

Computer-simulation of Adsorption and Diffusion of Hydrocarbons in Zeolites

Computer-simulation of Adsorption and Diffusion of Hydrocarbons in Zeolites

ACADEMISCH PROEFSCHRIFT

ter verkrijging van de graad van doctor
aan de Universiteit van Amsterdam,
op gezag van de Rector Magnificus
prof. mr. P. F. van der Heijden
ten overstaan van een door het college voor promoties ingestelde
commissie, in het openbaar te verdedigen in de Aula der Universiteit

op vrijdag 28 oktober 2005, te 11.00 uur

door

David Dubbeldam
geboren te Krimpen a/d Lek

Promotiecommissie

Promotor:

- prof. dr. ir. B. Smit

Overige leden:

- prof. dr. W. J. Briels
- prof. dr. D. Frenkel
- prof. dr. J. Kärger
- prof. dr. R. Krishna
- prof. dr. D. N. Theodorou
- prof. dr. J. M. Verstraten

Faculteit der Natuurwetenschappen, Wiskunde en Informatica

The research reported in this thesis was carried out at the Van 't Hoff Institute for Molecular Sciences, Faculty of Science, University of Amsterdam (Nieuwe Achtergracht 166, 1018 WV, Amsterdam, The Netherlands) with financial support from a PIONIER project of the council for chemical sciences of the Netherlands Organization for Scientific Research (NWO-CW).

Contents

CHAPTER 1 Introduction	1
I. Zeolites and molecular sieves	1
II. Properties	3
III. Context, scope, and structure of the thesis	5
A. The "window"-effect (chapters 3, 4, and 5)	5
B. Development of methods to compute very slow diffusion in confinement (chapters 3, 4)	6
C. Force field development (chapter 6, 7, and 8)	6
D. Development of methods to compute very slow diffusion in confinement <i>as a function of loading</i> (chapters 9, 10, and 12)	6
E. Flexibility influence on diffusion (chapter 10)	8
F. Understanding diffusion in confinement: Molecular Traffic Control (chapters 11 and 12)	9
Bibliography	9

CHAPTER 2 Molecular Simulation Techniques	11
I. Molecular Electrostatics	11
A. Introduction	11
B. Partial charges	12
C. Dispersive and repulsive interactions	12
D. Dielectric effects and polarizability	13
E. Force field development for simulations	17
II. Zeolite electrostatics	18
A. Dielectric effects and polarizability	18
B. Force field development for simulation	19
C. Force field functional forms	21
III. Boundary conditions	32
IV. Monte-Carlo (MC)	33
A. The Metropolis algorithm	33
B. Recycling of micro-states	33
C. Ensembles	34
D. Configurational-bias Monte-Carlo (CBMC)	41
E. Monte-Carlo moves	42
V. Molecular dynamics (MD)	43
VI. Ewald summation in periodic frameworks	45
A. Coulomb potential in periodic systems	45
B. Ewald Transformation	47
C. General formulism	48

D.	Charge only systems	58
E.	Electric-field dependent potentials	62
VII.	Rigid Frameworks	63
A.	Pressure and Stress	63
B.	Charged Frameworks	63
	Bibliography	65
<hr/>		
CHAPTER 3	Incommensurate Diffusion in Confined Systems	71
	Bibliography	76
<hr/>		
CHAPTER 4	Computer Simulation of Incommensurate Diffusion in Zeolites: Understanding Window-Effects	77
I.	Introduction	77
II.	Simulation model	79
III.	Transition State Theory	80
IV.	Reaction coordinate	83
V.	Zeolite Description	87
VI.	Results and Discussion	89
A.	Henry Coefficients and Isothermic Heats of Adsorption	89
B.	Diffusion	91
C.	Activation energies and frequency factors	94
D.	Free energy profiles	96
VII.	The window effect reexamined	98
VIII.	Conclusions	100
	Bibliography	100
<hr/>		
CHAPTER 5	Understanding the Window Effect in Zeolite Catalysis	103
	Bibliography	107
<hr/>		
CHAPTER 6	Force Field Parameterization through Fitting on Inflection Points in Isotherms	109
	Bibliography	113
<hr/>		
CHAPTER 7	United Atom Force Field for Alkanes in Nanoporous Materials	115
I.	Introduction	115
II.	Model	116
A.	Choice of models and methods	116
B.	Selection of experimental datasets	118
C.	Parameter Optimization Strategy	119
D.	Parameters from MFI/AFI-inflections	121
E.	Comparing this work and calibration data	123
F.	Comparing this work and preceding models	125
G.	Internal interaction parameters	125
III.	Validation and applications	126
A.	Extension to other sorbates in MFI	126
B.	Extension to mixtures in MFI	126
C.	Extension to low-coverage in MFI	128

D.	Extension to different topologies	130
IV.	Discussion	132
V.	Conclusions	133
	Bibliography	138
<hr/>		
CHAPTER 8	Understanding the role of sodium during adsorption: A force field for alkanes in sodium exchanged faujasites	141
I.	Introduction	141
II.	Methodology	143
A.	Model	143
B.	Parameter Optimization	145
III.	Applications	150
A.	Cation redistribution upon alkane adsorption	150
B.	Adsorption in low-coverage regime	150
C.	Adsorption in high-coverage regime	153
D.	Simultaneous Adsorption of more than one component	156
IV.	Conclusions	156
	Bibliography	157
<hr/>		
CHAPTER 9	Molecular Simulation of Loading Dependent Slow Diffusion in Confined Systems	163
	Bibliography	168
<hr/>		
CHAPTER 10	Molecular Simulation of Loading Dependent Diffusion in Nanoporous Materials using Extended Dynamically Corrected Transition State Theory	171
I.	Introduction	171
II.	Methodology	173
A.	Force field parameters for adsorption and diffusion of alkanes in siliceous nanoporous materials	173
B.	Molecular Dynamics (MD)	174
C.	Lattice random walk theory	177
D.	Correlations	179
E.	Dynamically corrected transition state theory (dcTST) at infinite dilution	180
F.	Importance-sampled MD at infinite dilution	182
G.	Dynamically corrected transition state theory at nonzero loading	183
H.	Zeolite descriptions and simulation details	186
III.	Results	188
A.	Infinite dilution	188
B.	Non-zero loading	191
IV.	Discussion	194
V.	Conclusions	196
	Bibliography	197
<hr/>		
CHAPTER 11	Molecular Path Control in Zeolite Membranes	201
I.	Introduction	201
II.	Model and computational details	202

III. Results	204
IV. Discussion	206
Bibliography	207
<hr/>	
CHAPTER 12 Applying Dynamically Corrected Transition State Theory in Complex Lattices	211
I. Introduction	211
II. Methods	213
A. Zeolite descriptions	213
B. Lattices	213
C. the dcTST method	216
D. Non-rectangular unit cells	218
E. Reaction coordinate	218
F. Force field potentials and simulation details	219
III. Results	221
A. ethane in ERI-type zeolite (anisotropic diffusion)	221
B. ethane in CHA-type zeolite	223
IV. Conclusions	223
Bibliography	224
<hr/>	
CHAPTER 13 Summary and conclusions	227
I. The "window"-effect (chapters 3, 4, and 5)	227
II. Development of methods to compute very slow diffusion in confinement (chapters 3, 4)	229
III. Force field development (chapter 6, 7, and 8)	231
IV. Development of methods to compute very slow diffusion in confinement <i>as a function of loading</i> (chapters 9, 10, and 12)	233
V. Flexibility influence on diffusion (chapter 10)	235
VI. Understanding diffusion in confinement: Molecular Path Control (chapters 11 and 12)	236
Bibliography	238
<hr/>	
CHAPTER 14 Samenvatting (Summary in Dutch)	241
<hr/>	
CHAPTER 15 Acknowledgments	245
<hr/>	
CHAPTER 16 Published Work	247

1

Introduction

I Zeolites and molecular sieves

A "molecular sieve" is a material with selective adsorption properties capable of separating components of a mixture on the basis of differences in molecular size, shape, and polarity. Examples of molecular sieves include zeolites, clays, and porous glasses. Zeolites are three-dimensional, microporous, crystalline solids with well-defined structures that contain aluminum, silicon, and oxygen. Their regular frameworks have void spaces (cavities or channels) that can host cations, water, or other molecules. The first zeolite was discovered by Cronstedt in 1756 who found that the mineral rapidly loses water on heating and seemed to boil. The name "zeolite" comes from the Greek words *zeo* (to boil) and *lithos* (stone).

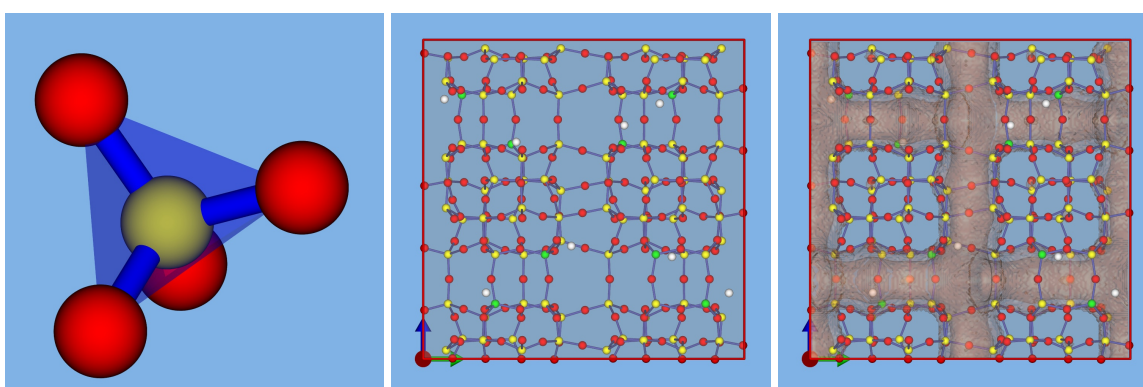


Figure 1: Zeolites are three-dimensional, microporous, crystalline solids with well-defined structures that contain aluminum (green), silicon (yellow), and oxygen (red) in their regular framework. Aluminosilicate zeolites induce a net negative framework charge compensated by non-framework cations (white). Left: the silicon and aluminum atoms are tetrahedrally coordinated with each other through shared oxygen atoms. Middle: an open framework structure made up of corner-sharing SiO_4 and AlO_4 tetrahedra. Right: zeolites have cavities or channels (brown).

Zeolites are based on TO_4 tetrahedra, where T is an aluminum or silicon atom. The vast 3-dimensional networks are a result of all four corners for the tetrahedra being shared, producing low density microporous materials. The Primary Building Units (PBU's) are the TO_4 tetrahedra, and they form Secondary Building Units (SBU's) that contain up to 16 T atoms. Examples are four rings (4R), five rings (5R), six rings (6R), eight rings (8R), double four rings (D4R), double six rings (D6R), double eight ring (D8R) etc. It can be noted that SBU's in the isolated state of highest possible symmetry are neither left- nor right-handed (non-chiral). It is the way that these SBUs join together that gives rise to the huge number of different zeolites. The SBUs join to form structurally and chemically important zeolite channels known as oxygen windows that pass through the zeolite and form a pore system. The pores passing through the zeolite in 1, 2, or 3 directions, vary in size and in the case of MFI-type zeolite can also be sinusoidal. A unit cell always contains the same number of SBU's, and although rare, some materials can have different combinations of SBU's within the zeolite framework. An important class of materials are the pentasil zeolites, named so because they are constructed of five-membered rings. The most important example is that of MFI-type zeolite shown in Fig. 1.

The framework aluminum and silicon are bound to each other through shared oxygen atoms. The SiO_4 units are neutral: $\text{Si}_4^+/\text{O}_4^-$ but the AlO_4 results in a net negative charge: $\text{Al}_3^+/\text{O}_4^-$. The net negative charge is balanced by cations that are present during the synthesis. These cations are highly mobile and can be exchanged for other cationic species. According to the so-called Löwenstein rule, Al-O-Al linkages in zeolitic frameworks are forbidden. As a result, all aluminate tetrahedra must be linked to four silicate tetrahedra, but a silicate tetrahedron may have five different possible environments: Si (0 Al, 4 Si), Si (1 Al, 3 Si), Si (2 Al, 2 Si), Si (3 Al, 1 Si) and Si (4 Al, 0 Si). In general the Löwenstein-rule is assumed to be the correct, but recent investigations into zeolites synthesised at high temperatures have shown non-Löwenstein distributions in sodalite materials.

Since 1982 several new families of molecular sieves based on AlPO_4 have been discovered. These aluminophosphates, silicoaluminophosphates, metalloaluminophosphates and metasilicoaluminophosphates are denoted as AlPO_4-n , SAPO- n , MeAPO- n and MeAPSO- n , respectively, where n is an integer indicating the structure type. Of the more than twenty AlPO_4 molecular sieves prepared so far, some have structures of known zeolites, but many have novel structures. When Si is incorporated in the AlPO_4-n framework, the product is known as SAPO. MeAPO or MeAPSO sieves are formed by the incorporation of a metal atom (Me) into an AlPO_4-n or SAPO framework. These metal atoms include Li, Be, Mg, Co, Fe, Mn, Zn, B, Ga, Fe, Ge, Ti and As. Most substituted AlPO_4-n 's have the same structure as AlPO_4-n , but several new structures were only found in SAPO, MeAPO and MeAPSO materials. Their frameworks carry an electric charge, potentially providing a further alteration of catalytic behavior. Recent advances in structural zeolite chemistry have been mainly in the areas of highly siliceous zeolites, aluminophosphates and related materials. Zeolite chemistry is thus no longer confined to aluminosilicates.

During the last years, two major trends could be observed in the synthesis community; the development of methods for the growth of "giant" zeolite crystals, and the exploration of nanometer-sized zeolite crystals. Large crystals are of interest as model host materials, e.g. for adsorption and/or diffusion studies. Shimizu and Hamada obtained MFI zeolite (silicalite-1) crystallites up to 4 mm in size. Nanosized zeolites have attracted a lot of attention due to the fact that they can be used as precursors for zeolite films or membranes. Several new synthetic zeolites have been obtained, e.g. Engelhard titanium silicate (ETS-4) having adjustable pore sizes depending on the content of water in

the pores. Another very interesting class of materials are the metal-organic frameworks (MOF) by using metal-organic building blocks linked by organic spacers. These materials seem to be promising candidates for metal-organic heterogeneous catalysis. Seo et al. showed that a homochiral metal-organic microporous material denoted as POST-1 is an active catalyst in transesterification reactions.

II Properties

Molecular sieves have found widespread industrial applications as highly selective adsorbents, ion exchangers and, most importantly, catalysts of exceptionally high activity and selectivity in a wide range of reactions. These applications include the drying of refrigerants, removal of atmospheric pollutants such as sulphur dioxide, cryo pumping, separation of air components, separation and recovery of normal paraffin hydrocarbons, recovering radioactive ions from waste solutions, catalysis of hydrocarbon reactions and the curing of plastics and rubber. Molecular sieves exhibit appreciable Brønsted acidity with shape-selective features not available in amorphous catalysts of similar composition.

Molecular sieves are selective, high-capacity adsorbents because of their high intracrystalline surface area and strong interactions with adsorbates. Molecules of different size generally have different diffusion properties in the same molecular sieve. Molecules are separated on the basis of size and structure relative to the size and geometry of the apertures of the sieve. Molecular sieves adsorb molecules, in particular those with permanent dipole moments, and exhibit other interactions not found in other sorbents. Different polar molecules have a different interaction with the molecular sieve framework, and may thus be separated by a particular molecular sieve. This is one of the major uses of zeolites. An example is the separation of N_2 and O_2 in the air on zeolite A, by exploiting different polarities of the two molecules.

The quantity of adsorbed gas or liquid depends on pressure, temperature, the nature of the adsorbate and the kind of the molecular sieve. Variations in the chemical composition of the sieve also affect adsorption. The adsorbed molecules can be removed by heating and/or evacuation. It is also known that the aluminum in materials such as VPI-5 may possess a higher coordination number than four, indicating that chemisorption of water occurs. The structure may also be changed while the adsorbed water is driven away. The ring sizes of molecular sieve may be determined by sorption of molecules of different size. Water and nitrogen are two of the smallest molecules which can easily penetrate almost the entire structures. These two molecules are normally used to determine the crystallinity of molecular sieves by comparing the adsorption volume with that of a standard sample.

Zeolites with low Si/Al ratios have strongly polar anionic frameworks. The exchangeable cations create strong local electrostatic fields and interact with highly polar molecules such as water. The cation-exchange behavior of zeolites depends on

- the nature of the cation species, the cation size (both anhydrous and hydrated) and cation charge,
- the temperature,
- the concentration of the cationic species in the solution,
- the anion associated with the cation in solution,

- the solvent (most exchange has been carried out in aqueous solutions, although some work has been done in organics),
- the structural characteristics of the particular zeolite.

Cation exchange in a zeolite is accompanied by an alteration of stability, adsorption behavior and selectivity, catalytic activity and other properties. In some cases, the introduction of a larger or smaller cation will decrease or enlarge the pore opening. The location of that cation within the crystal will also contribute to the size of pore opening. For example, the Na^+ form of zeolite A has a smaller effective pore dimension than would be expected for its 8-membered ring framework opening. This is due to sodium ion occupancy of sites where it will partially block the 8-membered ring window. When the Na^+ ion is exchanged for the larger K^+ ion, the pore diameter is reduced so that only the very small polar molecules will be adsorbed. If the divalent Ca^{2+} cation is used to balance of the framework charge, the effective pore opening widens, as only half the number of cations are needed. These ions occupy sites within the voids of the zeolite and do not reduce the effective pore diameter of the 8-membered ring. Highly and purely siliceous molecular sieves have virtually neutral frameworks, exhibit a high degree of hydrophobicity and no ion-exchange capacity.

The most important application of molecular sieves is as catalysts. Zeolites combine high acidity with shape selectivity, high surface area and high thermal stability and have been used to catalyze a variety of hydrocarbon reactions, such as cracking, hydrocracking, alkylation and isomerization. The reactivity and selectivity of zeolites as catalysts are determined by the active sites brought about by a charge imbalance between the silicon and aluminum atoms in the framework. Each framework aluminum atom induces a potential active acid site. In addition, purely siliceous and AlPO_4 molecular sieves have Brønsted acid sites whose weak acidity seems to be caused by the presence of terminal -OH bonds on the external surface of the crystal.

Shape selectivity, including reactant shape selectivity, product shape selectivity or transition-state shape selectivity, plays a very important role in molecular sieve catalysis. The channels and cages in a molecular sieve are similar in size to medium-sized molecules. Different sizes of channels and cages may therefore promote the diffusion of different reactants, products or transition-state species. High crystallinity and the regular channel structure are the principal features of molecular sieve catalysts. Reactant shape selectivity results from the limited diffusivity of some of the reactants, which cannot effectively enter and diffuse inside the crystal. Product shape selectivity occurs when slowly diffusing product molecules cannot rapidly escape from the crystal, and undergo secondary reactions. Restricted transition-state shape selectivity is a kinetic effect arising from the local environment around the active site: the rate constant for a certain reaction mechanism is reduced if the necessary transition state is too bulky to form readily.

An example of the effect of shape selective catalysis is the Methanol to Gasoline (MTG) process developed by the Mobil Oil Company. A stream of gaseous methanol is passed over a H-ZSM-5 catalyst bed and a dehydration-polymerization reaction takes place inside the pore. The resulting effect is a sharp cut off of product distribution at C_{11} (gasoline) length fractions. A result of this cut-off is that no extra reprocessing is needed to remove heavier residues. The impact of this has been immense, countries with no natural source of crude oil such as New Zealand are generating their own gasoline via the MTG process. It is likely to become even more popular over the next few decades as crude oil supplies become depleted.

III Context, scope, and structure of the thesis

Every gasoline molecule has seen the interior of a zeolite and therefore these nanoporous materials play a very important technological role. Given the importance of these materials it is surprising that the fundamentals of diffusion and shape selectivity – used to improve the octane number of gasoline – is so poorly understood. The reason is that experimentally it is very difficult to obtain information of the hydrocarbons inside to pores. The aim of my research during the PhD was to obtain a fundamental understanding of diffusion in zeolites by the application of molecular simulation techniques. Specifically, I used it as a technique to obtain a better understanding of the effect of the zeolite confinement on the properties of the adsorbed molecules. I set out to work on the following open-problems:

A The “window”-effect (chapters 3, 4, and 5)

One of the most controversial and intriguing phenomena in the zeolite literature is the window effect. Conventional zeolite-catalyzed (hydro)cracking yields a product distribution with a single maximum, which is consistent with the currently accepted reaction mechanisms. Chen et al. [1,2] discovered in 1968 that ERI-type zeolites yield a bimodal product distribution with maxima at n -C_{3–4} and n -C_{10–12}, but no product in the C_{7–9} range (the “window”). This suggests the possibility of *length selective* hydrocracking, enabling control over the length distribution of the product or reactant slate by selecting a zeolite with the appropriate window.

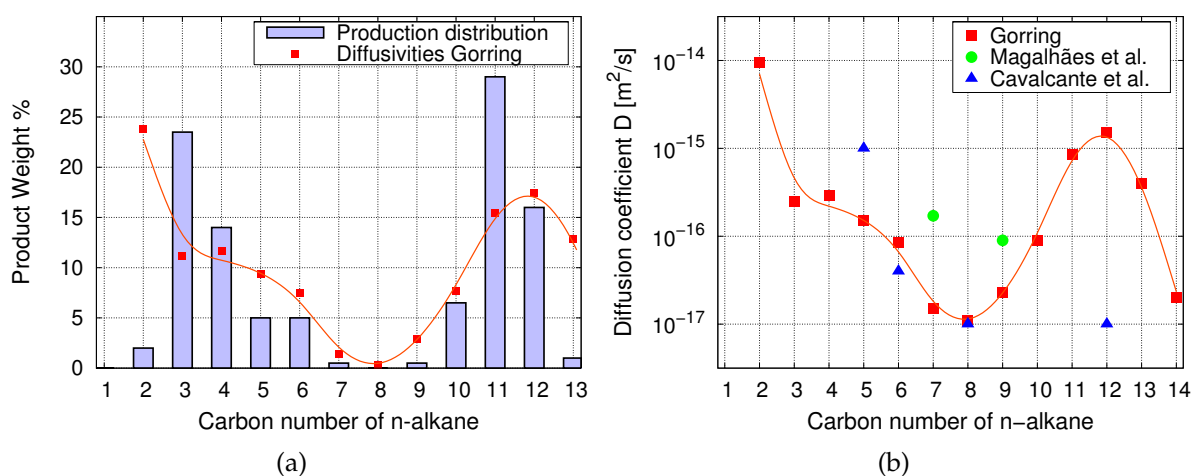


Figure 2: The window effect in ERI-type zeolites (a) a near-perfect correlation exists between the product distribution by Chen et al. [1, 2] and the diffusion coefficient as a function of n -alkane length by Goring [3], (b) Goring’s results are in disagreement with the results of Cavalcante et al. [4] and Magalhães et al. [5].

For a long time the window effect has been related nearly exclusively to the diffusion rate of n -alkanes in ERI-type zeolites. Goring showed that a near perfect correlation exists between the product distribution and the diffusion coefficient as a function of n -alkane length (Fig. 2(a)) [3]. Recent diffusion measurements by Cavalcante et al. [4] and Magalhães et al. [5] failed to reproduce the increase in diffusion rate for the appropriate

n-alkane lengths (Fig. 2(b)). This controversy motivated us to study the window-effect using molecular simulations focusing on the following questions

Does the window-effect exist? what is the reason for the product distribution?

B Development of methods to compute very slow diffusion in confinement (chapters 3, 4)

The diffusion coefficients in ERI-type zeolites are extremely low, as low as 10^{-17} m²/s. The first difficulty we encountered when studying diffusion behavior in zeolites using simulation is that many diffusional processes occur outside the time scale accessible to MD, which is currently typically limited to diffusion rates in the order of 10^{-12} m²/s. The first step in my PhD was

the development of a novel simulation Transition State Theory technique to study diffusion of linear alkanes in nanoporous materials with exceptionally low diffusion rates.

C Force field development (chapter 6, 7, and 8)

Different parameter sets yield different values of diffusivities. In Fig. 3 the MD-data of Fritzsche et al. at 173K for methane in LTA-type zeolite are shown [6,7], using two different parameters sets *A* and *B*. The diffusivities differ quantitatively by an order in magnitude, but also the qualitative behavior is different: set *B* *increases* with loading, while set *A* *decreases*. The critical unresolved question is:

which of the different potential parameter sets circulating in literature is the most physically realistic one? Is it possible to design a consistent and high-quality force field in a systematic way?

D Development of methods to compute very slow diffusion in confinement as a function of loading (chapters 9, 10, and 12)

Many of the processes of industrial importance occur at non-zero loading. A limited number of studies deal with non-zero loading. Tunca and Ford [10] used multidimensional TST to obtain the hopping rate of adsorbates from an α -cage in LTA-type zeolite as a function of loading. Various approximations were applied to make the simulations computationally feasible. In a subsequent study [11] the limitations of an empty receiving cage and the use of the Widom insertion method were avoided. Recently, Tunca and Ford presented a new hierarchical approach to the molecular modeling of diffusion and

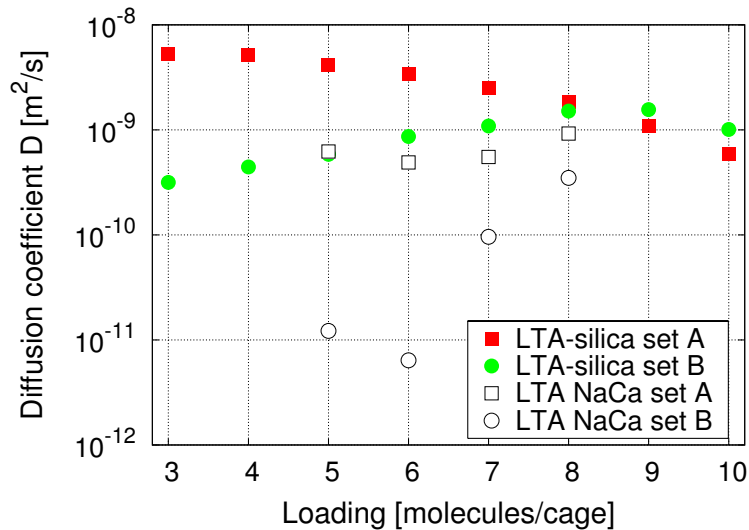


Figure 3: Diffusion coefficients of methane in LTA-type silica at 173K as a function of loading by MD simulations of Fritzsche et al. [6, 7]. Set A uses $\sigma = 3.14 \text{ \AA}$ and $\epsilon = 180 \text{ K}$ for the O-CH₄ interaction, while set B uses $\sigma = 3.46 \text{ \AA}$ and $\epsilon = 97.5 \text{ K}$

adsorption at nonzero loading in microporous materials [12]. Statistical mechanical partitions functions are calculated on molecular level models and used as an input to a coarse-grained model.

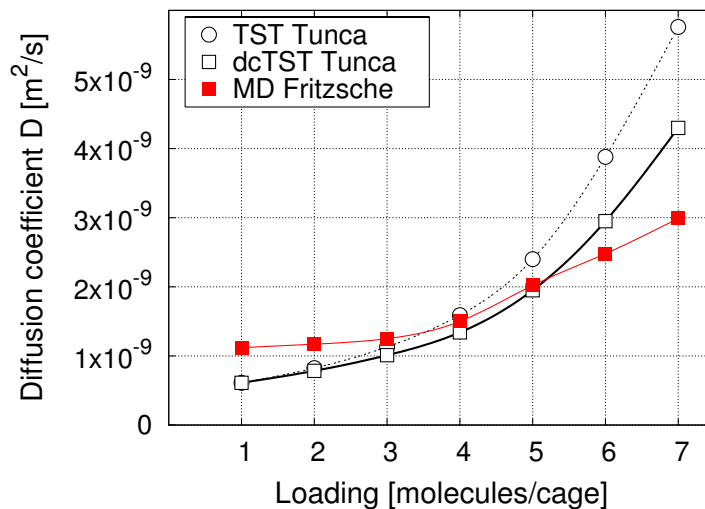


Figure 4: Diffusion coefficient of methane in LTA-type silica as a function of loading. The coarse-grained results of Tunca et al. using dynamically corrected and noncorrected TST are shown. The MD results were taken from Fritzsche et al. on an identical system.

Fig. 4 shows the diffusion coefficients of methane in LTA-type zeolite as a function of loading using the TST and dcTST method of Tunca et al. and the MD results of Fritzsche et al. on an identical system. Although adsorption is well represented by the method of Tunca et al., the coarse-grained self-diffusivity data under-predicted the diffusivity at low loading, while significantly over-predicting the diffusivities at higher loadings, in comparison to conventional MD. The obvious question to be answered is:

Can we do better? Can we develop a method that is capable of computing *quantitatively* the diffusivity of adsorbed molecules in confined systems at non-zero loading?

E Flexibility influence on diffusion (chapter 10)

The flexibility issue has long been an open one, and is thought to be closed: "In cation-free zeolites, diffusivities remain virtually unchanged for small molecules when including lattice vibrations". Fritzsche et al. studied methane in cation-free LTA-type zeolite, and their data is summarized in Fig. 5. By comparing with a model rigid LTA minimized using the same force field, they found almost no influence on the diffusion coefficient.

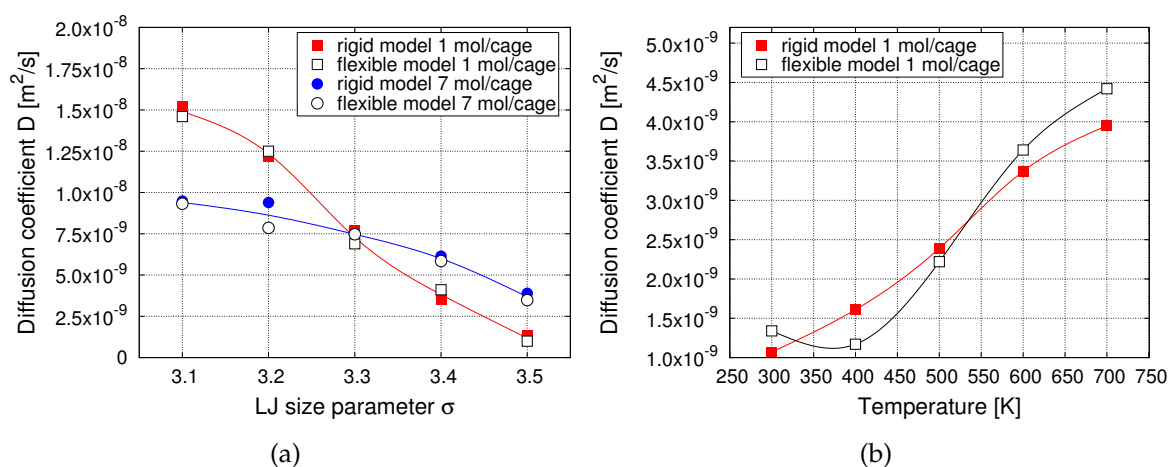


Figure 5: MD data of Fritzsche et al. [8] on methane in LTA-type silica (a) comparing a rigid and flexible model varying the LJ size parameter σ at a loading of 1 and 7 molecules per cage, (b) comparing a rigid and flexible model as a function of temperature at a loading of 1 molecule per cage. The flexible lattice model of Demontis et al. was used [9].

Assuming a good force field, a mismatch between experimental and computed diffusivities can only mean two things:

- the united-atom model is inadequate to properly describe diffusion,
- the framework flexibility should be properly modeled.

The first conclusion can only be drawn after considering the second. Therefore, the flexibility issue for diffusion has to be resolved for our systems and simulation conditions

Does flexibility influences diffusion? At what conditions and for what systems does flexibility matter, and when can it be neglected?

F Understanding diffusion in confinement: Molecular Traffic Control (chapters 11 and 12)

In contrast to adsorption, which is relatively well understood, diffusion in confinement is somewhat of a mystery. Current knowledge is so limited that one can not predict whether for a given molecule and adsorbate the diffusion coefficient will go up, go down, or remain constant as a function of loading. Therefore, our main objective to study diffusion in zeolites is

Predicting diffusion behavior for arbitrary topologies, adsorbates and loadings.

Bibliography

- [1] Chen, N.Y.; Garwood, William E.; Dwyer, Francis G., *Shape selective Catalysis in industrial Applications, 2nd edition, revised and expanded* Chemical Industries; New York, 1996.
- [2] Chen, N. Y.; Lucki, S. J.; Mower, E. B. *J. Catal.* **1969**, *13*, 329-332.
- [3] Gorring, L. R. *J. Catal.* **1993**, *31*, 13-26.
- [4] Cavalcante, C. L. ; Eić, M.; Ruthven, D. M.; Ocelli, M. L. *Zeolites* **1995**, *15*, 293-307.
- [5] Magalhães, F. D.; Laurence, R. L.; Conner, W. C. *J. AlChE.* **1996**, *42* 68-86.
- [6] Fritzsche, S.; Haberlandt, R.; Kärger, J.; Pfeifer, H.; Heinzinger, K.; Wolfsberg, M. *Chem. Phys. Lett.* **1995**, *242*, 361-366.
- [7] Fritzsche, S.; Gaub, M.; Haberlandt, R.; Hoffman, G. *J. Mol. Model.* **1996**, *9*, 286-292.
- [8] Fritzsche S.; Wolfsberg M.; Haberlandt R.; Demontis P.; Suffritti G. B.; Tilocca A., *J. Chem. Phys.* **296**, 253-258 (1998).
- [9] P. Demontis, G. B. Suffritti, S. Quartieri, E. S. Fois, and A. Gamba, *J. Phys. Chem.* **92**, 867-871 (1988).
- [10] C. Tunca and D. M. Ford, *J. Chem. Phys.* **111**, 2751 (1999).
- [11] C. Tunca and D. M. Ford, *J. Phys. Chem. B* **106**, 10982 (2002).
- [12] C. Tunca and D. M. Ford, *Chem. Eng. Sci.* **58**, 3373 (2003).

An overview chapter focusing on molecular simulations techniques applicable to periodic framework studies. The chapter is largely based on information from the following books: Understanding molecular simulations: from algorithms to applications by D. Frenkel and B. Smit [1], Computer simulations of liquids by M. P. Allen and D. J. Tildesley [2], Molecular Modeling: Principles and Applications by A. Leach [3], Introduction to Computational Chemistry by F. Jensen [4], Principles of Condensed Matter Physics by Paul M. Chaikin, T. C. Lubensky [5], and the manual of the software package DL_POLY [6].

D. Dubbeldam

2

Molecular Simulation Techniques

I Molecular Electrostatics

A Introduction

Electromagnetic interactions dominate on the molecular scale. This is clearest in the case of electrostatic interactions where charges on nuclei and electrons interact according to Coulomb's law:

$$U = \frac{1}{4\pi\epsilon_0} \frac{q_i q_j}{\epsilon_r r_{ij}} \quad (1)$$

where q_i and q_j are the magnitude of the charges, r_{ij} is their separation, ϵ_0 the permittivity of free space and ϵ_r the relative dielectric constant of the medium in which the charges are placed. Strictly speaking, Coulomb's law can only adequately describe the interaction of two point charges in a continuous medium. However, charges are not point charges and the medium is not continuous. For this reason, the Coulomb's law in its original form is a crude approximation. Intrinsic to the electrostatic problem is the question of how charges may be distributed in space and how such a distribution is described mathematically. A charge distribution can be either continuous or discrete. At the most fundamentally level, quantum mechanism teaches us that while the positive nuclear charge may be considered discrete on the atomic scale, the negative electronic charge is distributed continuously in the electronic clouds or orbitals, as dictated by the solutions of the electronic Schrödinger equation. Since the size of molecules precludes quantum mechanical molecular simulations, the basic continuous distribution is forsaken in favor of a discrete set of point charges, dipoles, and perhaps higher-order multipoles, all characterized by vanishingly small dimensions. The total electrostatic potential ϕ due to the charge distribution is then expressed as a sum of successive multipolar potentials: a monopolar potential ϕ_0 , a dipolar potential ϕ_1 , a quadrupolar potential ϕ_2 , etc. In principle, such a "distributed multipole" description can exactly describe the potential ϕ due to the true charge density, at point distant from the expansion centers where "penetration" effects are negligible. In practice this expansion is truncated, usually at low order, and often at the monopole

level in current force fields. The distributed monopoles are usually referred to as partial charges, since they need not have integral values. The long-range effects are most pronounced for the monopolar potential ϕ_0 . The monopole ($1/r$) dominates the dipole ($1/r^2$), dipole dominates quadrupole, etc.

B Partial charges

Electrostatic interactions are of fundamental importance. The most common approach is to place a partial charge at each atomic center (nucleus). These charges then interact by Coulomb's Law. The charge can take fractions of an electron and can be positive or negative. Charges on adjacent atoms (joined by one or two covalent) bonds are normally made invisible to one another - the interactions between these atoms being dealt with by covalent interactions. Note that the concept of a partial charge is only a convenient abstraction of reality. In practice many electrons and nuclei come together to form a molecule - partial charges give a crude representation of what a neighboring atom will on average "see" due to this collection.

The standard modern way to calculate partial charges is to perform a (reasonably high level) quantum chemical calculation for a small molecule which is representative of the group of interest. The electrostatic potential is then calculated from the orbitals obtained for many points on the molecular surface. A least squares fitting procedure is then used to produce a set of partial charges which produce potential values most consistent with the quantum calculations. Older procedures used methods in which orbital populations are simply split between atoms (Mulliken Population Analysis). All though much simpler, these charges do not produce a reasonable representation of the electrostatic potential around a molecule - which is usually what is of interest in a simulation. Using partial charges at nuclear centers is the crudest effective abstraction. To obtain a more accurate representation two approaches are common. The first is to add dipole, quadrupole and higher moments to the nuclear centers. The second is to introduce further non-nuclear centers - this is commonly done to represent the anisotropy in potential cause by lone pairs on oxygen atoms.

In many respects electrostatic interactions provided the biggest problems to computational studies. By their nature they are long range and dependent on the properties of the surrounding medium (see discussion of dielectric effects). A simple rule of thumb is that the more highly charged a system the harder it is to simulate - thus simulations of liquid argon can do a wonderful job, hydrocarbons are fairly easy, water becomes difficult and proteins more so. The limit is reached with nucleic acids like DNA which are aqueous complex salts (each base having a charge of minus two) with counter ions and solvent having important effects on structures. Usually some sort of "fudge" has to be made in simulations to keep DNA stable at all!

C Dispersive and repulsive interactions

At low temperatures gases such as argon liquefy. The attractive interactions which cause this are called dispersion. Although they also occur between charged atoms they are usually overwhelmed by the stronger electrostatic terms and so are normally only of importance for uncharged groups. To really understand dispersion effects one must turn to 2nd order perturbation theory in quantum mechanics. Imagine that we have an atom of argon. It can be considered to be like a large spherical jelly with a golf ball embedded

at the center. The golf ball is the nucleus carrying a large positive charge and the jelly represents the clouds of electrons whizzing about this. At a point external to the atom the net average field will be zero because the positively-charged nucleus' field will be exactly balanced by the electron clouds. However, atoms vibrate (even at 0K) and so that at any instant the cloud is likely to be slightly off center. This disparity creates an "instantaneous dipole". Suppose that we have another argon atom close to the first. This atom will see the electric field resulting from the instantaneous dipole. This field will effect the jelly inducing a dipole. The two dipoles attract one another - producing an attractive interaction.

The dispersion interaction can be shown to vary according to the inverse sixth power of the distance between the two atoms:

$$-\frac{B_{ij}}{r^6} \quad (2)$$

The factor B_{ij} depends on the nature of the pair of atoms interacting (in particular their polarizability). It is normal to parameterize the dispersion empirically using structural and energetic data from crystals of small molecules. It is *not* possible to use simple quantum chemical calculations to find parameters. This is because most quantum chemical calculations use the self consistent field approximation (SCF). Each electron is solved independently keeping the other orbitals frozen (in a self consistency). This effectively means that electrons only experience a time averaged picture of other electrons - so that dispersion cannot come into effect. More advanced methods in quantum chemistry introduce methods to tackle "electron correlation" to avoid this problem.

There are no physical arguments for choosing the repulsive term to vary as r^{-12} , this arises due to computational convenience. A more rigorous choice for the repulsive part of the potential would be an exponential term. The repulsive potential is dominated by the overlap between electron clouds on different atoms. As the electron density falls off roughly exponentially with distance from the nuclei, this repulsive interaction should have an exponential dependence with distance [7]. This leads to the Hill [8] or Buckingham potential. The use of Buckingham (exp-6) and Lennard-Jones 12-6 van der Waals potentials in MD simulations can quite successfully reproduce experimental thermodynamic data at low densities. However, they are less successful in producing a description of the repulsive regions of the potential energy surface (PES) that is in accord with the results of high-level ab initio computations. One final form occasionally used is the Morse potential. While this abandons the explicit r^{-6} dependence for the dispersion interaction, this is included within the exponential term, along with the other terms in the induced multipole-induced multipole series. Hayes et al. showed that Morse potentials can be parameterized to give excellent fits to both the attractive and repulsive regions of the PES for alkanes at high pressures and densities [9].

D Dielectric effects and polarizability

When two charges interact in a vacuum the energy of their mutual interaction is given by Coulomb's law:

$$U = \frac{1}{4\pi\epsilon_0} \frac{q_i q_j}{r_{ij}} \quad (3)$$

However, if the charges are in a space filled with a material the energy of the interaction is reduced by a factor known as the dielectric constant:

$$U = \frac{1}{4\pi\epsilon_0} \frac{q_i q_j}{\epsilon_r r_{ij}} \quad (4)$$

Here ϵ_r is the dielectric constant or to use the modern but little used alternative term relative permittivity. Table 1 quotes the value of the dielectric constant measured for a number of materials. The source of dielectric effects is that the electric field polarizes the material involved. Suppose that we have two charges interacting in a vacuum. We can draw the electric field lines (the direction in which a positive charge would be forced to move). These charges are then placed in a dielectric medium - which can be thought of as being composed of a large number of microscopic dipoles (a little rod with positive charge at one end and negative at the other). These line up along the field lines. A few important points can be made:

- every dipole lines up so that its positive end points toward the negative charge and vice-versa. This means that the electric field caused by the dipoles will oppose the original electric field at all places. This reduction in field causes a reduction in electric potential and thus a reduction in the interaction energy.
- the electric field between charges permeates the *whole* of space - it does not only depend on what is immediately in between the charges.

The polarizability of a molecule is a measure of its ability to respond to an electric field and acquire an electric dipole moment \mathbf{p} . Therefore, polarization is the separation of positive and negative charges in a system so that there is a net electric dipole moment per unit volume. Electric dipole moments can be induced by the electric field \mathbf{E} or can be permanent. There are several microscopic mechanisms of polarization in a dielectric material.

- Electronic polarization α_e
Electronic polarization α_e describes the displacement of the cloud of bound electrons with reference to the nucleus under an applied electric field. The atoms distort and the center of the atom's negative charge no longer coincides with the position of the nucleus, resulting in an electric dipole moment. Every atom can be polarized in this way. Electronic polarizability rises linearly with the inducing field up to very high field strengths. The contribution of the electronic polarization to the dielectric constant is usually small.
- Distortion (ionic) polarization α_d
Distortion polarization α_d (ionic polarization) relates to the distortion of the position of the nuclei by the applied field, thereby stretching or compressing the bond length, depending on the relative orientation between the ionic bond and the electric field. The molecule is bent and stretched by the applied field and changes its dipole moment accordingly. Nonpolar molecules may acquire an induced dipole moment in an electric field on account of the distortion the field causes in their electronic distributions and nuclear positions. Typically ionic polarization is important in ionic crystals below the infrared wavelengths.

water (20° C)	80.3
water (0° C)	87.7
ice polycrystalline (-10° C)	98
methanol	33.6
liquid H ₂ S (-85.5° C)	9.3
beeswax	2.9
alkanes	2.0-2.5
liquid Argon (-191° C)	1.5
vacuum	1.0 (by definition)
siliceous α -quartz	2.12
siliceous sodalite zeolite	1.7
siliceous faujasite zeolite	1.5

Table 1: The dielectric constant of selected materials relative to the dielectric constant of a vacuum.

CH ₄	methane	0 D	C ₆ H ₆	1-hexyne	0.83 D
CH ₄ O	methanol	1.7 D	C ₆ H ₆	benzene	0 D
C ₂ H ₄	ethene	0 D	C ₆ H ₅ NO ₂	nitrobenzene	4.22 D
C ₂ H ₆	ethane	0 D	NH ₃	ammonia	1.3 D
C ₃ H ₆	propene	0.366 D	CF ₄	carbon tetrafluoride	0 D
C ₃ H ₈	propane	0.084 D	HCl	hydrogen chloride	1.08 D
C ₄ H ₈	1-butene	0.34 D	CO	carbon monoxide	0.1 D
C ₄ H ₁₀	butane	<0.05 D	CO ₂	carbon dioxide	0 D
C ₄ H ₁₀ O	1-butanol	1.66 D	HO	hydroxyl radical	1.66 D
C ₅ H ₁₂	2-methylbutane	0.13 D	H ₂ O	water	1.85 D

Table 2: Selected values of electric dipole moments for molecules in the gas phase. The numerical values are expressed in Debye units D ($1 D = 3.33564 \times 10^{-30}$ Coulomb meter).

compound	α [Å ³]	α [a.u.]	compound	α [Å ³]	α [a.u.]
methane	2.6	17.23	water	1.48	10
ethane	4.4	30.2	ethene	4.1	27.7
propane	6.23	42.26	methanol	3.29	22.2
<i>n</i> -butane	8.02	54.82	ethanol	5.21	35.2
isobutane	8.01	54.75	1-propanol	7.1	47.9
<i>n</i> -pentane	9.88	67.14	1-butanal	8.99	60.67
<i>n</i> -hexane	11.78	79.51	nitrobenzene	13.54	91.37
<i>n</i> -heptane	13.61	91.89	propylene carbonate	8.8	59.38
He	0.2	1.35	Ar	1.66	11.2
H ₂	0.82	5.53	N ₂	1.77	11.94
CO	1.98	13.36	HF	0.51	3.44
HCl	2.63	17.75	NH ₃	2.22	14.98
CF ₄	0	0	SO ₂	4.34	29.3

Table 3: Selected values of static polarizabilities α for molecules in the gas phase. The units are volume units and atomic unit of electric polarizability ($1.648777274 \times 10^{-41}$ C²m²/J). It is common practice not to list α itself, but rather $\alpha/(4\pi\epsilon_0)$ ($\epsilon_0 = 8.854187817 \times 10^{-12}$ C² s²/(kg m³)) which has dimensions of volume.

- **Orientalional (dipolar) polarization α_d**
Orientalional polarization α_d arises when randomly oriented polar molecules are rotated and aligned by the application of an electric field so as to give rise to a net average dipole moment per molecule. The net effect is that each polar molecule is a small charge dipole which aligns with the applied electric field and influences the total electric field both inside and outside the material. Orientalional polarizability is limited to molecules that have significant permanent dipole moments, i.e. molecules that have a dipole moment even in the absence of an inducing field.

The average polarizability α_T in the medium is given by the sum

$$\alpha_T = \alpha_e + \alpha_i + \alpha_d \quad (5)$$

A polar molecule is a molecule with a permanent electric dipole moment. The permanent dipole moment is a result of the partial charges on the atoms in the molecule that arise from the different electronegativity or other features of bonding. Polar molecules may have their existing dipole moments modified by the applied field.

In a material, the dipole moment per unit volume is vector field known as the polarization vector \mathbf{P} . In the presence of electronic, ionic and dipolar polarization mechanisms, the total polarization of a medium \mathbf{P} will be the sum of all the contributions in terms of the local effective field acting on each individual molecule

$$\mathbf{P} = \alpha_e \mathbf{E}_{\text{local}} + \alpha_i \mathbf{E}_{\text{local}} + \alpha_d \mathbf{E}_{\text{local}} \quad (6)$$

where α_e , α_i , and α_d are the electronic, ionic, and dipolar polarizabilities. $\mathbf{E}_{\text{local}}$ is the local effective field at the site of an individual molecule that causes the induced polarization. In the simplest case (valid for gases) we can take the local field to be the same as the macroscopic field. In solids we have to consider the actual effective field acting on a molecule.

The quantitative relation between the dielectric constant and properties of the molecules is described by the Debye equation

$$\frac{\epsilon_r - 1}{\epsilon_r + 2} = \frac{\rho}{3\epsilon_0} (\alpha_e + \alpha_i + \alpha_d) \quad (7)$$

The dielectric constant ϵ_r of materials is high if its molecules are polar and highly polarizable. There are several ways to decrease the dielectric constant: reduction of the density ρ , the polarizabilities α_e and α_d , and also the dielectric constant is lowered when materials do not contain polar molecules. Reducing the number of ionic bonds in the material minimizes the distortion polarization. The electronic polarization is minimized by lowering the electron density in the material, i.e. introducing smaller elements.

We list selected values for dielectric constant, dipole moments, and polarizabilities in Table 1, 2, and 3, respectively. Water has a very high dipole moment due to the electronegativity of oxygen and the fact that hydrogen-oxygen bonds are short. In methanol one of the hydrogen atoms is replaced by a CH_3 group lengthening the bond and so reducing the dipole moment and consequently the dielectric constant by a factor of over 2. For H_2S the oxygen has been replaced by the much less electronegative sulphur atom and the bond lengths have been increased. This has the result that the compound is unable to form hydrogen bonds and is a gas at normal temperatures/pressures. Not surprisingly when liquefied its dielectric constant is one eighth that of water. Going down the list we find

that alkanes and organic, essentially unpolarized compounds have a dielectric constant of around 2 to 3 - this will be around the value found in lipid bilayers. The contribution to this of electron polarization can be estimated by comparison to liquid argon with a dielectric constant of 1.5. The dielectric constant of ice is around 100. Although ice is crystalline with the oxygen atoms confined to a tetrahedral pattern, Bernal and Fowler showed the dipole moments of individual water molecules to be randomly orientated [10]. The crystal does not have any restraining effect on their ability to reorient in an electric field.

So what implications does this have for interactions of importance to simulations? The first thing to note is that the concept of a dielectric constant is an essentially macroscopic concept. It relies on the fact that the space around the charges is uniformly filled with a large number of small dipole moments or polarizable atoms. As the separation of the charges is reduced to the same scale as the molecules which produce the dielectric effect this assumption breaks down. The medium surrounding two interaction will have some dielectric effect but it will not be as simple as a constant.

It is worth noting that typical empirical force fields use a dielectric constant of 1 to compute charge-charge interactions. Thus, any modulation of electrostatic interactions by electronic polarization must be implicit in other terms. For well-hydrated molecules, this may not be a problem because the orientational polarizability of water makes up for the lack of explicit electronic polarization. However, the neglect of electronic polarization is likely to be a significant problem in an interior of a protein, where orientational polarizability probably cannot compensate. An alternative approach is to use a "reaction field".

E Force field development for simulations

alkanes Alkanes are ubiquitous in industrial processes and form the building blocks of biological systems. Alkanes are generally inert to chemical reagents. Carbon-carbon and carbon-hydrogen bonds are strong, and do not break unless heated to high temperatures. Similar electronegativities result in little polarization, so generally unaffected by most bases. There are no unshared electrons in alkanes for attack by acids. They are non-polar and consists of a small number of groups, making them the logical starting point for potential model development.

Three accurate united-atom potential sets for *n*-alkanes have appeared recently. The TRAPPE (Martin and Siepmann [11]) and NERD models (Nath et al. [12]) use the Lennard-Jones potential to describe non-bonded interactions among methyl and methylene groups, while the model of Errington and Panagiotopoulos [13] uses the exponential-6 form. All three reproduce the experimental phase diagram and critical points. The exponential-6 model is slightly better with respect to representation of the vapor pressures. Deviations from experimental data for the exponential-6 united atom model are comparable to those for a recently developed all-atom TRAPPE model (Chen and Siepmann [14]). United-atom potentials for branched alkanes have been developed by Cui et al. [15], Martin and Siepmann [16], and for α -alkenes by Spyriouni et al. [17], Pascual et al. [18], and recently Jakobtorweihen et al. [19].

polar fluids There have been several recent studies of the phase behavior of polar compounds such as *n*-alkanols (van Leeuwen [20]), hydrogen sulfide (Kristof and Liszi [21]), and carbon sulfide (Kristof et al. [22]). However, no transferable force fields that can be used to obtain the phase behavior of polar fluids with reasonably accuracy are currently

available. Visco and Kofke studied two *ab initio* and one empirical potential model for hydrogen fluoride [23]. The *ab initio* models did not reproduce accurately the saturated liquid densities and none of the models predicted correctly the vapor pressure and heat of vaporization as functions of temperature.

water Because of the importance of water in biological and chemical systems, a large number of models have been proposed for atomistic simulations. Rigid fixed point charge models for water are often used in simulations of biological systems because of their simplicity and reasonable predictions of the structure and thermodynamics of liquid water at ambient conditions. Such models include TIP (Jorgensen et al. [24]) and SPC (Berendsen et al. [25]). All represent water as a single Lennard-Jones sphere within which are embedded positive and negative charges. None of the fixed point charge models can adequately reproduce thermodynamic and structural properties over a broad range. In the inclusion of only two-body interactions also results in a higher "effective" dipole moment relative to the gas phase. Several polarizable models for water are available in literature, but none seems to be better than the simple fixed points charged models with respect to the coexistence properties and critical parameters. Recent methodological developments permit incorporation of polarizability with a penalty of a factor 10 in CPU time relative to non-polarizable model calculations.

mixtures A key question for all force fields for atomistic simulations is their ability to predict properties of mixtures without use of additional adjustable parameters for the unlike-pair interactions. For mixtures of non-polar components such as alkanes or inert gases, there is considerable evidence that the newer force fields can be used for reliable predictions of mixture behavior. For mixtures with large differences in polar character between the components, current models do not result in quantitative agreement with experiments.

II Zeolite electrostatics

A Dielectric effects and polarizability

Brønsted sites [26] A Brønsted acidic proton consists of a hydrogen atom bonded to the oxygens atom that connects the tetrahedrally-coordinated framework cations (Fig. 1). The tetrahedra form a three-dimensional system by sharing of one oxygen atom between each two tetrahedra. The zeolite framework loses neutrality when lattice Si^{4+} framework cations become replaced by lattice Al^{3+} cations. The excess lattice negative charge now has to be compensated for by positively charged mobile cations. The zeolitic acidity can be generated in several ways. NH_4^+ ions can be introduced in the zeolite and by heating they can subsequently be decomposed into NH_3 and H^+ . The NH_3 molecule desorbs, and the proton is left bonded to a bridging lattice oxygen atom, which connects a tetrahedron with four valent (Si^{4+}) framework cation and one that contains a three valent (Al^{3+} , Ga^{3+} , Fe^{3+}) framework cation.

Formally the 3-fold coordination of the oxygen bridge is a nonclassical bonding situation, also known for instance for the hydronium ion H_3O^+ . Compared to silanol (Fig. 1(a)), which is only weakly acidic, the acidity of the proton is enhanced, which is due to a silanol that undergoes Lewis acid promotion by Al^{3+} . Quantum-chemical calculations

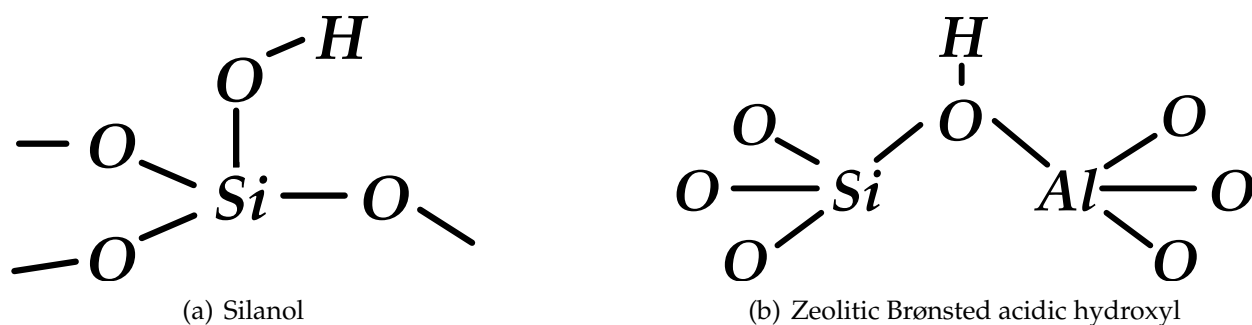


Figure 1: Schematic representation of (a) silanol, and (b) zeolitic Brønsted acidic hydroxyl.

indicate that the charge on the proton is very low (<0.1 eu). The stretching frequency of the zeolite OH group is significantly higher than the highest lattice fundamental modes, which have their maximum value around 1300 cm^{-1} . This does not imply that the OH bond is much stronger than the lattice TO bonds, but reflects the low proton mass. The value for the covalent OH bond strength on many different solids for the covalent dissociation energy is around 500 kJ/mol . This implies that the acidic nature of the OH group becomes apparent only when proton transfer itself, or the response of the OH group on an interacting basic molecule, is measured.

The polarizability of the zeolitic OH group is much higher than that of the free silanol group. This polarizability relates of course to the electronic interactions between the oxygen and neighboring atoms. The silanol group is less acidic than the zeolitic hydroxyl, because the negative charge on the oxygen atoms is only stabilized by orbital interactions with one Si^{4+} ion in the case of silanol, but by interactions with a Si^{4+} and another T^{3+} ion on the bridging site. Importantly, the OH as well as the lattice OT bonds have to be considered as strong covalent bonds superposed by small (long range) electrostatic interactions.

For siliceous FAU-type zeolite long-range electrostatic interactions contribute only $\approx 5\%$ to the calculated vibrational frequency differences. Siliceous zeolites are insulators with a very low dielectric constant. Only when cations such as Na^+ , K^+ or Mg^{2+} and Ca^{2+} are located in the zeolite micropore next to tetrahedra that contain trivalent cations such as Al^{3+} instead of Si^{4+} , are large electric fields generated. They are short ranged, and the positive cation charges are compensated for by the corresponding negative lattice charges. The Na^+ cation has only a weak covalent interaction. When Al^{3+} is substituted for one of the Si^{4+} framework ions, the geometry is changed. The Al-O distances are longer in alumina tetrahedra compared to that in the silicon tetrahedron, because of the weaker Al-O bond strength. The Si-O bond lengths that neighbor the Al-containing tetrahedron are shortened, and also the next neighbor bond lengths increase.

B Force field development for simulation

force field for alkanes in dehydrated siliceous zeolites The adsorption of hydrocarbons is dominated by dispersive forces. These interactions are notoriously difficult to describe using quantum chemical approaches. The next level of sophistication is to use an all-atom model. These models are commonly used in the simulations of proteins and other large systems. First attempts to simply use such a force field (Consistent Valence Force Field) for the adsorption of hydrocarbons in MFI gave a reasonable prediction of the adsorption

isotherms. However, the much simpler united atom models yielded a significantly more accurate description of the adsorption isotherms [27]. Of course, this observation is not surprising since the united atom models have been specifically optimized for this type of adsorption studies, whereas the all-atom model is a universal force field aimed at a myriad of different applications. To obtain the same degree of accuracy for the all-atom model as for the united atom model would require a dedicated optimization of the all-atom model parameters. Such an optimization will be cumbersome, for it is our impression that the physical information required for such an optimization is not experimentally available in sufficient detail.

The force field proposed we use is primarily designed to reproduce thermodynamic properties of guest molecules in a host system at minimal computational cost. The internal structure of the guests and the guest-guest interactions are of less importance because the properties are dominated by the strong interaction with the force field exerted by the host. Adsorption in cation-free structures takes place at sites with little or no electric field. For these reasons the united atom model [28] seems the most straightforward choice. We consider the CH_x groups as single, chargeless interaction centers with their own effective potentials.

The forcefield we use for siliceous zeolites does not contain an explicit polarization term. Polarization energies are typically less than 10% to 20% of the total energy, and even less for silicious zeolites. However, it should be note that the "average" polarization (and also framework flexibility) is included implicitly in the parameterization. The parameters are obtained empirically. Flexibility of the framework is not an issue for *adsorption of linear and branched alkanes*.

force field for alkanes in dehydrated aluminosilicates When cations such as Na^+ are introduced into the framework, strong and inhomogeneous electric fields are generated. In addition, the negatively charged oxygen atoms form a polarizable environment for adsorbed species. Therefore our model explicitly distinguishes silicon from aluminum with a difference of $0.3 e^-$ between q_{Si} and q_{Al} [29]. Different charges are used for oxygen atoms bridging two silicon atoms, q_{OSi} , and oxygen atoms bridging one silicon and one aluminum atom q_{OAl} . Using the relation $q_{\text{Si}} + (2q_{\text{OSi}}) = 0$ is obtained, making the zeolite neutral in the absence of aluminum, while q_{OAl} is chosen to make the total system charge equal to zero [30, 31].

In the force field we use, an "average" polarization is included implicitly in the parameterization by means of two effects:

- the polarization induced by the cation on the zeolite and on the alkanes. For the cation-zeolite interactions we used the approach of Auerbach [29], taking into account the polarization effects by adjusting the partial charges on the oxygen depending whether they are connected to Si or Al.
- Concerning the polarization effects for the cation-alkane interactions, alkanes are very difficult to polarize and therefore a logical approach was to use effective Lennard-Jones interactions between the cations and the alkanes.

future direction of force fields The polarization is not easy to treat within the approximation of the effective pair potentials because of the many-body origin of this phenomenon. Several models have attempted the explicit inclusion of polarization in simulations of

aluminosilicate systems. For bare aluminosilicates the shell potential model has widely been used in energy minimizations of crystal structures in order to describe the polarization of the oxygen atoms [32]. For heterogeneous systems, a potential model for hydrated aluminosilicates with electric field-dependent force field parameters for flexible water molecules has been proposed by Demontis et al. [33]. Application of the model to water-natrolite system showed a good agreement of the calculated and experimental infrared spectra. The introduction of electric field-dependent terms in the intramolecular potential of water can improve the reproduction of complex electronic effects by relative simple empirical functions. Toufar et al. combined classical Monte-Carlo techniques with the electronegativity equalization method (EEM) and applied this scheme to cation-water and zeolite-water clusters [34]. Smirnov and Bougeard used MD of hydrated aluminosilicate structures with the explicit inclusion of the polarization of both the adsorbent and the adsorbate molecules [35]. The approach was based on an electronegativity equalization (EE) model.

C Force field functional forms

The force field is the set of functions needed to define the interactions in a molecular system. These may have a wide variety of analytical forms with some basis in chemical physics. A classical force field consists at least of bonded and non-bonded terms:

$$U^{\text{total}} = U^{\text{bonded}} + U^{\text{non-bonded}} \quad (8)$$

with

$$U^{\text{bonded}} = U^{\text{bond}} + U^{\text{bend}} + U^{\text{torsion}} + U^{\text{intra VDW}} \quad (9)$$

$$U^{\text{non-bonded}} = U^{\text{VDW}} + U^{\text{Coulomb}} \quad (10)$$

Many, many force field exists. Among the force field implemented in the commercial Cerius software package we find: universal Force Field [36] (a generic forcefield optimized for organics, main group elements, and organometallic systems), Dreiding II [37] (for organics, biological compounds, main group elements, and polymers), CFF91 and CFF95 [38] (for organic systems and polymers), CVFF class II forcefields [39] for proteins and organics), PCFF [39] (for polymers and materials science applications), COMPASS 1.0 [40] (for condensed phase properties), GlassFF [41] (for silicates and glasses), MSXX [42] (for polyvinylfluoride polymers), Burchart [43] and BKS [43] (for zeolites), specialty forcefields for morphology prediction [44] and specialty forcefields for sorption calculations [45].

Several revised or newly developed general forcefields have been published in the past ten years. Among them are Discover (CVFF) [46], Discover (CFF) [47–49], MM2 [50–52], MM3 [53–58], MM4 [59, 59–63], Dreiding [37], SHARP [64, 65], VALBON [66, 67], UFF [36], CFF95 [38], AMBER [68–72], CHARMM [73–78], OPLS/Amber [79–82], Tripos [83], ECEPP/2 [84–86], GROMOS [87–89], and MMFF [90–95]. In one approach, forcefields were made to be very generic, so that broad coverage of the periodic table, including inorganic compounds, metals, and transition metals, could be achieved. At the extreme UFF was designed for simulating molecules containing any combination of elements in the periodic table. Simple functional forms are used for the diagonal terms in the force-constant matrix of these forcefields. To enable study of complex inorganic systems, for which the

traditional covalent models fail, new concepts were introduced in these forcefield developments. The parameters were defined empirically or by combining atomic parameters based on certain rules. Because of the generality of parameterization, these forcefields are normally expected to yield reasonable predictions of molecular structures. Validation studies with respect to other molecular properties, such as vibration frequencies and conformational properties, have been limited. In another direction, emphasis was given to improving the ability of classical forcefields having relatively simple functional forms to predict properties in a rather focused area of application (mostly biochemistry). For example, much attention has recently been given to the prediction of condensed-phase properties. This trend is clearly seen in new versions of AMBER and CHARMM. In particular, Jorgensen and coworkers published an OPLS/AMBER forcefield [80] in which the well-known OPLS forcefield approach was extended from the united-atom model [96–99] to an explicit all-atom forcefield.

Finally, attention has been paid to achieving high accuracy in predicting various molecular properties while maintaining a fairly broad coverage of the periodic table. The properties of interest include molecular structures, conformational properties, vibrational frequencies, heats of formation, etc. To achieve this goal, complicated functional forms including off-diagonal cross-coupling terms and high-order (cubic and quartic) energy terms are used in these forcefields. Forcefields such as MM3, MM4, CFF95 and MMFF belong in this category. The parameters were derived by fitting to high quality experimental data (MM3/MM4) or to *ab initio* (calculated quantum mechanically) data (CFF95, MMFF). With the great flexibility in functional form and the immense amounts of data in the training set, these forcefields are parameterized accurately. The calculation errors with them are often within experimental error. However, application of these forcefields to models in condensed phases has been limited to energy minimization of molecular crystals. Most of the well-parameterized forcefields, such as MM3, MM4, CHARMM, AMBER, CFF95, and MMFF, were designed mainly for biologically interesting molecules. The Merck Molecular Force Field (MMFF) represents a systematic attempt to combine the best features of such well-regarded force fields as MM3, OPLS, AMBER, and CHARMM into a single force field that is equally adept in small-molecule and macromolecular applications. In particular, MMFF strives for MM3-like accuracy for small molecules in a force field that can be used with confidence in condensed-phase simulations.

Surprisingly, these general force fields give very poor results for such a specialized system as adsorption and diffusion in nanoporous systems. When a zeolite framework is involved we have

$$U^{\text{total}} = U_g^{\text{bonded}} + U_h^{\text{bonded}} + U_{gg}^{\text{non-bonded}} + U_{gh}^{\text{non-bonded}} + U_{hh}^{\text{non-bonded}} \quad (11)$$

where *g* denotes *guest* and *h* denotes *host*. The thermodynamic properties of adsorbed molecules are overwhelmed by the strong adsorbent-adsorbate (host-guest) interactions, and these are not modeled in the force fields listed above. Even worse, it turns out that for simple molecules like alkanes, dedicated force fields like the TRAPPE models of Martin and Siepmann [11] perform just as well or *better*. Likewise, the united-atom model for adsorption and diffusion of alkanes in zeolites of Vlucht et al. [100] outperforms all models mentioned above. It seems that for high accuracy in specialized systems the generic force fields are to no avail.

The functional forms of the bonded and non-bonded terms found in many force fields are discussed below.

Bonding potential U^{bond}

Neighboring atoms bonds could be modeled by keeping them at a fixed bond-distance. However, the resulting dynamics would not be time-reversible. For our fully flexible molecule several potentials have been proposed in the literature. They are functions of the interatomic distances only, where the distance is defined as $\mathbf{r}_{ij} = \mathbf{r}_j - \mathbf{r}_i$.

the harmonic bond potential

$$U_{\text{harm}}(\mathbf{r}_{ij}) = \frac{1}{2}k(r_{ij} - r_{\text{eq}})^2 \quad (12)$$

$$\mathbf{f}_i(\mathbf{r}_{ij}) = k(r_{ij} - r_{\text{eq}}) \frac{\mathbf{r}_{ij}}{r_{ij}} \quad (13)$$

The motion is fastest at the equilibrium position and comes to a complete stop for an instant at the turning points, where all of the energy is potential energy. The probability of finding the object is highest at the turning point and lowest at the equilibrium point.

For larger displacements of the atoms (larger than 0.1 Å), the higher-order terms in the Taylor approximation to the potential become more important and the harmonic approximation describes the system less well. The disadvantage of the harmonic potential is that the force is too large at long distances.

the Morse potential bond The potential differs from the harmonic potential in having an asymmetric potential well, indicating that it is harder to compress a bond than to pull it apart. The potential has a zero force at infinite distance. Morse's function has the advantage that it more realistically describes the potential energy of diatomic molecules and still leads to an exactly solvable quantum mechanical equation. The Morse potential fits better over a wider range of internuclear distances but it fails at larger distances (London dispersion forces become important at larger distances).

$$U_{\text{Morse}}(\mathbf{r}_{ij}) = E_0 \left[\left\{ 1 - e^{-k(r_{ij} - r_{\text{eq}})} \right\}^2 - 1 \right] \quad (14)$$

$$\mathbf{f}_i(\mathbf{r}_{ij}) = 2E_0k \left(1 - e^{-k(r_{ij} - r_{\text{eq}})} \right) e^{-k(r_{ij} - r_{\text{eq}})} \frac{\mathbf{r}_{ij}}{r_{ij}} \quad (15)$$

where E_0 is the depth of the well in energy units, k defines the steepness of the well in Å⁻¹, and r_{eq} is the equilibrium distance in Å. The steepness parameters k can be expressed in terms of the reduced mass of the atoms i and j , the fundamental frequency ω_{ij} and the well depth E_0

$$k = \omega_{ij} \sqrt{\frac{\mu_{ij}}{2E_0}} \quad (16)$$

and because $\omega = \sqrt{k_h/\mu}$ one can rewrite k in terms of the harmonic force constant k_h

$$k = \sqrt{\frac{k_h}{2E_0}} \quad (17)$$

For small deviations $r_{ij} - r_{\text{eq}}$, one can expand the exp-term to first order in the Taylor expansion $\exp(-x) \approx 1 - x$. Substituting this in the functional form

$$\begin{aligned} U_{\text{Morse}}(\mathbf{r}_{ij}) &= E_0 \left[1 - e^{-k(r_{ij} - r_{\text{eq}})} \right]^2 \\ &= E_0 \left[1 - \left(1 - \sqrt{\frac{k_h}{2E_0}} (r_{ij} - r_{\text{eq}}) \right) \right]^2 \\ &= \frac{1}{2} k_h (r_{ij} - r_{\text{eq}})^2 \end{aligned} \quad (18)$$

One recovers the harmonic bond stretching potential.

Disadvantages of Morse potential are that it allows a bond to stretch to an unrealistic length and for a structure with long bonds there would be almost no force pulling the atoms together \rightarrow convergence might be problematic or nonphysical results might be obtained.

the m-n bond potential There have been many attempts to fit the bond energy curves with analytical functions. An early attempt due to Mie in 1903 and developed by Lennard-Jones, combines repulsive and attractive contributions as the sum of simple hyperbolic curves:

$$U_{m,n}(\mathbf{r}_{ij}) = \left(\frac{A}{r_{ij}^m} \right) - \left(\frac{B}{r_{ij}^n} \right) \quad (19)$$

$$\mathbf{f}_i(\mathbf{r}_{ij}) = \frac{nB}{r_{ij}^{n+1}} - \frac{mA}{r_{ij}^{m+1}} \quad (20)$$

The parameters m and n represent the strength of the repulsive and attractive contributions; in order for the repulsion to dominate the attraction as short distances m must be larger than n .

The 12-6 and 12-10 potentials are used for the modeling of hydrogens, 12-6 for non-polar hydrogens, 12-10 for polar hydrogens. This an optional hydrogen-bond term that augments the electrostatic description of the hydrogen bond. This term adds only about $0.5 \text{ kcal mol}^{-1}$ to the hydrogen-bond energy, so the bulk of the hydrogen-bond energy still arises from the dipole-dipole interaction of the donor and acceptor groups.

the Quartic potential A Taylor-expansion of the potential energy, similar to the simple harmonic potential, while keeping terms up to order 4.

$$U_{\text{quartic}}(\mathbf{r}_{ij}) = \frac{k}{2} (r_{ij} - r_{\text{eq}})^2 + \frac{k'}{3} (r_{ij} - r_{\text{eq}})^3 + \frac{k''}{4} (r_{ij} - r_{\text{eq}})^4 \quad (21)$$

$$\mathbf{f}_i(\mathbf{r}_{ij}) = \left[k(r_{ij} - r_{\text{eq}}) + k'(r_{ij} - r_{\text{eq}})^2 + k''(r_{ij} - r_{\text{eq}})^3 \right] \frac{\mathbf{r}_{ij}}{r_{ij}} \quad (22)$$

The force exerted on atoms labeled i and j is easily obtained using

$$f(i) = \left[\frac{\partial U_{\text{stretch}}(\mathbf{r}_{ij})}{\partial \mathbf{r}_{ij}} \right] \frac{\mathbf{r}_{ij}}{|\mathbf{r}_{ij}|} \quad f(j) = - \left[\frac{\partial U_{\text{stretch}}(\mathbf{r}_{ij})}{\partial \mathbf{r}_{ij}} \right] \frac{\mathbf{r}_{ij}}{|\mathbf{r}_{ij}|} \quad (23)$$

The contribution to the atom virial is

$$\mathcal{W} = -\mathbf{r}_{ij} \cdot \mathbf{f}_j \quad (24)$$

The contribution to the stress tensor σ is

$$\begin{pmatrix} \mathbf{r}_{ij}(x)\mathbf{f}_j(x) & \mathbf{r}_{ij}(x)\mathbf{f}_j(y) & \mathbf{r}_{ij}(x)\mathbf{f}_j(z) \\ \mathbf{r}_{ij}(y)\mathbf{f}_j(x) & \mathbf{r}_{ij}(y)\mathbf{f}_j(y) & \mathbf{r}_{ij}(y)\mathbf{f}_j(z) \\ \mathbf{r}_{ij}(z)\mathbf{f}_j(x) & \mathbf{r}_{ij}(z)\mathbf{f}_j(y) & \mathbf{r}_{ij}(z)\mathbf{f}_j(z) \end{pmatrix} \quad (25)$$

Bond-bending potential U^{bend}

The angle θ_{jik} is the angle between \mathbf{r}_{ij} and \mathbf{r}_{ik}

$$\theta = \cos^{-1} \left(\frac{\mathbf{r}_{ij} \cdot \mathbf{r}_{ik}}{r_{ij}r_{ik}} \right) \quad (26)$$

A general expression for most common angle potentials is

$$U(\theta_{jik}, r_{ij}, r_{ik}) = A(\theta_{jik}) \quad (27)$$

where $A(\theta)$ is a purely angular function.

With this reduction the force on an atom derived from the valence angle potential is given by

$$f_l^\alpha = -\frac{\partial U(\theta_{jik}, r_{ij}, r_{ik})}{\partial r_l^\alpha} \quad (28)$$

with atomic label l being one of i, j, k and α indicating the x, y, z component. The derivative is

$$-\frac{\partial U(\theta_{jik}, r_{ij}, r_{ik})}{\partial r_l^\alpha} = -\frac{\partial A(\theta_{jik})}{\partial r_l^\alpha} \quad (29)$$

The derivative of the angular function $A(\theta_{jik})$

$$-\frac{\partial A(\theta_{jik})}{\partial r_l^\alpha} = \frac{1}{\sin(\theta_{jik})} \frac{\partial A(\theta_{jik})}{\partial \theta_{jik}} \frac{\partial}{\partial r_l^\alpha} \left(\frac{\mathbf{r}_{ij} \cdot \mathbf{r}_{ik}}{r_{ij}r_{ik}} \right) \quad (30)$$

with

$$\frac{\partial}{\partial \mathbf{r}_i} \left(\frac{\mathbf{r}_{ij} \cdot \mathbf{r}_{ik}}{r_{ij}r_{ik}} \right) = -\frac{\partial}{\partial \mathbf{r}_j} \left(\frac{\mathbf{r}_{ij} \cdot \mathbf{r}_{ik}}{r_{ij}r_{ik}} \right) - \frac{\partial}{\partial \mathbf{r}_k} \left(\frac{\mathbf{r}_{ij} \cdot \mathbf{r}_{ik}}{r_{ij}r_{ik}} \right) \quad (31)$$

$$\frac{\partial}{\partial \mathbf{r}_j} \left(\frac{\mathbf{r}_{ij} \cdot \mathbf{r}_{ik}}{r_{ij}r_{ik}} \right) = \frac{\mathbf{r}_{ik}}{r_{ij}r_{ik}} - \cos(\theta_{jik}) \frac{\mathbf{r}_{ij}}{r_{ij}^2} \quad (32)$$

$$\frac{\partial}{\partial \mathbf{r}_k} \left(\frac{\mathbf{r}_{ij} \cdot \mathbf{r}_{ik}}{r_{ij}r_{ik}} \right) = \frac{\mathbf{r}_{ij}}{r_{ij}r_{ik}} - \cos(\theta_{jik}) \frac{\mathbf{r}_{ik}}{r_{ik}^2} \quad (33)$$

The atomic forces are then completely specified by the derivatives of the particular function $A(\theta_{jik})$.

the harmonic potential

$$U_{\text{harm}}(\theta_{jik}) = \frac{1}{2}k(\theta_{jik} - \theta_{\text{eq}})^2 \quad (34)$$

$$\mathbf{f}_i = -\mathbf{f}_j - \mathbf{f}_k \quad (35)$$

$$\mathbf{f}_j = \frac{k(\theta_{jik} - \theta_{\text{eq}})}{\sin(\theta_{jik})} \left[\frac{\mathbf{r}_{ik}}{r_{ij}r_{ik}} - \cos(\theta_{jik}) \frac{\mathbf{r}_{ij}}{r_{ij}^2} \right] \quad (36)$$

$$\mathbf{f}_k = \frac{k(\theta_{jik} - \theta_{\text{eq}})}{\sin(\theta_{jik})} \left[\frac{\mathbf{r}_{ij}}{r_{ij}r_{ik}} - \cos(\theta_{jik}) \frac{\mathbf{r}_{ik}}{r_{ik}^2} \right] \quad (37)$$

the quartic potential

$$U_{\text{quartic}}(\theta_{jik}) = \frac{1}{2}k(\theta_{jik} - \theta_{\text{eq}})^2 + \frac{1}{3}k'(\theta_{jik} - \theta_{\text{eq}})^3 + \frac{1}{4}k''(\theta_{jik} - \theta_{\text{eq}})^4 \quad (38)$$

$$\mathbf{f}_i = -\mathbf{f}_j - \mathbf{f}_k \quad (39)$$

$$\mathbf{f}_j = \frac{k(\theta_{jik} - \theta_{\text{eq}}) + k'(\theta_{jik} - \theta_{\text{eq}})^2 + k''(\theta_{jik} - \theta_{\text{eq}})^3}{\sin(\theta_{jik})} \left[\frac{\mathbf{r}_{ik}}{r_{ij}r_{ik}} - \cos(\theta_{jik}) \frac{\mathbf{r}_{ij}}{r_{ij}^2} \right] \quad (40)$$

$$\mathbf{f}_k = \frac{k(\theta_{jik} - \theta_{\text{eq}}) + k'(\theta_{jik} - \theta_{\text{eq}})^2 + k''(\theta_{jik} - \theta_{\text{eq}})^3}{\sin(\theta_{jik})} \sin(\theta_{jik}) \left[\frac{\mathbf{r}_{ij}}{r_{ij}r_{ik}} - \cos(\theta_{jik}) \frac{\mathbf{r}_{ik}}{r_{ik}^2} \right] \quad (41)$$

the harmonic cosine potential

$$U_{\text{harm cos}}(\theta_{jik}) = \frac{k}{2}(\cos(\theta_{jik}) - \cos(\theta_{\text{eq}}))^2 \quad (42)$$

$$\mathbf{f}_i = -\mathbf{f}_j - \mathbf{f}_k \quad (43)$$

$$\mathbf{f}_j = \frac{k(\cos(\theta_{jik}) - \cos(\theta_{\text{eq}}))}{\sin(\theta_{jik})} \left[\frac{\mathbf{r}_{ik}}{r_{ij}r_{ik}} - \cos(\theta_{jik}) \frac{\mathbf{r}_{ij}}{r_{ij}^2} \right] \quad (44)$$

$$\mathbf{f}_k = \frac{k(\cos(\theta_{jik}) - \cos(\theta_{\text{eq}}))}{\sin(\theta_{jik})} \left[\frac{\mathbf{r}_{ij}}{r_{ij}r_{ik}} - \cos(\theta_{jik}) \frac{\mathbf{r}_{ik}}{r_{ik}^2} \right] \quad (45)$$

In general, the contribution to the atom virial is

$$\mathcal{W} = -(\mathbf{r}_{ij} \cdot \mathbf{f}_j + \mathbf{r}_{ik} \cdot \mathbf{f}_k) \quad (46)$$

The bending potentials given here make *no* contribution to the virial.

The contribution to the stress tensor σ is $\sigma^{\alpha\beta} = r_{ij}^\alpha f_j^\beta + r_{ik}^\alpha f_k^\beta$

$$\begin{pmatrix} \mathbf{r}_{ij}(x)\mathbf{f}_j(x) + \mathbf{r}_{ik}(x)\mathbf{f}_k(x) & \mathbf{r}_{ij}(x)\mathbf{f}_j(y) + \mathbf{r}_{ik}(x)\mathbf{f}_k(y) & \mathbf{r}_{ij}(x)\mathbf{f}_j(z) + \mathbf{r}_{ik}(x)\mathbf{f}_k(z) \\ \mathbf{r}_{ij}(y)\mathbf{f}_j(x) + \mathbf{r}_{ik}(y)\mathbf{f}_k(x) & \mathbf{r}_{ij}(y)\mathbf{f}_j(y) + \mathbf{r}_{ik}(y)\mathbf{f}_k(y) & \mathbf{r}_{ij}(y)\mathbf{f}_j(z) + \mathbf{r}_{ik}(y)\mathbf{f}_k(z) \\ \mathbf{r}_{ij}(z)\mathbf{f}_j(x) + \mathbf{r}_{ik}(z)\mathbf{f}_k(x) & \mathbf{r}_{ij}(z)\mathbf{f}_j(y) + \mathbf{r}_{ik}(z)\mathbf{f}_k(y) & \mathbf{r}_{ij}(z)\mathbf{f}_j(z) + \mathbf{r}_{ik}(z)\mathbf{f}_k(z) \end{pmatrix} \quad (47)$$

Torsion potential U^{torsion}

Compared to bond-and bend forces, the torsional force is much weaker. Most variations in molecular structure and relative energies is due to complex interplay between torsional and non-bonded interactions.

The dihedral angle potentials describe the interaction arising from torsional forces in molecules. They require the specification of four atomic positions.

The dihedral angle is defined by

$$\phi_{ijkn} = \cos^{-1} (B(\mathbf{r}_{ij}, \mathbf{r}_{jk}, \mathbf{r}_{kn})) \quad (48)$$

where

$$B(\mathbf{r}_{ij}, \mathbf{r}_{jk}, \mathbf{r}_{kn}) = \frac{(\mathbf{r}_{ij} \times \mathbf{r}_{jk}) \cdot (\mathbf{r}_{jk} \times \mathbf{r}_{kn})}{|\mathbf{r}_{ij} \times \mathbf{r}_{jk}| |\mathbf{r}_{jk} \times \mathbf{r}_{kn}|} \quad (49)$$

With this definition, the sign of the dihedral angle is positive if the vector product $(\mathbf{r}_{ij} \times \mathbf{r}_{jk}) \cdot (\mathbf{r}_{jk} \times \mathbf{r}_{kn})$ is in the same direction as the bond vector \mathbf{r}_{jk} and negative if in the opposite direction. The angle ϕ is the angle between the ijk and jkl planes, with $\phi = 0$ corresponding to the *cis* configuration (i and l on the same side). This definition is called the *protein convention*.

The force on an atom arising from the dihedral potential is given by

$$\mathbf{f}_l = -\frac{\partial}{\partial \mathbf{r}_l} U(\phi_{ijkn}) \quad (50)$$

with l being one of i, j, k, n . This may be expanded into

$$-\frac{\partial}{\partial \mathbf{r}_l} U(\phi_{ijkn}) = \frac{1}{\sin(\phi_{ijkn})} \frac{\partial}{\partial \phi_{ijkn}} U(\phi_{ijkn}) \frac{\partial}{\partial \mathbf{r}_l} B(\mathbf{r}_{ij}, \mathbf{r}_{jk}, \mathbf{r}_{kn}) \quad (51)$$

The derivative of the function $B(\mathbf{r}_{ij}, \mathbf{r}_{jk}, \mathbf{r}_{kn})$ is

$$\begin{aligned} \frac{\partial}{\partial \mathbf{r}_l} = & \frac{1}{|\mathbf{r}_{ij} \times \mathbf{r}_{jk}| |\mathbf{r}_{jk} \times \mathbf{r}_{kn}|} \frac{\partial}{\partial \mathbf{r}_l} ((\mathbf{r}_{ij} \times \mathbf{r}_{jk}) \cdot (\mathbf{r}_{jk} \times \mathbf{r}_{kn})) \\ & - \frac{\cos(\phi_{ijkn})}{2} \left[\frac{1}{|\mathbf{r}_{ij} \times \mathbf{r}_{jk}|^2} \frac{\partial}{\partial \mathbf{r}_l} |\mathbf{r}_{ij} \times \mathbf{r}_{jk}|^2 + \frac{1}{|\mathbf{r}_{jk} \times \mathbf{r}_{kn}|^2} \frac{\partial}{\partial \mathbf{r}_l} |\mathbf{r}_{jk} \times \mathbf{r}_{kn}|^2 \right]_{\alpha} \end{aligned} \quad (52)$$

with

$$\begin{aligned} \frac{\partial}{\partial \mathbf{r}_i} ((\mathbf{r}_{ij} \times \mathbf{r}_{jk}) \cdot (\mathbf{r}_{jk} \times \mathbf{r}_{kn})) &= -\mathbf{r}_{jk} [\mathbf{r}_{jk} \mathbf{r}_{kn}]_{\alpha} + \mathbf{r}_{kn} [\mathbf{r}_{jk} \mathbf{r}_{jk}]_{\alpha} \\ \frac{\partial}{\partial \mathbf{r}_j} ((\mathbf{r}_{ij} \times \mathbf{r}_{jk}) \cdot (\mathbf{r}_{jk} \times \mathbf{r}_{kn})) &= -\mathbf{r}_{ij} [\mathbf{r}_{jk} \mathbf{r}_{kn}]_{\alpha} + \mathbf{r}_{jk} [\mathbf{r}_{jk} \mathbf{r}_{kn}]_{\alpha} \\ &+ \mathbf{r}_{kn} (-[\mathbf{r}_{ij} \mathbf{r}_{jk}]_{\alpha} - [\mathbf{r}_{jk} \mathbf{r}_{jk}]_{\alpha}) + 2\mathbf{r}_{jk} [\mathbf{r}_{ij} \mathbf{r}_{kn}]_{\alpha} \\ \frac{\partial}{\partial \mathbf{r}_k} ((\mathbf{r}_{ij} \times \mathbf{r}_{jk}) \cdot (\mathbf{r}_{jk} \times \mathbf{r}_{kn})) &= \mathbf{r}_{ij} ([\mathbf{r}_{jk} \mathbf{r}_{jk}]_{\alpha} + [\mathbf{r}_{jk} \mathbf{r}_{kn}]_{\alpha}) - \mathbf{r}_{jk} [\mathbf{r}_{ij} \mathbf{r}_{jk}]_{\alpha} \\ &+ \mathbf{r}_{kn} [\mathbf{r}_{ij} \mathbf{r}_{jk}]_{\alpha} - 2\mathbf{r}_{jk} [\mathbf{r}_{ij} \mathbf{r}_{kn}]_{\alpha} \\ \frac{\partial}{\partial \mathbf{r}_n} ((\mathbf{r}_{ij} \times \mathbf{r}_{jk}) \cdot (\mathbf{r}_{jk} \times \mathbf{r}_{kn})) &= -\mathbf{r}_{ij} [\mathbf{r}_{jk} \mathbf{r}_{jk}]_{\alpha} + \mathbf{r}_{jk} [\mathbf{r}_{ij} \mathbf{r}_{jk}]_{\alpha} \end{aligned} \quad (53)$$

and

$$\begin{aligned}
\frac{\partial}{\partial \mathbf{r}_i} |\mathbf{r}_{ij} \times \mathbf{r}_{jk}|^2 &= -2\mathbf{r}_{ij} [\mathbf{r}_{jk}\mathbf{r}_{jk}]_{\alpha} + 2\mathbf{r}_{jk} [\mathbf{r}_{ij}\mathbf{r}_{jk}]_{\alpha} \\
\frac{\partial}{\partial \mathbf{r}_j} |\mathbf{r}_{ij} \times \mathbf{r}_{jk}|^2 &= 2\mathbf{r}_{ij} [\mathbf{r}_{jk}\mathbf{r}_{jk}]_{\alpha} + 2\mathbf{r}_{ij} [\mathbf{r}_{ij}\mathbf{r}_{jk}]_{\alpha} - 2\mathbf{r}_{jk} [\mathbf{r}_{ij}\mathbf{r}_{ij}]_{\alpha} - 2\mathbf{r}_{jk} [\mathbf{r}_{ij}\mathbf{r}_{jk}]_{\alpha} \\
\frac{\partial}{\partial \mathbf{r}_k} |\mathbf{r}_{ij} \times \mathbf{r}_{jk}|^2 &= -2\mathbf{r}_{ij} [\mathbf{r}_{ij}\mathbf{r}_{jk}]_{\alpha} + 2\mathbf{r}_{jk} [\mathbf{r}_{ij}\mathbf{r}_{ij}]_{\alpha} \\
\frac{\partial}{\partial \mathbf{r}_n} |\mathbf{r}_{ij} \times \mathbf{r}_{jk}|^2 &= 0
\end{aligned} \tag{54}$$

and

$$\begin{aligned}
\frac{\partial}{\partial \mathbf{r}_i} |\mathbf{r}_{jk} \times \mathbf{r}_{kn}|^2 &= 0 \\
\frac{\partial}{\partial \mathbf{r}_j} |\mathbf{r}_{jk} \times \mathbf{r}_{kn}|^2 &= 2\mathbf{r}_{kn} [\mathbf{r}_{jk}\mathbf{r}_{kn}]_{\alpha} - 2\mathbf{r}_{jk} [\mathbf{r}_{kn}\mathbf{r}_{kn}]_{\alpha} \\
\frac{\partial}{\partial \mathbf{r}_k} |\mathbf{r}_{jk} \times \mathbf{r}_{kn}|^2 &= -2\mathbf{r}_{kn} [\mathbf{r}_{jk}\mathbf{r}_{jk}]_{\alpha} - 2\mathbf{r}_{kn} [\mathbf{r}_{jk}\mathbf{r}_{kn}]_{\alpha} + 2\mathbf{r}_{jk} [\mathbf{r}_{kn}\mathbf{r}_{kn}]_{\alpha} + 2\mathbf{r}_{jk} [\mathbf{r}_{jk}\mathbf{r}_{kn}]_{\alpha} \\
\frac{\partial}{\partial \mathbf{r}_n} |\mathbf{r}_{jk} \times \mathbf{r}_{kn}|^2 &= 2\mathbf{r}_{kn} [\mathbf{r}_{jk}\mathbf{r}_{jk}]_{\alpha} - 2\mathbf{r}_{jk} [\mathbf{r}_{jk}\mathbf{r}_{kn}]_{\alpha}
\end{aligned} \tag{55}$$

where

$$[\mathbf{ab}]_{\alpha} = \sum_{\beta} (1 - \delta_{\alpha\beta}) a^{\beta} b^{\beta} \tag{56}$$

$$\begin{aligned}
[\mathbf{ab}]_x &= a^y b^y + a^z b^z \\
[\mathbf{ab}]_y &= a^x b^x + a^z b^z \\
[\mathbf{ab}]_z &= a^x b^x + a^y b^y
\end{aligned}$$

Formally, the contribution to be added to the atomic virial is given by

$$\mathcal{W} = - \sum_{i=1}^4 \mathbf{r}_i \cdot \mathbf{f}_i \tag{57}$$

However it is possible to show that the dihedral makes *no* contribution to the atomic virial.

The contribution to be added to the atomic stress tensor is given by

$$\sigma^{\alpha\beta} = r_{ij}^{\alpha} p_i^{\beta} + r_{jk}^{\alpha} p_j^{\beta} + r_{kn}^{\alpha} p_n^{\beta} - \frac{\cos(\phi_{ijkn})}{2} \left(r_{ij}^{\alpha} g_i^{\beta} + r_{jk}^{\alpha} g_k^{\beta} + r_{jk}^{\alpha} h_j^{\beta} + r_{kn}^{\alpha} h_n^{\beta} \right) \tag{58}$$

with

$$\begin{aligned}
\mathbf{p}_i &= \frac{\mathbf{r}_{jk} [\mathbf{r}_{jk}\mathbf{r}_{kn}]_{\alpha} - \mathbf{r}_{kn} [\mathbf{r}_{jk}\mathbf{r}_{jk}]_{\alpha}}{|\mathbf{r}_{ij} \times \mathbf{r}_{jk}| |\mathbf{r}_{jk} \times \mathbf{r}_{kn}|} \\
\mathbf{p}_n &= \frac{\mathbf{r}_{jk} [\mathbf{r}_{ij}\mathbf{r}_{jk}]_{\alpha} - \mathbf{r}_{ij} [\mathbf{r}_{jk}\mathbf{r}_{jk}]_{\alpha}}{|\mathbf{r}_{ij} \times \mathbf{r}_{jk}| |\mathbf{r}_{jk} \times \mathbf{r}_{kn}|} \\
\mathbf{p}_{jk} &= \frac{\mathbf{r}_{jk} [\mathbf{r}_{jk}\mathbf{r}_{kn}]_{\alpha} - \mathbf{r}_{kn} [\mathbf{r}_{ij}\mathbf{r}_{jk}]_{\alpha} - 2\mathbf{r}_{jk} [\mathbf{r}_{ij}\mathbf{r}_{kn}]_{\alpha}}{|\mathbf{r}_{ij} \times \mathbf{r}_{jk}| |\mathbf{r}_{jk} \times \mathbf{r}_{kn}|} \\
\mathbf{g}_i &= \frac{2(\mathbf{r}_{ij} [\mathbf{r}_{jk}\mathbf{r}_{jk}]_{\alpha} - \mathbf{r}_{jk} [\mathbf{r}_{ij}\mathbf{r}_{jk}]_{\alpha})}{|\mathbf{r}_{ij} \times \mathbf{r}_{jk}|^2} \\
\mathbf{g}_k &= \frac{2(\mathbf{r}_{jk} [\mathbf{r}_{ij}\mathbf{r}_{ij}]_{\alpha} - \mathbf{r}_{ij} [\mathbf{r}_{ij}\mathbf{r}_{jk}]_{\alpha})}{|\mathbf{r}_{ij} \times \mathbf{r}_{jk}|^2} \\
\mathbf{h}_j &= \frac{2(\mathbf{r}_{jk} [\mathbf{r}_{kn}\mathbf{r}_{kn}]_{\alpha} - \mathbf{r}_{kn} [\mathbf{r}_{jk}\mathbf{r}_{kn}]_{\alpha})}{|\mathbf{r}_{jk} \times \mathbf{r}_{kn}|^2} \\
\mathbf{h}_n &= \frac{2(\mathbf{r}_{kn} [\mathbf{r}_{kn}\mathbf{r}_{kn}]_{\alpha} - \mathbf{r}_{jk} [\mathbf{r}_{jk}\mathbf{r}_{kn}]_{\alpha})}{|\mathbf{r}_{jk} \times \mathbf{r}_{kn}|^2}
\end{aligned} \tag{59}$$

the cosine potential

$$U_{ijkn} = A [1 + \cos(m\phi_{ijkn} - \delta)] \tag{60}$$

the harmonic potential

$$U_{ijkn} = \frac{1}{2}k(\phi_{ijkn} - \phi_{eq})^2 \tag{61}$$

the harmonic cosine potential

$$U_{ijkn} = \frac{1}{2}k(\cos(\phi_{ijkn}) - \cos(\phi_{eq}))^2 \tag{62}$$

the triple cosine potential The Pitzer potential used in OPLS is given by the first four terms of a Fourier series

$$U_{ijkn} = A_0 + \frac{1}{2}[A_1(1 + \cos(\phi)) + A_2(1 - \cos(2\phi)) + A_3(1 + \cos(3\phi))] \tag{63}$$

A_n gives the energy barrier to rotation, $n = 1, 2, 3$ in $n\phi$ the number of maxima (or minima) in one full rotation. The use of the sum allows for complex angular variation of the potential energy (in effect a truncated Fourier series is used). Barriers for dihedral angle rotation can be attributed to the exchange interaction of electrons in adjacent bonds. Steric effects can also be important. It was found that the Pitzer potential was insufficient to give a full representation of the energy barriers of dihedral angle change. Modern potential energy functions normally model the dependence of the energy on dihedral angle change by a combination of Pitzer potential terms and non-bonded effects.

the Ryckaert-Bellemans potential For alkanes the following dihedral potential the Ryckaert-Bellemans potentials are often used. Note that a conversion can be achieved by multiplying every coefficient by $(-1)^n$. The use of this potential implies exclusion of LJ-interactions between the first and last atom of the dihedral, and $\theta = \phi - \pi$ is defined according the *polymer convention* $\theta_{\text{trans}} = 0$.

$$U_{ijkn} = \sum_n C_n \cos^n(\theta) \quad (64)$$

The RB potential can also be used to include the OPLS dihedral potential. Because of the equalities $\cos(2\phi) = 2\cos^2(\phi) - 1$ and $\cos(3\phi) = 4(\cos^3(\phi) - 3\cos(\phi))$ one can translate the OPLS parameters to Ryckaert-Bellemans parameters as follows:

$$\begin{aligned} C_0 &= A_0 + A_2 + \frac{1}{2}(A_1 + A_3) \\ C_1 &= \frac{1}{2}(3A_3 + A_1) \\ C_2 &= -A_2 \\ C_3 &= -2A_3 \\ C_4 &= 0 \\ C_5 &= 0 \end{aligned} \quad (65)$$

with OPLS parameters in protein convention and Ryckaert-Bellemans in polymer convention.

non-Bonded Potentials U^{VDW}

In addition to the bonded interactions between atoms described above, force fields also contain non-bonded interactions. Non-bonded interactions act between atoms in the same molecule and those in other molecules. Force fields usually divide non-bonded interactions into two: Van der Waals interactions and electrostatic interactions.

pair-potentials In general, the system potential energy can be expressed as

$$U = \sum_i U_1(\mathbf{r}_i) + \sum_i \sum_{j>i} U_2(\mathbf{r}_i, \mathbf{r}_j) + \sum_i \sum_{j>i} \sum_{k>j>i} U_3(\mathbf{r}_i, \mathbf{r}_j, \mathbf{r}_k) + \dots \quad (66)$$

where the first term denotes the effect of external fields and other terms denote the interactions between particles. Among them, U_2 is the potential between pairs of particles, U_3 is the potential between triplets, and U_4 and U_5 are the interactions between quadruplets and quintuplets, respectively, etc. . . .

The dominant term is the two-body interaction and higher terms are usually neglected. In some cases, tree-body interactions are important, but they rapidly increase the time needed for simulation. The atomic pairwise potential is the foundation for evaluating molecular properties, because molecules are composed of atoms.

VDW potentials The most common potentials, as Lennard-Jones, have an infinite range. The problem of this is that we must analyze $n * (n - 1)$ pair-potentials each time step. It is not possible for large applications, and for this reason it is customary to establish a cutoff

radius r_c and disregard the interactions between atoms separated by more than r_c . This results in simpler programs and enormous savings of computer resources, because the number of atomic pairs separated by a distance r grows as r^2 and becomes quickly huge.

The force is derived from the potential as

$$f_j(r) = -\frac{1}{r_{ij}} \left[\frac{\partial}{\partial r} U(r_{ij}) \right] \mathbf{r}_{ij} \quad (67)$$

12 - 6 potential

$$U(r_{ij}) = \left(\frac{A_{ij}}{r_{ij}^{12}} \right) - \left(\frac{B_{ij}}{r_{ij}^6} \right) \quad (68)$$

$$-\frac{\partial}{\partial r} U(r_{ij}) = \frac{12}{r} \left[\frac{A}{r^{12}} - \frac{1}{2} \frac{B}{r^6} \right] \quad (69)$$

Lennard-Jones

$$U(r_{ij}) = 4\epsilon_{ij} \left[\left(\frac{\sigma_{ij}}{r_{ij}} \right)^{12} - \left(\frac{\sigma_{ij}}{r_{ij}} \right)^6 \right] \quad (70)$$

$$-\frac{\partial}{\partial r} U(r_{ij}) = \frac{48}{r} \left[\left(\frac{\sigma}{r} \right)^{12} - \frac{1}{2} \left(\frac{\sigma}{r} \right)^6 \right] \quad (71)$$

Buckingham potential

$$U(r_{ij}) = -\frac{A_{ij}}{r_{ij}^6} + B_{ij}e^{-C_{ij}r_{ij}} \quad (72)$$

$$-\frac{\partial}{\partial r} U(r_{ij}) = \frac{6}{r} \frac{A_{ij}}{r^6} + B_{ij}C_{ij}e^{-C_{ij}r_{ij}} \quad (73)$$

electrostatic interaction U^{Coulomb} The electrostatic interaction arises due to the unequal distribution of charge in a molecule. Within the force field framework this uneven distribution of charge can be modeled by placing point charges at each of the atomic sites. Due to charge conservation for a neutral molecule these sum to zero. The interaction between point charges is generally modeled by a Coulomb potential

$$U = \frac{1}{4\pi\epsilon_0} \frac{q_i q_j}{r_{ij}} \quad (74)$$

where ϵ_0 is the permittivity of free space, q are atomic charges, and r_{ij} is the distance between atom i and j . An alternative approach used in some force fields is to model the electrostatics using point dipoles on the atoms or bonds. This can be extended by placing point multipoles on the atomic sites, a method called Distributed Multipole Analysis (DMA).

III Boundary conditions

Periodic boundary conditions are commonly applied to overcome the problems of surface effects. The original simulation box, including all the atoms within it, is replicated throughout space. When a molecule in the original box moves, its periodic images in each of the surrounding boxes moves in exactly the same way. If a molecule leaves the central box, one of its images will enter the box through the opposite face. It is not necessary to store the coordinates and momenta of all the images, only the ones in the central box are needed, because the images can be obtained from translation operators. The boundary of the periodic box does not have any physical significance, only the shape and orientation is fixed.

Usually, one uses the minimum-image convention, where the distance between two particles is taken to be the shortest distance between their periodic images, and a truncation (and shifted such that the potential vanishes at the cutoff) of the potential at some distance smaller than half the box length to be consistent with the minimum image convention. The advantage of using a truncated and shifted potential is that the intermolecular forces are always finite. This is important because impulsive forces are hard to handle in MD simulations. The cutoff-distance has to be larger than the distance where pair-correlations are present, i.e. $g(r) \approx 1$ at the cutoff distance. The function $g(r)$ gives the probability of finding a pair of atoms a distance r apart, relative to the probability expected for a complete random distribution at the same density.

In crystallography, the crystal structure is defined by the unit cell, and by the fractional coordinates of the atoms within the unit cell. These coordinates form an orthonormal dimensionless \mathcal{S} -space. The transformation from \mathcal{S} -space to real \mathcal{R} -space can be carried out by the matrix \mathcal{H} :

$$\mathcal{H} = \begin{pmatrix} a & b \cos(\gamma) & c \cos(\beta) \\ 0 & b \sin(\gamma) & c\zeta \\ 0 & 0 & c\sqrt{1 - \cos^2\beta - \zeta^2} \end{pmatrix} \quad (75)$$

with

$$\zeta = \frac{\cos\alpha - \cos\gamma\cos\beta}{\sin\gamma} \quad (76)$$

Conversely, \mathcal{H}^{-1} transforms real coordinates to fractional coordinates. With the chosen \mathcal{H} the scaled box has a length of 1. Our potential forcefield is defined in real space, therefore it is convenient to store position in \mathcal{R} space, transform them to \mathcal{S} space, apply periodic boundary conditions in \mathcal{S} space, and transform back to \mathcal{R} space to compute distances within the simulation box

$$\begin{aligned} \mathbf{s} &= \mathcal{H}^{-1}\mathbf{r} \\ \mathbf{s}' &= \mathbf{s} - \text{rint}(\mathbf{s}) \\ \mathbf{r}' &= \mathcal{H}\mathbf{s}' \end{aligned} \quad (77)$$

where the "rint"-function returns the rounded integer value of its argument. The smallest perpendicular width of the unit cell has to be larger than twice the spherical cutoff in \mathcal{R} space.

For computational reasons a rectangular unit cell is preferred. Not only is the matrix conversion more expensive, if the the unit cell is severely distorted from cubic many distances will be calculated that are outside the cutoff in \mathcal{R} space reducing the efficiency.

However, for computation of free energy profiles in complex zeolite structures, the fractional space is often very convenient.

IV Monte-Carlo (MC)

A The Metropolis algorithm

The Markov Chain Monte Carlo method (MCMC) is an important tool to estimate the average properties of systems with a very large number of accessible states. Often the quantity of interest are not the configurational part of the partition function itself, but averages of the type

$$\langle A \rangle = \frac{\int e^{-\beta U(\mathbf{r}^N)} A(\mathbf{r}^N) d\mathbf{r}^N}{\int e^{-\beta U(\mathbf{r}^N)} d\mathbf{r}^N} \quad (78)$$

where $\beta = 1/(k_B T)$, with k_B the Boltzmann constant, and $U(\mathbf{r}^N)$ is the total energy of the system with N particles at positions \mathbf{r}^N . The configurational part of the partition function is denoted by Z

$$Z \equiv \int e^{-\beta U(\mathbf{r}^N)} d\mathbf{r}^N \quad (79)$$

the ration $e^{-\beta U}/Z$ is the probability density of finding the system in a configuration around \mathbf{r}^N . The Monte Carlo scheme makes use of the fact that only the relative probability of visiting points in configuration space is needed, *not* the absolute probability. To visit points with the correct frequency, the MCMC algorithm generates random trial moves from the current ("old") state (o) to a new state (n). To show that an arbitrary initial distribution eventually relaxes to the equilibrium distribution, it is often convenient to apply the condition of detailed balance (as is used in the original Metropolis scheme). If $P_B(o)$ and $P_B(n)$ denote the probability of finding the system in in state (o) and (n), respectively, and $\alpha(o \rightarrow n)$ and $\alpha(n \rightarrow o)$ denote the conditional probability to perform a trial move from $o \rightarrow n$ and $o \rightarrow n$, respectively, then the probability $P_{\text{acc}}(o \rightarrow n)$ to accept the trial move from $o \rightarrow n$ is related to $P_{\text{acc}}(n \rightarrow o)$ by the following

$$P_B(o)\alpha(o \rightarrow n)P_{\text{acc}}(o \rightarrow n) = P_B(n)\alpha(n \rightarrow o)P_{\text{acc}}(n \rightarrow o) \quad (80)$$

Metropolis et al. assumed that

$$\alpha(o \rightarrow n) = \alpha(n \rightarrow o) \quad (81)$$

and fixed the acceptance probability using

$$P_{\text{acc}}(o \rightarrow n) = \min\left(1, \frac{P_B(n)}{P_B(o)}\right) \quad (82)$$

B Recycling of micro-states

In the Metropolis scheme, the rejected trial states are not contributing to the average, but to the proper normalization. As a consequence, conventional Monte Carlo algorithms are wasteful because they tend to generate many trial states that are unused for averages and distributions. However, we can do better; the properties of the rejected states can

be included in the sampling by using the Waste-Recycled Monte Carlo (WRMC) method by D. Frenkel [101]. The weaker condition "balance" is both sufficient and necessary to guarantee that a particular Markov chain algorithm leads to equilibrium sampling. The balance condition requires only that the Markov chain leaves the equilibrium distribution invariant.

Assume that we start with an old configuration (o). Instead of generating a single new configuration we generate a *set* of possible new configurations, which we denote by $\{n\}$. Now, with the set ($o + \{n\}$) we do a thought experiment in which we sample states within this set only using the conventional Metropolis scheme. If we would carry out this simulation with an infinite number of steps, then we can exactly predict the ensemble average of an observable A of this set.

$$\langle A \rangle = \frac{\sum_{i=1}^n e^{-\beta U(i)} A(i)}{\sum_{i=1}^n e^{-\beta U(i)}} \quad (83)$$

Furthermore, the probability that the system is in state i after this simulation is given by

$$P(i) = \frac{e^{-\beta U(i)}}{\sum_{j=1}^n e^{-\beta U(j)}} \quad (84)$$

The sampling of the set ($o + \{n\}$) can be considered as a coarse-grained move in which the final configuration is selected with a probability given by Eq. 84. By averaging over *many* of these coarse-grained moves we obtain the correct ensemble average. All states that we have generated, both accepted and rejected, contribute to this ensemble average, but with a different weight.

It is important to note that this scheme only works if the underlying method to generate configurations obeys detailed balance. The whole set of coarse-grained moves obeys the weaker condition of balance, but still samples the correct distribution.

C Ensembles

canonical NVT ensemble

In the canonical ensemble, the number of particles N , the temperature T , and the volume V are constant. The partition function is

$$Z_{NVT} = \frac{1}{\Lambda^{3N} N!} \int e^{-\beta U} d\mathbf{r}^N \quad (85)$$

where $\Lambda = \sqrt{h^2 / (2\pi m k_B T)}$ is the thermal de Broglie wavelength. The probability of finding configuration \mathbf{r}^N is given by

$$\mathcal{N}(\mathbf{r}^N) \propto e^{-\beta U(\mathbf{r}^N)} \quad (86)$$

The average of the variable $A(\mathbf{r}^N)$ in the NVT ensemble is given by

$$\langle A(\mathbf{r}^N) \rangle = \frac{\int A(\mathbf{r}^N) e^{-\beta U} d\mathbf{r}^N}{\int e^{-\beta U} d\mathbf{r}^N} \quad (87)$$

Computing properties like the average energy is obvious, but pressure and the chemical potential are more difficult. The definition for pressure from thermodynamics is

$$p = k_B T \left(\frac{\partial \log Z_{NVT}}{\partial V} \right)_{N,T} \quad (88)$$

Making the coordinate change (assuming a cubic box for simplicity)

$$\mathbf{s}_i = \frac{\mathbf{r}_i}{L} \quad L = V^{\frac{1}{3}} \quad \text{for } i = 1, 2, \dots, N \quad (89)$$

we can write

$$\left(\frac{\partial \log Z_{\text{NVT}}}{\partial V} \right)_{N,T} = NV^{N-1} \int_0^1 \dots \int_0^1 e^{-\beta U} d\mathbf{s}^N - \beta V^N \int_0^1 \int_0^1 \int_0^1 e^{-\beta U} \frac{\partial U}{\partial V} \quad (90)$$

with

$$\frac{\partial U}{\partial V} = \sum_i \frac{dU(\mathbf{r}_i^\alpha)}{d\mathbf{r}_i^\alpha} \frac{d\mathbf{r}_i^\alpha}{dV} \quad (91)$$

$$= - \sum_i \mathbf{f}_i^\alpha \frac{1}{3} V^{-\frac{2}{3}} \mathbf{r}_i^\alpha \quad (92)$$

$$= - \frac{1}{3V} \sum_i \mathbf{f}_i \cdot \mathbf{r}_i \quad (93)$$

Conversion to the initial coordinates and using

$$\frac{\partial \log Z_{\text{NVT}}}{\partial V} = \frac{1}{Z_{\text{NVT}}} \frac{\partial Z_{\text{NVT}}}{\partial V} \quad (94)$$

we see that the first term is the density, and the second term is the ensemble average of the sum of the force times coordinate

$$pV = Nk_B T - \frac{1}{3} \langle \mathbf{f}_i \cdot \mathbf{r}_i \rangle \quad (95)$$

The second term on the right is called *the virial*, and this equation *the virial equation*.

A particularly simple and elegant method for measuring the chemical potential μ in a pure fluid or in a mixture is the Widom particle insertion method (WPI). From thermodynamics, we know that μ_a of species a is defined as

$$\mu_a = \left(\frac{\partial F}{\partial N_a} \right)_{N_{a \neq b}, VT} \quad (96)$$

where F is the Helmholtz free energy. The expression for the Helmholtz free energy is

$$F_{\text{NVT}} = -k_B T \ln Z_{\text{NVT}} \quad (97)$$

$$= -k_B T \ln \left(\frac{V^N}{\Lambda^{3N} N!} \right) - k_B T \ln \left(\int e^{-\beta U(\mathbf{s}^N)} d\mathbf{s}^N \right) \quad (98)$$

$$= F_{\text{NVT}}^{\text{id}} + F_{\text{NVT}}^{\text{ex}} \quad (99)$$

For large enough in Eq. 96, the chemical potential is given by

$$\mu = -k_B T \ln \frac{Z_{N+1}}{Z_N} \quad (100)$$

$$= -k_B T \ln \frac{V}{\Lambda^3(N+1)} - k_B T \ln \frac{\int e^{-\beta U(\mathbf{s}^{N+1})} d\mathbf{s}^{N+1}}{\int e^{-\beta U(\mathbf{s}^N)} d\mathbf{s}^N} \quad (101)$$

$$\equiv \mu_{\text{id}}(\rho) + \mu_{\text{ex}} \quad (102)$$

We now separate the potential energy function of the N -particle system, and the interaction energy of the $(N + 1)$ th particle with the rest

$$\Delta U \equiv U(\mathbf{s}^{N+1}) - U(\mathbf{s}^N) \quad (103)$$

and we can write

$$\mu_{\text{ex}} = -k_B T \ln \left(\int \langle e^{-\beta \Delta U} \rangle d\mathbf{s}^{N+1} \right) \quad (104)$$

where $\langle \dots \rangle$ denotes canonical ensemble averaging over the configurational space of the N -particle system.

Widom test-particle method.

- Perform NVT MC simulation for the system of N particles
- Calculate the average of the $e^{-\beta U(N+1)}$, by inserting the “ghost” particle at random positions inside the box, and calculating its interaction energy with the rest of the system, as if it were real.

This technique works fine at moderate densities around the critical point, but turns out to have problems at high densities around liquid-solid coexistence, because the probability to insert the “ghost” at the place where the $e^{-\beta U_{N+1}}$ is very small.

NPT ensemble

The constant volume ensemble is not very convenient for the study of phase transitions. Some experimental values, like the excess properties, are measured at constant pressure, not at constant volume, therefore it would be nice to have a method to simulate the isobaric conditions also. The average of the value $A(\mathbf{s}^N)$ in the NPT ensemble is given as:

$$\langle A \rangle_{\text{NPT}} = \frac{1}{Z_{\text{NPT}}} \int_0^\infty e^{-\beta PV} V^N \left(\int_0^1 A(\mathbf{s}^N) e^{-\beta U} d\mathbf{s}^N \right) dV \quad (105)$$

with

$$Z_{\text{NPT}} = \frac{\beta P}{\Lambda^{3N} N!} \int V^N e^{-\beta PV} \left(\int e^{-\beta U} d\mathbf{s}^N \right) dV \quad (106)$$

Here we again made the transformation to the “primed” coordinates, rescaling them by the box dimensions. If we perform a random walk in $\ln V$, the probability of finding volume V is given by

$$\mathcal{N}(\ln(V); \mathbf{s}^N) \propto e^{-\beta(PV+U)+(N+1)\ln V} \quad (107)$$

For a random walk in $\ln V$, instead of in V , the domain of this walk coincides with all possible values of V . Furthermore, the average step size turns out to be less sensitive to the density. Metropolis algorithm is implemented in the same way as for NVT ensemble, but now we also allow the volume to change. We have two kinds of the Monte Carlo moves: particles displacement, performed the same way as in the NVT simulations, and volume change. The acceptance criterion is, of course, modified now, as instead of the energy difference between the old and new states, it is based on the difference of enthalpies:

$$\Delta H = \Delta U + P(V' - V) - (N + 1) \frac{1}{\beta} \ln \frac{V'}{V} \quad (108)$$

$$\text{acc}(o \rightarrow n) = \min(1, e^{-\beta \Delta H}) \quad (109)$$

For the computation of the chemical potential we must evaluate

$$\mu = \frac{\partial G}{\partial N_{PT}} \quad (110)$$

Entirely analogous to the NVT case we find that $\mu = G(N + 1, P, T) - G(N, P, T)$ reads

$$\mu = -k_B T \ln \left\langle \frac{V}{\Lambda^3(N+1)} \int e^{-\beta \Delta U} d\mathbf{s}^{N+1} \right\rangle \quad (111)$$

$$= -k_B T \ln \frac{k_B T}{P \Lambda^3} - k_B T \ln \left\langle \frac{PV}{(N+1)k_B T} \int e^{-\beta \Delta U} d\mathbf{s}^{N+1} \right\rangle \quad (112)$$

$$= \mu_{\text{id}}(P) + \mu_{\text{ex}}(P) \quad (113)$$

We now define the ideal gas reference state at the same pressure, rather than at the same average density as the system under study. The fluctuating quantity that we are averaging is no longer $e^{-\beta \Delta U}$, but $V e^{-\beta \Delta U}$.

Gibbs ensemble

The Gibbs ensemble Monte Carlo simulation technique allows direct simulation of phase equilibria in fluids. Gibbs ensemble simulations are performed in two separate microscopic regions, each within periodic boundary conditions.

An n -component system at constant temperature T , total volume V , and total number of particles N is divided into two regions, with volumes V_I and $V_{II} = V - V_I$ and number of particles N_I and $N_{II} = N - N_I$. The partition function is given by

$$Q_{\text{NVT}}^{\text{Gibbs}} \equiv \frac{1}{\Lambda^{3N} N!} \sum_{N_I=0}^N \binom{N}{N_I} \int_0^V (V_I)^{N_I} (V_{II})^{N_{II}} \left(\int e^{-\beta U(\mathbf{s}^{N_{II}})} d\mathbf{s}_{II}^{N_{II}} \int e^{-\beta U(\mathbf{s}_I^{N_I})} d\mathbf{s}_I^{N_I} \right) dV_I \quad (114)$$

The probability of finding a configuration with N_I particles in box 1 with volume V_I , and positions $\mathbf{s}_1^{N_I}$ and $\mathbf{s}_2^{N_{II}}$ is given by

$$\mathcal{N}(N_I, V_I, \mathbf{s}_1^{N_I}, \mathbf{s}_2^{N_{II}}) \propto \frac{(V_I)^{N_I} (V_{II})^{N_{II}}}{N_I! N_{II}!} e^{-\beta (U(\mathbf{s}_1^{N_I}) + U(\mathbf{s}_2^{N_{II}}))} \quad (115)$$

In the Gibbs scheme we consider the following trial moves

- displacement of a randomly selected particle
The acceptance rule is identical to that used in a conventional NVT ensemble simulation
- change of box volumes while keeping the total volume constant
The acceptance rule for a random walk in $\ln(V_I/V_{II})$ is

$$\text{acc}(o \rightarrow n) = \min\left(1, \left(\frac{V_I(n)}{V_I(o)}\right)^{N_I+1} \left(\frac{V_{II}(n)}{V_{II}(o)}\right)^{N_{II}+1} e^{-\beta \Delta U(\mathbf{s}^N)}\right) \quad (116)$$

- transfer of a randomly selected particle from one box to the other
We can generate a new configuration n from configuration o (N_I particles in box 1) by removing a particle from box 1 and inserting this in box 2. At random, it is selected

to transfer a particle from box 1 to box 2 or vice versa. Out of the n components, one the components j is selected at random. A particle that obeys the first two choices is selected at random and transferred to a random position in the other box. The acceptance rule is given by

$$\text{acc}(o \rightarrow n) = \min \left(1, \frac{N_{I,j} V_{II}}{(N_{II,j} + 1) V_I} e^{-\beta(U(\mathbf{s}_i^N) - U(\mathbf{s}_o^N))} \right) \quad (117)$$

Alternatively, one can first select a particle at random from all N particles and then try to move this particle to the other simulation box. The acceptance rule is

$$\text{acc}(o \rightarrow n) = \min \left(1, \frac{V_{II}}{V_I} e^{-\beta(U(\mathbf{s}_i^N) - U(\mathbf{s}_o^N))} \right) \quad (118)$$

For pure component systems, the phase rule requires that only one intensive variable (the temperature) can be independently specified when two phases coexists. The vapor pressure is obtained from the simulation. By contrast, for multi-component systems pressure can be specified in advance, with the total system being considered at constant NPT. The only change necessary is that the volume changes in the two regions are now independent. The acceptance rule for a volume change of region I , while the other remains unchanged is given by

$$\text{acc}(o \rightarrow n) = \min \left(1, e^{-\beta \Delta U_I - \beta P(V_I(n) - V_I(o)) + (N_I + 1) \ln \frac{V_I(n)}{V_I(o)}} \right) \quad (119)$$

grand-canonical ensemble (μ, V, T)

In adsorption studies one would like to know the amount of materials adsorbed as a function of pressure and temperature of the reservoir with which the sieve is in contact. Therefore the natural ensemble to use is the grand-canonical ensemble (or μ, V, T ensemble). In this ensemble, the temperature T , the volume V , and the chemical potential μ are fixed. The partition function is given by

$$Z_{\mu VT} \equiv \sum_{N=0}^{\infty} \frac{e^{\beta \mu N} V^N}{\Lambda^{3N} N!} \int e^{-\beta U(\mathbf{s}^N)} d\mathbf{s}^N \quad (120)$$

with a corresponding probability density

$$\mathcal{N}_{\mu VT} \propto \frac{e^{\beta \mu N} V^N}{\Lambda^{3N} N!} e^{-\beta U(\mathbf{s}^N)} \quad (121)$$

Metropolis algorithm is implemented in the same way as for NVT ensemble, but now we also allow the number of particles to change. We have two additional Monte-Carlo moves. The creation of a particle is accepted with a probability

$$\text{acc}(N \rightarrow N + 1) = \min \left(1, \frac{V}{\Lambda^3(N + 1)} e^{\beta(\mu - U(N+1) + U(N))} \right) \quad (122)$$

and the removal of a particle is accepted with a probability

$$\text{acc}(N \rightarrow N - 1) = \min \left(1, \frac{\Lambda^3 N}{V} e^{-\beta(\mu + U(N-1) - U(N))} \right) \quad (123)$$

The equilibrium conditions are that the temperature and chemical potential of the gas inside and outside the adsorbent must be equal. The imposed chemical potential μ can be related to the fugacity f

$$\beta\mu = \beta\mu_{\text{id}}^0 + \ln(\beta f), \quad (124)$$

where μ_{id}^0 is the reference chemical potential. All information of the reference state drops out, because it simply acts as a shift of the chemical potential that has no effect on the observable thermodynamic properties of the system. The fugacity f_j of component j in the reservoir is defined as the partial pressure of component j in the reservoir under the condition that the reservoir would be an ideal gas. Using the ideal gas law

$$f_j V \beta = N_j \quad (125)$$

we obtain for the insertion and deletion of a particle in the system

$$\text{acc}(N \rightarrow N + 1) = \min \left(1, \frac{V \beta f}{(N + 1)} e^{-\beta(U(N+1) - U(N))} \right) \quad (126)$$

$$\text{acc}(N \rightarrow N - 1) = \min \left(1, \frac{N}{V \beta f} e^{-\beta(U(N-1) - U(N))} \right) \quad (127)$$

The pressure p is related to the fugacity f by

$$f = \phi p, \quad (128)$$

where ϕ is the fugacity coefficient computed directly from the equation of state of the vapor in the reservoir. For most adsorbates, the experimental equation of state is well known and we use the Peng-Robinson equation of state to convert the pressure to the corresponding fugacity, introducing only a small correction for the currently studied systems.

Semigrand ensemble

The quantity $\Delta\mu_{\text{ex}} \equiv (\mu_A - \mu_B)_{\text{ex}}$ is problematic to compute accurately. Fortunately, $\Delta\mu_{\text{ex}}$ can be obtained much more directly by measuring the Boltzmann factor associated with a virtual move, where a randomly selected particle of type B is transformed into type A . Then

$$\Delta\mu_{\text{ex}} = -k_B T \ln \left\langle \frac{N_B}{N_A + 1} e^{-\beta\Delta U^\pm} \right\rangle \quad (129)$$

where ΔU^\pm denotes the change in potential energy of the system if one particle of type B is changed into type A ; $-k_B T \ln(N_B / (N_A + 1))$ is simply the ideal mixing contribution to the chemical potential. For a perfect mixture (i.e. A and B have the same intermolecular interactions), $\ln \langle e^{-\beta\Delta U^\pm} \rangle$ is identically equal to 0. Therefore, we may obtain very good statistics on $\Delta\mu_{\text{ex}}$ even when the direct measurement of the excess chemical potential of the individual species would yield poor statistics.

The use of identity switch is a very efficient trial move. Out of n components, two components $i \neq j$ are selected. At random it is decided whether i is from box A and j from box B , or vice versa. In each box a particle is randomly selected with the desired identity. The acceptance rule is given by

$$\text{acc}(o \rightarrow n) = \min \left(1, \frac{N_i^A N_j^B}{(N_j^A + 1)(N_i^B + 1)} e^{-\beta\Delta U} \right) \quad (130)$$

This trial move is easily rewritten for use in grand-canonical simulations, because we can write

$$\frac{N_i^A}{N_j^A + 1} = \frac{f_i}{f_j} \quad (131)$$

The acceptance rules becomes

$$\text{acc}(o \rightarrow n) = \min \left(1, \frac{f_i N_j}{f_j (N_i + 1)} e^{-\beta \Delta U} \right) \quad (132)$$

This type of trial move in the grand-canonical ensemble is sometimes called semi-grand canonical ensemble.

Parallel tempering

The method of parallel tempering is a Monte Carlo scheme that has been derived to achieve good sampling of systems that have a free energy landscape with many local minima. In parallel tempering we consider n systems. In each of these systems we perform a simulation in the canonical ensemble, but each system is in a different thermodynamic state. Usually, but not necessarily, these states differ in temperature. In what follows we assume that this is the case. Systems with a sufficiently high temperature pass all barriers in the system. The low temperature systems, on the other hand, mainly probe the local energy minima. The idea of parallel tempering is to include MC trial moves that attempt to “swap” systems that belong to different thermodynamic states, e.g., to swap a high temperature system with a low temperature system. If the temperature difference between the two systems is very large, such a swap has a very low probability of being accepted. This is very similar to particle displacement in ordinary Monte Carlo. If one uses a very large maximum displacement a move has a very low probability of being accepted. The solution to this problem is to use many small steps. In parallel tempering we use intermediate temperatures in a similar way. Instead of making attempts to swap between a low and a high temperature, we swap between ensembles with a small temperature difference.

The total partition function of a system with n canonical subsystems (Z) equals

$$Z = \prod_{i=1}^{i=n} Z_{\text{NVT}}(i) \quad (133)$$

in which $Z_{\text{NVT}}(i)$ is the canonical partition function of the individual system i . For each of these systems, individual trial moves are performed. After a randomly selected number of trial moves, an attempt is made to exchange configurations. Two systems (i and $i + 1$) are selected at random. The trial move is accepted with probability

$$\text{acc}(i \leftrightarrow i + 1) = \min \left(1, e^{(\beta_{i+1} - \beta_i)(U_{i+1} - U_i)} \right) \quad (134)$$

and after an accepted move all particle positions are swapped. The acceptance rule for parallel tempering in the grand-canonical ensemble reads

$$\text{acc}(i \leftrightarrow i + 1) = \min \left(1, e^{(\beta_{i+1} - \beta_i)(U_{i+1} - U_i) - (\beta_{i+1} \mu_{i+1} - \beta_i \mu_i)(N_{i+1} - N_i)} \right) \quad (135)$$

Swap moves are very inexpensive because they do not involve additional calculations. Note that the swap moves do not disturb the Boltzmann distribution corresponding to

a particular ensemble. Therefore one can determine ensemble averages from every individual ensemble just as we do for an ordinary Monte Carlo simulations. This is an important advantage over simulated annealing. Parallel tempering is a true equilibrium Monte Carlo scheme.

D Configurational-bias Monte-Carlo (CBMC)

Conventional Monte Carlo is time-consuming for long chain molecules. The fraction of successful insertions into the sieve is too low. To increase the number of successfully inserted molecules we apply the CBMC technique. In the CBMC scheme it is convenient to split the total potential energy U of a trial site into two parts.

$$U = U^{\text{int}} + U^{\text{ext}}. \quad (136)$$

The first part is the internal, bonded potential U^{int} which is used for the generation of trial orientations. The second part of the potential, the external potential U^{ext} , is used to bias the selection of a site from the set of trial sites. This bias is exactly removed by adjusting the acceptance rules. In the CBMC technique a molecule is grown segment-by-segment. For each segment we generate a set of k trial orientations according to the internal energy U^{int} and compute the external energy $U_i^{\text{ext}}(j)$ of each trial position j of segment i . In this work the number of trial positions k for both NVT and μ VT is set to 10. We select one of these trial positions with a probability

$$P_i(j) = \frac{e^{-\beta U_i^{\text{ext}}(j)}}{\sum_{l=1}^k e^{-\beta U_i^{\text{ext}}(l)}} = \frac{e^{-\beta U_i^{\text{ext}}(j)}}{w(i)}. \quad (137)$$

The selected trial orientation is added to the chain and the procedure is repeated until the entire molecule has been grown. For this newly grown molecule we compute the so-called Rosenbluth factor

$$W^{\text{new}} = \prod_i w(i). \quad (138)$$

To compute the old Rosenbluth factor W^{old} of an already existing chain, $k - 1$ trial orientations are generated for each segment. These orientations, together with the already existing bond, form the set of k trial orientations. In a dynamic scheme, a Markov chain of states is generated. The average of a property is the average of over the elements of the Markov chain. For an infinite Markov chain the expression is exact. Every new configuration is accepted or rejected using an acceptance/rejection rule.

We have defined μ^{ex} as the difference in chemical potential of the interacting alkane and an alkane in the ideal gas state. The Rosenbluth weight $\langle W^{\text{IG}} \rangle$ of the reference state of the ideal gas is needed when comparing with real experimental data. When CBMC is used, it is straightforward to show that $e^{-\beta \Delta U}$ has to be replaced by $\frac{W(\text{new chain})}{W(\text{IG})}$ for inserting a particle and by $\frac{W(\text{IG})}{W(\text{old chain})}$ for the deletion of a particle. There are two ways to obey detailed balance:

- Every time a transfer attempt to and from the reservoir, the Rosenbluth factor W^{IG} is computed. Because the particle reservoir is an ideal gas, there are only intramolecular interactions present.
- Detailed balance is also obeyed when W^{IG} is replaced by $\langle W^{\text{IG}} \rangle$, i.e. the *average* Rosenbluth weight of a chain in the reservoir. This implies that $\langle W^{\text{IG}} \rangle$ has to be computed only *once* for a given molecule and temperature.

E Monte-Carlo moves

Several Monte Carlo moves can be employed during a simulation.

- Displacement move

A chain is selected at random and given a random displacement. The maximum displacement is taken such that 50% of the moves is accepted. The acceptance rule is

$$\text{acc}(\text{old} \rightarrow \text{new}) = \min\left(1, e^{-\beta(U^{\text{new}} - U^{\text{old}})}\right). \quad (139)$$

Note that the energy of the new configuration U^{new} and the energy of the old configuration U^{old} only differ in the external energy.

- Rotation move

A chain is selected at random and given a random rotation. The center of the rotation is the center of mass. The maximum rotation angle is selected such that 50% of the moves are accepted. The acceptance rule is given by Eq. 139. Again, the energy of the new configuration U^{new} and the energy of the old configuration U^{old} only differ in the external energy.

- Insertion move

A chain is grown at a random position. The acceptance rule for insertion of the particle is given by

$$\text{acc}(N \rightarrow N + 1) = \min\left(1, \frac{W^{\text{new}} \beta V}{N + 1} \frac{f}{\langle W^{\text{IG}} \rangle}\right). \quad (140)$$

- Deletion move

A chain is chosen at a random position and the old Rosenbluth factor is computed. The acceptance rule for deletion of the particle is given by

$$\text{acc}(N \rightarrow N - 1) = \min\left(1, \frac{N}{W^{\text{old}} \beta V} \frac{\langle W^{\text{IG}} \rangle}{f}\right). \quad (141)$$

- Full regrow move

A chain is selected at random and is completely regrown at a random position. This move is essential for N, V, T to change the internal configuration of a molecule, and during this move data for the average Rosenbluth weight can be collected. The acceptance rule for full regrow is given by

$$\text{acc}(\text{old} \rightarrow \text{new}) = \min\left(1, \frac{W^{\text{new}}}{W^{\text{old}}}\right). \quad (142)$$

- Partial regrow move

A chain is selected at random and part of the molecule is regrown. It is decided at random which part of the chain is regrown and with which segment the regrown is started. The acceptance rule for partial regrow is given by Eq. 142.

- Identity change move (mixtures)

The identity-change trial move is called semi-grand ensemble, but it can also be seen as a special case of the Gibbs ensemble. One of the components is selected at random and an attempt is made to change its identity. The acceptance rule is given by

$$\text{acc}(A \rightarrow B) = \min \left(1, \frac{W^{\text{new}} f_B \langle W_A^{\text{IG}} \rangle N_A}{W^{\text{old}} f_A \langle W_B^{\text{IG}} \rangle (N_B + 1)} \right), \quad (143)$$

where f_A and f_B are the fugacities of components A and B , and N_A and N_B are the number of particles.

The relative probabilities for attempting these moves were such that in the NVT -simulations 10% of the total number of moves were displacements, 10% rotations, 10% partial regrowths, and 70% regrowths of the entire molecule. For the case of grand-canonical simulations of the pure components the distribution of moves was: 15% displacements, 15% rotations, 15% partial regrowths, and 55% exchanges with the reservoir. For alkane mixtures the number of exchanges was reduced to 50% and the remaining 5% of the moves were attempts to change the identity of a molecule.

V Molecular dynamics (MD)

In MD successive configurations of the system are generated by integrating Newton's laws of motion. Newton's second law states $\mathbf{f} = m\mathbf{a}$, where \mathbf{f} is the force exerted on the particle, m the mass of the particle, and \mathbf{a} its acceleration. Integration of the equations of motion then yields a trajectory that describes the positions, velocities and accelerations of the particles as they vary with time. The Verlet algorithm is probably the most widely used method for integrating the equations of motion in a molecular dynamics simulation and is also our method of choice.

$$\mathbf{r}(t + \Delta t) = \mathbf{r}(t) + \mathbf{v}(t)\Delta t + \frac{\mathbf{f}(t)}{2m}\Delta^2 t \quad (144)$$

$$\mathbf{v}(t + \Delta t) = \mathbf{v}(t) + \frac{\mathbf{f}(t) + \mathbf{f}(t + \Delta t)}{2m}\Delta t \quad (145)$$

We can compute the new velocities only after we have computed the new positions and, from these, the new forces. The algorithm is fast, requires little memory (only \mathbf{r} , \mathbf{v} , \mathbf{f} are stored), is time reversible (as are Newton's equations), phase-space area-preserving, and exhibits little long time energy drift. To test the energy drift ΔE of the numerical integration algorithm for a given time step Δt after M integration steps, one usually computes

$$\Delta E(\Delta t) = \frac{1}{M} \sum_{i=1}^{i=M} \left| \frac{E(0) - E(i\Delta t)}{E(0)} \right| < 10^{-3}. \quad (146)$$

After equilibration, we perform the actual measurements by determining the average values of properties from the trajectories of the particles. The ergodic hypothesis states that ensemble averages can be obtained from time averages. A system is ergodic when every accessible point in configuration space can be reached in a finite number of steps from any other phase space. In practice, the ergodic hypothesis applies to systems with low free energy barriers.

The self-diffusion coefficients D_S^α in the direction $\alpha = x, y, z$ are computed by taking the slope of the mean-squared displacement (msd) at long times

$$D_S^\alpha = \frac{1}{2N} \lim_{t \rightarrow \infty} \frac{d}{dt} \left\langle \sum_{i=1}^N (r_{i\alpha}(t) - r_{i\alpha}(0))^2 \right\rangle \quad (147)$$

where N is the number of molecules, t the time, and $r_{i\alpha}$ the α -component of the center-of-mass of molecule i . Equivalently, D_α is given by the time integral of the velocity autocorrelation function

$$D_S^\alpha = \frac{1}{N} \int_0^\infty \left\langle \sum_{i=1}^N v_{i\alpha}(t) v_{i\alpha}(0) \right\rangle dt \quad (148)$$

where $v_{i\alpha}$ is the α -component of the center-of-mass-velocity of molecule i . A separation of time scales occurs for interacting particles roughly at the times between particle-particle and particle-zeolite collisions. The mean-squared displacement thus bends over to attain a different slope, and we are interested in the long-time diffusion coefficient. The collective diffusion coefficients D_C^α are given by

$$D_C^\alpha = \frac{1}{2N} \lim_{t \rightarrow \infty} \frac{d}{dt} \left\langle \left(\sum_{i=1}^N (r_{i\alpha}(t) - r_{i\alpha}(0)) \right)^2 \right\rangle \quad (149)$$

and

$$D_C^\alpha = \frac{1}{N} \int_0^\infty \left\langle \left(\sum_{i=1}^N v_{i\alpha}(t) \right) \left(\sum_{i=1}^N v_{i\alpha}(0) \right) \right\rangle dt \quad (150)$$

Collective diffusivity measures the transport of mass and the decay of density fluctuations in the system, while self-diffusion measures the diffusive motion of a single particle. The directionally averaged diffusion coefficient is given by

$$D = \frac{D_x + D_y + D_z}{3} \quad (151)$$

The calculation of the diffusion coefficients requires much memory and CPU power, especially when fluctuations decay slowly. The order- n algorithm to measure correlations allows us to measure fast and slow dynamics simultaneously at minimal computational cost by using adjustable sampling frequencies [1]. The order- n scheme is equally accurate as the conventional scheme but the saving in memory as well as CPU time is significant for computing the mean-squared displacements at long times.

In a conventional NVE Molecular Dynamics simulation, the total energy E , the number of particles N , and the volume V are constant. Hence, MD measures (time) averages in the microcanonical ensemble, while in a conventional Monte-Carlo simulation the canonical ensemble (NVT-ensemble) is probed. The extended Lagrangian approach has become one of the most important tricks for MD in the NVT ensemble and is completely dynamic in origin. The Nosé-Hoover Chain (NHC) formulation extends the Lagrangian with additional coordinates and velocities containing the system to a constant temperature NVT-ensemble. We use the NHC method as implemented by Martyna et al. [102] in which the dynamics is still reversible. The instantaneous kinetic temperature fluctuates, but the probability to find the system in a given energy state follows the Maxwell-Boltzmann velocity probability distribution function

$$P(v_x, v_y, v_z) = \left(\frac{m}{2\pi k_B T} \right)^{3/2} \exp \left(\frac{-m(v_x^2 + v_y^2 + v_z^2)}{2k_B T} \right) \quad (152)$$

which reduces to

$$P(v_x) = \sqrt{\frac{m}{2\pi k_B T}} \exp\left(\frac{-mv_x^2}{2k_B T}\right) \quad (153)$$

for the case of a single direction.

For the instantaneous temperature we measure the total kinetic energy of the system and divide this by the number of degrees of freedom N_f ($= 3N - 3$ for a system of N particles with fixed total momentum)

$$k_B T(t) = \sum_{i=1}^N \frac{m_i v_i^2(t)}{N_f} \quad (154)$$

The disadvantage of most methods for working at constant temperature is that the dynamics is changed in an artificial way. Because in our simulations we do not have photons or electrons, i.e. the system is mechanical, heat is transported at the speed of sound or slower. However, most thermostat methods have a coupling constant, i.g. the masses of the NHC, and the effect of the thermostat on the particles is instantaneous. The NHC masses should therefore be chosen as large as possible to alter the dynamics as little as possible. If this is taken care of, the non-physical effects for dynamical properties will be of order $(1/N)$ in general.

To prepare the system at the desired temperature in an equilibrium configuration we initialize the system by the following procedure

- N molecules are inserted into the framework at random positions as long as no overlaps occur with the framework or other particles, and as long as the positions are accessible from the main cages and channels.
- During the initializing period we perform an NVT MC simulation to rapidly achieve an equilibrium molecular arrangement.
- After the initialization step, we assign all the atoms velocities from the Maxwell-Boltzmann distribution at the desired average temperature. The total momentum of the system is set to zero. Next, we equilibrate the system further by performing a NVT MD simulation using the NHC thermostat.
- The equilibration is completed and during the production run we collect statistics using either the NVE or NVT-ensemble. Following this equilibration procedure, the average temperature using NVE over the entire production period is usually within a few Kelvin of the desired average temperature, while NVT would give the exact desired average temperature if simulated sufficiently long.

VI Ewald summation in periodic frameworks

A Coulomb potential in periodic systems

Suppose there are N point charges q_1, q_2, \dots, q_N at positions $\mathbf{r}_1, \mathbf{r}_2, \dots, \mathbf{r}_N$ within the unit cell U satisfying $q_1 + q_2 + \dots + q_N = 0$. The vectors \mathbf{a}_α , which need not be orthogonal, form the edges of the unit cell. The conjugate reciprocal vectors \mathbf{a}_α^* are defined by the relations

$$\mathbf{a}_\alpha^* \cdot \mathbf{a}_\beta = \delta_{\alpha\beta} \quad \alpha, \beta = \{x, y, z\} \quad (155)$$

Let \mathbf{a} be the 3×3 matrix having the lattice vectors a_α as columns. Note that the volume V of the unit cell is given by the determinant of \mathbf{a} . Furthermore \mathbf{a}^{-1} is the 3×3 matrix having the reciprocal lattice vectors \mathbf{a}_α^* as rows.

The point charge q_i as position \mathbf{r}_i has fractional coordinates $s_{\alpha i}$ defined by

$$s_{\alpha i} = \mathbf{a}_\alpha^* \cdot \mathbf{r}_i \quad (156)$$

The charges interact according to Coulomb's law with periodic boundary conditions. Thus a point charge q_i at position \mathbf{r}_i interacts with all other charges q_j (with $j \neq i$) at positions \mathbf{r}_j as well as with all of their periodic images at positions $\mathbf{r}_j + n_1\mathbf{a}_1 + n_2\mathbf{a}_2 + n_3\mathbf{a}_3$ for all integers n_1, n_2, n_3 . It also interacts with its own periodic images at $\mathbf{r}_i + n_1\mathbf{a}_1 + n_2\mathbf{a}_2 + n_3\mathbf{a}_3$ for all integers n_1, n_2, n_3 not all zero.

The electrostatic energy of the unit cell U can then be written

$$E(\mathbf{r}_1, \dots, \mathbf{r}_N) = \frac{1}{2} \sum_{\mathbf{n}} \sum_{ij} \frac{q_i q_j}{|\mathbf{r}_i - \mathbf{r}_j + \mathbf{n}|} \quad (157)$$

where the outer sum is over the vectors $\mathbf{n} = n_1\mathbf{a}_1 + n_2\mathbf{a}_2 + n_3\mathbf{a}_3$, the prime indicating that terms with $i = j$ for $\mathbf{n} = 0$ are omitted.

We define the reciprocal lattice vectors \mathbf{k} by $\mathbf{k} = k_1\mathbf{a}_1^* + k_2\mathbf{a}_2^* + k_3\mathbf{a}_3^*$ with k_1, k_2, k_3 integers not all zero. We define the structure factor $S(\mathbf{k})$ by

$$S(\mathbf{k}) = \sum_{j=1}^N q_j \exp(2\pi i \mathbf{k} \cdot \mathbf{r}_j) \quad (158)$$

$$= \sum_{j=1}^N q_j \exp[2\pi i (k_1 s_{1j} + k_2 s_{2j} + k_3 s_{3j})] \quad (159)$$

The structure factor $S(\mathbf{k})$ can be viewed as a discrete Fourier transform of a set of charges placed irregularly within the unit cell.

The technique of Ewald summation is popular in molecular dynamics simulation, even though it applies to a special case: namely, true periodic systems. By this we mean that the simulation region or unit cell is effectively replicated in all spatial directions, so that particles leaving the cell reappear at the opposite boundary. For systems governed by a short-ranged potential - say Lennard-Jones or hard spheres - it is sufficient to take just the neighboring simulation volumes into account, leading to the *minimum image* configuration. The potential seen by the particle is summed over all other particles or their periodic images, whichever is closest. For long-range potentials this arrangement is inadequate because the contributions from more distant images at $2L, 3L$ etc, are no longer negligible. One might argue that these contributions should more or less cancel, which they nearly do, but one has to take care in which order to do the sum: a simple example serves to illustrate the problem. Consider a system of two oppositely charged ions, periodically extended to form an infinite one-dimensional line of charges, each separated by a distance R . The potential energy of the reference ion with charge $-q$ is:

$$\begin{aligned} U &= -2q^2 \left(\frac{1}{R} - \frac{1}{2R} + \frac{1}{3R} - \frac{1}{4R} \dots \right) \\ &= -\frac{2q^2}{R} \left(1 - \frac{1}{2} + \frac{1}{3} - \frac{1}{4} \dots \right) \\ &= -\frac{2q^2}{R} \log 2 \end{aligned} \quad (160)$$

The factor $2 \log 2$ is the Madelung constant, which is of central importance in the theory of ionic crystals. The series is actually *conditionally convergent*, i.e. the results depends on the summation order. We can choose a different ordering, for example

$$1 + \frac{1}{3} - \frac{1}{2} + \frac{1}{5} + \frac{1}{7} - \frac{1}{4} + \frac{1}{9} + \dots \quad (161)$$

that is, two positive terms followed by a negative term. Then it can be shown it now converges to $\frac{3}{2} \log 2$, giving a 50% higher potential energy then before! In three dimensions, determination of the Madelung constant - and hence the lattice potential energy - is non-trivial because successive terms in the series must be arranged so that positive and negative contributions nearly cancel. This is exactly the problem we are faced with: in what order should we sum over image boxes. An intuitive and elegant way of doing this is to build up sets of images contained within successively larger spheres surrounding the simulation region. According to this scheme the energy is expressed as in Eq. 157.

B Ewald Transformation

The total electrostatic potential energy of interaction between point charges q_i at the positions \mathbf{r}_i is given by

$$U = \frac{1}{4\pi\epsilon_0} \sum_{i < j} \frac{q_i q_j}{|\mathbf{r}_i - \mathbf{r}_j|} = \frac{1}{8\pi\epsilon_0} \sum_{i \neq j} \frac{q_i q_j}{|\mathbf{r}_i - \mathbf{r}_j|} \quad (162)$$

In this expression, the first form explicitly counts all pairs, while the second form counts all interactions and divides by 2 to compensate for double counting.

For a finite system of charges, this expression can be evaluated directly. However, for a large or infinite system, the expression does *not* converge and numerical tricks must be used to evaluate the energy. In fact, for the infinite system, one has an infinite amount of charge and the energy of interaction is undefined. If the system is neutral, it is possible to define a meaningful interaction energy by use of an Ewald transformation.

The basic idea of the Ewald approach is as follows. The error function $\text{erf}(x)$ and its complement are defined as:

$$\text{erf}(x) = \frac{2}{\sqrt{\pi}} \int_0^x e^{-t^2} dt \quad (163)$$

$$\text{erfc}(x) = 1 - \text{erf}(x) = \frac{2}{\sqrt{\pi}} \int_x^\infty e^{-t^2} dt \quad (164)$$

Ewald noted that

$$\frac{1}{r} = \frac{\text{erf}(\alpha r)}{r} + \frac{\text{erfc}(\alpha r)}{r} \quad (165)$$

In this expression, the first term goes to a constant $\left(\frac{2\alpha}{\sqrt{\pi}}\right)$ as $r \rightarrow 0$, but has a long tail as $r \rightarrow \infty$. The second term has a singular behavior as $r \rightarrow 0$, but vanishes exponentially as $r \rightarrow \infty$. Ewald's idea is to replace a single divergent summation with two convergent summations. The first summation has a convergent summation in the form of its Fourier transform and the second has a convergent direct summation. Thus the calculation of the electrostatic energy would be evaluated using:

$$U = \frac{1}{8\pi\epsilon_0} \sum_{i \neq j} \frac{q_i q_j}{|\mathbf{r}_i - \mathbf{r}_j|} = \frac{1}{8\pi\epsilon_0} \left(\sum_{i \neq j} \frac{q_i q_j \text{erf}(\alpha |\mathbf{r}_i - \mathbf{r}_j|)}{|\mathbf{r}_i - \mathbf{r}_j|} + \sum_{i \neq j} \frac{q_i q_j \text{erfc}(\alpha |\mathbf{r}_i - \mathbf{r}_j|)}{|\mathbf{r}_i - \mathbf{r}_j|} \right) \quad (166)$$

For an appropriate choice of the parameter α , the second summation converges quickly and can be evaluated directly. The first term in the summation must be transformed into Fourier space.

In order to describe these summations explicitly, we assume that we have a periodic lattice so that every ion can be located by $\mathbf{r}_i = \mathbf{r}'_i + \mathbf{n}$, i.e. a location \mathbf{r}'_i within a unit cell and a periodic translation vector \mathbf{n} . In this way, the summation becomes

$$\sum_{ij} = N \sum_{i,j,\mathbf{n}}, \quad (167)$$

where N denotes the number of unit cells in the system. Since we have a periodic system, N is infinite, but the energy per unit cell U/N is well defined. The other identity that we must use is that a sum over lattice translation \mathbf{n} may be transformed into an equivalent sum over reciprocal lattice translations \mathbf{k} according to the identity:

$$\sum_{\mathbf{n}} \delta^3(\mathbf{t} - \mathbf{n}) = \frac{1}{V} \sum_{\mathbf{k}} e^{i\mathbf{k}\cdot\mathbf{r}}, \quad (168)$$

where V denotes the unit cell volume.

The first term thus becomes

$$\sum_{i \neq j} \frac{q_i q_j \operatorname{erf}(\alpha |\mathbf{r}_i - \mathbf{r}_j|)}{|\mathbf{r}_i - \mathbf{r}_j|} = \sum_{i,j} \frac{q_i q_j \operatorname{erf}(\alpha |\mathbf{r}_i - \mathbf{r}_j|)}{|\mathbf{r}_i - \mathbf{r}_j|} - \sum_{i=j} \frac{q_i q_j \operatorname{erf}(\alpha |\mathbf{r}_i - \mathbf{r}_j|)}{|\mathbf{r}_i - \mathbf{r}_j|} \quad (169)$$

$$= N \left(\sum_{i,j} q_i q_j \sum_{\mathbf{n}} \frac{\operatorname{erf}(\alpha |\mathbf{r}_i - \mathbf{r}_j + \mathbf{n}|)}{|\mathbf{r}_i - \mathbf{r}_j + \mathbf{n}|} - \frac{2\alpha}{\sqrt{\pi}} \sum_i q_i^2 \right) \quad (170)$$

where the last term comes from subtracting out the self-interaction ($i = j$) term from the complete lattice sum. Using the short hand notation \mathbf{r}_{ij} , the lattice sum can be evaluated

$$\frac{1}{V} \sum_{\mathbf{k}} \int e^{i\mathbf{k}\cdot\mathbf{r}} \frac{\operatorname{erf}(\alpha |\mathbf{r}_{ij} + \mathbf{n}|)}{|\mathbf{r}_{ij} + \mathbf{n}|} d^3r = \frac{4\pi}{V} \left(\sum_{\mathbf{k} \neq 0} \frac{e^{-i\mathbf{k}\cdot\mathbf{r}_{ij}} e^{-\frac{k^2}{\alpha^2}}}{k^2} + \frac{1}{2} \int_0^\alpha \frac{1}{u^3} du \right) \quad (171)$$

where the last term, which is infinite, comes from the $\mathbf{k} = 0$ contribution.

If the last term cannot be eliminated, it is clear that the electrostatic energy is infinite. The term can be eliminated if and only if the system is neutral. taking all the terms into account, we find the final Ewald expression to be

$$\frac{U}{V} = \sum_{i,j} \frac{q_i q_j}{8\pi\epsilon_0} \left(\frac{4\pi}{V} \sum_{\mathbf{k} \neq 0} \frac{e^{-i\mathbf{k}\cdot\mathbf{r}_{ij}} e^{-k^2/\alpha^2}}{k^2} - \frac{2\alpha}{\sqrt{\pi}} \delta_{ij} + \sum_{\mathbf{n}} \frac{\operatorname{erfc}(\alpha |\mathbf{r}_{ij} + \mathbf{n}|)}{|\mathbf{r}_{ij} + \mathbf{n}|} \right) \quad (172)$$

where the ' in the summation over the lattice translations \mathbf{n} indicates that all self-interaction terms should be omitted.

C General formulism

Consider a finite system of interacting molecules possessing atomic charges, dipoles, and anisotropic polarizabilities. We will start by focusing on the total potential energy of such a system arising from the long-range Coulomb and dipole interactions including

induction effects. Throughout, the Einstein summation convention is used for Greek letter indices. We employ the interactions tensors

$$\mathcal{T}_{ij} = \frac{1}{r_{ij}} \quad (173)$$

$$\mathcal{T}_{ij}^\alpha = \nabla_\alpha \mathcal{T}_{ij} = -\frac{r_{ij,\alpha}}{r_{ij}^3} \quad (174)$$

$$\mathcal{T}_{ij}^{\alpha\beta} = \nabla_\alpha \nabla_\beta \mathcal{T}_{ij} = \frac{3r_{ij,\alpha}r_{ij,\beta}}{r_{ij}^5} - \frac{\delta_{\alpha\beta}}{r_{ij}^3} \quad (175)$$

$$\mathcal{T}_{ij}^{\alpha\beta\gamma} = \nabla_\alpha \nabla_\beta \nabla_\gamma \mathcal{T}_{ij} = -\frac{15r_{ij,\alpha}r_{ij,\beta}r_{ij,\gamma}}{r_{ij}^7} + \frac{3(\delta_{\alpha\beta}r_{ij,\gamma} + \delta_{\alpha\gamma}r_{ij,\beta} + \delta_{\beta\gamma}r_{ij,\alpha})}{r_{ij}^5} \quad (176)$$

Here, $r_{ij,\alpha} = r_{j\alpha} - r_{i\alpha}$, where $r_{i\alpha}$ is the α -component of the position vector atom i . We define $\mathcal{T}_{ij} = \mathcal{T}_{ij}^\alpha = \mathcal{T}_{ij}^{\alpha\beta} = \mathcal{T}_{ij}^{\alpha\beta\gamma} \equiv 0$ when atoms i and j belong to the same molecule.

In addition, we define

$$\widehat{\mathcal{T}}_{ij} = \frac{\text{erfc}(\alpha r_{ij})}{r_{ij}} \quad (177)$$

$$\widehat{\mathcal{T}}_{ij}^\alpha = \nabla_\alpha \widehat{\mathcal{T}}_{ij} = -\left(\frac{2\alpha e^{-\alpha^2 r_{ij}^2}}{\sqrt{\pi} r_{ij}^2} + \frac{\text{erfc}(\alpha r_{ij})}{r_{ij}^3}\right) r_{ij,\alpha} \quad (178)$$

$$\begin{aligned} \widehat{\mathcal{T}}_{ij}^{\alpha\beta} = \nabla_\alpha \nabla_\beta \widehat{\mathcal{T}}_{ij} = & \left(\frac{6\alpha e^{-\alpha^2 r_{ij}^2}}{\sqrt{\pi} r_{ij}^4} + \frac{4\alpha^3 e^{-\alpha^2 r_{ij}^2}}{\sqrt{\pi} r_{ij}^2} + \frac{3\text{erfc}(\alpha r_{ij})}{r_{ij}^5}\right) r_{ij,\alpha} r_{ij,\beta} \\ & - \delta_{\alpha\beta} \left(\frac{2\alpha e^{-\alpha^2 r_{ij}^2}}{\sqrt{\pi} r_{ij}^2} + \frac{\text{erfc}(\alpha r_{ij})}{r_{ij}^3}\right) \end{aligned} \quad (179)$$

$$\begin{aligned} \widehat{\mathcal{T}}_{ij}^{\alpha\beta\gamma} = \nabla_\alpha \nabla_\beta \nabla_\gamma \widehat{\mathcal{T}}_{ij} \\ = -\left(\frac{30\alpha e^{-\alpha^2 r_{ij}^2}}{\sqrt{\pi} r_{ij}^6} + \frac{20\alpha^3 e^{-\alpha^2 r_{ij}^2}}{\sqrt{\pi} r_{ij}^4} + \frac{8\alpha^5 e^{-\alpha^2 r_{ij}^2}}{\sqrt{\pi} r_{ij}^2} + \frac{15\text{erfc}(\alpha r_{ij})}{r_{ij}^7}\right) r_{ij,\alpha} r_{ij,\beta} r_{ij,\gamma} \\ + \delta_{\alpha\beta} \left(\frac{6\alpha e^{-\alpha^2 r_{ij}^2}}{\sqrt{\pi} r_{ij}^4} + \frac{3\text{erfc}(\alpha r_{ij})}{r_{ij}^5}\right) r_{ij,\gamma} + \delta_{\alpha\gamma} \left(\frac{6\alpha e^{-\alpha^2 r_{ij}^2}}{\sqrt{\pi} r_{ij}^4} + \frac{3\text{erfc}(\alpha r_{ij})}{r_{ij}^5}\right) r_{ij,\beta} \\ + \delta_{\beta\gamma} \left(\frac{6\alpha e^{-\alpha^2 r_{ij}^2}}{\sqrt{\pi} r_{ij}^4} + \frac{3\text{erfc}(\alpha r_{ij})}{r_{ij}^5}\right) r_{ij,\alpha} \end{aligned} \quad (180)$$

and define

$$\widetilde{\mathcal{T}}_{ij} = \frac{\text{erfc}(\alpha d_{ij})}{d_{ij}} \quad (181)$$

$$\widetilde{\mathcal{T}}_{ij}^\alpha = \nabla_\alpha \widetilde{\mathcal{T}}_{ij} = -\left(\frac{2\alpha e^{-\alpha^2 d_{ij}^2}}{\sqrt{\pi} d_{ij}^2} + \frac{\text{erfc}(\alpha d_{ij})}{d_{ij}^3}\right) d_{ij,\alpha} \quad (182)$$

$$\begin{aligned} \widetilde{\mathcal{T}}_{ij}^{\alpha\beta} = \nabla_\alpha \nabla_\beta \widetilde{\mathcal{T}}_{ij} = & \left(\frac{6\alpha e^{-\alpha^2 d_{ij}^2}}{\sqrt{\pi} d_{ij}^4} + \frac{4\alpha^3 e^{-\alpha^2 d_{ij}^2}}{\sqrt{\pi} d_{ij}^2} + \frac{3\text{erfc}(\alpha d_{ij})}{d_{ij}^5}\right) d_{ij,\alpha} d_{ij,\beta} \\ & - \delta_{\alpha\beta} \left(\frac{2\alpha e^{-\alpha^2 d_{ij}^2}}{\sqrt{\pi} d_{ij}^2} + \frac{\text{erfc}(\alpha d_{ij})}{d_{ij}^3}\right) \end{aligned} \quad (183)$$

$$\begin{aligned}
\tilde{\mathcal{T}}_{ij}^{\alpha\beta\gamma} &= \nabla_\alpha \nabla_\beta \nabla_\gamma \tilde{\mathcal{T}}_{ij} \\
&= - \left(\frac{30\alpha e^{-\alpha^2 d_{ij}^2}}{\sqrt{\pi} d_{ij}^6} + \frac{20\alpha^3 e^{-\alpha^2 d_{ij}^2}}{\sqrt{\pi} d_{ij}^4} + \frac{8\alpha^5 e^{-\alpha^2 d_{ij}^2}}{\sqrt{\pi} d_{ij}^2} + \frac{15 \operatorname{erfc}(\alpha d_{ij})}{d_{ij}^7} \right) d_{ij,\alpha} d_{ij,\beta} d_{ij,\gamma} \\
&\quad + \delta_{\alpha\beta} \left(\frac{6\alpha e^{-\alpha^2 d_{ij}^2}}{\sqrt{\pi} d_{ij}^4} + \frac{3 \operatorname{erfc}(\alpha d_{ij})}{d_{ij}^5} \right) d_{ij,\gamma} + \delta_{\alpha\gamma} \left(\frac{6\alpha e^{-\alpha^2 d_{ij}^2}}{\sqrt{\pi} d_{ij}^4} + \frac{3 \operatorname{erfc}(\alpha d_{ij})}{d_{ij}^5} \right) d_{ij,\beta} \\
&\quad + \delta_{\beta\gamma} \left(\frac{6\alpha e^{-\alpha^2 d_{ij}^2}}{\sqrt{\pi} d_{ij}^4} + \frac{3 \operatorname{erfc}(\alpha d_{ij})}{d_{ij}^5} \right) d_{ij,\alpha}
\end{aligned} \tag{184}$$

where d_{ij} is the intramolecular distance between atom i and j .

After a generalization of the approach by Veseley, the total potential energy of a set of atoms possessing charges, dipoles, and anisotropic polarizabilities can be expressed as

$$\begin{aligned}
U &= U_{\text{int}} + U_{\text{pol}} \\
U_{\text{int}} &= \underbrace{\frac{1}{2} \sum_{i,j \neq i} q_i \mathcal{T}_{ij} q_j}_{\text{charge-charge}} + \underbrace{q_i \mathcal{T}_{ij}^\alpha \mu_{j,\alpha}}_{\text{charge-total dipole}} - \underbrace{\mu_{i,\alpha} \mathcal{T}_{ij}^\alpha q_j}_{\text{total dipole-charge}} - \underbrace{\mu_{i,\alpha} \mathcal{T}_{ij}^{\alpha\beta} \mu_{j,\beta}}_{\text{total dipole-total dipole}} \\
U_{\text{pol}} &= \frac{1}{2} \sum_i \mu_{i,\alpha}^{\text{ind}} \alpha_{i,\alpha\beta}^{-1} \mu_{i,\beta}^{\text{ind}}
\end{aligned} \tag{185}$$

where q_i is the charge on atom i , $\mu_{i,\alpha}$ the α -component of the total dipole moment of atom i , $\mu_{i,\alpha}^{\text{ind}}$ the α -component of the induced dipole moment of atom i , and $\alpha_{i,\alpha\beta}$ the $\alpha\beta$ -component of the polarizability tensor of atom i . The Einstein summation convention is used for Greek indices.

In Eq. 185 the four terms in U_{int} represent the charge-charge, the charge-total dipole, the total dipole-charge, and the total dipole-total dipole interaction respectively, whereas U_{pol} represents the work of forming the induced dipoles. The total dipole moment of atom i is given by

$$\mu_{i,\alpha} = \mu_{i,\alpha}^{\text{stat}} + \mu_{i,\alpha}^{\text{ind}}, \tag{186}$$

where $\mu_{i,\alpha}^{\text{stat}}$ denotes the α -component of the permanent (static) dipole moment of atom i .

By introducing a infinitesimal test charge ∂q at \mathbf{r} , the electrostatic potential at \mathbf{r} is defined according to

$$\phi(\mathbf{r}) \equiv \lim_{\delta q \rightarrow 0} \frac{\partial U}{\partial \delta q} \tag{187}$$

where U is the potential energy of the system including the test charge. The α -component of the electrostatic field is defined as

$$E_\alpha(\mathbf{r}) \equiv -\frac{\partial \phi(\mathbf{r})}{\partial r_\alpha}, \tag{188}$$

and the $\alpha\beta$ -component of the electric field gradient at \mathbf{r} as

$$E_{\alpha\beta}(\mathbf{r}) \equiv \frac{\partial E_\alpha(\mathbf{r})}{\partial r_\beta}. \tag{189}$$

The inclusion of the test charge in the summation of Eq. 185 and the application of Eqs. 187-189 on Eq. 185 gives the electrostatic potential, field, and field gradients. The corresponding quantities on atom i become (after omission of any self-terms):

$$\phi_i \equiv \phi(\mathbf{r}_i) = \sum_{j \neq i} \left(\mathcal{T}_{ij} q_j + \mathcal{T}_{ij}^\alpha \mu_{j,\alpha} \right), \quad (190)$$

$$E_{i,\alpha} \equiv E_\alpha(\mathbf{r}_i) = \sum_{j \neq i} \left(\mathcal{T}_{ij}^\alpha q_j + \mathcal{T}_{ij}^{\alpha\beta} \mu_{j,\beta} \right), \quad (191)$$

$$E_{i,\alpha\beta} \equiv E_{\alpha\beta}(\mathbf{r}_i) = - \sum_{j \neq i} \left(\mathcal{T}_{ij}^{\alpha\beta} q_j + \mathcal{T}_{ij}^{\alpha\beta\gamma} \mu_{j,\gamma} \right). \quad (192)$$

The induced dipole moments are determined by a minimization of U with respect to $\mu_{i,\alpha}^{\text{ind}}$, and we get

$$\mu_{i,\alpha}^{\text{ind}} = \alpha_{i,\alpha\beta} E_{i,\beta}, \quad (193)$$

where $E_{i,\alpha}$ is the α -component of the electrostatic field on atom i arising from other charges and total dipole moments as given by Eq. 191.

The potential energy is often separated into two physically appealing contributions: an electrostatic and an induction term. With the use of Eq. 186 and 193, Eq. 185 can be recast according to

$$U = U_{\text{elec}} + U_{\text{ind}} \quad (194)$$

where the electrostatic energy is given by

$$U_{\text{elec}} = \frac{1}{2} \sum_i \left(q_i \phi_i^{\text{stat}} - \mu_{i,\alpha}^{\text{stat}} E_{i,\alpha}^{\text{stat}} \right), \quad (195)$$

and the induction energy by

$$U_{\text{ind}} = - \frac{1}{2} \sum_i \mu_{i,\alpha}^{\text{ind}} E_{i,\alpha}^{\text{stat}}, \quad (196)$$

with ϕ_i^{stat} denoting the electrostatic potential and $E_{i,\alpha}^{\text{stat}}$ the α -component of the electrostatic field at atom i arising from other charges and static dipoles. The quantities ϕ_i^{stat} and $E_{i,\alpha}^{\text{stat}}$ are obtained from Eq. 190 and Eq. 191 by replacing $\mu_{j,\alpha}$ with $\mu_{j,\alpha}^{\text{stat}}$ according to

$$\phi_i^{\text{stat}} = \sum_{j \neq i} \left(\mathcal{T}_{ij} q_j + \mathcal{T}_{ij}^\alpha \mu_{j,\alpha}^{\text{stat}} \right), \quad (197)$$

and

$$E_{i,\alpha}^{\text{stat}} = \sum_{j \neq i} \left(\mathcal{T}_{ij}^\alpha q_j + \mathcal{T}_{ij}^{\alpha\beta} \mu_{j,\beta}^{\text{stat}} \right). \quad (198)$$

By taking the derivative of the total potential energy U given by Eq. 185 with respect to the position of atom i and noting that U is stationary with respect to variation of $\mu_{i,\alpha}^{\text{ind}}$, we obtain the α -component of the force on atom i arising from its interaction with atom j according to

$$f_{ij,\alpha} = q_i \mathcal{T}_{ij}^\alpha q_j + q_i \mathcal{T}_{ij}^{\alpha\beta} \mu_{j,\beta} - \mu_{i,\beta} \mathcal{T}_{ij}^{\beta\alpha} q_j - \mu_{i,\beta} \mathcal{T}_{ij}^{\beta\alpha\gamma} \mu_{j,\gamma}. \quad (199)$$

The α -component of the total force acting on atom i can conveniently be expressed as

$$f_{i,\alpha} = \sum_{j \neq i} f_{ij,\alpha} = q_i E_{i,\alpha} + \mu_{i,\beta} E_{i,\beta\alpha}, \quad (200)$$

where $E_{i,\alpha}$ is the α -component of the electrostatic field and $E_{i,\alpha\beta}$ the $\alpha\beta$ -component of the field gradient on atom i arising from other charges and total dipole moments as given by Eq. 191 and Eq. 192, respectively.

Finally, the virial Φ , which enters the expression for the pressure, $p = p_{\text{ideal}} - \Phi/3V$, is given by

$$\Phi = 3V \left\langle \frac{\partial U}{\partial V} \right\rangle, \quad (201)$$

where V denotes the volume of the system. Consider first the general case of pairwise interactions according to $U = \frac{1}{2} \sum_{i,j \neq i} u(r_{ij})$. The application of the Anderson scaling relation for cubic systems, $\mathbf{r}_{ij} = V^{1/3} \boldsymbol{\rho}_{pp'} + \mathbf{d}_i - \mathbf{d}_j$, where $\boldsymbol{\rho}_{pp'}$ is a scaled and volume independent center-of-mass-center-of-mass vector between molecules p and p' ($i \in p$ and $j \in p'$) and \mathbf{d}_i the location of atom i relative to the center-of-mass of its molecule, leads to

$$\begin{aligned} \Phi &= \frac{1}{2} \sum_{i,j \neq i} r_{ij} \frac{\partial u(r_{ij})}{\partial r_{ij}} - \frac{1}{2} \sum_{i,j \neq i} (\mathbf{d}_i - \mathbf{d}_j) \cdot \mathbf{r}_{ij} \frac{1}{r_{ij}} \frac{\partial u(r_{ij})}{\partial r_{ij}} \\ &= -\frac{1}{2} \sum_{i,j \neq i} \mathbf{r}_{ij} \cdot \mathbf{f}_{ij} + \sum_i \mathbf{d}_i \cdot \mathbf{f}_i \end{aligned} \quad (202)$$

where $\mathbf{f}_{ij} = -\nabla u(r_{ij}) = -(\mathbf{r}_{ij}/r_{ij}) \partial u(r_{ij})/\partial r_{ij}$ denotes the pairwise force and $\mathbf{f}_i = \sum_{j \neq i} \mathbf{f}_{ij}$ the total force acting on atom i . With the same approach applied on Eq. 185, we find that the virial for a molecular system composed of charges, static, and induced dipole moments formally is also given by

$$\Phi = -\frac{1}{2} \sum_{i,j \neq i} \mathbf{r}_{ij} \cdot \mathbf{f}_{ij} + \sum_i \mathbf{d}_i \cdot \mathbf{f}_i, \quad (203)$$

but with \mathbf{f}_{ij} and \mathbf{f}_i now given by Eq. 199 and Eq. 200, respectively.

In numerical applications, the procedure for calculating the electrostatic and induction contributions of the energy, forces, and the virial in a molecular system, where each molecule is described by atomic charges, dipole moments, and anisotropic polarizabilities, can be outlined as follows

1. Calculate the electrostatic potential ϕ_i^{stat} and the electrostatic field $E_{i,\alpha}^{\text{stat}}$ from charges and static dipole moments, according to Eq. 197 and Eq. 198, respectively.
2. Calculate the induced dipole moments $\mu_{i,\alpha}^{\text{ind}}$ either by prediction, or self-consistent iteration using Eq. 193 and $E_{i,\alpha} = E_{i,\alpha}^{\text{stat}} + E_{i,\alpha}^{\text{ind}}$ with $E_{i,\alpha}^{\text{ind}} = \sum_{j \neq i} \mathcal{T}_{ij}^{\alpha\beta} \mu_{j,\beta}^{\text{ind}}$.
3. Calculate the electrostatic energy U_{elec} and the induction energy U_{ind} from Eq. 195 and Eq. 196, respectively.
4. If the induced dipole moments were predicted above, calculate $E_{i,\alpha}^{\text{ind}}$.
5. Calculate the electrostatic field gradient $E_{i,\alpha\beta}$ from charges and total dipole moments according to Eq. 192.
6. Calculate the forces $f_{i,\alpha}$ from Eq. 200.
7. Calculate the virial Φ from Eq. 203.

The procedure is so far general in the sense that it is valid for a finite system with an arbitrary cutoff.

When applying truly periodic boundary conditions, the summations over $j \neq i$ are replaced by infinite lattice sums. These are conveniently evaluated by using the Ewald summation technique. In this approach a Gaussian charge distribution of equal magnitude and opposite sign is surrounding each charge making the interactions short-ranged. Of course, canceling charge distributions are also added, and after a Fourier transformation their contribution is readily given in a closed expression. In the Ewald formalism, the expression of a given property is conventionally divided into four different terms viz. (i) a real term arising from the short-range interaction in the real space, (ii) a reciprocal term arising from the long-range interaction in the reciprocal space (iii) a self-term correcting an overcounting in the reciprocal space, and (iv) a surface term appearing in systems with nonconducting surroundings.

In this section expressions will be provided for U , ϕ_i , $E_{i,\alpha}$, $E_{i,\alpha\beta}$, $f_{i,\alpha}$ and Φ for a truly infinite periodic system of charges, static dipoles, and anisotropic polarizabilities. The expressions correctly reduce to those for systems of only charges, or of only dipoles.

We define the volume $V = L_x L_y L_z$, where L_x , L_y , and L_z denote the lengths of the box edges. We define A_k according to

$$A_k = \frac{1}{k^2} e^{-\frac{k^2}{4\alpha^2}}, \quad (204)$$

and $Q^{q\mu}$ according to

$$\begin{aligned} Q^{q\mu} &= Q^q + Q^\mu \\ Q^q &= \sum_j q_j e^{-i\mathbf{k}\cdot\mathbf{r}_j} \\ Q^\mu &= Q^{\mu(\text{stat})} + Q^{\mu(\text{ind})} \\ &= \sum_j i \left(\boldsymbol{\mu}_j^{\text{stat}} \cdot \mathbf{k} \right) + \sum_j i \left(\boldsymbol{\mu}_j^{\text{ind}} \cdot \mathbf{k} \right) e^{i\mathbf{k}\cdot\mathbf{r}_j}, \end{aligned} \quad (205)$$

where $i^2 \equiv -1$. We will use $\bar{Q}^{q\mu}$ for the complex conjugate of $Q^{q\mu}$. The vector \mathbf{k} is defined as

$$\mathbf{k} = 2\pi \left(\frac{n_x}{L_x}, \frac{n_y}{L_y}, \frac{n_z}{L_z} \right), \quad (206)$$

where $\mathbf{n} = (n_x, n_y, n_z)$ is a vector of integers.

the potential energy For a system of charges, static dipoles, and anisotropic polarizabilities in an infinite lattice, the potential energy can be written as

$$\begin{aligned}
U = & \underbrace{\frac{1}{2} \sum_{i,j \neq i} \left(q_i \widehat{\mathcal{T}}_{ij} q_j + q_i \widehat{\mathcal{T}}_{ij}^{\alpha} \mu_{j,\alpha} - \mu_{i,\alpha} \widehat{\mathcal{T}}_{ij}^{\alpha} q_j - \mu_{i,\alpha} \widehat{\mathcal{T}}_{ij}^{\alpha\beta} \mu_{j,\beta} \right)}_{\text{Real part}} + \underbrace{\frac{2\pi}{V} \sum_{\mathbf{k} \neq 0} A_{\mathbf{k}} |Q^{q\mu}|^2}_{\text{Reciprocal part}} \\
& - \underbrace{\sum_i \left(\frac{\alpha}{\sqrt{\pi}} q_i^2 + \frac{2\alpha^3}{3\sqrt{\pi}} \mu_i^2 \right) - \frac{1}{2} \sum_p \sum_{i,j \neq i; j \in p} \left(q_i \widetilde{\mathcal{T}}_{ij} q_j + q_i \widetilde{\mathcal{T}}_{ij}^{\alpha} \mu_{j,\alpha} - \mu_{i,\alpha} \widetilde{\mathcal{T}}_{ij}^{\alpha} q_j - \mu_{i,\alpha} \widetilde{\mathcal{T}}_{ij}^{\alpha\beta} \mu_{j,\beta} \right)}_{\text{Self part}} \\
& + \underbrace{\frac{2\pi}{(2\epsilon_{\text{sur}} + 1)V} \left[\left(\sum_i q_i \mathbf{r}_i \right)^2 + 2 \left(\sum_i q_i \mathbf{r}_i \right) \cdot \left(\sum_j \boldsymbol{\mu}_j \right) + \left(\sum_i \boldsymbol{\mu}_i \right)^2 \right]}_{\text{Surface part}} + U_{\text{pol}}
\end{aligned} \tag{207}$$

where the four terms are the real, the reciprocal, the self, and the surface contribution, respectively, to the potential energy and U_{pol} represents the work of forming the induced dipoles.

In Eq. 207, U_{real} is obtained from Eq. 185 after considering the screening of the charges and the dipoles by the Gaussian distributions. Formally this is done by introducing the modified interactions tensors $\widehat{\mathcal{T}}$. In practice, this surmounts to replacing $r^{-(2n+1)}$, $n \in \{0, 1, 2, 3\}$, in the interaction energy expressions by its screened counterpart $\widehat{r^{-(2n+1)}}$, where

$$\frac{\widehat{1}}{r} = \frac{\text{erfc}(\alpha r)}{r} \tag{208}$$

and

$$\frac{\widehat{1}}{r^{2n+1}} = \frac{1}{r^2} \left[\frac{\widehat{1}}{r^{2n-1}} + \frac{(2\alpha^2)^n}{\sqrt{\pi}\alpha(2n-1)} e^{-\alpha^2 r^2} \right], \tag{209}$$

for $n > 0$. Note that this can straightforwardly be extended to higher order moments through the use of the recursion formula Eq. 209. From Eq. 207 and on, we assume that the Ewald convergence parameter α is chosen such that the screening is sufficiently large to ensure that only particles in the primary box need to be considered when calculating the real space sum. In the self-term U_{self} , the single sum over i is always present. In the remaining part, the index p runs over all particles and the notation $i, j \in p$ means that atomic sites i and j both reside within particle p . Hence, the double sum over i and j contributes only if atom i and j belongs to the same particle.

Finally, the surface term U_{sur} originates from the total dipole moment of the simulation box. The quantity ϵ_{sur} entering in U_{sur} is the dielectric constant of the continuum surrounding the replicated sample, and is often chosen to be either ∞ (tin foil conditions) or 1 (vacuum conditions). For systems such as ionic and dipolar ones, where long-range interactions are important, Ewald summation with tin foil boundary conditions corresponds to the physically most desirable situation.

The general energy expression reduces correctly for systems consisting of (i) only charges by setting $\boldsymbol{\mu}^{\text{stat}} = \boldsymbol{\mu}^{\text{ind}} = 0$ and (ii) only dipoles by setting $q = 0$ and $\boldsymbol{\mu}^{\text{ind}} = 0$.

the electrostatic potential The electrostatic potential on atom i arising from other charges and total dipole moments is obtained from Eq. 207, and becomes

$$\phi_i = \underbrace{\sum_{j \neq i} \left(\widehat{\mathcal{T}}_{ij} q_j + \widehat{\mathcal{T}}_{ij}^{\alpha} \mu_{j,\alpha} \right)}_{\text{real part}} + \underbrace{\frac{4\pi}{V} \sum_{\mathbf{k} \neq 0} A_k \text{Re} \left(e^{i\mathbf{k} \cdot \mathbf{r}_i} \bar{Q}^{q\mu} \right)}_{\text{reciprocal part}} - \underbrace{\frac{2\alpha}{\sqrt{\pi}} q_i - \sum_{j \neq i; j \in p} \left(\widetilde{\mathcal{T}}_{ij} q_j + \widetilde{\mathcal{T}}_{ij}^{\alpha} \mu_{j,\alpha} \right)}_{\text{self-term}} + \underbrace{\frac{4\pi}{(2\epsilon_{\text{sur}} + 1)V} \left[\mathbf{r}_i \cdot \sum_j \left(q_j \mathbf{r}_j + \boldsymbol{\mu}_j \right) \right]}_{\text{surface part}} \quad (210)$$

For systems of only atoms the sum in the self-term vanishes. For a system of charge neutral molecules we may write the surface term as

$$\phi_i^{\text{sur}} = -\frac{2\pi}{(2\epsilon_{\text{sur}} + 1)V} \sum_j \left[q_j (\mathbf{r}_j - \mathbf{r}_i)^2 + 2\boldsymbol{\mu}_i \cdot (\mathbf{r}_j - \mathbf{r}_i) \right]. \quad (211)$$

the electrostatic field Similarly, the expression for the corresponding α -component of the electrostatic field on atom i is obtained from Eq. 207, and we get

$$E_{i,\alpha} = \underbrace{\sum_{j \neq i} \left(\widehat{\mathcal{T}}_{ij}^{\alpha} q_j + \widehat{\mathcal{T}}_{ij}^{\alpha\beta} \mu_{j,\beta} \right)}_{\text{real part}} - \underbrace{\frac{4\pi}{V} \sum_{\mathbf{k} \neq 0} A_k k_{\alpha} \left[\text{Re} \left(i e^{i\mathbf{k} \cdot \mathbf{r}_i} \bar{Q}^{q\mu} \right) - \mu_{i,\beta} k_{\beta} \right]}_{\text{reciprocal part}} + \frac{4\pi}{3V} \mu_{i,\alpha} - \underbrace{\sum_{j \neq i; j \in p} \left(\widetilde{\mathcal{T}}_{ij}^{\alpha} q_j + \widetilde{\mathcal{T}}_{ij}^{\alpha\beta} \mu_{j,\beta} \right)}_{\text{self part}} - \underbrace{\frac{4\pi}{(2\epsilon_{\text{sur}} + 1)V} \sum_j \left(q_j r_{j,\alpha} + \mu_{j,\alpha} \right)}_{\text{surface part}} \quad (212)$$

In particular, for a system consisting of only charges the reciprocal term reduces to

$$E_{i,\alpha}^{\text{rec}} = -\frac{4\pi}{V} \sum_{\mathbf{k} \neq 0} A_k k_{\alpha} \text{Re} \left(i e^{i\mathbf{k} \cdot \mathbf{r}_i} \bar{Q}^q \right), \quad (213)$$

and for a system of only static dipoles it becomes

$$E_{i,\alpha}^{\text{rec}} = -\frac{4\pi}{V} \sum_{\mathbf{k} \neq 0} A_k k_{\alpha} \left[\text{Re} \left(i e^{i\mathbf{k} \cdot \mathbf{r}_i} \bar{Q}^{\mu(\text{stat})} \right) - \mu_{i,\beta}^{\text{stat}} k_{\beta} \right] + \frac{4\pi}{3V} \mu_{i,\alpha}^{\text{stat}} \quad (214)$$

where Q^q and $Q^{\mu(\text{stat})}$ were defined in Eq. 205. For an atomic system, the self term is zero. The α -component of the electrostatic field on atom i arising from other induced dipoles only, $E_{i,\alpha}^{\text{ind}}$, is needed later, and it is obtained from Eq. 212 by setting $Q_i = 0$ and by replacing $\mu_{i,\alpha}$ by $\mu_{i,\alpha}^{\text{ind}}$ and $Q^{q\mu}$ by $Q^{\mu(\text{ind})}$.

For the finite system, it can be shown after some algebra that (i) the induced dipole moments are still given by Eq. 193, but $E_{i,\alpha}$ is now given by Eq. 212, and (ii) the potential energy can again be separated into an electrostatic and induction term according to Eq. 194. The electrostatic term U_{ele} is still given by Eq. 195 and the induction term by Eq. 196, but ϕ_i^{stat} and $E_{i,\alpha}^{\text{stat}}$ are now given by Eq. 210 and Eq. 212, respectively, after replacing $\mu_{i,\alpha}$ with $\mu_{i,\alpha}^{\text{stat}}$ and $Q^{q\mu}$ by $Q^q + Q^{\mu(\text{stat})}$.

the electrostatic gradient The $\alpha\beta$ -component of the field gradient i on atom i is similarly obtained from Eq. 207, and it is given by

$$E_{i,\alpha\beta} = \underbrace{-\sum_{j \neq i} \left(\widehat{\mathcal{T}}_{ij}^{\alpha\beta} q_j + \widehat{\mathcal{T}}_{ij}^{\alpha\beta\gamma} \mu_{j,\gamma} \right)}_{\text{real part}} + \underbrace{\frac{4\pi}{V} \sum_{\mathbf{k} \neq 0} A_k k_\alpha k_\beta \left[\text{Re} \left(e^{i\mathbf{k} \cdot \mathbf{r}_i} \bar{Q}^{q\mu} \right) - q_i \right] - \frac{4\pi}{3V} q_i \delta_{\alpha\beta}}_{\text{reciprocal part}} + \underbrace{\sum_{j \neq i, j \in p} \left(\widetilde{\mathcal{T}}_{ij}^{\alpha\beta} q_j + \widetilde{\mathcal{T}}_{ij}^{\alpha\beta\gamma} \mu_{j,\gamma} \right)}_{\text{self term}} \quad (215)$$

For an atomic system, the self-term is zero. We note that $E_{i,\alpha\beta}^{\text{sur}}$ is zero.

the force The expressions for the α -component of the force on atom i is also readily available from Eq. 207 by taking its derivative with respect to $r_{i,\alpha}$. After some algebra, we get

$$f_{i,\alpha} = \underbrace{\sum_{j \neq i} \left(q_i \widehat{\mathcal{T}}_{ij}^\alpha q_j + q_i \widehat{\mathcal{T}}_{ij}^{\alpha\beta} \mu_{j,\beta} - \mu_{i,\beta} \widehat{\mathcal{T}}_{ij}^{\beta\alpha} q_j - \mu_{i,\beta} \widehat{\mathcal{T}}_{ij}^{\beta\alpha\gamma} \mu_{j,\gamma} \right)}_{\text{real part}} - \underbrace{\frac{4\pi}{V} \sum_{\mathbf{k} \neq 0} A_k k_\alpha \text{Re} \left[(iq_i - \mu_{i,\beta} k_\beta) e^{i\mathbf{k} \cdot \mathbf{r}_i} \bar{Q}^{q\mu} \right]}_{\text{reciprocal part}} - \underbrace{\sum_{j \neq i, j \in p} \left(q_i \widetilde{\mathcal{T}}_{ij}^\alpha q_j + q_i \widetilde{\mathcal{T}}_{ij}^{\alpha\beta} \mu_{j,\beta} - \mu_{i,\beta} \widetilde{\mathcal{T}}_{ij}^{\beta\alpha} q_j - \mu_{i,\beta} \widetilde{\mathcal{T}}_{ij}^{\beta\alpha\gamma} \mu_{j,\gamma} \right)}_{\text{self part}} - \underbrace{\frac{4\pi}{(2\epsilon_{\text{sur}} + 1)V} q_i \sum_j (q_j r_{j,\alpha} + \mu_{j,\alpha})}_{\text{surface part}} \quad (216)$$

Now, one can show that the use of $E_{i,\alpha}$ given by Eq. 212 and $E_{i,\alpha\beta}$ given by Eq. 215 leads exactly to Eq. 200. Moreover, Eq. 200 holds term wise. For a system consisting of only charges the reciprocal term reduces to

$$f_{i,\alpha}^{\text{rec}} = \frac{4\pi}{V} \sum_{\mathbf{k} \neq 0} A_k k_\alpha q_i \text{Im} \left[e^{i\mathbf{k} \cdot \mathbf{r}_i} \bar{Q}^q \right], \quad (217)$$

and for a system consisting of only static dipoles we have

$$f_{i,\alpha}^{\text{rec}} = \frac{4\pi}{V} \sum_{\mathbf{k} \neq 0} A_k k_\alpha k_\beta \mu_{i,\beta}^{\text{stat}} \text{Re} \left[e^{i\mathbf{k} \cdot \mathbf{r}_i} \bar{Q}^{\mu(\text{stat})} \right]. \quad (218)$$

We notice that the self-term is not constant due to the presence of $\mu_{i,\alpha}$. For an atomic system, the self-term is zero.

the virial Starting with Eq. 201 and Eq. 207, the virial is separated according to

$$\Phi = \Phi^{\text{real}} + \Phi^{\text{rec}} + \Phi^{\text{self}} + \Phi^{\text{sur}}. \quad (219)$$

With the help of Eq. 203, the real contribution to the virial can be expressed directly as

$$\Phi^{\text{real}} = -\frac{1}{2} \sum_{i,j \neq i} \mathbf{r}_{ij} \cdot \mathbf{f}_{ij} + \sum_i \mathbf{d}_{ij} \cdot \mathbf{f}_i^{\text{real}}, \quad (220)$$

where $\mathbf{f}_i^{\text{real}}$ is given by the first term of Eq. 216. In order to get the reciprocal contribution, we apply the scaling relation $\mathbf{r}_i = V^{1/3} \boldsymbol{\rho}_p + \mathbf{d}_i$, where $\boldsymbol{\rho}_p$ is a scaled and volume independent center-of-mass vector for molecule p ($i \in p$) and we note similarly that \mathbf{k} is volume independent. The use of U^{rec} and the derivatives

$$\frac{\partial A_k}{\partial V} = \frac{2}{3V} \left(1 + \frac{k^2}{4\alpha^2} \right) A_k \quad (221)$$

and

$$\frac{\partial |Q^{q\mu}|^2}{\partial V} = -\frac{2}{3V} \text{Re} \left[\left(Q^\mu + \sum_i \mathbf{k} \cdot \mathbf{d}_i (iq_i - \boldsymbol{\mu} \cdot \mathbf{k}) e^{i\mathbf{k} \cdot \mathbf{r}_i} \right) \bar{Q}^{q\mu} \right], \quad (222)$$

leads after some manipulations to

$$\Phi^{\text{rec}} = -\frac{4\pi}{V} \sum_{\mathbf{k} \neq 0} A_k \left[\text{Re} (Q^\mu \bar{Q}^{q\mu}) + \frac{1}{2} |Q^{q\mu}|^2 \left(1 - \frac{k^2}{2\alpha^2} \right) \right] + \sum_i \mathbf{d}_i \cdot \mathbf{f}_i^{\text{rec}}, \quad (223)$$

where $\mathbf{f}_{ij}^{\text{rec}}$ is defined by the second term of Eq. 216. In the polyatomic case a self-term arises, which is given by

$$\Phi^{\text{self}} = -\frac{1}{2} \sum_p \sum_{i,j \in p} \mathbf{d}_{ij} \cdot \mathbf{f}_{ij}^{\text{self}} \quad (224)$$

where $\mathbf{f}_{ij}^{\text{self}}$ is given by the third term of Eq. 216. In the case of a monoatomic system, the self contribution vanishes.

The surface term is obtained by substituting U_{sur} given by Eq. 207 into Eq. 201 according to

$$\Phi^{\text{sur}} = 3V \left[\frac{\partial U^{\text{sur},qq}}{\partial V} + \frac{\partial U^{\text{sur},q\mu}}{\partial V} + \frac{\partial U^{\text{sur},\mu\mu}}{\partial V} \right] \quad (225)$$

with

$$U^{\text{sur},qq} \equiv \frac{2\pi}{(2\epsilon_{\text{sur}} + 1)V} \left(\sum_i q_i \mathbf{r}_i \right)^2, \quad (226)$$

$$U^{\text{sur},q\mu} \equiv \frac{4\pi}{(2\epsilon_{\text{sur}} + 1)V} \left(\sum_i q_i \mathbf{r}_i \right) \cdot \left(\sum_j \boldsymbol{\mu}_j \right), \quad (227)$$

$$U^{\text{sur},\mu\mu} \equiv \frac{2\pi}{(2\epsilon_{\text{sur}} + 1)V} \left(\sum_i \boldsymbol{\mu}_i \right)^2 \quad (228)$$

With the scaling relation $\mathbf{r}_i = V^{1/3} \boldsymbol{\rho}_p + \mathbf{d}_i$, we get

$$\begin{aligned} \Phi^{\text{sur}} &= - \left(U^{\text{sur},qq} + 2U^{\text{sur},q\mu} + 3U^{\text{sur},\mu\mu} + \frac{4\pi}{(2\epsilon_{\text{sur}} + 1)V} \left[\left(\sum_j (q_j \mathbf{r}_j + \boldsymbol{\mu}_j) \right) \cdot \sum_i q_i \mathbf{d}_i \right] \right) \\ &= - (U^{\text{sur},qq} + 2U^{\text{sur},q\mu} + 3U^{\text{sur},\mu\mu}) + \sum_i \mathbf{d}_i \cdot \mathbf{f}_i^{\text{sur}} \end{aligned} \quad (229)$$

where $\mathbf{f}_i^{\text{sur}}$ is given by the fourth term if Eq. 216.

Hence, the substitution of Eq. 220, 223, 224, and 229 into Eq. 219 gives the final expression of the virial according to

$$\begin{aligned} \Phi &= \underbrace{-\frac{1}{2} \sum_{i,j \neq i} \mathbf{r}_{ij} \cdot \mathbf{f}_{ij}^{\text{real}}}_{\text{real part}} \underbrace{-\frac{4\pi}{V} \sum_{\mathbf{k} \neq 0} A_k \left[\text{Re} (Q^\mu \bar{Q}^{q\mu}) + \frac{1}{2} |Q^{q\mu}|^2 \left(1 - \frac{k^2}{2\alpha^2} \right) \right]}_{\text{reciprocal part}} \\ &\quad \underbrace{-\frac{1}{2} \sum_p \sum_{i,j \in p} \mathbf{d}_{ij} \cdot \mathbf{f}_{ij}^{\text{self}}}_{\text{self part}} \underbrace{-(U^{\text{sur},qq} + 2U^{\text{sur},q\mu} + 3U^{\text{sur},\mu\mu})}_{\text{surface part}} + \sum_i \mathbf{d}_i \cdot (\mathbf{f}_i^{\text{real}} + \mathbf{f}_i^{\text{rec}} + \mathbf{f}_i^{\text{sur}}) \end{aligned} \quad (230)$$

D Charge only systems

The expressions of the previous section reduce to the familiar ones for systems consisting of only charges. They are easily incorporated into the usual Ewald summation routines.

the potential energy The potential energy can be written as

$$U = U^{\text{real}} + U^{\text{rec}} + U^{\text{self}} \quad (231)$$

where

$$\begin{aligned} U^{\text{real}} &= \frac{1}{2} \sum_{i,j \neq i} q_i \hat{\mathcal{T}}_{ij} q_j \\ &= \frac{1}{2} \sum_{i,j \neq i} q_i q_j \frac{\text{erfc}(\alpha r_{ij})}{r_{ij}} \\ U^{\text{rec}} &= \frac{2\pi}{V} \sum_{\mathbf{k} \neq 0} A_k |Q^q|^2 \\ &= \frac{2\pi}{V} \sum_{\mathbf{k} \neq 0} \frac{1}{k^2} e^{-\frac{k^2}{4\alpha^2}} \left(\left| \sum_{i=1}^N q_i \cos(\mathbf{k} \cdot \mathbf{r}_i) \right|^2 + \left| \sum_{i=1}^N q_i \sin(\mathbf{k} \cdot \mathbf{r}_i) \right|^2 \right) \\ U^{\text{self}} &= - \sum_i \frac{\alpha}{\sqrt{\pi}} q_i^2 \end{aligned} \quad (232)$$

the electrostatic potential The electrostatic potential in atom i arising from other charges is given by

$$\phi_i = \phi_i^{\text{real}} + \phi_i^{\text{rec}} + \phi_i^{\text{self}} \quad (233)$$

where

$$\begin{aligned}
\phi_i^{\text{real}} &= \sum_{i,j \neq i} \hat{\mathcal{T}}_{ij} q_j \\
&= \frac{1}{2} \sum_{j \neq i} q_j \frac{\text{erfc}(\alpha r_{ij})}{r_{ij}} \\
\phi_i^{\text{rec}} &= \frac{4\pi}{V} \sum_{\mathbf{k} \neq 0} A_k \text{Re} (e^{i\mathbf{k} \cdot \mathbf{r}_i} \bar{Q}^q) \\
&= \frac{4\pi}{V} \sum_{\mathbf{k} \neq 0} \frac{1}{k^2} e^{-\frac{k^2}{4\alpha^2}} \left[\cos(\mathbf{k} \cdot \mathbf{r}_i) \sum_{j=1}^N q_j \cos(\mathbf{k} \cdot \mathbf{r}_j) + \sin(\mathbf{k} \cdot \mathbf{r}_i) \sum_{j=1}^N q_j \sin(\mathbf{k} \cdot \mathbf{r}_j) \right] \\
\phi_i^{\text{self}} &= -\frac{2\alpha}{\sqrt{\pi}} q_i
\end{aligned} \tag{234}$$

the electrostatic field The α -component of the electrostatic field on atom i is given by

$$E_{i,\alpha} = E_{i,\alpha}^{\text{real}} + E_{i,\alpha}^{\text{rec}} \tag{235}$$

where

$$\begin{aligned}
E_{i,\alpha}^{\text{real}} &= -\sum_{j \neq i} \hat{\mathcal{T}}_{ij}^{\alpha} q_j \\
&= \sum_{j \neq i} q_j \left(\frac{2\alpha e^{-\alpha^2 r_{ij}^2}}{\sqrt{\pi}} + \frac{\text{erfc}(\alpha r_{ij})}{r_{ij}} \right) \frac{r_{ij,\alpha}}{r_{ij}^2} \\
E_{i,\alpha}^{\text{rec}} &= -\frac{4\pi}{V} \sum_{\mathbf{k} \neq 0} A_k k_{\alpha} \text{Re} (i e^{i\mathbf{k} \cdot \mathbf{r}_i} \bar{Q}^q) \\
&= \frac{4\pi}{V} \sum_{\mathbf{k} \neq 0} \frac{1}{k^2} e^{-\frac{k^2}{4\alpha^2}} k_{\alpha} \left[\sin(\mathbf{k} \cdot \mathbf{r}_i) \sum_j q_j \cos(\mathbf{k} \cdot \mathbf{r}_j) - \cos(\mathbf{k} \cdot \mathbf{r}_i) \sum_j q_j \sin(\mathbf{k} \cdot \mathbf{r}_j) \right]
\end{aligned} \tag{236}$$

the electrostatic field gradient The $\alpha\beta$ -component of the field gradient on atom i is given by

$$E_{i,\alpha\beta} = E_{i,\alpha\beta}^{\text{real}} + E_{i,\alpha\beta}^{\text{rec}} \tag{237}$$

where

$$\begin{aligned}
E_{i,\alpha\beta}^{\text{real}} &= - \sum_{j \neq i} \hat{T}_{ij}^{\alpha\beta} q_j \\
&= - \sum_{j \neq i} q_j \left(\frac{6\alpha e^{-\alpha^2 r_{ij}^2}}{\sqrt{\pi} r_{ij}^2} + \frac{4\alpha^3 e^{-\alpha^2 r_{ij}^2}}{\sqrt{\pi}} + \frac{3\text{erfc}(\alpha r_{ij})}{r_{ij}^3} \right) \frac{r_{ij,\alpha} r_{ij,\beta}}{r_{ij}^2} \\
&\quad + \delta_{\alpha\beta} \sum_{j \neq i} q_j \left(\frac{2\alpha e^{-\alpha^2 r_{ij}^2}}{\sqrt{\pi}} + \frac{\text{erfc}(\alpha r_{ij})}{r_{ij}} \right) \frac{1}{r_{ij}^2} \\
E_{i,\alpha\beta}^{\text{rec}} &= \frac{4\pi}{V} \sum_{\mathbf{k} \neq 0} A_k k_\alpha k_\beta [\text{Re}(e^{-i\mathbf{k} \cdot \mathbf{r}_i} \bar{Q}^{q\mu}) - q_i] - \frac{4\pi}{3V} q_i \delta_{\alpha\beta} \\
&= \frac{4\pi}{V} \sum_{\mathbf{k} \neq 0} \frac{1}{k^2} e^{-\frac{k^2}{4\alpha^2}} k_\alpha k_\beta \left[\cos(\mathbf{k} \cdot \mathbf{r}_i) \sum_{j=1}^N q_j \cos(\mathbf{k} \cdot \mathbf{r}_j) + \sin(\mathbf{k} \cdot \mathbf{r}_i) \sum_{j=1}^N q_j \sin(\mathbf{k} \cdot \mathbf{r}_j) - q_i \right] \\
&\quad - \frac{4\pi}{3V} q_i \delta_{\alpha\beta}
\end{aligned} \tag{238}$$

the force The α -component of the force on atom i is given by

$$f_{i,\alpha} = f_{i,\alpha}^{\text{real}} + f_{i,\alpha}^{\text{rec}} \tag{239}$$

where

$$\begin{aligned}
f_{i,\alpha}^{\text{real}} &= - \sum_{j \neq i} q_i \hat{T}_{ij}^\alpha q_j \\
&= q_i \sum_{j \neq i} q_j \left(\frac{2\alpha e^{-\alpha^2 r_{ij}^2}}{\sqrt{\pi}} + \frac{\text{erfc}(\alpha r_{ij})}{r_{ij}} \right) \frac{r_{ij,\alpha}}{r_{ij}^2} \\
f_{i,\alpha}^{\text{rec}} &= \frac{4\pi}{V} \sum_{\mathbf{k} \neq 0} A_k k_\alpha q_i \text{Im}(e^{i\mathbf{k} \cdot \mathbf{r}_i} \bar{Q}^q) \\
&= q_i \frac{4\pi}{V} \sum_{\mathbf{k} \neq 0} \frac{1}{k^2} e^{-\frac{k^2}{4\alpha^2}} k_\alpha \left[\sin(\mathbf{k} \cdot \mathbf{r}_i) \sum_j q_j \cos(\mathbf{k} \cdot \mathbf{r}_j) - \cos(\mathbf{k} \cdot \mathbf{r}_i) \sum_j q_j \sin(\mathbf{k} \cdot \mathbf{r}_j) \right]
\end{aligned} \tag{240}$$

example In this case study we have four particles at different positions and with different charges. We are interested in the electrostatic potential, the electric field, the force, and the electric field gradient at the positions of the particles, which will be of vital value for future exploration of electric field-dependent potentials in molecular simulations. In addition, the electrostatic field and the electrostatic field gradients are also quantities of their own importance in spectroscopy, e.g. NMR quadrupole relaxation. In Fig. 2(a) we have four particles at which positions we would like to evaluate the electric properties. When there are more than two particles present, we must supplement Coulomb's law with the principle of superposition. That's all there is to electrostatics. The properties of a particle in Fig. 2(a) is given by the superposition of the fields of the other three particles (Fig. 2(b)) evaluated at the position of the chosen particle. The charges are taken to be static. Electricity and magnetism are distinct phenomena as long as charges and currents are static.

\mathbf{r}_i	q	potential	electric field	force	field gradient
(-1,0)	0.5	-0.664214	$\begin{pmatrix} 0.332107 \\ -0.176777 \\ 0 \end{pmatrix}$	$\begin{pmatrix} 0.166053 \\ -0.0883883 \\ 0 \end{pmatrix}$	$\begin{pmatrix} -0.0214466 & -0.265165 & 0 \\ -0.265165 & 0.541053 & 0 \\ 0 & 0 & -0.519607 \end{pmatrix}$
(1,0)	1.5	-1.16421	$\begin{pmatrix} -0.582107 \\ -0.176777 \\ 0 \end{pmatrix}$	$\begin{pmatrix} -0.87316 \\ -0.265165 \\ 0 \end{pmatrix}$	$\begin{pmatrix} 0.228553 & 0.265165 & 0 \\ 0.265165 & 0.416053 & 0 \\ 0 & 0 & -0.644607 \end{pmatrix}$
(0,1)	-0.75	0.789214	$\begin{pmatrix} -0.353553 \\ 0.394607 \\ 0 \end{pmatrix}$	$\begin{pmatrix} 0.265165 \\ -0.295955 \\ 0 \end{pmatrix}$	$\begin{pmatrix} -0.509803 & 0.53033 & 0 \\ 0.53033 & -0.0410534 & 0 \\ 0 & 0 & 0.550857 \end{pmatrix}$
(0,-1)	-1.25	1.03921	$\begin{pmatrix} -0.353553 \\ -0.519607 \\ 0 \end{pmatrix}$	$\begin{pmatrix} 0.441942 \\ 0.649508 \\ 0 \end{pmatrix}$	$\begin{pmatrix} -0.447303 & -0.53033 & 0 \\ -0.53033 & -0.166053 & 0 \\ 0 & 0 & 0.613357 \end{pmatrix}$

Table 4: Electrostatics case study: 4 ions. The potential energy $U_{\text{pot}} = -1.98467$.

\mathbf{r}_i	q	potential	electric field	force	field gradient
(-1,0)	0.5	0.21967	$\begin{pmatrix} -0.109835 \\ 0.265165 \\ 0 \end{pmatrix}$	$\begin{pmatrix} -0.0549175 \\ 0.132583 \\ 0 \end{pmatrix}$	$\begin{pmatrix} -0.242417 & 0.397748 & 0 \\ 0.397748 & 0.320083 & 0 \\ 0 & 0 & -0.077665 \end{pmatrix}$
(0,-1)	-1.25	0.68566	$\begin{pmatrix} -0.53033 \\ -0.34283 \\ 0 \end{pmatrix}$	$\begin{pmatrix} 0.662913 \\ 0.428538 \\ 0 \end{pmatrix}$	$\begin{pmatrix} -0.358915 & -0.795495 & 0 \\ -0.795495 & -0.077665 & 0 \\ 0 & 0 & 0.43658 \end{pmatrix}$
(1,0)	1.5	-0.633883	$\begin{pmatrix} -0.316942 \\ -0.441942 \\ 0 \end{pmatrix}$	$\begin{pmatrix} -0.475413 \\ -0.662913 \\ 0 \end{pmatrix}$	$\begin{pmatrix} 0.0959709 & 0.662913 & 0 \\ 0.662913 & 0.283471 & 0 \\ 0 & 0 & -0.379442 \end{pmatrix}$
(0,1)	-0.75	-0.271447	$\begin{pmatrix} 0.176777 \\ -0.135723 \\ 0 \end{pmatrix}$	$\begin{pmatrix} -0.132583 \\ 0.101792 \\ 0 \end{pmatrix}$	$\begin{pmatrix} -0.244638 & -0.265165 & 0 \\ -0.265165 & 0.224112 & 0 \\ 0 & 0 & 0.0205267 \end{pmatrix}$

Table 5: Electrostatics case study: two molecules. The Potential energy $U_{\text{pot}} = -0.745882$.

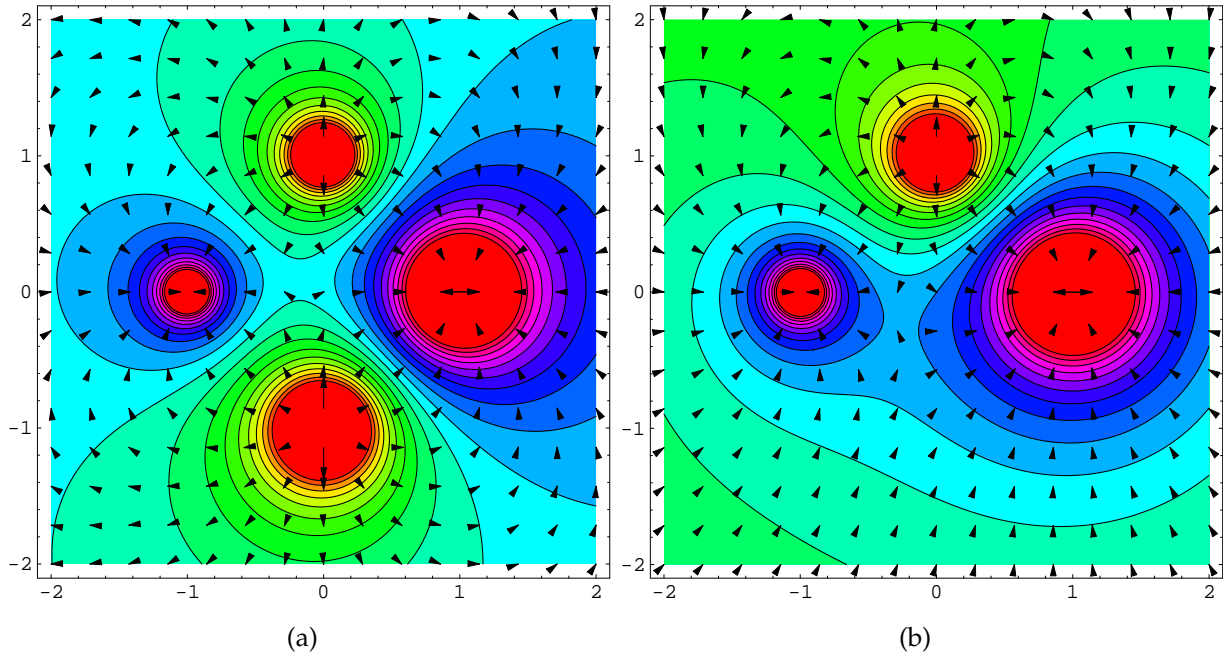


Figure 2: (a) Two positively charged ions: $q = 0.5$ at $(-1, 0)$ and $q = 1.5$ at $(1, 0)$ and two negatively charged ions: $q = -0.75$ at $(0, 1)$ and $q = -1.25$ at $(0, -1)$, (b) Two positively charged ions: $q = 0.5$ at $(-1, 0)$ and $q = 1.5$ at $(1, 0)$ and one negatively charged ion: $q = -0.75$ at $(0, 1)$.

E Electric-field dependent potentials

Let us consider a system of N charged particles, interacting with each other via a potential energy function depending on their positions and on the electric field acting upon each of them and generated by other particles (which also depend on the positions of the particles):

$$U = U(\mathbf{r}_1, \dots, \mathbf{r}_N | \mathbf{E}_1, \dots, \mathbf{E}_N) = U(\{\mathbf{r}_i\} | \{\mathbf{E}_j\}) \quad (i, j = 1, \dots, N) \quad (241)$$

where \mathbf{r}_i are the positions of the particles and \mathbf{E}_i are the electric fields. The force acting on a particle i is given by

$$\mathbf{f}_i = -\frac{\partial U}{\partial \mathbf{r}_i} = -\left(\frac{\partial U}{\partial \mathbf{r}_i}\right)_{\mathbf{E}} - \sum_j \frac{\partial U}{\partial \mathbf{E}_j} \frac{\partial \mathbf{E}_j}{\partial \mathbf{r}_i} \quad (242)$$

where \mathbf{E} stands for $\{\mathbf{E}_j\}$. In particular, it is worth to note that the terms in Eq. 242 including the $3N \times 3N$ matrix,

$$\frac{\partial \mathbf{E}_j}{\partial \mathbf{r}_i} \quad (243)$$

corresponds to many-body forces involving in principle *all* the particles of the system as it is better illustrated if the atom pair approximation is assumed. In this approximation, the potential energy is represented by the sum of pairwise interactions $U_p(\mathbf{r}_{ij} | \mathbf{E})$ between i and j . Therefore Eq. 242 and Eq. 243 become

$$U = \sum_i \sum_{j>i} U_p(\mathbf{r}_{ij} | \mathbf{E}) \quad (244)$$

$$\mathbf{f}_i = -\left(\sum_{j>i} \frac{\partial U_p(\mathbf{r}_{ij} | \mathbf{E})}{\partial \mathbf{r}_i}\right)_{\mathbf{E}} - \sum_{j>i} \frac{\partial U_p(\mathbf{r}_{ij} | \mathbf{E})}{\partial \mathbf{E}_i} \frac{\partial \mathbf{E}_i}{\partial \mathbf{r}_i} - \sum_{k \neq i} \sum_{j>k} \frac{\partial U_p(\mathbf{r}_{kj} | \mathbf{E})}{\partial \mathbf{E}_k} \frac{\partial \mathbf{E}_k}{\partial \mathbf{r}_i} \quad (245)$$

where, again, \mathbf{E} stands for $\{\mathbf{E}_i\}$ and the terms containing the electric field gradients have been grouped in two sums, the former including the gradient of the electric field acting on particle i for which the force is calculated, and the latter including the gradient of the electric field *acting on all the other particles multiplied by the derivatives, with respect to these electric fields, of the potential function terms involving particle j , even though these terms do not include explicitly any interaction with the particle i* . It is worthy to note that in general the last group of terms is not zero: indeed it ensured that the third law of the dynamics (as generalized for many-body forces) is obeyed.

VII Rigid Frameworks

A Pressure and Stress

There is no unique definition of the internal stress or pressure of framework system. The pressure of a system in space with periodic boundary conditions is defined in terms of the molecular virial

$$\mathcal{W} = \frac{1}{3} \sum_{i=1}^N \sum_{j \neq i}^N \mathbf{R}_{ij} \cdot \mathbf{F}_{ij} \quad (246)$$

But the framework has no center-of-mass, and so the quantity \mathbf{R}_{ij} can not be defined. The site-virial is of no assistance as the definition of the "internal" coordinate $\mathbf{p}_{i\alpha}$ involves the center-of-mass coordinate \mathbf{R}_i . Neither can one simply choose a convenient reference \mathbf{R}_i . Since the force exerted by a fluid acting on the framework is in general non-zero, the term

$$\sum_i \sum_{\alpha} \mathbf{p}_{i\alpha} \mathbf{f}_{i\alpha} = \sum_i \sum_{\alpha} \mathbf{r}_{i\alpha} \mathbf{f}_{i\alpha} - \sum_i \mathbf{R}_i \mathbf{F}_i \quad (247)$$

clearly depends on \mathbf{R}_i . The situation may also be viewed physically. The definition of pressure of a system is the derivative of the free energy with respect to volume. But with an infinite rigid framework the volume derivative can not be defined.

The useful quantity in this case is the partial pressure of the fluid. The partial pressure is that pressure it would exert if it would occupied the entire volume by itself. Dalton's law states that the total pressure exerted by a mixture is the sum of the partial pressures of the components.

B Charged Frameworks

A minor complication arises when using a framework which has a non-zero net electric charge. Although the system a whole may be electrically neutral, the omission of framework-framework interactions from the calculation also means the Ewald Fourier-contributions should be splitted into separate net-charged sums. Not only the interactions of a framework atoms with other framework atoms should be omitted, but also the interactions with all its images.

Splitting of the potential energy into separate contribution involves computing cross terms between component \mathcal{A} and \mathcal{B} . In real space this is trivially accomplished, but the reciprocal separation is more difficult. Cross term interaction energies in reciprocal space

are given by

$$U_{\mathcal{A},\mathcal{B}}^{\text{rec}} = \frac{2\pi}{V} \sum_{\mathbf{k} \neq 0} \frac{1}{k^2} e^{-\frac{k^2}{4\alpha^2}} \left[\left(\sum_{i \in \mathcal{A}} q_i \cos(\mathbf{k} \cdot \mathbf{r}_i) \right) \left(\sum_{i \in \mathcal{B}} q_i \cos(\mathbf{k} \cdot \mathbf{r}_i) \right) + \left(\sum_{i \in \mathcal{A}} q_i \sin(\mathbf{k} \cdot \mathbf{r}_i) \right) \left(\sum_{i \in \mathcal{B}} q_i \sin(\mathbf{k} \cdot \mathbf{r}_i) \right) \right]. \quad (248)$$

It is important to note that Eq. 248 only applies when both the separate sums over species A and B are charge neutral. This is in general not the case. For example, in Monte-Carlo adsorption simulations one often encounters a negatively charged zeolite charge-compensated by either cations or protons. All-silica zeolites devoid of cations are neutral, but framework ions as aluminum induce a net-charge.

It is custom to treat charged periodic systems via a uniform neutralizing background plasma. However, this leads to serious artifacts in both system energy and pressure and leads to unrealistic behavior. Bogusz et al. corrected these artifacts by instituting a net-charge correction term that consists of subtracting off the Ewald sum for a single particle with charge equal to the net charge. This correction implicitly restores α -independence in net-charged systems.

We define U_ζ as the reciprocal energy of single ion place at the center of charge \mathbf{o}

$$U_\zeta = \frac{2\pi}{V} \sum_{\mathbf{k} \neq 0} \frac{1}{k^2} e^{-\frac{k^2}{4\alpha^2}} \left[(\cos(\mathbf{k} \cdot \mathbf{o}))^2 + (\sin(\mathbf{k} \cdot \mathbf{o}))^2 \right] - \frac{\alpha}{\sqrt{\pi}}. \quad (249)$$

If only the energy is needed the particle can simply be placed at the origin. Note that the term then only depend on the shape and size of the simulation cell and has be computed only once if the cell does not change.

We define

$$Q(\mathcal{A}, \mathbf{k}) = \sum_{i \in \mathcal{A}} q_i e^{i(\mathbf{k} \cdot \mathbf{r}_i)} \quad (250)$$

The interaction energy of component \mathcal{A} and \mathcal{B} is given by

$$U_{\mathcal{A},\mathcal{B}}^{\text{rec}} = \frac{2\pi}{V} \sum_{\mathbf{k} \neq 0} \frac{1}{k^2} e^{-\frac{k^2}{4\alpha^2}} \text{Re} [Q(\mathcal{A}, \mathbf{k}) \overline{Q(\mathcal{B}, \mathbf{k})}] + \left(\sum_{i \in \mathcal{A}} q_i \right) \left(\sum_{i \in \mathcal{B}} q_i \right) U_\zeta - (1 - \delta_{\mathcal{A}\mathcal{B}}) \frac{\alpha}{\sqrt{\pi}} \sum_{i \in \mathcal{A},\mathcal{B}} q_i^2, \quad (251)$$

where $\delta_{ij} = 1$ if $i = j$, zero otherwise, denotes the Kronecker delta.

These expressions are valid in any kind of net-charge arrangement, including a net-charge of the total system.

Most Monte-Carlo moves are based on changing the coordinates of single chain and computing the energy difference of a new *trial*-chain with respect to the old chain. As the positions of all the other chains are unaltered it is unnecessary to recompute the reciprocal energy of the non-moving chains. An important example is a rigid zeolite. The precomputing and storing of the Ewald sums makes the Ewald-summation method the preferred method for Monte Carlo simulations.

We assume the simulation starts with a full computation of Eq. 251, and the sums per \mathbf{k} vector are stored in $Q(\mathcal{A}, \mathbf{k})$. For each of the n -specie the sums $Q(\mathcal{A}, \mathbf{k})$ and the net-charges per specie needs to be stored. After an accepted move the sums and net-charges

are updated

$$\begin{aligned} \forall \mathbf{k} Q(\mathcal{A}, \mathbf{k}) &\rightarrow Q(\mathcal{A}, \mathbf{k}) + Q(\text{New}, \mathbf{k}) - Q(\text{Old}, \mathbf{k}) \\ \mathcal{N}(\mathcal{A}) &\rightarrow \mathcal{N}(\mathcal{A}) + \sum_{i \in \text{New}} q_i - \sum_{i \in \text{Old}} q_i \end{aligned} \quad (252)$$

The difference of a trial-chain and the old chain belonging to specie \mathcal{A} can be calculated by

$$\begin{aligned} \Delta U_{\mathcal{A}}^{\text{rec}} &= \frac{2\pi}{V} \sum_{\mathbf{k} \neq 0} \frac{1}{k^2} e^{-\frac{k^2}{4\alpha^2}} \left[|Q(\mathcal{A}, \mathbf{k}) + Q(\text{New}, \mathbf{k}) - Q(\text{Old}, \mathbf{k})|^2 - |Q(\mathcal{A}, \mathbf{k})|^2 \right] \\ &+ \frac{\alpha}{\sqrt{\pi}} \left[\sum_{i \in \text{New}} q_i^2 - \sum_{i \in \text{Old}} q_i^2 \right] + \left[\left(\sum_{i \in \mathcal{A}} q_i + \sum_{i \in \text{New}} q_i - \sum_{i \in \text{Old}} q_i \right)^2 - \left(\sum_{i \in \mathcal{A}} q_i \right)^2 \right] U_{\zeta}, \\ U_{\mathcal{A}, \mathcal{B}}^{\text{rec}} &= \frac{2\pi}{V} \sum_{\mathbf{k} \neq 0} \frac{1}{k^2} e^{-\frac{k^2}{4\alpha^2}} \text{Re} \left[(Q(\mathcal{A}, \mathbf{k}) + Q(\text{New}, \mathbf{k}) - Q(\text{Old}, \mathbf{k})) \overline{Q}(\mathcal{B}, \mathbf{k}) - Q(\mathcal{A}, \mathbf{k}) \overline{Q}(\mathcal{B}, \mathbf{k}) \right] \\ &+ \left[\left(\sum_{i \in \mathcal{B}} q_i \right) \left(\sum_{i \in \text{New}} q_i \right) - \left(\sum_{i \in \mathcal{B}} q_i \right) \left(\sum_{i \in \text{Old}} q_i \right) \right] U_{\zeta}. \end{aligned} \quad (253)$$

Bibliography

- [1] Frenkel, D.; Smit, B., *Understanding molecular simulation 2nd edition* Academic Press; London, UK, 2002.
- [2] Allen, M. P.; Tildesley, D. J., *Computer simulation of liquids* Clarendon Press; Oxford, 1987.
- [3] Leach, A. R., *Molecular Modelling: Principles and Applications*, 2nd ed. Prentice Hall; Longman, Essex, England, 2001.
- [4] Jensen, Frank, *An Introduction to Computational Chemistry* John Wiley & Son Ltd; New York, 1998.
- [5] Chaikin, P. M.; Lubensky, T. C., *Principles of Condensed Matter Physics* Cambridge University Press; Cambridge, 1995.
- [6] Smith, W.; Forester, T. R. *J. Mol. Graphics* **1996**, *14*, 136-141.
- [7] Stone, A. J., *The Theory of Intermolecular Forces* Oxford University Press; Oxford, 1996.
- [8] Hill, R. *Proc. R. Soc. London* **1948**, *193*, 281-297.
- [9] Hayes, J. M.; J. C. Greer, D. A. Morton-Blake *J. Comp. Chem.* **2004**, *25*, 1953 - 1966.
- [10] Bernal, J. D.; Fowler, R. H. *J. Chem. Phys* **1933**, *1*, 515-548.
- [11] Martin, M. G.; Siepmann, J. I. *J. Chem. Phys* **1998**, *102*, 2569-2577.

- [12] Nath, S. K.; Escobedo, F. A.; Pablo, J. J. de *J. Chem. Phys* **1998**, *108*, 9905-9911.
- [13] Errington, J. R.; Panagiotopoulos, A. Z. *J. Phys. Chem. B* **1999**, *103*, 6314-6322.
- [14] Chen, B.; Siepmann, J. I. *J. Phys. Chem. B* **1999**, *103*, 5370-5379.
- [15] Cui, S. T.; Cummings, P. T.; Cochran, H. D. *Fluid Phase Equilibria* **1997**, *141*, 45-61.
- [16] Martin, M. G.; Siepmann, J. I. *J. Phys. Chem. B* **1999**, *103*, 4508-4517.
- [17] Spyriouni, T.; Economou, I. G.; Theodorou, D. N. *J. Am. Chem. Soc.* **1999**, *121*, 3407-3413.
- [18] Pascual, P.; Ungerer, P.; Tavitian, B.; Boutin, A. *J. Phys. Chem. B* **2004**, *108*, 393-398.
- [19] Jakobtorweihen, S.; Hansen, N.; Keil, F. J. *Mol. Phys.* **2005**, *103*, 471-489.
- [20] van Leeuwen, M. *Molec. Phys.* **1996**, *87*, 87-101.
- [21] Kristof, T.; Liszi, J. *J. Phys. Chem. B* **1997**, *101*, 5480-5483.
- [22] Kristof, T.; Liszi, J.; Szalai, I. *Molec. Phys.* **1996**, *89*, 931-942.
- [23] Visco Jr., D. P.; Kofke, D. A. *J. Chem. Phys* **1998**, *109*, 4015-4027.
- [24] Jorgensen, W. L.; Chadrsekhar, J.; Madura, J. D.; Impey, R. W.; Klein, M. L. *J. Chem. Phys* **1983**, *79*, 926-935.
- [25] Berendsen, H. J. C.; Postma, J. P. M.; Gunsteren, W. F. van ; Hermans, J., in *Intermolecular Forces*, edited by Pullman, B. Reidel; Dordrecht, 1981.
- [26] van Santen, R. A.; Kramer, G. J. *Chem. Rev.* **1995**, *95*, 637 - 660.
- [27] Macedonia, M. D.; Maginn, E. J. *Mol. Phys.* **1999**, *96*, 1375-1390.
- [28] Ryckaert, J. P.; Bellemans, A. *Faraday Discuss. Chem. Soc.* **1978**, *66*, 95-106.
- [29] Jaramillo, E.; Auerbach, S. M. *J. Phys. Chem. B* **1999**, *103*, 9589-9594.
- [30] Beerdsen, E.; Smit, B.; Calero, S. *J. Phys. Chem. B* **2002**, *106*, 10659-10667.
- [31] Beerdsen, E.; Dubbeldam, D.; Smit, B.; Vlugt, T. J. H.; Calero, S. *J. Phys. Chem. B* **2003**, *107*, 12088-12096.
- [32] Schroder, K. P.; Sauer, J. *J. Phys. Chem.* **1996**, *100*, 11043-11049.
- [33] Cicu, P.; Demontis, P.; Spanu, S.; Suffritti, G. B.; Tilocca, A. *J. Chem. Phys* **2000**, *112*, 8267-8278.
- [34] Toufar, H.; Baekelandt, B. G.; Janssens, G. O. A.; Mortier, W. J.; Schoonheydt, R. A. *J. Phys. Chem.* **1995**, *99*, 13876-13885.
- [35] Smirnov, K. S.; Bougeard, D. *Chem. Phys.* **2003**, *292*, 53-70.
- [36] Rappé, A. K.; Casewit, C. J.; Colwell, K. S.; Goddard, W. A.; Skiff, W. M. *J. Am. Chem. Soc.* **1992**, *114*, 10024-10035.

- [37] Mayo, S. L.; Olafson, B. D.; Goddard, W. A. *J. Phys. Chem.* **1990**, *94*, 8897-8909.
- [38] Maple, J. R.; Hwang, M.-J.; Stockfisch, T. P.; Dinur, U.; Waldman, M.; Ewig, C. S.; Hagler, A. T. *J. Comp. Chem.* **1994**, *15*, 162-182.
- [39] Sun, H.; Mumby, S. J.; Maple, J. R.; Hagler, A. T. *J. Am. Chem. Soc.* **1994**, *116*, 2978.
- [40] Sun, H.; Ren, P.; Fried, J. R. *Computational and Theoretical Polymer Sciences* **1998**, *8*, 229-246.
- [41] Garofalini, G. H.; Zirl, D. M. *J. Am. Ceram. Soc.* **1990**, *73*, 2848-2456.
- [42] Karasawa, N.; Goddard, W. A. *Macromolecules* **1992**, *25*, 7268.
- [43] de Vos Burchart, E.; Verheij, V. A.; van Bekkum, H. *Zeolites* **1989**, *9*, 432.
- [44] Lifson, ; Hagler, ; Dauber, *J. Am. Chem. Soc.* **1979**, *101*, 5111-5141.
- [45] Momany, F. A.; Carruthers, L. M.; McGuire, R. F.; Scheraga, H. A. *J. Phys. Chem.* **1974**, *78*, 1595-1620.
- [46] Dauber-Osguthorpe, P.; Roberts, V. A.; Osguthorpe, D. J.; Wolff, J.; Genest, M.; Hagler, A. T. *Proteins: Structure, Function and Genetics* **1988**, *4*, 31-47.
- [47] Hagler, A. T.; Ewig, C. S. *Comp. Phys. Comm.* **1994**, *84*, 131-155.
- [48] Hwang, M.-J.; Stockfisch, T. P.; Hagler, A. T. *J. Am. Chem. Soc.* **1994**, *116*, 195 -231.
- [49] Maple, J. R.; Hwang, M.-J.; Stockfisch, T. P.; Hagler, A. T. *Israel J. Chem.* **1994**, *34*, 195 -231.
- [50] Allinger, N. L. *J. Am. Chem. Soc.* **1977**, *99*, 8127-8134.
- [51] Allinger, N. L.; Kok, R.; Imam, M. R. *J. Comp. Chem.* **1988**, *9*, 591-595.
- [52] Lii, J.-H.; Gallion, S.; Bender, C.; Wikstrom, H.; Allinger, N. L.; Flurchick, K. M.; Teeter, M. M. *J. Comp. Chem.* **1989**, *10*, 503-513.
- [53] Allinger, N. L.; Yuh, Y. H.; Lii, J.-H. *J. Am. Chem. Soc.* **1989**, *111*, 8551-8565.
- [54] Hay, B. P.; Yang, L.; Lii, J.-H.; Allinger, N. L. *J. Molecular Structure* **1998**, *428*, 203-219.
- [55] Lii, J.-H.; Allinger, N. L. *J. Am. Chem. Soc.* **1989**, *111*, 8566-8575.
- [56] Lii, J.-H.; Allinger, N. L. *J. Am. Chem. Soc.* **1989**, *111*, 8576-8582.
- [57] Lii, J.-H.; Allinger, N. L. *J. Comp. Chem.* **1991**, *12*, 186-199.
- [58] Lii, J.-H.; Allinger, N. L. *J. Comp. Chem.* **1998**, *19*, 1001-1016.
- [59] Allinger, N. L.; Fan, Y. *J. Comp. Chem.* **1997**, *18*, 1827-1847.
- [60] Allinger, N. L.; Chen, K.; Katzenellenbogen, J. A.; Wilson, S. R.; Anstead, G. M. *J. Comp. Chem.* **1996**, *17*, 747-755.
- [61] Nevens, N.; Chen, K.; Allinger, N. L. *J. Comp. Chem.* **1996**, *17*, 669-694.

- [62] Nevens, N.; Lii, J.-H.; Allinger, N. L. *J. Comp. Chem.* **1996**, *17*, 695-729.
- [63] Nevens, N.; Allinger, N. L. *J. Comp. Chem.* **1996**, *17*, 730-746.
- [64] Allured, V. S.; Kelly, C. M.; Landis, C. R. *J. Am. Chem. Soc.* **1991**, *113*, 1.
- [65] Bearpark, M. J.; Robb, M. A.; Bernardi, F.; Olivucci, M. *Chem. Phys. Lett.* **1994**, *217*, 513.
- [66] Root, D. M.; Landis, C. R.; Cleveland, T. J. *J. Am. Chem. Soc.* **1993**, *115*, 4201.
- [67] Cleveland, T. J.; Landis, C. R. *J. Am. Chem. Soc.* **1996**, *118*, 6020.
- [68] Cornell, W. D.; Cieplak, P.; Bayly, C. I.; Gould, I. R.; Merz Jr., K. M.; Ferguson, D. M.; Spellmeyer, D. C.; Fox, T.; Caldwell, J. W.; Kollman, P. A. *J. Am. Chem. Soc.* **1992**, *117*, 5179-5197.
- [69] Pearlman, D. A.; Case, D. A.; Caldwell, J. C.; Seibel, G. L.; Singh, U. C.; Weiner, P.; Kollman, P. A., *AMBER 4.0* University of California Press; San Francisco, 1991.
- [70] Weiner, P. K.; Kollman, P. A. *J. Comp. Chem.* **1981**, *2*, 287-303.
- [71] Weiner, S. J.; Kollman, P. A.; Case, D. A.; Singh, U. C.; Ghio, C.; Alagona, G.; Profeta Jr., S.; Weiner, P.K. *J. Am. Chem. Soc.* **1984**, *106*, 765-784.
- [72] Weiner, S. J.; Kollman, P. A.; Nguyen, D. T.; Case, D. A. *J. Comp. Chem.* **1986**, *7*, 230-252.
- [73] Brooks, B. R.; Bruccoleri, R. E.; Olafson, B. D.; States, D. J.; Swaminathan, S.; Karplus, M. *J. Comp. Chem.* **1983**, *4*, 187-217.
- [74] Feller, S. E.; Yin, D. X.; MacKerell, R. W. Pastor A. D. *Biophys. J.* **1997**, *73*, 2269-2279.
- [75] MacKerell, A. D.; Bashford, D.; Bellott, M.; Dunbrack, R. L.; Evanseck, J. D.; Field, M. J.; Fischer, S.; Gao, J.; Guo, H.; Ha, S.; Joseph-McCarthy, D.; Kuchnir, L.; Kuczera, K.; Lau, F. T. K.; Michnick, C. Mattos S.; Ngo, T.; Nguyen, D. T.; Prodhom, B.; Reiher, W. E.; Roux, B.; Schlenkrich, M.; Smith, J. C.; Stote, R.; Straub, J.; Watanabe, M.; Wiorkiewicz-Kuczera, J.; Yin, D.; Karplus, M. *J. Phys. Chem. B* **1998**, *102*, 3586-3617.
- [76] Momany, F. A.; Rone, R. *J. Comp. Chem.* **1992**, *13*, 888-900.
- [77] Pavelites, J. J.; Gao, J.; Bash, P.A.; Mackerell Jr., A. D. *J. Comp. Chem.* **1997**, *18*, 221-239.
- [78] al., Schlenkrichat, in *Biological Membranes: A Molecular Perspective from Computation and Experiment*, edited by Merz, K.M.; Roux, B. Birkhauser; Boston, 1996, pp. 31-81.
- [79] Damm, W.; Frontera, A.; Tirado-Rives, J.; Jorgensen, W. L. *J. Comp. Chem.* **1997**, *18*, 1955-1970.
- [80] Jorgensen, W. L.; Maxwell, D. S.; Tirado-Rives, J. *J. Am. Chem. Soc.* **1996**, *118*, 11225-11236.
- [81] Jorgensen, W. L.; Tirado-Rives, J. *J. Am. Chem. Soc.* **1988**, *110*, 1657-1666.

- [82] Kaminski, G.; Duffy, E. M.; Matsui, T.; Jorgensen, W. L. *J. Phys. Chem.* **1994**, *98*, 13077-13082.
- [83] Clark, M.; van Opdenbosch, R. D. Kramer III N. *J. Comp. Chem.* **1989**, *10*, 982-1012.
- [84] Momany, F. A.; McGuire, R. F.; Burgess, A. W.; Scheraga, H. A. *J. Phys. Chem.* **1975**, *79*, 2361-2381.
- [85] Nemethy, G.; Pottle, M. S.; Scheraga, H. A. *J. Phys. Chem.* **1983**, *87*, 1883-1887.
- [86] Sippl, M. J.; Nemethy, G.; Scheraga, H. A. *J. Phys. Chem.* **1984**, *88*, 6231-6633.
- [87] Hermans, J.; Berendsen, H. J. C.; van Gunsteren, W. F.; Postma, J. P. M. *Biopolymers* **1984**, *23*, 1-.
- [88] Ott, K.-H.; Meyer, B. *J. Comp. Chem.* **1996**, *17*, 1068-1084.
- [89] van Gunsteren, W. F.; Daura, X.; Mark, A. E. *Encyclopaedia of Computational Chemistry* **1997**, *17*, .
- [90] Halgren, T. A. *J. Am. Chem. Soc.* **1992**, *114*, 7827-7843.
- [91] Halgren, T. A. *J. Comp. Chem.* **1996**, *17*, 490-519.
- [92] Halgren, T. A. *J. Comp. Chem.* **1996**, *17*, 520-552.
- [93] Halgren, T. A. *J. Comp. Chem.* **1996**, *17*, 553-586.
- [94] Halgren, T. A.; Nachbar, R. B. *J. Comp. Chem.* **1996**, *17*, 587-615.
- [95] Halgren, T. A.; Nachbar, R. B. *J. Comp. Chem.* **1996**, *17*, 616-641.
- [96] Jorgensen, W. L.; Madura, J. D.; Swenson, C. J. *J. Am. Chem. Soc.* **1984**, *106*, 6638.
- [97] Jorgensen, W. L.; Swenson, C. J. *J. Am. Chem. Soc.* **1985**, *107*, 569.
- [98] Jorgensen, W. L. *J. Phys. Chem.* **1986**, *90*, 6379.
- [99] Jorgensen, W. L. *J. Phys. Chem.* **1986**, *90*, 1276.
- [100] Vlugt, T.; Krishna, R.; Smit, B. *J. Phys. Chem. B.* **1999**, *103*, 1102-1118.
- [101] Frenkel, D. *PNAS* **2004**, *101*, 17571-17575.
- [102] Martyna, G. J.; Tuckerman, M.; Tobias, D. J.; Klein, M. L. *Mol. Phys.* **1996**, *87*, 1117-1157.

Molecular simulations corroborate the existence of the disputed window effect, i.e. an increase in diffusion rate by orders of magnitude when the alkane chain length increases so that the shape of the alkane is no longer commensurate with that of a zeolite cage. This window effect is shown to be characteristic for molecular sieves with pore openings that approach the diameter of the adsorbate. Furthermore, the physical compatibility between the adsorbate and the adsorbent has a direct effect on the heat of adsorption, the Henry coefficients, the activation energy, and the frequency factors.

D. Dubbeldam, S. Calero, T. L. M. Maesen, B. Smit

3

Incommensurate Diffusion in Confined Systems

Zeolites are confined systems with pore sizes comparable to the molecular size. These microporous materials are used for separations, water softeners, and as catalysts in many (petro)chemical applications. From a scientific point of view zeolites are ideal systems to study the effect of confinement on the properties of the adsorbed molecules [1–6]. The effect of confinement on diffusion is still poorly understood despite its importance for practical applications. Experimentally this is a very difficult subject; depending on the experimental technique the measured diffusion coefficients may differ many orders of magnitude [7].

Zeolites are designated by three capital letter codes derived from the names of the type materials: ERI (**E**rionite), CHA (**C**habazite), LTA (**L**inde **T**ype **A**), OFF (**O**ffretite), and MFI (**Z**SM-**5** **f**ive). In 1973 Gorrington reported an experimental study of diffusion of linear alkanes in ERI-type zeolite (a cage/window-type structure) as a function of chain length indicating a *window-effect* [8]. Surprisingly, the diffusion rates reportedly increase significantly going from C₈ to C₁₂ before the usual mono-

tonic decrease with chain length sets in. According to Gorrington the diffusion rate exhibits a maximum for C₁₂ because the shape is incommensurate with that of an ERI-type cage, so that C₁₂ is always inside an ERI-type window. Smaller molecules are commensurate with the ERI-type cage and remain trapped in its potential well.

Perhaps the simplest model for molecules that are either commensurate or incommensurate with the framework structure is the Frenkel-Kontorowa (FK) model [9] for adsorbed atoms on a periodic substrate. Models based on the FK-theory have been proposed by Ruckenstein and Lee [10], Derouane et al. [11], and by Nitsche and Wei [12] to explain the observed increase of the diffusion coefficient as a function of the chain length qualitatively. However, due to the simplifications the quantitative predictions of these models are poor. For example, these models can not predict the location and magnitude of the local maximum, nor can they describe the inner-cage behavior correctly. Recent attempts [13, 14] failed to experimentally corroborate Gorrington's diffusion data. The discrepancy between the experiments and the lack of a molecu-

lar model that quantitatively explains the window-effect motivated us to develop a molecular simulation method to quantitatively study diffusion in cage/window-type geometries.

In this work we focus on self-diffusion of linear alkanes in ERI-, CHA-, and LTA-type zeolites as a function of chain length. These types of zeolites have a cage/window-type structure with highly tortuous diffusion paths. The CHA-type cages are slightly shorter than the elongated ERI-type cages and both cage types are significantly smaller than the spherical LTA-type cages. Conventional molecular simulations are limited to relatively fast diffusing molecules [15, 16] or small rigid molecules [17]. Here, we combine the Configurational Bias Monte-Carlo (CBMC) method with rare-event molecular simulation techniques [18, 19]. The diffusion coefficients are 4-10 orders of magnitude lower than what currently can be computed by conventional molecular simulation methods.

We use the united-atom model [20] and consider the CH_3 and CH_2 groups as single interaction centers with their own effective potentials. The beads in the chain are connected by harmonic bonding potentials. The bond bending between three neighboring beads is modeled by a harmonic cosine bending potential and changes in the torsional angle are controlled by a Ryckaert-Bellemans potential. The beads in a chain separated by more than three bonds interact with each other through a Lennard-Jones potential. Lattice vibrations, intergrowths and defects, cations and associated aluminum atoms create strong disorder and complicate the diffusion process. In this work we focus on the influence of the confinement on the diffusion coefficient and therefore we use rigid all-silica ERI-, CHA-, and LTA-type molecular sieves. In all-silica structures the electric field does not vary much across the channels and cages, and Coulomb contributions to the energy of the hydrocarbons can be neglected. The chains

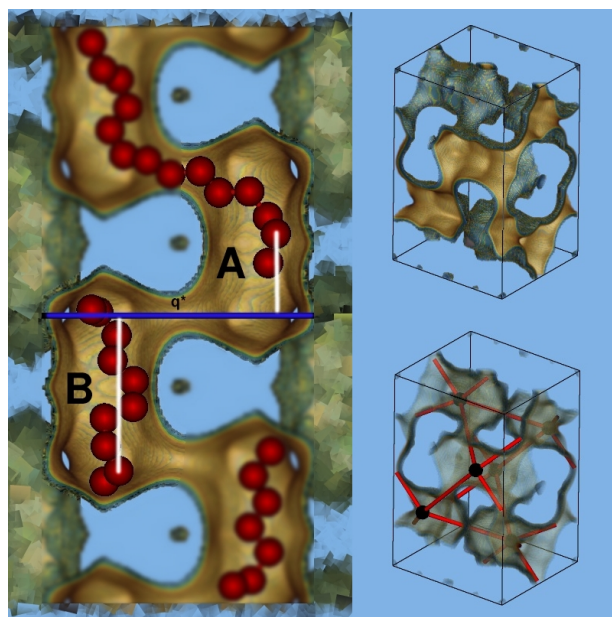


Figure 1: The reaction coordinate q is defined as the position of the second bead of a chain mapped orthogonal to the axis of projection (the line perpendicular to the window). The resulting free energy profile $F(q)$ indicates a high free energy barrier at the position of the window q^* separating cage A and B. On the right we show two pictures: the unit cell of ERI in 3D (top), and the connectivity of the cages within the unit cell (bottom). At infinite dilution the molecules perform a random walk on a lattice spanned by the cage-centers.

interact with the oxygens atoms of the zeolite through a Lennard-Jones potential. Further details, including the parameters, are given by Vlugt et al. [21] and Maesen et al. [22], who have shown that with these parameters one can reproduce the adsorption isotherms, heats of adsorption, and Henry coefficients of linear alkanes in all-silica zeolites accurately.

The structures of interest here consist of cages A and B separated by a narrow window forming a high free energy barrier. In the Bennet-Chandler approach [18, 19, 23] one computes the transmission rate over the barrier in two steps. First one computes the probability to find a chain on top of the barrier and subsequently the transmission coefficient κ , defined as the fraction

of particles coming from A that successfully reaches B out of those starting on top of the barrier. At infinite dilution the chains perform a random walk on a lattice spanned by the cage-centers. The transmission rates are then easily converted to diffusion coefficients. Transition State Theory (TST) assumes that no recrossing occurs ($\kappa = 1$) and predicts a transmission rate $k_{A \rightarrow B}^{\text{TST}}$ given by

$$k_{A \rightarrow B}^{\text{TST}} = \sqrt{\frac{k_B T}{2\pi m}} \frac{e^{-\beta F(q^*)}}{\int_{-\infty}^{q^*} e^{-\beta F(q)} dq},$$

where k_B is the Boltzmann constant, T the temperature, $\beta = 1/(k_B T)$, m the mass of the particle, and $F(q)$ the free energy as a function of q . The reaction coordinate q defines the progress of the diffusion event from cage A to cage B . We define q^* to be the location of the dividing barrier. The omission of the transmission coefficient κ is not allowed for our systems and we correct the TST results by computing the transmission coefficients in a separate Molecular Dynamics calculation. It is vital to choose an appropriate reaction coordinate. By trial and error we concluded that using the second bead of the chain gave near optimal results for the systems discussed here. The transmission coefficient $\kappa = 1$ for methane and within the range $\kappa = 0.1 - 0.3$ for other chain lengths. The more intuitive middle bead and center of mass gave very small transmission coefficients resulting in an extremely inefficient computation.

For long chains the conventional techniques are prohibitively expensive. However, the CBMC technique used to simulate adsorption isotherms [24] can be extended to compute the free energy of a chain. In a CBMC simulation chains are grown bead by bead biasing the growth process towards energetically favorable configurations avoiding overlap with the zeolite. During the growth the Rosenbluth factor is calculated. The average Rosenbluth factor is directly related to the excess chemical potential, free energy, and the Henry coefficient [19]. The CBMC algorithm greatly

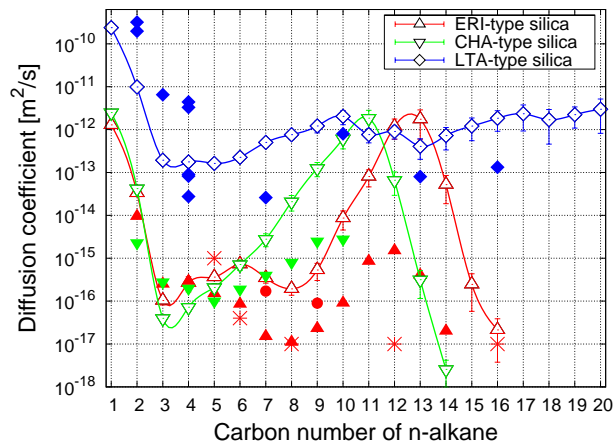


Figure 2: Diffusion coefficients as a function of chain length at 600 K for ERI-, CHA-, and LTA-type zeolite; \triangle ERI-type silica sim. results, \blacktriangle exp. results of Gorring [8], $*$ Cavalcante et al. [13], \bullet Magalhães et al. [14]; ∇ CHA-type silica sim. results, \blacktriangledown exp. results of Gorring [25]; \diamond LTA-type silica sim. results, \blacklozenge exp. compiled in Ref. [7].

improves the conformational sampling of molecules and increases the efficiency of chain insertions by many orders of magnitude. To compute the free energy as a function of the position in the zeolite, chains are inserted at random positions and grown using the CBMC scheme. The mapping of the second bead of a chain is depicted in Fig. 1. A part of the ERI-type silica with cages A and B (connected to other cages) is sliced half open. We show two examples: a C_{14} chain in cage A and a C_{10} chain in cage B . Free energy values are mapped onto the one-dimensional free energy profile $F(q)$ by orthogonal projection of the position of the second bead onto the line perpendicular to the window.

For most zeolites the diffusion coefficients of linear alkanes are monotonically decreasing as a function of chain length [7]. Fig. 2 shows a qualitatively different behavior in ERI- and CHA-type silica. We observe a range of intermediate chain lengths in which the diffusion coefficient is constant or increases with increasing chain length, followed by a pronounced local maximum.

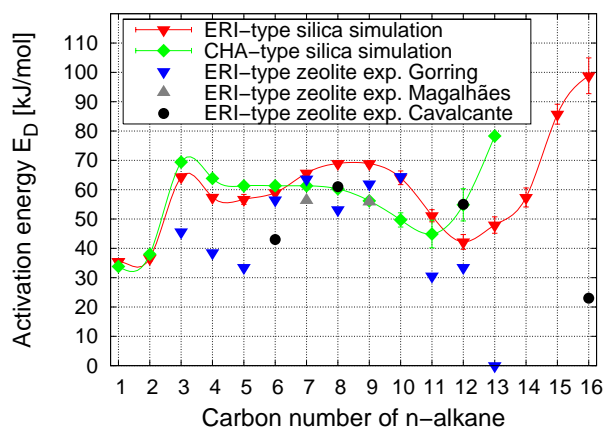


Figure 3: Activation energies obtained from fitting diffusion simulation results at 300, 400, 500, 600, and 700 K to the Arrhenius law compared to the experimental results taken from Goring [8], Cavalcante et al. [13], and Magalhães et al. [14].

Good quantitative agreement with the non-disputed experimental data for LTA-type zeolite is found, although one has to realize that the scatter in the experimental data can be as much as two orders of magnitude. We note that the input of our simulations is the crystal structure of LTA and the force field, which has been optimized for the adsorption in a silicalite. It is therefore encouraging that such a good agreement is obtained without any adjustment of the parameters. More importantly, our simulation reproduce the chain length dependence and is consistent with the experimental data of Goring [8]; we not only confirm the occurrence of a maximum for both ERI- and CHA-type zeolite at the same carbon number as observed experimentally, but also the shift of this maximum to lower carbon numbers for CHA-type silica. The increase in the diffusion rate originating from the geometry-chain interaction is a remarkable four orders of magnitude for both ERI- and CHA-type silicas. Additionally, we have computed the activation energies and frequency factors by fitting the diffusion results at several temperatures to the Arrhenius law. The simulation curves in Fig. 3 are qualitatively the inverse of the

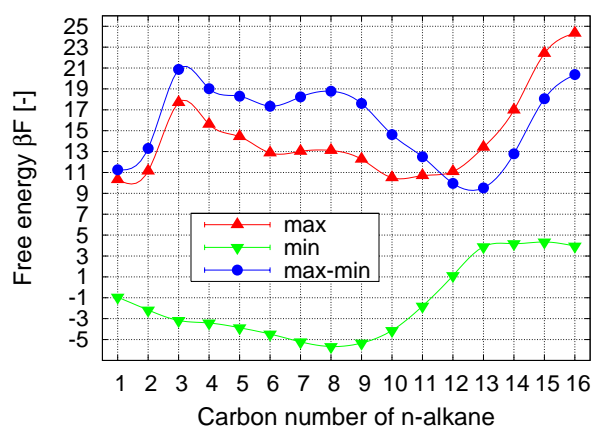


Figure 4: The free energy difference between maximum and minimum for ERI-type silica at 600 K.

general shape of the diffusion curves, i.e. if a chain has a high mobility the activation energy is low and visa versa. The frequency factors (data not shown) show a maximum where the diffusion also shows a maximum and where the activation energy is at a minimum. Visual inspection of the simulations snapshots and end-to-end distance histograms show that the chain is stretched across a cage tethered at opposite windows: C_{13} for ERI-type silica, C_{11} for CHA-type silica, and C_{23} for LTA-type silica. These chains correspond to the largest chains still able to fit into a single cage and have the lowest orientational freedom.

In simulations we are able to extract detailed information such as $F(q)$. The free energy differences for ERI-type silica are shown in Fig. 4 and are analyzed in terms of the value inside the cage and the value at the barrier. For the chains in the cage we observe that as we increase the chain length the minimum of the free energy decreases until we reach an optimum chain length beyond which the chain no longer fits comfortably in one cage. For chain lengths longer than this optimum length the free energy increases rapidly until the chain is so big that additional beads are added comfortably in the second cage and the minimum free energy is decreasing again. For the free energy of a chain on top of the

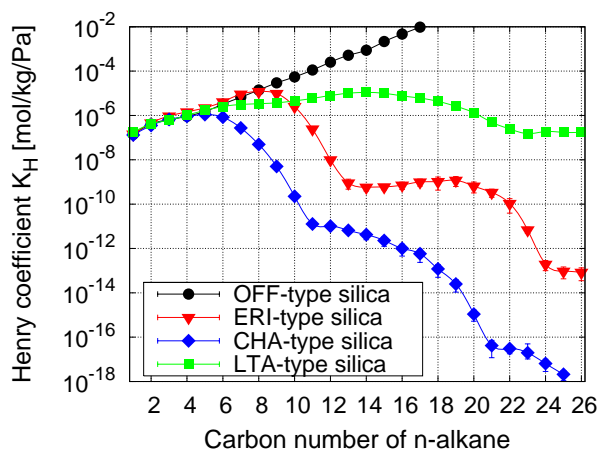


Figure 5: Henry coefficients in OFF-, ERI-, CHA- and LTA-type silica as a function of chain length at 600K.

barrier we observe an increase from C_1 to C_3 , as more beads are placed on top of the barrier. For C_3 all beads feel the influence of the window. Any additional bead will be placed in more favorable positions outside the window and therefore the barrier decreases for C_4 and continues to decrease until the chain is so large that it feels the limitations of the cage. Beyond this chain length the maximum of the free energy increases rapidly. Combining these effects gives the generic, non-monotonic diffusion behavior. First a decrease followed by a possible plateau, an increase, and finally a decrease again. Key parameters in this mechanism are the presence of a narrow window combined with a cage structure. By optimizing the effective cage size one can shift the location of the second maximum to a desired value.

We have argued that the maximum of the diffusion is related to a relative unfavorable adsorption for this chain length. This is also reflected in the Henry coefficient as a function of chain length shown in Fig. 5. At sufficiently low pressures the number of adsorbed molecules is proportional to the Henry coefficient. The Henry coefficients are directly related to the minimum of the free energy profile. The data for OFF-type silica shows the common behavior of

many channel-type zeolites. In contrast, cage/window-type zeolites show a typical non-monotonic, periodic dependence of the Henry coefficients on the chain length. The same applies to the heat of adsorption (data not shown). The local minima nicely correspond to the local maxima in the diffusion coefficient. The repeating period in the Henry coefficients corresponds to chains fitting into one, two, or three cages, respectively. We note that the period of LTA-type zeolite is large. The confinement determines the variety of conformations present and for LTA-type zeolites this entropy effect is large as chains up to C_{23} still fit into a single cage. An important argument against the existence of the window effect was that experimental data for LTA do not provide evidence in support of this effect [7]. Experimentally, the maximum chain length that has been studied is C_{16} . This chain length is in the plateau region; only for much longer chain lengths a moderate increase can be expected.

Our simulations show that the window effect is a very generic effect that can be found in an entire class of zeolites. When a chain is incommensurate with the cage structure the diffusion rate increases by orders of magnitude. The crossover points, at which a chain fits in n -cages and a longer one into $(n + 1)$ -cages, are directly related to the local minima in the Henry coefficients, the heats of adsorption, and the activation energies, and to the local maxima in the diffusion coefficients and the frequency factors. Although closely related, this is not necessarily an exact multiple of the window-to-window distance, nor is half the window-to-window distance the chain length which is always commensurate with the cage, as theory suggests. In fact, there can be more than one minimum of diffusion per period. From a simulation point of view it is encouraging that our method allows us to compute very low diffusion coefficients that vary six orders of magnitude for alkanes ranging from C_1 to C_{20} . It is par-

ticularly useful at conditions accessible to neither conventional simulation techniques nor experiments, but where diffusion limitations can be an important factor in understanding practical applications.

Acknowledgments

We would like to thank the Netherlands Research Council for Chemical Sciences (CW), the European Commission through a Marie Curie Individual Research Fellowship to SC, and ChevronTexaco for financial support.

Bibliography

- [1] K. Hahn, J. Kärger, and V. Kukla, *Phys. Rev. Lett.* **76**, 2762 (1996).
- [2] H. Jobic, J. Kärger, and M. Bee, *Phys. Rev. Lett.* **82**, 4260 (1999).
- [3] L. A. Clark, G. T. Ye, and R. Q. Snurr, *Phys. Rev. Lett.* **84**, 2893 (2000).
- [4] D. S. Sholl and K. A. Fichthorn, *Phys. Rev. Lett.* **79**, 3569 (1997).
- [5] R. C. Runnebaum and E. J. Maginn, *J. Phys. Chem. B.* **101**, 6394 (1997).
- [6] C. Rajappa and S. Yashonath, *J. Chem. Phys.* **110**, 5960 (1999).
- [7] J. Kärger and D. M. Ruthven, *Diffusion in Zeolites and other microporous solids* (John Wiley & Sons, Inc., New York, 1992).
- [8] R. L. Goring, *J. Catal.* **31**, 13 (1973).
- [9] Y. I. Frenkel and T. Kontorowa, *Phys. Z. Sowjetunion* **13**, 1 (1938).
- [10] E. Ruckenstein and P. S. Lee, *Phys. Lett. A* **56**, 423 (1976).
- [11] E. G. Derouane, J. M. Andre, and A. A. Lucas, *J. Catal.* **110**, 58 (1988).
- [12] J. M. Nitsche and J. Wei, *AIChE. J.* **37**, 661 (1991).
- [13] C. L. C. Jr, M. Eić, D. M. Ruthven, and M. L. Occelli, *Zeolites* **15**, 293 (1995).
- [14] F. D. Magalhães, R. L. Laurence, and W. C. Conner, *AIChE. J.* **68**, 42 (1996).
- [15] E. B. Webb, G. S. Grest, and M. Mondello, *J. Phys. Chem. B.* **103**, 4949 (1999).
- [16] D. Schuring, A. P. J. Jansen, and R. A. van Santen, *J. Phys. Chem. B.* **104**, 941 (2000).
- [17] S. M. Auerbach, *International reviews in physical chemistry* **19**, 155 (2000).
- [18] D. Chandler, *J. Chem. Phys.* **68**, 2959 (1978).
- [19] D. Frenkel and B. Smit, *Understanding molecular simulation 2nd edition* (Academic Press, London, UK, 2002).
- [20] J. P. Ryckaert and A. Bellemans, *Faraday Discuss. Chem. Soc.* **66**, 95 (1978).
- [21] T. Vlugt, R. Krishna, and B. Smit, *J. Phys. Chem. B.* **103**, 1102 (1999).
- [22] T. L. M. Maesen, M. Schenk, T. J. H. Vlugt, J. P. de Jonge, and B. Smit, *J. Catal.* **188**, 403 (1999).
- [23] C. H. Bennett, in *Diffusion in Solids: Recent Developments*, edited by A. Nowick and J. Burton (Academic Press, New York, 1975), pp. 73–113.
- [24] B. Smit and T. L. M. Maesen, *Nature* **374**, 42 (1995).
- [25] N. Chen, W. E. Garwood, and F. G. Dwyer, *Shape selective Catalysis in industrial Applications, 2nd edition, revised and expanded* (Chemical Industries, New York, 1996, with $r = 0.4 \mu\text{m}$).

Dedicated molecular simulation techniques afford the study of the abnormal adsorption and diffusion of linear alkanes in ERI-, CHA-, and LTA-type zeolites. The exceptionally slow diffusion rates required the development of a combination of rare-event transition state theory techniques and the configurational-bias Monte Carlo algorithm. The diffusion coefficients computed by this novel method agree well with the non-disputed rates determined experimentally for LTA-type sieves. The computed rates corroborate the non-monotonic variation of the diffusion rate with alkane chain length published by Goring, i.e. the rate increases by orders of magnitude when the molecular and cage shape are no longer commensurate, so that a molecule ends up stretched across a cage tethered at opposite windows. The simulations corroborate this "window-effect" for both ERI- and CHA-type sieves, and suggest that it is characteristic for all sieves with windows approximately 0.4 nm across. They predict that it also occurs for LTA-type sieves provided that the *n*-alkane is long enough to exceed the diameter of the LTA-type supercage.

D. Dubbeldam and B. Smit

4

Computer Simulation of Incommensurate Diffusion in Zeolites: Understanding Window-Effects

I Introduction

With the potential substitution of methyl-tertiarybutylether (MTBE) by ethanol in gasoline, it will be difficult to maintain gasoline volatility without removing a substantial amount of the volatile pentanes together with the MTBE. In the 1960-ies the selective hydrocracking of pentanes and hexanes under reforming conditions was commercialized using a catalyst based on an ERI-type zeolite [1]. One could envisage a resurgence of such a process if the catalyst could somehow be reformulated so as to exhibit a higher selectivity for pentane removal than the ERI-type zeolite. An impediment to such a development is that the fundamental operating principles of the ERI-type zeolite have never been fully under-

stood at a molecular level. This paper attempts to remedy this situation by applying state of the art molecular simulation techniques to assess the catalytically relevant diffusion and adsorption phenomena.

In 1973 Goring reported an experimental study of diffusion of several *n*-alkanes over zeolite T [2]. Zeolite T is a disordered intergrowth of OFF- and ERI-type zeolites: The OFF-type structure consists of channels 0.67 nm across, the ERI-type structure of cages linked by a highly tortuous diffusion path through 0.4 nm windows. Surprisingly, the diffusion and reaction rates in ERI-type zeolites reportedly increase significantly going from *n*-C₈ to *n*-C₁₂ before the usual monotonic decrease with alkane chain lengths sets in. According to Goring [2] and Chen [3, 4] the diffusion rate

exhibits a maximum for n -C₁₂ because the shape is incommensurate with that of an ERI-type cage, so that n -C₁₂ is always inside an ERI-type window. Smaller molecules are commensurate with the ERI-type cage and remain trapped in its potential well. Larger molecules also gain stability from the interactions with the cage. Gorring argued that the occurrence of the window effect might be a general phenomenon common to diffusion of long molecules in many zeolites, with the position of minima and maxima determined by identifiable crystal parameters.

The origin of the window effect is a relatively unfavorable adsorption for the chain lengths close to the cage size combined with a low orientational freedom as the chains are stretched across a cage tethered at opposite windows [5,6]. As the movement of the incommensurate chain is less impeded by the higher free energy barriers a commensurate chain would feel, it has an enhanced mobility around integer values of the ratio of the chain length to the period of a lattice. Perhaps the simplest model for molecules that are either commensurate or incommensurate with the framework structure is the 1938 Frenkel-Kontorowa (FK) model [7, 8] for adsorbed atoms on a periodic substrate. The model, consisting of a string of atoms connected by springs and subjected to a periodic potential, contains for a vanishing potential a "floating phase" which is incommensurate for almost all values of the ratio a/b , where a is the equilibrium lattice spacing of the harmonic chain and b the lattice period. Similar models have been proposed by Ruckenstein and Lee [9], Derouane et al. [10], and by Nitsche and Wei [11]. However, we are aware neither of theoretical studies closer to reality nor of additional experimental confirmation of the non-monotonic variation of diffusion with alkane chain length. On the contrary, recent attempts [12, 13] failed to corroborate Gorring's diffusion data.

An intensive research effort on mea-

suring diffusion rates in zeolites augmented the number of techniques to measure the diffusion rates, and the discrepancies between the rates obtained by the various methods. Thus, agreement between microscopic (pulsed field gradient NMR, quasi-elastic neutron scattering), mesoscopic (micro-FT IR), and macroscopic (membrane permeation, uptake methods, zero length column, frequency response) techniques is rare. As compared to Cavalcante et al. [12] and Magalhães et al. [13] Gorring used too much sample in his mass uptake measurements and changed his sorbate concentration too drastically, so that his data were prone to the intrusion of heat transfer and extra-crystalline mass transfer phenomena. The discrepancy between the experiments motivated us to develop a molecular simulation method that would allow us to study the adsorption and diffusion and shed some light on the experimental dispute. Furthermore, we hope to contribute valuable new insights to the theory of diffusion in zeolites.

In this paper we use configurational-bias Monte Carlo (CBMC) to obtain the Henry coefficients and heats of adsorption in OFF-, ERI-, CHA-, and LTA-type silica. We apply the transition state theory (TST) Bennet-Chandler approach [14, 15] and the techniques developed by Ruiz-Montero et al. [16], combined with CBMC, to calculate diffusion coefficients in ERI-type, CHA-type, and LTA-type silica. Both Henry coefficients and diffusion coefficients are calculated over a wide range of chain lengths and temperatures. The diffusion data is fitted with an Arrhenius law producing activation energies and frequency factors. For ERI- and CHA-type sieves we confirm the existence of the window-effect. The physical origin of the window-effect and the conditions under which the phenomenon occurs are studied in detail.

The remainder of this paper is organized as follows. First, we introduce our simulation model in Sec. II and review the relevant

theoretical foundations in Sec. III. Next we discuss the choice of the reaction coordinate needed in the transition state theory in Sec. IV. A detailed description of the zeolites is presented in Sec. V. In Sec. VI simulation results on adsorption, diffusion, activation energies, and frequency factors are reported and we discuss the comparison with the scattered experimental results. We discuss the comparison with some theoretical and experimental results in Sec. VII and end in Sec. VIII with some concluding remarks.

II Simulation model

We use the united atom model [17] and consider the CH₃ and CH₂ groups as single interaction centers with their own effective potentials. The pseudo-atoms in the chain are connected by harmonic bonding potentials. Bond bending between neighboring pseudo-atoms i , j , and k is modeled by a harmonic cosine bending potential, and changes in the torsional angle are controlled by a Ryckaert-Bellemans potential [18]. The pseudo-atoms in different molecules, or belonging to the same molecule but separated by more than three bonds, interact with each other through a shifted Lennard-Jones potential.

In the CBMC scheme it is convenient to split the total potential energy of a trial site into two parts. The first part is the internal, bonded potential U^{int} which is used for the generation of trial orientations. The second part of the potential, the external potential U^{ext} , is used to bias the selection of a site from the set of trial sites. Note that the split can be made completely arbitrary. The internal energy U^{int} is given by

$$U^{\text{int}} = U^{\text{bond}} + U^{\text{bend}} + U^{\text{torsion}}, \quad (1)$$

with

$$U^{\text{bond}} = \sum_{\text{bonds}} \frac{1}{2} k_1 (r - r_0)^2, \quad (2)$$

$$U^{\text{bend}} = \sum_{\text{bends}} \frac{1}{2} k_2 (\cos \theta - \cos \theta_0)^2, \quad (3)$$

$$U^{\text{torsion}} = \sum_{\text{torsions}} \sum_{n=0}^5 C_n \cos^n \phi, \quad (4)$$

where $k_1/k_B = 96500 \text{ K}/\text{\AA}^2$ is the bond force constant, $r_0 = 1.54 \text{ \AA}$ the reference bond length, $k_2/k_B = 62500 \text{ K}$ the bend force constant, $\theta_0 = 114^\circ$ the reference bend angle, ϕ the dihedral angle (defined as $\phi_{\text{trans}} = 0$), and where the torsion parameters are given by $C_0 = 1204.654$, $C_1 = 1947.740$, $C_2 = -357.845$, $C_3 = -1944.666$, $C_4 = 715.690$, $C_5 = -1565.572$ with C_n/k_B in K. The external energy U^{ext} consists of a guest-guest intermolecular energy, a guest-zeolite interaction, and an intra-molecular Lennard-Jones interaction

$$U^{\text{ext}} = U_{ij}^{\text{gg}} + U_{ij}^{\text{gz}} + U_{ij}^{\text{intra}}, \quad (5)$$

with

$$U_{ij}^{\text{gg,gz,intra}} = \sum_{\text{LJ-pairs}} 4\epsilon_{ij} \left[\left(\frac{\sigma_{ij}}{r_{ij}} \right)^{12} - \left(\frac{\sigma_{ij}}{r_{ij}} \right)^6 \right] - E_{\text{cut}}, \quad (6)$$

where r_{ij} is the distance between site i and site j , $r_{\text{cut}} = 13.8 \text{ \AA}$, the cutoff radius, and E_{cut} the energy at the cut-off radius. Jorgensen mixing rules, $\sigma_{ij} = \sqrt{\sigma_i \sigma_j}$ and $\epsilon_{ij} = \sqrt{\epsilon_i \epsilon_j}$, are used for the cross terms of the Lennard-Jones parameters, $\sigma = 3.75 \text{ \AA}$, $\epsilon/k_B = 98.0 \text{ K}$ for CH₃, and $\sigma = 3.95 \text{ \AA}$, $\epsilon/k_B = 46.0 \text{ K}$ for CH₂. The interactions between the zeolite and the guest molecules are assumed to be dominated by the oxygens atoms [19]. The interactions with the Si atoms are implicitly taken into account in this effective potential. The dispersive interactions with the oxygens are described with the Lennard-Jones potential with parameters $\sigma = 3.6 \text{ \AA}$ and $\epsilon/k_B = 80 \text{ K}$ for O-CH₂, $\epsilon/k_B = 58 \text{ K}$ for O-CH₃. Further details

are given by Vlugt et al. [20] and Maesen et al. [21], who have shown that with these parameters one can reproduce the adsorption isotherms, heats of adsorption, and Henry coefficients of various linear and branched alkanes in several zeolites accurately.

Instead of the experimentally studied cation-exchanged aluminosilicates, we use OFF-, ERI-, CHA-, and LTA-type silica devoid of cations. In all-silica sieves the electric field does not vary much across the channels and cages, and Coulomb forces can be neglected. The positions of the atoms are taken from Ref. [22]. The zeolite is considered to be rigid [19] as this allows for the use of efficient grid interpolation techniques to compute interactions and forces. In cation-free all-silica sieves, there is evidence that adsorption and diffusivities are virtually unchanged for small alkanes when lattice vibrations are included [23–25]. Although with a fixed framework a flexible molecule can not dissipate its energy, there is still some thermalization through the transfer of translational energy into the internal degrees of freedom of the molecule.

Conventional Monte Carlo (MC) is time-consuming for long chain molecules. The fraction of successful insertions into the sieve is too low. To increase the number of successfully inserted molecules we apply the CBMC technique [26,27]. In the CBMC technique a molecule is grown segment-by-segment. For each segment we generate a set of k trial orientations according to the internal energy U^{int} and compute the external energy $U_i^{\text{ext}}(j)$ of each trial position j of segment i . We select one of these trial positions with a probability

$$P_i(j) = \frac{e^{-\beta U_i^{\text{ext}}(j)}}{\sum_{l=1}^k e^{-\beta U_i^{\text{ext}}(l)}} = \frac{e^{-\beta U_i^{\text{ext}}(j)}}{w(i)}, \quad (7)$$

where $\beta = 1/(k_B T)$, with k_B the Boltzmann constant and T the temperature. The selected trial orientation is added to the chain and the procedure is repeated until the entire molecule has been grown. For this

newly grown molecule we compute the so-called Rosenbluth factor [28]

$$W = \prod_i w(i). \quad (8)$$

The Rosenbluth factor of the new configuration is related to the free energy F

$$F = -\frac{1}{\beta} \ln \frac{\langle W \rangle}{\langle W^{\text{id}} \rangle}, \quad (9)$$

where $\langle W^{\text{id}} \rangle$ is the Rosenbluth factor of an ideal chain (defined as a chain having only internal interactions), which can be calculated from a simulation of a single chain. In addition, the Rosenbluth factor is related to the Henry coefficient K_H

$$K_H = \beta \frac{\langle W \rangle}{\langle W^{\text{id}} \rangle}. \quad (10)$$

In the limit of zero coverage the Henry coefficient is related to the heat of adsorption Q_{st} via a thermodynamic relation [27]

$$Q_{\text{st}} = \frac{\partial \log(K_H)}{\partial \beta}. \quad (11)$$

Although this formula can be used to check the consistency, in practice it is more convenient to obtain the heat of adsorption in the infinite dilution limit from

$$Q_{\text{st}} = \langle U_{\text{gz}} \rangle - \langle U_z \rangle - \langle U_g \rangle - k_B T, \quad (12)$$

where $\langle U_{\text{gz}} \rangle$ and $\langle U_g \rangle$ are the ensemble average of the potential energy of the zeolite-guest system and the energy of an isolated ideal chain, respectively, and where the average zeolite energy $\langle U_z \rangle$ is zero for a rigid zeolite. The CBMC algorithm greatly improves the conformational sampling of molecules and increases the efficiency of chain insertions, required for the calculation of the free energy and Henry coefficients, by many orders of magnitude.

III Transition State Theory

ERI-, CHA-, and LTA-type zeolites consist of cages separated by 0.4 nm wide windows. These windows form large free energy barriers to diffusion. If the barrier is

much higher than $k_B T$, diffusion is an activated process. Once in a while a particle hops from one cage to the next, but the actual crossing time is negligible compared to the time a particle spends inside the cage. To compute the hopping rate from one cage to the next the rare-event simulation techniques of Bennet and Chandler [14, 15] can be readily applied. We give a brief overview of the main results of the Bennet-Chandler approach.

We consider a system which can be in two stable states, A and B . The reaction coordinate, a value that indicates the progress of the diffusion event from adsorption site A to site B , is denoted by q . Here, q is a function of the Cartesian coordinates, \dot{q} denotes the derivative in time, q^* is the location of the dividing surface, and q_A, q_B are the minima of the free energy corresponding to state A and B , respectively. We introduce two characteristic functions n_A and n_B that measure whether the system is in state A or B . A possible and often used definition is

$$n_A = \theta(q^* - q), \quad (13)$$

$$n_B = \theta(q - q^*), \quad (14)$$

where θ is the Heaviside function $\theta(x)$, which has value zero for $x < 0$ and value 1 for $x \geq 0$. With these definitions the transition rate $k_{A \rightarrow B}$ is given by [16]

$$k_{A \rightarrow B} = \underbrace{\frac{\langle \delta(q - q^*) \rangle}{\langle \theta(q^* - q) \rangle}}_{P(q)} \times \underbrace{\frac{\langle \dot{q} \delta(q - q^*) \theta(q(t) - q^*) \rangle}{\langle \delta(q - q^*) \rangle}}_{R(t)}, \quad (15)$$

where $P(q)$ is the equilibrium probability density of finding the system at the top of the barrier divided by the equilibrium probability of finding it at state A , and where $R(t)$ is the averaged flux at the top of the barrier multiplied by the probability that the system ends up in state B at time t . The expression is rigorously correct for arbitrary crossings provided that the barrier is much larger than $k_B T$. $P(q)$ is a *time-independent* equilibrium quantity and can be

computed explicitly

$$P(q) = \frac{\langle \delta(q - q^*) \rangle}{\langle \theta(q^* - q) \rangle} = \frac{e^{-\beta F(q^*)}}{\int_{-\infty}^{q^*} e^{-\beta F(q)} dq}, \quad (16)$$

where $F(q)$ is the free energy as a function of the diffusion path q . $R(t)$ is a conditional average, namely the product $\langle \dot{q}(0) \theta(q(t) - q^*) \rangle$, given that $q(0) = q^*$.

Using the assumption that the velocities of the atoms within the molecules follow a Maxwell-Boltzmann distribution, we can estimate from kinetic theory the long time value of $R(t)$ by $\frac{1}{2} |\dot{q}(0)| = \sqrt{\frac{k_B T}{2\pi m}}$, where m is the mass of the segments of the particle involved in the reaction coordinate (the total mass of the particle if the center of mass is used or the mass of only one segment if the reaction coordinate is a single segment like the middle bead in a molecule). Transition state theory predicts a crossing rate $k_{A \rightarrow B}^{\text{TST}}$ given by

$$k_{A \rightarrow B}^{\text{TST}} = \sqrt{\frac{k_B T}{2\pi m}} \frac{e^{-\beta F(q^*)}}{\int_{-\infty}^{q^*} e^{-\beta F(q)} dq}. \quad (17)$$

Calculating TST rate constants is therefore equivalent to calculating free energy differences. In the Bennet-Chandler approach it is sufficient to assign the barrier position q^* inside the barrier region. The result of the scheme does not depend on the specific location, although the statistical accuracy does. If the dividing surface is not at the top of the barrier the probability of finding a particle will be higher than at q^* , but the fraction of the particles that actually cross the barrier will be less than predicted by transition state theory. It is convenient to introduce the time-dependent transmission coefficient $\kappa(t)$, defined as the ratio

$$\begin{aligned} \kappa(t) &\equiv \frac{k_{A \rightarrow B}(t)}{k_{A \rightarrow B}^{\text{TST}}} \\ &= \frac{\langle \dot{q} \delta(q(0) - q^*) \theta(q(t) - q^*) \rangle}{\langle \frac{1}{2} |\dot{q}(0)| \delta(q(0) - q^*) \rangle}. \end{aligned} \quad (18)$$

The correction $\kappa(t)$ is the fraction of particles coming from the initial state that successfully reaches the final state out of those

that cross the dividing surface at $t = 0$. It corrects for trajectories which cross the transition state from A but fail to equilibrate in B. It can be shown that $\kappa(0) = 1$ and $k_{A \rightarrow B}(0) = k_{A \rightarrow B}^{\text{TST}}$. There is a large separation of time scales. The recrossings are completed in a time much less than the time to react and Eq. 18 will reach a plateau value κ . For classical systems $0 < \kappa \leq 1$ and Eq. 17 is corrected as

$$k_{A \rightarrow B} = \kappa k_{A \rightarrow B}^{\text{TST}}. \quad (19)$$

Standard Molecular Dynamics (MD) yields the transmission coefficients, a separate MC simulation the starting configurations. The reaction coordinate is restricted to the dividing surface q^* . The MC moves involved are translations of the reaction bead in the plane of the dividing surface and complete regrowing of the molecule starting from the restricted bead. Subsequently the transmission coefficient is calculated by standard MD in the micro canonical ensemble using a velocity Verlet integrator with a time step of 0.2 fs. The beads are given independent velocities, corresponding on average to the desired temperature, by sampling from a Maxwell-Boltzmann distribution. A molecule sampled at a particular temperature at the top of the barrier will acquire a huge velocity once it has arrived in the valley. No thermal equilibration takes place. In fact, the velocity is so high that it will very likely cross another window or (as in ERI- and CHA-type structures) bounce back from the opposite wall and recross the initial window again. For this reason it is necessary to terminate a trajectory once a valley has been reached. Failing to end the trajectory can lead to spurious, undamped oscillations in $\kappa(t)$.

The approach of $\kappa(t)$ to its plateau value can be quite slow [16]. Moreover, in the case of diffusive barrier crossings the transmission coefficient is quite small and κ can *not* be calculated accurately by using Eq. 15. The Bennet-Chandler approach becomes in-

efficient for systems with low transmission coefficients because the scheme prepares the system in a state that is not close to the steady-state situation. In addition, the scheme employs the θ -function to detect what state the system is in. The scheme can be improved by devising a perturbation that prepares the system immediately close to the steady-state, and by constructing a more continuous detection function.

One of the problems, when devising a more sophisticated scheme, is the lack of exact knowledge of the free energy of the system as a function of the order parameter. It is shown that in practice we need to approximate only $F(q)$ [16]. We denote our estimate of $F(q)$ by $F_{\text{est}}(q)$. Any reasonable guess will lead to a more rapid convergence than the delta function. Using the free energy estimate we can compensate approximately for the effect of the energy barrier. This leads to a more or less uniform distribution over the entire range of q . Only trajectories starting in the barrier region yield relevant information and therefore a weighting function $w(q)$ is applied, restricting the sampling to the barrier region

$$w(q) = \frac{e^{2\beta F_{\text{est}}(q)}}{\int_{q_A}^{q_B} e^{2\beta F_{\text{est}}(q)} dq}. \quad (20)$$

The following expression for $k_{A \rightarrow B}$ can be derived [16]

$$k_{A \rightarrow B} = \int_0^\infty \left\langle \dot{q}(0) \dot{q}(t) e^{\beta F_{\text{est}}(q(t)) - \beta F_{\text{est}}(q(0))} \right\rangle_w dt \frac{\int_{q_A}^{q_B} e^{2\beta F_{\text{est}}(q)} dq \langle w(q) \rangle_{\text{eq}}}{\left[\int_{q_A}^{q_B} e^{\beta F_{\text{est}}(q)} dq \right]^2 \langle n_A \rangle_{\text{eq}}}. \quad (21)$$

If $F(q)$ is known in advance or, as in our case, $F_{\text{est}}(q)$ is the best possible measurement in a simulation, then $F_{\text{est}}(q)$ and $F(q)$ become synonymous. This leads to a sim-

plification of the expressions

$$\kappa(t) = \int_0^\infty \left\langle \dot{q}(0) \dot{q}(t) e^{\beta F(q(t)) - \beta F(q(0))} \right\rangle_w dt$$

$$\frac{e^{\beta F(q^*)}}{\int_{q_A}^{q_B} e^{\beta F(q)} dq} \frac{2}{\langle |\dot{q}| \rangle}, \quad (22)$$

$$k_{A \rightarrow B} = \frac{\int_0^\infty \left\langle \dot{q}(0) \dot{q}(t) e^{\beta F(q(t)) - \beta F(q(0))} \right\rangle_w dt}{\langle n_A \rangle_{\text{eq}} \int_{q_A}^{q_B} e^{\beta F(q)} dq \int_{-\infty}^\infty e^{-\beta F(q)} dq}. \quad (23)$$

At infinite dilution the molecules perform a random walk on a lattice spanned by the cage-centers. The transmission rates are easily converted to diffusion coefficients if the jump distance and the number of equivalent diffusion paths are known [29]. Error calculations are performed for the measured quantities, including the free energy profiles $F(q)$, the heats of adsorption, the Henry coefficients, and the diffusion coefficients. Each insertion of a chain molecule is statistically independent and error bars are easily calculated for each point on the free energy profile and for the Henry coefficients. Error bars on the diffusion coefficients, obtained from the transmission rate k_{AB} , are less trivial. The complete free energy profile is regenerated for each point from their average value and error value σ , assuming a Gaussian distribution with width σ around its average value [30]. A smooth cubic approximation spline is fitted to the regenerated data and Eq. 16 is evaluated using the spline-approximation. The procedure is repeated many times and the error $P(q)$ is assumed to be twice the standard deviation in the resulting data-set (95 percent confidence interval). The error in the diffusion coefficient is then calculated by applying normal error propagation rules.

IV Reaction coordinate

To compute the free energy as a function of the position in the zeolite, one has to relate

a position in the channel or cage to a reaction coordinate q . Such a map should satisfy several criteria

- Every coordinate in the simulated volume should be uniquely designate a position in a single cage.
- All Cartesian space should be used and partitioned into equivalent regions in order to have a correct entropic contribution. Not only all pore volume should be used, but also the zeolite volume. The space-group of the zeolite indicates how to exploit the inherent symmetry.
- The mapping should achieve the highest free energy barrier. If not, the transmission coefficient can become very small, making the computation extremely inefficient or even impossible.

In addition, a linear mapping is preferred from a computational point of view, to avoid correcting the density distribution for the use of constraints [16].

We stress that choosing an appropriate reaction coordinate is vital. By trial and error we concluded that using the second bead of the alkane chain gave near optimal results for all alkane chains and zeolites discussed here. Chains are always newly grown starting from this bead. The mapping is depicted in Fig. 1, where a part of the ERI-type silica is shown with cages A and B (connected to other cages) sliced half open. Two examples of the mapping are depicted: a C_{14} chain in cage A and a C_{10} chain in cage B . Free energy values are mapped onto the one-dimensional free energy profile $F(q)$ by orthogonal projection of the position of the second bead onto the line perpendicular to the window. Only chains that have the smallest distance to either cage A or B (of all the cages in the zeolite) give a contribution to the transmission rate $k_{A \rightarrow B}$.

There are two ways to obtain an near-optimal mapping: try all beads, compute

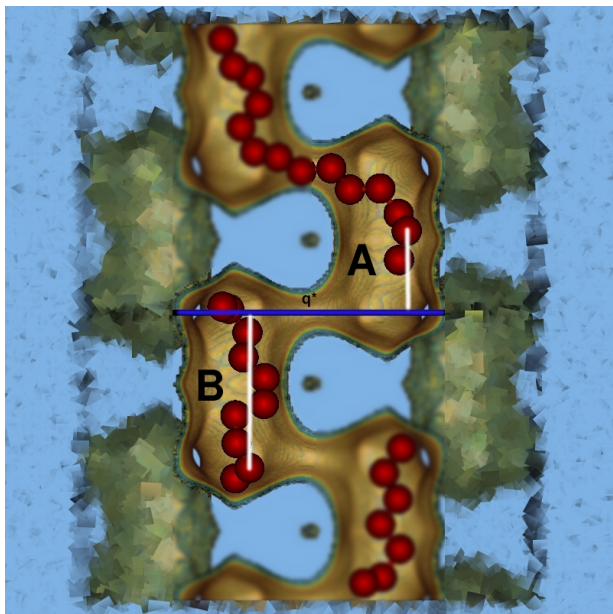


Figure 1: The reaction coordinate q , indicating the progress of the diffusion event from adsorption site A to adsorption site B, is defined as the position of the second bead of a chain mapped orthogonal to the axis of projection (the line perpendicular to the window). The resulting free energy profile $F(q)$ indicates a high free energy barrier at the position of the window q^* separating cage A and B. Shown here are two examples in ERI-type silica: C_{14} in cage A, and C_{10} in cage B. Also shown a C_8 molecule, but it would contribute to the diffusion between cage B and the C_8 cage (these contributions can be converted into a $k_{A \rightarrow B}$ contribution due to symmetry reasons). The C_8 molecules fit snugly inside the erionite cages, C_{10} adapts high energy configurations, while the C_{14} stretches energetically more favorable across two cages.

the free energy profiles and then choose the one which gives the highest free energy difference, or try all beads, compute the transmission coefficient κ and then choose the one which gives the highest κ . Fig. 2 shows the free energy profiles (raw, unsmoothed data) in ERI-type silica at 600 K for mappings using the various beads of C_9 as the order parameter. The maximum of the free energy is at the $q = 0$ position corresponding to the dividing window q^* , the minimum values are at $q \approx |4|$ correspond-

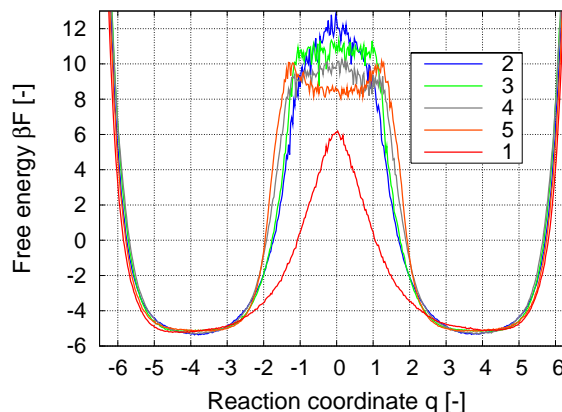


Figure 2: Free energy profiles $F(q)$ (raw, unsmoothed data) in ERI-type silica at 600 K for C_9 using bead 1, 2, 3, 4 and 5 as the mapping bead (lines from top to bottom at $q = 0$ in order of the legend).

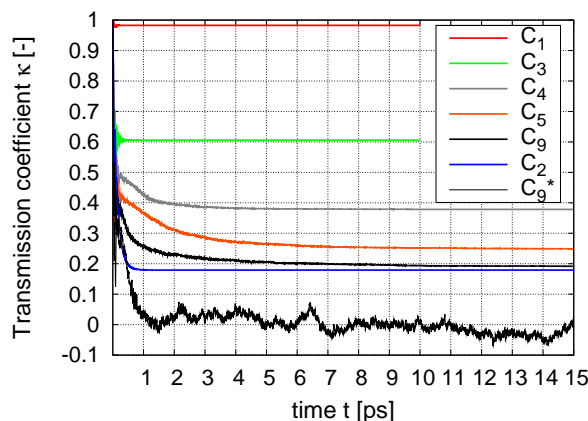


Figure 3: Transmission coefficients $\kappa(t)$ in ERI-type silica at 600 K plotted against simulation time for C_1 - C_5 and C_9 using the second-bead-mapping, and C_9^* using the middle-bead-mapping (lines from top to bottom in order of the legend).

ing to values deep inside cage A and B. We note that the x -axis corresponds to the line perpendicular to the window in Fig. 1. The second-bead-mapping gives the highest free energy barrier and in addition, the shape of the free energy profile indicates that molecules will fall off the barrier the fastest. With the second bead on top of the barrier the tail of the chain is bended and close to the wall. It has already one bead

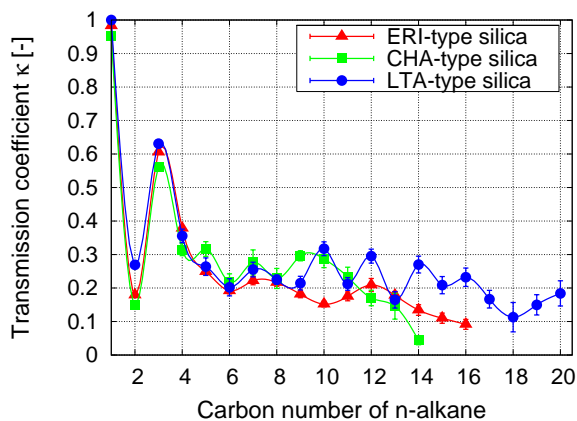


Figure 4: Transmission coefficients in ERI-, CHA-, and LTA-type silica plotted as function of carbon number of the *n*-alkane. Error bars are only shown when larger than the symbol size.

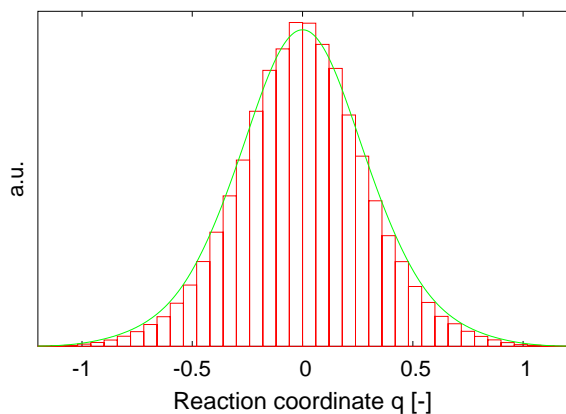


Figure 5: Histogram of the sampled positions of the second bead of propane in ERI-type silica. The $q = 0$ position corresponds to the position of the dividing window. The solid curve denotes the curve $e^{\beta F(q)}$ with $F(q)$ the spline fit through the free energy profile of propane.

through the window and combined with the asymmetry of the molecule it is dynamically most balanced. Using the middle-bead-mapping (bead 5) it is nearly impossible to obtain κ . The chains tend to sit comfortable in a (small) local free energy minimum and diffuses on top of the barrier without actually falling off the barrier. For other chain lengths similar results have been obtained.

In Fig. 3 we show the transmission coefficient $\kappa(t)$ for C_1 - C_5 , C_9 for ERI-type silica at 600 K with a second-bead-mapping. For comparison we show the result for C_9 with a middle-bead-mapping. The position of the middle bead can not be used, since $\kappa(t)$ does not reach a clear positive plateau value. Note that a change in the barrier height results in an exponential change of the transmission coefficient. Computing the transmission coefficient for the various mappings is therefore more sensitive. Fig. 4 shows the transmission coefficient κ as a function of chain length at 600 K for the zeolites ERI-, CHA-, and LTA-type silica. The second-bead-mapping works well and the transmission coefficients are for C_3 -plus of approximately equal magnitude ($\kappa = 0.1 - 0.3$). This facilitates the interpretation and comparison of the free energy profiles as a function of chain length.

The free energy profiles (in combination with the transmission coefficients) can be used to calculate $k_{A \rightarrow B}$. The Ruiz-Montero et al. method uses the free energy profile to define a weighting function $w(q)$ for sampling initial configurations. In Fig. 5 we show the histogram of the position of the second bead of propane chains around q^* in ERI-type silica. The shape of the distribution is proportional to $e^{\beta F_{\text{est}}(q)}$ with $F_{\text{est}}(q)$ the free energy profile of propane. The sampled configurations are then used to measure the diffusion coefficient on top of the barrier by calculating the velocity autocorrelation function taking the weighting function into account. In Table IV we compare the diffusion results for both methods for C_1 - C_9 in ERI-type silica at 600 K. The Bennet-Chandler method is performed using the second-bead-mapping, while the Ruiz-Montero et al. method is performed with the middle-bead-mapping. Note that the methods are equal for C_1 - C_4 . The results are consistent, and although the statistics is rather poor, the Ruiz-Montero et al. method worked for this poor choice of reaction coordinate where the Bennet-Chandler

n	$D^{\text{TST}} [m^2/s]$	$\kappa [-]$	$D_{\text{BC}} [m^2/s]$	$D_{\text{RM}} [m^2/s]$
1	$1.31e - 12 \pm 1.33e - 14$	0.983 ± 0.002	$1.3e - 12 \pm 1.3e - 14$	$1.3e - 12 \pm 2.4e - 14$
2	$1.85e - 13 \pm 3.06e - 15$	0.179 ± 0.002	$3.3e - 14 \pm 6.5e - 16$	$4.4e - 14 \pm 2.0e - 14$
3	$1.71e - 16 \pm 1.92e - 17$	0.606 ± 0.003	$1.0e - 16 \pm 1.2e - 17$	$1.0e - 16 \pm 8.5e - 18$
4	$7.46e - 16 \pm 1.03e - 16$	0.378 ± 0.007	$2.8e - 16 \pm 3.9e - 17$	$2.8e - 16 \pm 2.6e - 17$
5	$1.48e - 15 \pm 2.59e - 16$	0.249 ± 0.009	$3.7e - 16 \pm 6.6e - 17$	$4.3e - 16 \pm 5.0e - 17$
6	$3.86e - 15 \pm 8.14e - 16$	0.192 ± 0.009	$7.4e - 16 \pm 1.6e - 16$	$5.1e - 16 \pm 9.4e - 17$
7	$1.53e - 15 \pm 3.94e - 16$	0.222 ± 0.012	$3.4e - 16 \pm 8.9e - 17$	$2.6e - 16 \pm 2.2e - 16$
8	$8.95e - 16 \pm 3.00e - 16$	0.217 ± 0.012	$1.9e - 16 \pm 6.6e - 17$	$4.6e - 16 \pm 4.4e - 16$
9	$2.93e - 15 \pm 1.25e - 15$	0.182 ± 0.011	$5.3e - 16 \pm 2.3e - 16$	$4.1e - 16 \pm 3.8e - 16$

Table 1: Comparison of two transition state theory methods for computing diffusion constants in the zeolite erionite for $C_1 - C_9$. The Bennet-Chandler method uses the second-bead-mapping and dynamically corrects the transition state estimate k^{TST} with the transmission coefficient κ . The diffusion coefficient D_{BC} is computed as $\kappa \times D^{\text{TST}}$. The diffusion coefficients D_{RM} in the last column are obtained using the Ruiz-Montero et al. method. Here, the mapping used was the middle-bead-mapping, which did not work for the second-bead-mapping due to the extremely low transmission coefficients.

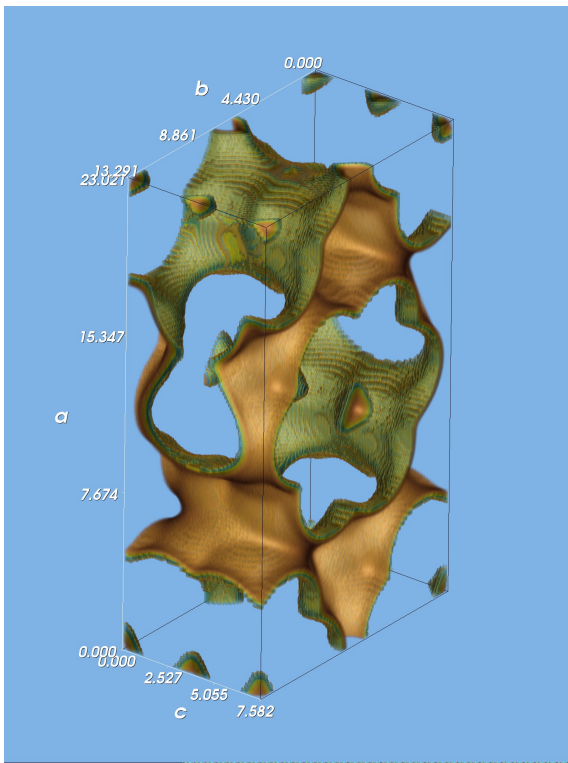
method completely failed. It provides much more freedom and worked for several mappings, including the ones which have inherent diffusive behavior on top of the barrier. The validity of the diffusion results was checked by using both methods.

V Zeolite Description

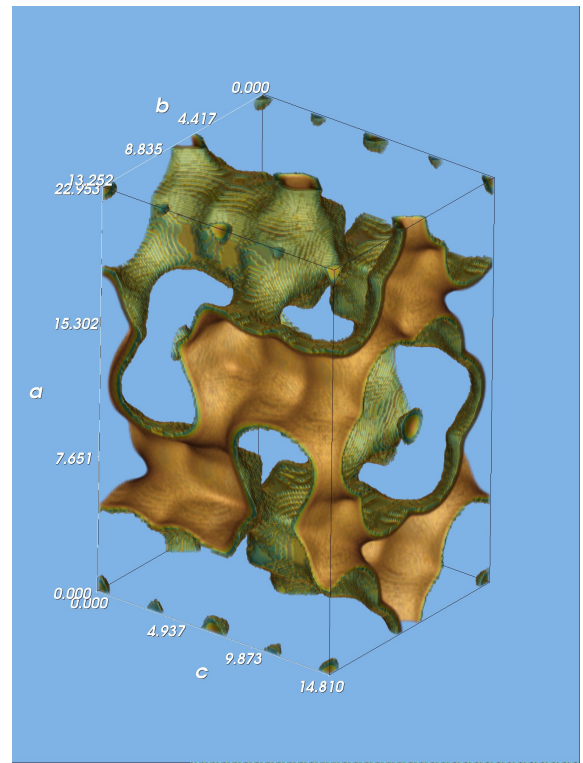
Small differences in the crystal structure of silica cause large differences in the diffusion rates of an alkane as a function of chain length. The OFF-type silica structure [31] crystallizes in the hexagonal-ditrigonal dipyramidal spacegroup $P\bar{6}m2$ with $a = 1.31$ nm, $b = 1.31$ nm, $c = 0.76$ nm, and $\alpha = \beta = 90^\circ$, $\gamma = 120^\circ$. In the absence of stacking faults OFF-type silica would consist of channels 0.67 nm across. The perpendicular 0.36-0.49 nm wide windows have a significantly slower diffusion rate, and are only accessible to small molecules. The pores are girthed at 0.76 nm intervals by 12T-membered ring structures of approximately 0.67×0.68 nm. The ERI-type silica structure [32] crystallizes in the hexagonal dipyramidal spacegroup $P6_3/mmc$ with $a = b = 1.31$ nm, $c = 1.52$ nm, and $\alpha = \beta = 90^\circ$, $\gamma = 120^\circ$. The elongated erionite cages are approximate the shape of 1.3×0.63 nm cylinders connected by 0.36×0.51 nm windows. Only linear molecules are able to penetrate the windows. There are three windows at the top of the cage rotated 120° with respect to each other. At the bottom of the cage there are also three windows rotated 120° with respect to each other. The top three windows are aligned with the windows at the bottom. Zeolite T is an intergrowth of OFF- and ERI-types zeolites [33]. It consists primarily of OFF-type zeolite interspersed by thin layers of ERI-type zeolite. Each ERI-type cage blocks an OFF-type channel and forces diffusion through the ERI-type window. The CHA-type structure [34] has the spacegroup $R\bar{3}m$ (a squashed cube) with $a = b = c = 0.942$

nm, and $\alpha = \beta = \gamma = 94.47^\circ$. The CHA-type cage is an ellipsoidal cavity of about 1.0×0.67 nm across, accessible through 0.38 nm wide windows. Only linear alkanes are able to penetrate the windows. There are three windows at the top of the cage rotated 120° with respect to each other. At the bottom of the cage there are also three windows rotated 120° with respect to each other. The bottom three are at a 60° angle relative to the top ones. The LTA-type structure [35] has a cubic spacegroup $Fm\bar{3}c$ with $a = b = c = 2.4555$ nm, and $\alpha = \beta = \gamma = 90^\circ$. The crystallographic unit cell consists of 8 large spherical cages (named α -cages) of approximately 1.12 nm interconnected via windows of about 0.41 nm diameter.

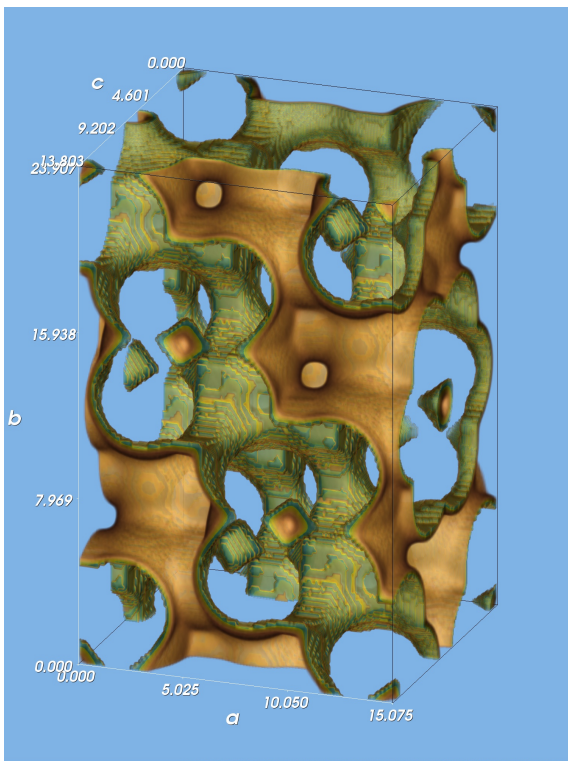
In Fig. 6(a), 6(b), 6(c), and 6(d) we show the volume-rendered pictures of the OFF-, ERI-, CHA-, and LTA-type silica, respectively. The unit cell is divided into $150 \times 150 \times 150$ voxels (constant valued volume-elements). At millions of random positions in the unit cell the free energy of a test-particle (methane molecule) is calculated and assigned to the appropriate voxel. To visualize this energy landscape the three-dimensional dataset is volume rendered [36, 37], removing the parts that generate overlap (the zeolite itself) by making it completely transparent. Low energy values are rendered with medium transparency, allowing the inside of the cages to be viewed as voids. Higher energy values are rendered less and less transparent until the energy approaches a cutoff energy and is regarded as part of the zeolite wall. Also color is assigned according to the energy value: brown for the inside view of a cage, green for the outside view of a cage. For simulation efficiency all structures are converted to orthorhombic periodic unit cells with dimensions $a = 2.3021$ nm, $b = 1.3291$ nm, and $c = 0.7582$ nm for OFF $a = 2.2953$ nm, $b = 1.3252$ nm, and $c = 1.481$ nm for ERI, $a = 1.5075$ nm, $b = 2.3907$ nm, and $c = 1.3803$ nm for CHA. In addition to the relevant cages and channels there are also topo-



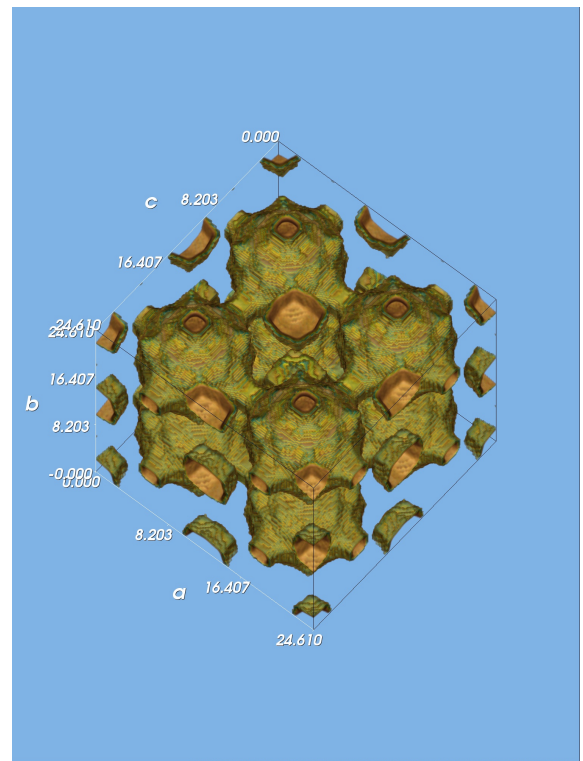
(a)



(b)



(c)



(d)

Figure 6: The structure of a single periodic unit cell of (a) OFF-type silica, (b) ERI-type silica, (c) CHA-type silica, and (d) LTA-type silica. Distance-labels are plotted in units Å.

logically disconnected pockets. A methane molecule does fit at that position, but it is not accessible from the main cages and channels. An example is the visibly disconnected SOD-type sodalite-cage (β -cage) in LTA. To obtain correct results it is necessary to artificially block the inaccessible pockets for adsorbing molecules.

To examine the critical molecular length at which molecules are forced to stretch into two cages the silica structures are probed with molecules of various lengths. The simulation snap-shots are visually inspected and end-to-end distance histograms (data not shown) are studied. The OFF-type channels can host all chain lengths. The largest molecule that fits in a single ERI-type cage is n -C₁₃. It assumes a serpentine-like configuration extending tethered between opposite windows which makes it about 1.6 nm long. Similarly, 1.35 nm long n -C₁₁ is the longest molecule that can be tethered between two opposing windows in a CHA-type cage. LTA-type cage can harbor molecules as long as n -C₂₂– n -C₂₄ in a conformation coiled like a snake in a basket. Pictures of these snapshots are published in Ref. [6].

VI Results and Discussion

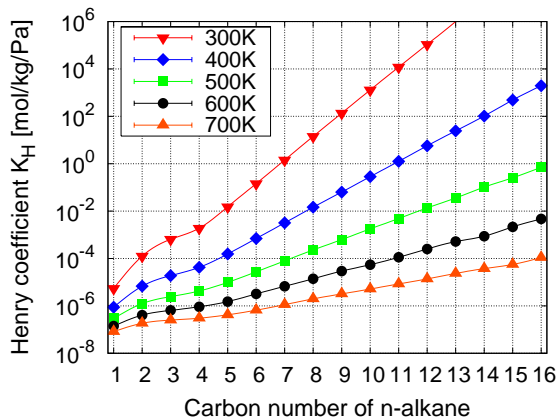
A Henry Coefficients and Iso-steric Heats of Adsorption

Molecular sieves have the ability to trap molecules, which can access their intra crystalline void volume. For low pressures the amount of adsorbed molecules is linearly related to the pressure, with the Henry coefficient as the proportionality constant. If the external pressures are sufficiently low, the Henry coefficient provides a good estimation of the extent of adsorption isotherms. In Fig. 7(a) the Henry coefficients at various temperatures as a function of chain length for OFF-type silica are shown. The Henry coefficients increases exponentially

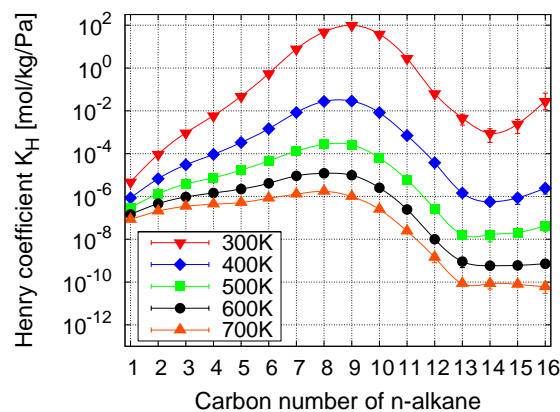
with alkane chain length, because the enthalpy gained by molecule-wall interaction outweighs the loss in entropy. Other channel structures like MFI-and TON-type silica exhibit a similar pattern.

ERI- and CHA-type zeolites show a markedly different behavior (Fig. 7(c)). A clear cage-effect of many orders of magnitude is present: a periodic, non-monotonic dependence of the Henry coefficient on chain length. The local maximum indicates that the shape of n -C₈– n -C₉ is commensurate with the shape of an ERI-type cage, whereas the shape of n -C₅– n -C₆ is commensurate with that of a CHA-type cage. A sharp decrease in the Henry coefficient is observed when molecules are forced to curl up, so as to fit into a single cage. When they are even longer, this conformation becomes too unfavorable, and they stretch across two cages instead. In ERI-type silica the first molecule to stretch across two cages is n -C₁₄, in CHA-type silica it is n -C₁₂. This neatly reflects the difference in size between the ERI-and CHA-type cages. Increasing the chain length improves adsorption again, until the molecule has to curl up and eventually has to stretch across three cages. As opposed to the small, elongated ERI- and CHA-type cages, molecules have more orientational freedom in the spherical, larger LTA-type cages. As a result, the n -alkane that fit best is more temperature dependent than for ERI- and CHA-type silica. At 300 K the molecule that fit most snugly is n -C₂₀, at 500 K it is n -C₁₄– n -C₁₈, while at 700 K the plateau stretches from n -C₆ to n -C₁₄. The largest molecules that fit inside a single cage are C₂₂–C₂₄, and represent the local minimum in the Henry coefficient.

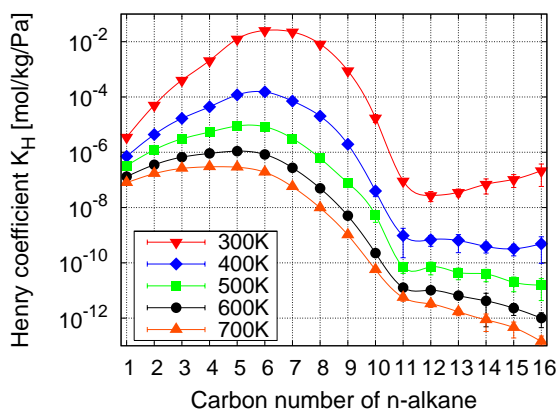
For all silicas studied here, the adsorption decreases with increasing temperature, since the thermal energy increase causes a lowering of the physisorption energy. The positions of the maxima, i.e. the best adsorbing molecules, shift towards lower chain lengths for increasing temperature. The maxima themselves become broadened



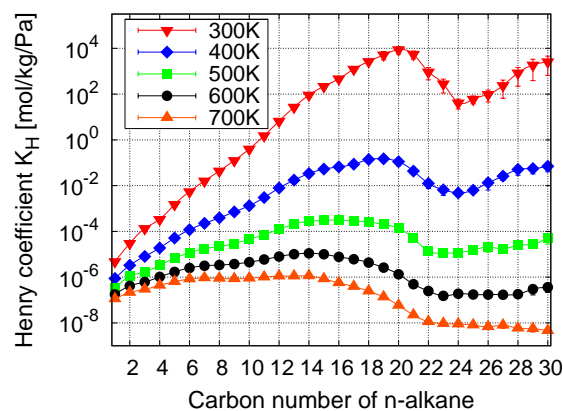
(a)



(b)



(c)



(d)

Figure 7: Henry coefficients as a function of chain length at various temperatures for (a) OFF-type silica, (b) ERI-type silica, (c) CHA-type silica, and (d) LTA-type silica. At low pressure the loading is linear in the pressure with the Henry coefficient as the proportionality constant. Error bars are only shown when larger than the symbol size.

and can even become large plateaus of equally well adsorbing molecules. Also the local minima shift towards lower chain lengths with increasing temperatures. The position of these minima indicates a cross-over point. Below this cross-over point the molecules fit into a single cage, above this point the chains start to find it energetically more favorable to stretch across two cages.

The heat of adsorption Q_{st} is related to the Henry coefficient. The isosteric heat of adsorption obtained from simulation is plotted in Fig. 8 as a function of chain length for OFF-, ERI-, CHA-, and LTA-type silica. The heat of adsorption is obtained from a single NVT (600K) simulation in the gas phase and a single simulation of one molecule adsorbed in ERI-type silica, measuring the average energies as needed in Eq. 12. The result is consistent with the thermodynamic limit Eq. 11, where we obtained the heat of adsorption as an average over a temperature range. The heat of adsorption has only a slight temperature dependence for these silicas. We were unable to find comparative experimental data on ERI-, CHA-, or LTA-type silica or aluminum phosphates. The heat of adsorption for OFF-type silica is directly proportional to the alkane length, while that of ERI- and CHA-type silica shows a non-monotonic, periodic behavior, with similar periods as the Henry coefficient data. The heat of adsorption Q_{st} in LTA-type silica is also non-monotonic, although only for alkanes longer than C_{21} (data not shown).

Many zeolites show a well defined linear variation of adsorption energy with carbon number and a linear relationship between the entropy and energy of adsorption (compensation effect). In Ref. [38] Ruthven and Kaul present such correlations for sorption of linear alkanes on the Na-form of zeolite X, the Na-form of zeolite Y, Ultra Stable zeolite Y, and silicalite. We found that pores with constrictions (*windows*) that approach the diameter of the adsorbate exhibit a dramatically different behavior. Instead

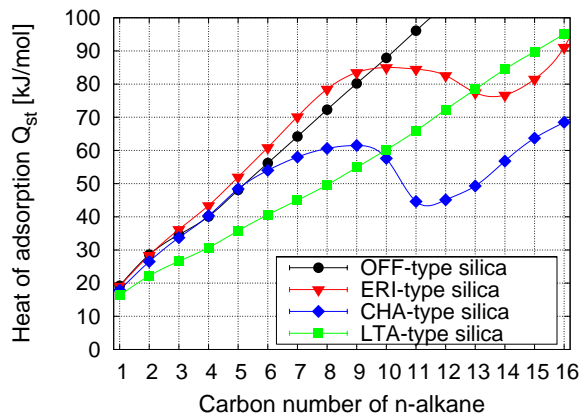


Figure 8: Heat of adsorption Q_{st} as a function of chain length of the alkanes adsorbed in OFF-, ERI-, CHA-, and LTA-type silica at 600 K using Eq. 12. Error bars are only shown when larger than the symbol size.

of attractive adsorbate-adsorbent interactions, windows exert repulsive adsorbate-adsorbent interactions that increase the adsorption enthalpy of any n-alkane partially adsorbed inside such a window. Accordingly, the usual compensation between adsorption enthalpy and adsorption entropy ceases as soon as n-alkanes become too long to fit comfortably inside the wider part of these pores (*cages*) [6]. Our simulations indicate that the compensation theory is true for channel-type zeolites, but for cage/window-type zeolites with windows smaller than approximately 0.45 nm the results apply only to effective chain lengths much smaller than the cage size. At higher carbon numbers the data deviates and the linear relationship breaks down.

B Diffusion

The simulation results of diffusion of n-alkanes in ERI-type silica as a function of chain length at several fixed temperatures are presented in Fig. 9(left), while the experimental results found by Gorring on a potassium-exchanged intergrowth of OFF- and ERI-type zeolites are plotted in Fig. 9(right). The order of magnitude and over-

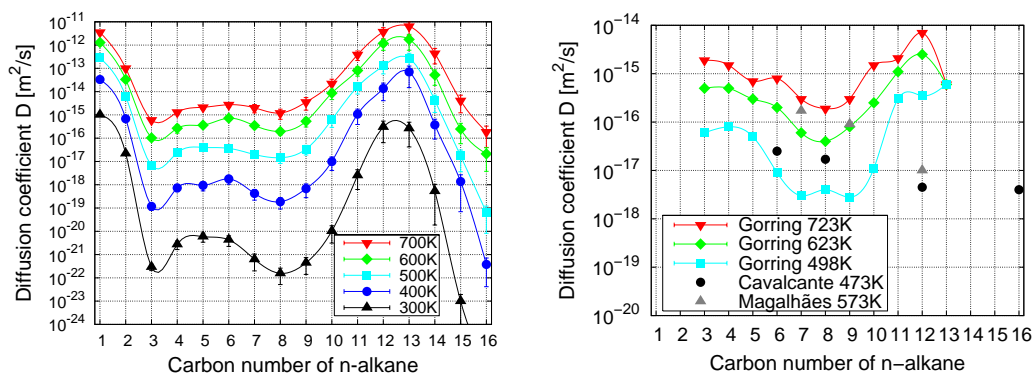


Figure 9: Diffusion coefficients as a function of chain length at various temperatures in ERI-type zeolite, (left) silica simulation results, (right) experimental results of Goring on a potassium-exchanged OFF/ERI intergrowth [2], Cavalcante et al. [12], and Magalhães et al. [13]. Error bars on the simulation data are only shown when larger than the symbol size.

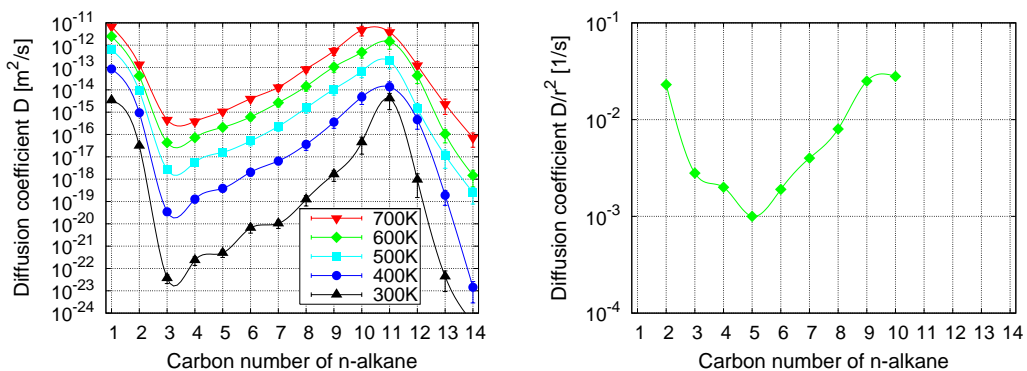


Figure 10: Diffusion coefficients as a function of chain length at various temperatures in CHA-type zeolite, (left) silica simulation results, (right) experimental results of Goring on H-CHA [3] (the crystal size r is unknown). Error bars on the simulation data are only shown when larger than the symbol size.

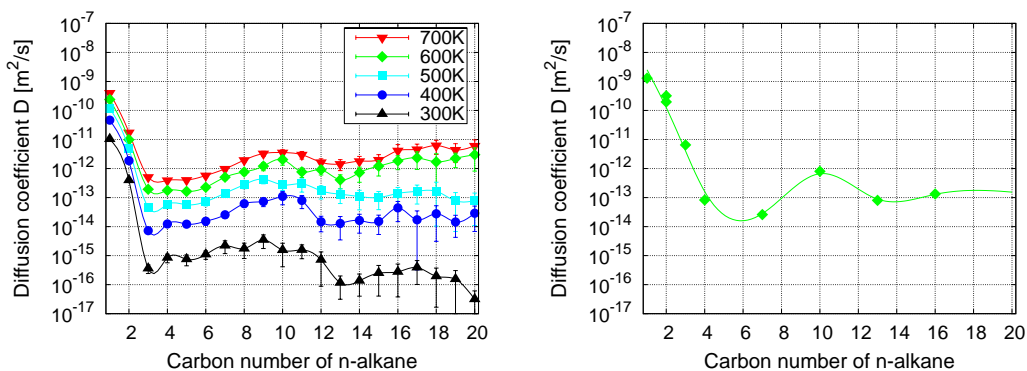


Figure 11: Diffusion coefficients as a function of chain length at various temperatures in LTA-type zeolite, (left) silica simulation results, (right) experimental results of Eic and Ruthven [39] on the Ca/Na-form of LTA-type zeolite. Error bars on the simulation data are only shown when larger than the symbol size.

all trend is well reproduced. The simulation data clearly supports the existence of a diffusional window-effect. The positions of the minima at C_8 and the maxima at C_{12} - C_{13} are well in agreement with Gorrings' experimental data. In addition to the C_8 minimum, the simulation data shows a second local minimum at C_3 .

In Fig. 10(left) we plot the simulation results for CHA-type silica and the experimental curve of Gorrings is shown in Fig. 10(right). Also the simulated data for CHA-type silica corroborate the existence of a diffusional window effect with the the maximum diffusion rate at C_{10} - C_{11} . The overall shape of the diffusion curve is satisfactorily reproduced. The simulation data finds the local minima at C_3 , while Gorrings results indicates a C_5 minimum, although the difference is small.

The behavior found for ERI- and CHA-type silica is markedly different from that of LTA-type silica (Fig. 11 left). The experimental results taken from Ref. [39, 40] are plotted in Fig. 11(right). The activation energies reported in the references are used to extrapolate the experimental diffusion coefficients to 600 K. In Ref. [39] the authors explicitly state that no evidence for a window effect in LTA-type zeolites has been found. Our simulation data agrees qualitatively well with the experimental results and also the order of magnitude is well reproduced for LTA-type silica. A possible window-effect is, however, expected at higher chain lengths (C_{23} - C_{24}) than have been studied experimentally. In addition, our simulation data seem to suggest that the slight decrease in diffusion beyond the C_{10} -region corresponds to the critical length where molecules feel the limitation of the cage and start to fold or coil.

For all silicas studied here, the diffusion coefficient decreases with decreasing temperature. The positions of the maxima and minima shift towards lower chain lengths for decreasing temperature. The window-effect in ERI- and CHA-type silica is sev-

eral orders in magnitude and increases with lower temperatures. LTA-type silica does not possess an order of magnitude window effect in the C_1 - C_{20} range, but shows complex intra-cage behavior. The agreement between simulated data on a cation-free LTA-type sieve and the experimental data on a cation loaded LTA-type zeolite is remarkable.

Gorrings provided an explanation for the window-effect in terms of a match between the effective length of a molecule and the size of the zeolite cage (the window-to-window distance) [2]. Eic and Ruthven applied similar logic to LTA-type zeolites [39]. They argued that the maximum activation energy should then occur at C_{13} - C_{14} in the LTA-type structure. When they found that the activation energy increased monotonically with carbon until C_{16} they dismissed the window effect. Our simulations indicate that they did not take adequately into effect that molecules usually curl and fold into energetically more favorable conformations, and thereby reduce their effective length [6]. Simulations predict that a window effect for LTA-type silica will occur, not at the chain lengths predicted by Eic and Ruthven, but around chain length C_{24} .

We obtained convincing evidence of a diffusional window-effect for both ERI- and CHA-type silica with positions for the maxima of diffusion corresponding to the cage size, as suggested by Gorrings. The simulations results agree qualitatively with Gorrings' experimental results, but deviate somewhat for small chain lengths in ERI-type silica. Discrepancies are not surprising, since we model Gorrings' complicated intergrowth of ERI- and OFF-type zeolites loaded with potassium cations with ERI-type silica. Fig. 12 depicts two OFF-type channels, one of which is blocked by an ERI-type intergrowth. ERI-type moieties only block the OFF-type channels for molecules larger than C_4 . A portion of the small molecules can easily "navigate" around the ERI-type block. They have so

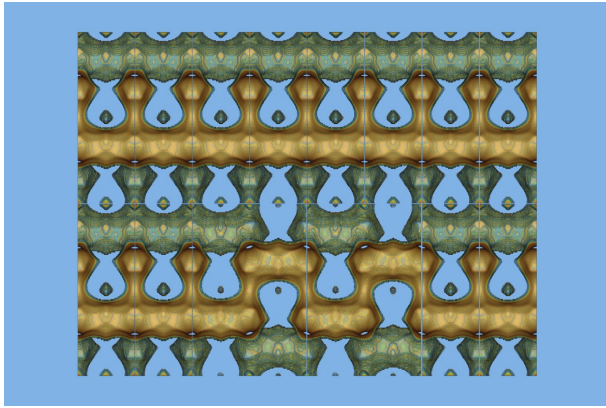


Figure 12: Zeolite T is a disordered intergrowth of OFF- and ERI-type zeolite and crystallographic not well defined. Although OFF-type zeolite is dominating, it is believed that ERI-type zeolite is the controlling bottleneck for diffusion. The top channel is an unobstructed of-fretite channel, the bottom channel is blocked by two unit cells ERI-type zeolite. The exact arrangement of the ERI-type intergrowth inside OFF-type zeolite is unknown, although ERI-type zeolite is thought to form thin layers converting OFF-type zeolite into a zeolite which can only adsorb linear molecules.

much orientational freedom that the diffusion path into the OFF-type side-cages is just as tortuous as the diffusion into the ERI-type moieties. These diffusional short cuts for n -C₄-minus could contribute to change in diffusion rate by orders of magnitude.

C Activation energies and frequency factors

For the OFF/ERI intergrowth [2, 12, 13] and both the Ca/Na- and Na-forms of LTA-type zeolites [39, 40] experimental data on diffusion activation energies are available. There are also some data on frequency factors in the K-form of the OFF/ERI intergrowth [2] and the Ca/Na-form of the LTA-type zeolite [39]. In our simulations we use all-silica with the equivalent framework structure, but without non-framework cations. Accordingly, the simulation data show the

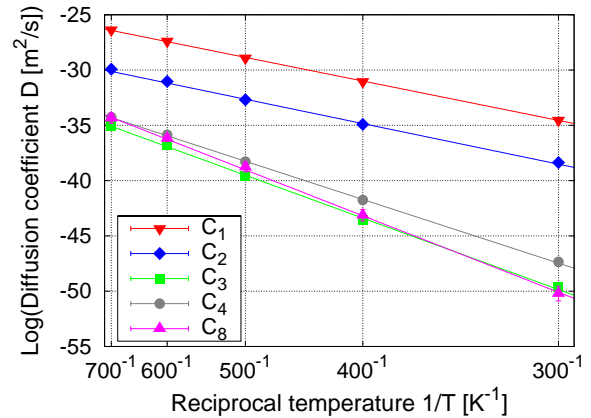


Figure 13: The natural logarithm of the diffusion coefficient in ERI-type silica plotted against the reciprocal temperature for C₁-C₄, C₈. The data is fitted with a straight line over the complete simulated temperature range showing Arrhenius-type behavior of the form $D_{\infty}e^{-E_D/k_B T}$. Error bars are only shown when larger than the symbol size.

influences of the structure of the zeolite itself and exclude loading and cation-effects.

To calculate the activation energy and frequency factor in simulation we exploit the fact that diffusion in cage-zeolites can be described as an activated process. If the jump distance is l and we have n equivalent jump sites, and d is the dimensionality, we can use the Einstein equation and relate the diffusion coefficient to the jump rate

$$D(T) = \frac{nl^2\nu_0}{2d} e^{-\frac{E_V+E_A}{k_B T}} = D_{\infty} e^{-\frac{E_D}{k_B T}} \quad (24)$$

Here, ν_0 can be thought of as an attempt frequency (frequency of oscillation) at the free energy minima, E_A the hopping activation energy, and E_V the vacancy formation energy. At infinite dilution the vacancy formation energy is zero. The self-diffusion activation energy E_D is the energy needed to "activate" the diffusion (with $e^{-\frac{E_D}{k_B T}}$ the probability that the molecule has enough energy). The pre-exponential factor or frequency factor D_{∞} is a material property of both the zeolite as well as the diffusing molecule. It accounts for directional steric

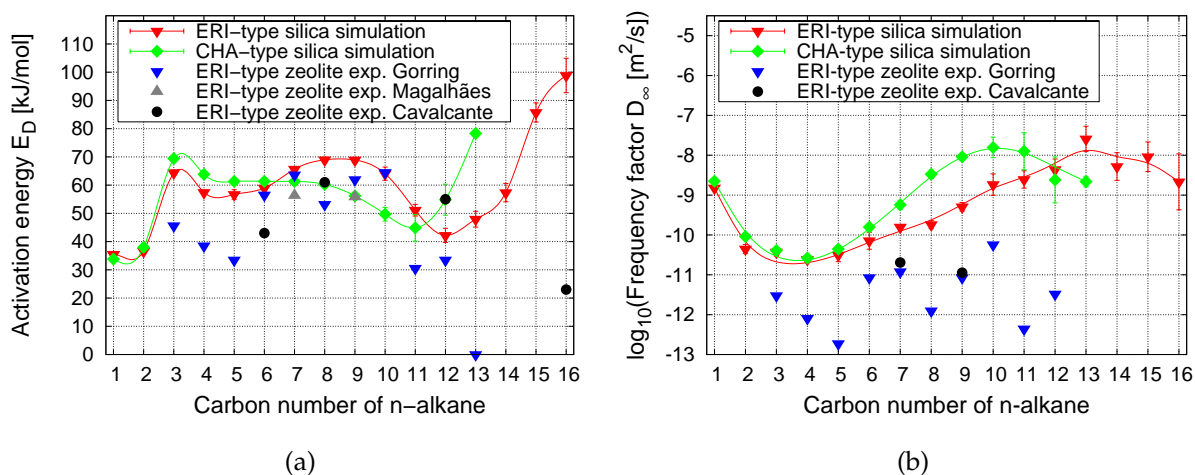


Figure 14: Fit to the Arrhenius expression for ERI- and CHA-type silica, (a) activation energies in units kJ/mol, (b) logarithm of the frequency factors D_0 in units m^2/s , both as a function of chain length. The simulation results are compared to the experimental results obtained by Gorring [2], Cavalcante et al. [12], and Magalhães et al. [13]. Error bars on the simulation data are only shown when larger than the symbol size.

effects that are difficult to predict.

Fig. 13 plots the logarithm of the diffusion coefficient as a function of inverse temperature for several chain lengths in the ERI-type silica. Over the complete temperature range (300-700 K) Arrhenius-type behavior of the form $D_\infty e^{-E_D/k_B T}$ is found. The slope of a fitted line in the figure corresponds to $-E_D$ and the value at infinite temperature is D_∞ . The activation energy is related to the height of the energy barrier arising from the repulsive forces involved in penetrating the relatively small windows of the zeolite framework. The nature of the surface and the precise shape of the pore appear to be of secondary importance [40]. The precise form of the frequency factor D_∞ varies with the shape of the free energy barrier.

The activation energy for diffusion E_D is plotted in Fig. 14(a) for ERI- and CHA-type silica. The simulation curve is qualitatively the inverse of the general shape of the diffusion curves, i.e. if a molecule has a high mobility the activation energy is small and visa versa. The experimental results for ERI-type zeolites are more difficult to interpret. The diffusion path of a C₁₃ is still quite

tortuous and an activation energy of zero is doubtful. Measuring diffusion of C₁₃ or higher accurately in ERI-type zeolites or intergrowths between ERI- and OFF-type zeolites might prove to be beyond current experimental techniques. The order of magnitude of the C₆-C₁₂ range is however quite well represented by our simulation data. We find significantly higher activation energies for C₃-C₅.

In Fig. 14(b) the frequency factors for ERI- and CHA-type silica are shown. Gorring found a compensation effect where the D_∞ increases as the activation energy E_D increases. The simulation results show only structural effects and the curves are relatively straightforward to interpret. The molecules in the C₂-C₅ range have the highest orientational freedom, while for higher chain lengths the alkane gets more and more constrained. This effect continues up to the C₁₀ for CHA-type silica and C₁₂-C₁₃ for ERI-type silica. These molecules represent local maxima. Longer molecules have to stretch through a window into two cages, leading again to more orientational freedom. We note that the maximum in the frequency factor corresponds to the minimum

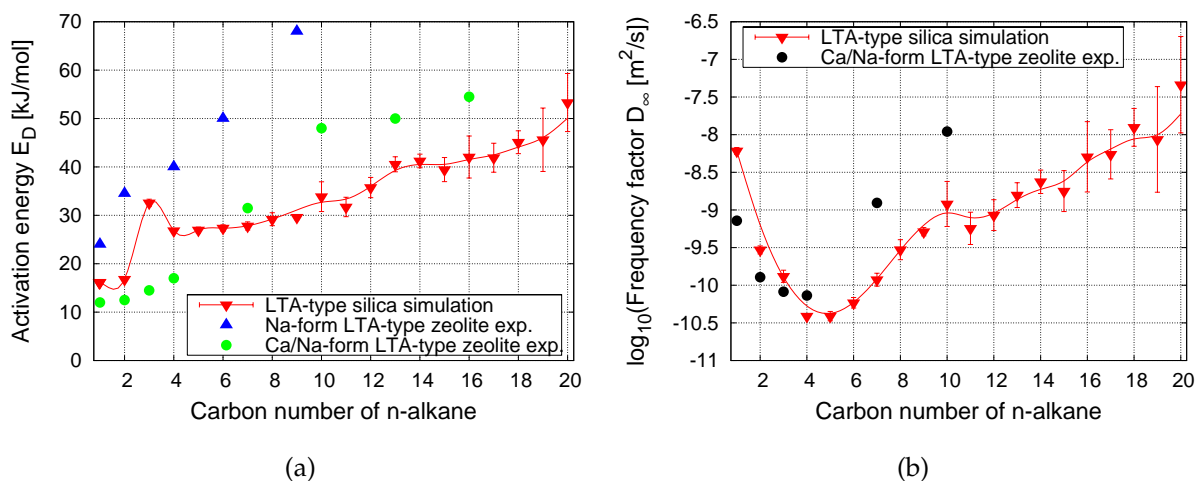


Figure 15: Fit to the Arrhenius expressions for LTA-type silica, (a) activation energies in units kJ/mol , (b) logarithm of the frequency factors D_0 in units m^2/s , both as a function of chain length. The results are compared to the experimental results obtained by Eic and Ruthven [39], and data published in Ref. [40]. Error bars on the simulation data are only shown when larger than the symbol size.

of the activation energy and the maximum in the diffusion constant.

In Fig. 15(a) the activation energy obtained for LTA-type silica from simulation is plotted along with experimental results for the Na- and Ca/Na-form of LTA-type zeolites from Refs. [39,40]. For a given chain length the activation energy for diffusion in the Na-form of LTA-type zeolites is higher than for the Ca/Na-form reflecting their difference in the pore size. We were unable to find data on the all-silica version of the LTA-type zeolite, but despite this the qualitative agreement with the Ca/Na-form of the LTA-type zeolite is already reasonable and agreement with a cation-free LTA-type sieve is expected to be quantitatively better. Fig. 15(b) shows the frequency factors. Both data sets suggest that C_4 - C_5 has the most orientational freedom and lead to the lowest attempt-frequency. Unlike ERI- and CHA-type silica, LTA-type silica exhibits a compensation-effect, i.e. the activation energy increases and the frequency factor concomitantly. The former increases because the higher mobility that comes with an increase in temperature impedes diffusion through a window, the latter because

the same mobility results in more attempts to pass through the window. Apparently both of these effects cancel out each other.

We note that the LTA-type cavities are large enough to contain molecules up to C_{23} . They can bend, fold, or coil like a spring. In addition to inter-cage entropic barriers (i.e. windows) also intra-cage entropic energy barriers can be present. For lower temperatures the temperature dependence of the frequency factor becomes important. For ethane molecules at low temperatures (150-300 K) diffusion can even decrease with increasing temperatures because heating the system moves the molecule away from the window, increasing the entropic barrier for cage-to-cage motion [41].

D Free energy profiles

The Henry coefficient can be considered as a spatial average of the free energy over the complete zeolite space (see Eq. 10). In simulations we are able to extract more detailed information such as the free energy of a molecule as a function of position. This is not an easily obtainable quantity in experiments. In addition to the potential energy,

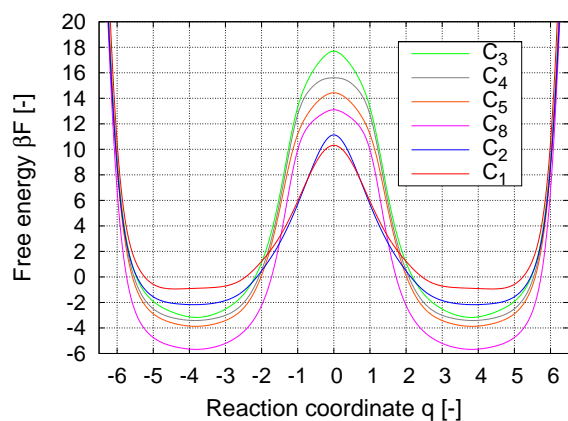


Figure 16: Free energy profiles for C_1 - C_5 , C_8 in ERI-type silica in dimensionless units as a function of the dimensionless reaction coordinate q (lines from top to bottom at $q = 0$ in order of the legend). The 8T-ring window corresponds to $q = 0$, $q \approx |4|$ corresponds to a location deep inside cage A or B, respectively.

the free energy $F(q)$ also contains an entropy contribution and is directly related to the probability of the molecule to be found at position q (see Eq. 16). We have plotted the free energy profiles (spline fits) in dimensionless units for C_1 - C_5 , C_8 in Fig. 16 at 600 K in erionite. The description as an activated process is well justified, as $\Delta F \gg k_B T$.

The free energy difference of ERI- (Fig. 17 top), CHA- (Fig. 17 middle), and LTA-type silica (Fig. 17 bottom) can be analyzed in terms of the value inside the cage and the value at the barrier. The simulations show that the dominating contribution to the diffusion coefficient is the height of the free energy barrier associated with the window between the cages. This height is given by the free energy difference between a molecule positioned in the cage and a molecule on top of the barrier. The depth of the free energy is directly related to the Henry coefficients. For the molecules in the cage we observe that as we increase the chain length the minimum of the free energy decreases until we reach an optimal chain length beyond which the n -alkanes no longer fit comfortably in one cage. For chain lengths

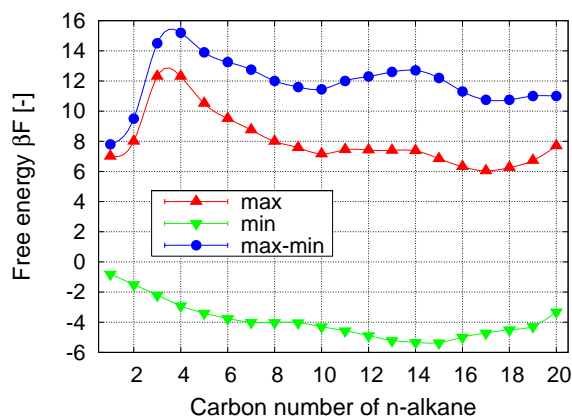
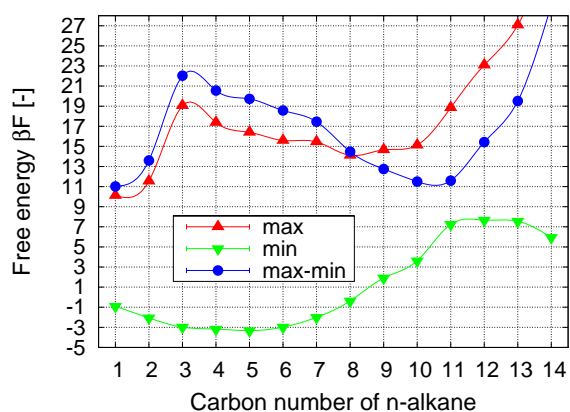
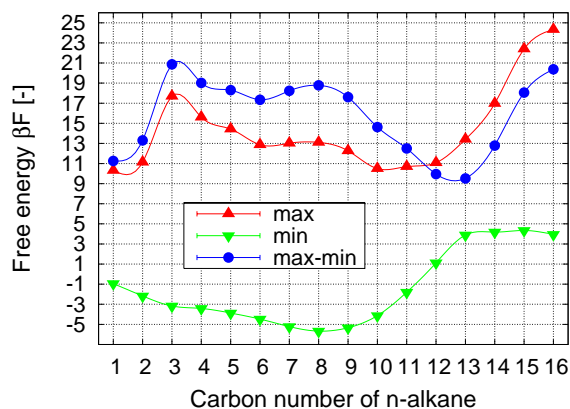


Figure 17: The free energy maximum, minimum, and difference between maximum and minimum in dimensionless units for (top) ERI-type silica, (middle) CHA-type silica, and (bottom) LTA-type silica at 600 K.

longer than this optimal length the free energy increases rapidly until the molecule is so big that additional atoms are added comfortably in the second cage and the minimum free energy is decreasing again. For the free energy of a molecule on top of the

barrier we observe an increase from C_1 to C_3 , as more atoms are placed on top of the barrier. For C_3 all atoms feel the influence of the window. Any additional atom will be placed in more favorable positions outside the window and therefore the barrier decreases for n - C_4 and continues to decrease until the molecule is so large that it feels the limitations of the cage. Beyond this chain length the maximum of the free energy increases rapidly. Combining these effects gives the generic diffusion behavior as a non-monotonic function of chain length. First a decrease followed by a possible plateau, an increase, and finally a decrease again. Key parameters in this mechanism are the presence of a narrow window combined with a cage structure. By optimizing the effective cage size one can shift the location of the second maximum to a desired value.

VII The window effect re-examined

The idea of adsorption on a periodic substrate that forms periodic arrays that are either commensurate or incommensurate with the substrate originates from the 1938 Frenkel-Kontorowa (FK) model [7, 8, 42]. The adsorbed atoms at positions x_n are treated as a harmonic chain with equilibrium lattice spacing a . The substrate is a one-dimensional periodic lattice with period b . The interaction between the n^{th} adsorbed atom and the periodic substrate is described by a potential energy $V(x_n)$. The model contains a "floating phase" in which the equilibrium lattice spacing a of the adsorbed lattice can be an arbitrary multiple of the substrate periodicity b . The diffusion and thermodynamic characteristics of molecules whose shape is commensurate with that of the zeolite pore is very different from that of the incommensurate ones. It has been demonstrated that molecular sieves favor the formation of reaction inter-

mediates that have a shape commensurate with their pore shape [43].

The similar models of Nitsche and Wei [11] and Ruckenstein and Lee [9] use stiff rods to model n -alkanes. Due to the simplifications the model can not predict the location of the maximum, nor can it describe the intra-cage behavior correctly, i.e. the minima. The entropy effect (there is variety of conformations depending on the structure of the adsorbate) has been ignored and only a one-dimensional diffusion path is taken into account. Despite these simplifications, they corroborate the essence of the window effect: a stochastic motion through a regular array of potential barriers. An earlier proposed model by Derouane et al. [10] analyzed Goring's results in terms of energy and surface curvature effects by applying a segmentational diffusion principle, i.e. a translation occurs by successive segmental displacements. All segments are affected by different free energy environments. The model includes two distinct trapping cases: a portion of the molecule lying in the cage, and the remaining portion lying in the interconnecting window space or the opposite filling order. For the sake of simplicity the probability of the cases is equally weighted. In contrast to the other models the authors attribute the changes in the diffusivity to a variation in the sticking force. Due to the distinction between a cage and window region this model captures the physics of the intra cage behavior somewhat better than the rod models.

Tsekov and Smirniotis [44] extended the concept of resonance diffusion by Ruckenstein and Lee [9] to include the effect of the zeolite structure and the alkane vibrations. As the mechanics of crossing channels is hard to describe with a theoretical model, it is again restricted to channel-type zeolites like those with LTL-type structure. They demonstrate that the existence of a sequence of expansions and apertures alone is not enough. The energy barrier should be sufficiently high to observe the

diffusion peaks. Talu et al. [45] found experimental evidence of a resonance diffusion effect in silicalite. Their results obtained by steady-state single-crystal membrane technique agreed well with the MD results of Runnenbaum and Maginn [46]. In the latter report it has been suggested that although resonance diffusion is a real effect in zeolite, it will only occur under special conditions: low temperature, rigid sorbate, smooth channels, and low loadings. The acceleration of the diffusion rate due to resonance effects does not exceed a factor of two. Therefore, the authors attribute the more dramatic acceleration reported by Gorrington to other effects.

It is important to note that in our approach *all* possible configurations (translations, rotations, and internal configurational changes) and as a consequence *all* possible diffusion paths through the zeolite are represented with the proper weight. As such the techniques can be straightforwardly applied to other cage/window-type zeolites. The heats of adsorption and the Henry coefficients shed light on a possible window-effect, before computing the more computationally demanding diffusion coefficients at interesting chain lengths.

We would like to comment on the positions and total amount of the cations within the zeolite structure and of their relevance for the obtained results. The available experimental data on zeolites with window-effects is contradictory and very scattered. There exists systematic data for *n*-alkanes up to C₁₄ on potassium-exchanged OFF/ERI intergrowths [2], up to C₁₂ on proton-exchanged CHA-type zeolites [3], and for a few selected alkanes on various types of ERI/OFF intergrowths by Cavalcante et al. [12] and Magalhães et al. [13] [13]. Lattice intergrowths and defects, cations, and associated aluminum atoms create strong disorder, increase the hopping activation energy, inhibit the mobility of sorbates, and slow down the diffusion process. Factors such as the existence of several

different energetically favorable cation sites complicate the diffusion process. In addition, our Henry coefficients indicate abnormally low adsorption in ERI- and CHA-type zeolites for chain lengths close to or longer than the cage-size.

The positions of ions are of critical importance if they are located in the windows obstructing the diffusion. The difference between the Na-form of the LTA-type zeolite and the Ca/Na-form is a striking example [40]. The Ca/Na-form (zeolite 5A) has 4 calcium and 4 sodium ions per cage. None of the windows is blocked by an ion and the free diameter of the windows is 5 Å. The Na-form (zeolite 4A) contains 12 sodiums per cage and 100% of the windows are occupied with an ion, reducing the effective window size to 4 Å. Exchange with potassium would reduce the window size to 3 Å (zeolite 3A). The difference in diffusion is large: the coefficients in 4A are 4 orders of magnitude lower than that in 5A. The Ca-form of CHA-type zeolite is another example where the ions are located in the windows [47]. However, the positions are dependent on pretreatment of the zeolite sample (the dehydration steaming process).

Although the locations of protons can potentially be determined by neutron diffraction in an empty zeolite, they are easily displaced by diffusing adsorbates and considering their small size the impediment of diffusion is expected to be small. In accordance with this view our all-silica CHA-type zeolite results agree well with the H-CHA experimental results, although a quantitative comparison is difficult due to the unknown crystal size in the experiment. We note that the original cracking data of Chen was performed using H-ERI. The actual samples used by Gorrington [2], Cavalcante et al. [12], and Magalhães et al. were rather different in composition of cations and intergrowth ratio. However, in some forms of the ERI-type zeolite [48] and the Ca/Na-form of the LTA-type zeolite [40] the ions are known to be located in the cages

and not in the windows. Hence, they are expected to have a somewhat better adsorption inside the cage (Henry coefficients) but the maximum of the free energy at the windows may be virtually unchanged. Therefore, the order of magnitude difference in diffusion could possibly also be found in some of the cation-loaded versions of ERI-type zeolite.

To unambiguously detect the window effect in reality is by far no trivial task, both in view of the requirements for the experimental techniques and the quality of the nanoporous materials. In view of the difficulties, it would be of high interest to the simulation community to experimentally validate the diffusion behavior of alkanes as a function of chain length in ERI-, CHA-, and LTA-type silica or their aluminum phosphate analogues (viz. AlPO-17 [49], AlPO-34 and SAPO-42, respectively). We note that recently an all-silica form of the CHA-type zeolite has been synthesized [50].

VIII Conclusions

We studied the effect of the zeolite structure on the diffusion of *n*-alkanes as a function of carbon number. The ERI-, CHA-, and LTA-type frameworks consist of cages separated by small windows, but differ in the size and shape of the cages and in the orientation of the windows with respect to the cage. In contrast to channel zeolites like those of the OFF-type, the cage/window-type zeolites showed a cage effect for adsorption and diffusion: a non-monotonic, periodic dependence of the Henry coefficients, heats of adsorption, and diffusion coefficients on the chain length. The simulations corroborate the existence of the window effect in ERI- and CHA-type silica with the positions of the minima and maxima determined by size and orientational crystal parameters. When a molecule is incommensurate with the cage structure the diffu-

sion rate increases by orders of magnitude. The corresponding chain length is the maximum length at which a molecule still fits in a single cage: C_{13} for ERI-type silica, C_{11} for CHA-type silica, and C_{23} for LTA-type silica. These crossover points are directly related to the local minima in the Henry coefficients, the heats of adsorption, and the activation energies, and to the local maxima in the diffusion coefficients and the frequency factors. In the controversy about the experimental results we side with Goring, who was the first and only to report experimental data indicating the "window-effect". This opens the possibility of length selective cracking, where the length distribution is controlled by choosing structures with the appropriate cage size.

Acknowledgments

We thank T. L. M. Maesen, S. Calero, R. Krishna, T. Vlugt, P. Bolhuis, E. J. Meijer, T. van Erp, M. Schenk and D. Frenkel for valuable discussions, suggestions and comments on our manuscript. The investigations are supported in part by the Netherlands Research Council for Chemical Sciences (CW).

Bibliography

- [1] Chen, N. Y.; Maziuk, J.; Schwartz, A. B.; Weisz, P. B. *Oil Gas J.* **1968**, *66*, 154-157.
- [2] Goring, L. R. *J. Catal.* **1993**, *31*, 13-26.
- [3] Chen, N.Y.; Garwood, William E.; Dwyer, Francis G., *Shape selective Catalysis in industrial Applications, 2nd edition, revised and expanded* Chemical Industries; New York, 1996.
- [4] Chen, N. Y.; Lucki, S. J.; Mower, E. B. *J. Catal.* **1969**, *13*, 329-332.

- [5] Dubbeldam, D.; Calero, S.; Maesen, T. L. M.; Smit, B. *Phys. Rev. Lett.* **2003**, in press.
- [6] Dubbeldam, D.; Calero, S.; Maesen, T. L. M.; Smit, B. *Angew. Chem. Int. Ed.* **2003**, in press.
- [7] Frenkel, Y. I.; Kontorowa, T. *Phys. Z. Sowietunion* **1938**, *13*, 1.
- [8] Kontorowa, T.; Frenkel, Y. I. *Zh. Eksp. Teor. Fiz.* **1938a,b**, *8*, 89,1340.
- [9] Ruckenstein, E.; Lee, P. S. *Phys. Lett. A* **1976**, *56*, 423-424.
- [10] Derouane, E. G.; Andre, J. M.; Lucas, A. A. *J. Catal.* **1988**, *110*, 58-73.
- [11] Nitsche, J. M.; Wei, J. J. *AIChE*. **1991**, *37*, 661-670.
- [12] Jr, C. L. Cavalcante; Eić, M.; Ruthven, D. M.; Occelli, M. L. *Zeolites* **1995**, *15*, 293-307.
- [13] Magalhães, F. D.; Laurence, R. L.; Conner, W. C. *J. AIChE*. **1996**, *42-86*, 68.
- [14] Chandler, D. J. *Chem. Phys* **1978**, *68*, 2959.
- [15] Bennett, C. H., in *Diffusion in Solids: Recent Developments*, edited by Nowick, A.S.; Burton, J.J. Academic Press; New York, 1975, pp. 73-113.
- [16] Ruiz-Montero, M. J.; Frenkel, D.; Brey, J. J. *Mol. Phys.* **1996**, *90*, 925-941.
- [17] Ryckaert, J. P.; Bellemans, A. *Faraday Discuss. Chem. Soc.* **1978**, *66*, 95-106.
- [18] Ryckaert, J. P.; Bellemans, A. *Chem. Phys. Lett.* **1975**, *30*, 123-106.
- [19] Bezus, A. G.; Kiselev, A. V.; Lopatkin, A. A.; Du, P. Q. *J. Chem. Soc., Faraday Trans. II* **1978**, *74*, 367-379.
- [20] Vlugt, T.; Krishna, R.; Smit, B. *J. Phys. Chem. B.* **1999**, *103*, 1102-1118.
- [21] Maesen, T. L. M.; Schenk, M.; T. J. H. Vlugt, J. P. de Jonge; Smit, B. *J. Catal.* **1999**, *188*, 403-412.
- [22] <http://www.iza-structure.org/databases/>.
- [23] Demontis, P.; Suffritti, G. B.; Fois, E. S.; Quartieri, S. *J. Phys. Chem.* **1992**, *96*, 1482-1490.
- [24] Fritzsche, S.; Wolfsberg, M.; Haberlandt, R.; Demontis, P.; Suffritti, G. B.; Tilocca, A. *Chem. Phys. Lett.* **1998**, *296*, 253.
- [25] Vlugt, T. J. H.; Schenk, M. *J. Phys. Chem. B.* **2002**, *106*, 12757-12763.
- [26] Frenkel, D.; Smit, B., *Understanding molecular simulation 2nd edition* Academic Press; London, UK, 2002.
- [27] Smit, B.; Siepmann, J. I. *J. Phys. Chem.* **1994**, *98*, 8442-8452.
- [28] Rosenbluth, M.; Rosenbluth, A. *J. Chem. Phys* **1955**, *23*, 356-359.
- [29] Smit, B.; Daniël, L.; Loyens, J. C.; Verbist, Guy L. M. *Faraday Discuss. Chem. Soc.* **1997**, *106*, 93-104.
- [30] Press, W.H.; Flannery, B.P.; Teukolsky, S.A.; Vetterling, W.T., *Numerical Recipes in C* Cambridge University Press; New York, 1988.
- [31] Alberti, A.; Cruciani, G.; Galli, E.; Vezzalini, G. *Zeolites* **1996**, *17*, 457-461.
- [32] Pluth, J. J.; Smith, J. V.; Bennett, J. M. *Acta Cryst* **1986**, *C42*, 283-286.
- [33] Bennet, J. M.; Gard, J. A. *Nature* **1967**, *214*, 1005-1006.
- [34] Calligaris, M.; Nardin, G.; Randaccio, L. *Zeolites* **1983**, *3*, 205-208.
- [35] Pluth, J. J.; Smith, J. V. *Zeolites* **1980**, *102*, 4704-4708.

- [36] Schroeder, Will; Martin, Ken; Lorensen, Bill, *The Visualization Toolkit: an object-oriented approach to 3D graphics* Prentice-Hall, Inc; Upper Saddle River, New Jersey 07458, 1996.
- [37] <http://public.kitware.com/VTK/>.
- [38] Ruthven, D. M.; Kaul, B. K. *Adsorption* **1998**, *4*, 269-273.
- [39] Eic, M.; Ruthven, D. M. *Zeolites* **1988**, *8*, 472-479.
- [40] Kaerger, Joerg; Ruthven, Douglas M., *Diffusion in Zeolites and other microporous solids* John Wiley & Sons, Inc.; New York, 1992.
- [41] Schüring, A.; Auerbach, S. M.; Fritzsche, S.; Haberlandt, R. *J. Chem. Phys* **2002**, *116*, 10890-10894.
- [42] Braun, O. M.; Kivshar, Y. *Phys. Rep.* **1998**, *306*, 1-108.
- [43] Schenk, M.; Smit, B.; Vlugt, T. J. H.; Maesen, T. L. M. *Angew. Chem. Int. Ed.* **2001**, *40*, 736-739.
- [44] Tsekov, R.; Smirniotis, P. G. *J. Phys. Chem. B.* **1998**, *102*, 9385-9391.
- [45] Talu, O.; Sun, M. S.; Shah, D. B. *J. AlChE.* **1998**, *44*, 681-694.
- [46] Runnebaum, R. C.; Maginn, E. J. *J. Phys. Chem. B.* **1997**, *101*, 6394-6408.
- [47] Grey, T.; Gale, J.; Nicholson, D.; Peterson, B. *Microporous and Mesoporous Materials* **1999**, *31*, 45-59.
- [48] Alberti, A.; Martucci, A.; Galli, E.; Vezzalini, G. *Zeolites* **1997**, *19*, 349-352.
- [49] Pluth, J. J.; Smith, J. V. *Acta Cryst.* **1986**, *42*, 283-286.
- [50] Díaz-Cabanas, M.-J.; Barrett, P. A.; Cambor, M. A. *Chem. Comm.* **1998**, *17*, 1881-1882.

Traditionally, cracking mechanisms in the zeolite literature have assumed full adsorption. Our simulations indicate abnormally low adsorption in ERI-, AFX-, CHA-, RHO-, and KFI-type zeolites for chain lengths close to or longer than the cage-size. Very long molecules adsorb partially into a cage near the outer surface. After scission the non-adsorbed part can end up in the product or re-adsorb and undergo another scission. This mechanism is characteristic for cage/window-type zeolites with small windows close to the diameter of the adsorbate. The newly gained understanding of length-selective hydrocracking affords prediction of selectivity as a function of cage-size.

D. Dubbeldam, S. Calero, T. L. M. Maesen, and B. Smit

5

Understanding the Window Effect in Zeolite Catalysis

The *window*-effect is one of the most controversial and intriguing phenomena in the zeolite literature. Chen et al. discovered in 1968 that ERI-type zeolites yield a bimodal product distribution with maxima at n -C₃₋₄ and n -C₁₀₋₁₂, but no products in the C₅₋₈ range (the *window*) [1]. Conventional zeolite-catalyzed (hydro)cracking yields a product distribution with only a single maximum, which is consistent with the currently accepted reaction mechanisms [2, 3]. A comprehensive and fundamental understanding of the product selectivity associated with these catalytic processes is of considerable practical significance, as the results of Chen would open the possibility of *length-selective hydrocracking* [4]. Where the mandatory addition of volatile ethanol to gasoline is imminent [5-7], the more volatile components that are currently part of gasoline will have to be removed so as to maintain gasoline volatility. This revives the interest in a process to selectively hydrocrack the linear pentanes and hexanes so as to reduce volatility and increase the octane number. Such a process was commercialized in the 1960's, went by the name

selectoforming [8], and used ERI-type zeolite cages. Improvements on such a process would involve a better understanding of the hydrocracking process of linear alkanes up to a certain chain length. The newly gained understanding affords a prediction of length-selective hydrocracking.

For a long time the window effect has been related almost exclusively to the diffusion rate of n -alkanes in ERI-type zeolites. Goring showed that the product distribution and the diffusion coefficient as a function of n -alkane length correlate extremely well [9]. The low diffusion coefficients for n -C₇ to n -C₉ suggest that these molecules diffuse too slowly to leave the zeolite without cracking; the high diffusion coefficients for n -C₁₀ to n -C₁₂ suggest that these molecules diffuse rapidly enough to escape. However, recent diffusion measurements by Cavalcante et al. [10] and Magalhães et al. [11] failed to reproduce the increase in diffusion coefficient for the appropriate n -alkane lengths. This controversy motivated us to simulate the window-effect at the molecular level using advanced molecular simulations [12-14]. In these

Configurational-Bias Monte Carlo simulations molecules are grown atom by atom biasing the growth process towards energetically favorable configurations avoiding overlap with the zeolite. During the growth we compute the Rosenbluth factor, which is directly related to the excess chemical potential, the free energy, and the Henry coefficient [15].

Although our simulations of the diffusion [16] confirm the experimental observations of Goring, the results nevertheless point to an alternative mechanism based on anomalously low adsorption of long molecules. At sufficiently low pressures the amount of adsorbed molecules is directly proportional to the pressure. The proportionality constant is known as the Henry coefficient, and shown in Fig. 1 as a function of chain length for various zeolites. OFF-type sieves exhibit the usual monotonic increase of the Henry coefficient with n -alkane length. Longer n -alkanes have more attractive adsorbent-adsorbate interactions, and -therefore- a lower adsorption enthalpy. Longer n -alkanes also have fewer conformations in the adsorbed phase as compared to the gas phase, and -therefore- a lower adsorption entropy. The decrease in enthalpy offsets the decrease in entropy, so that the Gibbs free energy of adsorption decreases (and the Henry coefficient increases) with lengthening of the n -alkane. We found that pores with constrictions (*windows*) that approach the diameter of the adsorbate exhibit a dramatically different behavior. Instead of attractive adsorbate-adsorbent interactions, these windows exert repulsive adsorbate-adsorbent interactions that increase the adsorption enthalpy of any n -alkane partially adsorbed inside such a window. Accordingly, the usual compensation between adsorption enthalpy and adsorption entropy ceases as soon as n -alkanes become too long to fit comfortably inside the wider part of these pores (*cages*). For these longer n -alkanes the loss of entropy with increasing

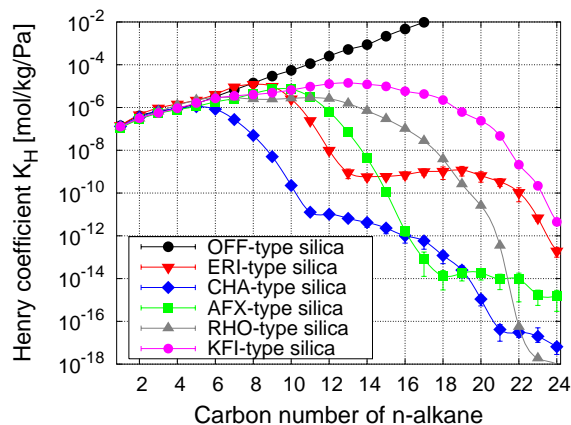


Figure 1: Henry coefficients at 600K for various types of zeolites as a function of alkane chain length. At sufficiently low pressures the amount of adsorbed molecules is linearly related to the pressure with the Henry coefficient as the proportionality constant.

length dominates their adsorption properties. For example, n -C₁₃ in an ERI-type cage predominantly adsorbs in a limited number of curled conformations, whereas n -C₁₄ has to stretch through a window into two cages. For even longer n -alkanes this pattern is repeated, now involving a second window. The Henry coefficients of molecular sieves with <0.45 nm windows exhibit periodic behavior (Fig. 1). The local minima correspond to alkanes that barely fit into n cages, so that alkanes one methylene group longer require $n + 1$ cages. Our simulations indicate that all molecular sieves with a window smaller than the 0.45 nm across EUO-type window exhibit such a remarkable decrease of the Henry coefficient with n -alkane length. To the best of our knowledge there are no experimental data available for comparison. In fact, anomalously low adsorption has never been cited when interpreting the catalytic or diffusion data on the large number of zeolites that should exhibit this window or cage effect in adsorption. In what follows we will amend this situation for ERI- and AFX-type zeolites.

Our simulations for ERI-type zeolite indicate that exactly for n -C₉ and longer n -

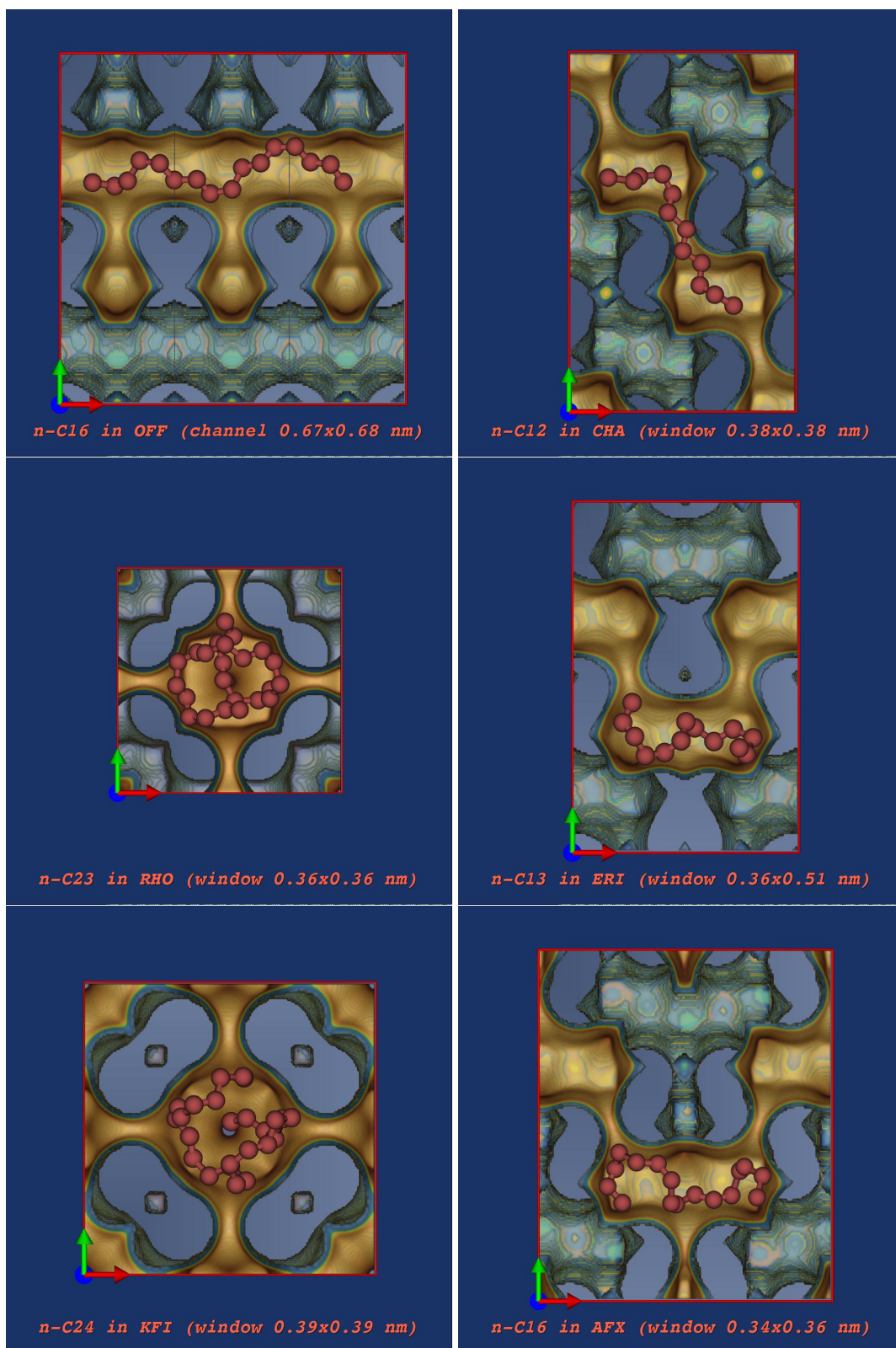


Figure 2: The crystalline structures OFF-, ERI-, RHO-, CHA-, KFI-, and AFX-type zeolites. The size of the CHA-, ERI-, and AFX-type cages limit the *n*-alkanes to 11, 13, and 16 carbon atoms, respectively. The large cages of RHO- and KFI-type zeolites accommodate molecules up to *n*-C₂₄ and *n*-C₂₆, respectively, in snake-in-a-basket conformations. The red balls represent CH₃- or CH₂-groups. Arrows at the origin are 0.3 nm in length.

alkanes the amount adsorbed decreases. This nicely corresponds with the observed decline in activity [17], and if we assume that the hydroconversion in ERI is similar to that of zeolites with windows nearly twice as wide (e.g. FAU-type zeolites), this decline may be seen as indirect evidence for our Henry coefficients. The selectivity as observed by Chen [1] concerns *n*-alkanes as long as *n*-C₃₆. It is important to note that the window effect has become associated only with a high *n*-C_{10–12} yield. However, a closer inspection of the raw data of Chen et al. published for *n*-C₃₆ reveals additional yield maxima at *n*-C_{24–26} and at *n*-C_{15–17} in the complete chromatogram of the *n*-C₃₆ cracking products. From the calculated variation of Henry coefficients with chain length it is immediately apparent that the complete *n*-C₃₆ adsorption can be excluded, and yet ERI-type zeolites crack *n*-C₃₆ shape selectively. The preferential yield of *n*-C_{24–26} and *n*-C_{15–17} is indicative of consecutive scissions of C_{10–12} fragments from *n*-C₃₆. The maximum at *n*-C_{10–12} indicates that the most rapidly diffusing cracking product can escape complete consumption into more refractory alkanes with six or fewer carbon atoms. This selective cracking process leaves minima at *n*-C_{18–23} and at *n*-C_{13–14}. A reasonable explanation for persistence of shape-selective cracking of very long alkanes by ERI-type zeolites is that these long molecules adsorb partially in the surface pockets created by the ERI-type cages at the outer crystal surface. Full adsorption by more than 12 carbon atoms is unlikely. The adsorbed *n*-C_{10–12} part is chopped off, and the non-adsorbed part is released. Released parts end up in the product slate or undergo further scission reactions. This process becomes less selective with an increasing number of cracking steps due to concomitant isomerization reactions. AFX-type zeolites exhibit a hydrocracking pattern similar to ERI-type zeolites. This is not surprising, for these zeolites only differ in cage size. Similar to ERI-type ze-

olites [4], AFX-type zeolites preferentially hydrocrack shorter rather than longer *n*-alkanes [18] when given a choice. Thus, they consume exclusively *n*-C₆ when processing a mixture of *n*-C₆ and *n*-C₁₆, even though they hydroconvert more than 50% of either *n*-C₆ or *n*-C₁₆ when processing them separately. Inspection of our Henry coefficients shows that *n*-C₆ adsorbs fully, whereas *n*-C₁₆ can only adsorb partially. Since partial adsorption is thermodynamically highly unfavorable [19], fully adsorbing molecules can effectively block adsorption and hydroconversion for partially adsorbing molecules.

Naturally, windows approaching the diameter of the adsorbate are a barrier to both adsorption and diffusion, and these two factors cannot be seen in isolation. Diffusion rates determine the impact of the very low adsorption on catalysis. Its impact will be higher when the diffusion is slower, because the path through consecutive windows is highly tortuous (as in ERI-, AFX-, and CHA-type zeolites). Its impact will be lower when the diffusion is faster because the path through consecutive windows is straight (as in RHO- and KFI-type zeolites) (Fig. 2).

This newly gained understanding of length-selective hydrocracking affords a prediction of selectivity as a function of cage size. We would predict that the larger AFX-type cage shifts the cracking selectivity by 2 carbon atoms towards longer *n*-alkanes as compared to the smaller ERI-type cage, and that the even smaller CHA-type cages shift the cracking selectivity further towards *n*-C₅. We further predict that RHO- and KFI-type zeolites afford length-selective hydrocracking of *n*-alkanes longer than those removed by AFX-type zeolites.

In summary, we refute some of the traditional cracking mechanisms found in zeolite literature based on full adsorption. The simulation results indicate abnormally low adsorption in ERI-, AFX-, CHA-, RHO-, and KFI-type zeolites for chain lengths close to

or longer than the cage size. Hence, very long molecules adsorb partially into a cage near the outer surface. After scission the non-adsorbed part can end up in the product or re-adsorb and undergo another scission. This mechanism is characteristic for cage/window-type zeolites with small windows close to the diameter of the adsorbate. The newly gained understanding of length-selective hydrocracking affords prediction of selectivity as a function of cage size.

Acknowledgment

We would like to thank the Netherlands Research Council for Chemical Sciences (CW), the European Commission for a Marie Curie Fellowship to S. C., ChevronTexaco for financial support, and C. Wilson, C. H. Roemkens, A. Kuperman, S. I. Zones, and R. Krishna for their comments on our manuscript.

Bibliography

- [1] N. Y. Chen, S. J. Lucki, E. B. Mower, *J. Catal.* **1969**, *13*, 329-332.
- [2] J. Weitkamp, S. Ernst, L. Puppe in *Catalysis and Zeolites* (Eds.: J. Weitkamp, L. Puppe), Springer, Berlin, **1999**, pp. 326-376.
- [3] J. A. Martens, P. A. Jacobs in *Zeolite Microporous Solids: Synthesis, Structure, and Reactivity* (Eds.: E. G. Derouane, F. Lemos, C. Naccache, F. Ramão-Ribeiro), Kluwer, Amsterdam, **1992**, pp. 511-529.
- [4] J. Wei, *Ind. Eng. Chem. Res.* **1994**, *33*, 2467-2472.
- [5] M. Radler, *Oil Gas J.* **2002**, *100*, 5-9.
- [6] K. Watkins, *C&En News* **2001**, *79*, 21-21.
- [7] M. Lorenzetti, *Oil Gas J.* **2003**, *101*, 20-22.
- [8] N. Y. Chen, J. Maziuk, A. B. Schwartz, P. B. Weisz, *Oil Gas J.* **1968**, *66*, 154-157.
- [9] L. R. Gorrington, *J. Catal.* **1993**, *31*, 13-26.
- [10] C. L. Cavalcante Jr.; M. Eić, D. M. Ruthven, M. L. Ocelli, *Zeolites* **1995**, *15*, 293-307.
- [11] F. D. Magalhães, R. L. Laurence, W. C. Conner, *J. AlChE.* **1996**, *42*, 68-86.
- [12] B. Smit, T. L. M. Maesen, *Nature* **1995**, *374*, 42-44.
- [13] T. J. H. Vlugt, R. Krishna, B. Smit, *J. Phys. Chem. B.* **1999**, *103*, 1102-1118.
- [14] T. L. M. Maesen, M. Schenk, T. J. H. Vlugt, J. P. de Jonge, B. Smit, *J. Catal.* **1999**, *188*, 403-412.
- [15] D. Frenkel, B. Smit in *Understanding molecular simulation 2nd edition*, Academic Press, London, UK, **2002**.
- [16] D. Dubbeldam, S. Calero, T. L. M. Maesen, B. Smit, *Phys. Rev. Lett.* **2003**, in press.
- [17] N. Y. Chen, W. E. Garwood, *Advan. Chem.* **1973**, *121*, 575-582.
- [18] D. S. Santilli, S. I. Zones, *Catalysis Letters* **1990**, *7*, 383-387.
- [19] E. B. Webb III; G. S. Grest, *J. Chem. Phys.* **2002**, *116*, 6311-6321.

We present a method to determine potential parameters in molecular simulations of confined systems through fitting on experimental isotherms with inflection points. The procedure uniquely determines the adsorbent-adsorbate interaction parameters, and is very sensitive to the size-parameter. The inflection points in the isotherms are often related to a subtle interplay between different adsorption sites. If a force field can predict this interplay, it also reproduces the remaining part of the isotherm correctly, i.e. the Henry coefficients and saturation loadings.

D. Dubbeldam, S. Calero, T. J. H. Vlugt, R. Krishna,
T. L. M. Maesen, E. Beerdsen, and B. Smit

6

Force Field Parameterization through Fitting on Inflection Points in Isotherms

The effect of confinement on adsorption and diffusion is still poorly understood despite its importance for practical applications. The performance of molecular sieves in separation and catalytic processes depends critically on the match between sieve topology and the shape and size of the adsorbate [1]. It is therefore of considerable industrial importance to explore the adsorption and diffusion of linear and branched alkanes in different topologies using realistic simulations at the microscopic level [2]. Different parameter sets yield values of diffusivities that differ not only quantitatively but also show a different qualitative dependence on the molecular loading [3]. The critical unresolved question is: which of these parameter sets is the most physically realistic one? Here, we hope to remedy this situation.

Potential parameter sets can be checked only via comparison with experiment. For diffusion the comparison is complicated by large discrepancies between microscopic and macroscopic experimental measurement methods, and even within the same measurement technique there are many dis-

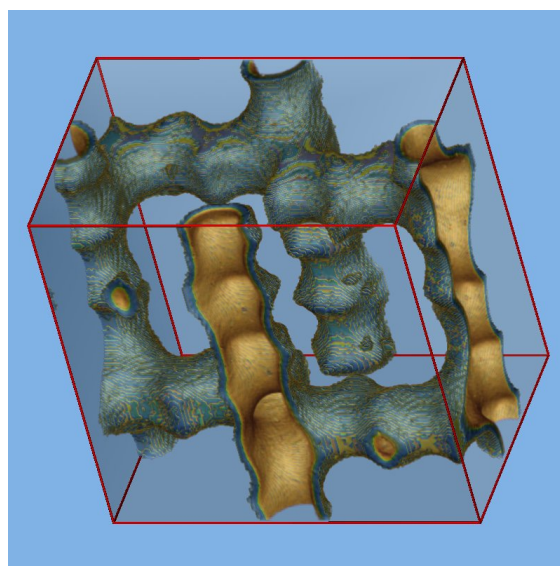


Figure 1: (color online). *Silicalite-1 has linear channels intersected with zig-zag channels four times per periodic unit cell.*

agreements between various studies. However, adsorption results seem to be well established and provide a more solid basis for a detailed comparison between experiment and simulation. Moreover, a large amount of data exists on adsorption of hydrocarbons in siliceous zeolites.

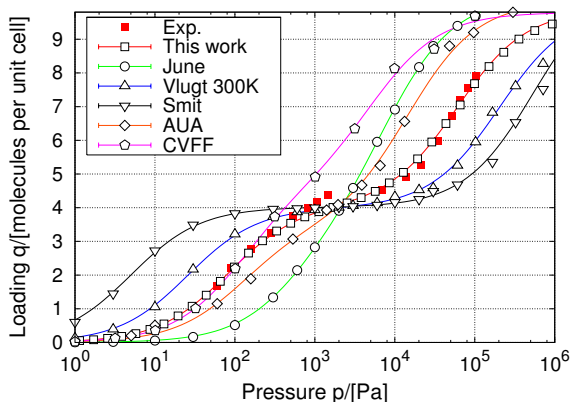


Figure 2: (color online). Isotherms of 2-methylpropane at 308 K in silicalite-1 compared to various computational models.

Silicalite-1 (Fig. 1) consists of a three-dimensional pore system with straight parallel channels, intersected by zig-zag channels [4]. The channels of approximately 6 Å in diameter lead to shape selectivity, especially for the isomers of hexane which have dimensions close to the silicalite-1 pores. The linear channels intersect with the zig-zag channels four times per unit cell. Interestingly, for *n*-heptane, and for the branched alkanes in silicalite-1 a kink in the isotherm is observed [5]. This inflection is directly related to the number of intersections in the structure and occurs at *exactly* 4 molecules per unit cell. As these inflections are caused by a subtle interplay between the size and configuration of the molecule and two different adsorption sites, it becomes clear that the adsorbent-adsorbate potential size-parameter σ is the most sensitive parameter in the force field.

In general, adsorption in any periodic structure will have steps or kinks. The reason is that steps and kinks signal transitions between different types of packing and similar to adsorption on substrates, at low loadings the packing of molecules will often be imposed by the sieve while at higher loading such packing is only by exception commensurate with the packing of the adsorbed molecules. This change in packing is reflected in a kink or plateau in an ad-

sorption isotherm. To illustrate our method we exploit the close physical connection between potential parameters and inflection points in isotherms to optimize a forcefield for adsorption and diffusion of alkanes in siliceous zeolites.

We use the united-atom model [6] and consider the CH_x groups as single interaction centers with their own effective potentials. The beads in the chain are connected by harmonic bonding potentials. A harmonic cosine bending potential models the bond bending between three neighboring beads, a Ryckaert-Bellemans potential controls the torsional angle. The beads in a chain separated by more than three bonds interact with each other through a Lennard-Jones potential. The Lennard-Jones potentials are shifted and cut at 12 Å. The interactions between the rigid framework and the guest molecules are assumed to be dominated by the oxygen atoms [7]. Some of the alkane-alkane interactions are taken from Ref. [8].

In adsorption studies, the natural ensemble to use is the grand-canonical ensemble (or μ, V, T ensemble). The adsorbed phase is simulated by specifying the temperature T , the volume V , and the chemical potential μ . At these conditions the number of adsorbed molecules is computed. We convert the imposed chemical potential to the corresponding pressure using the Peng-Robinson equation of state. To successfully insert and remove molecules we use the configurational-bias Monte Carlo (CBMC) technique [9], in which chains are grown bead by bead biasing the growth process towards energetically favorable configurations. This bias is exactly removed by adjusting the acceptance rules. Further details are given in Refs. [5].

In Fig. 2 we show the influence of the size parameter $\sigma_{\text{O-CH}_x}$ on the inflection of 2-methylpropane ($\text{CH}_3\text{-CH}[\text{-CH}_3]\text{-CH}_3$) in silicalite-1. The experimental data are taken from Ref. [10] and simulation data from Refs. [5, 11–14]. The models of Smit et

al. and Vlugt et al. exaggerated the inflections because their size-parameters were too large. The models of Pascual et al., June et al., and the all-atom CVFF force field did not show a clear inflection at all because their size-parameters were too small. Although the size-parameters differ by less than 10%, the shape of the isotherms is dramatically different. The model of June et al. uses a small value of $\sigma = 3.364 \text{ \AA}$, the AUA-model uses $\sigma_{\text{O-CH}_3} = 3.30 \text{ \AA}$, $\sigma_{\text{O-CH}_2} = 3.23 \text{ \AA}$, and $\sigma_{\text{O-CH}} = 3.18 \text{ \AA}$. The models of Vlugt et al. and Smit et al. use a fixed σ ; $\sigma_{\text{O-CH}_3} = \sigma_{\text{O-CH}_2} = \sigma_{\text{O-CH}} = 3.60 \text{ \AA}$ for the Vlugt-model, and $\sigma_{\text{O-CH}_3} = \sigma_{\text{O-CH}_2} = \sigma_{\text{O-CH}} = 3.64 \text{ \AA}$ for the Smit-model. The model proposed in this work uses $\sigma_{\text{O-CH}_3} = 3.48 \text{ \AA}$, $\sigma_{\text{O-CH}_2} = 3.58 \text{ \AA}$, and $\sigma_{\text{O-CH}} = 3.92 \text{ \AA}$. It yields exact overlap with experimental data and the inflection is reproduced faithfully. We stress that only a single strength/size parameter pair is able to describe the inflection and the entire isotherm properly. This is in contrast with the common belief that for each value of σ there is a corresponding ϵ that can describe the isotherm correctly [8, 15].

In practice we proceed as follows. A reasonable starting size parameter is chosen. For this parameter we iteratively search for the corresponding strength parameter ϵ that matches the experimental data at a pressure significantly below the inflection. The entire isotherm is then followed for increasing pressure until a deviation from the experimental data is observed. The "updated" size parameter is then found by choosing a higher value for a deviation to the left of the experimental data, and by choosing a lower value for the size parameter for a deviation to the right of the experimental data. This scheme proceeds iteratively until the entire experimental isotherm is accounted for. The adsorbent-adsorbate parameters obtained from fitting to inflections are listed in Table 1 and the errors in the size- and strength-parameters are limited to no more than 0.01 \AA and 5 K, respectively.

	O	CH ₄	CH ₃	CH ₂	CH	C
CH ₄	115.0	158.50	130.84	94.21	51.91	11.26
	3.47	3.72	3.74	3.84	4.17	4.87
CH ₃	93.0	130.84	108.00	77.77	42.85	9.30
	3.48	3.74	3.76	3.86	4.19	4.90
CH ₂	60.5	94.21	77.77	56.00	30.86	6.69
	3.58	3.84	3.86	3.96	4.30	5.03
CH	40.0	51.91	42.85	30.85	17.00	3.69
	3.92	4.17	4.19	4.30	4.67	5.46
C	10.0	11.26	9.30	6.69	3.69	0.80
	4.56	4.87	4.90	5.03	5.46	6.38

Table 1: Force field guest-host and guest-guest interactions of hydrocarbons in cation-free nanoporous materials. Lennard-Jones parameters, ϵ/k_B [K] in top-left corner, σ [\AA] in bottom-right corner of each field. Some of the alkane-alkane interactions are taken from Ref. [8] and optimized to reproduce vapor-liquid coexistence curves of the phase diagrams. The parameters may be combined with any reasonable internal interaction model.

Ethane, *n*-heptane, and 2-methylpropane exhibit isotherms of the Brunauer type-VI in silicalite-1. Experimental data are taken from Sun et al. [10, 16], Choudhary et al. [17], and Zhu et al. [18, 19]. Ethane ($\text{CH}_3\text{-CH}_3$) shows a small inflection point in the adsorption isotherm at high loading [20]. The $\epsilon_{\text{O-CH}_3}$ and $\sigma_{\text{O-CH}_3}$ are uniquely obtainable from the ethane isotherm (Fig. 3 top). When the channel interiors are occupied the probability distribution shows a remarkable order: a repeating pattern of ethane molecules "locked" in the zig-zag channels between two intersections. The $\epsilon_{\text{O-CH}_2}$ and $\sigma_{\text{O-CH}_2}$ are obtained from *n*-heptane. The inflection behavior of *n*-heptane ($\text{CH}_3\text{-CH}_2\text{-CH}_2\text{-CH}_2\text{-CH}_2\text{-CH}_2\text{-CH}_3$) is well established [9, 16]. Smit and Maesen explained this effect in terms of *commensurate freezing*: *n*-heptane has a size commensurate with the size of the zig-zag channel. At high pressures the molecules shift from a random distribution to a distribution where the molecules are localized exclusively in the channels and not at the

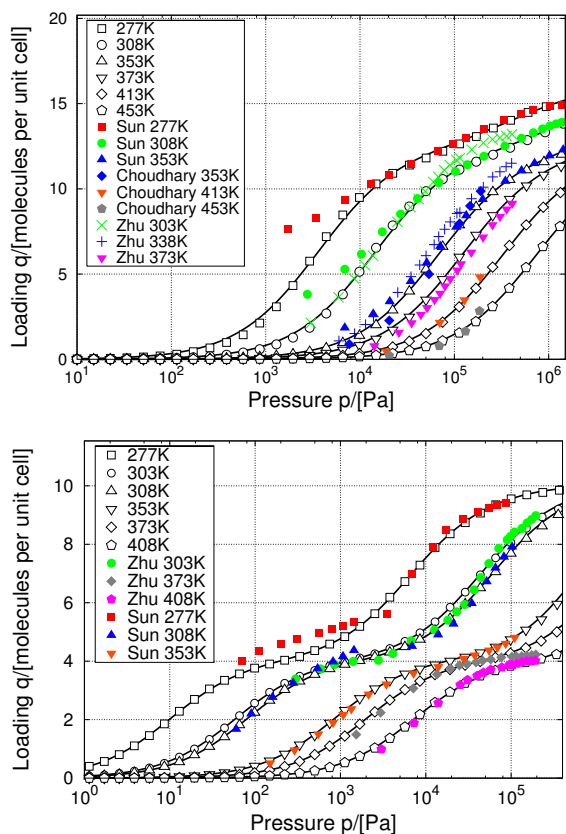


Figure 3: (color online). Fitting to the isotherms of ethane (top), and 2-methylpropane (bottom) in silicalite-1 at various temperatures.

intersections. Various branched molecules show inflections for another reason [5]. 2-methylpropane preferentially adsorbs at the intersections. At a loading of four molecules per unit cell the intersections are fully occupied and additional molecules have to be pushed into the channels requiring a significantly higher driving force [21]. The $\epsilon_{\text{O-CH}}$ and $\sigma_{\text{O-CH}}$ are uniquely obtainable from the isotherm of 2-methylpropane (Fig. 3 bottom).

For 3-methylpentane ($\text{CH}_3\text{-CH}_2\text{-CH}[\text{-CH}_3]\text{-CH}_2\text{-CH}_3$) in silicalite-1 (Fig. 4) the prediction of our isotherms obtained from simulation is in excellent agreement with Zhu et al. [22] and Jolimaitre et al. [23]. Thus, the agreement between simulated and experimental data on the adsorption of molecules not part of the calibration set is remarkably good. The accuracy of the model and the successful extension to other

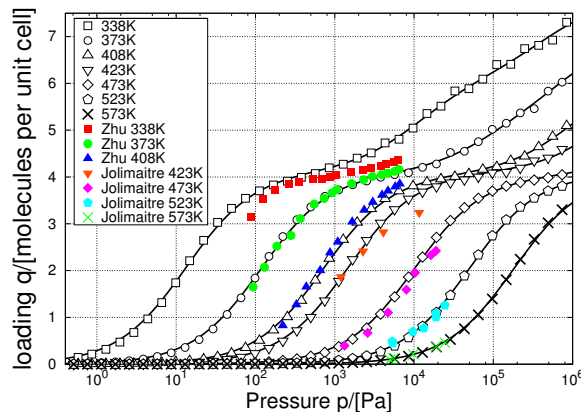


Figure 4: (color online). Prediction of the isotherm of 3-methylpentane in silicalite-1 at various temperatures.

sorbates, mixtures, and topologies will be published elsewhere.

In Table 2 we compare our simulation results on low-coverage adsorption properties with the experimental results on silicalite-1 from Denayer et al. [24]. It is noteworthy that also Denayer's data set was not part of the set used as a basis for our force field. The quantitative agreement and consistency on low-coverage properties of simulated and experimental data is therefore truly remarkable. The value of $\sigma_{\text{O-CH}_x}$ also has an effect on the maximum loading and packing efficiency. De Meyer et al. [25] performed experiments of long chain n -alkanes in silicalite. Experiments show that the maximum packing is approximately 53.2 carbon atoms per unit cell for $n\text{-C}_{14}$, while the current model yields 52.5 carbon atoms per unit cell in excellent agreement with experiment.

Although the fitting procedure is applied to hydrocarbons, it is by no means restricted to alkanes. In the literature many isotherms with inflections can be found and these molecules are easily included. Examples include adsorbates in clays [26], aromatic molecules in silicalite, gasses, alkanes and cyclo-alkane isomers in AFI, adsorbates in silica gels, water and methonal in FER, and benzene, acetonitrile, water in mesoporous materials like MCM-41 silica.

CN	K_H 573K [mol/kg/Pa]		K_∞ [mol/kg/Pa]		$-\Delta H$ [kJ/mol]	
	Sim.	Exp.	Sim.	Exp.	Sim.	Exp.
5	3.04×10^{-6}	2.99×10^{-6}	2.33×10^{-11}	2.64×10^{-11}	56.13	55.7
6	6.10×10^{-6}	5.93×10^{-6}	6.07×10^{-12}	6.07×10^{-12}	65.87	66.0
7	1.23×10^{-5}	1.22×10^{-5}	1.53×10^{-12}	1.29×10^{-12}	75.77	76.7
8	2.43×10^{-5}	2.49×10^{-5}	3.67×10^{-13}	3.25×10^{-13}	85.82	86.6
9	4.61×10^{-5}	4.73×10^{-5}	8.59×10^{-14}	8.41×10^{-14}	95.81	96.1
relation			Sim.		Exp.	
$-\Delta H = \alpha \text{CN} + \beta$			$\alpha = 9.93$		$\alpha = 10.1$	
$-\Delta S = \gamma \text{CN} + \delta$			$\gamma = 11.65$		$\gamma = 11.99$	
$-\ln(K_\infty) = -A\Delta H + B$			$A = 0.141, B = 16.54$		$A = 0.143, B = 16.4$	

Table 2: Comparison of our simulations results of low-coverage properties in silicalite-1 with the experimental results of Denayer et al. [24]. Both the Denayer and the simulation Henry coefficients K_H of the linear alkanes have been fitted to $K_H = K_\infty e^{\frac{-\Delta H}{RT}}$ in the temperature range $T=473\text{-}673$ K. Here, K_∞ denotes the pre-exponential Henry coefficient, ΔH the enthalpy of adsorption, and $R = 8.31451$ J/mol/K the gas constant. The entropy ΔS per carbon number is related to the slope of $\ln(K_\infty)$ plotted as a function of Carbon Number (CN) [24].

For systems that lack inflection data, the strategy would be to use an initial set of parameters to identify for which type of sieve an inflection can be expected. Experiments can then focus at accurately determining the location of such an inflection rather than determining "at random" entire isotherms for many different systems.

The fitting to well-established inflection points in the isotherms has many advantages and overcomes problems that have so far impeded the development of more accurate force fields. We obtain a unique set of parameters that all directly relate to a well-defined physical property. Therefore, the parameters are much better transferable to other systems than parameters from previous attempts. By explicitly fitting to entire adsorption isotherms we guarantee the proper reproduction of properties such as Henry coefficients, heats of adsorption, adsorption entropies, and saturation loadings.

We would like to thank the Netherlands Research Council for Chemical Sciences (CW), the European Commission, ChevronTexaco, and the Deutsche Forschungsgemeinschaft (DFG) for financial support. Corresponding author:

D.Dubbeldam@uva.nl

Bibliography

- [1] J. M. Thomas, *Sci. Am.* **266**, 82 (1992).
- [2] W. O. Haag, in *Zeolites and Related Microporous Materials: State of the Art 1994*, Studies in Surface Science and Catalysis, edited by J. Weitkamp, H. G. Karge, H. Pfeifer, and W. Hölderich (Elsevier, Amsterdam, 1994), Vol. 84, pp. 1375–1394.
- [3] S. Fritzsche, M. Gaub, R. Haberlandt, and G. Hofmann, *J. Mol. Model.* **2**, 286 (1996).
- [4] <http://www.iza-structure.org/databases/>.
- [5] T. J. H. Vlugt, R. Krishna, and B. Smit, *J. Phys. Chem. B.* **103**, 1102 (1999).
- [6] J. P. Ryckaert and A. Bellemans, *Faraday Discuss. Chem. Soc.* **66**, 95 (1978).
- [7] A. G. Bezus, A. V. Kiselev, A. A. Lopatkin, and P. Q. J. Du, *J. Chem. Soc., Faraday Trans. II* **74**, 367 (1978).

- [8] M. G. Martin, A. P. Thompson, and T. M. Nenoff, *J. Chem. Phys.* **114**, 7174 (2001).
- [9] B. Smit and T. L. M. Maesen, *Nature* **374**, 42 (1995).
- [10] M. S. Sun, D. B. Shah, and O. Talu, *J. Phys. Chem. B.* **102**, 1466 (1998).
- [11] R. L. June, A. T. Bell, and D. N. Theodorou, *J. Phys. Chem* **96**, 1051 (1992).
- [12] B. Smit, L. D. J. C. Loyens, and G. L. M. M. Verbist, *Faraday Discuss.* **106**, 93 (1997).
- [13] P. Pascual, P. Ungerer, B. Tavitian, P. Pernot, and A. Boutin, *Phys. Chem. Chem. Phys.* **5**, 3684 (2003).
- [14] M. D. Macedonia and E. J. Maginn, *Mol. Phys.* **96**, 1375 (1999).
- [15] B. Smit, *J. Phys. Chem.* **99**, 5597 (1995).
- [16] M. S. Sun, O. Talu, and D. B. Shah, *J. Phys. Chem.* **100**, 17276 (1996).
- [17] V. R. Choudhary and S. Mayadevi, *Zelolites* **17**, 501 (1996).
- [18] W. Zhu, F. Kapteijn, and J. A. Moulijn, *Phys. Chem. Chem. Phys.* **2**, 1989 (2000).
- [19] W. Zhu, F. Kapteijn, and J. A. Moulijn, *Adsorption* **6**, 159 (2000).
- [20] Z. Du, T. J. H. Vlugt, B. Smit, and G. Manos, *AIChE J.* **44**, 1756 (1998).
- [21] T. J. H. Vlugt, W. Zhu, F. Kapteijn, J. A. Moulijn, B. Smit, and R. Krishna, *J. Am. Chem. Soc.* **120**, 5599 (1998).
- [22] W. Zhu, F. Kapteijn, B. van der Linden, and J. A. Moulijn, *Phys. Chem. Chem. Phys.* **3**, 1755 (2001).
- [23] E. Jolimaitre, M. Tayakout-Fayolle, C. Jallut, and K. Ragil, *Ind. Eng. Chem. Res.* **40**, 914 (2001).
- [24] I. C. Arik, J. F. Denayer, and G. V. Baron, *Microporous and Mesoporous Mat.* **60**, 111 (2003).
- [25] K. M. A. D. Meyer, S. Chempath, J. F. M. Denayer, J. A. Martens, R. Q. Snurr, and G. V. Baron, *J. Phys. Chem. B.* **107**, 10760 (2003).
- [26] D. Cao, W. Wang, and X. Duan, *J. Colloid Interface Sci.* **254**, 1, (2002).

A novel united atom force field affords accurate and quantitative reproduction of the adsorption properties of linear and branched alkanes in nanoporous framework structures. The force field was generated by adjusting the parameters so as to faithfully reproduce the experimentally determined isotherms (particularly the inflection points) on MFI-type zeolite over a wide range of pressures and temperatures. It reproduces extremely well the Henry coefficients, heats of adsorption, pre-exponential factors, entropies of adsorption, and maximum loading. It is shown that the extension of the force field from MFI to other nanoporous framework topologies is successful, that it affords the prediction of topology-specific adsorption properties, and that it can be an effective tool to resolve the many discrepancies among experimental data sets.

D. Dubbeldam, S. Calero, T. J. H. Vlucht,
R. Krishna, T. L. M. Maesen, and B. Smit



United Atom Force Field for Alkanes in Nanoporous Materials

I Introduction

Molecular sieves are of importance for many refinery and petrochemical processes such as the separation of linear and branched alkanes [1]. The pore sizes of these nanoporous materials are of the same order of magnitude as those of the adsorbing molecules so that adsorption can occur selectively. The performance of molecular sieves in separation and catalytic processes depends critically on the match between sieve topology and the shape and size of the adsorbate [2]. It is therefore of considerable industrial importance to explore the adsorption of linear and branched alkanes in different topologies using realistic simulations at the microscopic level [3].

Many molecular simulation studies have aimed at providing accurate data at a microscopic level under catalytic process conditions [4]. At these conditions adsorption properties are not readily amenable to ex-

perimental evaluation, but they are still accessible to molecular simulations. However, the simulation results are not beyond dispute, for there is no consensus on which force field is best suited to study e. g. the adsorption of hydrocarbons in nanoporous materials. Some groups claim that an all-atom representation is required [5], while others assume that a united atom approach should suffice [6, 7]. It is also argued that three-body interactions are required for these systems [8]. Within these approaches different parameter sets have been published. Despite these differences most studies claim a good agreement with experimental data, so that it is not trivial to select the best force field to address future practical catalytic or separation problems.

From a molecular simulation point of view the development of a reliable force field for as wide a variety of systems as possible is of preeminent importance. Notwithstanding the plethora of published experi-

mental data, these experimental results involve different zeolite samples or different experiments so that it is difficult to unambiguously compare one experiment with the next. When different experimental data are used as a calibration point to develop a molecular simulation model the result is a different set of parameters or potentials. In this work we develop a unique set of parameters. Although we use this approach to develop a significantly more accurate force field for hydrocarbons in nanoporous materials than previous attempts, a similar optimization strategy can be used for other systems.

The novel parameter-optimization starts by obtaining a reduced set of reliable experimental data sets, preferably of several independent research groups, to calibrate the simulations results. Next, we fit, starting with the smallest number of free parameters, and increase the number of parameters incrementally. The most important part is to analyze the physical connection between a parameter and the various adsorption properties. For example, we found that fitting to inflections in isotherms uniquely determines the adsorbate-adsorbent interaction parameters, and is very sensitive to the size-parameters. Inflection points in the isotherm are often related to a subtle interplay between different adsorption sites. It turns out that if our force field can predict this interplay, it also reproduces the remaining part of the isotherm correctly. Once a reasonable set of parameters had been obtained, we reexamined the experimental data set and included those data that were consistent with the original data set. This extended data set was subsequently used to further refine the parameters. This procedure was repeated until all experimental data were accounted for. The resulting force field not only yields a superior description of the experimental data that formed the basis for the fitting procedure, but also yields an excellent description of reference systems which were not included in the cali-

bration set.

The remainder of this paper is organized as follows. In section II we explain the new fitting procedure. The choice of the model is discussed, followed by a screening of the experimental data used in the fitting procedure. The parameter optimization strategy is explained and we present the final parameter set. This section is concluded with a detailed comparison of this work with various other models proposed in literature. We show in section III that this procedure leads to an excellent description of adsorption properties not included in the initial optimization procedure: other sorbates, mixtures, low-coverage properties (Henry coefficients, enthalpies and entropies of adsorption), and other topologies. As an application we have scrutinized the available experimental data indicating common sources for error. We end with some concluding remarks on the applicability of the model.

II Model

A Choice of models and methods

The first step in an optimization strategy is the selection of the type of force field. In the literature one can find claims that very different force fields yield an equally good description of the adsorption isotherms. However, the following practical considerations limit the choice. The adsorption of hydrocarbons is dominated by dispersive forces. These interactions are notoriously difficult to describe using quantum chemical approaches. The most successful approach is a hybrid technique where, in addition to the *ab-initio* quantum chemical calculation, the dispersive interactions are taken into account using ad-hoc empirical potentials [9].

The next level of sophistication is to use an all-atom model. These models are commonly used in the simulations of proteins

framework	density [kg/m ³]	cells			unit cell size [nm]		
		x	y	z	x	y	z
MFI	1796.358	2	2	4	4.0044	3.9798	5.3532
TON	1968.733	3	3	7	4.1577	5.2260	3.5266
AFI	1729.848	2	3	5	4.7548	4.1178	4.2420
DDR	1759.963	2	3	1	4.8012	4.1580	4.0892
MWW	1673.460	1	2	1	2.4447	2.8228	2.4882

Table 1: Unit cells used in the simulation. For convenience the crystallographic cells are converted to orthorhombic cells.

and other large systems. First attempts to simply use such a force field (Consistent Valence Force Field) for the adsorption of hydrocarbons in MFI gave a reasonable prediction of the adsorption isotherms. However, the much simpler united atom models yielded a significantly more accurate description of the adsorption isotherms [5]. Of course, this observation is not surprising since the united atom models have been specifically optimized for this type of adsorption studies, whereas the all-atom model is a universal force field aimed at a myriad of different applications. To obtain the same degree of accuracy for the all-atom model as for the united atom model would require a dedicated optimization of the all-atom model parameters. Such an optimization will be cumbersome, for it is our impression that the physical information required for such an optimization is not experimentally available in sufficient detail. Thus, it is not straightforward to obtain a physically realistic value for e. g. the ratio of the size parameters for C and H atoms. Optimization of the all-atom model will be more difficult commensurate with its higher level of detail and sophistication, even if the pertinent information were available. It requires fine tuning a larger number of parameters and - accordingly - a significantly larger experimental data set than is needed for the united atom model. In our opinion, the currently available experimental data suffice to optimize the united atom model, but not the all-atom model.

The force field proposed here is primarily designed to reproduce thermodynamic properties of guest molecules in a host system at minimal computational cost. The internal structure of the guests and the guest-guest interactions are of less importance because the properties are dominated by the strong interaction with the force field exerted by the host. Adsorption in cation-free structures takes place at sites with little or no electric field. For these reasons the united atom model [10] seems the most straightforward choice. We consider the CH_x groups as single, chargeless interaction centers with their own effective potentials. The beads in the chain are connected by harmonic bonding potentials. A harmonic cosine bending potential models the bond bending between three neighboring beads, a Ryckaert-Bellemans potential controls the torsional angle. The beads in a chain separated by more than three bonds interact with each other through a Lennard-Jones potential. The Lennard-Jones potentials are shifted and cut at 12 Å. Analytical tail-corrections do not apply in zeolites [5]. A truncated and shifted potential is equally suitable to Monte Carlo and Molecular Dynamics. Flexibility of the framework is not an issue for adsorption of linear and branched alkanes [11]. The interactions between the rigid framework and the guest molecules are assumed to be dominated by the oxygen atoms [12]. We have used the crystallographic structures of van Koningsveld et al. [13], B. Marler [14], S. Qiu et al. [15], H. Gies [16], and M. A. Cam-

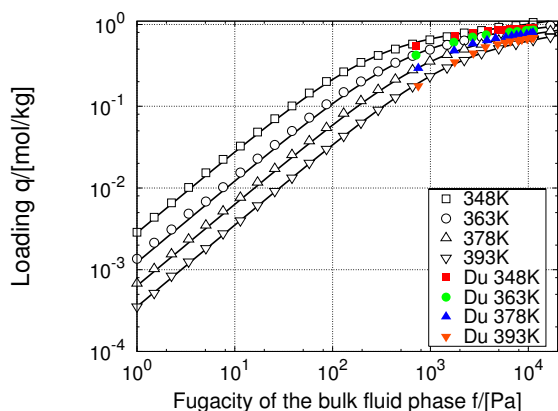


Figure 1: Isotherm of *n*-hexane in MWW at various temperatures. The experimental data are taken from Du et al. [49].

blor et al. [17]. The used unit cells and their sizes are listed in Table 1.

The conventional simulation techniques to compute adsorption isotherms are prohibitively expensive for long alkanes. The Configurational Bias Monte Carlo (CBMC) technique simulates the adsorption isotherms at affordable cost [18]. In a CBMC simulation chains are grown bead by bead biasing the growth process towards energetically favorable configurations, and avoiding overlap with the zeolite. During the growth the Rosenbluth factor is calculated. The average Rosenbluth factor is directly related to the excess chemical potential, the free energy, and the Henry coefficient K_H [19, 20]. The CBMC algorithm greatly improves the conformational sampling of molecules and increases the efficiency of chain insertions by many orders of magnitude. More details on the simulations can be found in Refs. [7, 19, 20] and in the Appendix.

B Selection of experimental datasets

The parameters in current force fields for adsorption in porous media are usually tuned to reproduce heats of adsorption and Henry coefficients. However, it is difficult to identify unambiguously correct physical

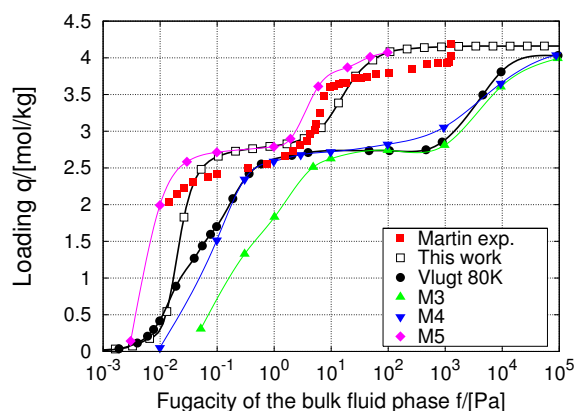


Figure 2: Isotherm of methane at 77 K in an aluminophosphate $AlPO_4-5$ (AFI-topology). The experimental data are taken from Martin et al. [21], the M3, M4, and M5 simulation data from Ref. [8], and the simulation data of Vlugt are from Ref. [65].

values for these parameters. Figure 1 illustrates the problem. It shows the experimentally determined *n*-hexane adsorption by a MWW-type zeolite along with our prediction from simulation. The loading is directly proportional to the pressure only at the extremely low pressures in the Henry regime. When plotted on log-log scale it becomes apparent that most available experimental isotherms are not inside but outside the Henry regime. Experimentally, it is quite difficult to obtain reliable measurements at very low pressures. Usual experimental procedures to obtain Henry coefficients involve fitting the measured data with an equation for an isotherm, followed by extrapolation to zero pressure and loading. In the absence of actual low pressure data, this introduces significant errors. The margin for error increases further, when the heats of adsorption are determined from the temperature dependence of the Henry coefficients. Our results strongly indicate that in many instances extrapolation to zero loading was not justified, because of a lack of low pressure data, a lack of high pressure data, or because there were altogether too few experimental data points.

A better approach would be to fit on en-

model	O-CH ₃		O-CH ₂		O-CH	
	σ [Å]	ϵ/k_B [K]	σ [Å]	ϵ/k_B [K]	σ [Å]	ϵ/k_B [K]
AUA	3.30	106	3.23	89.84	3.18	69.05
June et al.	3.364	83.8	3.364	83.8	-	-
This work	3.48	93	3.58	60.5	3.92	40
Vlugt et al.	3.60	80	3.60	58	3.60	58
Smit et al.	3.64	87.5	3.64	54.4	3.64	51.3

Table 2: Adsorbent-adsorbate interaction size parameters σ and strength parameters ϵ used in various united atom models.

tire isotherms. However, several problems arise. At very high pressures (to determine the saturation loading) a commonly occurring experimental difficulty is that adsorption is not restricted to the pores defined by the framework topology under investigation, but also occurs at the exterior crystal surface. Since the texture of the crystals and crystal agglomerates varies widely, the maximum loading reported in literature tends to show a wide scatter. An example is methane in tubular AFI-like structures. Figure 2 shows the isotherm of methane in an AFI-type aluminophosphate at 77 K. AFI-type structures consist of straight, non-intersecting channels that are 0.73 nm \times 0.73 nm in diameter. The experimental results of Martin et al. [21] illustrate a problem frequently encountered when trying to link experiments on the AFI-type pores to simulation. Simulation uses perfect crystals, while the pores in the actual samples used by Martin are (partially) blocked. Due to the one-dimensional character, a very small structural imperfection can block off a large part of the zeolite. In fact, Martin et al. studied several samples of different origin and found significantly different adsorption capacities. The authors estimate the ideal sorption capacity at 6 molecules per unit cell (4.16 mol/kg), which matches our maximum loading from simulation. At 1000 Pa, condensation on the external surface intrudes the experimental measurements, whereas simulation uses fugacity and is not hampered by this transition from gas to liquid phase adsorption.

C Parameter Optimization Strategy

Instead of calibrating a force field with extrapolated experimental data, we propose to calibrate it by explicitly fitting the entire isotherm over a wide range of pressures and temperatures. If this procedure were followed for individual molecules it would not necessarily yield a consistent force field, for many different sets of model parameters are able to properly reproduce one and the same isotherm. A necessary and sufficient procedure is to utilize isotherms that exhibit inflection points, and use these inflection points as calibration points for the parameter optimization.

It is instructive to discuss the role of the size-parameter $\sigma_{\text{O-CH}_x}$. In Figure 3 we show the influence of the σ parameters on the inflection of 2-methylpropane in MFI. The O-CH parameters remain fixed at $\sigma = 3.92$ Å and $\epsilon/k_B = 40$ K, while $\epsilon_{\text{O-CH}_3}$ is examined over a range of reasonable values for two values of $\sigma_{\text{O-CH}_3}$: one significantly too small and one significantly too large. A crucial observation is that only a single strength/size parameter pair is able to describe the inflection and the entire isotherm properly. This is in contrast with the common belief that for each value of σ there is a corresponding ϵ that can describe the isotherm correctly [22]. The shape of the isotherm and the inflection points are the most sensitive to the size-parameter of the interactions, whereas the loading at a given pressure is most sensitive to the strength-

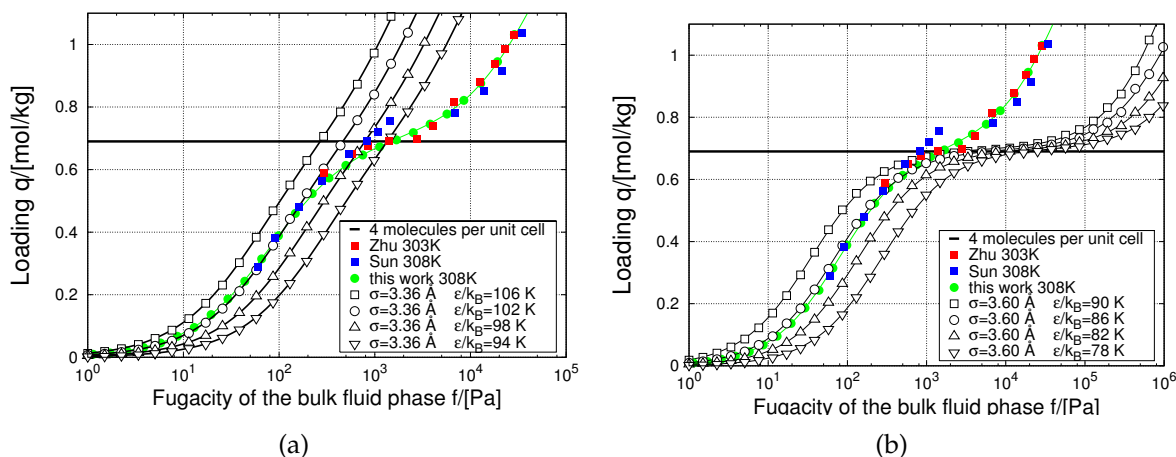


Figure 3: Isotherms of 2-methylpropane at 308 K in MFI. The O-CH parameters remain fixed at $\sigma = 3.92 \text{ \AA}$ and $\epsilon/k_B = 40 \text{ K}$, while $\epsilon_{\text{O-CH}_3}$ is examined over a range of reasonable values for two fixed values of $\sigma_{\text{O-CH}_3}$ a) a rather too small of $\sigma_{\text{O-CH}_3} = 3.36 \text{ \AA}$ and b) a too high value of $\sigma_{\text{O-CH}_3} = 3.60 \text{ \AA}$. Only a single parameter pair, $\epsilon_{\text{O-CH}_3}/k_B = 93$ and $\sigma_{\text{O-CH}_3} = 3.48$ combined with the CH parameters (Table 2), is able to describe the experimental data of Sun et al. [36] and Zhu et al. [33].

parameter of the interaction. A higher strength parameter ϵ induces an increased loading, and a lower strength parameter results in a decrease in loading (for a fixed pressure). The amount of inflection is controlled by the size parameter σ . These properties can be exploited to obtain unique parameters.

In practice we proceed as follows. A reasonable starting size parameter is chosen. For this parameter we iteratively search for the corresponding strength parameter that matches the experimental data at a pressure significantly below the inflection. The entire isotherm is then followed for increasing pressure until a deviation from the experimental data is observed. The “updated” size parameter is then found by choosing a higher value for a deviation to the left of the experimental data, and by choosing a lower value for the size parameter for a deviation to the right of the experimental data. This scheme proceeds iteratively until the entire experimental isotherm is accounted for.

In Figure 4 we show the influence of the σ parameter on the inflection of 2-methylpropane in MFI. Although the size-

parameters listed in Table 2 differ by less than 10%, the shape of the isotherms is dramatically different. The model of June et al. [23] uses a small value of $\sigma = 3.364 \text{ \AA}$, the AUA-model [24] uses $\sigma_{\text{O-CH}_3} = 3.30 \text{ \AA}$, $\sigma_{\text{O-CH}_2} = 3.23 \text{ \AA}$, and $\sigma_{\text{O-CH}} = 3.18 \text{ \AA}$. The models of Vlught et al. [7] and Smit et al. [25] use a fixed σ ; $\sigma_{\text{O-CH}_3} = \sigma_{\text{O-CH}_2} = \sigma_{\text{O-CH}} = 3.60 \text{ \AA}$ for the Vlught-model, and $\sigma_{\text{O-CH}_3} = \sigma_{\text{O-CH}_2} = \sigma_{\text{O-CH}} = 3.64 \text{ \AA}$ for the Smit-model. The model proposed in this work uses $\sigma_{\text{O-CH}_3} = 3.48 \text{ \AA}$, $\sigma_{\text{O-CH}_2} = 3.58 \text{ \AA}$, and $\sigma_{\text{O-CH}} = 3.92 \text{ \AA}$. It yields exact overlap with experimental data and the inflection is reproduced faithfully. In the remainder of this paper we will demonstrate their accuracy.

The fitting to well-established inflection points in the isotherms has many advantages and overcomes problems that have so far impeded the development of more accurate force fields.

- We obtain a unique set of parameters that all relate directly to a well defined physical property. We therefore expect these parameters to be much better transferable to other systems than

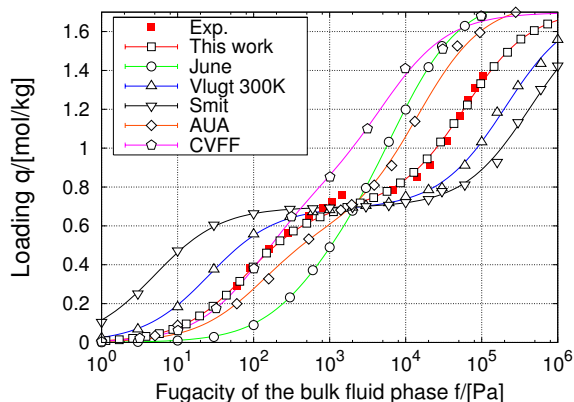


Figure 4: Isotherms of 2-methylpropane at 308 K in MFI compared to various computational models. The experimental data are taken from Ref. [36], the simulation data from June et al. [23], Vlugt et al. [7], Smit et al. [25], AUA from Pascual et al. [24], and CVFF from Macedonia et al. [5].

previous attempts.

- The parameters are determined accurately. The inflection in an isotherm is extremely sensitive to the size-parameter $\sigma_{\text{O-CH}_x}$.
- By explicitly fitting to entire adsorption isotherms we guarantee the proper reproduction of properties such as Henry coefficients, heats of adsorption, adsorption entropies, and maximum loadings.
- Inflections are found at moderate pressures and here the experimental data is most reliable. Experimentally there is minimal intrusion from adsorption at the exterior surface.
- The inflection is directly related to the structure e. g. for *n*-heptane and 2-methylpropane in MFI the inflection occurs exactly at 4 molecules per unit cell.

D Parameters from MFI/AFI-inflections

The isotherms measured on MFI are optimally suited for calibration of a force field, because they have been reported by many different experimental research groups, and the fundamental reason for their shapes is very well established. The MFI-type structure consist of a three-dimensional pore system with straight, parallel channels intersected by zig-zag channels. The linear channels intersect with the zig-zag channels four times per unit cell. Interestingly, for *n*-hexane, *n*-heptane, and for the branched alkanes in MFI a kink in the isotherm is observed [7]. This inflection is directly related to the number of intersections in the structure and occurs at *exactly* 4 molecules per unit cell. The fundamental understanding of the inflection points affords an independent check on the consistency of experimental data. If isotherms do not show an inflection point at the correct loading they can be summarily excluded.

Ethane, *n*-heptane, and 2-methylpropane exhibit isotherms of the Brunauer type-VI in MFI. Ethane shows a small inflection point in the adsorption isotherm at high loading [26]. The $\epsilon_{\text{O-CH}_3}$ and $\sigma_{\text{O-CH}_3}$ are uniquely obtainable from the ethane isotherm. When the channel interiors are occupied the probability distribution shows a remarkable order: a repeating pattern of ethane molecules "locked" in the zig-zag channels between two intersections. The $\epsilon_{\text{O-CH}_2}$ and $\sigma_{\text{O-CH}_2}$ are obtained from *n*-heptane. The inflection behavior of *n*-heptane is well established [18, 27]. Smit and Maesen explained this effect in terms of *commensurate freezing*: *n*-heptane has a size commensurate with the size of the zig-zag channel. At high pressures the molecules shift from a random distribution to a distribution where the molecules are localized exclusively in the channels and not at the intersections. Various branched molecules show inflections for another rea-

	O	CH ₄	CH ₃	CH ₂	CH	C
CH ₄	115.00 3.47	158.50 3.72	130.84 3.74	94.21 3.84	51.91 4.17	11.26 4.87
CH ₃	93.00 3.48	130.84 3.74	108.00 3.76	77.77 3.86	42.85 4.19	9.30 4.90
CH ₂	60.50 3.58	94.21 3.84	77.77 3.86	56.00 3.96	30.86 4.30	6.69 5.03
CH	40.00 3.92	51.91 4.17	42.85 4.19	30.85 4.30	17.00 4.67	3.69 5.46
C	10.00 4.56	11.26 4.87	9.30 4.90	6.69 5.03	3.69 5.46	0.80 6.38
bond	$U^{\text{bond}} = \frac{1}{2}k_1(r - r_0)^2$ $k_1/k_B = 96500 \text{ K}/\text{\AA}^2, r_0 = 1.54 \text{ \AA}$					
bend	$U^{\text{bend}} = \frac{1}{2}k_2(\cos \theta - \cos \theta_0)^2$ $k_2/k_B = 62500 \text{ K}, \theta_{\text{eq}} = 114^\circ$					
torsion	$U^{\text{torsion}} = \sum_{n=0}^5 \eta_n \cos^n \phi$ $(x_1 \dots x_i) - A - B - (y_1 \dots y_j)$					η_n/k_B in K
type 1	C _x -CH ₂ -CH ₂ -C _x			<i>n</i> -butane		
type 2	H-CH-CH ₂ -C _x			2-methylbutane		
type 3	C _x -C-CH ₂ -C _x			2,2-dimethylbutane		
type 4	C _x -C-C-C _x			2,2,3,3-tetramethylbutane		
type 5	C _x -C-CH-H			2,2,3-trimethylbutane		
type 6	H-CH-CH-H			2,3-dimethylbutane		
	η_0	η_1	η_2	η_3	η_4	η_5
type 1	1204.654	1947.740	-357.845	-1944.666	715.690	-1565.572
type 2	1367.086	4360.147	416.005	-6499.427	-832.004	1646.129
type 3	1293.324	3879.849	0	-5173.163	0	0
type 4	2045.657	6136.797	0	-8182.447	0	0
type 5	1575.127	4725.259	0	-6300.384	0	0
type 6	1092.268	2822.786	-908.033	-3007.027	1816.066	-1816.059

Table 3: Force field guest-host and guest-guest interactions of hydrocarbons in cation-free nanoporous materials. Lennard-Jones parameters, ϵ/k_B [K] in top-left corner, σ [Å] in bottom-right corner of each field, bond and bend parameters, and the torsion potential: the torsion type on the left, on the right an example of a molecule with this type of torsion potential, and on the bottom the parameters. Some of the alkane-alkane interactions are taken from Ref. [66] and optimized to reproduce vapor-liquid coexistence curves of the phase diagrams, the internal bond from Ref. [67], the internal bend from Ref. [41], and the torsion from T. J. H. Vlugt and M. Frash [68].

son [7]. 2-methylpropane preferentially adsorbs at the intersections. At a loading of four molecules per unit cell the intersections are fully occupied and additional molecules must be pushed into the channels requiring a significantly higher driving force [28]. The $\epsilon_{\text{O-CH}}$ and $\sigma_{\text{O-CH}}$ are uniquely obtainable from the isotherm of 2-methylpropane. Detailed inspection of the experimental data showed that for ethane, 2-methylpropane, and *n*-heptane several independent groups provided consistent data and we used these data as our primary set of experimental data. As basis for calibration we utilized the experimental data from several different research groups of Cavalcante et al. [29], Jolimaître et al. [30, 31], Eder et al. [32], Zhu et al. [33–35], Sun et al. [27, 36], and Choudhary et al. [37].

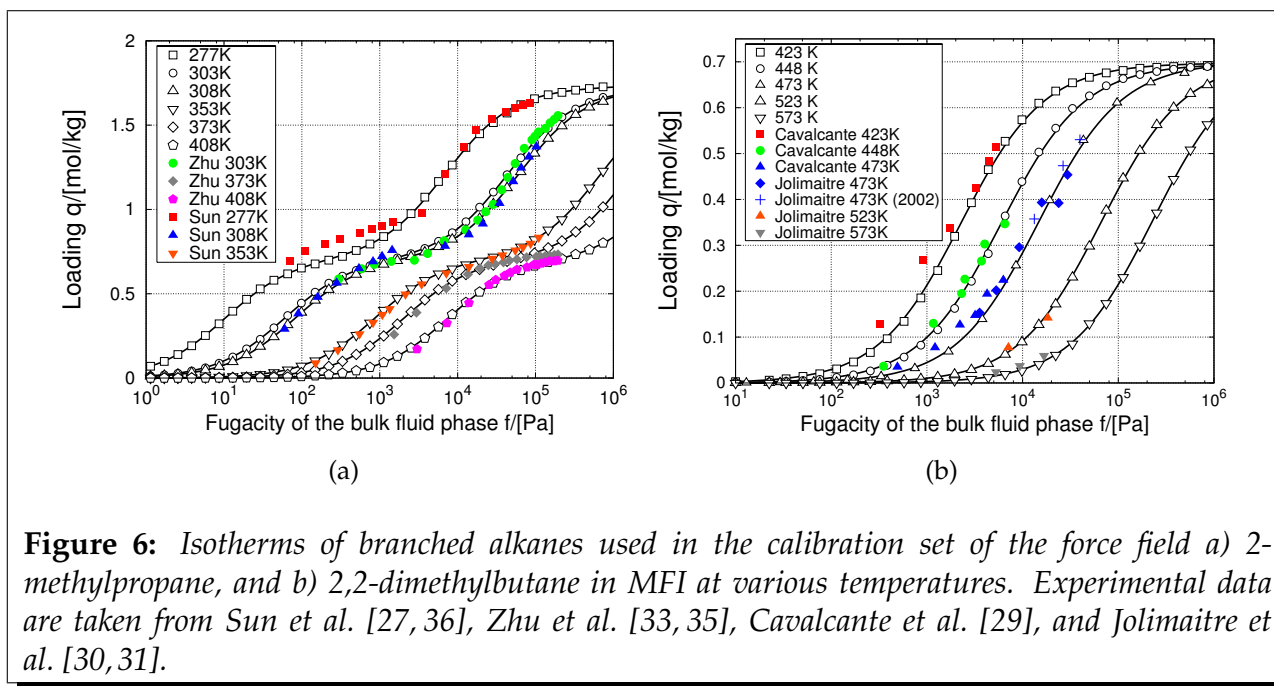
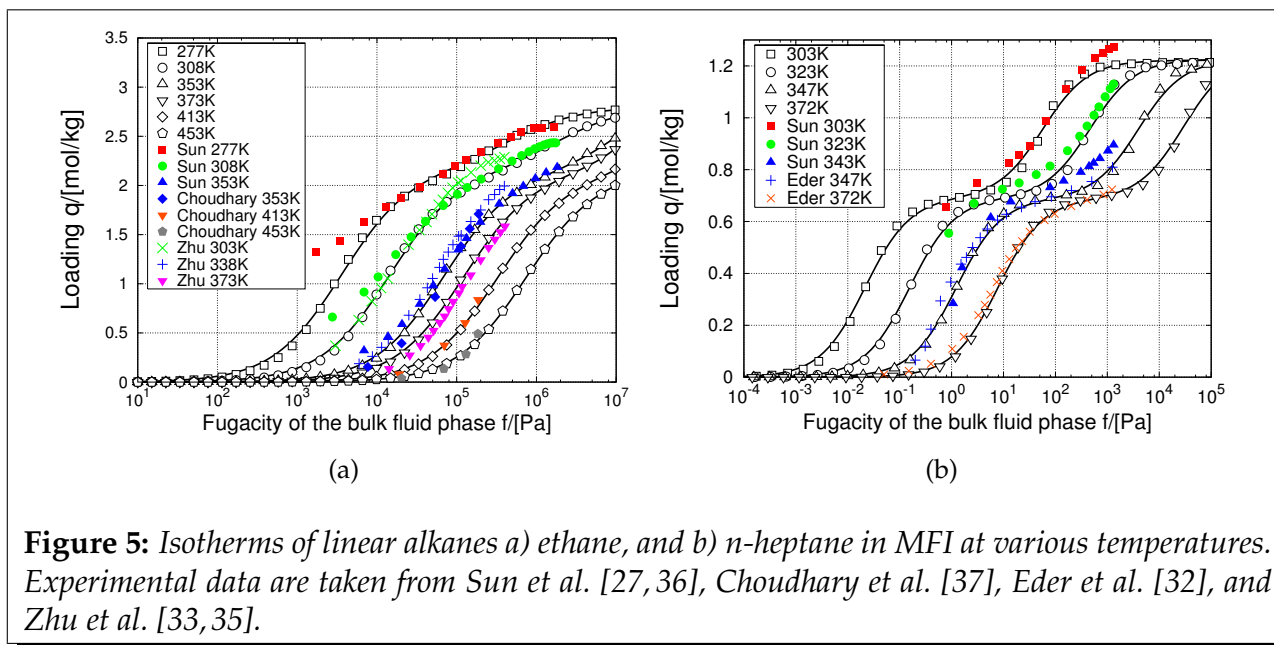
Whereas inflection points in the isotherms of MFI-type zeolites can be used to calibrate most of the parameters, it does not afford calibration of the parameters for CH_4 . For this molecule we resorted to AFI-type sieves. The isotherms for CH_4 at 77 K have a clearly defined inflection point at 4 molecules per unit cell (2.77 mol/kg) loading. Therefore $\epsilon_{\text{O-CH}_4}$ and $\sigma_{\text{O-CH}_4}$ are obtained from the isotherm of methane in AFI. There are no experimental isotherms of double branched alkanes with an inflection, so that the $\epsilon_{\text{O-C}}$ and $\sigma_{\text{O-C}}$ could not be uniquely and accurately determined. Their initial values had to be estimated from mixing rules. Calibration of these values utilizing an entire isotherm of 2,2-dimethylbutane in MFI indicated that the initial estimates were essentially correct. The resulting force field is described by the parameters listed in Table 3.

E Comparing this work and calibration data

The inflection of methane in AFI at 77 K is found at the experimental pressure, and the isotherm shape is satisfactorily reproduced (Figure 2). The $\epsilon_{\text{O-CH}_4}$ and $\sigma_{\text{O-CH}_4}$

could be uniquely determined, with an accuracy better than 0.02 Å for σ and better than 5 K for ϵ/k_B . Figure E shows the results of the fitting procedure of ethane and *n*-heptane in MFI along with the experimental basis set. The $\epsilon_{\text{O-CH}_3}$ and $\sigma_{\text{O-CH}_3}$ parameters are uniquely fixed with a precision better than 0.01 Å for σ and better than 1 K for ϵ/k_B . The simulation results for ethane are in excellent agreement with the experimental data from Choudhary et al. (Figure 5(a)). The agreement with the data from Zhu et al. and Sun et al. is fair, for the former deviate at low pressures and the latter at high pressures. Considering the good agreement between the simulations and experiments, the results may be interpreted as indirect evidence for the ethane inflection, even though the experimental high pressure confirmation is missing. Normal heptane has a much more pronounced inflection behavior (Figure 5(b)). The $\epsilon_{\text{O-CH}_2}$ and $\sigma_{\text{O-CH}_2}$ are uniquely fixed with a precision better than 0.02 Å for σ and better than 5 K for ϵ/k_B . The simulated isotherms overlap perfectly with data of Eder et al. and well with the data of Sun et al. The few high pressure points of Sun et al. at 303 K are in disagreement with the simulations and with most experimental data on maximum loadings (1.25 mol/kg Yang and Rees [38] and 1.265 mol/kg van Well et al. [39]).

The 2-methylpropane isotherms are compared in Figure 6(a) to the data of Sun et al. and Zhu et al. The agreement is again excellent, except for the low pressure part of the Sun data for 277 K. The experimental loadings are probably too high because the inflection is expected at 4 molecules per unit cell (0.6935 mol/kg). The $\epsilon_{\text{O-CH}}$ and $\sigma_{\text{O-CH}}$ are uniquely fixed with a precision better than 0.01 Å for σ and better than 1 K for ϵ/k_B . Figure 6(b) shows the double branched 2,2-dimethylbutane isotherm. The simulation data overlaps with Jolimaître et al., and Cavalcante and Ruthven.



F Comparing this work and preceding models

To show the improvement of this work compared to previous approaches we refer again to Figure 2. The figure shows another important point. Our approach clearly outperforms complex all-atom models containing two- and three-body dispersion interactions between guest and framework atoms (up to quadrupole terms), induced interactions (polarization), and repulsive terms. As an example, the M3, M4, and M5 models are taken from Ref. [8]. These three models differ only by a slight change in repulsive interaction. The M5 model is the best of the three, but not better than our significantly less complex united atom approach. The success of the united atom model supports the notion that adsorption properties are dominated by dispersive forces, and that a united atom model captures these satisfactorily.

We also refer again to Figure 4 to discuss the comparison with various united atom approaches previously proposed in literature. The figure showed the inflection in the isotherm of 2-methylpropane at 308 K in MFI. The models of Smit et al. and Vlught et al. exaggerated the inflections because their size-parameters were too large. The models of Pascual et al., June et al., and the all-atom CVFF force field did not show a clear inflection at all because their size-parameters were too small.

The value of $\sigma_{\text{O-CH}_x}$ also has an effect on the maximum loading and packing efficiency. De Meyer et al. [40] performed both experiments and simulations of long chain n -alkanes in MFI. Experiments show that the maximum packing is approximately 53.2 carbon atoms per unit cell for n -C₁₄ and longer n -alkanes, while simulations using the model of Vlught et al. find a value of 49.0 carbon atoms per unit cell. The current model yields 52.5 carbon atoms per unit cell in excellent agreement with experiment, but not with the model of Vlught et al.

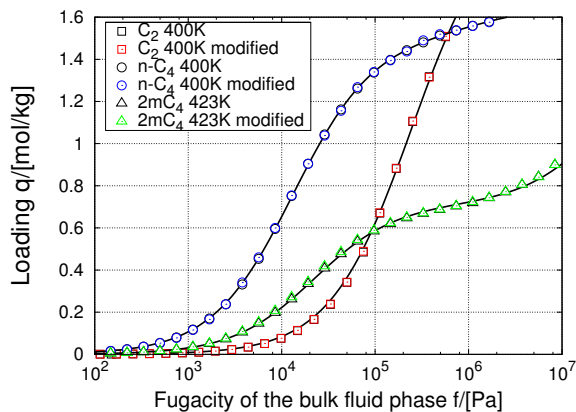


Figure 7: Isotherms of ethane, butane, and 2-methylbutane compared to isotherms obtained using different internal interaction potentials and parameters as described in the text.

This is another indication that the value for $\sigma_{\text{O-CH}_x}$ in the Vlught model is too high.

G Internal interaction parameters

To test the dependence of the adsorbent-adsorbate interaction parameters derived in this work on the internal interaction parameters, we apply different sets to ethane, butane, and 2-methylbutane and compare the isotherms with the loadings obtained using the internal interactions of this work (Table 3). We modified the harmonic cosine potential to a fixed distance of 1.54 Å and recomputed the isotherm of ethane. The butane model was modified to the TraPPE-UA model [41], which uses a fixed bond distance of 1.54 Å, and a bending and torsion potential of the form

$$U^{\text{bend}} = \sum_{\text{bends}} \frac{1}{2} k_{\theta} (\theta - \theta_0)^2, \quad (1)$$

with $k_{\theta}/k_B = 62500$ K, $\theta_0 = 114^\circ$, and

$$U^{\text{torsion}} = \sum_{\text{torsions}} \eta_0 + \eta_1 [1 + \cos(\phi)] + \eta_2 [1 - \cos(2\phi)] + \eta_3 [1 + \cos(3\phi)] \quad (2)$$

with $\eta_n/k_b = \{0, 335.03, -68.19, 791.32\}$. Another possible combination of parameters applied to 2-methylbutane is a fixed

bond length of 1.53 Å, a bending potential of the form Eq. 1 with $k_\theta/k_B = 85000$ K, $\theta_0 = 113^\circ$, and the torsion potential of the this work. The results for the three test-cases shown in Figure 7 suggests a minimal dependency of the adsorption results on the internal interaction parameters, and that the adsorbent-adsorbate interaction parameters may be combined with any other physically reasonable internal interaction model. The results are also largely independent of the intermolecular potentials, because these too are dominated by the adsorbent-adsorbate interactions.

III Validation and applications

A Extension to other sorbates in MFI

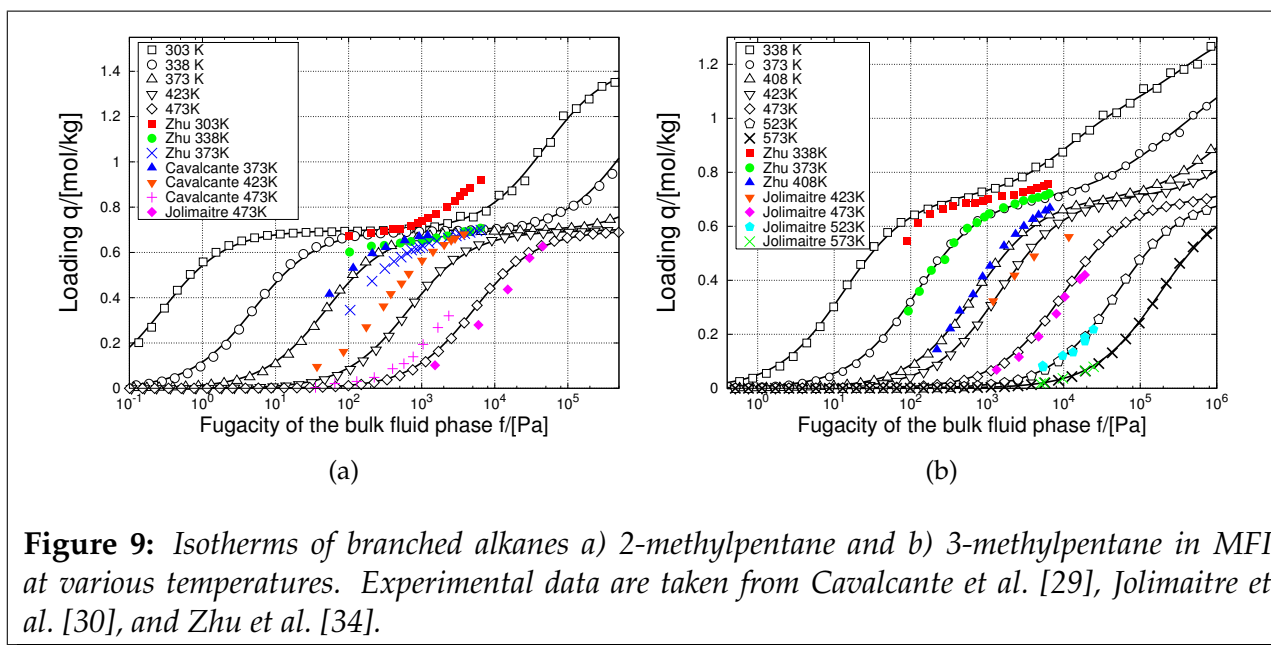
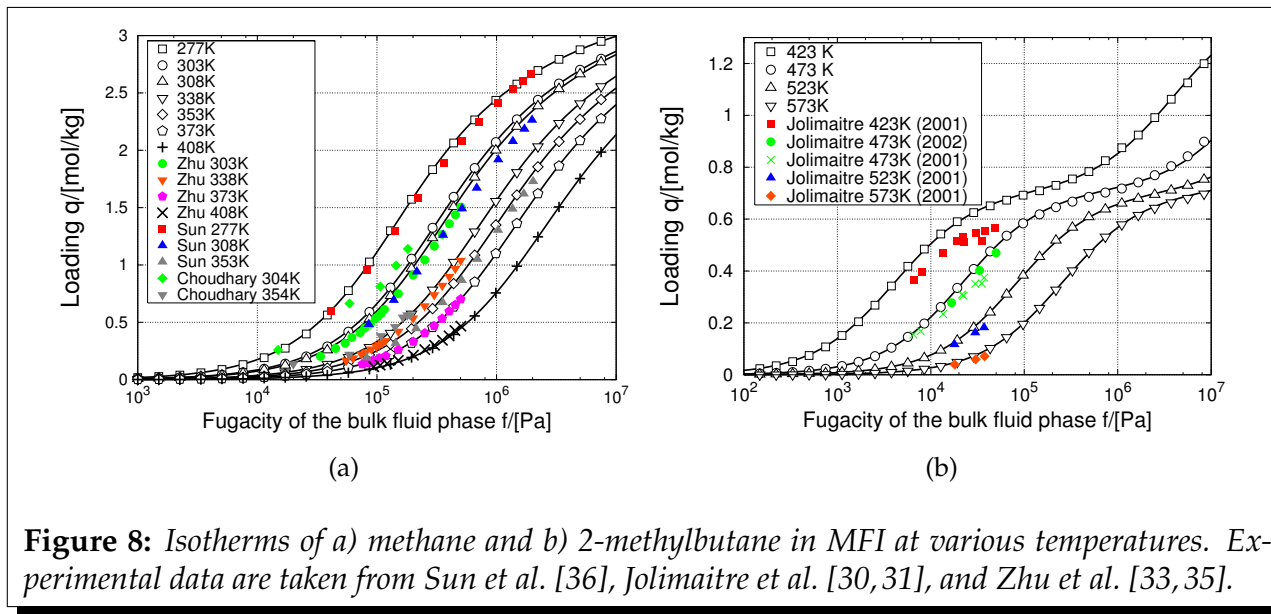
To demonstrate that our parameters are transferable to other molecules in MFI we have selected methane, 2-methylbutane, 2-methylpentane, and 3-methylpentane. The simulated and experimental isotherms for methane on MFI are shown in Figure 8(a). The agreement of the simulations and experiments is satisfactory considering the scatter in the experimental data sets. The temperature dependence, the amount adsorbed, and the shape of the isotherms are well reproduced. For 2-methylbutane (Figure 8(b)) we find excellent agreement with Jolimaitre et al. The data are obtained using pulse chromatography and uptake measurements, and are in good agreement with each other. Once again we find a deviation at the lowest temperature. Reasons for deviations include adsorption in mesopores and on the external surface, and at low temperatures the sorption equilibration of particularly branched molecules materializes extremely slowly.

Figure 9(a) shows the computed isotherms for 2-methylpentane com-

pared to Jolimaitre et al., Zhu et al., and Cavalcante et al. The discrepancy between the experimental sets is clearly visible. A likely cause for the difficulty in obtaining reliable data on 2-methylpentane is that the molecule is asymmetric and too long to easily change orientation at the intersections. For the more symmetric and smaller 2-methylbutane molecule this is less of a problem. The optimal packing at a certain pressure is hard to attain, in both experiment and simulation. The Cavalcante loading is too high in comparison with ours. The agreement with Jolimaitre is reasonable, although only one temperature is available. The data of Zhu et al. deviates at higher temperatures. For 3-methylpentane (Figure 9(b)) we find excellent agreement with Zhu et al. and Jolimaitre et al. Thus, the agreement between simulated and experimental data on the adsorption of molecules not part of the calibration set is remarkably good, especially when the disagreement between the experimental data from various sources is taken into consideration.

B Extension to mixtures in MFI

Binary mixtures represent a critical test for our force field. Figure 10 compares the loading of the individual components of a mixture of *n*-hexane and 2-methylpentane as a function of 2-methylpentane in the gas phase at 433 K and 6.6 kPa as obtained by simulation with those obtained through experiments [42]. The loadings of the individual components at fractional compositions zero and one correspond to the pure component values, and agree well with the simulation results. The simulation results show no clear preference for either *n*-hexane or 2-methylpentane in this temperature and pressure region. The experimental results show a small preferential adsorption of *n*-hexane compared to 2-methylpentane. We note that the agreement with experiment is significantly improved



CN	K_H 573K [mol/kg/Pa]		K_∞ [mol/kg/Pa]		$-\Delta H$ [kJ/mol]	
	Sim.	Exp.	Sim.	Exp.	Sim.	Exp.
5	3.04×10^{-6}	2.99×10^{-6}	2.33×10^{-11}	2.64×10^{-11}	56.13	55.7
6	6.10×10^{-6}	5.93×10^{-6}	6.07×10^{-12}	6.07×10^{-12}	65.87	66.0
7	1.23×10^{-5}	1.22×10^{-5}	1.53×10^{-12}	1.29×10^{-12}	75.77	76.7
8	2.43×10^{-5}	2.49×10^{-5}	3.67×10^{-13}	3.25×10^{-13}	85.82	86.6
9	4.61×10^{-5}	4.73×10^{-5}	8.59×10^{-14}	8.41×10^{-14}	95.81	96.1
relation			Sim.		Exp.	
$-\Delta H = \alpha \text{CN} + \beta$			$\alpha = 9.93$		$\alpha = 10.1$	
$-\Delta S = \gamma \text{CN} + \delta$			$\gamma = 11.65$		$\gamma = 11.99$	
$-\ln(K_\infty) = -A\Delta H + B$			$A = 0.141, B = 16.54$		$A = 0.143, B = 16.4$	

Table 4: Comparison of our simulations results of low-coverage properties in MFI with the experimental results of Denayer et al. [44]. Both the Denayer and the simulation Henry coefficients K_H of the linear alkanes have been fitted to $K_H = K_\infty e^{\frac{-\Delta H}{RT}}$ in the temperature range $T=473$ - 673 K. Here, K_∞ denotes the pre-exponential Henry coefficient, ΔH the enthalpy of adsorption, and $R = 8.31451$ J/mol/K the gas constant. The entropy ΔS per carbon number is related to the slope of $\ln(K_\infty)$ plotted as a function of Carbon Number (CN) [44].

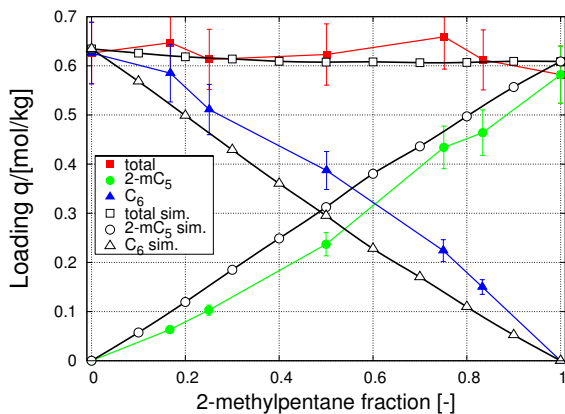


Figure 10: Hexane and 2-methylpentane loading in MFI as a function of 2-methylpentane fraction in the gas phase in a binary mixture at 433 K and 6.6 kPa. Experimental data are taken from Schuring et al. [42].

compared to the model of Vlugt et al. Their model yielded a loading that is too high (0.69 mol/kg for *n*-hexane and 0.65 mol/kg for 2-methylpentane), and a small preference for the branched instead of the experimentally preferred linear alkane [42]. The pressure is too low to observe the exclusion effect of branched molecules compared to their linear isomers due to the *configurational entropy* effect [43].

C Extension to low-coverage in MFI

The force field developed thus far yields isotherm data that agree not only qualitatively, but also quantitatively with many experimental data sets, such as Sun et al., Jolimaitre et al., Choudhary et al., Zhu et al., and Eder et al. Surprisingly, the agreement between the experimental data, and between simulated and experimental data breaks down at low coverage. This is especially striking because most of these data were obtained by extrapolating the very same isotherms to low pressure and loading. An analysis of the experimental data reported by Denayer and coworkers [44] sheds light on the likely reasons for these discrepancies. In marked contrast to other experimentalists, Denayer took special care to verify that the results were indeed obtained in the Henry-regime.

In this section we compare our simulation results with the experimental results from Denayer et al. on MFI. The results are summarized in Table 4. It is noteworthy that Denayer's data set was not part of the set used as a basis for our force field. The

CN	guest	K_H 573K Sim. [mol/kg/Pa]	K_H 573K Exp. [mol/kg/Pa]	$-\Delta H$ 300K Sim. [kJ/mol]	$-\Delta H$ 573K Exp. [kJ/mol]	values from literature [kJ/mol]
5	n -C ₅ 2-mC ₄	3.04×10^{-6} 2.72×10^{-6}	4.74×10^{-6} 3.34×10^{-6}	57.93 55.77	57.7 56.1	60.0 64.5 57.4 56.1 58.4
6	n -C ₆ 2-mC ₅ 3-mC ₅	6.1×10^{-6} 5.98×10^{-6} 4.0×10^{-6}	9.73×10^{-6} 6.04×10^{-6} 5.23×10^{-6}	68.06 67.88 65.00	68.8 66.8 66.0	69.9 70.0 72.0 71.5 67.8 58.5 64.0 62.8 61.5 63.0 62.7 66.4 66.8 60.0 54.4 68.4 63.0 67.7 55.0 58.4 54.4 54.4
	2,2-dmC ₄	2.93×10^{-6}	3.33×10^{-6}	62.20	63.9	
	2,3-dmC ₄	4.18×10^{-6}	3.12×10^{-6}	65.7	63.4	
7	n -C ₇ 2-mC ₆ 3-mC ₆ 2,3-dmC ₅	1.23×10^{-5} 1.08×10^{-5} 9.46×10^{-6} 5.5×10^{-6}	1.96×10^{-5} 1.10×10^{-5} 1.04×10^{-5} 4.24×10^{-6}	78.32 79.33 77.00 76.18	79.6 78.4 78.0 74.1	82.6 84.0 84.5 - - -
8	n -C ₈ 2-mC ₇ 3-mC ₇ 4-mC ₇	2.43×10^{-5} 2.10×10^{-5} 1.66×10^{-5} 2.19×10^{-5}	3.91×10^{-5} 2.15×10^{-5} 1.8×10^{-5} 1.8×10^{-5}	89.95 88.75 88.27 89.33	90.7 88.6 88.5 88.7	96.0 100.7 89.0 - -

Table 5: Comparison of our simulations results of the Henry coefficients K_H and enthalpies of adsorption ΔH of linear and branched alkanes in MFI with the experimental results of Denayer and coworkers on protonated MFI [45]. The values for the heat of adsorption are taken from Refs. [7, 44].

quantitative agreement and consistency on low-coverage properties of simulated and experimental data is therefore truly remarkable. We reproduce the chain length dependence of the enthalpy of adsorption and the entropy of adsorption, as well as the absolute values of Henry coefficients, pre-exponential factors, and enthalpies of adsorption.

A point of continued interest is the variation of the heat of adsorption with carbon number. Figure 11 shows this variation as obtained from simulation and from various experimental groups. Our results are consistent with Denayer et al. data at 573 K, and also with other experimental data obtained around 300 K. Sun et al. for C₁-C₁₂ derived his heats of adsorption from isotherms through extrapolation. These vary clearly in a more erratic fashion with carbon number than the data obtained through dedicated experiments at low pressure. A visual inspection of the simulated and most of the experimental data suggests that there are two linear correlations between the heat of adsorption and the Carbon Number (CN), one for C₁-C₅, and another for C₆-C₁₂. Our simulation at 300 K indicates a slope of 9.22×CN for C₁-C₅, and a slope of 11.3×CN for C₆-C₁₂. Various different values have been reported in the literature 9.81, 10.08, 10.2, 11.0, 11.3, and 12 kJ/mol carbon number. We note that simulation models of June et al., and Vlugt et al. do not resolve these two distinct regimes. The model of Smit et al. resolves two regimes with a crossover at C₈ instead of C₆.

Compared to linear alkanes, far fewer experimental data are available on the adsorption of branched alkanes in MFI. A detailed study of linear and branched alkanes in protonated MFI is available from Denayer et al. [45]. Despite the absence of protons in the simulated framework structure and the presence of protons in the experimental sample, the agreement between simulated and experimental Henry coeffi-

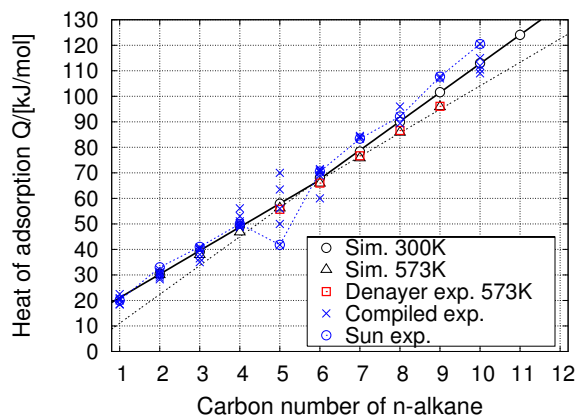


Figure 11: Comparison of computed heats of adsorption with experimental data for methane up to n-dodecane in MFI. Experimental data are taken from Sun et al. [27, 36], and Denayer et al. [44], and values found in the literature as compiled by Refs. [7, 44].

icients in Table A is fair. Both the simulations and the data of Denayer et al. agree on the ordering of the Henry coefficients for a set of isomers: linear > 2-methyl > 3-methyl > dibranched. The same order applies to the heats of adsorption. Comparison between simulated and experimental heats of adsorption from sources other than Denayer and coworkers does not seem to be a meaningful endeavor, for the scatter in the experimentally data in Table A (compiled by Refs. [7, 44]) is huge.

The good match between simulated and a single set of experimental data outside our calibration set strongly suggests that the pulse chromatographic technique used by Denayer is uniquely suited to obtain reliable low coverage data, and that extrapolation of isotherms from intermediate to low coverage tends to introduce major errors.

D Extension to different topologies

Validation of our model for *siliceous* zeolites other than MFI relies on the relatively few data available for DDR [46, 47], TON [48], and MWW [49]. The DDR topology

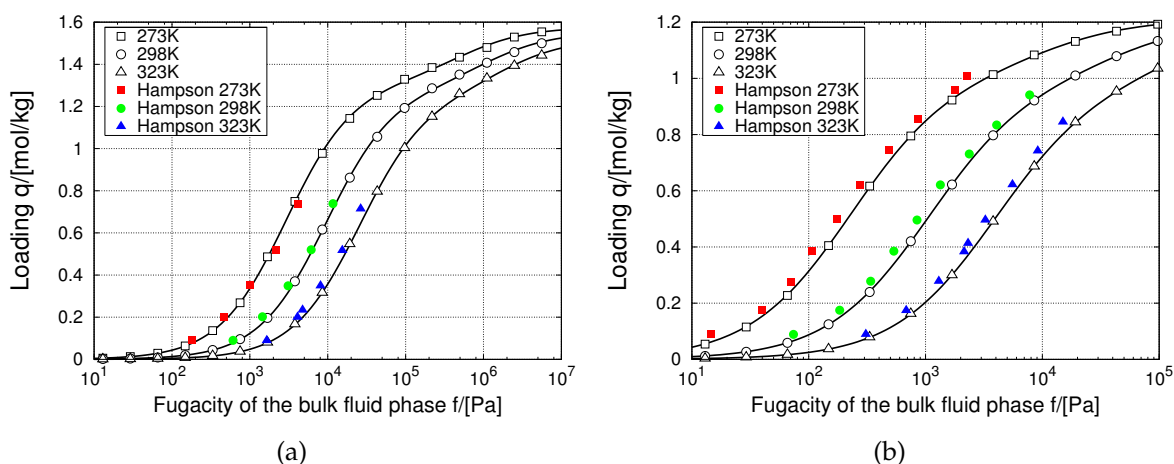


Figure 13: Isotherms of linear alkanes a) ethane and b) propane in TON at various temperatures. Experimental data are taken from Hampson and Rees [48].

consists of 19-hedron cavities connected through 8-ring windows of $0.35 \text{ nm} \times 0.44 \text{ nm}$ across into an hexagonally arranged two-dimensional cage/window-type systems. Figure 12 shows our simulation results for ethane compared with the experimental data of Zhu et al. for DDR. The agreement is excellent and we find overlap at all temperatures. The heat of adsorption computed at 300 K for ethane is 28.96 kJ/mol , while Zhu et al. found 24.74 kJ/mol when he used the virial form of the thermodynamic equilibrium equation to extrapolate the data to low loading. The Henry coefficients obtained in this way are fitted to the van't Hoff equation to provide the heat of adsorption. However, a closer inspection of the data plotted at log-log reveals that the data of Zhu et al. are too far outside the Henry regime to produce reliable results.

The TON topology consists of narrow, unidimensional 10-ring channels with small apertures of $0.46 \text{ nm} \times 0.57 \text{ nm}$. Hampson and Rees measured adsorption data for ethane and propane on TON [48]. Our simulation data and the experimental data are in excellent agreement. For C_2 and C_3 the simulated (32.0 and 41.6 kJ/mol) and experimental heat of adsorption (31.9 and 42.0 kJ/mol) are virtually identical. If framework flexibility were to

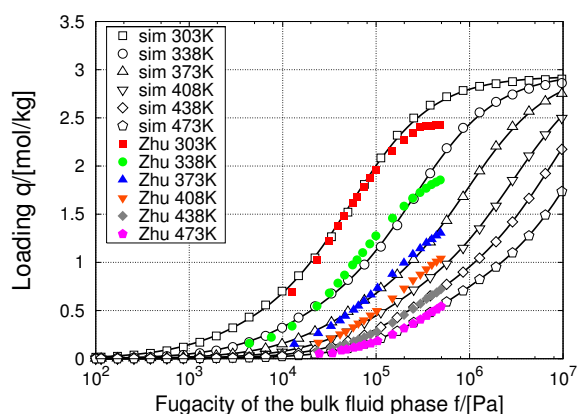


Figure 12: Isotherm of ethane in DDR at various temperatures. Experimental data are taken from Zhu et al. [46].

be important it would be in this highly confined environment. The agreement of simulation utilizing the model with a completely fixed framework corroborates earlier suggestions that framework flexibility does not significantly influence the adsorption properties, even in tight confinements. For a comparison of the heat of adsorption obtained from simulations based on TON and those obtained from experiments on TON aluminosilicates, the differences are apparent, particularly for longer alkanes. These are probably caused by adsorption on the Brönsted acid sites [50]. For TON zeolite with a Si/Al ratio of 30 Denayer et al.

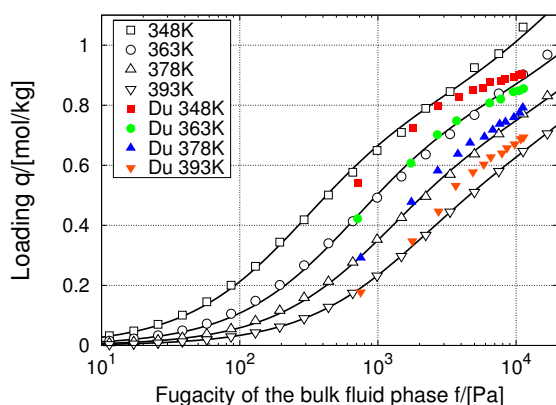


Figure 14: Isotherm of *n*-hexane in MWW at various temperatures. Experimental data is taken from Du et al. [49].

[45] found: *n*-pentane 62.1 kJ/mol (simulation 61.96 kJ/mol), *n*-hexane 75.0 kJ/mol (simulation 72.5 kJ/mol), *n*-heptane 87.9 kJ/mol (simulation 83.6 kJ/mol), *n*-octane 100.5 kJ/mol (simulation 95.1 kJ/mol).

MWW structures have two independent 10-ring pore systems, a large cavity (0.71 nm × 1.8 nm) pore system, and a channel-type (0.4 nm × 0.55 nm) pore system. The computed isotherms for *n*-hexane at various temperatures are shown in Figure 14. The experimental results are the data of Du et al. [49]. Considering the complexity of the experimental measurements the agreement is good. Much of the complexity originates from the existence of 0.9 nm deep pockets on the external surface that may have adsorption properties similar to that of the intra-crystalline region. This phenomenon obscures especially the lower temperature results of Du et al.

The heats of adsorption computed at 300 K are 54.0 kJ/mol for *n*-hexane, 59.15 kJ/mol for 3-methylpentane, and 59.24 kJ/mol for 2-methylpentane. Du et al. obtained 38.0 kJ/mol for *n*-hexane computed from the van 't Hoff plot, and 46.9 kJ/mol from the isotherms. The former is inaccurate because the data were determined too far outside the Henry regime, the latter is inaccurate due to intrusion by external surface adsorption at low temper-

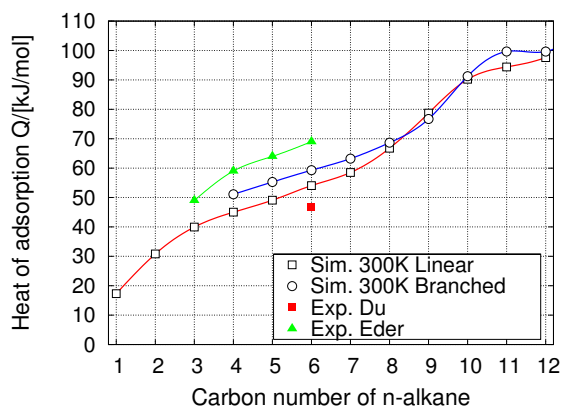


Figure 15: Heat of adsorption of linear and mono-branched alkanes as a function of carbon number in MWW, computed at 300 K. Experimental data are taken from Du et al. [49], and Eder et al. [50] on a protonated MWW zeolite.

ature. Interestingly, the heat of adsorption is not directly proportional to the carbon number (Figure 15), because the MWW combines two effects: the linear behavior of channel-type zeolites, and the nonlinear, periodic behavior of the heat of adsorption in cage/window-type systems [51, 52].

IV Discussion

Simulations are becoming increasingly less expensive, faster, and more accurate. Simulations utilizing the current force field afford valuable guidance for experimental adsorption research. Firstly, it can serve as a reference. Before doing any experiments, the model can predict the type of the isotherm, low-coverage properties such as the heats of adsorption and Henry coefficients, and the maximum loading. Interesting pressure and temperatures regimes can be identified, and the range of the Henry regime can be established. A second practical use of these simulations is to resolve experimental discrepancies. As an example we have scrutinized the available experimental data and have highlighted the lack of low or high pressure data as a common source for error. Experimental mea-

measurements in suboptimal pressure regimes can explain the high scatter found in the Henry coefficients and heats of adsorption as reported by various groups. A third advantage of simulations is its predictive power. We predict a surprisingly non-linear dependence of the heat of adsorption on carbon number for MWW-type zeolites, that might inspire experimentalists to verify this dependence. A fourth use of simulations is the explanation of adsorption data on a molecular level. Simulations can forge the connection between the location of the adsorbates inside the channels and cages and peculiarities (such as inflection points) in the adsorption isotherm. These explanatory data are very difficult to obtain experimentally. For adsorption of mixtures in zeolites, CBMC simulations have revealed new ways of separating linear and branched alkanes by exploiting subtle entropy effects [53].

We like to comment on the application of the current model to diffusion in molecular sieves. The currently proposed model faithfully reproduces the inflection points in isotherms. Proper reproduction of the inflection is necessary, since an inflection in the isotherm leads to a sharp inflection in the diffusion behavior [54, 55]. The adsorbent-adsorbate parameters are uniquely determined and in that sense the model can be directly applied to diffusion in zeolites. However, it remains to be seen if the united atom approximation also holds for diffusion in molecular sieves. There seems to be some indication that framework vibrations can alter the diffusivities of tightly fitting molecules [56,57], even though this appears not to be the case for the diffusion of small alkanes through cation-free sieves [58,59]. We stress that to compare a flexible framework with a rigid framework, the flexibility should be modeled in such a way that the two structures are on average identical. This implies that the reference bond lengths should be taken from the rigid structure [11].

In most nanoporous framework structures, the large oxygen atoms shield the much smaller silicon, aluminum, and phosphorus atoms. Therefore, the model only needs to consider interactions between the adsorbate and the oxygen atoms, provided there is no net negative electrical charge on the framework [12]. Theoretical studies have suggested that the electron density on a cation-free framework is lower in an aluminophosphate than in silica, which would induce a lower polarization and a lower heat of adsorption for alkanes. Some authors found experimental support for this theory, whereas others found none (see for discussion Ref. [60] and reference therein). If the latter are correct, this would extend the applicability of our parameters to aluminophosphates, and possibly even to more recently described nanoporous framework materials based on sulphur or nitrogen instead of oxygen atoms. In principle, one can extend the force field to adsorption of alkanes in pillared clays [61]. A further extension would be to include more types of pseudo atoms. Although the fitting procedure is applied to hydrocarbons, it is by no means restricted to alkanes. In the literature many isotherms with inflections can be found and these molecules can easily be included.

V Conclusions

A united atom model is presented that is capable of a quantitative prediction of adsorption properties of both linear and branched alkanes in cation-free molecular sieves. Very good agreement between experimental and simulated isotherms was found for AFI-, MFI-, TON-, DDR- and MWW-type structures over a wide range of pressures and temperatures. The simulations highlight three common sources for discrepancies between experimental data sets: 1) a lack of low pressure data, 2) a lack of high pressure data, and 3) the too short

experimental equilibration times. These can explain the large scatter in the experimentally reported values for the heat of adsorption and the Henry coefficients. The united atom molecular simulation results afford selection of the experimentally most sound values, and afford prediction of these values if none are available experimentally. This should be of great value when studying the use of nanoporous framework structures in industrial separation or catalytic processes and is particularly advantageous for mixtures, for which very few experimental data are available.

Acknowledgments

We would like to thank the Netherlands Research Council for Chemical Sciences (CW) and E. Beerdsen, P. Bolhuis, E. J. Meijer, M. Dreischor, and M. Schenk for valuable discussions, suggestions and comments on our manuscript.

Appendix

Adsorption ensemble. In adsorption studies one would like to know the amount of materials adsorbed as a function of pressure and temperature of the reservoir with which the sieve is in contact. Therefore the natural ensemble to use is the grand-canonical ensemble (or μ, V, T ensemble). In this ensemble, the temperature T , the volume V , and the chemical potential μ are fixed. The equilibrium conditions are that the temperature and chemical potential of the gas inside and outside the adsorbent must be equal. The imposed chemical potential μ can be related to the fugacity f

$$\beta\mu = \beta\mu_{\text{id}}^0 + \ln(\beta f), \quad (3)$$

where $\beta = 1/(k_B T)$, with k_B the Boltzmann constant, and μ_{id}^0 is the reference chemical potential. The pressure p is related to the fugacity f by

$$f = \phi p, \quad (4)$$

where ϕ is the fugacity coefficient computed directly from the equation of state of the vapor in the reservoir. For all adsorbates, the experimental equation of state is well known and we use the Peng-Robinson equation of state to convert the pressure to the corresponding fugacity, introducing only a small correction for the currently studied systems.

Configurational Bias Monte Carlo (CBMC). Conventional Monte Carlo is time-consuming for long chain molecules. The fraction of successful insertions into the sieve is too low. To increase the number of successfully inserted molecules we apply the CBMC technique [6,20,62]. In the CBMC scheme it is convenient to split the total potential energy U of a trial site into two parts.

$$U = U^{\text{int}} + U^{\text{ext}}. \quad (5)$$

The first part is the internal, bonded potential U^{int} which is used for the generation of trial orientations. The second part of the potential, the external potential U^{ext} , is used to bias the selection of a site from the set of trial sites. This bias is exactly removed by adjusting the acceptance rules. In the CBMC technique a molecule is grown segment-by-segment. For each segment we generate a set of k trial orientations according to the internal energy U^{int} and compute the external energy $U_i^{\text{ext}}(j)$ of each trial position j of segment i . In this work the number of trial positions k for both NVT and μ VT is set to 10. We select one of these trial positions with a probability

$$P_i(j) = \frac{e^{-\beta U_i^{\text{ext}}(j)}}{\sum_{l=1}^k e^{-\beta U_i^{\text{ext}}(l)}} = \frac{e^{-\beta U_i^{\text{ext}}(j)}}{w(i)}. \quad (6)$$

The selected trial orientation is added to the chain and the procedure is repeated until the entire molecule has been grown. For this newly grown molecule we compute the so-called Rosenbluth factor

$$W^{\text{new}} = \prod_i w(i). \quad (7)$$

To compute the old Rosenbluth factor W^{old} of an already existing chain, $k - 1$ trial orientations are generated for each segment. These orientations, together with the already existing bond, form the set of k trial orientations. In a dynamic scheme, a Markov chain of states is generated. The average of a property is the average of over the elements of the Markov chain. For an infinite Markov chain the expression is exact. Every new configuration is accepted or rejected using an acceptance/rejection rule.

We have defined μ^{ex} as the difference in chemical potential of the interacting alkane and an alkane in the ideal gas state. The Rosenbluth weight $\langle W^{\text{IG}} \rangle$ of the reference state of the ideal gas has to be computed in separate simulation. This quantity is needed when comparing with real experimental data.

Energy computation. We describe in some detail the computation of the energies using CBMC for our molecular united atom model. The total energy U is split into two contributions

$$U = U^{\text{int}} + U^{\text{ext}}. \quad (8)$$

The internal energy U^{int} is given by

$$U^{\text{int}} = U^{\text{bond}} + U^{\text{bend}} + U^{\text{torsion}}, \quad (9)$$

with

$$U^{\text{bond}} = \sum_{\text{bonds}} \frac{1}{2} k_1 (r - r_0)^2, \quad (10)$$

$$U^{\text{bend}} = \sum_{\text{bends}} \frac{1}{2} k_2 (\cos \theta - \cos \theta_0)^2, \quad (11)$$

$$U^{\text{torsion}} = \sum_{\text{torsions}} \sum_{n=0}^5 \eta_n \cos^n \phi, \quad (12)$$

where $k_1/k_B = 96500 \text{ K}/\text{\AA}^2$ is the bond energy constant, $r_0 = 1.54 \text{ \AA}$ the reference bond length, $k_2/k_B = 62500 \text{ K}$ the bend energy constant, $\theta_0 = 114^\circ$ the reference bend angle, ϕ the dihedral angle (defined as $\phi_{\text{trans}} = 0$), and η_n/k_B in K denote the

six torsion parameters. The torsion potential around $A - B$ is not split up in several torsions. When $A = \text{CH}_2$ or $B = \text{CH}_2$ a dummy hydrogen is added to this group. The dummy atom does not have any non-bonded interactions, only bendings and a single torsion interaction. The external energy U^{ext} consists of a guest-guest intermolecular energy U^{gg} , a host-guest interaction U^{hg} , and an intra-molecular Lennard-Jones interaction U^{intra} for beads in a chain separated by more than three bonds

$$U^{\text{ext}} = U_{ij}^{\text{gg}} + U_{ij}^{\text{hg}} + U_{ij}^{\text{intra}}, \quad (13)$$

with

$$U_{ij}^{\text{gg,hg,intra}} = \sum_{\text{LJ-pairs}} 4\epsilon_{ij} \left[\left(\frac{\sigma_{ij}}{r_{ij}} \right)^{12} - \left(\frac{\sigma_{ij}}{r_{ij}} \right)^6 \right] - E_{\text{cut}}, \quad (14)$$

where r_{ij} is the distance between site i and site j , $r_{\text{cut}} = 12.0 \text{ \AA}$, the cutoff radius, E_{cut} the energy at the cut-off radius, and $U_{ij}^{\text{gg,hg,intra}} = 0$ when $r_{ij} > r_{\text{cut}}$. The Lennard-Jones potential consists of two parameters, σ is the size-parameter, and ϵ is the strength-parameter. The force field is described by the parameters listed in Table 3.

Monte Carlo moves. Several Monte Carlo moves can be employed during a simulation.

- Displacement move

A chain is selected at random and given a random displacement. The maximum displacement is taken such that 50% of the moves is accepted. The acceptance rule is

$$\text{acc}(\text{old} \rightarrow \text{new}) = \min \left(1, e^{-\beta(U^{\text{new}} - U^{\text{old}})} \right). \quad (15)$$

Note that the energy of the new configuration U^{new} and the energy of the old configuration U^{old} only differ in the external energy.

- **Rotation move**
A chain is selected at random and given a random rotation. The center of the rotation is the center of mass. The maximum rotation angle is selected such that 50% of the moves are accepted. The acceptance rule is given by Eq. 15. Again, the energy of the new configuration U^{new} and the energy of the old configuration U^{old} only differ in the external energy.

- **Insertion move**
A chain is grown at a random position. The acceptance rule for insertion of the particle is given by

$$\text{acc}(N \rightarrow N + 1) = \min \left(1, \frac{W^{\text{new}} \beta V}{N + 1} \frac{f}{\langle W^{\text{IG}} \rangle} \right). \quad (16)$$

- **Deletion move**
A chain is chosen at random and the old Rosenbluth factor is computed. The acceptance rule for deletion of the particle is given by

$$\text{acc}(N \rightarrow N - 1) = \min \left(1, \frac{N}{W^{\text{old}} \beta V} \frac{\langle W^{\text{IG}} \rangle}{f} \right). \quad (17)$$

- **Full regrow move**
A chain is selected at random and is completely regrown at a random position. This move is essential for N, V, T to change the internal configuration of a molecule, and during this move data for the average Rosenbluth weight can be collected. The acceptance rule for full regrow is given by

$$\text{acc}(\text{old} \rightarrow \text{new}) = \min \left(1, \frac{W^{\text{new}}}{W^{\text{old}}} \right). \quad (18)$$

- **Partial regrow move**
A chain is selected at random and part

of the molecule is regrown. It is decided at random which part of the chain is regrown and with which segment the regrown is started. The acceptance rule for partial regrow is given by Eq. 18.

- **Identity change move (mixtures)**
The identity-change trial move [63] is called semi-grand ensemble, but it can also be seen as a special case of the Gibbs ensemble. One of the components is selected at random and an attempt is made to change its identity. The acceptance rule is given by [64]

$$\text{acc}(A \rightarrow B) = \min \left(1, \frac{W^{\text{new}} f_B \langle W_A^{\text{IG}} \rangle N_A}{W^{\text{old}} f_A \langle W_B^{\text{IG}} \rangle (N_B + 1)} \right), \quad (19)$$

where f_A and f_B are the fugacities of components A and B , and N_A and N_B are the number of particles.

The relative probabilities for attempting these moves were such that in the NVT -simulations 10% of the total number of moves were displacements, 10% rotations, 10% partial regrowths, and 70% regrowths of the entire molecule. For the case of grand-canonical simulations of the pure components the distribution of moves was: 15% displacements, 15% rotations, 15% partial regrowths, and 55% exchanges with the reservoir. For alkane mixtures the number of exchanges was reduced to 50% and the remaining 5% of the moves were attempts to change the identity of a molecule.

Duration/length of simulation. Simulations are performed in cycles. The number of cycles needed for equilibration depends on the number of molecules. We define a cycle to consist of smaller steps proportional to the number number of molecules with 20 as the minimum.

$$N_{\text{cycles}} = \max(20, N) \times N_{\text{steps}}. \quad (20)$$

property	formula	units
Henry coefficient K_H	$K_H = \frac{1}{RT\rho_f} \frac{\langle W \rangle}{\langle W^{IG} \rangle}$	mol/kg/Pa
Internal energy ΔU	$\Delta U = \langle U_{hg} \rangle - \langle U_h \rangle - \langle U_g \rangle$	J/mol
Helmholtz free energy ΔA	$\Delta A = -RT \ln \frac{\langle W \rangle}{\langle W^{IG} \rangle}$	J/mol
Gibbs free energy ΔG	$\Delta G = \Delta A - RT$	J/mol
Isosteric enthalpy of adsorption ΔH	$\Delta H = -\frac{\partial \ln(K_H)}{\partial (RT)^{-1}} = \Delta U - RT$	J/mol
Isosteric heat of adsorption Q	$Q = -\Delta H$	J/mol
Entropy ΔS	$\Delta S = \frac{\Delta U - \Delta A}{T} = \frac{\Delta H - \Delta G}{T}$	J/(mol K)

Table 6: Adsorption properties computed at the infinite dilution from a NVT-simulation. The Rosenbluth factor $\langle W \rangle$, the Rosenbluth factor of an ideal chain $\langle W^{IG} \rangle$, the ensemble average of the potential energy of the host-guest system $\langle U_{hg} \rangle$, the energy of an isolated ideal chain $\langle U_g \rangle$, and the average host energy $\langle U_h \rangle$ (zero for a rigid framework) are computed from two independent simulations of a single chain: a NVT-simulation of a chain adsorbed in the framework, and a NVT-simulation of an isolated chain in the ideal gas phase. Here, T is the temperature, $R = 8.31451$ J/(mol K) the gas constant, and ρ_f in kg/m^3 the density of the framework.

In each step one Monte Carlo move is performed. For molecules smaller than pentane at least 5×10^5 cycles are used to compute the isotherms. For longer molecules and all NVT-simulations we used at least 1×10^6 cycles.

Computation of low-coverage adsorption properties. If the chemical potential is sufficiently low the loading q is proportional to the Henry coefficient K_H and the pressure

$$q = K_H p. \quad (21)$$

The Henry coefficient is related to the Rosenbluth factor

$$K_H = \frac{1}{RT\rho_f} \frac{\langle W \rangle}{\langle W^{IG} \rangle}. \quad (22)$$

where ρ_f is the density of the framework. The chemical potential is related to the Helmholtz free energy A

$$\mu = \left(\frac{\partial A}{\partial N} \right)_{V,T}. \quad (23)$$

In the infinite dilution limit

$$\Delta A = A(1) - A(0) = \mu. \quad (24)$$

Therefore the Helmholtz free energy can be computed from a NVT-simulation

$$\Delta A = -RT \ln \frac{\langle W \rangle}{\langle W^{IG} \rangle}. \quad (25)$$

The entropy ΔS is given by

$$\Delta S = \frac{(\Delta U - \Delta A)}{T}, \quad (26)$$

or equivalently

$$\Delta S = \frac{(\Delta H - \Delta G)}{T}. \quad (27)$$

In the limit of zero coverage the Henry coefficient is related to the enthalpy of adsorption at a fixed loading ΔH via a thermodynamic relation

$$\Delta H = -\frac{\partial \ln(K_H)}{\partial (RT)^{-1}}. \quad (28)$$

In a simulation the isosteric enthalpy can be computed more conveniently from the internal energy difference

$$\Delta H = \Delta U - RT. \quad (29)$$

From Eq. 26, Eq. 27, and Eq. 29 we obtain for the Gibbs free energy difference ΔG at infinite dilution

$$\Delta G = \Delta A - RT. \quad (30)$$

The formulas are summarized in Table 6.

Bibliography

- [1] Blauwhoff, P. M. M.; Gosselink, J. W.; Kieffer, E. P.; Sie, S. T.; Stork, W. H. J., in *Catalysis and Zeolites*, edited by Weitkamp, J.; Puppe, L. Springer; Berlin, 1999, pp. 437–538.
- [2] Thomas, J. M. *Solid acid catalysts. Sci. Am.* **1992**, 266, 112-118.
- [3] Haag, W. O., in *Zeolites and Related Microporous Materials: State of the Art 1994*, Studies in Surface Science and Catalysis, edited by Weitkamp, J.; Karge, H. G.; Pfeifer, H.; Hölderich, W. Elsevier; Amsterdam, 1994, Vol. 84, pp. 1375–1394.
- [4] Rozanska, X.; van Santen, R. A.; Hutschka, F. S. *Progress in Theoretical Chemistry and Physics* **2001**, 1-28.
- [5] Macedonia, M. D.; Maginn, E. J. *Mol. Phys.* **1999**, 96, 1375-1390.
- [6] Smit, B.; Siepmann, J. I. *J. Phys. Chem.* **1994**, 98, 8442-8452.
- [7] Vlugt, T. J. H.; Krishna, R.; Smit, B. *J. Phys. Chem. B.* **1999**, 103, 1102-1118.
- [8] Lachet, V.; Boutin, A.; Pellenq, R. J.-M.; Nicholson, D.; Fuchs, A. H. *J. Phys. Chem.* **1996**, 100, 9006-9013.
- [9] Clark, L. A.; Sierka, M.; Sauer, J. J. *Am. Chem. Soc.* **2003**, 125, 2136-2141.
- [10] Ryckaert, J. P.; Bellemans, A. *Faraday Discuss. Chem. Soc.* **1978**, 66, 95-106.
- [11] Vlugt, T. J. H.; Schenk, M. J. *Phys. Chem. B.* **2002**, 106, 12757-12763.
- [12] Bezus, A. G.; Kiselev, A. V.; Lopatkin, A. A.; Du, P. Q. *J. Chem. Soc., Faraday Trans. II* **1978**, 74, 367-379.
- [13] van Koningsveld, H.; van Bekkum, H.; Jansen, J. C. *Acta Cryst.* **1987**, B43, 127-132.
- [14] Marler, B. *Zeolites* **1987**, 7, 393-397.
- [15] Qiu, S.; Pang, W.; Kessler, H.; Guth, J. L. *Zeolites* **1989**, 9, 440-444.
- [16] Gies, H. Z. *Kristallogr.* **1986**, 175, 93-104.
- [17] Cambor, M. A.; Corma, A.; Diaz-Cabanas, M.-J.; Baerlocher, Ch. *J. Phys. Chem. B.* **1998**, 102, 44-51.
- [18] Smit, B.; Maesen, T. L. M. *Nature* **1995**, 374, 42-44.
- [19] Smit, B.; Siepmann, J. I. *J. Phys. Chem.* **1996**, 98, 8442-8452.
- [20] Frenkel, D.; Smit, B., *Understanding molecular simulation 2nd edition* Academic Press; London, UK, 2002.
- [21] Martin, C.; Tosi-Pellenq, N.; Patarin, J.; Coulomb, J. P. *Langmuir* **1998**, 14, 1774-1778.
- [22] Smit, B. *J. Phys. Chem.* **1995**, 99, 5597-5603.
- [23] June, R. L.; Bell, A. T.; Theodorou, D. N. *J. Phys. Chem* **1992**, 96, 1051-1060.
- [24] Pascual, P.; Ungerer, P.; Tavitian, B.; Pernot, P.; Boutin, A. *Phys. Chem. Chem. Phys.* **2003**, 5, 3684-3693.
- [25] Smit, B.; Loyens, L. D. J. C.; Verbist, G. L. M. M. *Faraday Discuss.* **1997**, 106, 93-104.
- [26] Du, Z.; Vlugt, T. J. H.; Smit, B.; Manos, G. *AIChE J.* **1998**, 44, 1756-1764.

- [27] Sun, M. S.; Talu, O.; Shah, D. B. *J. Phys. Chem.* **1996**, *100*, 17276-17280.
- [28] Vlugt, T. J. H.; Zhu, W.; Kapteijn, F.; Moulijn, J. A.; Smit, B.; Krishna, R. *J. Am. Chem. Soc.* **1998**, *120*, 5599-5600.
- [29] Cavalcante, C. L.; Ruthven, D. M. *Ind. Eng. Chem. Res.* **1995**, *34*, 177-184.
- [30] Jolimaitre, E.; Tayakout-Fayolle, M.; Jallut, C.; Ragil, K. *Ind. Eng. Chem. Res.* **2001**, *40*, 914-926.
- [31] Jolimaitre, E.; Ragil, K.; Tayakout-Fayolle, M.; Jallut, C. *AIChE J.* **2002**, *48*, 914-926.
- [32] Eder, L. *Thermodynamics and siting of alkane adsorption in molecular sieves* **1996**, Ph. D. Thesis.
- [33] Zhu, W.; Kapteijn, F.; Moulijn, J. A. *Phys. Chem. Chem. Phys.* **2000**, *2*, 1989-1995.
- [34] Zhu, W.; Kapteijn, F.; van der Linden, B.; Moulijn, J. A. *Phys. Chem. Chem. Phys.* **2001**, *3*, 1755-1761.
- [35] Zhu, W.; Kapteijn, F.; Moulijn, J. A. *Adsorption* **2000**, *6*, 159-167.
- [36] Sun, M. S.; Shah, D. B.; Talu, O. *J. Phys. Chem. B.* **1998**, *102*, 1466-1473.
- [37] Choudhary, V. R.; Mayadevi, S. *Zeolites* **1996**, *17*, 501-507.
- [38] Yang, Y.; Rees, L. V. C. *Microporous Mater.* **1997**, *12*, 223-228.
- [39] van Well, W. J. M.; Wolthuizen, J. P.; Smit, B.; van Hoof, J. H. C.; van Santen, R. A. *Angew. Chem. Int. Ed.* **1995**, *34*, 2543-2544.
- [40] Meyer, K. M. A. De; Chempath, S.; Denayer, J. F. M.; Martens, J. A.; Snurr, R. Q.; Baron, G. V. *J. Phys. Chem. B.* **2003**, *107*, 10760-10766.
- [41] Martin, M. G.; Siepmann, J. I. *J. Phys. Chem. B.* **1999**, *103*, 4508-4517.
- [42] Schuring, D.; Koriabkina, A. O.; de Jong, A. M.; Smit, B.; van Santen, R. A. *J. Phys. Chem. B* **2001**, *105*, 7690-7698.
- [43] Krishna, R.; Calero, S.; Smit, B. *Chem. Eng. J.* **2002**, *88*, 81-94.
- [44] Arik, I. C.; Denayer, J. F.; Baron, G. V. *Microporous and Mesoporous Mat.* **2003**, *60*, 111-114.
- [45] Denayer, J. F.; Souverijns, W.; Jacobs, P. A.; Martens, J. A.; Baron, G. V. *J. Phys. Chem. B* **1998**, *102*, 4588-4597.
- [46] Zhu, W.; Kapteijn, F.; Moulijn, J. A.; den Exter, M. C.; Jansen, J. C. *Langmuir* **2000**, *16*, 3322-3329.
- [47] Zhu, W.; Kapteijn, F.; Moulijn, J. A.; Jansen, J. C. *Phys. Chem. Chem. Phys.* **2000**, *2*, 1773-1779.
- [48] Hampson, J. A.; Rees, L. V. C. *Stud. Surf. Sci. Catal.* **1994**, *83*, 197-208.
- [49] Du, H.; Kalyanaraman, M.; Cambor, M. A.; Olsen, D. H. *Microporous and Mesoporous Mat.* **2000**, *40*, 305-312.
- [50] Eder, F.; Lercher, J. A. *J. Phys. Chem. B* **1997**, *101*, 1273.
- [51] Dubbeldam, D.; Calero, S.; Maesen, T. L. M.; Smit, B. *Phys. Rev. Lett.* **2003**, *90*, 245901.
- [52] Dubbeldam, D.; Calero, S.; Maesen, T. L. M.; Smit, B. *Angew. Chem. Int. Ed.* **2003**, *42*, 3624-3626.
- [53] Krishna, R.; Smit, B.; Calero, S. *Chem. Soc. Rev.* **2002**, *31*, 185-194.
- [54] Krishna, R.; Paschek, D. *Chem. Eng. J.* **2002**, *85*, 7-15.
- [55] Krishna, R.; Vlugt, T. J. H.; Smit, B. *Chem. Eng. Sci.* **1999**, *54*, 1751-1757.

- [56] Sastre, G.; Catlow, C. R. A.; Corma, A. *J. Phys. Chem. B.* **1999**, *103*, 5187.
- [57] Bouyermaouen, A.; Bellemans, A. *J. Chem. Phys.* **1998**, *108*, 2170.
- [58] Demontis, P.; Suffritti, G. B.; Fois, E. S.; Quartieri, S. *J. Phys. Chem.* **1992**, *96*, 1482-1490.
- [59] Fritzsche, S.; Wolfsberg, M.; Haberlandt, R.; Demontis, P.; Suffritti, G. B.; Tilocca, A. *Chem. Phys. Lett.* **1998**, *296*, 253.
- [60] Eder, F.; Lercher, J. A. *J. Phys. Chem.* **1996**, *100*, 16460-16462.
- [61] Cao, D.; Wang, W.; Duan, X. *J. Colloid Interface Sci.* **2002**, *254*, 1-7.
- [62] Smit, B. *Mol. Phys.* **1995**, *85*, 153-172.
- [63] Martin, M. G.; Siepmann, J. I. *J. Am. Chem. Soc.* **1997**, *119*, 8921-8924.
- [64] Panagiotopoulos, A. Z. *Int. J. Thermophys.* **1989**, *10*, 447-457.
- [65] Maris, T.; Vlugt, T. J. H.; Smit, B. *J. Phys. Chem. B.* **1998**, *102*, 7183-7189.
- [66] Martin, M. G.; Thompson, A. P.; Nenoff, T. M. *J. Chem. Phys.* **2001**, *114*, 7174-7181.
- [67] Nath, S. K.; Escobedo, F. A.; de Pablo, J. J. *J. Chem. Phys.* **1998**, *108*, 9905-9911.
- [68] Personal communication T. J. H. Vlugt and M. Frash.

We have developed a united atom force field able to accurately describe the adsorption properties of linear alkanes in the sodium form of FAU-type zeolites. This force field successfully reproduces experimental adsorption properties of *n*-alkanes over a wide range of sodium cation densities, temperatures, and pressures. The force field reproduces the sodium positions in dehydrated FAU-type zeolites known from crystallography and it predicts how the sodium cations redistribute when *n*-alkanes adsorb. The cations in the sodalite cages are significantly more sensitive to the *n*-alkane loading than those in the supercages. We provide a simple expression that adequately describes the *n*-alkane Henry coefficient and adsorption enthalpy as a function of sodium density and temperature at low coverage. This expression affords an adequate substitute for complex configurational-bias Monte Carlo simulations. The applicability of the force field is by no means limited to low pressure and pure adsorbates, for it also successfully reproduces the adsorption from binary mixtures at high pressure.

S. Calero, D. Dubbeldam, R. Krishna, B. Smit, T. J. H. Vlugt,
J. F. M. Denayer, J. A. Martens, and T. L. M. Maesen



Understanding the role of sodium during adsorption: A force field for alkanes in sodium exchanged faujasites

I Introduction

Research activity on zeolites, and on adsorption and heterogeneous catalysis in general, has experienced increased interest in the last few years [1–4]. Zeolitic materials have outstanding properties due to their regular structures and high internal surface areas and they are used in industry as ion exchangers, catalysts and adsorbents [5, 6]. Molecular simulations are a powerful tool for gaining insight into these industrial processes at a molecular level. With the decreasing cost of computer simulations there is an increasing demand for the use of detailed simulations to predict the properties

resulting from the interaction of molecules and zeolites.

FAU-type zeolites are the most widely used zeolites in catalysis and separation processes [2, 7–9]. In their synthesized form the composition of the unit cell is $\text{Na}_x\text{Al}_x\text{Si}_{192-x}\text{O}_{384}$, where $96 \geq x \geq 0$. FAU-type zeolites have been labeled either X and Y depending on their framework aluminum density (x). Zeolite X has a framework aluminum density between 96 and 77 aluminum atoms per unit cell, whereas zeolite Y contains fewer than 77 framework aluminum atoms per unit cell. The FAU-type pore structure consists of sodalite cages arranged in 1.2 nm wide supercages

accessible through 0.72 nm windows. Since the sodalite cages are not readily accessible for alkanes, adsorption tends to be limited to the supercages.

The adsorption properties of FAU-type zeolites containing framework aluminum and sodium cations depend on the interaction of the zeolite framework and the non-framework cations with the adsorbate molecules. Therefore, a thorough characterization involving all interactions between these elements (zeolite framework, adsorbates and non-framework cations) is a missing key-ingredient for understanding their performance as adsorbents.

A variety of computational studies have been reported on the location of cations in adsorbate-free faujasites [10–18]. Most of these studies used force fields with the same partial charge on silicon and aluminum. However, due to the close proximity between cations and framework atoms this approach is unsuited for modeling cations in zeolites and it cannot account for the allocation of cations to specific positions [11, 13, 14, 17–19]. Simulations with force fields distinguishing aluminum from silicon have also been performed, but these were mostly limited to zeolites with alternating silicon and aluminum to minimize the number of different types of bridging oxygen atoms [11, 20]. More importantly, these simulations completely ignored cation mobility [11]. Not until the publication of a force field by Auerbach et al. [14] in 1999 were these constraints overcome.

Computer simulation studies on the adsorption of molecules in cation-free FAU-type silica have also been reported [21]. There are a few simulations on the adsorption behavior of hydrocarbons in the sodium form of FAU-type zeolites ("Na-FAU") focusing on halocarbons [12, 22–25] and aromatics [26, 27]. There are hardly any simulations involving linear alkanes on Na-FAU except for a few studies on the adsorption of the smallest, and com-

putationally least expensive, hydrocarbons; methane [21, 28–30, 32] and ethane [33]. In 1978 Bezus et al. [28] used an atomistic representation in Monte Carlo simulations of methane in zeolite NaX. A decade later, Yashonath et al. [34], reported the first Monte Carlo study of the adsorption of a single methane molecule in NaY and Woods and Rowlinson [29] computed the adsorption isotherms and isosteric heats of adsorption of methane in NaX and NaY using Grand Canonical Monte Carlo (GCMC) simulations. In both cases the Kiselev potential model was used [35] where interactions between methane and the atoms of the framework were modeled in terms of a short-range Lennard-Jones potential and a long range Coulombic term. It is important to note that these simulations treated sodium cations as immobile and do not establish distinctions between silicon and aluminum and therefore cannot correctly allocate specific cation positions.

More recently, Maddox and Rowlinson [36] have studied the adsorption of nitrogen and methane mixtures in NaX using the GCMC technique. As before, sodium cations were considered as an immobile part of the zeolitic framework and the interactions with the adsorbates were defined through the Kiselev potential model. Later studies increased the complexity of the potential model obtaining relatively good agreement with experimental adsorption data for methane [31]. Adsorption of ethane in NaY has been studied by Henson et al. using both inelastic neutron scattering and ab initio calculations [33]. They used the same set of parameters as Mellot et al. [12] in their simulations of chloroform in NaY. Finally, Yashonath et al. have also performed simulations of propane [37, 38], *n*-butane [39], and several *n*-alkanes [40] in NaY but again discounting sodium mobility.

In this paper we present a force field where the nature, density, and mobility of the non-framework cation, the density of

the framework aluminum, and all host-guest interactions are carefully taking into account. In section II we explain the general computational methodology, the choice of our model and the parameter optimization strategy. We also report a complete validation of the force field, as it accurately reproduces the sodium cation locations in adsorbate-free zeolites and the adsorption isotherms of *n*-alkanes (from methane to *n*-decane) in Na-FAU. In section III we analyze the applications of this force field. We 1) address the question of cation location during adsorption, subsequently we 2) simplify the results with an empirical expression for Henry coefficients and heats of adsorption as a function of the sodium concentration, temperature, and linear alkane, and finally we 3) extend our calculations to mixtures of alkanes at high pressure. In section IV we give some concluding remarks.

II Methodology

The development of our force field required 1) a model for the framework structure, 2) the partial charges of the zeolite atoms and 3) the interatomic potentials as well as 4) an unambiguous optimization of potential parameters using CBMC simulations. The conventional simulation techniques to compute adsorption isotherms are prohibitively expensive for long alkanes whereas the CBMC technique simulates them at affordable cost [41]. In a CBMC simulation molecules are grown bead by bead biasing the growth process towards energetically favorable configurations avoiding overlap with the zeolite. During the growth the Rosenbluth factor is calculated. The average Rosenbluth factor is directly related to the free energy and the Henry coefficient [42, 43].

Simulations are performed in cycles and in each cycle one move is chosen at random with a fixed probability of performing a molecule displacement (0.15), rota-

tion around the center of mass (0.15), exchange with the reservoir (0.55), and partial regrowth of a molecule (0.15). For mixtures we include an exchange of the type of molecules (0.05) and an exchange with the reservoir (0.5). The maximum translational and rotational displacements are adjusted to achieve an acceptance probability of 50%. The total number of cations remains constant during simulations so only translation movements and regrowth at a random position in the zeolite are considered for this type of particles. The regrowing at a new, randomly selected position bypasses energy barriers.

Henry coefficients were computed in the NVT ensemble including translation (0.1), rotation (0.1), partial regrowths (0.1) and regrowths of the entire molecule (0.7). For the NVT simulations the total number of cycles was at least 1×10^7 . For the grand-canonical simulations the number of cycles for one-component isotherms was 2×10^7 and at least 3×10^7 for the mixtures. More details on this simulation technique can be found elsewhere [42, 44, 45, 58, 59].

A Model

The FAU-type framework was built from silicon, aluminum, and oxygen utilizing the crystallographic positions of these atoms in dehydrated NaX [19]. Zeolites structures with lower framework aluminum densities were obtained by randomly substituting aluminum by silicon. This procedure automatically satisfies the Löwenstein rule and it should afford a reasonable approximation of the framework aluminum distributions obtained by experimental methods [46–49]. The charge distribution on the oxygen framework was considered static; i.e. polarization of oxygen by nearby sodium cations was neglected. Our model explicitly distinguishes silicon from aluminum with a difference of $0.3 e^-$ between q_{Si} and q_{Al} [14]. Different charges are used for oxygen atoms bridging two silicon atoms, q_{OSi} , and oxy-

	O _{Si}	O _{Al}	Si	Al	Na	CH ₄	CH ₃	CH ₂
CH ₄	115 3.47	115 3.47	-	-	582.17 2.72	158.5 3.72	130.84 3.74	94.21 3.84
CH ₃	93.0 3.48	93.0 3.48	-	-	443.73 2.65	130.84 3.74	108.0 3.76	77.7 3.86
CH ₂	60.5 3.58	60.5 3.58	-	-	310.0 2.95	94.21 3.84	77.7 3.86	56.0 3.96
Na	23.0 3.4	23.0 3.4	-	-	124.4 2.16	582.17 2.72	443.73 2.65	310.0 2.95
charge	q=-1.025	q=-1.2	q=+2.05	q=+1.75	q=+1.0	-	-	-
bond	$U^{\text{bond}} = \frac{1}{2}k_1(r - r_0)^2$ $k_1/k_B = 96500 \text{ K}/\text{\AA}^2, r_0 = 1.54 \text{ \AA}$							
bend	$U^{\text{bend}} = \frac{1}{2}k_2(\cos \theta - \cos \theta_0)^2$ $k_2/k_B = 62500 \text{ K}, \theta_0 = 114^\circ$							
torsion	$U^{\text{torsion}} = \sum_{n=0}^5 \eta_n \cos^n \phi$ $\eta_{n=0\dots5}/k_B = \{1204.654, 1947.740, -357.845, -1944.666, 715.690, -1565.572\}$							
LJ	$U_{ij}^{\text{gg,hg,intra}} = \begin{cases} 4\epsilon_{ij} \left[\left(\frac{\sigma_{ij}}{r_{ij}} \right)^{12} - \left(\frac{\sigma_{ij}}{r_{ij}} \right)^6 \right] - E_{\text{cut}} & \text{if } r < r_{\text{cut}} \\ 0 & \text{if } r \geq r_{\text{cut}} \end{cases}$							

Table 1: Lennard-Jones parameters, ϵ/k_B [K] in top-left corner, σ [\AA] in bottom-right corner of each field, partial charges [e] of the framework and the sodium cations, and the bond, bend, and torsion potential and parameters. The O-CH_x interactions are taken from our previous works [58,59], O_{Al} are the oxygens bridging one silicon and one aluminum atom, and O_{Si} are oxygens bridging two silicon atoms, $r_{\text{cut}} = 12$ [\AA] the cutoff distance, and E_{cut} denotes the energy at the cutoff radius (shifted potential).

gen atoms bridging one silicon and one aluminum atom q_{OAl} . q_{OSi} is obtained using the relation $q_{\text{Si}} + (2q_{\text{OSi}}) = 0$, making the zeolite neutral in the absence of aluminum, while q_{OAl} is chosen to make the total system charge equal to zero [50,51]. All partial charges are listed in Table 1.

The non-framework sodium cation density was adjusted to match the framework aluminum density and the density of the zeolites is determined by the framework atoms (aluminum, silicon and oxygen) and the non-framework cations (sodium). In our model, the sodium cations can move freely and adjust their position depending on their interactions with the framework atoms, other sodium cations, and alkane molecules. To sample cation motions we use displacements and insertions at new randomly selected positions. These random insertions bypass energy barriers.

Molecular simulations using flexible zeolites show that a flexible lattice can po-

tentially influence diffusion properties [52]. To diffuse inside a zeolite the molecules have to pass energy barriers posed by channels and intersections. In a flexible zeolite framework fluctuations can affect the size of the channels and intersections and, thereby, the height of these energy barriers. However, our study focuses at the low energy, equilibrium configurations, so that the fluctuations in the higher energy configurations in flexible zeolite models are negligible [53]. The interactions between guest molecules (alkanes and sodium cations) with the zeolite host framework are modeled by Lennard-Jones and Coulombic potentials. The Coulomb interactions in the system are calculated using the Ewald summation [42]. The alkanes are described with a united atom model, in which CH_x groups are considered as a single interaction centers with their own effective potentials [54]. The beads in the chain are connected by harmonic bonding potentials.

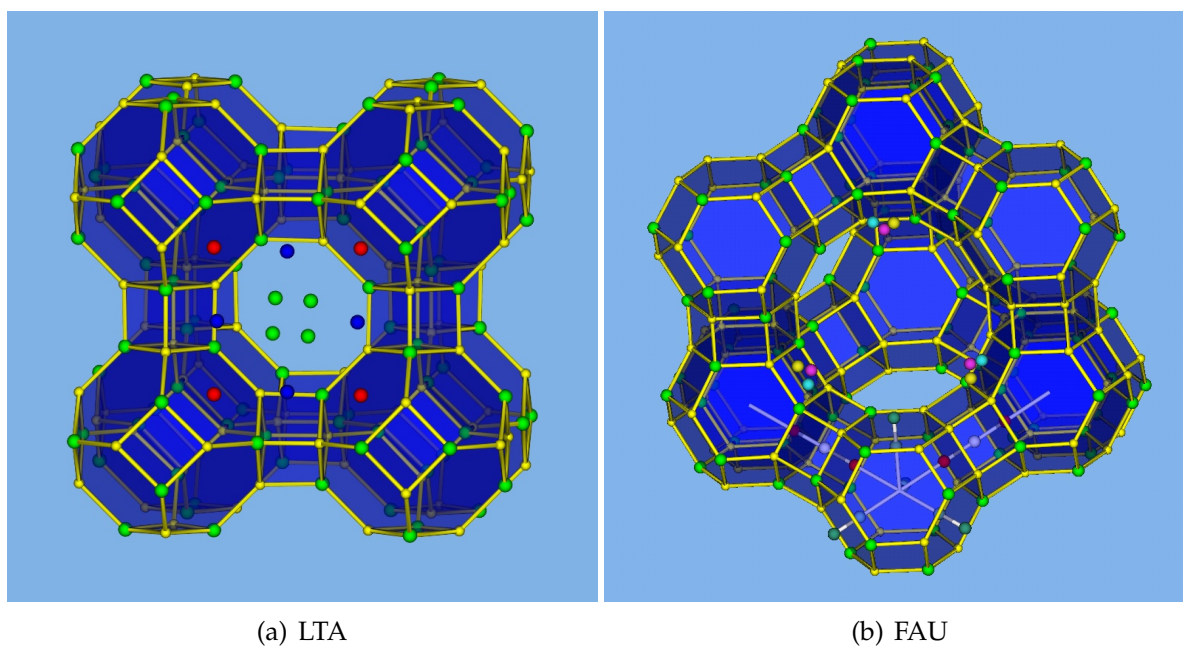


Figure 1: Positions of non-framework Na^+ cations in (a) LTA-type zeolites, (b) FAU-type zeolites.

The bond bending between three neighboring beads is modeled by a harmonic cosine bending potential and changes in the torsional angle are controlled by a Ryckaert-Bellemans potential. The beads in a chain separated by more than three bonds interact with each other through a Lennard-Jones potential. The interactions of the adsorbed molecules with the zeolite are dominated by the dispersive forces between the pseudo-atoms and the oxygen atoms of the zeolite [28, 35, 44] meaning that the silicon van der Waals interactions are taken into account through an effective potential with only the oxygen atoms.

In the force field described here an “average” polarization is included implicitly in the parameterization by means of two effects: the polarization induced by the cation on the zeolite and on the alkanes. For the cation-zeolite interactions we used the approach of Auerbach [14], taking into account the polarization effects by adjusting the partial charges on the oxygen depending whether they are connected to Si or Al. Concerning the polarization effects for the cation-alkane interactions, alkanes are very difficult to polarize and therefore a logi-

cal approach was to use effective Lennard-Jones interactions between the cations and the alkanes.

B Parameter Optimization

This work is concerned with a realistic description of the interaction between the sodium cations, the zeolite framework, and the alkanes. It turns out that the sodium cation distribution is a key factor to understand the adsorptive properties of the Na-FAU family of materials. However, diffraction methods are not always able to provide this information fully accurately. Even for well studied systems such adsorbate-free NaX or NaY the precise location of some cations has remained uncertain [19, 55, 56]. In marked contrast, there is general agreement on the sodium distribution in LTA-type zeolites. Especially, LTA-type zeolites with alternating silicon and aluminum atoms have a highly symmetrical ion-distribution. The sodium form of such an LTA-type zeolite has 12 sodiums per supercage distributed amongst 3 crystallographic sites (see Figure 1): in the center of the 6-ring (type 1), in the 8-ring window

	This work	Other work experimental data								simulation data	
		[19]	[56]	[75]	[11]	[77]	[73]	[18]	[78]	[14]	[81]
Na(I)-O(3)	2.53	2.74	2.71	2.71		2.71		2.3-2.4	2.56	2.11-2.29	
Na(I)-O(2)	3.53	3.55									
Na(I)-O(1)	3.74	3.82									
Na(I')-O(3)	2.5	2.24-2.36	2.24	2.32	2.24	2.44	2.27		2.25	2.07-2.27	2.14
Na(I')-O(2)	3.11	2.94-2.97		2.97	2.9		2.93		3.08		
Na(II)-O(2)	2.47	2.34	2.39	2.34	2.36	2.33	2.35		2.34	2.15-2.36	2.4
Na(II)-O(4)	3.06	2.89	2.86	2.89	2.9		2.88		3.1		
Na(II')-O(2)	2.52										
Na(II')-O(4)	3.31										
Na(III'a)-O(4)	2.64	2.22			2.77				2.3	2.26	2.37
Na(III'a)-O(1)	2.9	2.85			2.58				2.87		
Na(III'b)-O(4)	2.5	2.58					2.56				
Na(III'b)-O(1)	2.74	2.61					2.44				
Na(III'c)-O(4)	2.51	2.41									
Na(III'c)-O(1)	2.67	2.44									

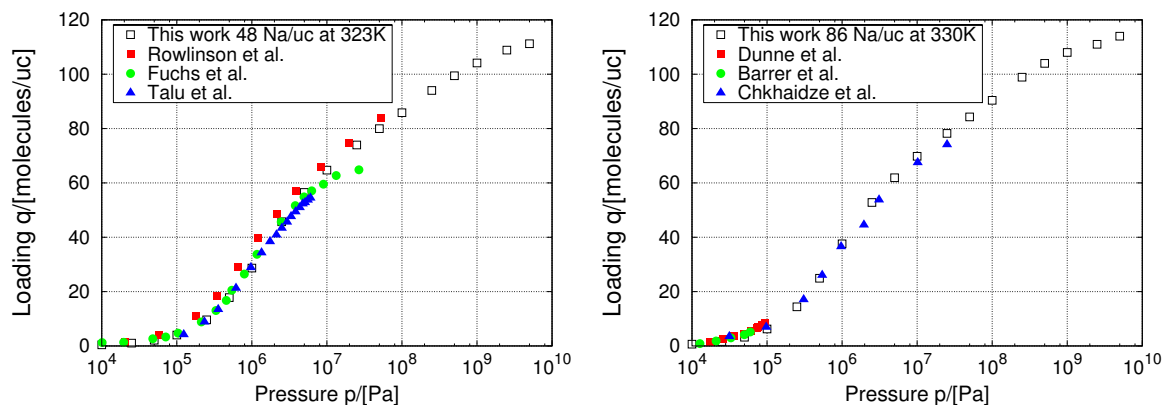
Table 2: Sodium-Oxygen distances [\AA] in faujasites.

(type 2), and opposite to a 4-ring (type 3) [57]. Crystallographic studies indicate that these sites are occupied for 97.2, 24.2, and 6.6 %, respectively. Molecular simulations with our optimized force field yield occupations of 100, 23.9 and 6.25 %, respectively. In addition the crystallographic locations of the sites obtained through molecular simulations are within 0.2 \AA from those obtained through X-ray diffraction.

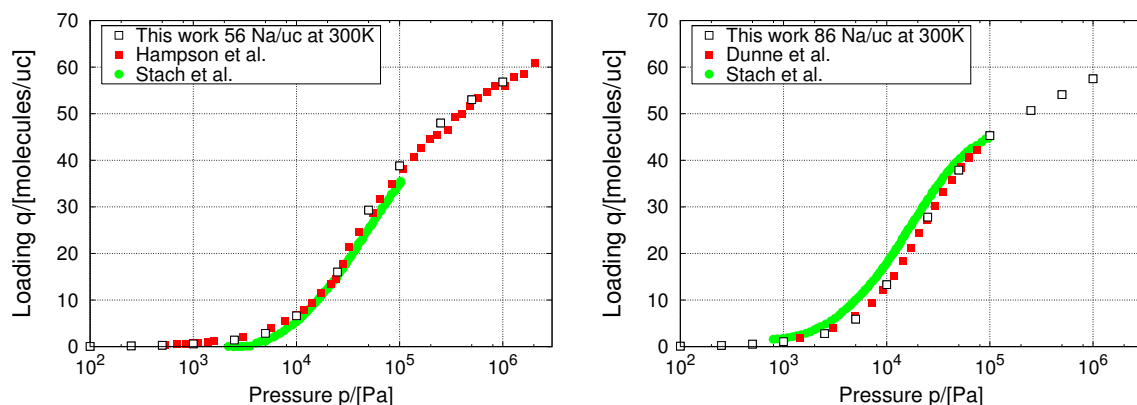
Using this set of parameters derived from this high alumina LTA-type zeolite, we performed simulations to obtain the average sodium-oxygen distances in FAU-type zeolite. The typical sites for sodium in adsorbate-free FAU-type zeolites are depicted schematically in Figure 1. Sites I, I' and II' are in the sodalite cages and hexagonal prisms while sites II, III, and III' are in the supercages. More specifically, site I is the hexagonal prism, sites I' and II' inside the sodalite cage, site II is located at the center of the hexagonal prisms but displaced from this point into the supercage and site III is in the supercage on a twofold axis opposing a four-ring between two twelve-rings. Some studies report three additional supercage III' sites within 2.8 \AA site III. The resulting sodium-oxygen distances are listed in Table 2. Although our results are within 0.2 \AA of the experiments, our dis-

tances are slightly larger than reported experimentally. The scatter in the experimental data makes it difficult to assess whether this points to a systematic deviation.

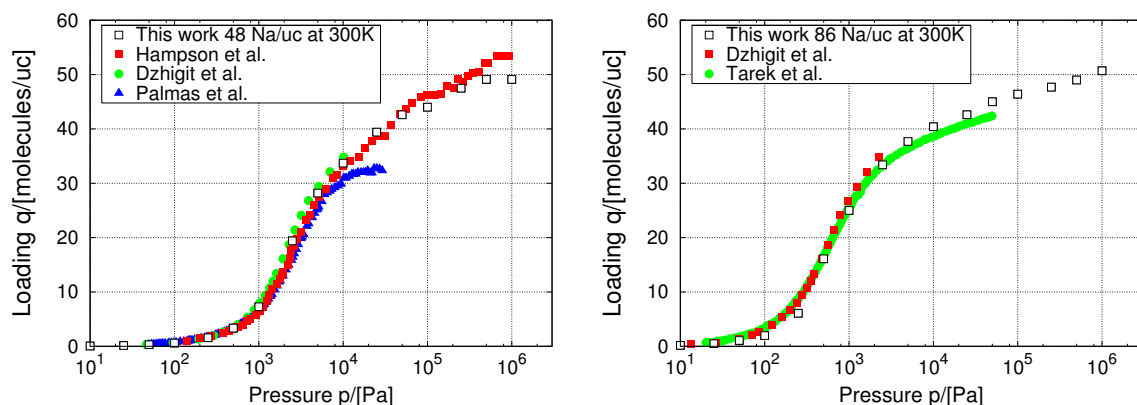
The alkane-sodium, alkane-alkane, and alkane-zeolite interaction parameters were obtained by calibrating the force field through explicitly fitting a full isotherm over a wide range of pressures, temperatures and sodium densities. We fit complete adsorption isotherms, because experimental determination of the adsorption properties at very low and at very high coverage is fraught with difficulty resulting in a large spread in experimentally determined Henry coefficients and saturation loadings, respectively [58, 59]. Experimental agreement on data in the intermediate coverage regime is significantly better. We start by obtaining a reduced set of reliable experimental data, of several independent research groups, to calibrate the simulation results. Next we fit, starting with the smallest number of free parameters, and increase the number of parameters incrementally. Once a reasonable set of parameters has been obtained, we re-examined the experimentally available data and included the data that are consistent with the original data set. This extended data set was subsequently used for further refinement of the



(a) methane in (left) NaY and (right) NaX

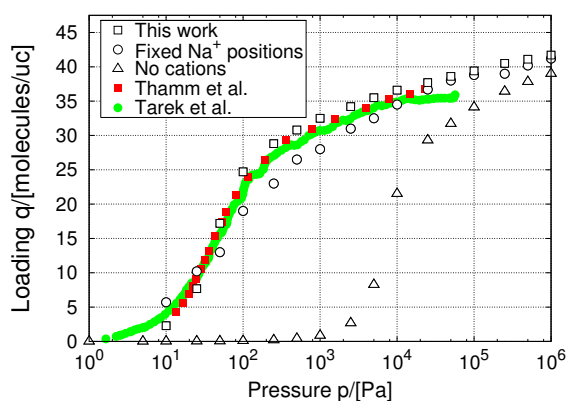


(b) ethane in (left) NaY and (right) NaX

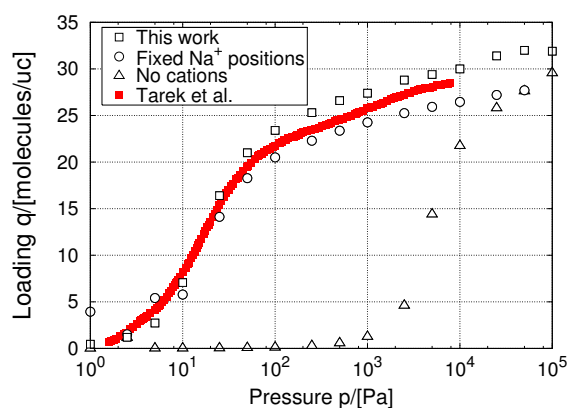


(c) propane in (left) NaY and (right) NaX

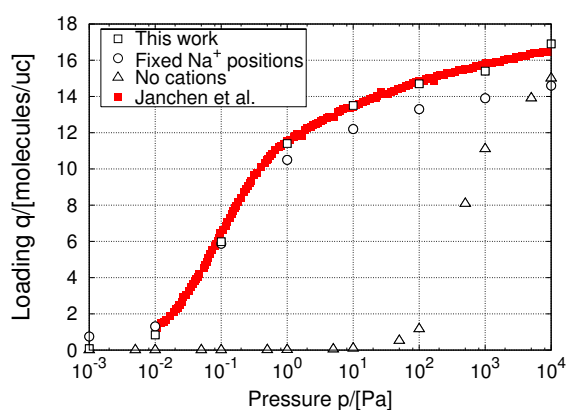
Figure 2: Adsorption isotherms of (a) methane, (b) ethane, and (c) propane in (left) NaY and (right) NaX-type faujasite. Comparison with experiment data [27, 60–70].



(a) *n*-butane in NaX



(b) *n*-pentane in NaX



(c) *n*-decane in NaX

Figure 3: Adsorption isotherms in NaX zeolites with mobile cations (this work), fixed cations, and without cations (a) *n*-butane in at 300K, (b) *n*-pentane at 333K, and (c) *n*-decane at 413K. Comparison with experimental data [64,71,72].

parameters. The procedure was repeated to obtain a best fit with the majority of the experimental data. The resulting force field parameters are listed in Table 1. Except for NaX, aluminum atoms are asymmetrically arranged in the simulation box. Thus, to compute a reliable quantity in the thermodynamic limit, we averaged over different aluminum atom arrangements in the simulation cell. Figure B shows the excellent agreement of our computed isotherms for methane, ethane, and propane with available experimental data [29, 60–70]. Previous GCMC simulation data (only available for methane [29, 31]) were included for comparison. The number of sodium cations and the temperature used for each isotherm were chosen to facilitate comparison with the experimental data, in principle treated with equal weight, and simulations were performed in all pressure range. Hence, methane isotherms in Figure 2(a) were obtained for structures with 60 and 86 Na^+ at 298K and 330K, ethane isotherms, Figure 2(b), were obtained for structures with 56 and 86 Na^+ at 300K, and propane isotherms, Figure 2(c), were obtained for structures with 58 and 86 at 300K and 293K, respectively. Figure 2(c) shows the experimental discrepancies of Dzhigit et al. [66] and Hampson et al. [67] with Palmas et al. [68]. These discrepancies are most likely due to factors such as structural imperfections, adsorption at the crystal surface, and pore-blocking that can render a large part of the zeolite inactive. The additional advantage of our simulations is to resolve these experimental discrepancies since they use "perfect" crystals and restrict the adsorption to the zeolite pores.

The resulting force field not only reproduces the experimental data from the calibration set, but also yields an extraordinarily good description of data not included in the calibration set. To validate the reliability of our force field, we compute adsorption isotherms of longer hydrocarbons (from *n*-butane to *n*-decane) com-

pare them with those available from experimental data [64, 68, 71, 72]. We compute adsorption isotherms of alkanes at several temperatures in FAU-type zeolites with different Na^+ cation densities. It is noteworthy that our computed isotherms reproduce the experimental isotherm shape and also the experimental saturation capacity of the validation data set. As an example, Figure 3(a) shows the excellent agreement of the computed isotherm for *n*-butane compared to Thamm et al. [71] at 300K in Na-FAU with 82 sodium and aluminum atoms per unit cell. The agreement with experimental data of Tarek et al. [64] in NaX with 86 sodium and aluminum per unit cell for *n*-butane (300K) and *n*-pentane (333K) is also remarkable (see Figure 3(a) and 3(b)) and it becomes outstanding in Figure 3(c) for decane in NaX with 83 sodium and aluminum atoms per unit cell at 413K.

The adsorption of alkanes is strongly determined by the sodium cations in faujasites. The effect of cations is twofold; 1) they create additional adsorption sites and 2) they occupy free volume. In cage-like structures the first effect dominates at low and intermediate loadings below the excluded volume effect. For a channel structure the excluded volume effect is compensated for the adsorption effect at low loading. The effect of cations on FAU-type structures is therefore much larger than for MFI [50]. We would like to highlight that both, sodium density and sodium mobility are essential factors during adsorption of alkanes in faujasites. Figure B compares the adsorption isotherms for *n*-butane, *n*-pentane, and *n*-decane obtained using the new force field with isotherms in a) FAU without cations and b) FAU with a fixed cation distribution. The comparison between isotherms in the structures with and without cations shows that the pressure needed to reach a certain loading in the structure without cations is up to 3 orders of magnitude higher than the one needed in the structure with cations. The second comparison shows that mobil-

ity of cations is indispensable to reproduce adsorption of alkanes in sodium faujasites. Simulations using frozen cations overestimate the adsorption of alkanes at low pressures and underestimate the adsorption of alkanes at high pressures.

Having established that the force field reproduces the calibration and validation data sets extremely well, we can now show how this force field readily yields information on a molecular level that would be extremely cumbersome to obtain through experimental studies.

III Applications

A Cation redistribution upon alkane adsorption

Low occupancies of cations at specific crystallographic locations tend to interfere with a complete determination of the cation distribution by crystallographic methods such as X-ray diffraction. Furthermore, very small amounts of adsorbates (particularly water) have a pronounced effect on the location of sodium cations. As a first application, our force field provides information about the cation redistribution upon alkane adsorption in the sodium forms of FAU-type zeolites. We used FAU-type zeolites with 96 and 58 sodium and aluminum atoms per unit cell (FAU-96 and FAU-58, respectively) at 300K. The study was carried out in two steps. First we performed simulations for the adsorbate-free zeolites to compare the force field for sodium with available experimental data, and subsequently we performed simulations with a loading up to 44 molecules of *n*-butane per unit cell, i.e. up to approximately the *n*-butane saturation loading (loading obtained at 1×10^6 Pa).

The sodium cation occupancies obtained from our simulations for the adsorbate-free FAU-type zeolites are fully consistent with the available experimental [11,19,56,73–80]

and simulation data [14,81] as shown in Table B. For FAU-96 the simulation results are in excellent agreement with experiment, and cations occupy predominantly sites I', II, and III'a. For FAU-58 simulations locate the sodium cations at sites I', I, and II. Within experimental error, the match between simulations and experiments is again remarkable. These results further corroborate our force field. Subsequently, *n*-butane adsorption was simulated (Table B). The adsorption of *n*-butane clearly redistributes the sodium cations. In FAU-58, *n*-butane adsorption enhances the population of sites II' and III, and delocalized sites in the supercage at the cost of sites I' and II. In FAU-96, *n*-butane adsorption induces a smaller sodium migration from site I' to sites I and III'. Furthermore *n*-butane adsorption counteracts the migration of sodium from site I' to the supercage as a result of an increase in temperature.

B Adsorption in low-coverage regime

Henry coefficients and heats of adsorption of linear alkanes were computed for a wide range of temperatures and the full range of aluminum (and sodium) densities. The obtained values were fitted to an empirical expression that describes the *n*-alkane Henry coefficient K_H [mol kg⁻¹ Pa⁻¹] as a function of sodium density N_S [cations per unit cell], the temperature T [K], and the carbon number CN .

$$\ln K_H = \frac{1}{T^2} [(144.1N_S + 27438.4)CN - 49567.3] + \frac{1}{T} [(4.37N_S + 432.8)CN + 1111.13] - (0.00135N_S + 0.3716)CN - 17.634 \quad (1)$$

The temperature derivative of this equation provides an expression for the adsorption

58 Na ⁺ /uc	I	I'	II	III'a	III'b	III'c
This work	7.3	15.7	31.6	3.4		
Marra et al. [76]	9.3	13.7	25.3		3.5	
Grey et al. [75]	4.3	18.9	32			
Lim and Grey [74]	3	17	30			
Van Dun et al. [80]	7.04	13.76	29.44		3.76	
<i>Boutin et al. [81]</i>	6	20	32			
Fitch et al. [56]	7.1	18.6	32.2			
Jirak et al. [79]	4	17.6	32		1.4	
Newsam et al. [78]	10	12	32		4	
Eulenberger et al. [79]	8	18.88	30.08		0.04	
96 Na ⁺ /uc	I	I'	II	III'a	III'b	III'c
This work		32	32	32		
Cheetham et al. [11]		32	32	32		
<i>Auerbach et al. [14]</i>	3	29	32	27	5	
<i>Boutin et al. [81]</i>		32	32	31	1	
Olson [19]	2.9	29.1	31	10.6	8.6	10.6
Zhu and Seff [73]		29.5	35.2	18	10	

Table 3: Sodium cation distributions (sodium cations per site per unit cell) in bare sodium faujasites at 10K. Previous simulation data used for comparison are shown in italics.

<i>n</i> -butane loading 58 Na ⁺ /uc	I	I'	II	II'	III'a	III'b	III'c	Other
0	5.3	13.7	25.7	2.0	4.2	3.6	1	2.5
0.6	5.0	5.8	17.8	5.1	13.3	4	1.7	5.3
3	5.0	6.0	17.2	5.0	13.3	4	1.6	6
27	5.0	6.0	17.4	5.0	12.5	4.8	1.8	5.5
37	5.0	5.8	19.5	5.1	11.6	5.8	1.9	3.3
42	5.0	6.0	18.3	5.0	12.2	4.8	2.7	4.0
46	5.0	5.6	19.9	5.4	10.7	6.0	2.5	3.0
<i>n</i> -butane loading 96 Na ⁺ /uc	I	I'	II	II'	III'a	III'b	III'c	Other
0	4.2	24.8	32	0	33.4	0.9	0.7	0
0.6	0.5	31.1	32	0	27	2.5	2.9	0
3	0.9	30.8	32	0	26.5	2.8	3.0	0
27	2.0	28.6	32	0	26.7	4.0	2.6	0
37	1.8	28.5	32	0	26.6	2.3	2.8	0
42	1.7	29.3	32	0	26.1	3.6	3.3	0
46	1.0	30.5	32	0.1	23.7	5.6	3.0	0.2

Table 4: Sodium cation distributions (sodium cations per site per unit cell) in *n*-butane loaded sodium faujasites at 300K. The loading of *n*-butane is given in molecules per unit cell.

Na ⁺ /uc	methane		ethane		propane		n-butane	
	This work	Others	This work	Others	This work	Others	This work	Others
0	12.2	14.0 [89]	16.6	-	21.1	-	25.6	-
14	12.7	-	17.8	-	23.7	28.1 [66]	27.9	-
48	14.1	<i>17.8 [31]</i> <i>15.5 [32]</i>	20.6	-	27.0	-	34.2	22.5 [40]
52	14.3	15.2 [82]	20.8	21.3 [82]	27.3	27.3 [82]	33.8	33.4 [82]
54	14.3	-	21.1	26.5 [69]	28.3	31.3 [66]	35.2	41.4 [71]
56	14.4	-	21.4	23.6 [90]	28.5	29.6 [90]	34.5	-
57	14.5	-	21.3	-	28.6	28.5 [66]	34.8	-
60	14.6	18.9 [62]	21.5	-	28.5	-	35.0	-
76	15.2	-	22.9	-	30.2	35.0 [66]	35.5	-
82	15.5	18.8 [61]	28.4	25.9 [61]	31.2	-	39.1	46.1 [71]
83	15.6	20.1 [70] 15.2 [28]	23.4	-	31.4	-	39.3	-
86	15.7	19.2 [60] 17.6 [91]	23.6	27.0 [60] 25.1 [91]	31.5	32.4 [64] 31.0 [66]	39.3	39.1 [64]
Na ⁺ /uc	n-pentane		n-hexane		n-heptane		n-octane	
	This work	Others	This work	Others	This work	Others	This work	Others
48	41.0	28.9 [40]	47.8	34.8 [40]	54.6	40.4 [40]	61.4	45.2 [40]
52	40.3	39.4 [82]	46.8	45.5 [82]	53.0	51.9 [82]	59.8	57.5 [82]
57	41.9	-	50.1	56.0 [92]	55.6	-	62.4	-
86	47.2	46.6 [64]	55.1	54.1 [64] 56.0 [93]	63.0	61.6 [64] 63.5 [94]	72.0	-
Na ⁺ /uc	n-nonane		n-decane		n-undecane		n-dodecane	
	This work	Others	This work	Others	This work	Others	This work	Others
32	60.0	-	67.1	74.0 [72]	71.6	-	77.5	-
48	68.1	56.1 [40]	72.4	-	78.9	-	85.4	-
52	66.3	63.4 [82]	72.8	70.8 [82]	79.3	77.4 [82]	85.8	81.7 [82]
57	69.3	-	78.4	81.6 [72]	83.0	-	89.8	-
83	78.9	-	89.3	91.9 [72]	94.7	-	102.7	-

Table 5: Heats of adsorption of n-alkanes in sodium faujasites. The heats of adsorption are obtained using our empirical expression at the temperatures referred on the experimental works that we use for comparison. When available, previous simulation data are also included in italics. For the values without comparison the temperature used is 503K and in all cases heats of adsorption are given in kJ/mol.

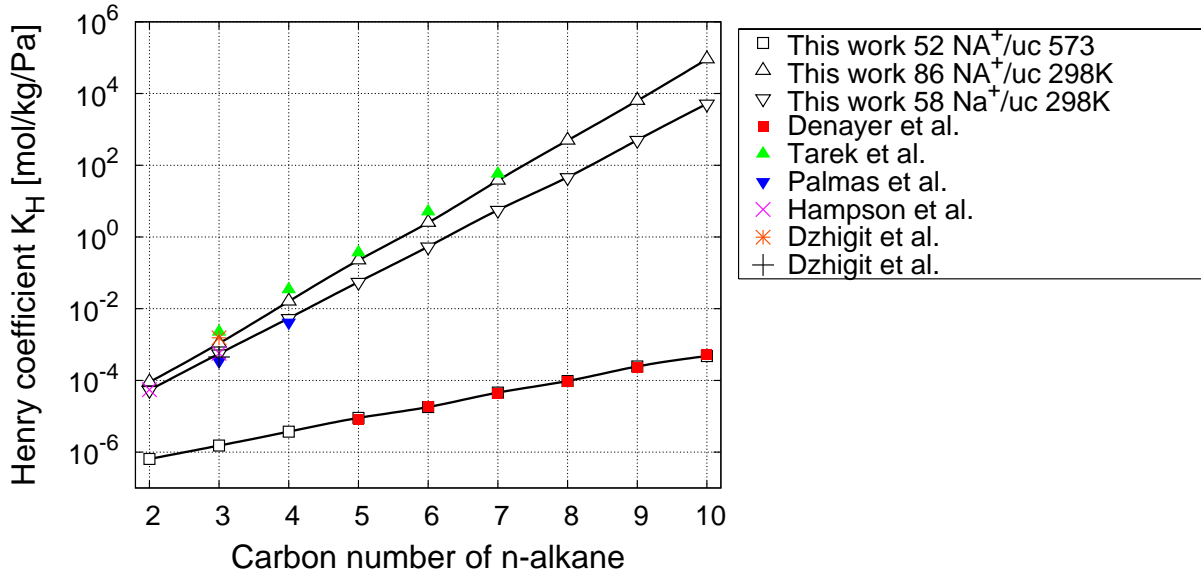


Figure 4: Henry coefficients of linear alkanes in sodium faujasites at several temperatures obtained from our empirical expression. In all cases the deviation between our empirical eq. 1 and the computed results is smaller than the symbol size. Available experimental and simulation sets are included for comparison [64–66, 68, 82, 90].

enthalpy ΔH_0 [kJ/mol]:

$$-\Delta H_0 = \frac{2}{T} [(144.1N_S + 27438.4)CN - 49567.3] \quad (2)$$

$$(4.37N_S + 432.8)CN + 1111.13$$

Figure 4 compares the Henry coefficients obtained for n -alkanes from this empirical expression with available experimental data [64–68, 82]. The calculated heats of adsorption of methane to n -dodecane in faujasite structures are given in Table B. Comparison with the large experimental data set available is also included in the table and shown as a function of the carbon number in Figures 5(a) and 5(b), respectively. It is noteworthy that these data were not part of the calibration of validation data. The remarkable quantitative agreement and consistency on low-coverage properties of simulated and experimental data thus further corroborates and validates the new force field.

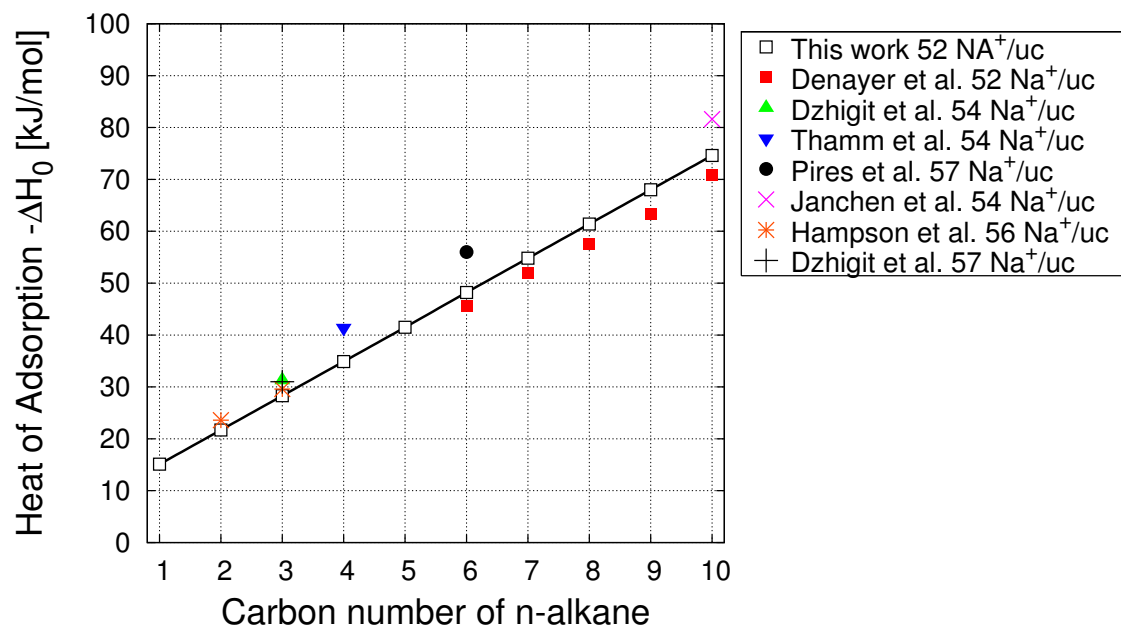
C Adsorption in high-coverage regime

The applicability of the force field is by no means limited to low pressure for it also reproduces accurately the adsorption of alkanes at high pressures. The saturation capacities of n -alkanes (methane to n -hexadecane) were computed for several Na-faujasites structures. From our simulations we can conclude that 1) saturation capacities θ_{sat} [molecules per unit cell] are roughly independent on the amount of sodium non-framework cations and 2) they can be fit to a second order exponential decay as a function of the carbon number (CN):

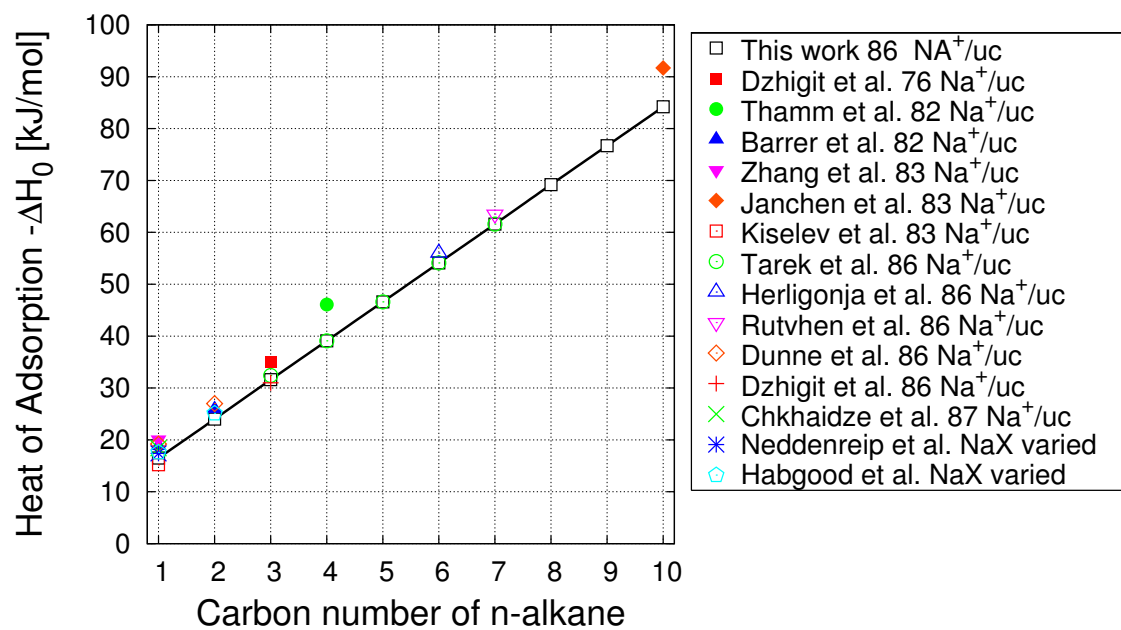
$$\theta_{\text{sat}}[\text{molecules/uc}] = 144.9e^{-\frac{CN}{1.7}} + 50.6e^{-\frac{CN}{9.3}} + 2.6 \quad (3)$$

$$\theta_{\text{sat}}[\text{molecules/uc}] = \theta_{\text{sat}}[\text{mol/kg}]N_{\text{AV}}\rho[\text{kg/m}^3]V[\text{m}^3], \quad (4)$$

where N_{AV} is Avogadro's number, ρ the zeolite density, and V the volume of the unit cell. The saturation capacity [mol kg⁻¹]



(a) NaY



(b) NaX

Figure 5: Heat of adsorption of linear alkanes in sodium faujasites obtained from our empirical expression for (a) NaY zeolites, (b) NaX zeolites. In all cases the deviation between our empirical eq. 2 and computed results is smaller than the symbol size. Available experimental and simulation sets are included for comparison [66, 68, 70–72, 82, 90–92, 92–96].

Pressure [Pa]		Loading [molecules/uc]		Molar fraction C ₈		K = $\frac{X_{C_8}^u(1-X_{C_8}^g)}{X_{C_8}^g(1-X_{C_8}^u)}$	
p_{C_8}	$p_{C_{10}}$	n_{C_8}	$n_{C_{10}}$	$X_{C_8}^g$	$X_{C_{10}}^g$	$K_{\text{simulation}}$	$K_{\text{Satterfield}}$
7.46×10^3	9.386×10^4	0.096	18.287	0.074	0.0052	0.07	2.00
7.365×10^6	9.2635×10^7	0.297	19.411	0.074	0.0151	0.19	
Pressure [Pa]		Loading [molecules/uc]		Molar fraction C ₈		K = $\frac{X_{C_8}^u(1-X_{C_8}^g)}{X_{C_8}^g(1-X_{C_8}^u)}$	
p_{C_8}	$p_{C_{12}}$	n_{C_8}	$n_{C_{12}}$	$X_{C_8}^g$	$X_{C_{12}}^g$	$K_{\text{simulation}}$	$K_{\text{Satterfield}}$
8.81×10^3	9.252×10^4	0.069	16.556	0.087	0.0042	0.04	1.7
8.69093×10^6	9.130907×10^7	0.564	16.432	0.087	0.0332	0.36	
Pressure [Pa]		Loading [molecules/uc]		Molar fraction C ₈		K = $\frac{X_{C_8}^u(1-X_{C_8}^g)}{X_{C_8}^g(1-X_{C_8}^u)}$	
p_{C_8}	$p_{C_{14}}$	n_{C_8}	$n_{C_{14}}$	$X_{C_8}^g$	$X_{C_{14}}^g$	$K_{\text{simulation}}$	$K_{\text{Satterfield}}$
1.011×10^4	9.121×10^4	1.983	13.298	0.100	0.1298	1.35	2.9
9.97943×10^6	9.002057×10^7	2.563	12.372	0.100	0.1716	1.87	

Table 6: Simulated and experimental [88] liquid phase adsorption from a mixture of *n*-octane and *n*-decane, *n*-dodecane, and *n*-tetradecane, respectively. In agreement with recent experiments [87], the simulations only qualitatively reproduce the preference for the shorter *n*-octane over the longer *n*-alkane for *n*-octane/*n*-tetradecane mixtures.

along with the expression for the Henry coefficients (eq. 1) allow the direct estimation of the adsorption isotherms of linear alkanes in sodium faujasites. The above correlations for the Henry coefficient and the saturation capacity can be used to obtain rough estimate of the complete adsorption isotherm, by using the Langmuir isotherm in the form:

$$\theta = \frac{K_{\text{HP}} p}{1 + (K_{\text{H}}/\theta_{\text{sat}}) p} \quad (5)$$

Where θ is the loading of alkane in the zeolite in mol per kilogram and p is the system pressure in Pa. Calculations using the above expression are in good agreement with the adsorption isotherms obtained from CBMC.

D Simultaneous Adsorption of more than one component

Of particular interest for the catalytic use of zeolites is the adsorption selectivity from mixtures of alkanes. In zeolites with extremely large pores one would expect that the alkane with the highest boiling point adsorbs preferentially. Remarkably, LTA- [83], FAU- [84], MFI- [85], and BEA-type zeolites [86] occasionally prefer absorbing the n -alkane with the lower boiling point, because it has a higher packing efficiency (i.e. a lower adsorption entropy) than the longer n -alkane with a higher boiling point [9, 84]. Experimental reproduction of the initially reported entropic preference of NaY for n -octane instead of n -decane, n -dodecane or n -tetradecane proved difficult [87] despite indications that adequate measures were taken to minimize intrusion from variations in sample preparation [88]. Recent experiments established that NaY does prefer adsorbing the shorter, lower boiling alkane from a mixture n -heptane and n -nonane at high pressure. Simulations using the best force field available at the time [50] corroborate the experiments in that they show

a change in preference from n -nonane to n -heptane at sufficiently high pressure [9]. However, the cross-over pressure is significantly higher than observed experimentally. In marked contrast, repeating the simulations with the force field for sodium discussed in the current paper the cross-over pressure yields nearly quantitative agreement (Figure 6). This is notable, for it illustrates the successful application of the force field to systems very different from the calibration data. In agreement with recent experiments, the force field does not reproduce the preference of NaY for n -octane instead of n -decane or n -dodecane reported in the 1970-ies (Table B). It does qualitatively corroborate a preference for adsorbing n -octane instead of n -tetradecane (Table B). Without further experimental work it is difficult to fathom why the first report on adsorption entropy effects with FAU-type zeolites is not fully consistent with present-day research.

IV Conclusions

We have developed and validated a united atom force field for alkanes in the sodium form of FAU- type zeolites that explicitly distinguishes Si and Al atoms through the different type of framework oxygen atoms and that accounts for the density, mobility, and interactions with the adsorbate of the non-framework cation. The force field reproduces accurately the sodium positions in dehydrated FAU-type zeolites known from crystallography and the available experimental adsorption properties of n -alkanes in faujasites over a wide range of sodium cation densities, temperatures, and pressures.

The applicability of this force field is manifold since it has been fitted in such a way that it is not limited to low pressure and pure adsorbents, for it also successfully reproduces the adsorption of binary mixtures at high pressure. Firstly the force field

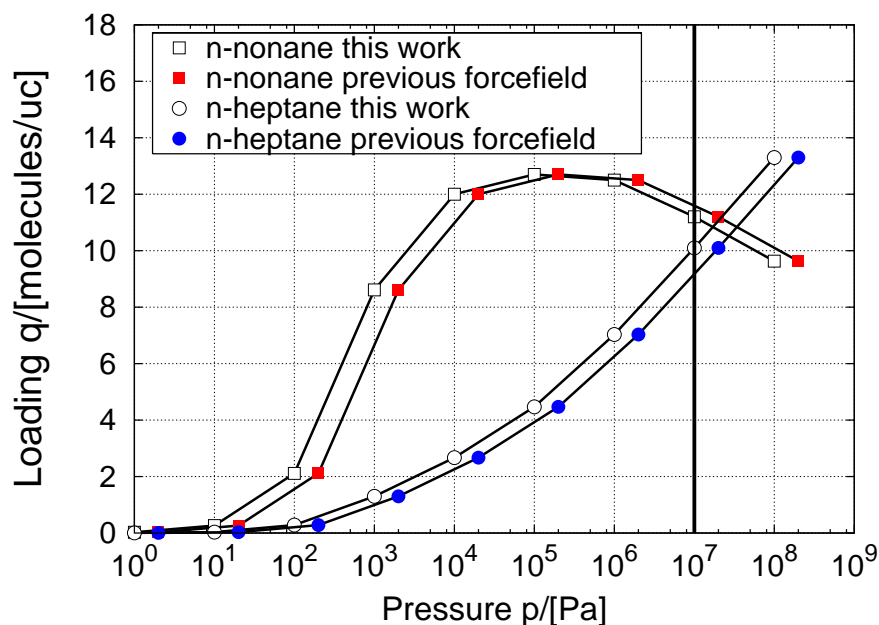


Figure 6: Adsorption isotherms of an equimolar mixture of *n*-nonane and *n*-heptane mixture obtained with CBMC simulations using (1) the previous available force field [50], and (2) our new developed force field (this work). The experimentally predicted cross-over pressure is also included for comparison (vertical line).

is suitable to predict sodium cation redistribution when *n*-alkanes adsorb showing that cations in the sodalite cages are significantly more sensitive to the *n*-alkane loading than those in the supercages. Secondly, the force field is also suitable to predict adsorption properties in the low pressure regime. From the resulting simulation data we have obtained a simple empirical expression that describes the *n*-alkane Henry coefficient and adsorption enthalpy as a function of sodium density and temperature at low coverage affording an adequate substitute for complex configurational-bias Monte Carlo simulations.

Acknowledgments

We would like to thank the Netherlands Research Council for Chemical Sciences, the European Commission for a Marie Curie Individual Research Fellowship to S.C and Chevron Texaco for financial support. J.F.M. Denayer is grateful to the

F.W.O.-Vlaanderen for a fellowship as post-doctoral researcher. J.A.Martens acknowledges the Flemish Government for a concerted research action on the understanding of the elementary active site in catalysis.

Bibliography

- [1] Barthomeuf, D. *Catal. Rev.-Sci. Eng.* **1996**, *38*, 521-612.
- [2] Hattori, H. *Chem. Rev.* **1995**, *95*, 537-558.
- [3] Sanchez-Sanchez, M.; Blasco, T. *J. Am. Chem. Soc.* **2002**, *124*, 3443-3456.
- [4] Concepcion-Heydorn, P.; Jia, C.; Herein, D.; Pfander, N.; Karge, H. G.; Jentoft, F. C. *J. Mol. Catal.* **2000**, *162*, 227-246.
- [5] Schenk, M.; Calero, S.; Maesen, T. L. M.; van Benthem, L. L.; Verbeek, M. G.; Smit, B. *Angew. Chem., Int. Ed.* **2002**, *41*, 2499-2502.

- [6] Schenk, M.; Smit, B.; Vlucht, T. J. H.; Maesen, T. L. M. *Angew. Chem., Int. Ed.* **2001**, *40*, 736-739.
- [7] Satterfield, C. N.; Cheng, C. S. *AIChE J.* **1972**, *18*, 720-723.
- [8] Breck, D. W. *Zeolite Molecular Sieves*; Wiley: New York, 1974.
- [9] Denayer, J. F. M.; Ocakoglu, R. A.; Huybrechts, W.; Dejonckheere, B.; Jacobs, P.; Calero, S.; Krishna, R.; Smit, B.; Baron, G. V.; Martens, J. A. *J. Catal.* **2003**, *220*, 66-73.
- [10] Smirnov, K. S.; Lemarie, M.; Bremard, C.; Bougeard, D. *Chem. Phys.* **1994**, *179*, 445-454.
- [11] Vitale, G.; Mellot, C. F.; Bull, L. M.; Cheetham, A. K. *J. Phys. Chem. B* **1997**, *101*, 4559-4564.
- [12] Mellot, C. F.; Davidson, A. M.; Eckert, J.; Cheetham, A. K. *J. Phys. Chem. B* **1998**, *102*, 2530-2535.
- [13] Auerbach, S. M.; Bull, L. M.; Henson, N. J.; Metiu, H. I.; Cheetham, A. K. *J. Phys. Chem.* **1996**, *100*, 5923-5930.
- [14] Jaramillo, E.; Auerbach, S. M. *J. Phys. Chem. B* **1999**, *103*, 9589-9594.
- [15] Ciruolo, M. F.; Norby, P.; Hanson, J. C.; Corbin, D. R.; Grey, C. P. *J. Phys. Chem. B* **1999**, *103*, 346-356.
- [16] Krause, K.; Geidel, E.; Kindler, J.; Forster, H.; Smirnov, K. S. *Vib. Spectrosc.* **1996**, *12*, 45-52.
- [17] Schrimpf, G.; Schlenkrich, M.; Brickmann, J.; Bopp, P. *J. Phys. Chem.* **1992**, *96*, 7404-7410.
- [18] Engelhardt, G. *Microporous Mater.* **1997**, *12*, 369-373.
- [19] Olson, D. H. *Zeolites* **1995**, *15*, 439-443.
- [20] Blake, N. P.; Weakliem, P. C.; Metiu, H. *J. Phys. Chem. B* **1998**, *102*, 67-74.
- [21] Fuchs, A. H.; Cheetham, A. K. *J. Phys. Chem. B* **2001**, *105*, 7375-7383.
- [22] Mellot, C. F.; Cheetham, A. K.; Harms, S.; Savitz, S.; Gorte, R. J.; Myers, A. L. *J. Am. Chem. Soc.* **1998**, *120*, 5788-5792.
- [23] Mellot, C. F.; Cheetham, A. K.; Harms, S.; Savitz, S.; Gorte, R. J.; Myers, A. L. *Langmuir* **1998**, *14*, 6728-6733.
- [24] Jaramillo, E.; Grey, C. P.; Auerbach, S. M. *J. Phys. Chem. B* **2001**, *105*, 12319-12329.
- [25] Mellot, C. F.; Cheetham, A. K. *J. Phys. Chem. B* **1999**, *103*, 3864-3868.
- [26] Gener, I.; Buntinx, G.; Bremard, C. *Microporous Mesoporous Mater.* **2000**, *41*, 253-268.
- [27] Lachet, V.; Boutin, A.; Tavitian, B.; Fuchs, A. H. *Faraday Discussions* **1997**, 307-323.
- [28] Bezus, A. G.; Kiselev, A. V.; Lopatkin, A. A.; Pham, Q. D. *J. Chem. Soc., Faraday Trans. 2* **1978**, *74*, 367-369.
- [29] Woods, G. B.; Rowlinson, J. S. *J. Chem. Soc., Faraday Trans. 2* **1989**, *85*, 765-781.
- [30] Ghorai, P. K.; Sluiter, M.; Yashonath, S.; Kawazoe, Y. *J. Am. Chem. Soc.* **2003**, *125*, 16192-16193.
- [31] Pellenq, R. J. M.; Tavitian, B.; Espinat, D.; Fuchs, A. H. *Langmuir* **1996**, *12*, 4768-4783.
- [32] Yashonath, S.; Demontis, P.; Klein, M. L. *J. Phys. Chem.* **1991**, *95*, 5881-5889.
- [33] Henson, N. J.; Eckert, J.; Hay, P. J.; Redondo, A. *Chem. Phys.* **2000**, *261*, 111-124.

- [34] Yashonath, S.; Thomas, J. M.; Nowak, A. K.; Cheetham, A. K. *Nature* **1988**, *331*, 601-604.
- [35] Kiselev, A. V.; Lopatkin, A. A.; Shulga, A. A. *Zeolites* **1985**, *5*, 261-267.
- [36] Maddox, M. W.; Rowlinson, J. S. *J. Chem. Soc., Faraday Trans.* **1993**, *89*, 3619-3621.
- [37] Sayeed, A.; Mitra, S.; Kumar, A. V. A.; Mukhopadhyay, R.; Yashonath, S.; Chaplot, S. L. *J. Phys. Chem. B* **2003**, *107*, 527-533.
- [38] Mukhopadhyay, R.; Sayeed, A.; Rao, M. N.; Anilkumar, A. V.; Mitra, S.; Yashonath, S.; Chaplot, S. L. *Chem. Phys.* **2003**, *292*, 217-222.
- [39] Bandyopadhyay, S.; Yashonath, S. *J. Chem. Phys.* **1996**, *105*, 7223-7226.
- [40] Rajappa, C.; Bandyopadhyay, S.; Subramanian, Y. *Bull. Mater. Sci.* **1997**, *20*, 845-878.
- [41] Smit, B.; Maesen, T. *Nature* **1995**, *374*, 42-44.
- [42] Frenkel, D.; Smit, B. *Understanding Molecular Simulations: From Algorithms to Applications*, 2nd Ed.; Academic Press: San Diego, CA, 2002.
- [43] Dubbeldam, D.; Calero, S.; Maesen, T. L. M.; Smit, B. *Phys. Rev. Lett.* **2003**, *90*(24), Art. No. 245901.
- [44] Vlugt, T. J. H.; Krishna, R.; Smit, B. *J. Phys. Chem. B* **1999**, *103*, 1102-1118.
- [45] Smit, B.; Siepmann, J. I. *J. Phys. Chem.* **1994**, *98*, 8442-8452.
- [46] Melchior, M. T.; Vaughan, D. E. W.; Jacobson, A. J. *J. Am. Chem. Soc.* **1982**, *104*, 4859-4864.
- [47] Herrero, C. P. *J. Chem. Soc., Faraday Trans.* **1991**, *87*, 2837-2841.
- [48] Vega, A. J. *J. Phys. Chem.* **1996**, *100*, 833-836.
- [49] Peterson, B. K. *J. Phys. Chem. B* **1999**, *103*, 3145-3150.
- [50] Beerdsen, E.; Smit, B.; Calero, S. *J. Phys. Chem. B* **2002**, *106*, 10659-10667.
- [51] Beerdsen, E.; Dubbeldam, D.; Smit, B.; Vlugt, T. J. H.; Calero, S. *J. Phys. Chem. B* **2003**, *107*(44), 12088-12096.
- [52] Kärger, J.; Vasenkov, S.; Auerbach, S. M. Diffusion in zeolites. In *Handbook of Zeolite Science and Technology*; Auerbach, S. M., Carrado, K. A., Dutta, P. K., Eds.; Marcel Dekker: New York, 2003; pp. 341-422.
- [53] Vlugt, T. J. H.; Schenk, M. *J. Phys. Chem. B* **2002**, *106*, 12757-12763.
- [54] Ryckaert, J. P.; Bellemans, A. *Faraday Discuss. Chem. Soc.* **1978**, *66*, 95-106.
- [55] Mortier, W. J.; Bossche, E. V. d.; Uytterhoeven, J. B. *Zeolites* **1984**, *4*, 41-44.
- [56] Fitch, A. N.; Jobic, H.; Renouprez, A. *J. Phys. Chem.* **1986**, *90*, 1311-1318.
- [57] Pluth, J. J.; Smith, J. V. *J. Am. Chem. Soc.* **1980**, *102*, 4704-4708.
- [58] Dubbeldam, D.; Calero, S.; Vlugt, T. J. H.; Krishna, R.; Maesen, T. L. M.; Beerdsen, E.; Smit, B. *Phys. Rev. Lett.* **2004**, *93*(8), Art. No. 088302
- [59] Dubbeldam, D.; Calero, S.; Vlugt, T. J. H.; Krishna, R.; Maesen, T. L. M.; Smit, B. *J. Phys. Chem. B* **2004**, *108*(33), 12301-12313.
- [60] Dunne, J. A.; Rao, M.; Sircar, S.; Gorte, R. J.; Myers, A. L. *Langmuir* **1996**, *12*, 5896-5904.
- [61] Barrer, R. M.; Sutherland, J. W. *Proc. R. Soc. London, Ser. A*, **1956**, *237*, 439-463.

- [62] Talu, O.; Zhang, S. Y.; Hayhurst, D. T. *J. Phys. Chem.* **1993**, *97*, 12894-12898.
- [63] Chkhaidze, E. V.; Fomkin, A. A.; Serpinski, V. V.; Tsitsishvili, G. V. *Bull. Acad. Sci. USSR Chem. Sci.* **1985**, *34*, 886-890.
- [64] Tarek, M.; Kahn, R.; Delara, E. C. *Zeolites* **1995**, *15*, 67-72.
- [65] Dzhigit, O. M.; Kiselev, A. V.; Rachmanova, T. A. *J. Chem. Soc., Faraday Trans. 2* **1979**, *75*, 2662-2677.
- [66] Dzhigit, O. M.; Kiselev, A. V.; Rachmanova, T. A. *Zeolites* **1984**, *4*, 389-397.
- [67] Hampson, J. A.; Rees, L. V. C. In *Zeolites and Microporous Crystals*, Proceedings of the International Symposium on Zeolites and Microporous Crystals, Nagoya-shi, Japan, Aug 22-25, 1993; Hattori, T., Yashima, T., Eds.; Elsevier; Amsterdam, 1994; Vol. 83, pp 197-208.
- [68] Palmas, S.; Polcaro, A. M.; Carta, R.; Tola, G. *J. Chem. Eng. Data* **1991**, *36*, 1-4.
- [69] Stach, H.; Lohse, U.; Thamm, H.; Schirmer, W. *Zeolites* **1986**, *6*, 74-90.
- [70] Zhang, S. Y.; Talu, O.; Hayhurst, D. T. *J. Phys. Chem.* **1991**, *95*, 1722-1726.
- [71] Thamm, H.; Stach, H.; Schirmer, W.; Fahlke, B. *Z. phys. Chemie (Leipzig)* **1982**, *263*, 461-469.
- [72] Janchen, J.; Stach, H. *Zeolites* **1985**, *5*, 57-59.
- [73] Zhu, L.; Seff, K. *J. Phys. Chem. B* **1999**, *103*, 9512-9518.
- [74] Lim, K. H.; Grey, C. P. *J. Am. Chem. Soc.* **2000**, *122*, 9768-9780.
- [75] Grey, C. P.; Poshni, F. I.; Gualtieri, A. F.; Norby, P.; Hanson, J. C.; Corbin, D. R. *J. Am. Chem. Soc.* **1997**, *119*, 1981-1989.
- [76] Marra, G. L.; Fitch, A. N.; Zecchina, A.; Ricchiardi, G.; Salvalaggio, M.; Bordiga, S.; Lamberti, C. *J. Phys. Chem. B* **1997**, *101*, 10653-10660.
- [77] Eulenberger, G. R.; Shoemaker, D. P.; Keil, J. G. *J. Phys. Chem.* **1967**, *71*, 1812-1819.
- [78] Newsam, J. M.; Jacobson, A. J.; Vaughan, E. W. *J. Phys. Chem.* **1986**, *90*, 6858-6864.
- [79] Jirak, Z.; Vratislav, S.; Bosacek, V. *J. Phys. Chem. Solids* **1980**, *41*, 1089-1095.
- [80] Vandun, J. J.; Dhaeze, K.; Mortier, W. J. *J. Phys. Chem.* **1988**, *92*, 6747-6754.
- [81] Buttefey, S.; Boutin, A.; Mellot-Draznieks, C.; Fuchs, A. H. *J. Phys. Chem. B* **2001**, *105*, 9569-9575.
- [82] Denayer, J. F. M.; Baron, G. V. *Adsorption* **1997**, *3*, 251-265.
- [83] Sundstrom, D. W.; Krautz, F. G. *J. Chem. Eng. Data* **1968**, *13*, 223-226.
- [84] Satterfield, C. N.; Smeets, J. K. *AIChE J.* **1974**, *20*, 618-619.
- [85] Denayer, J. F. M.; De Meyer, K.; Martens, J. A.; Baron, G. V. *Angew. Chem., Int. Ed.* **2003**, *42*, 2774-2777.
- [86] Denayer, J. F.; Ocakoglu, A. R.; De Jonckheere, B. A.; Martens, J. A.; Thybaut, J. W.; Marin, G. B.; Baron, G. V. *Int. J. Chem. React. Eng.* **2003**, *1*, A36.
- [87] Denayer, J. F.; Bouyermaouen, A.; Baron, G. V. *Ind. Eng. Chem. Res.* **1998**, *37*, 3691-3698.
- [88] Satterfield, C. N.; Hayhurst, D. T. *AIChE J.* **1974**, *20*, 1023-1024.
- [89] Yang, L.; Trafford, K.; Kresnawahjuesa, O.; Sepa, J.; Gorte, R. J.; White, D. J. *J. Phys. Chem. B* **2001**, *105*, 1935-1942.

- [90] Hampson, J. A.; Rees, L. V. C. *J. Chem. Soc., Faraday Trans.* **1993**, *89*, 3169-3176.
- [91] Habgood, H. W. *Can. J. Chem.* **1964**, *42*, 2340-2350.
- [92] Pires, J.; Decarvalho, M. B.; Ribeiro, F. R.; Derouane, E. *Appl. Catal.* **1989**, *53*, 273-277.
- [93] Hercigonja, R. V.; Radak, V. M.; Gal, I. *J. Zeolites* **1992**, *12*, 54-55.
- [94] Ruthven, D. M.; Doetch, I. H. *AIChE J.* **1976**, *22*, 882-886.
- [95] Dunne, J. A.; Mariwals, R.; Rao, M.; Sircar, S.; Gorte, R. J.; Myers, A. L. *Langmuir* **1996**, *12*, 5888-5895.
- [96] Neddenreip, R. J. *J. Colloid Interface Sci.* **1968**, *28*, 293-304.

An extension to Transition State Theory is presented that is capable of computing quantitatively the diffusivity of adsorbed molecules in confined systems at non-zero loading. This extension to traditional Transition State Theory yields a diffusivity in excellent agreement with that obtained by conventional Molecular Dynamics simulations. While Molecular Dynamics calculations are limited to relatively fast diffusing molecules or small rigid molecules, our approach extends the range of accessible times scales significantly beyond currently available methods. It is applicable in any system containing free energy barriers and for any type of guest molecule.

E. Beerdsen, B. Smit, and D. Dubbeldam



Molecular Simulation of Loading Dependent Slow Diffusion in Confined Systems

The adsorption and diffusion of molecules in confined systems is of great importance to many industrial processes such as the separation of linear and branched alkanes. The performance of confinements in separation and catalytic processes depends critically on the match between the confinement and the shape and size of the adsorbate [1]. Because diffusion is the rate limiting factor in many catalytic processes, diffusion in systems like zeolites has been widely studied [2–9]. However, in contrast to adsorption and separation, the diffusion of molecules in tight confinement is not yet well understood.

One of the difficulties encountered when studying diffusion behavior is that many processes occur outside the timescale accessible to Molecular Dynamics (MD), which is typically limited to diffusion rates in the order of 10^{-12} m²/s. To overcome this, some studies have used dynamically corrected Transition State Theory (dcTST) methods [10–13]. Hitherto, studies were limited to

the infinite dilution limit, whereas many of the processes of practical importance occur at non-zero loading. Coarse-grained kinetic Monte Carlo (kMC) studies have pointed at the difficulties in taking into account the various correlations induced by particle-particle interactions [11,14]. In this letter we resolve this problem by extending dcTST to include diffusion of molecules at non-zero loading. We show that these correlations can be taken into account by a proper definition of an effective hopping rate of a *single* particle. This hopping rate can be computed accurately using rare event simulation techniques at the conditions of interest.

A suitable and well-studied system to study diffusion in confinement is the LTA-type zeolite shown in Fig. 1. The system consists of cubically arranged cages of about 10 Å in size, where each cage has fifteen and twelve distinct adsorption sites for methane and ethane, respectively. The cages are connected by narrow windows that form large free energy barriers. For

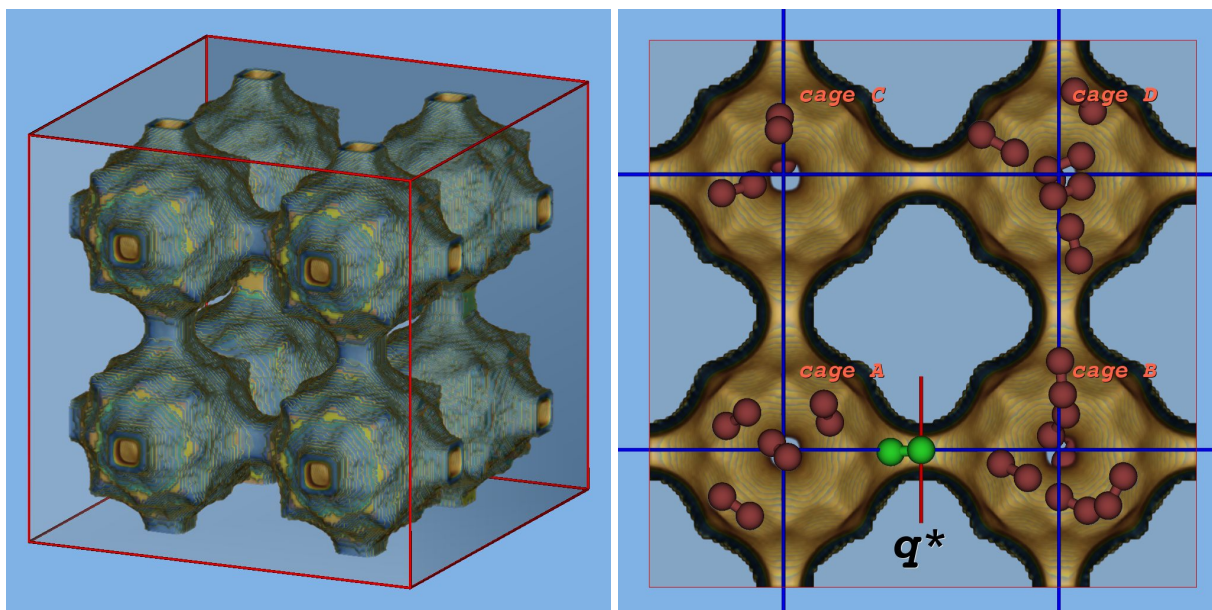


Figure 1: (color online) (top) A unit cell of the LTA-type zeolite. The dimensions of the cubic unit cell are 24.555 \AA . It contains 8 cages connected in a cubic arrangement and each cage is connected to six other cages, by windows of about 5 \AA in diameter. (bottom) Typical snapshot of ethane ($\text{CH}_3 - \text{CH}_3$) at an average loading of 4 molecules per cage at 750K, constraining one tagged molecule at the dividing surface q^* . The hopping events are coarse-grained on a lattice spanned by the cage-centers.

small molecules, the positions in the windows regions are favorable adsorption sites, and the windows form *entropic*, not *energetic* barriers. An advantage of this system is that studying diffusion of small molecules with MD is still feasible, and this allows a detailed comparison with our new approach. In this system, diffusion can be considered an activated process, in which the particle hops from one cage to the next, and the actual crossing time is negligible compared to the time a particle spends inside the cage. One can exploit the large separation in time scales using rare-event simulation techniques. We consider a system which can be in two stable states, *A* and *B* with a dividing free energy barrier between them. We define a reaction coordinate q , that indicates the progress of the diffusion event from cage *A* to cage *B*, as the Cartesian coordinate along the axis parallel to the line connecting the center points of *A* and *B*. The location of the dividing barrier is denoted by q^* (see Fig. 1). In

the Bennett-Chandler approach [15–17] one computes the hopping rate over the barrier in two steps. First, the relative probability $P(q^*)$ is computed to find a particle on top of the barrier, given that it is in state *A*, and subsequently the averaged velocity at the top of the barrier $\sqrt{k_B T / 2\pi m}$ (assuming that the particle velocities follow a Maxwell-Boltzmann distribution) and the probability κ that the system ends up in state *B*. The transmission rate $k_{A \rightarrow B}$ from cage *A* to cage *B* is then given by

$$k_{A \rightarrow B} = \kappa \times \sqrt{\frac{k_B T}{2\pi m}} \times P(q^*) \quad (1)$$

with

$$P(q^*) = \frac{e^{-\beta F(q^*)}}{\int_{\text{cage A}} e^{-\beta F(q)} dq}, \quad (2)$$

where $\beta = 1/(k_B T)$, k_B is the Boltzmann constant, T the temperature, m the mass involved in the reaction coordinate, and $F(q)$ the free energy as a function of q . In first

order approximation, TST assumes that all particles that reach the barrier with a velocity towards B do end up in B , i.e. $\kappa = 1$.

In dynamically corrected TST (dcTST), the transmission coefficient κ corrects for recrossing events, i.e. it corrects for trajectories which cross the transition state from A but fail to end up in B . In general, the reaction coordinate q is a function of the configuration of the whole system, i.e. $q = q(\mathbf{r}_1, \dots, \mathbf{r}_N)$. However, we can choose q as the position of one of the atoms of the diffusing molecules [13]. This choice of order parameter underestimates the free energy of the true transition state, but the dynamical correction κ is the *exact* correction compensating our choice of reaction coordinate [16]. The recrossings are fast events and can be computed using MD as the fraction of particles coming from the initial state A that successfully reaches the final state B out of those that cross the dividing surface at $t = 0$. The transmission coefficient reaches a clear plateau value as a function of time, indicating all short time scale recrossings have been eliminated.

In the limit of infinite dilution there are no interparticle correlations and the particles perform a random walk on a lattice spanned by the cage-centers. The transmission rates are then easily converted to self-diffusion coefficients by:

$$D_S = k_{A \rightarrow B} \lambda^2 = \frac{1}{6} k \lambda^2, \quad (3)$$

with λ the center-to-center lattice distance of the LTA cages (12.2775 Å). Because we calculate the hopping rate from A to B in one direction only, $k_{A \rightarrow B} = 1/6 k$.

The extension of dcTST to finite loading is nontrivial. Conventional methods use a hierarchical approach to compute elementary hopping rates for use in a subsequent kMC scheme to obtain self and collective diffusion coefficients [2, 3, 10, 14, 18]. Let us consider the class of window/cage-type systems (e.g. methane in LTA) where the barriers are *entropical* in nature. At nonzero

loading a molecule hopping from A to B induces a vacancy. The vacancy induces an increased probability of particles to hop to cage A . These correlated jumps may significantly influence the hopping process and should be included in order to obtain a correct diffusion coefficient. In a kMC simulation, the surrounding particles remain in their fixed positions (no two jumps can occur at the same time) and thus these correlations are suppressed. We are not aware of a scheme that results in effective kMC hopping rates that regain these correlations.

We take a different view-point on computing diffusivities in such systems. The correlations can be taken into account by a proper definition of an effective hopping rate of a *single* particle. We compute the self-diffusion coefficient directly. This is done by computing the hopping rate of a molecule over a typical length-scale λ given by the smallest repeating zeolite-structure (i.e. from the center of cage A to the center of cage B , implicitly integrating over all adsorption sites in the cage, irrespective of whether these are well-defined or not). The other particles are regarded as a contribution to the external field exerted on the tagged particle. Since we look at a single tagged particle, the diffusion coefficient can still be computed from the hopping rate by using Eq. 3 at any loading, rendering it unnecessary to perform N -particle kMC simulations. Now, $k_{A \rightarrow B}$ is the *effective* hopping rate, *including* all jump correlations and averaged over all orientations and loading fluctuations. The external field is maintained by an MC *NVT* simulation (fixed total number of particles, volume, and temperature) in the 'background'. By using an MC approach that includes translational, orientational, and regrow moves, we automatically average over cage distributions, positions, and orientations of neighboring molecules. To speed up these simulations for longer molecules by several orders of magnitude, these techniques can be combined with configurational bias

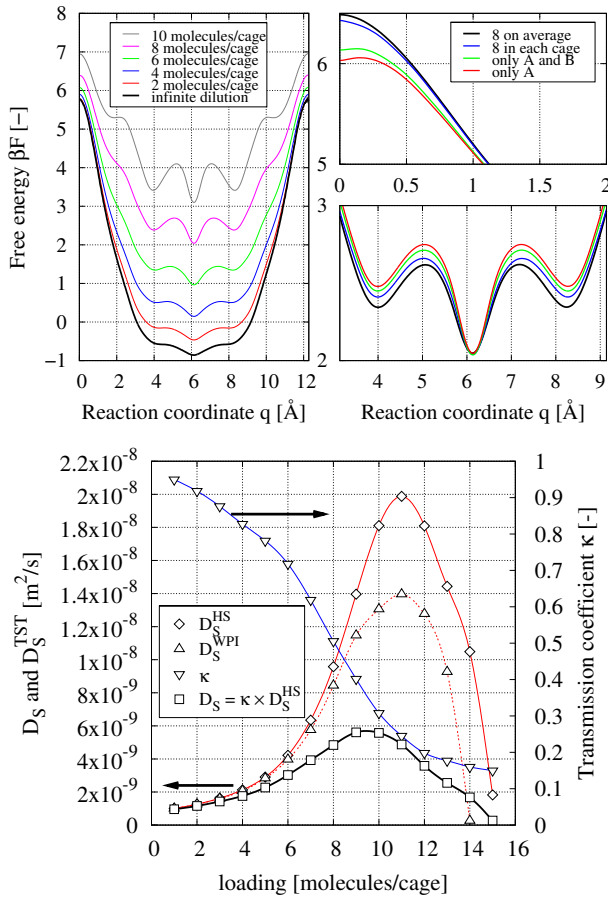


Figure 2: (color online) (top left) Free energy profiles of methane in LTA at 600K for various loadings, obtained using the HS method, (top right) Details from free energy profiles for 8 molecules per cage, using different environments (bottom) D_S^{HS} , D_S^{WPI} , and D_S (left axis) and transmission coefficients (right axis) as a function of loading.

Monte Carlo (CBMC) [17].

The proposed method relies on the direct inclusion of all interparticle correlations in the *effective* hopping rate of a particle traveling from cage A to cage B. In our calculations, we have observed that to obtain agreement with MD results, one cannot limit the free energy calculation to the two cages A and B for which the hopping is computed. It is essential to average over fluctuations in the number of particles in the neighboring cages. By ‘closing off’ cages, the system is intrusively changed. Fig. 2(top right) compares the correct free

energy (very large simulation box with on average 8 molecules per cage), with approximations by simulating a fixed number of 8 particles in cage A only, A and B only and simulations with a fixed number of exactly 8 particles in each cage. These small differences in the free energies result in diffusion coefficients that deviate up to 60%. If we surround cage A with one shell of neighboring cages, we obtain results that are identical to those obtained in the very large system. Inclusion of a second ring of cages is not necessary, as jump correlations over distances larger than two cages vanish. A similar influence is observed in the calculation of the transmission coefficient. Successful hopping events may induce a chain of hops of other particles, and this can influence the transmission coefficient. Only at low loadings we obtain agreement with MD.

We now discuss the two steps in the computation of the hopping rate using our approach in detail.

The probability $P(q)$ During an NVT-ensemble MC simulation at the required loading we measure the free energy $F(q)$ by using either the Widom Particle Insertion (WPI) method or Histogram Sampling (HS). WPI uses a probe particle that is inserted at random positions, to measure the energy required for or obtained by insertion of the particle in the system. This energy is mapped onto the reaction coordinate q , using $\beta F(q) = -\ln \langle e^{-\beta \Delta U} \rangle_N$, to produce a free energy profile, where $\langle e^{-\beta \Delta U} \rangle_N$ is the average Boltzmann factor over all positions in the slice perpendicular to the reaction coordinate. A “ghost particle” is used as the measuring probe, but the other particles in the system do not feel its presence. In the HS method, a histogram is made of the particle positions, mapped on the reaction coordinate. From the histogram a free energy profile is computed, by using $\beta F(q) = -\ln \langle P(q) \rangle$. If needed, statistics can be improved by using importance sampling [17].

At higher loadings, WPI is known to give erroneous results [17]. In Fig. 2(top left) we have plotted the free energy profiles as obtained from the HS method, for various loadings, and in Fig. 2(bottom) the D_S^{HS} and D_S^{WPI} as a function of loading. At loadings as low as 6 methane molecules per cage the WPI method starts to deviate.

The transmission coefficient κ We compute the fraction of particles starting on top of the barrier with a velocity towards B that successfully reach cage B . Starting configurations are generated using MC with one particle constrained to the dividing surface and $N - 1$ particles moving around freely (see Fig. 1 (right)). These configurations are then used to compute the ratio in unconstrained NVT -MD simulations, starting with velocities sampled from a Maxwell-Boltzmann distribution at the desired temperature. For this snapshot cage B contains more molecules than cage A , and the barrier-molecule has a high probability of recrossing to cage A . In general, the transmission coefficient is much lower than one for chain molecules (*even* at infinite dilution). Note that during the computation none of the windows are blocked and simultaneous jumps (e.g. from cage C to cage A , and cage D to cage B) are allowed.

Fig. 2(bottom) shows the individual components of the diffusion process, $\sqrt{k_B T / 2\pi m} \times P(q^*)$ and κ as a function of loading for methane in LTA. Although the transmission coefficient shows a monotonic decrease with density, the diffusion coefficient goes through a maximum. The driving force behind the initial increase in diffusion is a loss of guest-host attraction inside the cages. This interaction is being replaced by less favorable inter-particle interaction, causing an increase of the free energy in the cage regions and thus a net decrease of the free energy barrier (Fig. 2(bottom)). Eventually, the free energy barrier increases again, due to packing and

free-volume effects, causing a decrease of the diffusion coefficient. While the transmission coefficient only slightly changes the qualitative behavior of the diffusion as a function of loading, it has a profound quantitative influence (Fig. 2(bottom)).

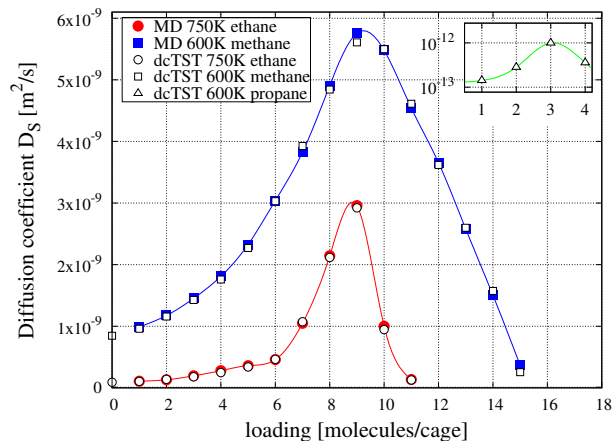


Figure 3: (color online) Diffusion of methane, ethane and propane in LTA, as a function of loading, at 600K, 750K and 600K respectively, computed by extended dcTST (HS method) and MD.

To validate our method, we show the diffusion in LTA of methane at 600K and ethane at 750K using both MD and extended dcTST. In addition we show the diffusion of propane at 600K, using only dcTST, for which the diffusion is too slow to compute with MD. The LTA-type system used here is a cation-free version of the commonly used LTA 5A zeolite (4 Na^+ and 4 Ca^+ per cage). The system size was a cubic box of 24.555 Å, containing 8 cages in total. We used a united-atom model [19], in which we consider CH_x groups as single interaction centers with their own effective Lennard-Jones potentials. We used the position of the CH_4 -group, one of the CH_3 -groups and the middle CH_2 -group as the dcTST reaction coordinate for methane, ethane and propane, respectively [13]. The interactions between the rigid framework and the guest molecules are assumed to be dominated by the oxygen atoms [20]. The potential parameters are optimized to re-

produce adsorption properties in pure silica confinements [21, 22]. In the MD simulations we used a time step of 0.5 fs with the velocity-verlet integration scheme. The *NVT* ensemble was imposed using a Nose-Hoover thermostat. The duration of the computation was such that the error bars are smaller than the symbol size. As is shown in Fig. 3, our extended dcTST method and MD agree quantitatively. The presented methodology provides a general framework for computing diffusivities of molecules in systems where diffusion is sufficiently slow, due to free energy barriers, irrespective of whether these are energetical or entropical in nature. Longer molecules are efficiently handled and likewise, diffusion in mixtures can easily be computed; any type of particle can be considered part of the external field. A quantitative comparison with PGF-NMR experimental results requires including the ions in the simulations. Beerdsen et al. have extended the united-atom model with cations [23], and our dcTST method already includes the necessary tools.

In summary, our method applies dcTST at non-zero loadings without introducing assumptions not already present in traditional TST methods. It can be used to explain diffusion behavior as a function of loading in any system with enough energy dissipation between hops, so that random walk theory (the assumption of equilibration between two subsequent jumps) and TST are valid, as we show here for alkanes in LTA. The method gives results in excellent agreement with MD, but is also applicable in the regime of very slow diffusion where MD can not be used. This extends the range of accessible time scales significantly beyond currently available methods. Furthermore, the method enables us to express loading effects in terms of free energy differences.

We thank Prof. Auerbach for his comments on the manuscript, the Netherlands Research Council (CW) and the

Deutsche Forschungsgemeinschaft (DFG, priority program SPP 1155) for financial support, and NWO/NCF for computational resources. Corresponding author: beerdsen@science.uva.nl

Bibliography

- [1] J. M. Thomas, Solid acid catalysts. *Sci. Am.* **266**, 112 (1992).
- [2] C. Saravanan, F. Jousse, and S. M. Auerbach, *Phys. Rev. Lett.* **80**, 5754 (1998).
- [3] E. J. Maginn, A. T. Bell, and D. N. Theodorou, *J. Phys. Chem.* **100**, 7155 (1996).
- [4] K. Hahn, J. Karger, and V. Kukla, *Phys. Rev. Lett.* **76**, 2762 (1996).
- [5] H. Jobic, J. Karger, and M. Bee, *Phys. Rev. Lett.* **82**, 4260 (1999).
- [6] L. A. Clark, G. T. Ye, and R. Q. Snurr, *Phys. Rev. Lett.* **84**, 2893 (2000).
- [7] D. S. Sholl and K. A. Fichthorn, *Phys. Rev. Lett.* **79**, 3569 (1997).
- [8] S. Fritzsche, M. Gaub, R. Haberlandt, and G. Hofmann, *J. Mol. Model* **2**, 286 (1996).
- [9] E. B. Webb, G. S. Grest, and M. Mondello, *J. Phys. Chem. B.* **103**, 4949 (1999).
- [10] R. L. June, A. T. Bell, and D. N. Theodorou, *J. Phys. Chem.* **95**, 8866 (1991).
- [11] S. M. Auerbach, *International reviews in physical chemistry* **19**, 155 (2000).
- [12] F. Jousse and S. M. Auerbach, *J. Chem. Phys.* **107**, 9629 (1997).
- [13] D. Dubbeldam, S. Calero, T. L. M. Maesen, and B. Smit, *Phys. Rev. Lett.* **90**, 245901 (2003).

- [14] C. Tunca and D. M. Ford, *Chem. Eng. Sci.* **58**, 3373 (2003).
- [15] C. H. Bennett, in *Diffusion in Solids: Recent Developments*, edited by A. Nowick and J. Burton (Academic Press, New York, 1975), pp. 73–113.
- [16] D. Chandler, *J. Chem. Phys.* **68**, 2959 (1978).
- [17] D. Frenkel and B. Smit, *Understanding molecular simulation 2nd edition* (Academic Press, London, UK, 2002).
- [18] K. F. Czaplewski and R. Q. Snurr, *AIChE Journal* 2223 (1999).
- [19] J. P. Ryckaert and A. Bellemans, *Faraday Discuss. Chem. Soc.* **66**, 95 (1978).
- [20] A. G. Bezus, A. V. Kiselev, A. A. Lopatkin, and P. Q. J. Du, *J. Chem. Soc., Faraday Trans. II* **74**, 367 (1978).
- [21] D. Dubbeldam, S. Calero, T. Vlugt, R. Krishna, T. Maesen, E. Beerdsen, and B. Smit, *Phys. Rev. Lett.* **93**, 088302 (2004).
- [22] D. Dubbeldam, S. Calero, T. Vlugt, R. Krishna, T. Maesen, and B. Smit, *J. Phys. Chem. B.* **108**, 12301 (2004).
- [23] E. Beerdsen, B. Smit, and S. Calero, *J. Phys. Chem. B* **106**, 10659 (2002).

A dynamically corrected Transition State Theory method is presented that is capable of computing quantitatively the self-diffusivity of adsorbed molecules in confined systems at non-zero loading. This extension to traditional Transition State Theory is free of additional assumptions and yields a diffusivity identical to that obtained by conventional Molecular Dynamics simulations. While Molecular Dynamics calculations are limited to relatively fast diffusing molecules, our approach extends the range of accessible times scales significantly beyond currently available methods. We show results for methane, ethane, and propane in LTL- and LTA-type zeolites over a wide range of temperatures and loadings, and demonstrate the extensibility of the method to mixtures.

D. Dubbeldam, E. Beerdsen, T. J. H. Vlucht, and B. Smit

10

Molecular Simulation of Loading Dependent Diffusion in Nanoporous Materials using Extended Dynamically Corrected Transition State Theory

I Introduction

Molecular simulation [1, 2] has evolved over the years as a powerful tool to study equilibrium and transport properties of molecules adsorbed in nanoporous materials. It provides an understanding of the microscopic dynamics underlying the macroscopic properties of industrial interest such as for instance the separation of mixtures of molecules [3]. The use of zeolites as a means for chemically clean separations can be considered a prime example of how nanomaterials are able to exploit the critical match between the confinement and the shape and size of the adsorbate. One of the difficulties encountered when studying diffusion behavior in zeolites using simulation is that many processes occur outside the

time scale accessible to MD, which is currently typically limited to diffusion rates in the order of 10^{-12} m²/s.

New methods have been developed for circumventing this time scale problem [4]. Systems characterized by a sequence of rare events can be described by Transition State Theory (TST) methods like the Bennett-Chandler approach [5,6], the Ruiz-Montero method [7], path sampling [8], transition interface sampling [9, 10], hyperdynamics [11], parallel replica dynamics [12], temperature-accelerated dynamics [13], and on-the-fly kinetic Monte Carlo [14]. In principle, all of these methods have the potential to be orders of magnitude more efficient while still retaining full atomistic detail. In TST approximations one computes a rate constant between

states A and B by computing the equilibrium particle flux through the dividing surface. The dividing surface should uniquely divide two connected states, and in general the TST rate is an upper bound on the exact rate. The exact rate can be recovered by running short MD trajectories from the dividing surface to compute a dynamical correction (dc) [1].

Many groups have worked on the time scale problem for diffusion in confinement. The approach of June et al. [15] models self-diffusion of Xenon and SF₆ in silicalite at infinite dilution as a series of uncorrelated jumps between potential energy minima (sites). The rate constants for jumping between the sites are converted to diffusivities by generating continuous-time/discrete-space Monte-Carlo random walks. The computed diffusivities were reasonably close to the values computed using conventional MD. Snurr et al. [16] developed a hierarchical approach for predicting isotherms of benzene in silicalite. The method can be applied to other systems when molecules adsorb at well-defined sites. In a subsequent paper, Snurr et al. [17] investigated the dynamical behavior of benzene using TST. Diffusion paths connecting pairs of potential energy minima are constructed through saddle points (transition states). Given the rate constants, the self-diffusivity was computed with a kinetic Monte-Carlo simulation. Maginn et al. [18] presented a hierarchical approach for simulating the diffusion of *n*-alkanes up to C₂₀ in silicalite using modest computational resources. The simulation strategy utilized concepts from Brownian motion theory and transition state theory. Jousse and Auerbach [19] used TST to compute exact rate coefficients for benzene jumps in Na-Y zeolite. Forester and Smith [20] used constrained reaction coordinate dynamics (Bluemoon ensemble) to characterize the free energy profile of benzene in silicalite-1 at 300K along the mean reaction path for diffusion. The free energies, com-

puted with estimates of the transmission coefficient, were used to obtain rate constants for diffusion between the main adsorption sites. Subsequent diffusive Monte Carlo simulations provided the self-diffusion coefficients. Mossel et al. [21, 22] studied the diffusion of benzene and *p*-xylene in zeolite NaY by means of constrained reaction coordinate dynamics. MD simulations were used to determine the potential of mean force along the coordinate perpendicular to the window connecting two supercages of the zeolite. Diffusion coefficients and activation energies were determined from a hopping model that considers dynamical corrections. Ghorai et al. [23] estimated the rate of passage of CCl₄ through the 8-ring window in a model of zeolite A by combining a direct evaluation of the free energy profile and an adaptation of the rare events method. The system contains on average one particle per cage, and because particle-particle interactions rarely occur under this condition the free energy is evaluated from the one-particle partition function. The self-diffusion of ethane in cation-free LTA-type zeolite has been studied by Schüring et al. [24] using MD and TST (without dynamical correction) for various temperatures. The bare TST jump rates were similar to the MD jump rates (where also the MD results were not corrected for short-time recrossings). Dubbeldam et al. [25,26] applied dynamically corrected Transition State Theory (dcTST) to study abnormal diffusion of linear alkane molecules (C₁-C₂₀) in ERI-, CHA-, and LTA-type zeolites at infinite dilution. The exceptionally slow diffusion rates required the combination of rare-event TST techniques with the configurational-bias Monte Carlo (CBMC) algorithm [1, 27]. The diffusivities were evaluated on a lattice spanned by the cage-centers.

It is important to note that these works have been performed at infinite dilution, even though many of the processes of industrial importance occur at non-zero load-

ing. A limited number of studies deal with non-zero loading. Tunca and Ford [28] used multidimensional TST to obtain the hopping rate of adsorbates from an α -cage in LTA-type zeolite as a function of loading. Various approximations were applied to make the simulations computationally feasible. In a subsequent study [29] the limitations of an empty receiving cage and the use of the Widom insertion method were avoided. Recently, Tunca and Ford presented a new hierarchical approach to the molecular modeling of diffusion and adsorption at nonzero loading in microporous materials [30]. Although adsorption was well represented, the coarse-grained self-diffusivity data under-predicted the diffusivity at low loading, while significantly over-predicting the diffusivities at higher loadings, in comparison to conventional MD.

Coarse-grained kinetic Monte Carlo (kMC) studies have pointed at the difficulties of computing an elementary hopping rate taking into account the various correlations induced by particle-particle interactions [30,31]. Very recently, Beerdsen et al. [32] extended the dcTST Bennett-Chandler approach to include diffusion of molecules at non-zero loading. It was shown that the particle-particle correlations can be taken into account by a proper definition of an effective hopping rate of a *single* particle. The self-diffusivity was computed directly by computing the hopping rate of a molecule over a typical length scale given by the smallest repeating zeolite-structure, i.e. from the center of cage A to the center of cage B. The use of kinetic Monte Carlo and its underlying assumptions are therefore avoided. Implicitly one integrates over all adsorption sites in the cage, irrespective whether these are well-defined or not. All other particles are regarded as a contribution to the external field exerted on this tagged particle. The dcTST extension to finite loadings yielded excellent agreement with that obtained

by conventional MD simulations and is applicable in any system containing high free energy barriers and for any type of guest molecule. In this work, we elaborate on the concepts introduced by Beerdsen et al., and show results for methane, ethane, and propane in LTL-, and LTA-type zeolites over a wide range of temperatures and loadings.

The remainder of the paper is organized as follows. In section II we explain the used methods and concepts. First the force field is described, and we present shortly the canonical MD algorithm focusing on maintaining temperature control and obtaining diffusion coefficients. Next we discuss some concepts from random walk theory, e.g. jump rates and memory effects. We show that TST is fully compatible and consistent with random walk theory and present our dcTST at nonzero loading. Section III starts with results on the infinite dilution case. Two different sets of parameters from literature are used and the difference indicates that the physics of adsorption and diffusion in zeolites is often highly parameter dependent. The main emphasis of the paper lies on the diffusivity results of methane, ethane, and propane in LTL- and LTA-type zeolites using dcTST compared to MD as a function of loading. For LTA-type zeolite we present additional results of a mixture of methane and ethane. We end with a general discussion on lattices, correlations, and dcTST in section IV, and conclusions in section V.

II Methodology

A Force field parameters for adsorption and diffusion of alkanes in siliceous nanoporous materials

Zeolites are confined systems with pore sizes comparable to the molecular size. Adsorption in cation-free zeolite structures

usually takes place at specific sites with little or no electric field. For this reason the united-atom model [33] seems the most straightforward choice. We consider the CH_x groups as single, chargeless interaction centers with their own effective potentials. The beads in the chain are connected by harmonic bonding potentials. A harmonic cosine bending potential models the bond bending between three neighboring beads. The Lennard-Jones potentials are shifted and cut at 12 Å. Analytical tail-corrections do not apply in zeolites [34]. A truncated and shifted potential is equally suitable to Monte Carlo and Molecular Dynamics. Flexibility of the framework is not an issue for adsorption of linear and branched alkanes [35]. For methane in LTA-type zeolite it was found that self-diffusion coefficients obtained with flexible and with rigid lattices are practically the same [36] (in the discussion section we will further comment on this). The interactions between the rigid framework and the guest molecules are assumed to be dominated by the oxygen atoms [37]. The interaction parameters of alkanes listed in Table 1 for use in molecular simulations of confined systems are obtained uniquely and accurately through fitting on experimental isotherms with inflection points [38, 39]. Recently, it was shown that these parameters also give near-quantitative agreement for collective and transport diffusivity for ethane in silicalite compared to neutron scattering experiments [40]. Details on the simulations can be found in Refs. [38, 41].

The parameters listed in Table 2 are used mainly for simulation comparison to the work of Schüring et al. [24, 42], and because the very small size parameters enhance diffusion by two orders of magnitude for ethane in LTA-type zeolite compared to the parameters of Dubbeldam et al. Although the parameters of Schüring et al. are probably less realistic in our opinion, they are convenient to compare the diffusion of ethane from a simulation-method point of

	O	CH_4	CH_3	CH_2
CH_4	115.00 3.47	158.50 3.72	130.84 3.74	94.21 3.84
CH_3	93.00 3.48	130.84 3.74	108.00 3.76	77.77 3.86
CH_2	60.50 3.58	94.21 3.84	77.77 3.86	56.00 3.96
bond	$U^{\text{bond}} = \frac{1}{2}k_1(r - r_0)^2$ $k_1/k_B = 96500 \text{ K}/\text{Å}^2, r_0 = 1.54 \text{ Å}$			
bend	$U^{\text{bend}} = \frac{1}{2}k_2(\cos \theta - \cos \theta_0)^2$ $k_2/k_B = 62500 \text{ K}, \theta_0 = 114^\circ$			

Table 1: Force field of Dubbeldam et al. [38, 39] for guest-host and guest-guest interactions of hydrocarbons in cation-free nanoporous materials. Lennard-Jones parameters, ϵ/k_B [K] in top-left corner, σ [Å] in bottom-right corner of each field, bond and bend parameters

view by MD and dcTST in LTA-type zeolite.

	O	Si	CH_3
CH_3	142 3.17	82 2.12	104 3.78
bond	$U^{\text{bond}} = \frac{1}{2}k_1(r - r_0)^2$ $k_1/k_B = 96500 \text{ K}/\text{Å}^2, r_0 = 1.54 \text{ Å}$		

Table 2: Force field parameters used by Schüring et al. for ethane in LTA-type zeolite [24], for guest-host and guest-guest interactions of hydrocarbons in cation-free nanoporous materials. Lennard-Jones parameters, ϵ/k_B [K] in top-left corner, σ [Å] in bottom-right corner of each field, bond and bend parameters

B Molecular Dynamics (MD)

In MD simulations [1, 2, 43], successive configurations of the system are generated by integrating Newton’s laws of motion, which then yields a trajectory that describes the positions, velocities and accelerations of the particles as they vary with time. The self-diffusion coefficients D_s^α in the direction $\alpha = x, y, z$ are computed by taking the slope of the mean-squared displacement

(msd) at long times

$$D_S^\alpha = \frac{1}{2N} \lim_{t \rightarrow \infty} \frac{d}{dt} \left\langle \sum_{i=1}^N (r_{i\alpha}(t) - r_{i\alpha}(0))^2 \right\rangle \quad (1)$$

where N is the number of molecules, t the time, and $r_{i\alpha}$ the α -component of the center-of-mass of molecule i . Equivalently, D_α is given by the time integral of the velocity autocorrelation function

$$D_S^\alpha = \frac{1}{N} \int_0^\infty \left\langle \sum_{i=1}^N v_{i\alpha}(t) v_{i\alpha}(0) \right\rangle dt \quad (2)$$

where $v_{i\alpha}$ is the α -component of the center-of-mass-velocity of molecule i . A separation of time scales occurs for interacting particles roughly at the times between particle-particle and particle-zeolite collisions. The mean-squared displacement thus bends over to attain a different slope, and we are interested in the long-time diffusion coefficient. The collective diffusion coefficients D_C^α are given by

$$D_C^\alpha = \frac{1}{2N} \lim_{t \rightarrow \infty} \frac{d}{dt} \left\langle \left(\sum_{i=1}^N (r_{i\alpha}(t) - r_{i\alpha}(0)) \right)^2 \right\rangle \quad (3)$$

and

$$D_C^\alpha = \frac{1}{N} \int_0^\infty \left\langle \left(\sum_{i=1}^N v_{i\alpha}(t) \right) \left(\sum_{i=1}^N v_{i\alpha}(0) \right) \right\rangle dt \quad (4)$$

Collective diffusivity measures the transport of mass and the decay of density fluctuations in the system, while self-diffusion measures the diffusive motion of a single particle. The directionally averaged diffusion coefficient is given by

$$D = \frac{D_x + D_y + D_z}{3} \quad (5)$$

Note that in simple fluids there is only a time scale separation for the self-motion, not for the collective motion. In nanoporous materials, both the displacements of the single particles as well as the

displacements of the total center of mass are restricted by the confinement and the time scale separation is also present in collective diffusion. This is very much related to the diffusion of polymers in melts where similar time scale separations occur [44]. In Fig. 1 we show the mean-squared displacements of the self-and collective motions at 300K of methane in LTA-type zeolite at an average loading of 8 molecules per cage. Several regimes can be identified for this system,

1. At very short time scales both the self and collective motion are ballistic, and the msd is proportional to t^2 .
2. While initially the same, the msd of self-motion is lowered in comparison to the collective motion due to back-correlation mechanisms that also occur in simple fluids. The onset of regime II is signaling the average mean free time before particles collide.
3. Regime three is dominated by a confinement-effect and particles have not yet been able, on average, to hop to the next confinement. The msd of single particles is restricted to approximately the cage size squared, but results in cancellation for the collective behavior. The msd of self-motion is therefore higher than for collective motion.
4. With increasing times the particles are increasingly able to leave the confinement, and both self-and collective motion increase eventually to a linear diffusive regime IV. Here, particles originating from *different* cages start to collide, and self-motion is again lowered in comparison with collective motion. For collective motion the onset of this hydrodynamical regime is a combined effect of confinement and the time particles start to leave the cage (because here, a change in the collective motion

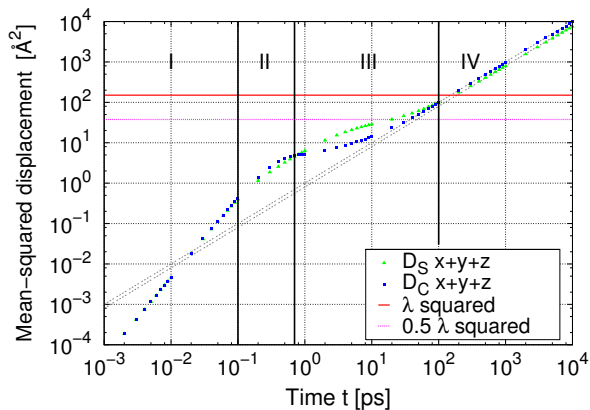


Figure 1: Mean-squared displacement of self-diffusivity D_S and collective diffusivity D_C for methane in LTA-type zeolite at 300K at an average loading of 8 molecules per cage. We can identify four distinct regimes (see text). For reference, we show $(\frac{1}{2}\lambda)^2$ and λ^2 , with $\lambda = 12.2775 \text{ \AA}$ the cage-center to cage-center lattice distance. The dotted lines are of slope unity and indicate normal diffusive behavior.

can only be accomplished by cage-to-cage hops of single particles). The onset for self-motion for cage/window-type systems is the cage-size squared, i.e. the average time for a particle to leave a cage.

The calculation of the diffusion coefficients requires much memory and CPU power, especially when fluctuations decay slowly. The order- n algorithm to measure correlations allows us to measure fast and slow dynamics simultaneously at minimal computational cost by using adjustable sampling frequencies [1]. The order- n scheme is equally accurate as the conventional scheme but the saving in memory as well as CPU time is significant for computing the mean-squared displacements at long times.

In a conventional NVE Molecular Dynamics simulation, the total energy E , the number of particles N , and the volume V are constant. Hence, MD measures (time) averages in the microcanonical ensemble, while in a conventional Monte-

Carlo simulation the canonical ensemble (NVT-ensemble) is probed. The extended Lagrangian approach has become one of the most important tricks for MD in the NVT ensemble and is completely dynamic in origin. The Nosé-Hoover Chain (NHC) formulation extends the Lagrangian with additional coordinates and velocities containing the system to a constant temperature NVT-ensemble. We use the NHC method as implemented by Martyna et al. [45] in which the dynamics is still reversible. The instantaneous kinetic temperature fluctuates, but the probability to find the system in a given energy state follows the Maxwell-Boltzmann distribution.

For the instantaneous temperature we measure the total kinetic energy of the system and divide this by the number of degrees of freedom $N_f (= 3N - 3$ for a system of N particles with fixed total momentum)

$$k_B T(t) = \sum_{i=1}^N \frac{m_i v_i^2(t)}{N_f} \quad (6)$$

The disadvantage of most methods for working at constant temperature is that the dynamics is changed in an artificial way. Because in our simulations we do not have photons or electrons, i.e. the system is mechanical, heat is transported at the speed of sound or slower. However, most thermostat methods have a coupling constant, i.e. the mass of the NHC, and the effect of the thermostat on the particle is instantaneous. The NHC mass should therefore be chosen as small possible to alter the dynamics as little as possible. If this is taken care of, the non-physical effects will be of order $(1/N)$ in general.

Fig. 2 shows the importance of adequate temperature control. Ideally, a flexible zeolite would provide excellent thermostating of adsorbed molecules. However, for computational reasons many authors keep the framework rigid, and the thermostating issue arises. In the NVE-ensemble the particles do not exchange energy with

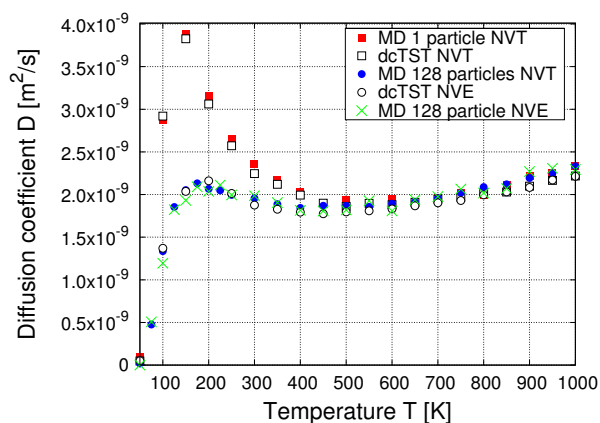


Figure 2: Self-diffusion of ethane at infinite dilution in LTA-type silica using the parameter sets of Schüring et al. The infinite dilution case using MD is simulated by switching the ethane intermolecular forces off, i.e. the particles do not interact (except through the thermostat in NHC-NVT simulations).

the heat bath and thermalization occurs through mutual interactions between the adsorbates. Moreover, rather unphysical ballistic motion may occur, and particles may be stuck in local free energy barriers. The non-physical effects of the NHC thermostat using a single molecule are clearly present in both MD and dcTST. We note that at high temperatures the thermostat effects are small, but they become significant at very low temperatures. This implies that single particle diffusion coefficients or correlations *should* be computed in the NVE-ensemble, unless a sufficient number of particles is used. At infinite dilution this can be accomplished by switching the intermolecular forces off, i.e. the particles do not interact except through the thermostat in NVT NHC simulations. However, even if this taken care of, the NHC method is only capable of maintaining adequate temperature control in equilibrium, and therefore breaks down in the limit of high potential energy barriers [46]. Entropical barriers (e.g. due to constrictions and apertures in zeolite cages and channels) represent no problem.

To prepare the system at the desired temperature in an equilibrium configuration

we initialize the system by the following procedure

- N molecules are inserted into the framework at random positions as long as no overlaps occur with the framework or other particles, and as long as the positions are accessible from the main cages and channels.
- During the initializing period we perform an NVT MC simulation to rapidly achieve an equilibrium molecular arrangement.
- After the initialization step, we assign all the atoms velocities from the Maxwell-Boltzmann distribution at the desired average temperature. The total momentum of the system is set to zero. Next, we equilibrate the system further by performing a NVT MD simulation using the NHC thermostat.
- The equilibration is completed and during the production run we collect statistics using either the NVE or NVT-ensemble. Following this equilibration procedure, the average temperature using NVE over the entire production period is usually within a few Kelvin of the desired average temperature, while NVT would give the exact desired average temperature if simulated sufficiently long.

C Lattice random walk theory

Diffusive motion of particles occurs by a series of discrete steps separated by elastic collisions, localized vibrations, and short shuffles. Diffusion is an irreversible macroscopic process, but is actually comprised of reversible microscopic steps, and may be well described by random walk theory. A random walk is a simple mathematical model for the movement of a particle on a lattice under the influence of some random or stochastic force affecting its direction of

motion. It is particularly attractive because in many instances analytical solutions can be worked out for both static as well as dynamic properties. From the internal (crystal) structure a lattice can be constructed that determines the lattice topology and the lattice distances. The dynamics of the random walk is uniquely determined once the jumping frequencies k_i for a lattice direction i are specified. The jump frequency is defined as

$$k = \frac{\langle \text{number of successful hops} \rangle}{\text{unit of time}} \quad (7)$$

The total jumping frequency k_{tot} is related to the specific jumping frequencies k_i for a given structure by a summation over the lattice connectivity Z :

$$k_{\text{tot}} = \sum_{i=1}^Z k_i \quad (8)$$

For a jump to be truly random, each of the possible jump directions is chosen with equal probability, the probability that the new lattice site is empty does not enter into any equation (the particles can overlap). The expected value $\langle \mathbf{r}(t) \rangle = 0$, and the driving force $\nabla \mu = 0$ for a simple regular random walk (necessary for the measurement of the self-diffusivity D_s). However, in real systems, jumps are usually correlated by defined interactions between jumping particles.

Let k_i be the average frequency that a random walker (an atom or molecule) jumps for lattice vector λ_i , and $\mathbf{r}(t)$ is the position of a particular random walker. The position of a particle (relative to the starting position) after a time t (or $n = kt$ hops) will be:

$$\mathbf{r}(t) = \sum_{i=1}^n \lambda_i \quad (9)$$

where n_i is the number of jumps in lattice direction λ_i on a regular lattice with connectivity Z . In primitive cubic crystals there exists one lattice site per unit cell surrounded by $Z = 6$ neighbors, the lattice

vectors are $\lambda_i = \{\{1, 0, 0\}, \{0, 1, 0\}, \{0, 0, 1\}, \{\bar{1}, 0, 0\}, \{0, \bar{1}, 0\}, \{0, 0, \bar{1}\}\}$. The distance between two particles should increase with time, which is measured by the spread of the distribution $\langle \mathbf{r}(t) \rangle$

$$\langle \mathbf{r}^2(t) \rangle = \left\langle \sum_{i=1}^n \lambda_i \cdot \lambda_i + 2 \sum_{i=1}^{n-1} \sum_{j=i+1}^n \lambda_i \cdot \lambda_j \right\rangle \quad (10)$$

written as a sum of diagonal and off-diagonal terms.

For the one-dimensional lattice, the two-dimensional square lattice, and the three-dimensional cubic lattice, all the jumping frequencies k_i and jump vectors are equivalent. Using the relationship $\lambda_i \cdot \lambda_j = |\lambda_i| |\lambda_j| \cos \Delta\phi_{ij}$, where $\Delta\phi_{ij}$ is the angle between the i^{th} and j^{th} jump-vectors. Therefore,

$$\mathbf{r}^2(t) = n \lambda^2 + 2 \left(\sum_{i=1}^{n-1} \sum_{j=i+1}^n |\lambda_i| |\lambda_j| \cos \Delta\phi_{ij} \right) \quad (11)$$

$$= n \lambda^2 + \sum_{i=1}^n \sum_{\substack{j=1 \\ j \neq i}}^n |\lambda_i| |\lambda_j| \cos \Delta\phi_{ij} \quad (12)$$

$$= n \lambda^2 \left(1 + \frac{1}{n} \left\langle \sum_{i=1}^n \sum_{j=1}^n \cos \Delta\phi_{ij} \right\rangle \right) \quad (13)$$

because $\Delta\phi_{ij} = -\Delta\phi_{ji}$. We can write

$$\langle \mathbf{r}(t)^2 \rangle = n f \lambda^2 = Z k_i f \lambda^2 t, \quad (14)$$

and apply Einstein's equation

$$\langle \mathbf{r}(t)^2 \rangle = 2dDt \quad (15)$$

to yield

$$D = \frac{Z}{2d} f k_i \lambda^2 = f k_{A \rightarrow B} \lambda^2 \quad (16)$$

$$= \frac{1}{2d} f k_{\text{tot}} \lambda^2 \quad (17)$$

This relates the macroscopic self-diffusivity to the jump frequency k , lattice hop distance λ and correlation factor f . The basic

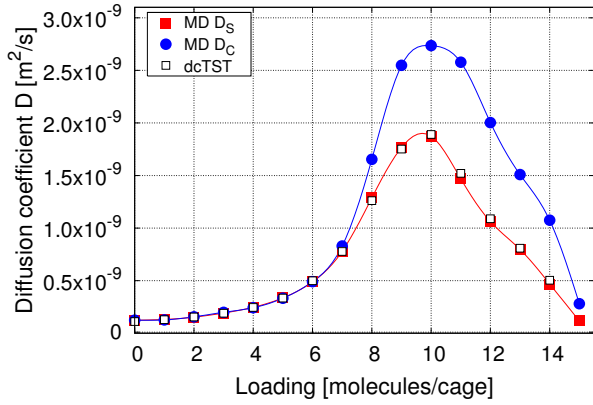


Figure 3: Self-diffusivity D_S and collective diffusivity D_C for methane in LTA-type zeolite at 300K as a function of loading.

assumption of the random walk model is the quick loss of memory of the molecules between consecutive jumps, i.e. a molecule will proceed with a probability independent of its history. The correlation factor f

$$f \equiv 1 + \frac{1}{n} \left\langle \sum_{i=1}^n \sum_{j=1}^n \cos \Delta\phi_{ij} \right\rangle \quad (18)$$

contains *all* memory-effects, arising from ordering and interparticle interactions.

The regular random walk has no “memory” of the previous step when determining the current one. This feature can be applied to a wide range of physical problems, but there are a number of other interesting problems for which this is not the case. In a persistent walk, the transition (or step) probability depends upon the previous transition, and a particle has a retention to the directional over a certain number of trajectory steps. In order for a simplistic regular lattice model to be valid, the loss of memory is an important condition that has to be satisfied.

D Correlations

The collective diffusivity contains all the dynamical correlations. Here, the motion results from the jumps of *different* particles at different times. In contrast, for self-diffusivity the motion results from the

jumps of a *tagged* particle at different times. Memory effects [47, 48] have a tendency to decrease D_S with respect to D_C , indicating it is somehow related to the well-known back-correlation mechanism where a diffusing particle has a higher probability to jump backwards than in any other direction, simply because the originating site is guaranteed to be empty. Most of the memory effect arise from ordering and interparticle interactions, the latter giving the leading contribution. Fig. 3 shows the self- and collective diffusivity of methane in LTA-type zeolite at 300K as a function of loading. In the low loading limit both diffusivities converge, because particle-particle interactions vanish. However, at a loading of 7 molecule per cage or higher the correlations are clearly visible. Although in principle conventional MD captures all relevant correlations, the dcTST method by Beerdsen et al. not only captures these correlations correctly but is also suitable for systems with large free energy barriers [32]. These correlations, originating from particle-particle interactions, are significant at higher loadings as is evidenced by the large difference between collective and self-diffusivity.

Memory effect are stronger on single particle motion than on the collective motion, where most of the back-correlations cancel out. For a Langmuir gas, where the only interaction is the site exclusion, they cancel out *exactly*. Correlations between successive jumps can be studied by considering *directional* correlations between two jumps separated by m previous jumps by a tagged particle. For a Langmuir gas the factor f reduces in the high loading limit to [47]

$$f = \frac{1 + \langle \cos \phi \rangle}{1 - \langle \cos \phi \rangle} \quad (19)$$

as a correlation factor for vacancy diffusion, where ϕ is the angle between two consecutive single particle jumps. This equation assumes that the predominant memory contribution comes from the back-correlation between two consecutive single-

particle jumps ($m = 1$). Eq. 19 is very much related to the end-to-end distance of an isolated, infinitely long, hypothetical model chain comprised of bonds of fixed lengths joined with fixed bend angles [49]. Unlike the freely joined case, the fixing of the angles ϕ imposes correlations.

A particle residing in a lattice point once in a while jumps to a neighboring site. If thermalization occurs we call it a *single jump*, otherwise we speak of a *long jump* or a *multi-jump*. These kinetic correlations become important at low loadings and in channel-type structures with smooth walls, e.g. carbon nanotubes. However, for entropy dominated barriers (e.g. methane and ethane in LTA-type zeolites) one can usually neglect kinetic correlations.

E Dynamically corrected transition state theory (dcTST) at infinite dilution

At infinite dilution and sufficient dissipation the correlation factor $f = 1$ (there are no memory-effects), and Eq. 16 reduces to

$$D = k_i \lambda^2 = k_{AB} \lambda^2 \quad (20)$$

The lattice distance λ is fixed and a property that can be obtained from crystal X-ray-scattering experiments. Therefore, Eq. 20 defines k_i as the hopping rate from lattice point A (in equilibrium) to a neighboring lattice point B (in equilibrium). Note that an attempt of a hop is always successful, and that a particle cannot have a position in between the lattice points, i.e. the jump is instantaneous and discrete. In principle, one could use MD simulations to determine this rate by computing the average residence time that a particle is in a cage. However, such a computation using MD proves cumbersome. Firstly, an A-to-B order parameter has to be defined, secondly, a criteria should be used to distinguish unsuccessful hops on a very short time scale from the successful AB-hop on a much longer time scale (the

equilibrium one), and thirdly, very few trajectories will involve motion from exactly point A to point B.

Dynamically corrected transition state theory overcomes these problems by computing precisely what we need: the hopping rate from lattice point A (in equilibrium) to a neighboring lattice point B (in equilibrium). In other words, dcTST is fully compatible and complementary to lattice random walk theory. We consider a system which can be in two stable states, A and B. The reaction coordinate, a parameter that indicates the progress of the diffusion event from region A to region B, is denoted by q . Here, q is a function of the Cartesian coordinates, \dot{q} denotes its time derivative, q^* is the location of the dividing surface, and q_A, q_B are the minima of the free energy corresponding to state A and B, respectively. In general, the reaction coordinate q is a function of the configuration of the whole system, i.e. $q = q(\mathbf{r}_1, \dots, \mathbf{r}_N)$. However, we can choose q as the position of one of the atoms of the diffusing molecules [25]. We introduce two characteristic functions n_A and n_B that measure whether the system is in state A or B. A possible and often used definition is

$$n_A = \theta(q^* - q), \quad (21)$$

$$n_B = \theta(q - q^*), \quad (22)$$

where θ is the Heaviside function $\theta(x)$, which has value zero for $x < 0$ and value of unity for $x \geq 0$. With these definitions the transition rate $k_{A \rightarrow B}$ is given by [7]

$$k_{A \rightarrow B} = \underbrace{\frac{\langle \delta(q^* - q) \rangle}{\langle \theta(q^* - q) \rangle}}_{P_{\in A}(q^*)} \times \underbrace{\frac{\langle \dot{q}(0) \delta(q^* - q(0)) \theta(q(t) - q^*) \rangle}{\langle \delta(q^* - q(0)) \rangle}}_{R(t)}, \quad (23)$$

where δ is the Dirac delta function, $\langle n_A \rangle$ is the equilibrium mole fraction of particles in state A, $P_{\in A}(q^*)$ is the equilibrium

probability density of finding the system at the top of the barrier divided by the equilibrium probability of finding it at state A , and where $R(t)$ is the averaged particle flux at the top of the barrier multiplied by the probability that the system ends up in state B at time t . From detailed balance follows

$$\frac{k_{A \rightarrow B}}{k_{B \rightarrow A}} = \frac{\langle n_B \rangle}{\langle n_A \rangle} \quad (24)$$

where

$$\langle n_A \rangle = \frac{\int_A e^{-\beta F(q)} dq}{\int_{A+B} e^{-\beta F(q)} dq} \quad (25)$$

$$\langle n_B \rangle = \langle 1 - n_A \rangle \quad (26)$$

The expression Eq. 23 is rigorously correct for arbitrary crossings provided that

- the actual crossing time is negligible compared to the time a particle spends inside the cage, i.e. there is a large separation in time scales. This condition is satisfied when the free energy barrier is much larger than $k_B T$.
- the velocity distribution at the dividing surface is known (The order parameter q is taken to be the position of a particle and therefore \dot{q} is simply the velocity of a particle. In TST it is assumed that the top of the barrier is in equilibrium and hence these velocities follow directly from the Maxwell-Boltzmann distribution).

At infinite dilution the molecules perform a random walk on a lattice spanned by the cage-centers. The transmission rates are easily converted to diffusion coefficients if the jump distance and the number of equivalent diffusion paths are known.

Eq. 23 is a product of a static and a dynamic term

- the probability $P_{\in A}(q^*)$ of finding the system at the top of the barrier is a *time-independent* equilibrium quantity and

can be computed explicitly

$$\begin{aligned} P_{\in A}(q^*) &= \frac{\langle \delta(q^* - q) \rangle}{\langle \theta(q^* - q) \rangle} \\ &= \frac{e^{-\beta F(q^*)}}{\int_{\text{cage A}} e^{-\beta F(q)} dq}, \end{aligned} \quad (27)$$

where $F(q)$ is the free energy as a function of the diffusion path q .

- the flux $R(t)$ through the dividing surface is a conditional average, namely the product $\dot{q}(0)\theta(q(t) - q^*)$, given that $q(0) = q^*$. Using the assumption that the velocities of the atoms follow the Maxwell-Boltzmann distribution, we can estimate from kinetic theory the long time value of $R(t)$ by $\langle \frac{1}{2} |\dot{q}(0)| \rangle = \sqrt{\frac{k_B T}{2\pi m}}$, where m is the mass of the segments of the particle involved in the reaction coordinate (the total mass of the particle if the center of mass is used or the mass of only one segment if the reaction coordinate is a single segment like the middle bead in a molecule). Transition state theory predicts a crossing rate $k_{A \rightarrow B}^{\text{TST}}$ given by

$$k_{A \rightarrow B}^{\text{TST}} = \sqrt{\frac{k_B T}{2\pi m}} \frac{e^{-\beta F(q^*)}}{\int_{\text{cage A}} e^{-\beta F(q)} dq}. \quad (28)$$

Calculating TST rate constants is therefore equivalent to calculating free energy differences.

The TST particle flux estimation $\sqrt{\frac{k_B T}{2\pi m}}$ contains spurious crossings, i.e. some particles that cross the transition state from A in reality would fail to equilibrate in B . The correction $\kappa(t)$ is defined as the ratio between the real rate and the TST expression.

$$\begin{aligned} \kappa(t) &\equiv \frac{k_{A \rightarrow B}(t)}{k_{A \rightarrow B}^{\text{TST}}} \\ &= \frac{\langle \dot{q}(0) \delta(q(0) - q^*) \theta(q(t) - q^*) \rangle}{\langle \frac{1}{2} |\dot{q}(0)| \delta(q(0) - q^*) \rangle}. \end{aligned} \quad (29)$$

It is the probability that a particle that starts with an initial velocity \dot{q} from the dividing surface will, in fact, cross the barrier, and therefore $\kappa(t)$ corrects for trajectories which cross the transition state from A but fail to equilibrate in B. The numerator in Eq. 18 counts trajectories with a positive, but also with a negative weight. It can be shown that $\lim_{t \rightarrow 0^+} \kappa(t) = 1$ and $\lim_{t \rightarrow 0^+} k_{A \rightarrow B}(t) = k_{A \rightarrow B}^{\text{TST}}$. There is a large separation of time scales. The transmissions are completed in a time much less than the time to react, and Eq. 18 will reach a plateau value κ . For classical systems $0 < \kappa \leq 1$ and Eq. 28 is corrected as

$$k_{A \rightarrow B} = \kappa k_{A \rightarrow B}^{\text{TST}}. \quad (30)$$

Standard Molecular Dynamics (MD) yields the transmission coefficients, a separate MC simulation is used to generate the starting configurations. The reaction coordinate is restricted to the dividing surface q^* . The MC moves involved are translations of the reaction bead in the plane of the dividing surface and complete regrowing of the molecule starting from the restricted bead. Subsequently, the transmission coefficient is calculated by standard MD in the NVE ensemble. The beads are given independent velocities, corresponding on average to the desired temperature, by sampling from the Maxwell-Boltzmann distribution.

In the Bennett-Chandler approach it is sufficient to assign the barrier position q^* inside the barrier region. The result of the scheme does not depend on the specific location, although the statistical accuracy does. If the dividing surface is not at the top of the barrier the probability of finding a particle will be higher than at the optimal q^* , but the fraction of the particles that actually cross the barrier will be less than predicted by transition state theory.

F Importance-sampled MD at infinite dilution

The approach of $\kappa(t)$ to its plateau value can be quite slow [7]. Moreover, in the case of diffusive barrier crossings the transmission coefficient is quite small and as a consequence many trajectories have to be generated for an accurate value of κ . The Bennett-Chandler approach becomes inefficient for systems with low transmission coefficients because the scheme employs the noisy θ -function to detect what state the system is in [50]. The scheme can be improved by constructing a more continuous detection function. More importantly, using the free energy we can compensate approximately for the effect of the free energy barrier. This leads to a more or less uniform tagged-particle density distribution over the entire range of q . However, only trajectories starting in the barrier region yield relevant information and therefore a weighting function $w(q)$ is applied, restricting the sampling to the barrier region.

A general expression from transition state theory for the rate of hopping from region A to region B over a barrier is [7]:

$$k_{A \rightarrow B} = - \left\langle \dot{q}(0) n_A(t) \frac{\partial \chi(q(0))}{\partial q} \right\rangle \quad (31)$$

where $\chi(q)$ is a dimensionless function describing the initial distribution function

$$\rho(q, t=0) = \rho_{\text{eq}}(q) \chi(q) \quad (32)$$

The initial distribution $\chi(q)$ can be approximated well by the steady-state distribution determined from the Fokker-Planck equation

$$\chi(q) = \frac{1}{\langle n_A \rangle} \left[1 - \frac{\int_{q_A}^q e^{\beta F(q')} dq'}{\int_{q_A}^{q_B} e^{\beta F(q')} dq'} \right] \quad (33)$$

and varies rapidly with q in the barrier region and slowly elsewhere, so that $\chi'(q)$ se-

lects initial configurations in the barrier region

$$\frac{\partial \chi(q)}{\partial q} = -\frac{1}{\langle n_A \rangle} \frac{e^{\beta F(q)}}{\int_{q_A}^{q_B} e^{\beta F(q)} dq} \quad (34)$$

We choose

$$n_A(q) = 1 - \frac{\int_{q_A}^q e^{(a-1)\beta F(q')} dq'}{\int_{q_A}^{q_B} e^{(a-1)\beta F(q')} dq'} \quad (35)$$

$$w(q) = e^{a\beta F(q)} \quad (36)$$

$$\pi(q) \propto e^{(a-1)\beta F(q)} \quad (37)$$

where $a > 0$ is a biasing parameter, leading to

$$k_{A \rightarrow B} = \frac{1}{\langle n_A \rangle} \frac{\left\langle \int_0^\infty \dot{q}(t) \dot{q}(0) \frac{w(q(t)) e^{-\beta F(q(t))}}{w(q(0)) e^{-\beta F(q(0))}} dt \right\rangle_\pi}{\int_{q_A}^{q_B} e^{\beta F(q)} dq \int_{-\infty}^\infty e^{-\beta F(q)} dq} \quad (38)$$

Although Eq. 38 can be considered a TST method using a more continuous "detector" function than the noisy θ -function, it can also be viewed as an MD method in a different, more convenient ensemble $\pi(q) \propto w(q)e^{-\beta F(q)}$. Starting configurations are sampled in the π -ensemble and subsequently a weighted velocity autocorrelation is computed. Note that the dynamics is still generated using the microcanonical ensemble (conventional MD). Importance-sampled MD is especially applicable to systems with erratic free energy landscapes, e.g. multiple barriers of possibly different heights.

G Dynamically corrected transition state theory at nonzero loading

The extension of dcTST to finite loading is nontrivial. Conventional methods use a hierarchical approach to compute elementary hopping rates $k_{A \rightarrow B}^{\text{iso}}$ between *isolated* cages A and B for use in a subsequent kMC scheme to obtain diffusion coefficients. However, the fundamental question is whether it is *possible* to compute an

elementary hopping rate $k_{A \rightarrow B}^{\text{iso}}$, in which the contributions of other cages are separated from the contribution of only the cages A and B. Let us consider the class of window/cage-type systems (e.g. methane in LTA) where the barriers are *entropical* in nature. At nonzero loading a molecule hopping from A to B induces a vacancy. While in principle a particle originating from any of the surrounding cages could fill the vacancy, hierarchical approaches will allow only a molecule from B to return to A (e.g. by blocking all windows except the window between cages A and B). The fundamental assumption of kMC (no two jumps can occur at the same time) artificially suppresses these correlated jumps, and we are not aware of a scheme that result in effective kMC hopping rates that regain those correlations.

Beerdse et al. [32] proposed a method to compute diffusivity values directly in systems with high free energy barriers (e.g. cage/window-type zeolites). Here, long time, large distance memory effects are negligible, because once a molecule jumps thermal equilibration takes place and next-nearest cage correlations are rare. It is therefore sufficient to include correlations *during* the jump across the barrier. Hence, we compute

$$D(c) = \frac{1}{6} k_{A \rightarrow B}^{\text{eff}}(c) \lambda^2 \quad (39)$$

$$k_{A \rightarrow B}^{\text{eff}}(c) = f(c) k_{A \rightarrow B}(c) \quad (40)$$

where c denotes the loading in molecules per unit cell, or mol/kg. But rather than attempting to compute $k_{A \rightarrow B}(c=0)$ or $k_{A \rightarrow B}^{\text{iso}}$ from a molecular simulation and the correlation factor $f(c)$ from a coarse-grained kinetic Monte-Carlo method, Beerdse et al. compute $k_{A \rightarrow B}^{\text{eff}}(c)$ *directly* from a molecular simulation.

$k_{A \rightarrow B}^{\text{eff}}(c)$ is the hopping rate of a single tagged particle at an average loading c from cage A to cage B under the influence of an external field exerted caused by the

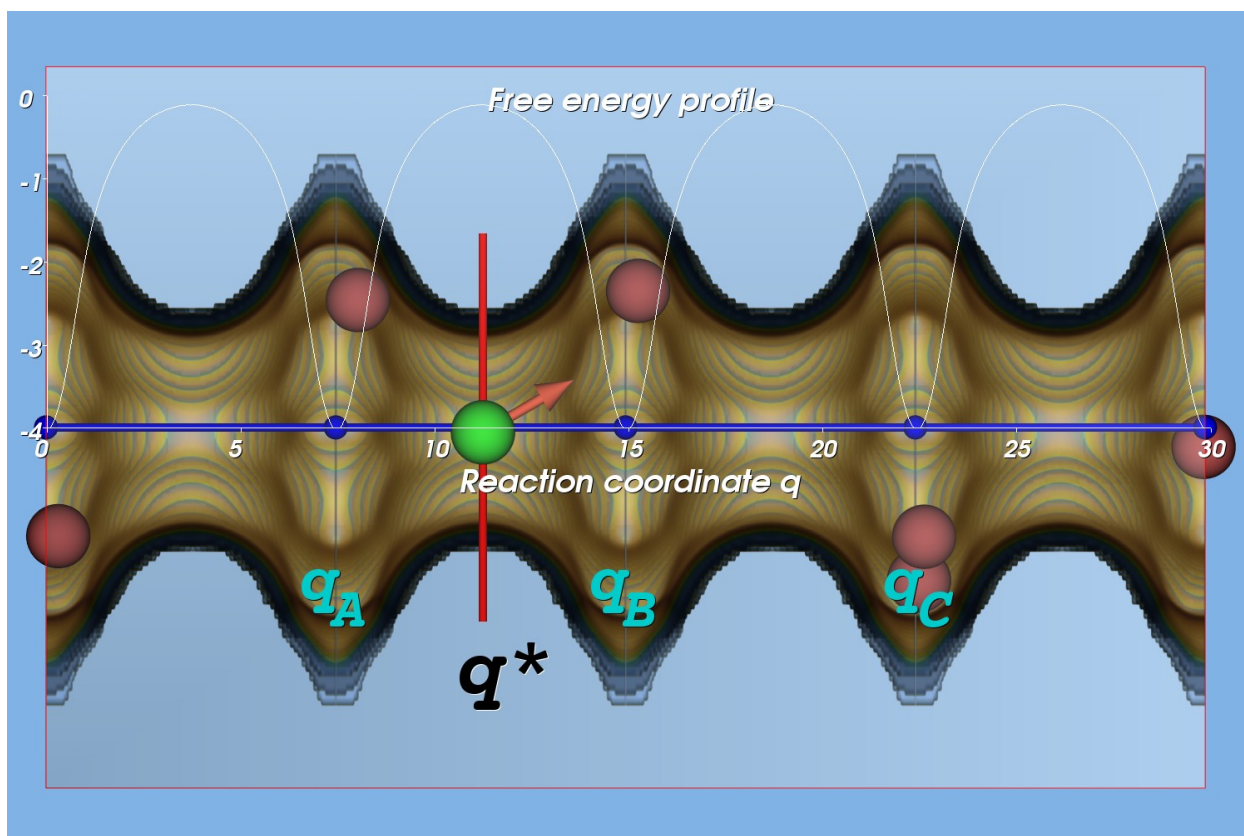


Figure 4: A typical snapshot of a tagged methane particle (green color) in LTL-type zeolite restrained to the barrier q^* surface at an average loading of 3 methane molecules per unit cell (there are two parallel channels per unit cell) at 300K. Four unit cells of 7.474 \AA in length are shown. The constrictions are caused by the 12-T-membered rings, which form free energy barriers impeding diffusion. The free energy profile in dimensionless units at this average loading is plotted in white, where the reaction coordinate is chosen parallel to the channel direction. If the free energy barriers are high enough, diffusion can be considered a hopping process from minima (q_A , q_B , q_C etc).

molecular sieve and the other $N - 1$ particles.

By including the nearest neighboring cages, all relevant short-time correlations are properly captured, including the dominant short-time back-correlation effects due to particle-particle interactions. Correlations at much longer times than $1/k$ are negligible in cage/window-type systems. The computation once again consists of two parts

- The probability density $P_{\in A}(q^*)$ of finding the system at the top can be computed explicitly by computing free energy profiles making use of Eq. 27. During an separate MC simulation in

the NVT-ensemble at the desired loading we measure the free energy $F(q)$ by using Histogram Sampling (HS). In the HS method, a histogram is made of the particle positions, mapped on the reaction coordinate. From the histogram a free energy profile is computed, by using

$$\beta F(q) = -\ln \langle P(q) \rangle. \quad (41)$$

At conditions where conventional MC is still feasible, all particles can be considered equivalent and all contributions can be used.

When displacement of particles is impeded by high free energy barriers, conventional HS becomes infeasible. A

single tagged particle can be biased to achieve improved statistics by using importance sampling. As a biasing potential the Widom Particle Insertion (WPI) profile can be used. WPI uses a probe particle that is inserted at random positions, to measure the energy required for or obtained by insertion of the particle in the system. This energy is mapped onto the reaction coordinate q , using

$$\beta F(q) = -\ln \langle e^{-\beta \Delta U} \rangle_N, \quad (42)$$

to produce a free energy profile, where $\langle e^{-\beta \Delta U} \rangle_N$ is the average Boltzmann factor over all positions in the slice perpendicular to the reaction coordinate. A "ghost particle" is used as the measuring probe, but the other particles in the system do not feel its presence. At higher loadings, WPI is known to give erroneous results [1, 32] and therefore the WPI method is not used to compute $F(q)$ directly, but rather to estimate the biasing function when needed.

- The particle flux $R(t)$ through the dividing surface can be computed from the fraction of particles starting on top of the barrier that successfully reach cage B. The other particles present in the system influence this fraction. Starting configurations are generated with one particle constrained to the dividing surface and $N - 1$ particles moving around (see Figs. 4 and 5). These configurations are then used to compute the particle flux in unconstrained NVE-MD simulations, starting with velocities sampled from a Maxwell-Boltzmann distribution at the desired temperature.

In Fig. 4 an instructive snapshot of methane in LTL-type zeolite at a loading of 3 molecules per unit cell at 300K is shown. The free energy profile consists of maxima, corresponding to geometric constrictions,

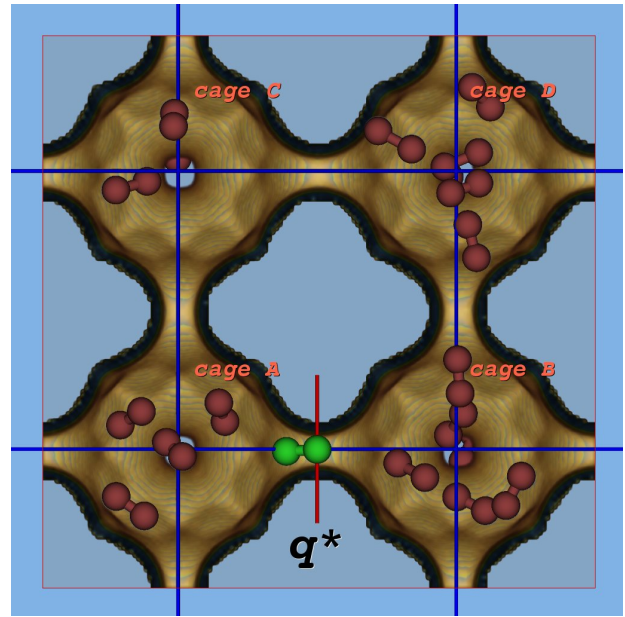


Figure 5: A typical snapshot of ethane ($\text{CH}_3 - \text{CH}_3$) in LTA-type zeolite at an average loading of 4 molecules per cage at 750K, constraining one tagged molecule at the dividing surface q^* . The hopping events are coarse-grained on a lattice spanned by the cage-centers.

and minima, corresponding to the apertures. A natural hopping lattice is formed by the one-dimensional sequences of free energy minima (q_A, q_B, q_C , etc). As can be seen from this snapshot, there are strong adsorption-sites where the curvature of the zeolite is the highest and commensurate with the shape of the particle. Particles reside in these minima for a long time, before a thermal excitation will eventually give the particles enough mobility to cross the free energy barrier and proceed to a neighboring lattice site. The latter process is a *fast* process in comparison to the time a particle spends near the lattice points.

Fig. 5 shows a snapshot of ethane at an average loading of 4 molecules per cage at 750 K in LTA-type zeolite. The lattice, formed by the cage centers, is the three-dimensional cubic lattice. For this snapshot cage B contains more molecules than cage A, and the barrier-molecule has a high probability of recrossing to cage A. The time-dependent transmission coeffi-

cient will reach a plateau value κ . However, because during a successful hop cage A donated a particle, while cage B received an additional particle, there is a slightly higher probability for the particle to return to A on a time scale *larger* than the thermalization time. However, for our systems this effect is negligible. Note that during the computation none of the windows is blocked and simultaneous jumps (e.g. from cage C to cage A , and cage D to cage B) are allowed.

The extension of the importance-sampled MD method Eq. 38 to non-zero loading is similar. The method can be summarized as follows.

- The free energy profiles at the desired average loading are measured as described above.
- The free energy minima q_A and q_B , and the corresponding hopping lattice are identified.
- A biasing profile $w(q)$ is constructed ranging from q_A to q_B using Eq. 36.
- Starting configurations are sampled in the interval q_A to q_B with the bias potential $w(q)$ operating on the tagged particle, leaving the others $N - 1$ free to move (unbiased).
- These starting configurations of N particles are integrated using MD for short times t_{\max} , and Eq. 38 is evaluated. The time t_{\max} is chosen such that the integral appearing in Eq. 38 has converged. The trajectories are stopped after t_{\max} time has elapsed or when $q < q_A$ or when $q > q_B$.

As mentioned, in general, the reaction coordinate q is a function of the configuration of the whole system. For dcTST simulations at a certain loading, we choose the reaction coordinate as the position of one of the atoms of the *tagged* molecule [32]. Although it can not be excluded that better reaction coordinates exists, for physical reasons our

choice seems optimal. The diffusion mechanism is divided in two parts. The first is a static term, corresponding to locations of preferable adsorption sites and estimations of free energy barriers in between, the latter (or actually the inverse of the transmission coefficient: the recrossing) corresponds to collision frequencies, which generally increase with loading. As such the dcTST method is able to explain different diffusion regimes over loading, and provides insight into the mechanisms behind an increase or decrease in diffusivity with loading [51].

H Zeolite descriptions and simulation details

To test and explore the limits of our dcTST method, we have selected two types of zeolites: the one-dimensional channel LTL-type zeolite structure and three-dimensional cage/window LTA-type zeolite structure. The LTA-type zeolite is selected because diffusion is slow, but just fast enough for the smallest alkanes to allow for a comparison of dcTST with MD. Here, dcTST is expected to work flawlessly. In LTL-type zeolite the diffusion is relatively fast, the free energy barriers low, and the system is close to the limits of TST, i.e. in this system it is more difficult to envision a clear separation of time scales. Moreover, the system is one-dimensional and correlations between diffusing particles are even higher.

LTL-type zeolites are used industrially for the aromatization of alkanes. The structure [52] has spacegroup P_6/mmm with $a = 1.84, b = 1.84, c = 0.752$ nm, and $\alpha = \beta = 90, \gamma = 120$. For computational efficiency the unit cell is converted to a rectangular cell. LTL-type zeolite provides a pore system having cancrinite cages (11-hedra) alternating with hexagonal prisms (8-hedra) stacked in columns parallel to the c -axis. The channels thus formed have nearly planar 12-membered rings with a free diameter of approximately 0.71 nm and expansions

LTL			LTA		
molec./uc	unit cells	N	molec./cage	unit cells	N
1	1x2x128	256	1	2x2x2	64
2	1x2x64	256	2	2x2x2	128
3	1x2x64	384	3	2x2x2	192
4	1x2x32	256	4	2x2x2	256
5	1x2x32	320	5	2x2x2	320
6	1x2x32	384	6	2x2x2	384
7	1x2x16	224	7	2x2x2	448
8	1x2x16	256	8	1x1x1	64
9	1x2x16	288	9	1x1x1	72
10	1x2x16	320	10	1x1x1	80
11	1x2x16	352	11	1x1x1	88
12	1x2x16	384	12	1x1x1	96
13	1x2x16	416	13	1x1x1	104
14	1x2x16	448	14	1x1x1	112
15	1x2x16	480	15	1x1x1	120
16	1x2x16	512	16	1x1x1	128
density [kg/m ³]					
1626.94			1285.228		
unit cell sizes [nm]			unit cell angles [°]		
x	y	z	α	β	γ
3.1984	1.8466	0.7476	90	90	90
2.4555	2.4555	2.4555	90	90	90

Table 3: Simulation details for the LTL- and LTA-type zeolite. Crystallographic positions are taken from Refs. [52, 53]. A single unit cell of LTL-type zeolite contains 2 channels, a single unit cell of LTA-type zeolite consists of 8 α -cages. Simulation of one-dimensional channels requires special attention. Here, diffusion results are very much dependent on the length of the channel, and surprisingly long channels are needed to reliably extrapolate to macroscopic diffusion coefficients [54].

of approximately 0.126 nm (see Fig. 4).

The single largest use of zeolites is the use of LTA-type zeolites for laundry detergents. LTA-type zeolite is also used for separations of small molecules from air by exploiting different polarities of molecules, and for bulk separations of linear and branched alkanes. The LTA-type structure [53] has a cubic spacegroup $Fm\bar{3}c$ with $a = b = c = 2.4555$ nm, and $\alpha = \beta = \gamma = 90^\circ$. The crystallographic unit cell consists of 8 large spherical cages (named α -cages) of approximately 1.12 nm interconnected via windows of about 0.41 nm diameter (see Fig. 5).

In addition to the relevant cages and channels there are also topologically disconnected pockets. A methane molecule does fit at that position, but it is not accessible from the main cages and channels. Both LTA (sodalite-cages), as well as LTL, have disconnected pockets. To obtain correct results in MC-simulations it is necessary to ensure that molecules will not be inserted into inaccessible pockets for adsorbing molecules.

We have summarized the details of our periodic simulation boxes in Table 3. Simulation of one-dimensional channels requires special attention. Here, diffusion results

are very much dependent on the length of the channel, and surprisingly long channels are needed to reliably extrapolate to macroscopic diffusion coefficients [54].

III Results

A Infinite dilution

methane, ethane, and propane in LTL-zeolite

Fig. 6 shows the free energy profiles $F(q)$ of methane along the channel direction. Two free energy minima are separated by a 12-ring forming the free energy barrier at q^* . For this system and the chosen reaction coordinate, the transmission coefficient is nearly equal to one, and the dcTST diffusion can be directly computed using Eq. 20 and Eq. 28. The free energy barrier ranges from about $10 k_B T$ at 100K to less than $3 k_B T$ at 1000K.

The transmission coefficient can only be assumed equal to one for a single, spherical particle providing the exact barrier is known, and only at infinite dilution. Even for methane in LTL the barrier is only known approximately because of the atomic structure of the window, although the value is very close to one using the window as the dividing surface. In Fig. 7 the transmission coefficient $\kappa(t)$ for propane using the second/middle-bead as the reaction coordinate is shown as a function of time for various temperatures. The starting configurations are sampled using a Monte-Carlo scheme at the desired temperature restricting the growing bead at the dividing surface. This distribution of configurations is temperature dependent, and also the transmission coefficient is temperature dependent. In general, the transmission coefficient increases with temperature, because a higher fraction of configurations has sufficient kinetic energy to overcome the free energy part resulting from a non-optimal reaction coordinate and dividing

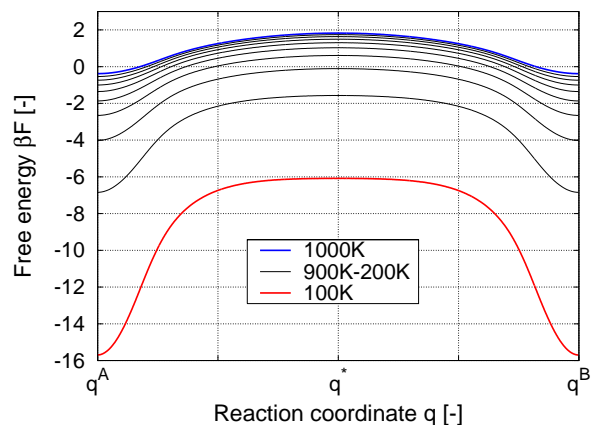


Figure 6: Free energy profiles $F(q)$ of methane in LTL at various temperatures (100K to 1000K in steps of 100K) and infinite dilution. The reaction coordinate is chosen along the z-channel direction (lines from top to bottom in order of the legend).

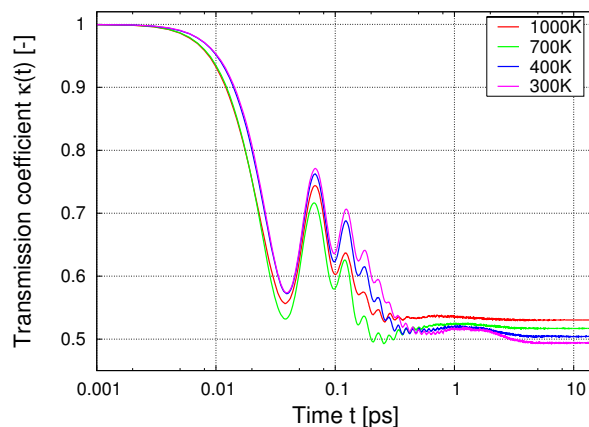


Figure 7: Transmission coefficient $\kappa(t)$ for propane in LTL-type zeolite at infinite dilution using the second/middle-bead as a function of time for various temperatures.

surface choice. The transmission coefficient starts at one (by definition, because a particle cannot revert its velocity within a single integration step), and slowly converges to a limiting plateau value at about 15 ps. It is this plateau value κ that is of interest, signaling all short-time recrossing are eliminated. The intermediate oscillatory behavior is caused by the bond-springs within the molecule itself. From the point of view of the reaction coordinate (the position of the second/middle-bead), the other beads connected to the middle-bead with springs are

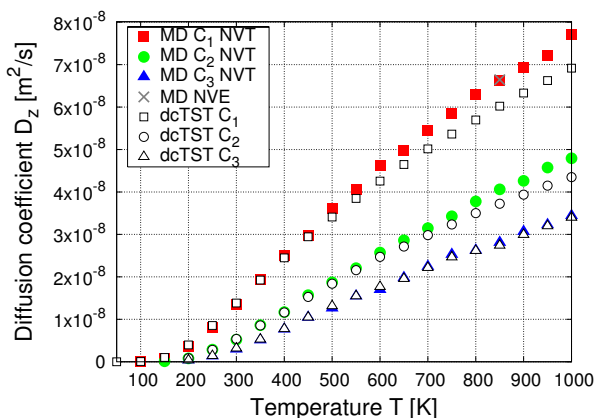


Figure 8: Diffusion of methane, ethane, and propane in LTL-type zeolite at infinite dilution computed by dcTST and MD.

just an external field in addition to the zeolite.

The transmission rates can be computed from the free energy profiles using Eq. 28, 30, and transmission coefficients, and then converted to diffusion coefficients using Eq. 20. The methane, ethane, and propane diffusivities computed from dcTST are compared to reference MD simulations in Fig. 8. The MD simulations were performed in the NVE and NVT ensembles (NHC thermostat) with 128 non-interacting particles. For methane, up to 450K dcTST gives equivalent results to MD, but at higher temperatures the methods diverge. For ethane, the methods diverge at 550K, while for propane both methods overlap. Where the methods diverge, the free energy barriers become too low for TST to be valid, because there is no longer a clear separation of time scales. The methane molecules do not equilibrate properly leading to enhanced diffusion due to kinetic correlations, i.e. the increased probability of particles to continue in their current direction.

There are several ways to include kinetic correlations, amongst them are the dynamical corrections as formulated by Voter and Doll [55] using multistate systems and the recently proposed Ruiz-Montero method (Eq. 38 with $a = 2$) [7]. The method of Voter and Doll would extend the two-state

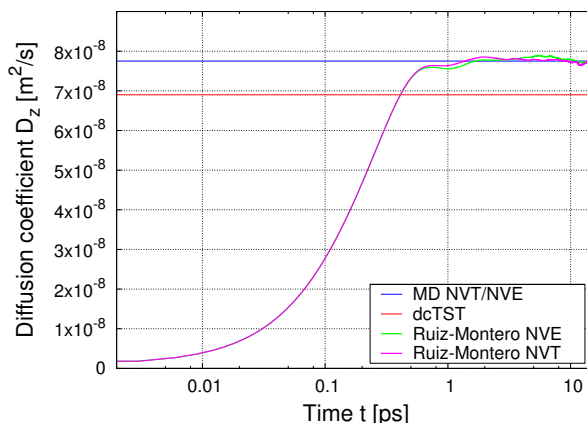


Figure 9: Diffusion of methane at 1000K in LTL-type zeolite at infinite dilution computed by dcTST and MD compared to the Ruiz-Montero method.

system A and B , to a multistate system A, B, C, D, \dots by computing the hopping rates k_{ij} , dynamical corrections κ_{ij} , and lattice distances λ_{ij} between state i and j . Note that the dynamical correction in this formulation is not restricted between 0 and 1, but can potentially increase beyond unity when kinetic correlations are abundant. However, at the highest temperatures reported here, the time scales of thermalization and k^{-1} become inseparable, so we pursue here the alternative Ruiz-Montero route. Fig. 9 shows the Ruiz-Montero method ($a = 2$) at 1000K for methane in LTL-type zeolite. The Eq. 38 is reaching a plateau value in time, equal to the MD-results. These results differ from the dcTST value due to presence of kinetic directional correlations, which are included using (importance-sampled) MD-methods. However, computing Eq. 38 is very time consuming and the dcTST method is preferable for cage/window-type systems with higher free energy barriers.

methane in LTA-type zeolite

At infinite dilution, the barrier for diffusion of methane in LTA-type zeolite at 300K is much higher than in LTL-type zeolite. The barrier is approximately $8.5 k_B T$ and

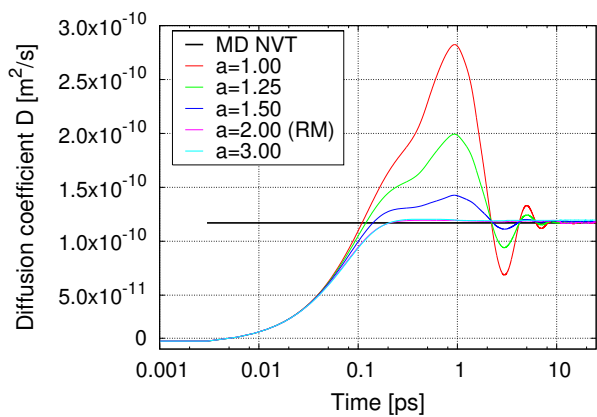


Figure 10: Diffusion of methane over a high free energy barrier in LTA-type zeolite at 300K and infinite dilution using various biasing functions (Eq. 43).

sharply peaked). In Fig. 10 we compare various biasing functions for the importance-sampled MD method. A biasing weighting function of

$$w(q) = \frac{e^{a\beta F(q)}}{\int e^{a\beta F(q)} dq} \quad (43)$$

using $a = 1$ flattens the free energy landscape and the initial configurations are sampled uniformly. However, for diffusion only the configurations in the barrier region yield relevant information, and with $a \gg 1$ as a biasing function the configurations are indeed restricted to the barrier regions, and all trajectories contribute significantly to the diffusion coefficient. The results show that for sharply peaked barriers a high biasing function achieves fast convergence. For these barriers the Bennett-Chandler method works well, because diffusive behavior is negligible and dynamic corrections are easily evaluated. However, the importance-sampled MD method is also applicable in the diffusive regime where $\kappa \ll 1$.

ethane in LTA-type zeolite

Ethane molecules in LTA perform jumps on a simple cubic lattice. It was found that self-diffusion *decreases* with increasing tempera-

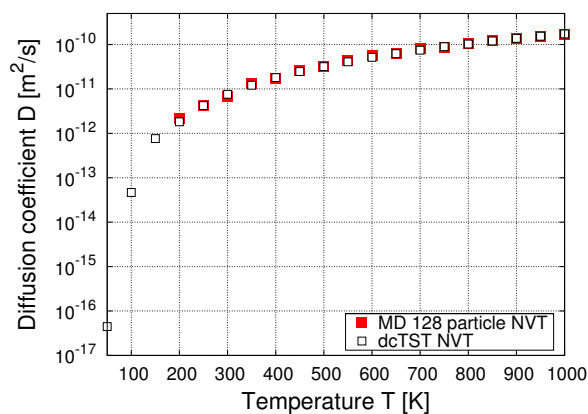


Figure 11: Self-diffusion of ethane at infinite dilution in LTA-type silica using the parameter set of Dubbeldam et al. The infinite dilution case using MD is simulated by switching the ethane intermolecular forces off, i.e. the particles do not interact (except through the thermostat in NHC-NVT simulations).

ture at low temperatures [24]. At low temperatures the molecules become less confined in the windows as temperature increases. Heating the system, ethane moves away from the windows, which increases the entropic barrier for cage-to-cage motion. Fig. 11 shows that the behavior found by Schüring et al. [24] is strongly dependent on the parameter set (Tables 3 and 2). The parameter set of Dubbeldam et al. [38] does not show a decrease with increasing temperature although for both parameters sets the local activation energy depend on temperature. The size-parameter used by Schüring et al. is so small that ethane at low temperature is found *in* the windows itself, and heating shifts the adsorption sites to just in front of the windows. In contrast, the set of Dubbeldam et al. has a larger size-parameter for ethane and also at low temperature the adsorption sites are always in front of window, reducing the behavior found by Schüring et al. However, the phenomenon is likely to be generic and present in cage/window-type systems and applicable to small molecules. It shows how much the actual adsorption sites can depend on temperature and simulation parameters.

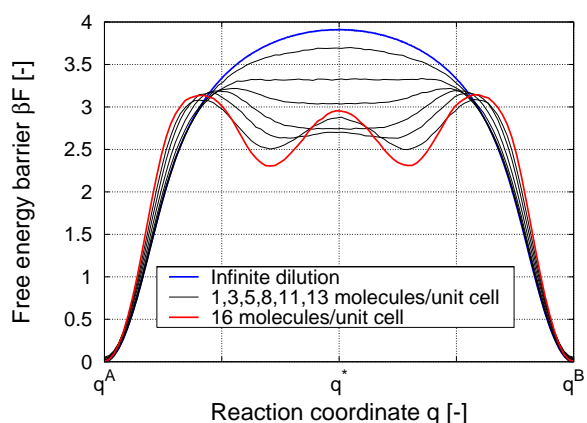


Figure 12: Free energy profiles $F(q)$ at 300K of methane in LTL at various loadings (infinite dilution, 1, 3, 5, 8, 11, 13, and 16 molecules per unit cell). The reaction coordinate is chosen along the z -channel direction (lines from top to bottom in order of the legend).

B Non-zero loading

methane, ethane, propane in LTL-type zeolite

The free energy barriers for various loadings of methane in LTL-type zeolite are plotted in Fig. 12. In comparison to the infinite dilution case, the free energy barrier initially decreases. Adding particles to the system induces an effectively “smoother” channel. For increasing loadings the top of the barrier flattens and eventually transforms into a barrier region with two local free energy minima.

Fig. 13 shows the diffusion behavior as a function of loading in LTL-type zeolite for methane, ethane, and propane at 300K. The TST diffusivities based on the free energy profiles (e.g. for methane shown in Fig. 12) increase, while the dcTST values decrease and are equal to the conventional MD results. Clearly the transmission coefficient not only quantitatively, but also qualitatively, correct the TST results. The good agreement between dcTST and MD for LTL-type zeolites is encouraging. The diffusion of alkanes in LTL-type zeolite is quite fast, and the fact that our dcTST method also works for such low free energy barriers as

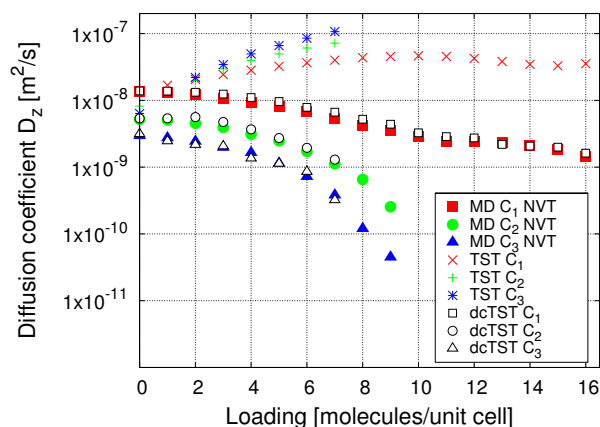


Figure 13: Diffusion of methane, ethane, and propane at 300K as a function of loading in LTL-type zeolite computed by TST, dcTST and MD.

in LTL-type zeolite is surprising.

Although this region of diffusion is fully accessible to conventional MD, the dcTST method has a very important advantage: it enables us to explain the qualitative behavior of diffusion in terms of free energy difference and transmission coefficients. For example, initially the diffusion of methane in LTL-type zeolite does not change much with loading. The MD results would suggest the fundamental reason could be that particles hardly notice each other at these lower loadings. However, the picture painted by the dcTST is quite different. There are two effects: 1) the free energy barrier decreases over loading (which means an increase in diffusion) rendering the channel environment more “uniform”, and 2) as loading increases the transmission coefficient decreases due to an increased collision frequency. At low loading the two effects almost counterbalance each other, but at higher loadings the rapid increase in collision frequency wins.

An important observation made by Beerdsen et al. [51] is that the appearance of the two local minima on top of the free energy barrier at around 11 molecules per unit cell for methane cause an inflection at the corresponding loading in the diffusion curves. This inflection is similarly found in the adsorption isotherms,

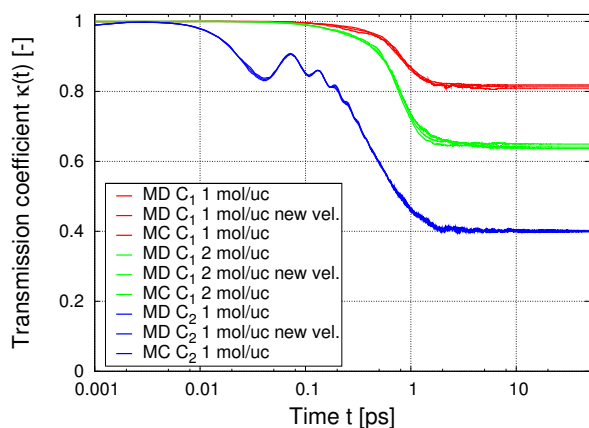


Figure 14: Transmission coefficient $\kappa(t)$ at 300K for methane and ethane in LTL-type zeolite using the first-bead as a function of time for various loadings. The starting configurations are sampled with MC or with MD, where the velocities are either taken from the trajectory or newly resampled from the Maxwell-Boltzmann distribution. The differences are negligible.

and both are related to a change in packing. They show that the dcTST method can generally be used to qualitatively explain the self and collective diffusion behavior of a molecule/zeolite-combination as a function of loading, by carefully analyzing the change in free energy (packing effects).

The appearance of extra adsorption sites over loading, and the change of packing, shows that the choice of the random walk lattice can not solely be based on a lattice of adsorption sites at low loading. The adsorption-site lattice needed to describe diffusion over adsorption sites depends on the zeolite, the guest, the temperature, *and* on the loading of the zeolite. In fact, for every zeolite, guest, temperature, and loading the lattice should be reconstructed. However, for very slow diffusion in cage/window-type zeolites the rate determining step is the cage-to-cage motion and all the details of intra-cage diffusion are present in the free energy profile. For very fast diffusion the adsorption-site lattice does not make sense either as there is too much correlation present between the hops at such a lattice, i.e. the separation of

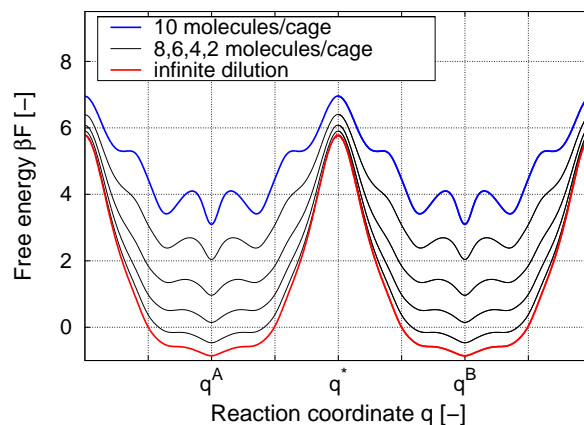
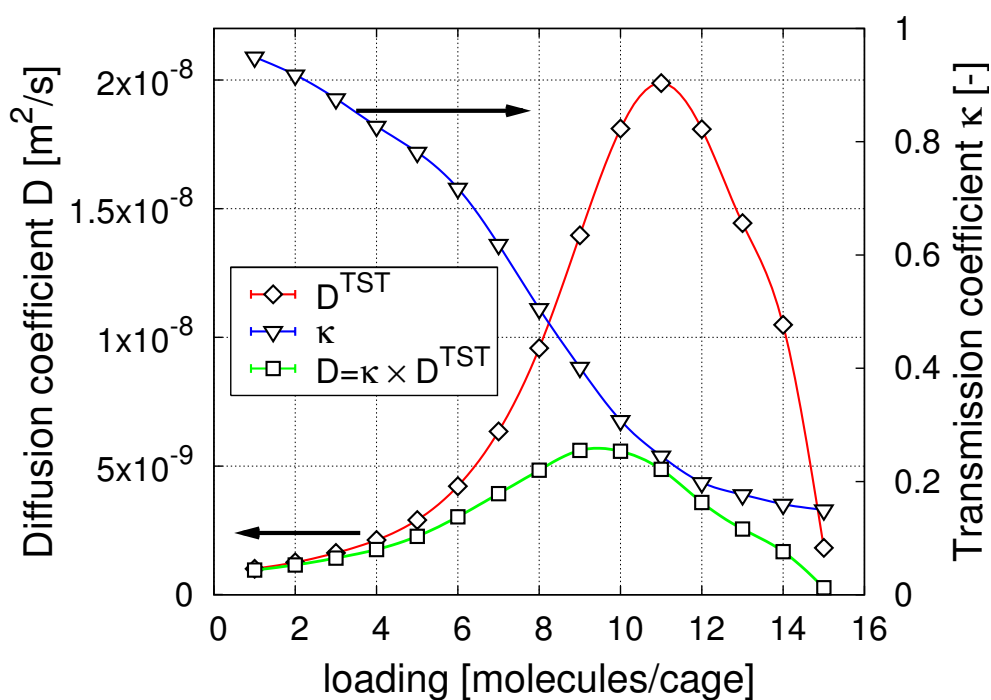


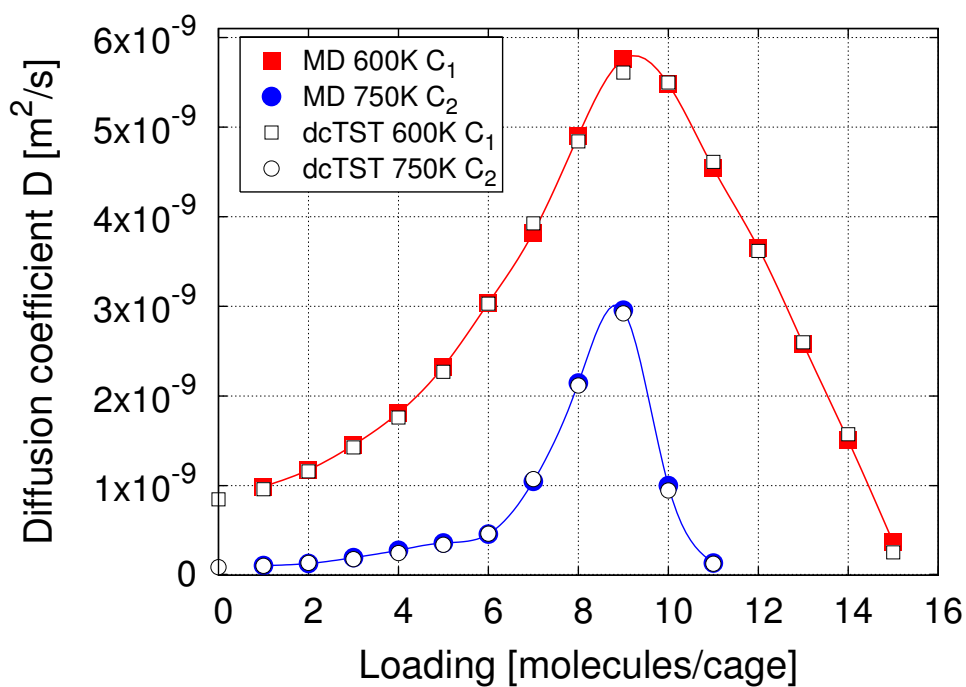
Figure 15: Free energy profiles of methane in LTA-type zeolite at 600K for various loadings (10, 8, 6, 4, 2 molecules per cage, and infinite dilution).

time scales vanishes and the description as "hopping" breaks down. The natural lattice to use would be an effective lattice of cage-center to cage-center.

For zeolites accessible to conventional MD the free energy can be obtained using either MC or MD, and we found no differences between both methods. In contrast, the sampling of configurations with a tagged particle restricted to the dividing barrier surface requires more thought. In Fig. 14 we show results for the transmission coefficients using MC and MD. The MD results are splitted in two types: 1) both the positions and velocities are stored, and 2) only the positions are taken from MD trajectories, the velocities are resampled from a Maxwell-Boltzmann distribution. As can be seen, reinitializing the velocities holds equal results, and one can conclude from the result that the velocities in this system are indeed Maxwell-Boltzmann distributed, even *on top* of the barrier. For systems with higher free energy barriers configurations are adequately sampled with biased MC, while conventional MD would become impossible.



(a)



(b)

Figure 16: *dcTST and MD in LTA-type zeolite a) the TST, and dcTST diffusivities for methane at 600K as a function of loading using the left axis, and the transmission coefficient κ using the right axis, b) diffusion of methane and ethane in LTA-type zeolite, as a function of loading, at 600K and 750K, respectively.*

methane, ethane in LTA-type zeolite

Fig. 15 shows the free energy profiles at 600K for methane in LTA-type zeolite for various loadings. Relative to the infinite dilution case, the addition of particles to the cages leads to an increase of the free energy inside the cage, while the free energy at the barrier remains unchanged up to intermediate loading. The inner-cage surface of LTA-type zeolite is adsorbophylic (wetting regime), and upon increased adsorption favorable adsorbate-adsorbent interactions are being replaced by less favorable interaction with other particles.

Fig. 16(a) shows the individual components of the diffusion process, D^{TST} and κ as a function of loading for methane in LTA. Although the transmission coefficient shows a monotonic decrease with density, the diffusion coefficient goes through a maximum. The driving force behind the initial increase in diffusion is a loss of guest-host attraction inside the cages. Eventually, the free energy barrier increases again, due to packing and free-volume effects, causing a decrease of the diffusion coefficient. While the transmission coefficient only slightly changes the qualitative behavior of the diffusion as a function of loading, it has a profound quantitative influence. We show the diffusion in LTA of methane at 600K and ethane at 750K using both MD and extended dcTST. Our extended dcTST method and MD again agree quantitatively.

methane/ethane-mixture in LTA-type zeolite

In Fig. 17 we plotted the results for a 50%-50% mixture of methane and ethane in LTA-type zeolite, as a function of loading at 300K. For each of the components the free energy and transmission coefficients are computed. For the κ -computation a single molecule of the component is restricted to the barrier, while the other molecules of the same component, and all molecules of the

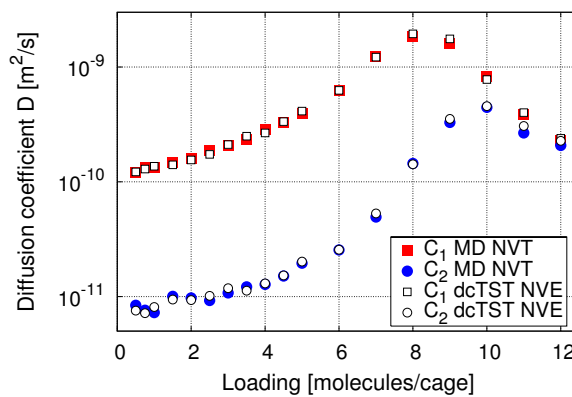


Figure 17: Self-diffusion in a 50%-50% mixture of methane and ethane in LTA-type zeolite, as a function of loading at 300K.

other component are free to move. Again, our extended dcTST method and MD agree quantitatively.

IV Discussion

We have shown that our method is applicable to simulating self-diffusion in any elementary topology. The extension of Eq. 16 to more complex structures and lattices is a geometric exercise to be published elsewhere [56]. The connection between the random walk lattice and the zeolite structure is found by an analysis of the free energy profiles. The diffusion of a tagged molecule is computed over that typical length scale given by the smallest repeating zeolite-structure, i.e. from the center of cage A to the center of cage B . One automatically averages over all adsorption sites in the cage, irrespective whether the adsorption sites are strong or weak, or even ill-defined, i.e. for purely entropic barriers. For most lattices the equivalent of Eq. 16 has been worked out. Since the lattice is not based on specific adsorption sites, often the same lattice can be used for all temperatures and loadings, although sometimes at high loadings new barriers may be formed.

Tunca and Ford [28–30] computed elementary hopping rates using multidimen-

sional TST for use in a subsequent coarse-grained kinetic Monte Carlo (kMC) scheme. Besides the various approximation to make the computation tractable, this approach relies on the computation of an *elementary* hopping rate. The fundamental question about hierarchical approaches is “Is it possible to compute an elementary hopping rate?”. In our calculations, we have observed that to obtain agreement with MD results, one cannot limit the free energy calculation to the two cages A and B for which the hopping is computed. It is essential to average over fluctuations in the number of particles in the neighboring cages [32]. By ‘closing off’ cages, the system is intrusively changed and we are not aware of any other scheme that can separate the contributions of other cages from the contribution of only the cages A and B. The omitted correlations are not the same as those regained by a kMC simulation later and therefore further corrections are needed to obtain results in exact agreement with MD.

We explicitly avoid the use of kMC and compute the self-diffusion coefficient directly. The diffusion constant we compute is the self-diffusion of a tagged molecule traveling from cage A to cage B considering all other particles as an external field. The external field is maintained by an MC NVT simulation (fixed total number of particles, volume, and temperature) of spectator molecules in the “background”. By using an MC approach that includes translational, orientational and regrow moves, we average over cage distributions, positions and orientations of neighboring molecules. This renders it unnecessary to sample the complete phase space by integrating over all particle positions and orientations, weighed with the correct Boltzmann weight. In addition to being computationally much cheaper, it also allows for the use of advanced simulation techniques such as CBMC, which speeds up simulations of longer molecules by orders of magnitude. Longer molecules are effi-

ciently handled and likewise, diffusion in mixtures can easily be computed; all particles are considered part of the external field, irrespective of the type of particle. The LTA-type system used here is a cation-free version of the commonly used LTA 5A zeolite (4 Na⁺ and 4 Ca⁺ per cage). A quantitative comparison with PFG-NMR experimental results requires including the ions in the simulations. Beerdsen et al. [57] and Calero et al. [58] have extended the united-atom model with cations, and our dcTST method already includes the necessary tools.

The diffusion behavior of ethane in LTA as a function of temperature has been well studied. In contrast to a previous study of Schüring et al. [24, 42], we found that ethane molecules in LTA-type zeolite perform hops on a regular cubic lattice, even when we used the smaller size-parameters of Schüring et al. However, these authors computed k_{AB} from MD using the number of cage visits divided by the MD-time. Such an approach overestimates the actual self diffusivity by nearly an order of magnitude for ethane in LTA-type zeolite at 100K. Using the center-of-mass of ethane as the order parameter, they overestimate the rate, because a molecule coming from A will show diffusive behavior in the barrier region and change cage many times before equilibrating in A (recrossing) or B (transmission). Only the successful transmission should be counted and Schüring et al. found that the correlation factor f (Eq. 19) computed using a molecular simulation approximately corrects for this. Our results show that a proper computation of the effective rate constant *including* the transmission coefficient leads to exact agreement between dcTST and MD. We stress that κ and f are different concepts. The similarity in behavior for this specific system originates from the fact that κ is dominated by back-correlations, and for a cubic lattice Eq. 19 computes the same. However, the computation of f using Eq. 19 is limited to the MD time scale.

We would like to comment on the use

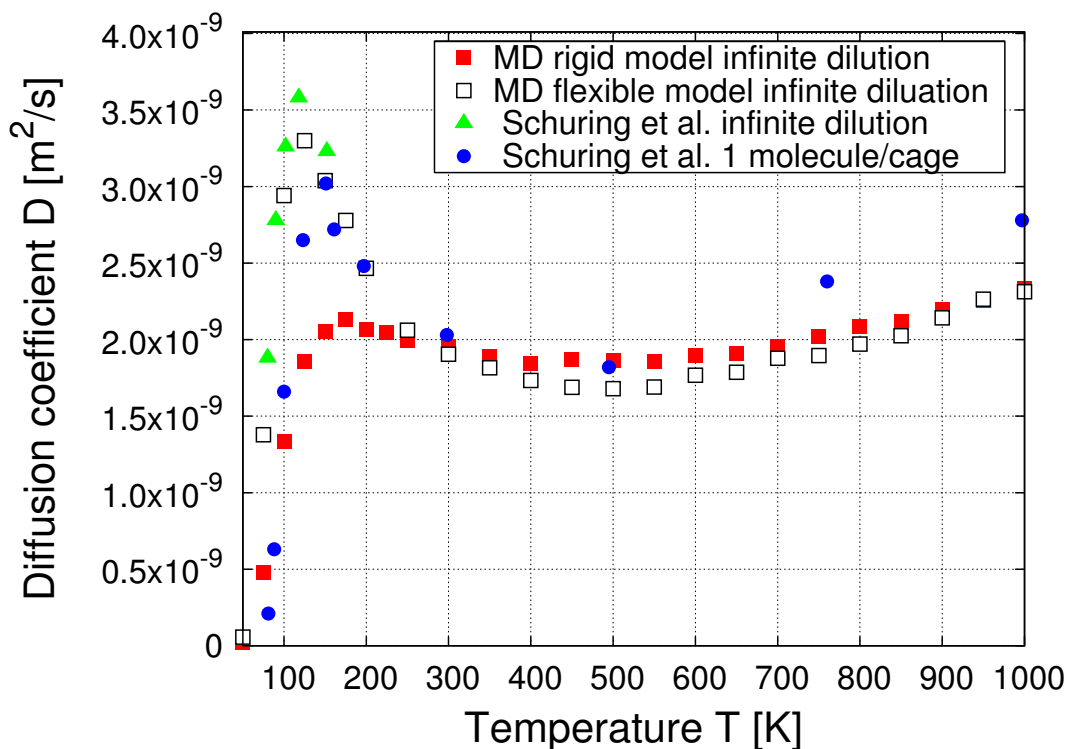


Figure 18: Self-diffusivity of ethane using the LJ-parameters of Table 2, comparing the results of a rigid zeolite to the flexible model of Demontis et al. [59, 60]. Error-bars are smaller or comparable to the symbol size. For comparison we have added the results of Schüring et al. [42] for the infinite dilution case, and for 1 molecule per cage.

of flexible zeolites in regard to our dcTST method. Although for computational reasons we kept the zeolite rigid, our method is fully applicable to flexible zeolites. In Ref. [36] it was found that self-diffusion coefficients for methane in LTA-type zeolite obtained with flexible and with rigid lattices are practically the same. In Fig. 18 we show the self-diffusivity of ethane using the LJ-parameters of Table 2 and compare the results of a rigid zeolite to the flexible model of Demontis et al. [59, 60]. Error-bars are smaller or comparable to the symbol size. We have added the results of Schüring et al. [42] for the infinite dilution case, and for 1 molecule per cage. The data of Schüring et al. compare well and are consistent with our simulations. An important observation is that the differences between flexible and rigid LTA-type zeolite for ethane are significant and temperature dependent. In the low temperature-region

the ethane molecule is tightly confined in the window itself, while at higher temperature the molecule is less tightly confined and located just in front of the window. The method proposed in this paper would allow a detailed investigation of the effect of framework flexibility on slow-diffusing molecules.

V Conclusions

Our method applies dcTST at non-zero loadings without introducing assumptions not already present in traditional TST methods. It can be used to explain diffusion behavior as a function of loading in any system with enough energy dissipation between hops, so that random walk theory (the assumption of equilibration between two subsequent jumps) and TST are valid, as we showed here for small alkanes in LTL- and LTA-type zeolites. The method

gives results in exact agreement with MD, but is also applicable in the regime of very slow diffusion where MD can not be used. This extends the range of accessible time scales significantly beyond currently available methods. Furthermore, the method enables us to express loading effects in terms of free energy differences. It can be used in any lattice and any adsorbate, and also for mixtures.

Acknowledgments

We thank D. Frenkel, T. S. van Erp and S. Calero for their comments on the manuscript, the Netherlands Research Council (CW) and the Deutsche Forschungsgemeinschaft (DFG, priority program SPP 1155) for financial support, and NWO/NCF for computational resources.

Bibliography

- [1] D. Frenkel and B. Smit, *Understanding molecular simulation 2nd edition* (Academic Press, London, UK, 2002).
- [2] M. P. Allen and D. J. Tildesley, *Computer simulation of liquids* (Clarendon Press, Oxford, 1987).
- [3] J. M. Thomas, Solid acid catalysts. *Sci. Am.* **266**, 112 (1992).
- [4] A. F. Voter, F. Montalenti, and T. C. Germann, *Annu. Rev. Mater. Res.* **32**, 321 (2002).
- [5] C. H. Bennett, in *Diffusion in Solids: Recent Developments*, edited by A. Nowick and J. Burton (Academic Press, New York, 1975), pp. 73–113.
- [6] D. Chandler, *J. Chem. Phys.* **68**, 2959 (1978).
- [7] M. J. Ruiz-Montero, D. Frenkel, and J. J. Brey, *Mol. Phys.* **90**, 925 (1996).
- [8] P. G. Bolhuis, C. Dellago, and D. Chandler, *Faraday Discuss.* **110**, 421 (1998).
- [9] T. S. van Erp, D. Moroni, and P. G. Bolhuis, *J. Chem. Phys.* **118**, 7762 (2003).
- [10] D. Moroni, P. G. Bolhuis, and T. S. van Erp, *J. Chem. Phys.* **120**, 4055 (2004).
- [11] A. F. Voter, *Phys. Rev. Lett.* **78**, 3908 (1997).
- [12] A. F. Voter, *Phys. Rev. B* **57**, 13985 (1998).
- [13] M. R. Sorensen and A. F. Voter, *J. Chem. Phys.* **112**, 9599 (2000).
- [14] G. Henkelman and H. Jónsson, *J. Chem. Phys.* **115**, 9657 (2001).
- [15] R. L. June, A. T. Bell, and D. N. Theodorou, *J. Phys. Chem.* **95**, 8866 (1991).
- [16] R. Q. Snurr, A. T. Bell, and D. N. Theodorou, *J. Phys. Chem.* **98**, 5111 (1994).
- [17] R. Q. Snurr, A. T. Bell, and D. N. Theodorou, *J. Phys. Chem.* **98**, 11948 (1994).
- [18] E. J. Maginn, A. T. Bell, and D. N. Theodorou, *J. Phys. Chem.* **100**, 7155 (1996).
- [19] F. Jousse and S. M. Auerbach, *J. Chem. Phys.* **107**, 9629 (1997).
- [20] T. R. F. TR and W. Smith, *J. Chem. Soc. Faraday Trans.* **93**, 3249 (1997).
- [21] T. Mosell, G. Schrimpf, and J. Brickmann, *J. Phys. Chem. B.* **101**, 9476 (1997).
- [22] T. Mosell, G. Schrimpf, and J. Brickmann, *J. Phys. Chem. B.* **101**, 9485 (1997).
- [23] P. K. Ghorai, S. Yashonath, and R. M. Lynden-Bell, *Mol. Phys.* **100**, 641 (2002).

- [24] A. Schüring, S. M. Auerbach, S. Fritzsche, and R. Haberlandt, *J. Chem. Phys.* **116**, 10890 (2002).
- [25] D. Dubbeldam, S. Calero, T. L. M. Maesen, and B. Smit, *Phys. Rev. Lett.* **90**, 245901 (2003).
- [26] D. Dubbeldam and B. Smit, *J. Phys. Chem. B.* **107**, 12138 (2003).
- [27] B. Smit and J. I. Siepmann, *J. Phys. Chem.* **98**, 8442 (1994).
- [28] C. Tunca and D. M. Ford, *J. Chem. Phys.* **111**, 2751 (1999).
- [29] C. Tunca and D. M. Ford, *J. Phys. Chem. B* **106**, 10982 (2002).
- [30] C. Tunca and D. M. Ford, *Chem. Eng. Sci.* **58**, 3373 (2003).
- [31] S. M. Auerbach, *International reviews in physical chemistry* **19**, 155 (2000).
- [32] E. Beerdsen, B. Smit, and D. Dubbeldam, *Phys. Rev. Lett.* **93**, 248301 (2004).
- [33] J. P. Ryckaert and A. Bellemans, *Faraday Discuss. Chem. Soc.* **66**, 95 (1978).
- [34] M. D. Macedonia and E. J. Maginn, *Mol. Phys.* **96**, 1375 (1999).
- [35] T. J. H. Vlugt and M. Schenk, *J. Phys. Chem. B.* **106**, 12757 (2002).
- [36] S. Fritzsche, M. Wolfsberg, R. Haberlandt, P. Demontis, G. B. Suffritti, and A. Tilocca, *Chem. Phys. Lett.* **296**, 253 (1998).
- [37] A. G. Bezus, A. V. Kiselev, A. A. Lopatkin, and P. Q. J. Du, *J. Chem. Soc., Faraday Trans. II* **74**, 367 (1978).
- [38] D. Dubbeldam, S. Calero, T. J. H. Vlugt, R. Krishna, T. L. M. Maesen, and B. Smit, *J. Phys. Chem. B.* **108**, 12301 (2004).
- [39] D. Dubbeldam, S. Calero, T. J. H. Vlugt, R. Krishna, T. L. M. Maesen, E. Beerdsen, and B. Smit, *Phys. Rev. Lett.* **93**, 088302 (2004).
- [40] C. Shang-Shan, H. Jobic, M. Plazanet, and D. Sholl, To be published (2005).
- [41] T. J. H. Vlugt, R. Krishna, and B. Smit, *J. Phys. Chem. B.* **103**, 1102 (1999).
- [42] A. Schüring, S. M. Auerbach, S. Fritzsche, and R. Haberlandt, in *Random Walk Treatment of Dumb-Bell molecules in an LTA Zeolite and in Chabazite*, Proceedings of the 14th International Zeolite Conference, edited by E. van Steen, L. Callanan, and M. Claeys (Elsevier, Cape Town, 2004), pp. 2110–2117.
- [43] D. C. Rapaport, *The art of molecular dynamics simulation* (Cambridge University Press, Cambridge, 1995).
- [44] K. Kremer and G. S. Grest, *J. Chem. Phys.* **92**, 5057 (1990).
- [45] G. J. Martyna, M. Tuckerman, D. J. Tobias, and M. L. Klein, *Mol. Phys.* **87**, 1117 (1996).
- [46] Y. Liu and M. E. Tuckerman, *J. Chem. Phys.* **112**, 1685 (2000).
- [47] I. Vattulainen, S. C. Ying, T. Ala-Nissila, and J. Merikoski, *Phys. Rev. B* **59**, 7697 (1999).
- [48] T. Ala-Nissila, R. Ferrando, and S. C. Ying, *Advances in Physics* **51**, 949 (2002).
- [49] P. J. Flory, *Statistical Mechanics of Chain Molecules* (Interscience, Wiley, New York, 1969), pp. 16–17.
- [50] G. W. N. White, S. Goldman, and C. G. Gray, *Mol. Phys.* **98**, 1871 (2000).
- [51] E. Beerdsen, D. Dubbeldam, and B. Smit, To be published (2005).

- [52] R. M. Barrer and H. Villiger, *Z. Kristallogr.* **128**, 352 (1969).
- [53] J. J. Pluth and J. V. Smith, *J. Am. Chem. Soc.* **102**, 4707 (1980).
- [54] H. L. Tepper and W. J. Briels, *J. Chem. Phys.* **116**, 9464 (2002).
- [55] A. F. Voter and J. D. Doll, *J. Chem. Phys.* **82**, 80 (1985).
- [56] D. Dubbeldam, E. Beerdsen, S. Calero, and B. Smit, To be published (2005).
- [57] E. Beerdsen, B. Smit, and S. Calero, *J. Phys. Chem. B* **106**, 10659 (2002).
- [58] S. Calero, D. Dubbeldam, R. Krishna, B. Smit, T. J. H. Vlugt, J. F. M. Denayer, J. A. Martens, and T. L. M. Maesen, *J. Am. Chem. Soc.* **126**, 11377 (2004).
- [59] P. Demontis, G. B. Suffritti, S. Quartieri, E. S. Fois, and A. Gamba, *Zeolites* **7**, 522 (1987).
- [60] P. Demontis, G. B. Suffritti, S. Quartieri, E. S. Fois, and A. Gamba, *J. Phys. Chem.* **92**, 867871 (1988).

We report molecular simulations of diffusion in confinement showing a phenomenon which we denote as Molecular Path Control (MPC); depending on loading, molecules follow a preferred pathway. MPC raises the important question to which extent the loading may affect the molecular trajectories in nanoporous materials. Through MPC one is able to manually adjust the ratio of the diffusivities through different types of pores, and as an application one can direct the flow of diffusing particles in membranes forward or sideward by simply adjusting the pressure, without the need for mechanical parts like valves. We show that the key ingredient of MPC is the anisotropic nature of the nanoporous material which results in a complex interplay between different diffusion paths as a function of loading. These paths may be controlled by changing the loading, either through a change in pressure or temperature.

D. Dubbeldam, E. Beerdsen, S. Calero, and B. Smit



Molecular Path Control in Zeolite Membranes

I Introduction

Among other emerging membrane technologies like polymer-inorganic composites, carbon films, and micro- and mesoporous silica films, zeolite membranes offer outstanding potential for molecular recognition at the subnanometer level and the ability to operate at high temperatures [1, 2]. Zeolites are crystalline structures made up of "T-atoms", where T is an aluminum or silicon atom, which are tetrahedrally bonded to each other with oxygen bridges. Because of the regularity of the crystalline structure and the pores with Angstrom-size dimensions, these crystals, when grown together to form a membrane, can operate as separation devices for gas and liquid mixtures. From a scientific point of view zeolites are ideal systems to study the effect of confinement on the properties of the ad-

sorbed molecules.

Transport of adsorbates in nanoporous adsorbents such as zeolites is determined by a complex interplay between adsorbent-adsorbate and adsorbate-adsorbate interactions. Molecules diffuse through the pores via various diffusion mechanisms [3]. Although interesting effects like single-file diffusion [4], incommensurate diffusion [5, 6] and levitation effects [7] are well-known, most of the effects of confinement on diffusion remain poorly understood. This is particularly true for loading effects in materials with different channels and/or cages in the x , y , and z -direction. Anisotropic single-component diffusion in silicalite has been known for a long time [8–12]. In general, the diffusion coefficients in the different directions can have different dependencies on temperature and loading. A limited number of studies deal with non-

zero loading. Bussai et al. [13] found little change in anisotropy for water in silicalite as a function of loading. In this work, we report a reversal of anisotropy, i.e. at low loading the diffusivity in the z -direction is two times *faster* than in the xy -direction for both the self- and collective diffusivity, while for higher loadings this changes into a z -diffusivity that is more than two times *slower*. This behavior is due to a complete change in the diffusion mechanism. Our results raise the new and unanswered question to which extent the loading may affect the molecular trajectories in nanoporous materials. Here, we focus on what we have named Molecular Path Control (MPC) where one and the same molecular species follows different pathways, depending on the loading. As a specific MPC example, we study the mechanism behind *tunable* anisotropy of ethane in ERI-type zeolite membranes, but the concepts are by no means limited to zeolite materials.

II Model and computational details

In our simulations, we neglect cations and study rigid, all-silica versions of the ERI- and CHA-type zeolites. Zeolites are designated by three capital letter codes derived from the names of the type materials, e.g. ERI (**E**rionite), and CHA (**C**habazite). The positions of the atoms are taken from Ref. [14] and Ref. [15], respectively. Following the work of Bezus et al. [18], the zeolites are modeled as a rigid network of oxygen atoms. This is a very common approximation because the large oxygen atoms essentially shield the much smaller silicon atoms and lattice flexibility is not important for small alkanes in all-silica zeolites [19]. The rectangular simulation box sizes we used are $4.5906 \times 3.9756 \times 4.443$ nm for ERI-type zeolite, and $3.015 \times 4.7814 \times 2.7606$ nm for CHA-type zeolite. Tests on larger systems did not show any signifi-

cant finite-size effects. Periodic boundary conditions were employed. Adsorption in cation-free structures takes place at sites with little or no electric field. For these reasons the united atom model [16] is a straightforward choice. We consider the CH_3 groups as single, chargeless interaction centers with their own effective potentials. The beads of ethane are connected by an harmonic bonding potential $U^{\text{bond}} = \frac{1}{2}k_1(r - r_0)^2$, with $k_1/k_B = 96500 \text{ K}/\text{\AA}^2$ and $r_0 = 1.54 \text{ \AA}$. The non-intramolecular energy is described with a LJ-potential using parameters $\sigma_{\text{O-CH}_3} = 3.17 \text{ \AA}$, $\epsilon_{\text{O-CH}_3}/k_B = 142 \text{ K}$, $\sigma_{\text{Si-CH}_3} = 2.12 \text{ \AA}$, $\epsilon_{\text{Si-CH}_3}/k_B = 82 \text{ K}$, and $\sigma_{\text{CH}_3-\text{CH}_3} = 3.78 \text{ \AA}$, $\epsilon_{\text{CH}_3-\text{CH}_3}/k_B = 104 \text{ K}$, which were taken from Ref. [17]. The accuracy of the simulation techniques have been verified in several publications [6, 20–23] in which comparisons were made with experimental data and can be considered state-of-the-art for computing adsorption and diffusivities in nanoporous materials.

The simulations were performed using two different methods: conventional Molecular Dynamics (MD) and the recently proposed dynamically corrected Transition State Theory (dcTST) [24, 25]. In MD simulations [26–28], successive configurations of the system are generated by integrating Newton’s laws of motion, which then yields a trajectory that describes the positions, velocities and accelerations of the particles as they vary with time. We used the velocity Verlet integration scheme with a timestep of 0.5 fs. The relative energy drift was smaller than 10^{-4} . For temperature control we employed the Nosé-Hoover chain (NHC) method as formulated by Martyna et al. [29]. Molecules were inserted into the framework at random positions as long as no overlaps occurred with the framework or other particles. During the initialization period we performed an NVT Monte-Carlo simulation to rapidly achieve an equilibrium molecular arrangement. After the initialization period, we assigned velocities from the Maxwell-Boltzmann dis-

tribution at the desired average temperature to all the atoms. The total momentum of the system was set to zero. Next, we equilibrated the system further by performing an NVT MD simulation using the NHC thermostat. After the equilibration was completed, during the production run of more than 20 ns, we collected statistics using the NVT-ensemble. Simulations using the NVE-ensemble gave equivalent results. More details can be found in Ref. [25].

Although MD and dcTST give equivalent diffusivity results for these systems, dcTST is also applicable in the regime of very slow diffusion, where MD cannot be used, and the behavior is better understood by analyzing the free energy profiles and lattice information provided by the dcTST method. In the dcTST-formalism, the diffusion mechanism is divided in two parts. The first is a static term, corresponding to locations of preferable adsorption sites and the free energy barriers in between, the second term generally decreases with loading and corresponds to the inverse of the collision frequency. As such, the dcTST method is able to explain different diffusion regimes over loading, and provides insight into the mechanisms behind an increase or decrease in diffusivity with loading [24].

Using the dcTST method of Beerdsen et al. [24, 25] the self-diffusivity is calculated directly by computing the hopping rate of a molecule over a typical length scale λ given by the smallest repeating zeolite-structure. The transmission rates are easily converted to diffusion coefficients once the lattice distances and connectivities are known. In ERI-type lattices, shown in Fig. 3, diffusion in the xy -plane occurs isotropically on an hexagonal lattice

$$D_{xy} = \frac{1}{4} k_{xy} \lambda_{xy}^2 \quad (1)$$

with λ_{xy} the lattice displacement distance, and k_{xy} the corresponding hopping rate. In ERI-type zeolite, each hop in the z direction is preceded by a hop in xy -direction, and

diffusion is anisotropic:

$$D_z = \frac{1}{2} \frac{k_{xy} k_z}{k_{xy} + k_z} \lambda_z^2 \quad (2)$$

Using MD, the self-diffusion coefficients D_S^α in the direction $\alpha = x, y, z$ are computed by taking the slope of the mean-squared displacement (msd) at long times

$$D_S^\alpha = \frac{1}{2N} \lim_{t \rightarrow \infty} \frac{d}{dt} \left\langle \sum_{i=1}^N (r_{i\alpha}(t) - r_{i\alpha}(0))^2 \right\rangle \quad (3)$$

where N is the number of molecules, t the time, and $r_{i\alpha}$ the α -component of the center-of-mass of molecule i . The collective diffusion coefficients D_C^α are calculated from

$$D_C^\alpha = \frac{1}{2N\xi} \lim_{t \rightarrow \infty} \frac{d}{dt} \left\langle \left(\sum_{i=1}^N (r_{i\alpha}(t) - r_{i\alpha}(0)) \right)^2 \right\rangle \quad (4)$$

where the term $1/\xi$ is the so-called thermodynamic factor (related to the compressibility of the system), which can easily be evaluated from the adsorption isotherm [30]. Collective diffusivity measures the transport of mass and the decay of density fluctuations in the system, while self-diffusion measures the diffusive motion of a single particle [30]. The collective diffusivity D_C is also known as the transport diffusivity D_T , defined as the proportionality constant between the macroscopic flux and concentration gradient, and is the quantity of experimental interest. In zeolite literature, sometimes the "corrected" diffusivity is used. This type of diffusivity is obtained from the collective (or transport) diffusion by removal of the thermodynamic factor. The "corrected" diffusivity can directly be related to the mean-square displacement of the collective coordinate $\mathbf{R} = \sum_{i=1}^N \mathbf{r}_i$ (which is N times the coordinate of the center of mass), in analogy to the self-diffusivity. We note that the thermodynamic factor has no influence on ratio of diffusivities.

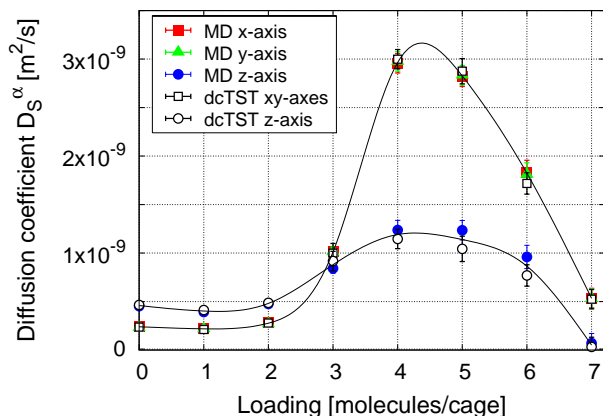


Figure 1: Anisotropic self-diffusivity D_s^α of ethane in ERI-type zeolite computed by dcTST and conventional MD at 600K.

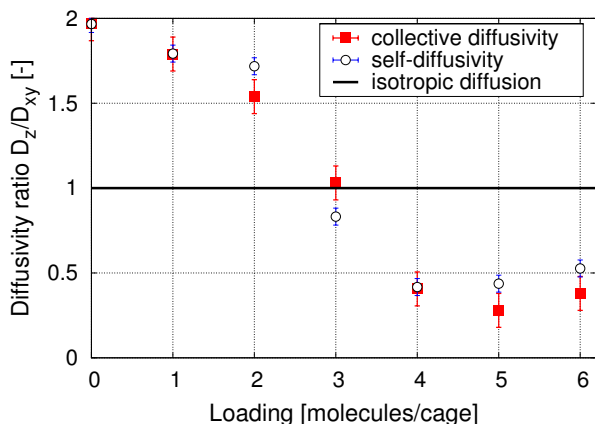


Figure 2: Anisotropic diffusivity ratio D_z/D_{xy} of ethane in ERI-type zeolite computed by MD at 600K for self and collective diffusion.

III Results

In Fig. 1 we have plotted the self-diffusivity of ethane in ERI-type zeolite at 600K as a function of loading. The ratios D_z/D_{xy} of the self and collective diffusivities are shown in Fig. 2. Very surprisingly, at low loading the diffusivity in the z -direction is two times *faster* than in the xy -direction for both the self- and collective diffusivity, while for higher loadings this changes into a z -diffusivity that is more than two times *slower*. This behavior directly shows that the molecules follow different pathways when the loading is changed.

The dcTST gives equivalent results to conventional MD. Importantly, the method

allows for a more detailed analysis in terms of free energy profiles and transmission coefficients. Eq. 2 shows that diffusion in the z -direction is dependent on both the hopping rate in the z -direction *and* in the xy -direction. An investigation of these hopping rates is made by analyzing the free energy barriers for diffusion in the xy -plane. For the diffusion in the xy -plane we find "normal" behavior, typical for cage/window-type zeolites [24]: the diffusivity increases with loading, because the free energy barrier for diffusion decreases. This is due to the finite volume of a cage, where adding particles to the cage results in more repulsive interactions. In the z -direction, we find different behavior. Initially, at low loadings, there are no intracage barriers, and therefore the barriers to diffusion are formed by the xy -barriers, i.e. the eight-ring windows between the adjacent cages. At higher loadings, the xy -barriers decrease and new barriers are formed at the centers of the cages. Eventually the barriers at the centers of the cages dominate the diffusion mechanism, thereby reversing the anisotropy of the diffusion.

It is interesting to note that when the elongation of the erionite-cages is removed, i.e. in CHA-type zeolites (Fig. 4), no significant anisotropy is observed in our simulations (Fig. 5). We note that the lattice is only slightly distorted from a cubic lattice and due to symmetry reasons the free energy profiles are all equivalent, i.e. there is only one hopping rate k from a cage to *any* of the neighboring cages in CHA-type zeolites. The orientationally averaged diffusion coefficient is *not* affected in CHA-type lattices by the distortion effect, but the individual components are, although the effect for 94.07° compared to 90° is negligibly small (less than 2%). Therefore, diffusion in CHA-type zeolite can be considered isotropic in practice. Also experimentally, tracer diffusion measurements in natural chabazite by Raman spectroscopy did not indicate any substantial deviation from isotropic diffu-

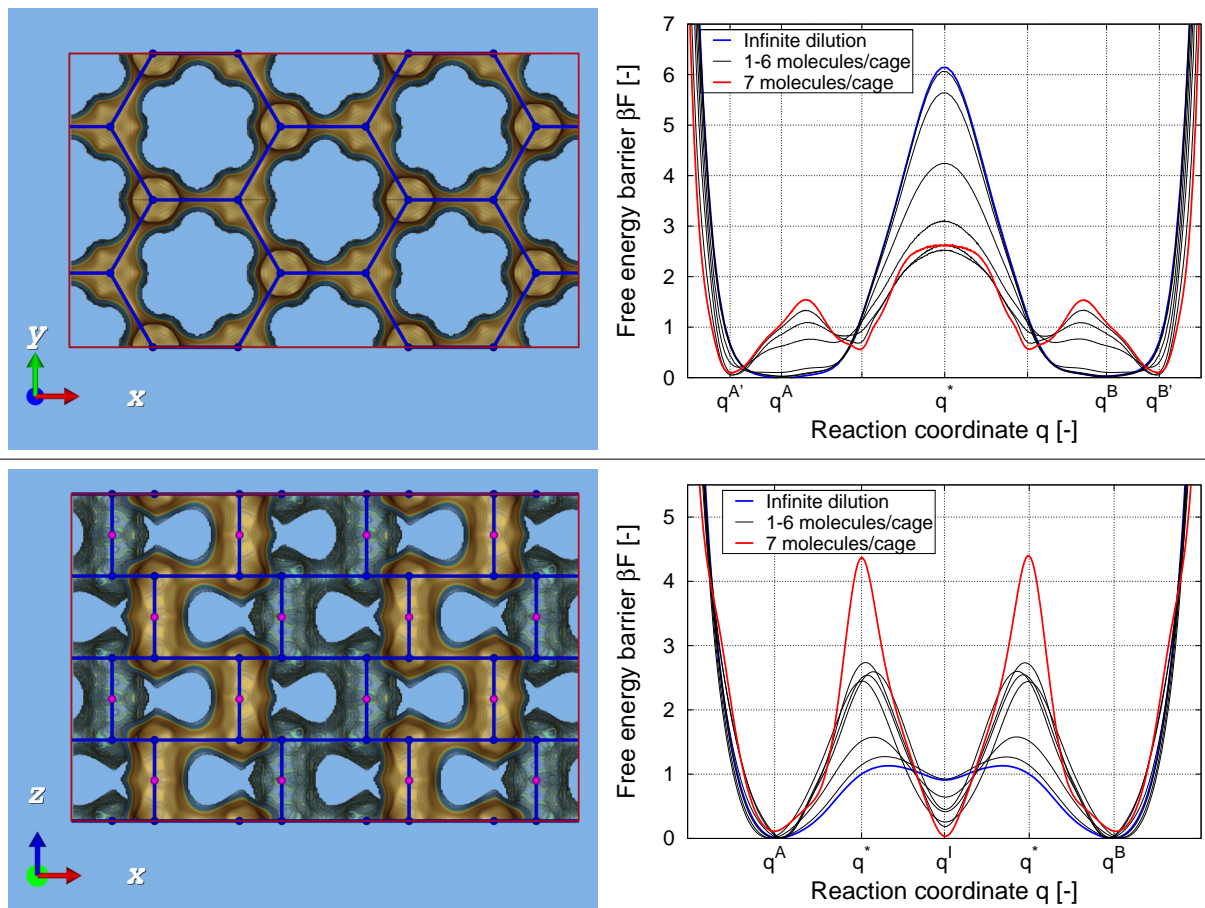


Figure 3: The ERI-type silica structure crystallizes in the hexagonal dipyramidal spacegroup $P6_3/mmc$ with $a = b = 1.327$ nm, $c = 1.505$ nm, and $\alpha = \beta = 90^\circ$, $\gamma = 120^\circ$. We show the topology of the ERI-type lattice (left-top) in xy -direction the hopping takes place on an hexagonal lattice, (left-bottom) in the z -direction a displacement has to be preceded first by an xy -hop. The lattice is drawn in blue dots connected by blue lines of lattice distance $\lambda \approx 0.75$ nm for x , y , and z directions. Free energy profiles $\beta F(q)$ at 600K of ethane in ERI at various loadings (infinite dilution, 1, 2, 3, 4, 5, 6, and 7 molecules per ERI-type cage) (right-top) in the hexagonal xy -plane with q^A the center of a cage, and q^B the center of a neighboring cage, (right-bottom) in the z -direction across a cage with q^A the top of the cage, q^l the middle of the cage, and q^B the bottom of the cage, respectively.

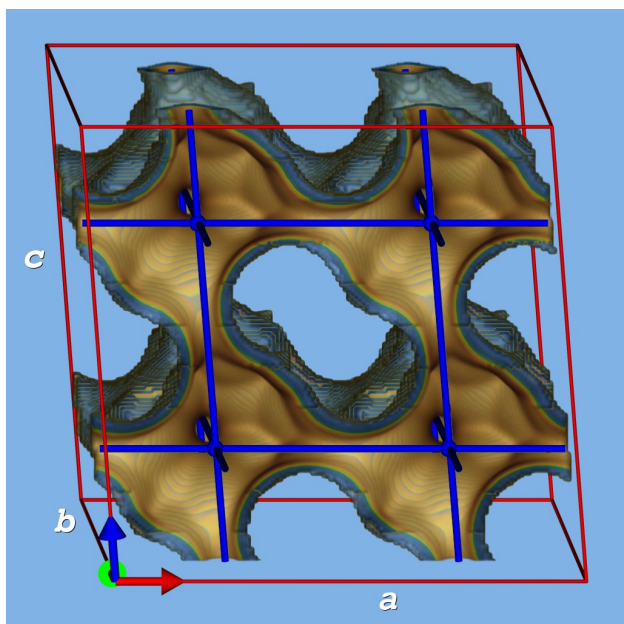


Figure 4: The CHA-type structure [15] has the spacegroup $R\bar{3}m$ (a squashed cube) with $a = b = c = 0.9459$ nm, and $\alpha = \beta = \gamma = 94.07^\circ$. The topology of the CHA-type lattice is shown, where the lattice is drawn in blue dots connected by blue lines.

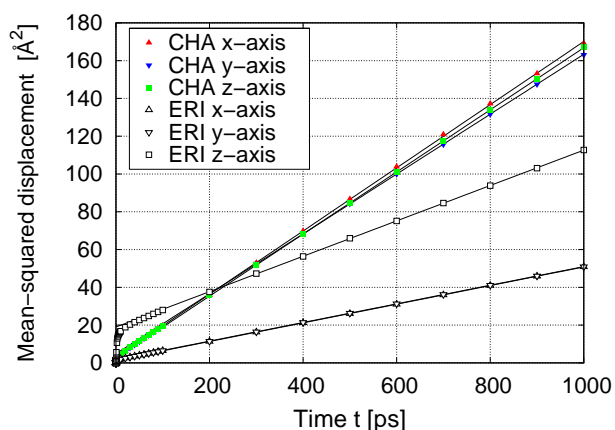


Figure 5: Mean-squared displacements of self-diffusivity of ethane in CHA- and ERI-type zeolite at 600K. The diffusion coefficients in the direction $\alpha = x, y, z$ are computed by taking the slope of the mean-squared displacements at long times.

sion [31]. However, using the pulsed field gradient NMR technique, Bär et al. [32] reported an orientation-dependent diffusivity with a ratio between the maximum and minimum diffusivity of a factor of two, also for water in natural chabazite.

IV Discussion

We stress that the concept of Molecular Traffic Control [33] is different from our Molecular Path Control. It is thought that the origin of MTC lies in the mutual correlation in the movement of a multicomponent fluid through two types of pores [34]. MTC has never been convincingly established and has remained a controversial subject for over two decades now, although recently some theoretical progress has been achieved [35–37]. The current work demonstrates only how the diffusivity of *one* component may vary between pore systems in the same zeolite. The concept of MTC requires various molecules (reactants and products) to exhibit preferences for different pore systems. However, our results show that these preferences might not only be due to shape-selectivity, but also due to (local) differences in loading. Moreover, the fact that a *single* component can be tuned to show a preference of one type of pore over another and that this preference can be manually adjusted, might be considered even more surprising. This implies the ability of directing adsorbates at the molecular level.

MPC originates from the anisotropic nature of the nanoporous material, e.g. the presence of different channel-types or elongated cages. Our results suggest that it is possible to actively design and screen for zeolites with molecular path control properties. As an example, we reported the diffusion of ethane in an erionite-type structure with different diffusion paths, which may be controlled by changing the loading or pressure and temperature. However, the phenomenon is general and by no means limited to zeolites. We have shown that the crucial ingredient is the asymmetric nature of a structure which can be exploited, even for a single component fluid, by using appropriate operating conditions.

Acknowledgments

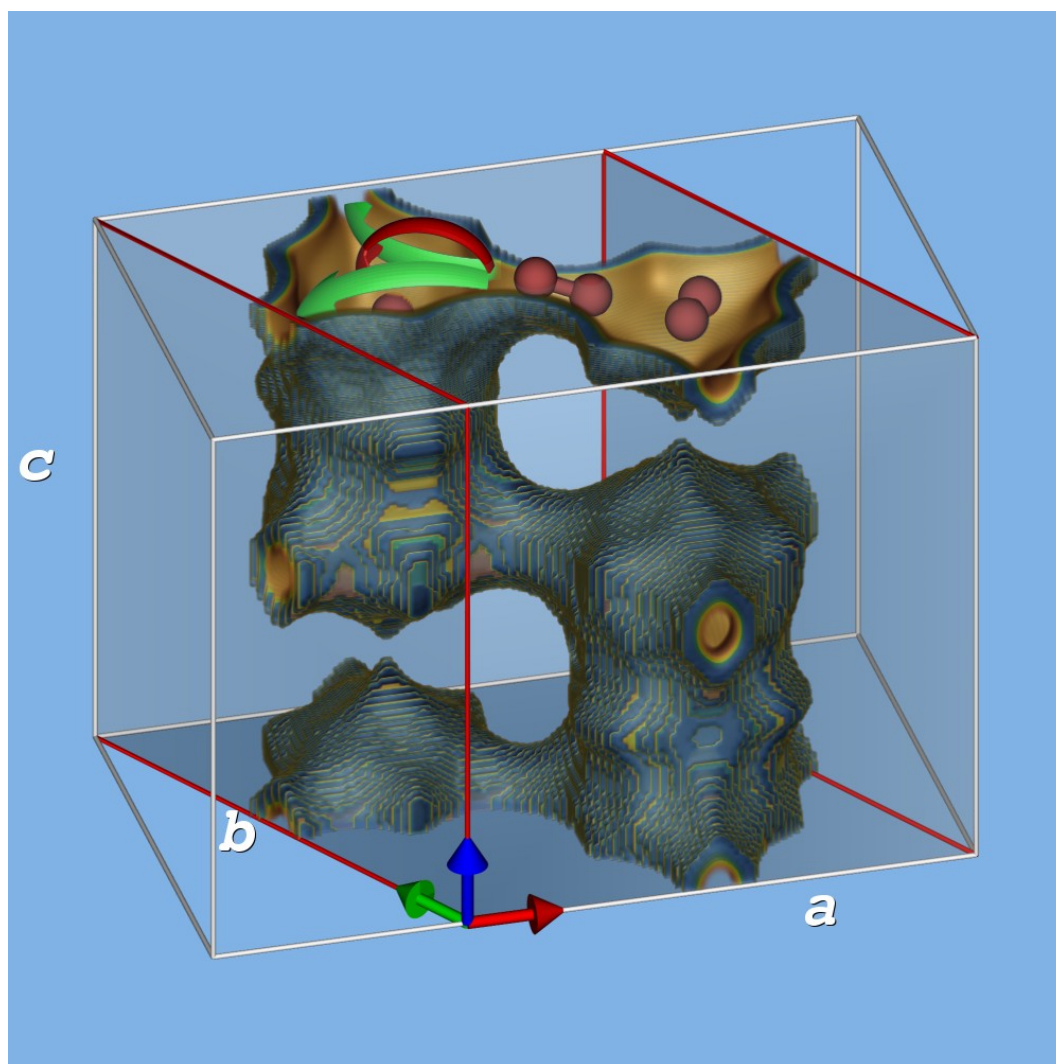
We thank T. J. H. Vlugt for his comments on the manuscript, the Netherlands Research Council (CW), the Deutsche Forschungsgemeinschaft (DFG, priority program SPP 1155), the Spanish Ministry of Science and Technology (Ramón y Cajal Program and VEM2003 20574 C03 01), the European Commission (ERG) for financial support, and NWO/NCF for computational resources.

Bibliography

- [1] Davis, M. E. (2003) *Science* **300**, 438–439.
- [2] Lai, Z, Bonilla, G, Diaz, I, Nery, J. G, Sujaoti, K, Amat, M. A, Kokkoli, E, Terasaki, O, Thompson, R. W, Tsapatsis, M, & Vlachos, D. G. (2003) *Science* **300**, 456–460.
- [3] Kärger, J & Ruthven, D. M. (1992) *Diffusion in Zeolites and other microporous solids*. (John Wiley & Sons, Inc., New York).
- [4] Hahn, K, Kärger, J, & Kukla, V. (1996) *Phys. Rev. Lett.* **76**, 2762–2765.
- [5] Gorring, R. L. (1993) *J. Catal.* **31**, 13–26.
- [6] Dubbeldam, D, Calero, S, Maesen, T. L. M, & Smit, B. (2003) *Phys. Rev. Lett.* **90**, 245901.
- [7] Ghorai, P. K, Yashonath, S, Demontis, P, & Suffritti, G. B. (2003) *J. Am. Chem. Soc.* **125**, 7116–7123.
- [8] June, R. L, Bell, A. T, & Theodorou, D. N. (1990) *J. Phys. Chem.* **94**, 8232–8240.
- [9] Kärger, J. (1991) *J. Phys. Chem.* **95**, 5558–5560.
- [10] Hong, U, Kärger, J, Kramer, R, Pfeifer, H, Seiffert, G, Muller, U, Unger, K. K, Luck, H. B, & Ito, T. (1991) *Zeolites* **11**, 816–821.
- [11] June, R. L, Bell, A. T, & Theodorou, D. N. (1992) *J. Phys. Chem.* **96**, 1051–1060.
- [12] Maginn, E. J, Bell, A. T, & Theodorou, D. N. (1996) *J. Phys. Chem.* **100**, 7155–7173.
- [13] Bussai, C, Fritzsche, S, Haberlandt, R, & Hannongbua, S. (2003) *J. Phys. Chem. B.* **107**, 12444–12450.
- [14] Gard, J. A & Tait, J. M. (1973) ed. Uytterhoeven, J. B. (Proceedings of the Third International Conference on Molecular Sieves; Recent Progress Reports, Leuven University Press, Zurich), pp. 94–99.
- [15] Calligaris, M, Nardin, G, & Randaccio, L. (1983) *Zeolites* **3**, 205–208.
- [16] Ryckaert, J. P & Bellemans, A. (1978) *Faraday Discuss. Chem. Soc.* **66**, 95–106.
- [17] Schüring, A, Auerbach, S. M, Fritzsche, S, & Haberlandt, R. (2002) *J. Chem. Phys.* **116**, 10890–10894.
- [18] Bezus, A. G, Kiselev, A. V, Lopatkin, A. A, & Du, P. Q. J. (1978) *J. Chem. Soc., Faraday Trans. II* **74**, 367–379.
- [19] Vlugt, T. J. H & Schenk, M. (2002) *J. Phys. Chem. B.* **106**, 12757–12763.
- [20] Calero, S, Dubbeldam, D, Krishna, R, Smit, B, Vlugt, T. J. H, Denayer, J. F. M, Martens, J. A, & Maesen, T. L. M. (2004) *J. Am. Chem. Soc.* **126**, 11377–11386.
- [21] Dubbeldam, D, Calero, S, Vlugt, T. J. H, Krishna, R, Maesen, T. L. M, Beerdsen, E, & Smit, B. (2004) *Phys. Rev. Lett.* **93**, 088302–1.

- [22] Dubbeldam, D, Calero, S, Vlugt, T. J. H, Krishna, R, Maesen, T. L. M, & Smit, B. (2004) *J. Phys. Chem. B.* **108**, 12301–12313.
- [23] Vlugt, T. J. H, Krishna, R, & Smit, B. (1999) *J. Phys. Chem. B.* **103**, 1102–1118.
- [24] Beerdsen, E, Smit, B, & Dubbeldam, D. (2004) *Phys. Rev. Lett.* **93**, 248301.
- [25] Dubbeldam, D, Beerdsen, E, Vlugt, T. J. H, & Smit, B. (2005) *J. Chem. Phys.* **122**, 224712.
- [26] Allen, M. P & Tildesley, D. J. (1987) *Computer simulation of liquids.* (Clarendon Press, Oxford).
- [27] Rapaport, D. C. (2004) *The art of molecular dynamics simulation 2nd edition.* (Cambridge University Press, Cambridge).
- [28] Frenkel, D & Smit, B. (2002) *Understanding molecular simulation 2nd edition.* (Academic Press, London, UK).
- [29] Martyna, G. J, Tuckerman, M, Tobias, D. J, & Klein, M. L. (1996) *Mol. Phys.* **87**, 1117–1157.
- [30] Ala-Nissila, T, Ferrando, R, & Ying, S. C. (2002) *Advances in Physics* **51**, 949–1078.
- [31] Goryainov, S. V & Belitsky, I. A. (1995) *Phys. Chem. Miner.* **22**, 433–452.
- [32] Bär, N.-K, Kärger, J, Pfeifer, H, Schäfer, H, & Schmitz, W. (1998) *Microp. Mesop. Materials* **22**, 289–295.
- [33] Derouane, E. G & Gabelica, Z. (1980) *J. Catal.* **65**, 486–489.
- [34] Clark, L. A, Ye, G. T, & Snurr, R. Q. (2000) *Phys. Rev. Lett.* **84**, 2893–2896.
- [35] Bräuer, P, Brzank, A, & Kärger, J. (2003) *J. Phys. Chem. B.* **107**, 1821–1831.
- [36] Neugebauer, N, Bräuer, P, & Kärger, J. (2000) *J. of Catal.* **194**, 1–3.
- [37] Bräuer, P, Neugebauer, N, & Kärger, J. (2001) *Coll. and Surf.* **187-188**, 459–467.

Illustration of Molecular Path Control



Molecular Path Control (MPC) in nanoporous materials. A periodic unitcell of erionite-type zeolites is shown. At low loading molecules diffuse twice as fast in the c -direction compared to the hexagonal ab -plane, while at higher loadings the opposite is observed due to a blockage formed by molecules at the center of the elongated cages. MPC offers the ability of directing molecules at the molecular level by simply adjusting the pressure.

We apply the dynamically corrected Transition State Theory to confinements with complex structures. This method is able to compute self-diffusion coefficients for adsorbate-adsorbent system far beyond the timescale accessible to Molecular Dynamics. Two exemplary cage/window-type confinements are examined: ERI- and CHA-type zeolites. In ERI-type zeolite each hop in the z direction is preceded by an hop in xy -direction, and diffusion is anisotropic. We show that the crystallographic symmetries (monoclinic and trigonal, respectively) can be exploited to simplify the description of the hopping mechanism. The free energy profiles are more easily evaluated in fractional, dimensionless space. The lattice for CHA-type zeolite is a rhombohedral Bravais lattice, and diffusion is anisotropic, albeit only slightly, but the orientational averaged diffusion coefficient is unaffected compared to a cubic lattice. The anisotropical behavior of ERI-type cages reverse with loading, i.e. at low loading the diffusion in the z -direction is two times faster than in the xy -direction, while for higher loadings this changes to a z -diffusivity that is more than two times slower. At low loading the diffusion is impeded by the eight-ring windows, i.e. the exits out of the cage to the next, but at higher loadings the barrier is formed by the center of the cages.

D. Dubbeldam, E. Beerdsen, S. Calero, and B. Smit

12

Applying Dynamically Corrected Transition State Theory in Complex Lattices

I Introduction

Transport of adsorbates in nanoporous adsorbents such as zeolites is determined by a complex interplay between adsorbent-adsorbate and adsorbate-adsorbate interactions. From a scientific point of view zeolites are ideal systems to study the effect of confinement on the properties of the adsorbed molecules because of their regularity and periodicity. Although interesting effects like single-file diffusion [1–3], incommensurate diffusion [4–7], and levitation ef-

fects [8] are well-known, most of the effects of confinement on diffusion remain poorly understood. This is particularly true for loading effects in materials with different channels and/or cages in the x , y , and z -direction.

Although Molecular Dynamics (MD) is a very powerful technique to study these effects, MD is typically limited to diffusion rates in the order of 10^{-12} m²/s. To overcome this, some studies have used dynamically corrected Transition State Theory (dcTST) methods (see Ref. [9] and refer-

ences therein). Hitherto, studies were limited to the infinite dilution limit, whereas many of the processes of practical importance occur at non-zero loading. Beerdsen et al. [10] resolved this problem by extending the dcTST Bennett-Chandler approach to include diffusion of molecules at non-zero loading using only assumptions already present in TST. It was shown that the particle-particle correlations can be taken into account by a proper definition of an effective hopping rate of a *single* particle. The self-diffusivity was computed directly by computing the hopping rate of a molecule over a typical length-scale given by the smallest repeating zeolite-structure, e.g. from the center of cage A to the center of cage B. The use of kinetic Monte Carlo is explicitly avoided. Implicitly one integrates over all adsorption sites in the cage, irrespective whether these are well-defined or not. All other particles are regarded as a contribution to the external field exerted on this tagged particle. The dcTST extension to finite loadings yielded excellent agreement with that obtained by conventional MD simulations and is applicable in any system containing high free energy barriers and for any type of guest molecule.

The method of Beerdsen et al. can be used to explain diffusion behavior as a function of loading in any system with enough energy dissipation between hops, so that random walk theory (the assumption of equilibration between two subsequent jumps) and TST are valid. The diffusion mechanism is divided in two parts. The first is a static term, corresponding to locations of preferable adsorption sites and estimations of free energy barriers in between, the latter (or actually the inverse of the transmission coefficient: the recrossing) corresponds to collision frequencies, which generally increase with loading. As such the dcTST method is able to explain different diffusion regimes over loading, and provides insight into the mechanisms behind an increase or decrease in diffusivity with loading.

In this work, we apply the dcTST method to ERI- and CHA-type zeolite, where diffusion is characterized by complex diffusion paths. Each hop in the z direction is preceded by an hop in xy -direction. Experimentally, there are contradictory results whether or not diffusion in CHA-type zeolites is anisotropic. Bär et al. studied diffusion of water in natural chabazite and found an orientation-dependent diffusivity ($D_z/D_{xy} \approx 0.4$) [13]. However, tracer diffusion measurements by Goryainov et al. of water in natural chabazite by Raman spectroscopy did not indicate any significant anisotropic diffusion [14].

Here, we study anisotropic diffusion in ERI- and CHA-type zeolites using MD and the dcTST method. The remainder of this paper is organized as follows. In section II we start with a detailed description of the ERI- and CHA-type zeolites. Like most confinements, these zeolites can be described using the concept of rare-event hopping on a lattice. For CHA-type zeolite this is a rhombohedral lattice, while for ERI-type zeolite the lattice is non-Bravais. Next, we describe the dcTST method to compute the effective hopping rate for these lattices. We then show how to use the inherent symmetry of the unit cells of ERI- and CHA-type structures using non-rectangular unit cells. The reaction coordinate onto which the free energy is projected to compute the free energy barriers is more conveniently described in the fractional and dimensionless orthonormal basis. In the results section III we show results for ethane at 600K in ERI- and CHA-type zeolites using dcTST and MD. The free energy profiles, the transmission coefficients, the hopping rate, and self-diffusion coefficients for both zeolites are evaluated. Here, we explain our choice of the hopping lattice, being closely related to the computed free energy profiles. We end with some conclusions on anisotropic behavior in zeolite as a function of loading, and why the dcTST method is a suitable method to provide detailed insight into

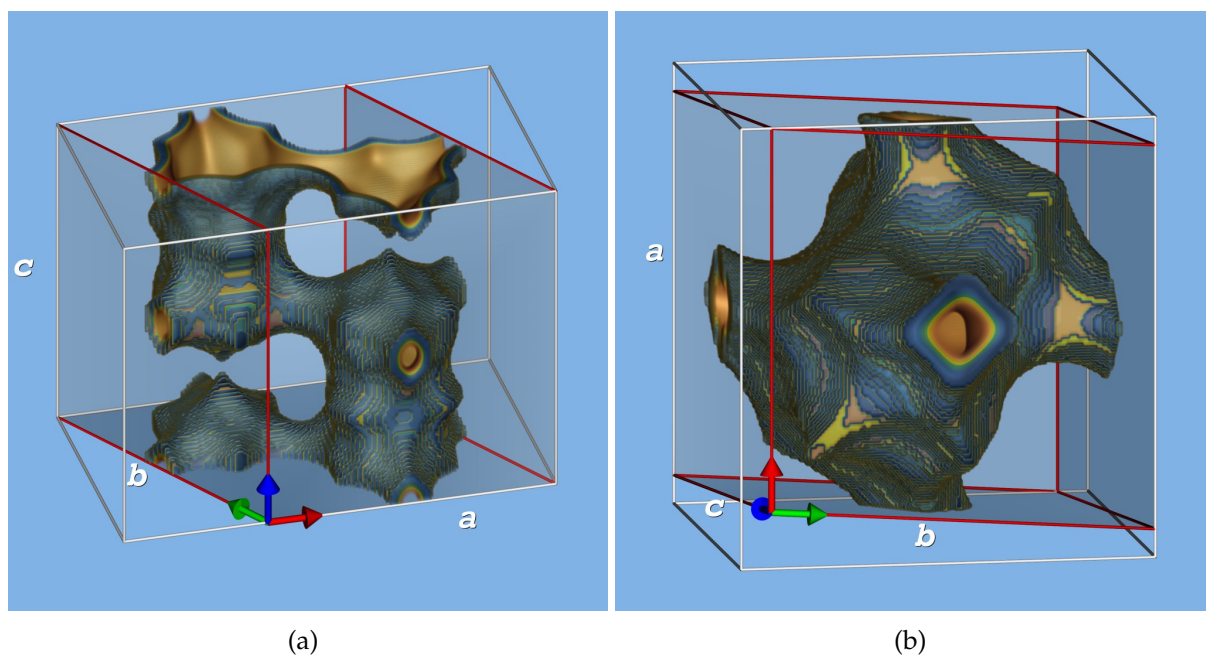


Figure 1: A unit cell of (a) ERI-type zeolite, and (b) CHA-type zeolite. The ERI-type silica structure [11] crystallizes in the hexagonal dipyramidal spacegroup $P6_3/mmc$ with $a = b = 1.327$ nm, $c = 1.505$ nm, and $\alpha = \beta = 90^\circ$, $\gamma = 120^\circ$. The CHA-type structure [12] has the spacegroup $R\bar{3}m$ (a squashed cube) with $a = b = c = 0.9459$ nm, and $\alpha = \beta = \gamma = 94.07^\circ$. A unit cell of erionite contains two cages, while a unit cell of chabazite contains a single cage.

mechanisms behind it.

II Methods

A Zeolite descriptions

The ERI-type silica structure [11] crystallizes in the hexagonal dipyramidal spacegroup $P6_3/mmc$ with $a = b = 1.327$ nm, $c = 1.505$ nm, and $\alpha = \beta = 90^\circ$, $\gamma = 120^\circ$. The elongated erionite cages approximate the shape of 1.3×0.63 nm cylinders connected by 0.36×0.51 nm windows. Only linear molecules are able to penetrate the eight-membered ring windows. There are three windows at the top of the cage rotated 120° with respect to each other. At the bottom of the cage there are also three windows rotated 120° with respect to each other. The top three windows are aligned with the windows at the bottom. Each ERI-type unit cell contains two erionite cages as shown in Fig. 1(a). The connectivity of the

cages is shown in Fig. 2(a).

The CHA-type structure [12] has the spacegroup $R\bar{3}m$ (a squashed cube) with $a = b = c = 0.9459$ nm, and $\alpha = \beta = \gamma = 94.07^\circ$. The framework contains double six-membered rings joined together through four-membered rings. The resulting three-dimensional structure has large ellipsoidal chabazite (CHA) cages. Small guest molecules can enter the cages through eight-membered 0.38 nm wide ring windows. Only linear alkanes are able to penetrate the windows. Each CHA-type unit cell contains a single chabazite cage as shown in Fig. 1(b). The connectivity of the cages is shown in Fig. 2(b).

B Lattices

A lattice is an infinite periodic array of points. In principle the lattice is completely described by three basis vectors \mathbf{a} , \mathbf{b} , \mathbf{c} , and the angles between these vectors α , β and γ . The lattice can be mapped into itself by

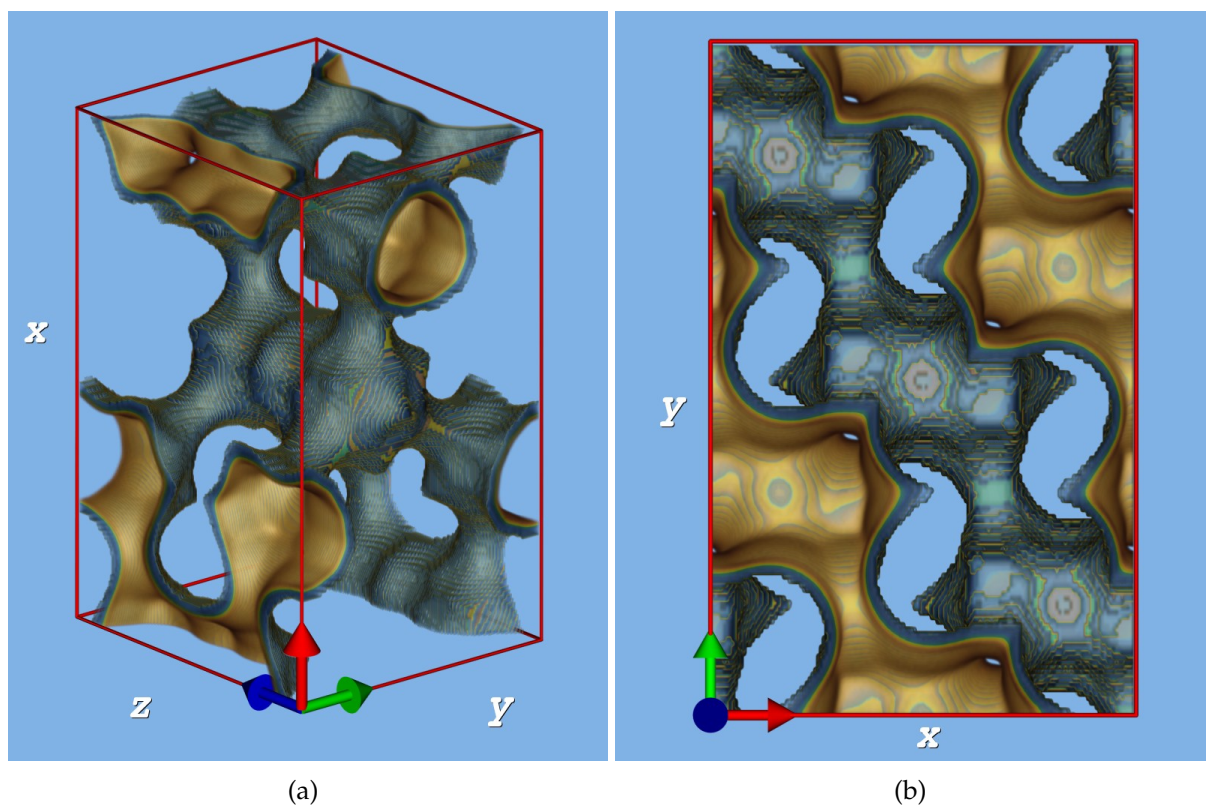


Figure 2: The structure of a rectangular periodic unit cell of (a) ERI-type zeolite, (b) CHA-type zeolite, showing the connectivity. Each erionite cage has six exits: three windows at the top of the cage rotated 120° with respect to each other, and three windows at the bottom of the cage. The top three windows are aligned with the windows at the bottom. Also the chabazite cage has 6 exits: three at the left, rotated approximately 120° with respect to each other, and three at the right part of the cage. The right and left part are approximately rotated 60° with respect to each other.

translation operations and by other symmetry operations. The Wigner-Seitz cell enclosing a point is the region of space that is closer to that lattice point than to any other lattice point. There is only one lattice point in the primitive unit cell thus formed. The symmetry of the unit cell is used to classify structures and how they fill space. In two dimensions there are only five lattices, called Bravais lattices, that fill space and defined by how you rotate the cell content and get the same cell back, and if there are any mirror planes within the cell (the square, hexagonal, rectangular, center rectangular, and oblique lattices). In three dimensions there are seven lattice systems (triclinic, monoclinic, orthorhombic, tetragonal, cubic, trigonal, hexagonal). The general lattice is triclinic, all others are derived

by putting constraints on the triclinic lattice. Note that we now have different lattice types: primitive (one lattice point), body-centered (two lattice points), face-centered (four lattice points), side-centered (two lattice points).

For use in the dcTST method, it turns out that often lattices are needed of two or more different types, i.e. a quasiperiodic nonrandom assembly of two or more types that fill space. These lattices are not Bravais lattices. In analogy to crystallographic lattices, one may fill space by tessellation or tiling a finite number of proto-tiles to fill space without gaps or overlap. These Wigner-Seitz cell (or Voronoï cell) cells form the lattice tiling.

A random walk is a simple mathematical model for the movement of a particle on a lattice under the influence of some ran-

dom or stochastic force affecting its direction of motion. Let k_i be the average frequency that a random walker (an atom or molecule) jumps for lattice vector λ_i , and $\mathbf{r}(t)$ is the position of a particular random walker. The total jumping frequency k is related to the specific jumping frequencies k_i for a given structure by a summation over the lattice connectivity Z :

$$k = \sum_{i=1}^Z k_i \quad (1)$$

In the limit of infinite dilution there are no interparticle correlations and the particles perform a random walk on a lattice spanned by for example the cage-centers. For Bravais lattices, the transmission rates are then easily converted to self-diffusion coefficients by for example

$$D_S = \frac{1}{2d} k \lambda^2 \quad (2)$$

where d denotes the spatial dimensionality, for the one dimensional lattice, two dimensional square and hexagonal lattice, and for the three dimensional simple cubic lattice, respectively.

For non-Bravais lattices, the diffusion coefficient can be easily evaluated numerically for any nonrandom quasiperiodic tessellation, but often it is possible to find analytical expressions. Consider an hop from A to C with an intermediate state B . We have

$$\frac{P_{B \rightarrow A}}{P_{B \rightarrow C}} = \frac{k_{B \rightarrow A}}{k_{B \rightarrow C}} \quad (3)$$

$$P_{B \rightarrow A} + P_{B \rightarrow C} = 1 \quad (4)$$

and therefore

$$P_{B \rightarrow C} = P_{B \rightarrow A} \frac{k_{B \rightarrow C}}{k_{B \rightarrow A}} \quad (5)$$

$$= (1 - P_{B \rightarrow C}) \frac{k_{B \rightarrow C}}{k_{B \rightarrow A}} \quad (6)$$

$$(7)$$

from which $P_{B \rightarrow C}$ can be solved

$$P_{B \rightarrow C} = \frac{k_{B \rightarrow C}}{k_{B \rightarrow A} + k_{B \rightarrow C}} \quad (8)$$

The hopping rate from A to C is the hopping rate from A to B times the probability $P_{B \rightarrow C}$ to go from B to C

$$k_{A \rightarrow C} = k_{A \rightarrow B} P_{B \rightarrow C} \quad (9)$$

In general a serial combination of hops is then described by

$$k_{A \rightarrow C} = \frac{k_{A \rightarrow B} k_{B \rightarrow C}}{k_{B \rightarrow A} + k_{B \rightarrow C}} \quad (10)$$

Eq. 10 proves convenient for finding the relation between hopping rates and diffusion coefficient on non-Bravais lattices. The relation between $k_{A \rightarrow B}$ and $k_{B \rightarrow A}$ is given by

$$\frac{k_{A \rightarrow B}}{k_{B \rightarrow A}} = \frac{\langle n_B \rangle}{\langle n_A \rangle} \quad (11)$$

where $\langle n_A \rangle = 1 - \langle n_B \rangle$ is the equilibrium mole fraction of particles in state A . For a symmetric barrier $\langle n_A \rangle = \langle n_B \rangle$ and therefore $k_{A \rightarrow B} = k_{B \rightarrow A}$.

In ERI-type lattice the diffusion in the xy -plane occurs isotropically on an hexagonal lattice

$$D_{xy} = \frac{1}{4} k_{xy} \lambda_{xy}^2 \quad (12)$$

with λ_{xy} the lattice displacement distance, and k_{xy} the corresponding hopping rate. The z -diffusion is dependent on the hopping in the xy plane. The lattice displacement vector λ_z is orthogonal to λ_r , and using Eq. 10 plus the symmetry of the lattice, we find

$$D_z = \frac{1}{2} \frac{k_{xy} k_z}{k_{xy} + k_z} \lambda_z^2 \quad (13)$$

To convert the hopping rate in CHA-type zeolites to a diffusion coefficient we note that the lattice is slightly distorted from a cubic lattice. The orientational averaged diffusion coefficient is *not* affected in CHA-type lattices but the individual components are, albeit that the distortion effect for the CHA-type lattice is negligibly small (smaller than 2%). Therefore diffusion in CHA-type zeolite can be considered isotropic in practice.

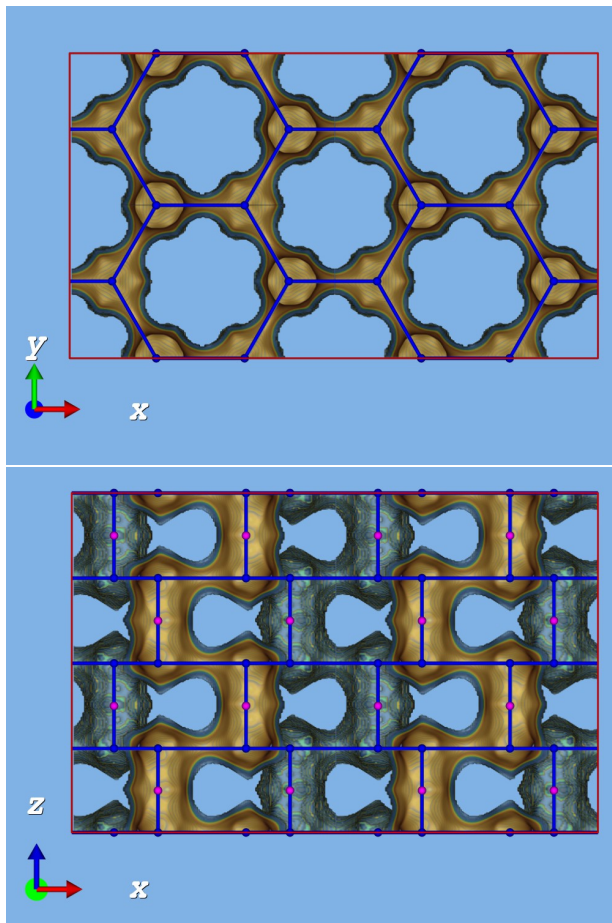


Figure 3: The topology of the ERI-type lattice in (a) xy -direction the hopping takes place on a hexagonal lattice, in (b) the z -direction a displacement has to be preceded first by a xy -hop. The lattice is drawn in blue dots connected by blue lines of lattice distance $\lambda \approx 0.75$ nm for x , y , and z directions.

C the dcTST method

Slow diffusion of molecules in zeolites can be considered an activated process, in which the particle hops from one free energy minimum to the next, and the actual crossing time is negligible compared to the time a particle spends inside the cage. One can exploit the large separation in time scales using rare-event simulation techniques, We consider a system which can be in two stable states, A and B with a dividing free energy barrier between them. The reaction coordinate q , indicates the progress of the diffusion event

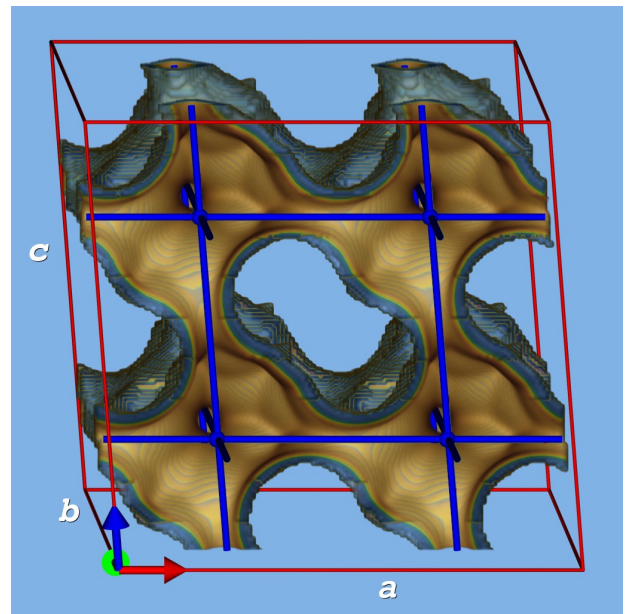


Figure 4: The topology of the CHA-type lattice. The lattice is drawn in blue dots connected by blue lines of lattice distance $\lambda \approx 0.9459$ nm for a , b , and c directions.

from cage A to cage B . The location of the dividing barrier is denoted by q^* . We introduce two characteristic functions n_A and n_B that measure whether the system is in state A or B . A possible and often used definition is

$$n_A = \theta(q^* - q), \quad (14)$$

$$n_B = \theta(q - q^*), \quad (15)$$

where θ is the Heaviside function $\theta(x)$, which has value zero for $x < 0$ and value one for $x \geq 0$.

In the Bennett-Chandler approach [9, 15, 16] one computes the hopping rate over the barrier in two steps

$$k_{A \rightarrow B} = \underbrace{\frac{\langle \delta(q^* - q) \rangle}{\langle \theta(q^* - q) \rangle}}_{P(q^*)} \times \underbrace{\frac{\langle \dot{q}(0) \delta(q^* - q(0)) \theta(q(t) - q^*) \rangle}{\langle \delta(q^* - q(0)) \rangle}}_{R(t)}, \quad (16)$$

where δ is the Dirac delta function.

The probability $P(q^*) / P(q)$ is the equilibrium probability density of finding the system at the top of the barrier divided by the equilibrium probability of finding it at state A . During an NVT -ensemble MC simulation at the required loading we measure the free energy $F(q)$ by using Histogram Sampling (HS). In the HS method, a histogram is made of the particle positions, mapped on the reaction coordinate. From the histogram a free energy profile is computed, by using

$$\beta F(q) = -\ln \langle P(q) \rangle. \quad (17)$$

The reaction coordinate is formed by a curve from lattice point to a neighboring lattice point, mapping the Wigner-Seitz volumes of A and B onto the curve. Inclusion of the full Wigner-Seitz volumes ensures the correct inclusion of entropy. This is especially important if the Widom-particle-insertion (WPI) method is used to compute the free energy. WPI uses a probe particle that is inserted at random positions, to measure the energy required for or obtained by insertion of the particle in the system. This energy is mapped onto the reaction coordinate q , using

$$\beta F(q) = -\ln \langle e^{-\beta \Delta U} \rangle_N \quad (18)$$

to produce a free energy profile, where $\langle e^{-\beta \Delta U} \rangle_N$ is the average Boltzmann factor over all positions in the slice corresponding to the reaction coordinate. A "ghost particle" is used as the measuring probe, but the other particles in the system do not feel its presence. At higher loadings, WPI is known to give erroneous results [17]. However, the WPI-profile can still be used as a biasing profile for the importance sampling techniques to improve statistics [17]. Note that only one tagged particle is biased, the other particles are free to move, and the free energy of the tagged particle is computed. If unbiased HS is feasible, then all particle contributions can be used.

the flux $R(t)$ through the dividing surface $R(t)$ is the averaged flux at the top of the barrier multiplied by the probability that the system ends up in state B at time t . $R(t)$ is a conditional average, namely the product $\dot{q}(0) \theta(q(t) - q^*)$, given that $q(0) = q^*$. We compute the fraction κ of particles starting on top of the barrier with a velocity towards B that successfully reach cage B . Starting configurations are generated using MC with one particle constrained to the dividing surface and $N - 1$ particles moving around freely. These configurations are then used to compute the ratio in unconstrained NVE -MD simulations, starting with velocities sampled from a Maxwell-Boltzmann distribution at the desired temperature. If the chosen dividing surface is the true dividing surface we can estimate from kinetic theory the long time value of $R(t)$ by $\frac{1}{2} |\dot{q}(0)| = \sqrt{\frac{k_B T}{2\pi m}}$. The dimensionless transmission coefficient κ corrects for particles that cross the transition state from A but fail to equilibrate in B .

$$\kappa(t) \equiv \frac{k_{A \rightarrow B}(t)}{k_{A \rightarrow B}^{\text{TST}}} = \frac{\langle \dot{q}(0) \delta(q(0) - q^*) \theta(q(t) - q^*) \rangle}{\langle \frac{1}{2} |\dot{q}(0)| \delta(q(0) - q^*) \rangle}. \quad (19)$$

We can then write

$$\begin{aligned} k_{A \rightarrow B} &= R(t) P(q^*) \\ &= \kappa \sqrt{\frac{k_B T}{2\pi m}} \frac{e^{-\beta F(q^*)}}{\int_{\text{cage } A} e^{-\beta F(q)} dq} \end{aligned} \quad (20)$$

For systems with erratic free energy landscapes, e.g. multiple of barriers of different heights, the dcTST method can be generalized using

$$k_{A \rightarrow B} = \frac{1}{\langle n_A \rangle} \frac{\left\langle \int_0^\infty \dot{q}(t) \dot{q}(0) \frac{w(q(t)) e^{-\beta F(q(t))}}{w(q(0)) e^{-\beta F(q(0))}} dt \right\rangle_\pi}{\int_{q_A}^{q_B} e^{\beta F(q)} dq \int_{-\infty}^\infty e^{-\beta F(q)} dq} \quad (21)$$

with a biasing function $w(q)$ operating on the range q^A to q^B , i.e. on the λ region

$$\begin{aligned} w(q) &= e^{a\beta F(q)} \\ \pi(q) &\propto e^{(a-1)\beta F(q)} \end{aligned} \quad (22)$$

where $a > 0$ is an integer to be freely chosen. A value of $a = 1$ would flatten the free energy landscape, a value of $a = 2$ would reproduce the Ruiz-Montero method (if the approximate free energy is taken to be the true free energy), and in the limit of $a \rightarrow \infty$ and a single free energy barrier the method reduces to the Bennet-Chandler method. Although Eq. 21 can be considered a TST method using a more continuous "detector" function than the noisy θ -function, it can also be viewed as a MD method in a different, more convenient ensemble $\pi(q) \propto w(q)e^{-\beta F(q)}$. Starting configurations at the desired loading are sampled using NVT-MC (with the biased, tagged particle in the π -ensemble) and subsequently a weighted velocity autocorrelation of the tagged particle is computed using conventional NVE-MD.

D Non-rectangular unit cells

ERI-and CHA-type zeolite come in both rectangular unit cells, as well as their crystallographic non-rectangular definitions. In crystallography, the crystal structure is defined by the unit cell, and by the fractional coordinates of the atoms within the unit cell. These coordinates form an orthonormal dimensionless \mathcal{S} -space. \mathcal{S} space is often more convenient for the computation of the free energy profiles. The transformation from \mathcal{S} -space to real \mathcal{R} -space can be carried out by the matrix \mathcal{H} :

$$\mathcal{H} = \begin{pmatrix} a & b \cos(\gamma) & c \cos(\beta) \\ 0 & b \sin(\gamma) & c\zeta \\ 0 & 0 & c\sqrt{1 - \cos^2\beta - \zeta^2} \end{pmatrix} \quad (23)$$

with

$$\zeta = \frac{\cos\alpha - \cos\gamma \cos\beta}{\sin\gamma} \quad (24)$$

Conversely, \mathcal{H}^{-1} transforms real coordinates to fractional coordinates. With the chosen \mathcal{H} the scaled box has a length of 1. Our potential forcefield is defined in real space, therefore it is convenient to store position in \mathcal{R} space, transform them to \mathcal{S} space, apply periodic boundary conditions in \mathcal{S} space, and transform back to \mathcal{R} space to compute distances within the simulation box

$$\begin{aligned} \mathbf{s} &= \mathcal{H}^{-1}\mathbf{r} \\ \mathbf{s}' &= \mathbf{s} - \text{rint}(\mathbf{s}) \\ \mathbf{r}' &= \mathcal{H}\mathbf{s}' \end{aligned} \quad (25)$$

where the "rint"-function returns the rounded integer value of its argument. The smallest perpendicular width of the unit cell has to be larger than twice the spherical cutoff in \mathcal{R} space.

For computational reasons a rectangular unit cell is preferred. Not only is the matrix conversion more expensive, if the the unit cell is severely distorted from cubic many distances will be calculated that are outside the cutoff in \mathcal{R} space reducing the efficiency. However, for computation of free energy profiles in complex zeolite structures, the fractional space is often very convenient.

E Reaction coordinate

In general, the reaction coordinate q is a function of the configuration of the whole system, i.e. $q = q(\mathbf{r}_1, \dots, \mathbf{r}_N)$. However, we can choose q as the position of one of the two beads of ethane [6,7]. This choice of order parameter underestimates the free energy of the true transition state, but the dynamical correction κ is the *exact* correction compensating our choice of reaction coordinate [16]. In the Bennett-Chandler approach it is sufficient to chose a reaction coordinate q and assign the barrier position q^* inside the barrier region. The result of the scheme does not depend on the specifics of the reaction coordinate and location, although the statistical accuracy *does*.

The monoclinic unit cell definition for an ERI-type cage is shown in Fig. 1(a). Because two cages are present in the unit cell definition it is convenient to be able to select a single cage by using

$$q = \begin{cases} s_x + (1 - s_y) < 1 & \text{for cage A} \\ s_x + (1 - s_y) > 1 & \text{for cage B} \end{cases} \quad (26)$$

where s are the fractional coordinates of a single ERI-type unit cell in \mathcal{S} -space. For xy -computations the barrier is located at $s_{xy} = \{\frac{1}{2}, \frac{1}{2}\}$, and by symmetry all positions in the unit cell can be mapped on the reaction coordinate. For the z -computation we select only cage A and use

$$q = s_z \quad (27)$$

The barrier at the center of the cage is located at $s = \{\frac{1}{3}, \frac{2}{3}, \frac{3}{4}\}$, while the free energy minima q^A and q^B are located at $s = \{\frac{1}{3}, \frac{2}{3}, \frac{1}{2}\}$ and $s = \{\frac{1}{3}, \frac{2}{3}, 1\}$, respectively. Using the projection Eq. 27 and the positions of cage A only, q^A is located at $s_z = \frac{1}{2}$, the barrier q^* at $s_z = \frac{3}{4}$, and q^B at $s_z = 1$.

The unit cell definition for a CHA-type cage is shown in Fig. 1(b) (the rhombohedral lattice can be thought of as a cube slightly pulled along its space diagonal). The reaction coordinate can now be chosen from the center of the cage ($\mathbf{s}_0 = \{0.5, 0.5, 0.5\}$) to any of the six exits through the center of the windows ($\mathbf{s}_1 = \{1, 0.5, 0.5\}$, $\mathbf{s}_2 = \{0.5, 1, 0.5\}$, $\mathbf{s}_3 = \{0.5, 0.5, 1\}$, $\mathbf{s}_4 = \{0, 0.5, 0.5\}$, $\mathbf{s}_5 = \{0.5, 0, 0.5\}$, $\mathbf{s}_6 = \{0.5, 0.5, 0\}$), i.e. the space is simply mapped onto the three orthonormal axes in scaled space. The other half of the profile, i.e. from q^* to q^B follows by symmetry. Due to symmetry reasons, the free energy profiles are all equivalent, and there is only one hopping rate k from a cage to any of the neighboring cages in CHA-type zeolites.

F Force field potentials and simulation details

We neglect cations and study rigid, all-silica versions of the ERI- and CHA-type zeolites. The positions of the atoms are taken from Ref. [11] and [12], respectively. Ref. [12], respectively. Following the work of Bezus et al. [18], the zeolites are modeled as a rigid network of oxygen atoms. This is a very common approximation because the large oxygen atoms essentially shield the much smaller silicon atoms and lattice flexibility is not important for small alkanes in all-silica zeolites [19]. The simulation box sizes we used are $3 \times 3 \times 3$ (perpendicular widths are $3.447647 \times 3.447647 \times 4.515$ nm) for ERI-type zeolite, and $3 \times 3 \times 3$ (perpendicular widths are $2.809895 \times 2.809895 \times 2.809895$ nm) for CHA-type zeolite. Tests on larger systems did not show any significant finite-size effects. Periodic boundary conditions were employed. Adsorption in cation-free structures takes place at sites with little or no electric field. For these reasons the united atom model [20] seems the most straightforward choice. We consider the CH_3 groups as single, chargeless interaction centers with their own effective potentials. The beads of ethane are connected by an harmonic bonding potential

$$U^{\text{bond}} = \frac{1}{2}k_1(r - r_0)^2 \quad (28)$$

with $k_1/k_B = 96500 \text{ K}/\text{\AA}^2$ and $r_0 = 1.54 \text{ \AA}$. The non-intramolecular energy consists of a guest-guest intermolecular energy U^{gg} , a host-guest interaction U^{hg} ,

$$U^{\text{ext}} = U_{ij}^{\text{gg}} + U_{ij}^{\text{hg}} \quad (29)$$

with

$$U_{ij}^{\text{gg,hg}} = \sum_{\text{LJ-pairs}} 4\epsilon_{ij} \left[\left(\frac{\sigma_{ij}}{r_{ij}} \right)^{12} - \left(\frac{\sigma_{ij}}{r_{ij}} \right)^6 \right] - E_{\text{cut}}, \quad (30)$$

where r_{ij} is the distance between site i and site j , $r_{\text{cut}} = 12.0 \text{ \AA}$, the cutoff radius, E_{cut} the

energy at the cut-off radius, and $U_{ij}^{\text{gg,hg}} = 0$ when $r_{ij} > r_{\text{cut}}$. The parameters $\sigma_{\text{O-CH}_3} = 3.17 \text{ \AA}$, $\epsilon_{\text{O-CH}_3}/k_B = 142 \text{ K}$, $\sigma_{\text{Si-CH}_3} = 2.12 \text{ \AA}$, $\epsilon_{\text{Si-CH}_3}/k_B = 82 \text{ K}$, and $\sigma_{\text{CH}_3-\text{CH}_3} = 3.78 \text{ \AA}$, $\epsilon_{\text{CH}_3-\text{CH}_3}/k_B = 104 \text{ K}$ were taken from Ref. [21]. Although the size parameters are rather small, for this study we prefer to use these parameters because then diffusion of ethane in ERI- and CHA-type zeolite is still feasible using conventional MD.

The simulations were performed using two different methods: conventional Molecular Dynamics (MD) and the recently proposed dynamically corrected Transition State Theory (dcTST) [9, 10]. In MD simulations [17, 22, 23], successive configurations of the system are generated by integrating Newton's laws of motion, which then yields a trajectory that describes the positions, velocities and accelerations of the particles as they vary with time. We used the velocity Verlet integration scheme with a timestep of 0.5 fs. The relative energy drift was smaller than 10^{-4} . For temperature control we employed the Nosé-Hoover chain (NHC) method as formulated by Martyna et al. [24]. Molecules were inserted into the framework at random positions as long as no overlaps occurred with the framework or other particles. During the initialization period we performed an NVT Monte-Carlo (MC) simulation to rapidly achieve an equilibrium molecular arrangement. After the initialization period, we assigned velocities from the Maxwell-Boltzmann distribution at the desired average temperature to all the atoms. The total momentum of the system was set to zero. Next, we equilibrated the system further by performing an NVT MD simulation using the NHC thermostat. After the equilibration was completed, during the production run of more than 20 ns, we collected statistics using the NVT-ensemble. Simulations using the NVE-ensemble gave equivalent results. More details can be found in Ref. [9].

Transmission coefficients are computed

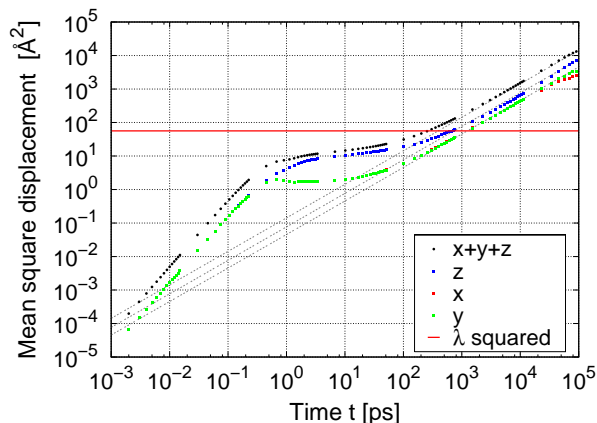
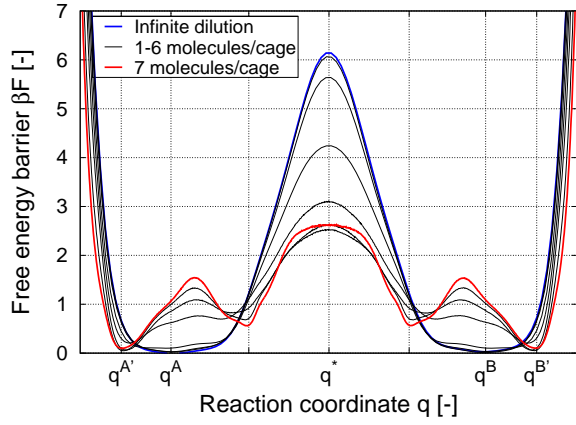
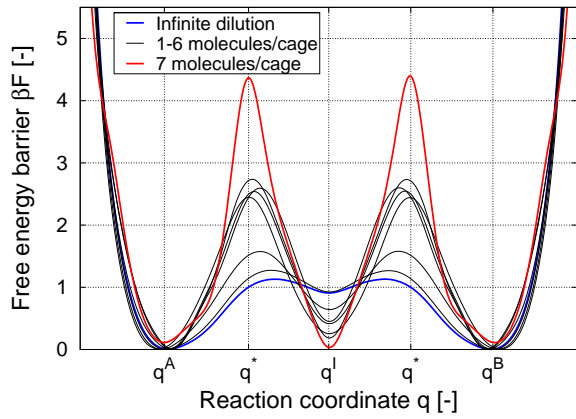


Figure 5: Mean square displacement of ethane in ERI-type zeolite at 600K and a loading of one molecule per cage. The msd is equal for x - and y -directions, and different in the z -direction. The horizontal line is the cage-to-cage hopping distance λ (approximately 7.5 \AA for both xy - and z -direction). The different regimes of diffusion are clearly visible, and only after a single cage-crossing the msd has become linear (a straight line of slope one in log-log scale). The slope over the linear regime corresponds to the limit of long times and can then be reliably measured. The diffusion coefficient is the slope at long times divided by two times the number of spatial dimensions.

from at least 50000 independent configurations. These configurations are obtained from Monte-Carlo simulations, where every 500 cycles a configurations is stored. A cycle is defined as N steps, where N is the amount of molecules, and a step is one Monte-Carlo move (translation, rotation, full regrow). On average there is one Monte-Carlo move per particle in a single cycle. The free-energy profiles are obtained using MD and MC, and both gave equivalent results.



(a)



(b)

Figure 6: Free energy profiles $F(q)$ at 600K of ethane in ERI at various loadings (infinite dilution, 1, 2, 3, 4, 5, 6, and 7 molecules per erionite cage) in the (a) hexagonal xy -plane with q^A the center of a cage, and q^B the center of a neighboring cage, (b) in the z -direction across a cage with q^A the top of the cage, q^I the middle of the cage, and q^B the bottom of the cage, respectively.

III Results

A ethane in ERI-type zeolite (anisotropic diffusion)

Diffusion in ERI-type is strongly anisotropic. In Fig. 5 we show the measured mean square displacements for ethane obtained using MD at 600K and a loading of one molecule per cage. Msd are equal for x - and y -directions, and different in the z -direction. The units are convenient

for simulation purposes, because distances are often defined in Ångstroms, and the relevant time scale is in the picosecond range. Slopes of msd are therefore in units of $1 \times 10^{-8} \text{ m}^2/\text{s}$. The different regimes of diffusion are clearly visible, and only after a single cage-crossing the msd has become linear (a straight line of slope one in log-log scale). For interacting particles there are timescale separations occurring roughly at the times between particle-particle and particle-zeolite collisions. The mean-squared displacement thus bends over to attain a different slope, and we are interested in the long-time diffusion coefficient. The self-diffusion coefficients D_α in the direction $\alpha = x, y, z$ are computed by taking the slope at long times

$$D_\alpha = \frac{1}{2N} \lim_{t \rightarrow \infty} \frac{1}{t} \left\langle \sum_{i=1}^N (r_{i\alpha}(t) - r_{i\alpha}(0))^2 \right\rangle \quad (31)$$

where N is the number of molecules, t the time, and $r_{i\alpha}$ the α -component of the center-of-mass of molecule i . The diffusion coefficients at one molecule per cage 600K are $D_{xy} = 2.1 \times 10^{-9} \text{ m}^2/\text{s}$ and $D_z = 4.2 \times 10^{-9} \text{ m}^2/\text{s}$. This indicates the diffusion is a rare event and the windows form obstructions to diffusion. Because $D_z \approx 2D_{xy}$ there are apparently no significant free energy barriers inside an erionite cage at low loading.

The hopping lattice for most cage/window-type zeolites are formed by the lattice spanned by their cage centers. However, for elongated cages like erionite, intra-cage barriers are formed at higher loadings. For an analysis we measure the free energy profiles along the cage-length (the z -direction), and along the center-to-center line in the hexagonal xy -plane. The profiles of ethane plotted in Fig. 6 over various loadings indicate that indeed there are inner cage barriers, and for the xy plane the barrier is formed by the dividing 8-ring window. The diffusion coefficient in the z -direction depends on both the hopping rate in z -direction as well

as the xy -direction (Eq. 13), because each hop in the z -direction has to be preceded by a hop in the xy -plane.

The free energy barrier in the xy -plane is a sharply peaked, and therefore the transmission coefficient is straightforward to evaluate using the Bennet-Chandler approach. The transmission coefficients $\kappa(t)$ are shown in Fig. 7. The starting configurations constrained to the top of the barrier q^* were sampled using a Monte-Carlo scheme. After approximately 10 picoseconds the time dependent transmission coefficient $\kappa(t)$ reached its plateau value κ . Using Eq. 16 and Eq. 12 the hopping rate and diffusion coefficient in the xy -plane can be computed.

The free energy in the z -direction across an erionite cage is initially rather flat, and with increasing loading a clear free energy minimum is formed in the center of the cage. There are two solutions to this problem. The first would be to use a different hopping lattice and include the purple points in Fig. 3 in the hopping lattice. An hop in z -direction is now a sequential process of two hops and the total hopping rate can be obtained using Eq. 10. A second method, and the method of our choice here, is to use biased MD to compute the total hopping rate from the top of the cage to the bottom of the cage *directly*. The reasons are twofold, firstly the method is applicable to low free energy barriers and secondly, the method is able to compute hopping rates over complicated free energy landscapes such as, in this case, two barriers. The reaction coordinate is the projection on the z -axes (Eq. 27), where q_A denotes the top of the cage, q_B the bottom of the cage, and q_I the intermediate free energy minimum. There are two barriers, one separating q_A and q_I , and another one between q_I and q_B . The biased MD method computes the total hopping rate from q_A to q_B by computing an effective diffusion coefficient over the entire q domain (q^A to q_B), i.e. there is no separate computation of the transmission coefficient.

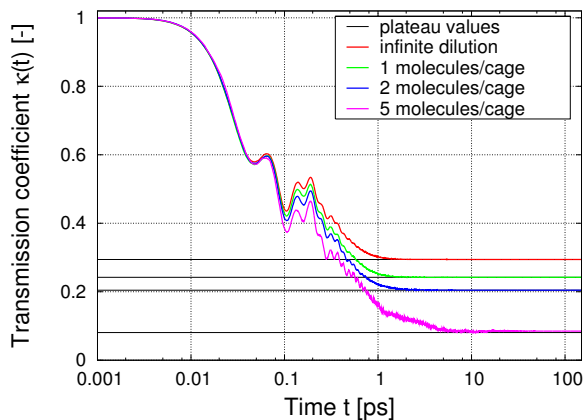


Figure 7: Transmission coefficient $\kappa(t)$ for ethane at 600K in ERI-type zeolite as a function of time for various loadings.

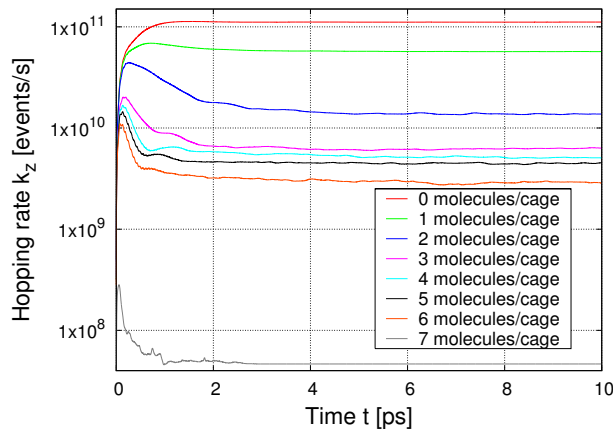


Figure 8: Intra-cage hopping rate in the z -direction obtained using Biased MD for ethane in elongated ERI-type cages at 600K.

The results are shown in Fig. 8. The plateau value at long times is the hopping rate of interest.

The self-diffusion coefficients of ethane in ERI-type zeolite at 600K using dcTST and conventional MD are shown in Fig. 9. Surprisingly, the anisotropical behavior of ERI-type cages reverse with loading, i.e. at low loading the diffusion in the z -direction is two times *faster* than in the xy -direction, while for higher loadings this changes to a diffusion that is more than two times *slower*. Although MD and dcTST give equivalent diffusivity results, the behavior is better understood by analyzing the free energy profiles (and transmission coefficients). At low

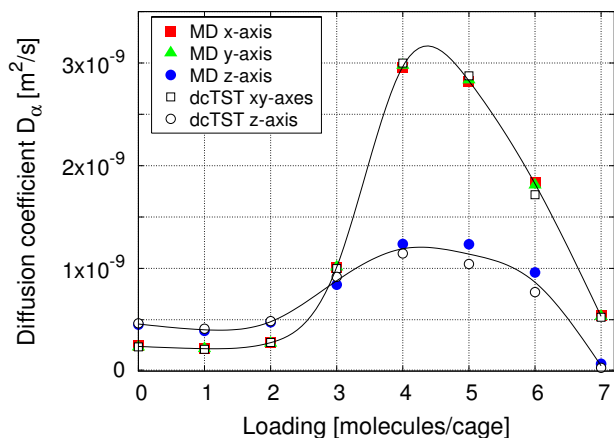


Figure 9: Anisotropic diffusion of ethane in ERI-type zeolite computed by dcTST and conventional MD at 600K.

loading the diffusion is impeded by the eight-ring windows, i.e. the exits out of the cage to the next, but at higher loadings the barrier is formed by the center of the cages.

B ethane in CHA-type zeolite

A similar free energy analysis as for ERI-type zeolites can be performed for CHA-type zeolites. However, here, the free energy profiles and transmission rates are equal for a , b , and c directions. Hence, there is only one hopping rate, and any anisotropy is entirely due to the degree of distortion from a cube. In Fig. 10 we show the free energy profiles for CHA-type zeolites. The barrier is formed by the eight-membered ring for all loadings, and at higher loadings some inner-cage reorganization is observed as more and more molecule has to be accommodate inside the chabazite cage.

Our simulations indicate no significant anisotropy (less than 2%) and therefore we plot the orientational averaged self-diffusivity only, for both MD and dcTST in Fig. 11. A similar diffusivity behavior to ERI-type zeolites is observed for CHA-type cages. Indeed, the increase in diffusivity is a general feature present due to cage-confinement. The maximum in the diffusivity is shifted to lower loading, consistent

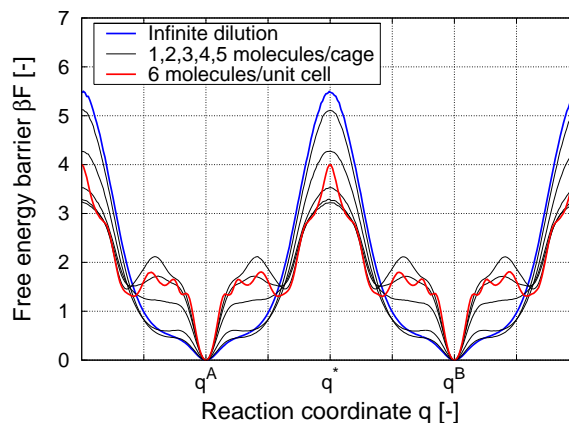


Figure 10: Free energy profiles $F(q)$ at 600K of ethane in CHA at various loadings (infinite dilution, 1, 2, 3, 4, 5, and 6 molecules per chabazite cage). The reaction coordinate is the position of the first bead along the centerline connecting the center-points of two cages. (lines from top to bottom in order of the legend).

with the smaller cage size of chabazite in comparison to erionite.

As mentioned, the diffusion in CHA-type zeolite can be considered isotropic in practice. Indeed, tracer diffusion measurements of water in natural chabazite by Raman spectroscopy did not indicate any substantial deviation from diffusion isotropy [14]. However, using the pulsed field gradient NMR technique Bär et al. [13] reported an orientation-dependent diffusivity with a ratio between the maximum and minimum diffusivity of a factor of two, also for water in natural chabazite. Such a significant anisotropy can potentially originate from a significant symmetry breaking in the zeolite sample, caused by for instance a non-random arrangement of cations and/or imperfections inside the crystal.

IV Conclusions

The dcTST gives equivalent results to conventional MD, but is also applicable in the regime of very slow diffusion where MD can not be used. Moreover, the method allows for a more detailed analysis in terms

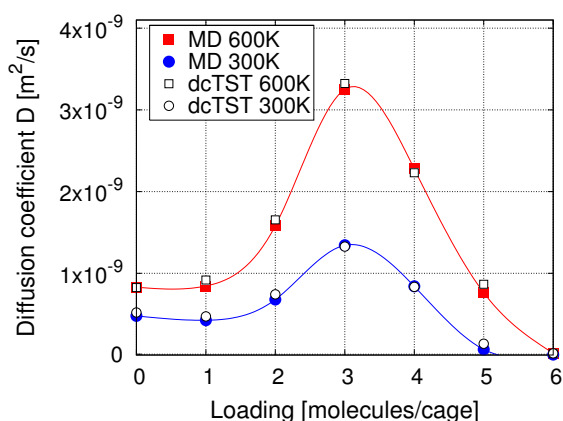


Figure 11: Orientationally averaged diffusion of ethane in CHA-type zeolite computed by dcTST and conventional MD at 300K and 600K.

of free energy profiles and transmission coefficients. The first is a static term, corresponding to locations of preferable adsorption sites and estimations of free energy barriers in between, the latter (or actually the inverse of the transmission coefficient: the recrossing) corresponds to collision frequencies, which generally increase with loading. Here, we have shown how to apply the dcTST to nontrivial lattices: (a) ERI-type lattices are non-Bravais, (b) CHA-type lattices are rhombohedral. Both zeolites are cage/window-type zeolites, and in both zeolites the diffusion increase with loading and decrease only close to saturation loading. The diffusion of CHA-type zeolites is nearly isotropic, the diffusion of ERI-type zeolites is strongly anisotropic. Surprisingly, the anisotropical behavior of ERI-type cages reverse with loading, i.e. at low loading the diffusion in the z -direction is two times *faster* than in the xy -direction, while for higher loadings this changes to a diffusion that is more than two times *slower*. Although MD and dcTST give equivalent diffusivity results, the behavior is better understood by analyzing the free energy profiles (and transmission coefficients). At low loading the diffusion is impeded by the eight-ring windows, i.e. the exits out of the cage to the next, but at higher loadings the

barrier is formed by the center of the cages.

Acknowledgments

We thank T. J. H. Vlugt and T. S. van Erp for their comments on the manuscript, the Netherlands Research Council (CW), the Deutsche Forschungsgemeinschaft (DFG, priority program SPP 1155), and the Spanish Ministry of Science and Technology (Ramón y Cajal Program and VEM2003 20574 C03 01) for financial support, and NWO/NCF for computational resources.

Bibliography

- [1] V. Gupta, S. S. Nivarthi, A. V. McCormick, and H. T. Davis, *Chem. Phys. Lett.* **247**, 596 (1995).
- [2] V. Kukla, J. Kornatowski, D. Demuth, I. Girnus, H. Pfeifer, L. V. C. Rees, S. Schunk, K. K. Unger, and J. Kärger, *Science* **272**, 702 (1996).
- [3] K. Hahn, J. Kärger, and V. Kukla, *Phys. Rev. Lett.* **76**, 2762 (1996).
- [4] R. L. Goring, *J. Catal.* **31**, 13 (1993).
- [5] K. Yoo, R. Tsekov, and P. G. Smirniotus, *J. Phys. Chem. B.* **7**, 13593 (2003).
- [6] D. Dubbeldam, S. Calero, T. L. M. Maesen, and B. Smit, *Phys. Rev. Lett.* **90**, 245901 (2003).
- [7] D. Dubbeldam and B. Smit, *J. Phys. Chem. B.* **107**, 12138 (2003).
- [8] P. K. Ghorai, S. Yashonath, P. Demonstis, and G. B. Suffritti, *J. Am. Chem. Soc.* **125**, 7116 (2003).
- [9] D. Dubbeldam, E. Beerdsen, T. J. H. Vlugt, and B. Smit, *J. Chem. Phys.* **122**, 224712 (2005).
- [10] E. Beerdsen, B. Smit, and D. Dubbeldam, *Phys. Rev. Lett.* **93**, 248301 (2004).

- [11] J. A. Gard and J. M. Tait, *Proceedings of the Third International Conference on Molecular Sieves; Recent Progress Reports*, edited by J. B. Uytterhoeven (Leuven University Press, Zurich, 1973), pp. 94–99.
- [12] M. Calligaris, G. Nardin, and L. Rاندaccio, *Zeolites* **3**, 205 (1983).
- [13] N.-K. Bär, J. Kärger, H. Pfeifer, H. Schäfer, and W. Schmitz, *Microp. Mesop. Materials* **22**, 289 (1998).
- [14] S. V. Goryainov and I. A. Belitsky, *Phys. Chem. Miner.* **22**, 433 (1995).
- [15] C. H. Bennett, in *Diffusion in Solids: Recent Developments*, edited by A. Nowick and J. Burton (Academic Press, New York, 1975), pp. 73–113.
- [16] D. Chandler, *J. Chem. Phys.* **68**, 2959 (1978).
- [17] D. Frenkel and B. Smit, *Understanding molecular simulation 2nd edition* (Academic Press, London, UK, 2002).
- [18] A. G. Bezus, A. V. Kiselev, A. A. Lopatkin, and P. Q. J. Du, *J. Chem. Soc., Faraday Trans. II* **74**, 367 (1978).
- [19] T. J. H. Vlugt and M. Schenk, *J. Phys. Chem. B.* **106**, 12757 (2002).
- [20] J. P. Ryckaert and A. Bellemans, *Faraday Discuss. Chem. Soc.* **66**, 95 (1978).
- [21] A. Schüring, S. M. Auerbach, S. Fritzsche, and R. Haberlandt, *J. Chem. Phys.* **116**, 10890 (2002).
- [22] M. P. Allen and D. J. Tildesley, *Computer simulation of liquids* (Clarendon Press, Oxford, 1987).
- [23] D. C. Rapaport, *The art of molecular dynamics simulation 2nd edition* (Cambridge University Press, Cambridge, 2004).
- [24] G. J. Martyna, M. Tuckerman, D. J. T. M. L., and Klein, *Mol. Phys.* **87**, 1117 (1996).

Summary and conclusions

I The "window"-effect (chapters 3, 4, and 5)

One of the most controversial and intriguing phenomena in the zeolite literature was the window effect. Conventional zeolite-catalyzed (hydro)cracking yields a product distribution with a single maximum, which is consistent with the currently accepted reaction mechanisms. Chen et al. [1,2] discovered in 1968 that ERI-type zeolites yield a bimodal product distribution with maxima at n -C₃₋₄ and n -C₁₀₋₁₂, but no product in the C₇₋₉ range (the "window"). This suggests the possibility of *length selective* hydrocracking, enabling control over the length distribution of the product or reactant slate by selecting a zeolite with the appropriate window.

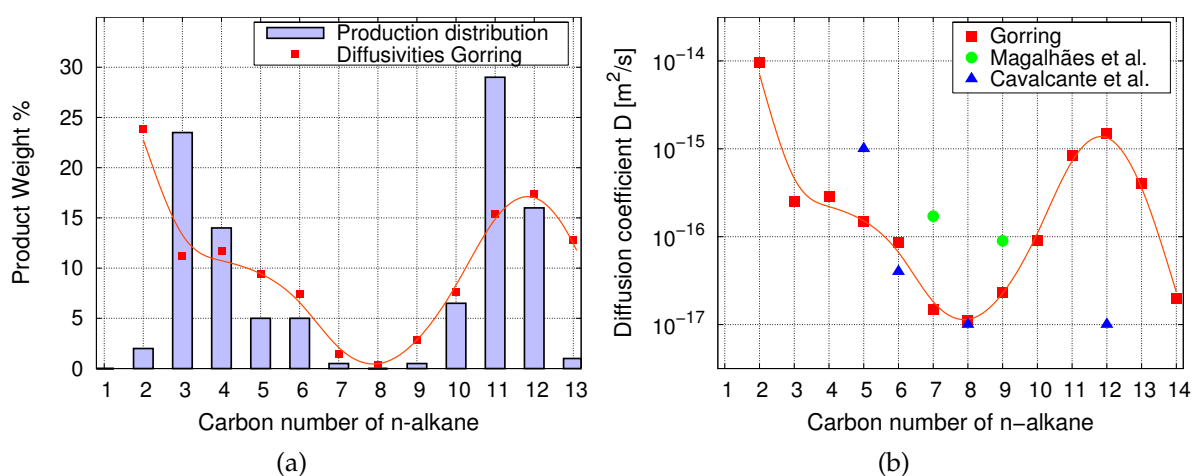


Figure 1: The window effect in ERI-type zeolites (a) a near-perfect correlation exists between the product distribution by Chen et al. [1,2] and the diffusion coefficient as a function of n -alkane length by Gorrings [3], (b) Gorrings's results are in disagreement with the results of Cavalcante et al. [4] and Magalhães et al. [5].

For a long time the window effect had been related nearly exclusively to the diffusion rate of n -alkanes in ERI-type zeolites. Gorrings showed that a near perfect correlation exists between the product distribution and the diffusion coefficient as a function of n -alkane length (Fig. 1(a)) [3]. Recent diffusion measurements by Cavalcante et al. [4] and Magalhães et al. [5] failed to reproduce the increase in diffusion rate for the appropriate n -alkane lengths (Fig. 1(b)). This controversy motivated us to study the window-effect using molecular simulations focussing on the following questions

Does the window-effect exist? what is the reason for the product distribution?

and constitute the first three chapters (3, 4, and 5).

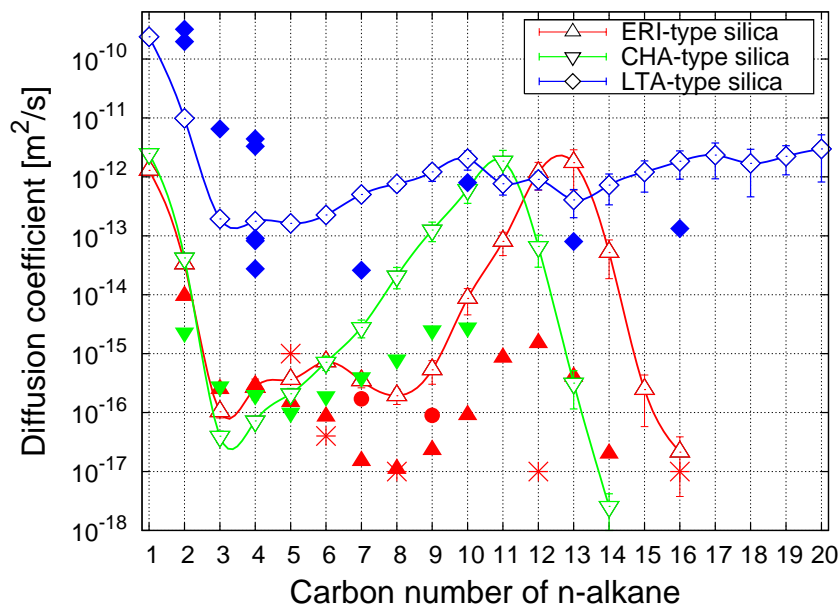


Figure 2: Diffusion coefficients as a function of chain length at 600 K for ERI-, CHA-, and LTA-type zeolite; \triangle ERI-type silica sim. results, \blacktriangle exp. results of Gorring [3], $*$ Cavalcante et al. [4], \bullet Magalhães et al. [5]; ∇ CHA-type silica sim. results, \blacktriangledown exp. results of Gorring [1]; \diamond LTA-type silica sim. results, \blacklozenge exp. compiled in Ref. [6].

The molecular simulations of chapter 3 and 4, shown in Fig. 2, corroborated the existence of the disputed window effect, i.e. an increase in diffusion rate by orders of magnitude when the alkane chain length increases so that the shape of the alkane is no longer commensurate with that of a zeolite cage. This window effect was shown to be characteristic for molecular sieves with pore openings that approach the diameter of the adsorbate. Our simulations reproduced the chain length dependence and are consistent with the experimental data of Gorring [3]; we not only confirmed the occurrence of a maximum for both ERI- and CHA-type zeolite at the same carbon number as observed experimentally, but also the shift of this maximum to lower carbon numbers for CHA-type silica. The increase in the diffusion rate originating from the geometry-chain interaction is a remarkable four orders of magnitude for both ERI- and CHA-type silicas !!! In the controversy about the experimental results we side with Gorring, who was the first and only to report experimental data indicating the "window-effect". This opens the possibility of length selective cracking, where the length distribution is controlled by choosing structures with the appropriate cage size.

Although our simulations confirmed the experimental observations of Gorring, the results nevertheless pointed to an alternative mechanism based on anomalously low adsorption of long molecules. It is important to note that the window effect has become associated only with a high n -C₁₀₋₁₂ yield. However, a closer inspection of the raw data of Chen et al. published for n -C₃₆ reveals additional yield maxima at n -C₂₄₋₂₆ and at n -C₁₅₋₁₇ in the complete chromatogram of the n -C₃₆ cracking products (Fig. 3). From the

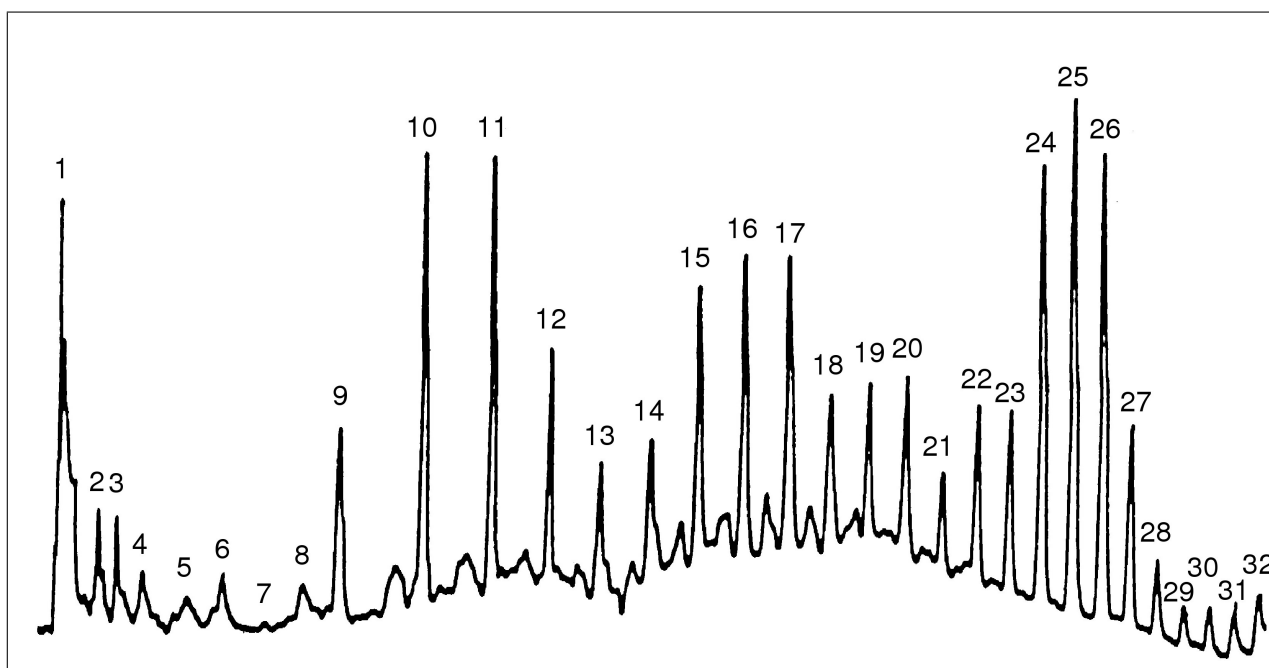


Figure 3: The complete chromatogram of the $n\text{-C}_{36}$ cracking products [1, 2].

calculated variation of Henry coefficients with chain length it is immediately apparent that the complete $n\text{-C}_{36}$ adsorption can be excluded, and yet ERI-type zeolites crack $n\text{-C}_{36}$ shape selectively. The preferential yield of $n\text{-C}_{24-26}$ and $n\text{-C}_{15-17}$ is indicative of consecutive scissions of C_{10-12} fragments from $n\text{-C}_{36}$. The maximum at $n\text{-C}_{10-12}$ indicates that the most rapidly diffusing cracking product can escape complete consumption into more refractory alkanes with six or fewer carbon atoms. This selective cracking process leaves minima at $n\text{-C}_{18-23}$ and at $n\text{-C}_{13-14}$. A reasonable explanation for persistence of shape-selective cracking of very long alkanes by ERI-type zeolites is that these long molecules adsorb partially in the surface pockets created by the ERI-type cages at the outer crystal surface. Full adsorption by more than 12 carbon atoms is unlikely. The adsorbed $n\text{-C}_{10-12}$ part is chopped off, and the non-adsorbed part is released. Released parts end up in the product slate or undergo further scission reactions. This process becomes less selective with an increasing number of cracking steps due to concomitant isomerization reactions.

The proposed mechanism is characteristic for cage/window-type zeolites with small windows close to the diameter of the adsorbate. The newly gained understanding of length-selective hydrocracking affords prediction of selectivity as a function of cage size.

II Development of methods to compute very slow diffusion in confinement (chapters 3, 4)

The diffusion coefficients in ERI-type zeolites are extremely slow, as low as 10^{-17} m^2/s . The first difficulty we encountered when studying diffusion behavior in zeolites using simulation is that many diffusional processes occur outside the time scale accessible to MD, which is currently typically limited to diffusion rates in the order of 10^{-12} m^2/s . The first step in my PhD was

the development of a novel simulation Transition State Theory technique to study diffusion of linear alkanes in nanoporous materials with exceptionally slow diffusion rates.

which required the combination of rare-event transition state theory techniques and the configurational-bias Monte Carlo algorithm (CBMC).

The conventional simulation techniques are prohibitively expensive for long alkanes. The CBMC technique greatly improves the conformational sampling of molecules and increases the efficiency of chain insertions by many orders of magnitude. In a CBMC simulation chains are grown bead by bead biasing the growth process towards energetically favorable configurations, and avoiding overlap with the zeolite. During the growth the Rosenbluth factor is calculated. The average Rosenbluth factor is directly related to the excess chemical potential, the free energy, and the Henry coefficient K_H .

Diffusion can be considered an activated process, if the free energy barrier impeding diffusion is much higher than $k_B T$, where k_B is the Boltzmann constant and T the temperature. We define a reaction coordinate q , that indicates the progress of the diffusion event from cage i to cage j . The location of the dividing barrier is denoted by q^* . Once in a while a particle hops from one cage to the next, and the actual crossing time is negligible compared to the time a particle spends inside the cage. One can exploit the large separation in time scales using rare-event simulation techniques. In Transition State Theory (TST) approximations one computes a rate constant between states A and B by computing the equilibrium particle flux through the dividing surface. The dividing surface should uniquely divide two connected states, and in general the TST rate is an upper bound on the exact rate. The exact rate can be recovered by running short MD trajectories from the dividing surface to compute a dynamical correction (dc) κ_{ij} . The rate coefficient for a jump from site i to site j can be expressed as

$$k_{i \rightarrow j} = \kappa_{ij} k_{i \rightarrow j}^{\text{TST}} \quad (1)$$

where κ_{ij} is the classical transmission coefficient and

$$k_{i \rightarrow j}^{\text{TST}} = \sqrt{\frac{k_B T}{2\pi m}} \frac{Z^S}{Z_i} \quad (2)$$

where m is the reduced mass associated with the reaction coordinate, Z^S is the configurational partition function on the dividing surface, Z_i is the configurational partition function in the reactant state i . The ratio of the partition function can be expressed in terms of the free energy surface $F(q)$

$$\frac{Z^S}{Z_i} = \frac{e^{-\beta F(q^*)}}{\int_i e^{-\beta F(q)} dq} \quad (3)$$

Our novel method combined the two algorithms. Calculating the equilibrium particle flux through the dividing surface is equivalent to a free energy computation as function of a "reaction coordinate", which monitors the progress of the diffusion event. At infinite dilution, free energy can be probed by the Widom particle insertion method, where chains are grown at random positions and the resulting contribution mapped onto the reaction

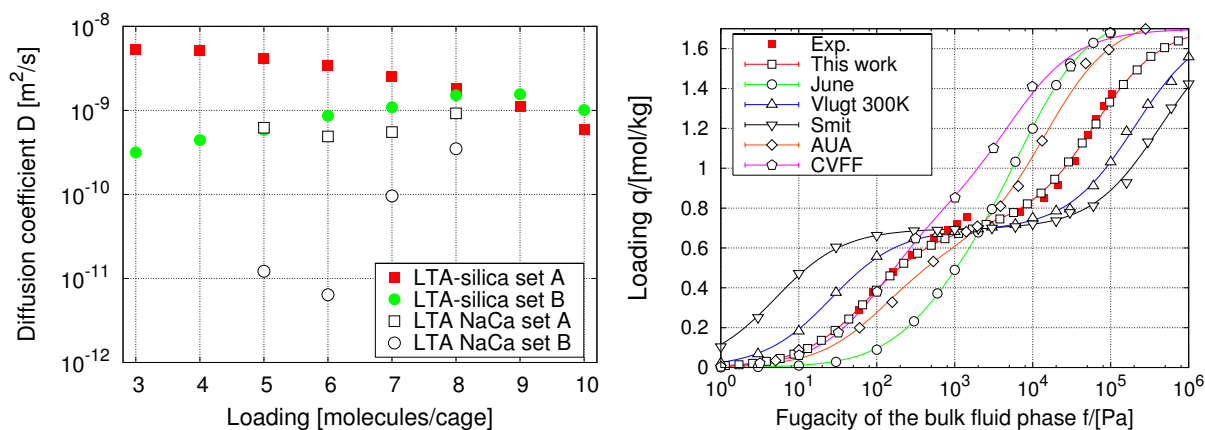


Figure 4: Force fields (a) diffusion coefficients of methane in LTA-type silica at 173K as a function of loading by MD simulations of Fritzsche et al. [7,8]. Set A uses $\sigma = 3.14 \text{ \AA}$ and $\epsilon = 180 \text{ K}$ for the O-CH_4 interaction, while set B uses $\sigma = 3.46 \text{ \AA}$ and $\epsilon = 97.5 \text{ K}$, (b) Isotherms of 2-methylpropane at 308 K in MFI compared to various computational models. The experimental data are taken from Ref. [9], the simulation data from June et al. [10], Vlugt et al. [11], Smit et al. [12], AUA from Pascual et al. [13], and CVFF from Macedonia et al. [14].

coordinate. The crucial link was to take the position of one of the beads as the reaction coordinates. This renders it unnecessary to sample the complete phase space by integrating over all internal particle coordinates and orientations, weighed with the correct Boltzmann weight. The resulting computational algorithm is 6-10 orders of magnitude more efficient compared to the conventional simulation techniques.

III Force field development (chapter 6, 7, and 8)

Different parameter sets yield different values of diffusivities. In Fig. 4, the MD-data of Fritzsche et al. at 173K for methane in LTA-type zeolite are shown [7, 8], using two different parameters sets A and B. The diffusivities differ quantitatively by an order in magnitude, but also the qualitative behavior is different: set B increases with loading, while set A decreases. The critical unresolved question was:

which of the different potential parameter sets circulating in literature is the most physically realistic one? Is it possible to design a consistent and high-quality force field in a systematic way?

Potential parameter sets can be checked only via comparison with experiment. For diffusion the comparison is complicated by large discrepancies between microscopic and macroscopic experimental measurement methods, and even within the same measurement technique there are many disagreements between various studies. However, adsorption results seem to be well established and provide a more solid basis for a detailed comparison between experiment and simulation. Moreover, a large amount of data exists on adsorption of hydrocarbons in siliceous zeolites.

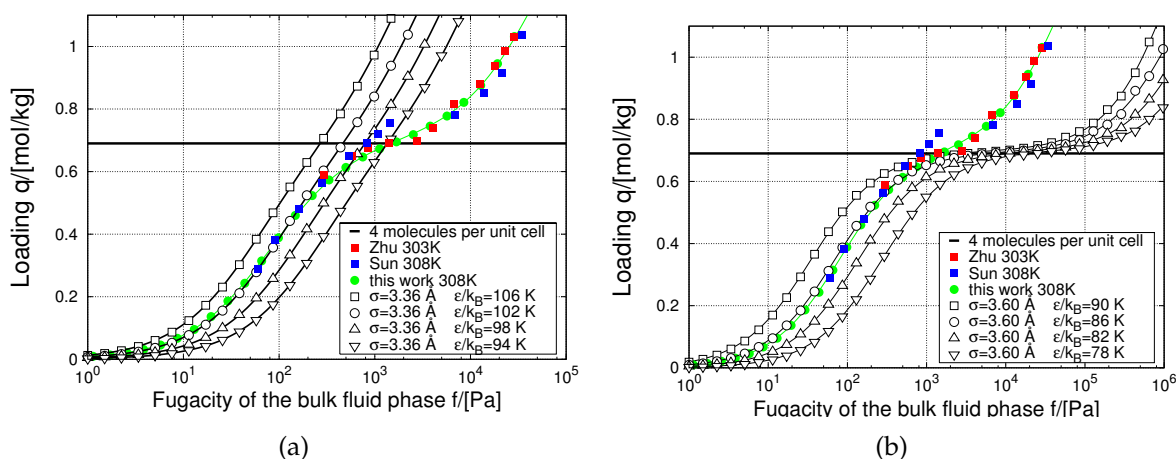


Figure 5: Isotherms of 2-methylpropane at 308 K in MFI. The O-CH parameters remain fixed at $\sigma = 3.92 \text{ \AA}$ and $\epsilon/k_B = 40 \text{ K}$, while $\epsilon_{\text{O-CH}_3}$ is examined over a range of reasonable values for two fixed values of $\sigma_{\text{O-CH}_3}$: a) a rather too small of $\sigma_{\text{O-CH}_3} = 3.36 \text{ \AA}$ and b) a too high value of $\sigma_{\text{O-CH}_3} = 3.60 \text{ \AA}$. Only a single parameter pair, $\epsilon_{\text{O-CH}_3}/k_B = 93$ and $\sigma_{\text{O-CH}_3} = 3.48$ combined with the CH parameters (Table 2), is able to describe the experimental data of Sun et al. [9] and Zhu et al. [15].

It is instructive to discuss the role of the size-parameter $\sigma_{\text{O-CH}_3}$. In Fig. 5 we show the influence of the σ parameters on the inflection of 2-methylpropane in MFI. The O-CH parameters remain fixed at $\sigma = 3.92 \text{ \AA}$ and $\epsilon/k_B = 40 \text{ K}$, while $\epsilon_{\text{O-CH}_3}$ is examined over a range of reasonable values for two values of $\sigma_{\text{O-CH}_3}$: one significantly too small and one significantly too large. A crucial observation is that only a single strength/size parameter pair is able to describe the inflection and the entire isotherm properly. This is in contrast with the common belief that for each value of σ there is a corresponding ϵ that can describe the isotherm correctly [16]. The shape of the isotherm and the inflection points are the most sensitive to the size-parameter of the interactions, whereas the loading at a given pressure is most sensitive to the strength-parameter of the interaction. A higher strength parameter ϵ induces an increased loading, and a lower strength parameter results in a decrease in loading (for a fixed pressure). The amount of inflection is controlled by the size parameter σ . These properties can be exploited to obtain unique parameters.

We refer to Fig. 4 to discuss the comparison with various united atom approaches previously proposed in literature. The figure showed the inflection in the isotherm of 2-methylpropane at 308 K in MFI. The models of Smit et al. and Vlucht et al. exaggerated the inflections because their size-parameters were too large. The models of Pascual et al., June et al., and the all-atom CVFF force field did not show a clear inflection at all because their size-parameters were too small. The question was "Which of the different potential parameter sets circulating in literature is the most physically realistic one?" We can state that for alkanes in siliceous zeolites our new force field is a big improvement over previous force fields. For further improvement and refinement more experimental data is needed.

The fitting to well-established inflection points in the isotherms has many advantages and overcame problems that had impeded the development of more accurate force fields. We obtained a unique set of parameters that all directly related to well-defined physical properties. Therefore, the parameters were much better transferable to other systems than

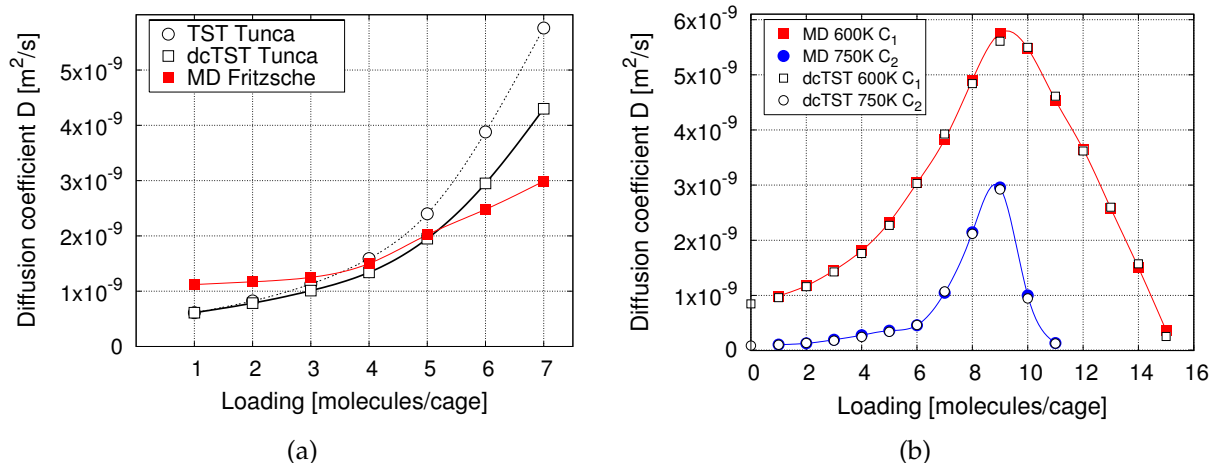


Figure 6: Diffusion coefficient of (a) methane in LTA-type silica as a function of loading. The coarse-grained results of Tunca et al. using dynamically corrected and noncorrected TST are shown. The MD results were taken from Fritzsche et al. on an identical system, (b) methane and ethane in LTA-type zeolite, as a function of loading, at 600K and 750K, respectively, using our dcTST method.

parameters from previous attempts. By explicitly fitting to entire adsorption isotherms we guarantee the proper reproduction of properties such as Henry coefficients, heats of adsorption, adsorption entropies, and saturation loadings.

Because this methodology can be applied to the important practical problem of force field development for zeolites including cations and also beyond the field of zeolites, it justified publication in Journal of the American Chemical Society and Physical Review Letters, respectively.

IV Development of methods to compute very slow diffusion in confinement as a function of loading (chapters 9, 10, and 12)

Many of the processes of industrial importance occur at non-zero loading. A limited number of studies deal with non-zero loading. Tunca and Ford [22] used multidimensional TST to obtain the hopping rate of adsorbates from an α -cage in LTA-type zeolite as a function of loading. Various approximations were applied to make the simulations computationally feasible. In a subsequent study [23] the limitations of an empty receiving cage and the use of the Widom insertion method were avoided. Recently, Tunca and Ford presented a new hierarchical approach to the molecular modeling of diffusion and adsorption at nonzero loading in microporous materials [24]. Statistical mechanical partitions functions are calculated on molecular level models and used as an input to a coarse-grained model. Tunca and Ford advocate separate calculations of Z^S and Z_i , as opposed to the conventional approach of calculating ratios of partitions functions *viz.* free energies (Eq. 3). They developed a recursive algorithm for building up $(N + 1)$ -body partition functions from N -body partitions functions

Fig. 6 shows the diffusion coefficients of methane in LTA-type zeolite as a function of

loading using the TST and dcTST method of Tunca et al. and the MD results of Fritzsche et al. on an identical system. Although adsorption was well represented by the method of Tunca et al., the coarse-grained self-diffusivity data under-predicted the diffusivity at low loading, while significantly over-predicting the diffusivities at higher loadings, in comparison to conventional MD. The discrepancies might stem from various sources:

- only one pair of isolated cage is treated.
- multi-jumps, involving three or more cages, are neglected.
- the intra cage dynamics is always fast in comparison to the rate of escape from the cage.
- for the purpose of calculating the partition function the molecules are restricted to a set of distinguishable cages.
- a "pore-pairwise" additivity of the excess Helmholtz free energy is assumed.
- the use of a kinetic Monte Carlo scheme on a lattice level where the equilibrium and dynamical properties are evaluated.

The obvious question to be answered was:

Could we do better? Could we develop a method that is capable of computing *quantitatively* the diffusivity of adsorbed molecules in confined systems at non-zero loading?

In chapter 9, published as a letter in Physical Review Letters, an extension to Transition State Theory was presented that is capable of computing quantitatively the diffusivity of adsorbed molecules in confined systems at non-zero loading. It was shown that the particle-particle correlations can be taken into account by a proper definition of an effective hopping rate of a *single* particle. The self-diffusivity was computed directly by computing the hopping rate of a molecule over a typical length scale given by the smallest repeating zeolite-structure, i.e. from the center of cage A to the center of cage B. The use of kinetic Monte Carlo and its underlying assumptions are therefore avoided. Implicitly one integrates over all adsorption sites in the cage, irrespective whether these are well-defined or not. All other particles are regarded as a contribution to the external field exerted on this tagged particle. The dcTST extension to finite loadings yielded excellent agreement with that obtained by conventional MD simulations and is applicable in any system containing high free energy barriers and for any type of guest molecule. While Molecular Dynamics calculations are limited to relatively fast diffusing molecules or small rigid molecules, our approach extends the range of accessible times scales significantly beyond currently available methods. In Chapter 10, results were shown for methane, ethane, and propane in LTL- and LTA-type zeolites over a wide range of temperatures and loadings, and demonstrated the extensibility of the method to mixtures.

V Flexibility influence on diffusion (chapter 10)

The flexibility issue had long been an open one, and was thought to be closed: "In cation-free zeolites, diffusivities remain virtually unchanged for for small molecules when including lattice vibrations". Fritzsche et al. studied methane in cation-free LTA-type zeolite, and their data is summarized in Fig. 7. By comparing with a model rigid LTA minimized using the same force field, they found almost no influence on the diffusion coefficient.

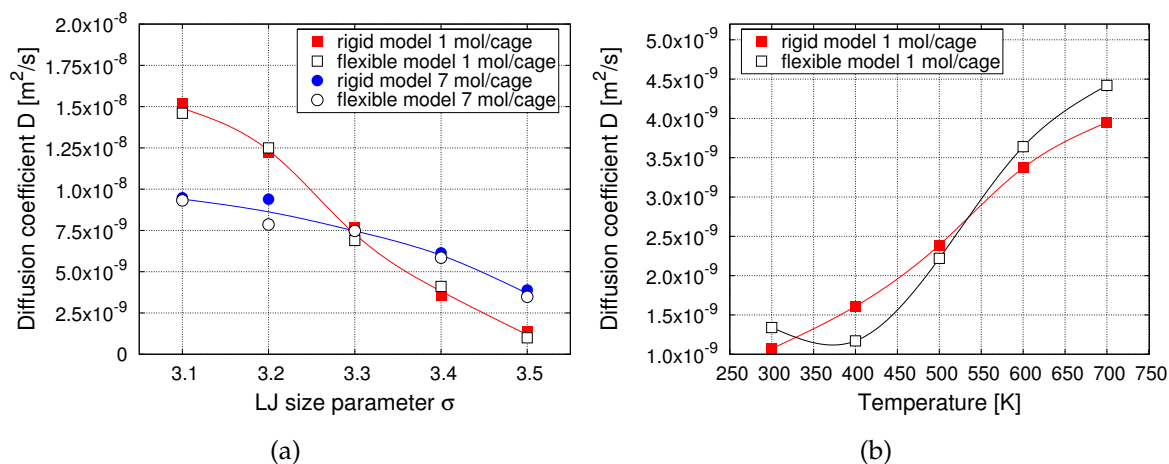


Figure 7: MD data of Fritzsche et al. [17] on methane in LTA-type silica (a) comparing a rigid and flexible model varying the LJ size parameter σ at a loading of 1 and 7 molecules per cage, (b) comparing a rigid and flexible model as a function of temperature at a loading of 1 molecule per cage. The flexible lattice model of Demontis et al. was used [18].

The force fields developed in chapter 6 and 7 have one extremely important consequence: they allow a detailed investigation of the importance of lattice vibrations. The reason is that the found parameters are *unique* and hence the only parameters to describe adsorption properly. Because flexibility of the framework is not an issue for adsorption of linear and branched alkanes [21], a mismatch between experimental and computed diffusivities can only mean two things:

- the united-atom model is inadequate to properly describe diffusion,
- the framework flexibility should be properly modeled.

Since the first conclusion can only be drawn after considering the second, the flexibility issue for diffusion had to be resolved for our systems and simulation conditions

Does flexibility influences diffusion? At what conditions and for what systems does flexibility matter, and when can it be neglected?

In Ref. [17] it was found that self-diffusion coefficients for methane in LTA-type zeolite obtained with flexible and with rigid lattices are practically the same. In Fig. 8 the self-diffusivity of ethane was shown using the LJ-parameters of Schüring et al. [19] and the

results of a rigid zeolite to the flexible model of Demontis et al. [18,20] were compared. The error-bars on our simulations are smaller or comparable to the symbol size, and can be considered highly accurate. The data was obtained by averaging over 20 independent simulations and the error bars were computed from twice the standard deviation for that set (95 percent confidence interval). We have added the results of Schüring et al. [19] for the infinite dilution case, and for 1 molecule per cage. The data of Schüring et al. compare well and are consistent with our simulations. An important observation is that the differences between flexible and rigid LTA-type zeolite for a small alkane like ethane in a cation-free zeolite are significant and *temperature* dependent. We note that Fritzsche's conclusions were drawn from data only *above* 300K. In the low temperature-region the ethane molecule is tightly confined in the window itself, while at higher temperature the molecule is less tightly confined and located just in front of the window. The dcTST method of chapter 9 and 10 would allow a detailed investigation of the effect of framework flexibility on slow-diffusing molecules.

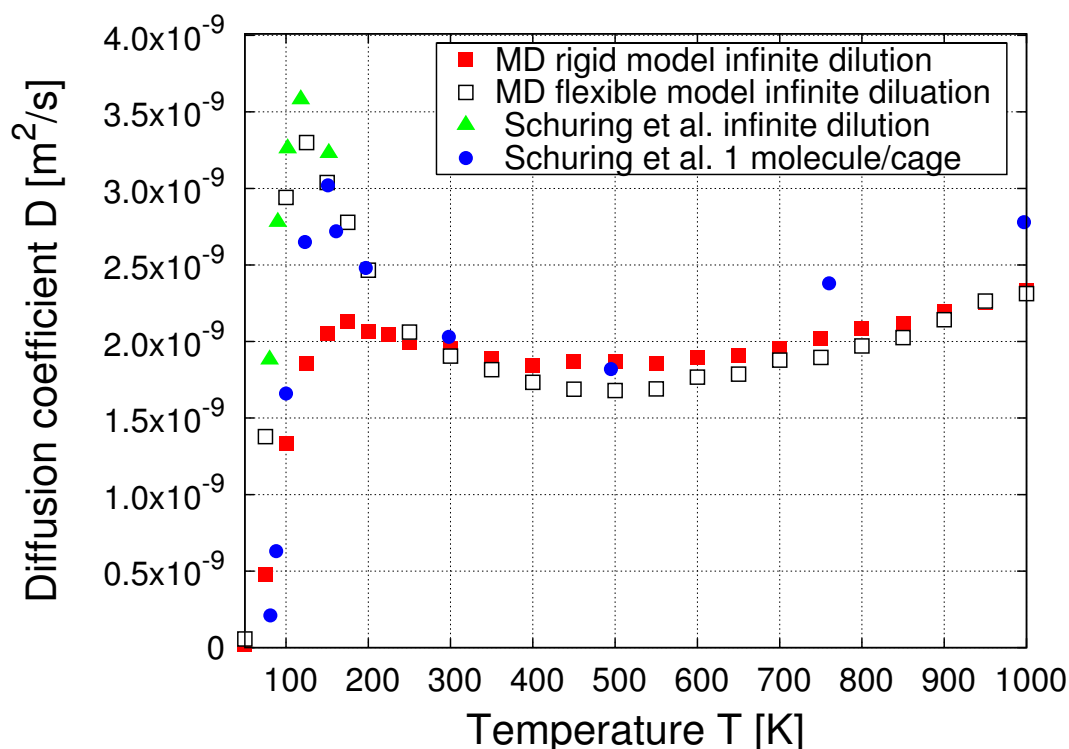


Figure 8: Self-diffusivity of ethane using the LJ-parameters of Schüring et al. [19] comparing the results of a rigid zeolite to the flexible model of Demontis et al. [18,20]. Error-bars are smaller or comparable to the symbol size. For comparison we have added the results of Schüring et al. [19] for the infinite dilution case, and for 1 molecule per cage.

VI Understanding diffusion in confinement: Molecular Path Control (chapters 11 and 12)

In contrast to adsorption, which is relatively well understood, diffusion in confinement was somewhat of a mystery. Previous knowledge was so limited that one could not predict whether for a given molecule and adsorbate the diffusion coefficient will go up, go

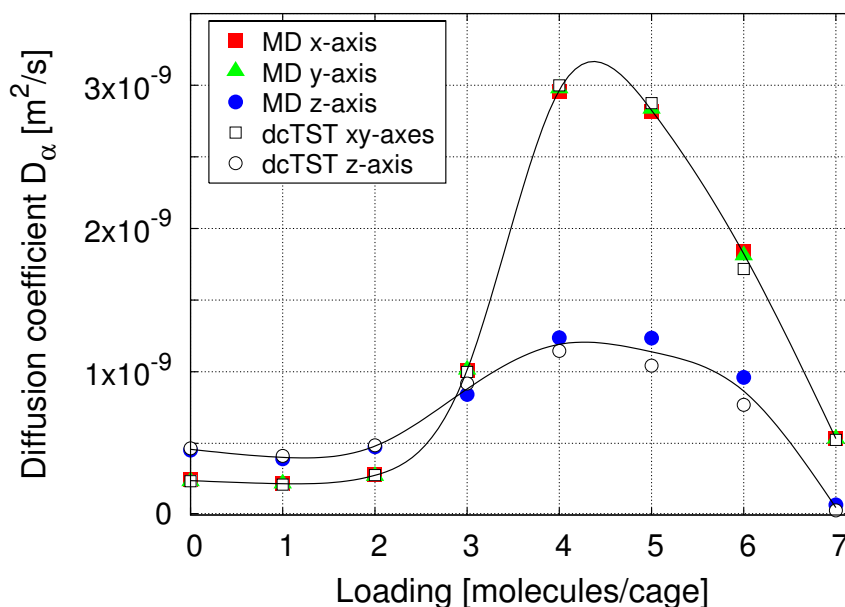


Figure 9: Anisotropic self-diffusivity D_α ($\alpha = x, y, z$) of ethane in ERI-type zeolite computed by dcTST and conventional MD at 600K.

down, or remain constant as a function of loading. Therefore, our main objective to study diffusion in zeolite was

Predicting diffusion behavior for arbitrary topologies, adsorbates and loadings.

The dcTST method can be used to explain diffusion behavior as a function of loading in any system with enough energy dissipation between hops, so that random walk theory (the assumption of equilibration between two subsequent jumps) and TST are valid. The diffusion mechanism is divided in two parts. The first is a static term, corresponding to locations of preferable adsorption sites and estimations of free energy barriers in between, the second corresponds to collision frequencies, which generally increase with loading. As such, the dcTST method is able to explain different diffusion regimes over loading, and provides insight into the mechanisms behind an increase or decrease in diffusivity with loading. The method is a significant breakthrough in the field of diffusion in confinement, and provides a full understanding of the molecular factors involved.

The last two chapters (11 and 12) dealt with applying the dynamically corrected Transition State Theory to confinements with complex structures and a new phenomenon in ERI-type zeolites was found: the anisotropical behavior of ERI-type cages reverses with loading, i.e. at low loading the diffusion in the z-direction is two times faster than in the xy-direction, while for higher loadings this changes into a z-diffusivity that is more than two times slower (Fig. 9). To our knowledge, this is the first time a form of molecular path control has been found for an one-component system.

The simulations were performed using two different methods: conventional Molecular Dynamics (MD) and the dynamically corrected Transition State Theory (dcTST) of chapter 9. Although MD and dcTST give equivalent diffusivity results, the behavior is better understood by analyzing the free energy profiles and lattice information provided by the dcTST method. Diffusion in the z-direction is dependent on both the hopping rate in the z-direction *and* in the xy-direction. An investigation of these hopping rates was made by

analyzing the free energy barriers for diffusion in the xy -plane. For the diffusion in the xy -plane we found "normal" behavior, typical for cage/window-type zeolite [25]. The diffusivity increases with loading, because the free energy barrier for diffusion decreases. This is due to the finite volume of a cage, where adding particles to the cage results in more repulsive interactions. In the z -direction, we found that, although initially the barriers are much smaller than in the xy -direction at low loading, the barriers for z -diffusion start to dominate the diffusion mechanism. At low loading the diffusion is impeded by the eight-ring windows, i.e. the exits out of the cage to the next, but at higher loadings the barrier is formed by the center of the cages.

When the elongation of the erionite-cages is removed, i.e. in CHA-type zeolites, no significant anisotropy, nor molecular path control is observed. These results suggest that it is possible to actively design and screen for zeolites with molecular path control properties. The key ingredient we report here is the elongation of the cages underlying tortuous diffusion paths which results in a complex interplay between different diffusion paths. These paths may then be controlled by changing the loading or pressure, and temperature.

Bibliography

- [1] Chen, N.Y.; Garwood, William E.; Dwyer, Francis G., *Shape selective Catalysis in industrial Applications, 2nd edition, revised and expanded* Chemical Industries; New York, 1996.
- [2] Chen, N. Y.; Lucki, S. J.; Mower, E. B. *J. Catal.* **1969**, *13*, 329-332.
- [3] Gorrington, L. R. *J. Catal.* **1993**, *31*, 13-26.
- [4] Jr, C. L. Cavalcante; Eic, M.; Ruthven, D. M.; Occelli, M. L. *Zeolites* **1995**, *15*, 293-307.
- [5] Magalhães, F. D.; Laurence, R. L.; Conner, W. C. *J. AlChE.* **1996**, *42* 68-86.
- [6] Kärger, Joerg; Ruthven, Douglas M., *Diffusion in Zeolites and other microporous solids* John Wiley & Sons, Inc.; New York, 1992.
- [7] Fritzsche, S.; Haberlandt, R.; Kärger, J.; Pfeifer, H.; Heinzinger, K.; Wolfsberg, M. *Chem. Phys. Lett.* **1995**, *242*, 361-366.
- [8] Fritzsche, S.; Gaub, M.; Haberlandt, R.; Hoffman, G. *J. Mol. Model.* **1996**, *9*, 286-292.
- [9] Sun, M. S.; Shah, D. B.; Talu, O. *J. Phys. Chem. B.* **1998**, *102*, 1466-1473.
- [10] June, R. L.; Bell, A. T.; Theodorou, D. N. *J. Phys. Chem* **1992**, *96*, 1051-1060.
- [11] Vlugt, T. J. H.; Krishna, R.; Smit, B. *J. Phys. Chem. B.* **1999**, *103*, 1102-1118.
- [12] Smit, B.; Loyens, L. D. J. C.; Verbist, G. L. M. M. *Faraday Discuss.* **1997**, *106*, 93-104.
- [13] Pascual, P.; Ungerer, P.; Tavitian, B.; Pernot, P.; Boutin, A. *Phys. Chem. Chem. Phys.* **2003**, *5*, 3684-3693.
- [14] Macedonia, M. D.; Maginn, E. J. *Mol. Phys.* **1999**, *96*, 1375-1390.
- [15] Zhu, W.; Kapteijn, F.; Moulijn, J. A. *Phys. Chem. Chem. Phys.* **2000**, *2*, 1989-1995.

- [16] Smit, B. J. *Phys. Chem.* **1995**, *99*, 5597-5603.
- [17] Fritzsche S.; Wolfsberg M.; Haberlandt R.; Demontis P.; Suffritti G. B.; Tilocca A., *J. Chem. Phys.* **296**, 253-258 (1998).
- [18] P. Demontis, G. B. Suffritti, S. Quartieri, E. S. Fois, and A. Gamba, *J. Phys. Chem.* **92**, 867871 (1988).
- [19] A. Schüring, S. M. Auerbach, S. Fritzsche, and R. Haberlandt, in *Random Walk Treatment of Dumb-Bell molecules in an LTA Zeolite and in Chabazite*, Proceedings of the 14th International Zeolite Conference, edited by E. van Steen, L. Callanan, and M. Claeys (Elsevier, Cape Town, 2004), pp. 2110–2117.
- [20] P. Demontis, G. B. Suffritti, S. Quartieri, E. S. Fois, and A. Gamba, *Zeolites* **7**, 522 (1987).
- [21] T. J. H. Vlugt and M. Schenk, *J. Phys. Chem. B.* **106**, 12757 (2002).
- [22] C. Tunca and D. M. Ford, *J. Chem. Phys.* **111**, 2751 (1999).
- [23] C. Tunca and D. M. Ford, *J. Phys. Chem. B* **106**, 10982 (2002).
- [24] C. Tunca and D. M. Ford, *Chem. Eng. Sci.* **58**, 3373 (2003).
- [25] E. Beerdsen, B. Smit, and D. Dubbeldam, *Phys. Rev. Lett.* **93**, 248301 (2004).

Samenvatting (Summary in Dutch)

Zeolieten zijn drie dimensionale micro poreuze vaste materialen met de eigenschap dat het moleculen van vergelijkbare grootte als de poriën kan adsorberen. Bekende toepassingen zijn waspoeder en katebakkorrels. Voor petrochemische toepassingen, zoals bijvoorbeeld het verhogen van het octaan gehalte van benzine, worden zeolieten gebruikt met goede scheidingseigenschappen tussen lineaire en vertakte alkanen. Sommige zeolieten bestaan uit kanalen, anderen bestaan uit kooien die verbonden zijn door nauwe windows. Het is met name deze laatste klasse van zeolieten waar het proefschrift zich op richt. Hoewel het proefschrift een studie van adsorptie en diffusie van alkanen in zeolieten is, draagt het ook bij aan het verbeteren van de huidige simulatie methoden. Het probleem is dat de benodigde rekentijd voor simulaties van diffusie in kooi/window zeolieten te groot is om met conventionele methoden te kunnen doen. Dit is inherent aan de structuur van kooi/window zeolieten, omdat de diffusie snelheid van moleculen erg traag is in vergelijking met kanaal zeolieten. Ter illustratie, kanaal-vormige zeolieten vertonen diffusie-snelheden in de orde grootte van 10^{-8} m²/s, conventionele methoden gebaseerd op het oplossen van de bewegingsvergelijkingen van Newton kunnen tot ongeveer 10^{-11} m²/s aan, maar de diffusie in kooi/window structuren is in de orde grootte van 10^{-14} m²/s of lager.

Hoofdstuk 1 is een generieke introductie tot zeolieten en beschrijft de structuur en context van het proefschrift. Daarna worden in hoofdstuk 2 de details gegeven van de simulatie methoden. De daarop volgende hoofdstukken zijn geordend per onderwerp.

Hoofdstuk 3, 4 en 5 gaan over het "window-effect", een oud, en al 35 jaar lang onopgelost probleem. In 1968 deed Chen "kraak"-experimenten in ERI-type zeolieten. Beginnend met lange alkanen breken de moleculen in de aanwezigheid van deze zeolieten in steeds kleinere stukken. Opmerkelijk genoeg waren er echter geen lengtes terug te vinden van 7/8/9 C-atomen, maar wel veel moleculen van lengtes 3/4 en 10/11/12. Drie jaar later deed Gorrington diffusie metingen aan hetzelfde systeem en ontdekte dat precies bij lengtes 3/4 en 10/11/12 de diffusie het snelst ging. Een mogelijke verklaring van de lengte verdeling kon dus zijn dat lange moleculen het zeoliet binnengaan, in stukken kraken, en dat de snelst bewegende moleculen er ook het eerst weer uit komen. Aan de buitenkant van het zeoliet zul je dan voornamelijk lengtes van 3/4 en 10/11/12 vinden.

Recentelijk zijn de metingen van Gorrington overgedaan door Cavalcante en Magalhães. Zij hadden veel kritiek op de wijze van uitvoering van de experimenten door Gorrington, en meenden dat Gorrington met zijn methode en experimentele set-up nooit de juiste diffusie had kunnen meten. De resultaten van Cavalcante en Magalhães waren niet in overeenstemming met Gorrington: zij vonden dat diffusie over keten lengte bleef dalen en er was dus geen relatief hogere diffusie bij lengte 10/11/12. Deze bevindingen motiveerden ons om naar dit systeem te gaan kijken met behulp van computer simulaties.

De lange-tijd beweging van moleculen in ERI-type zeolieten is zo traag dat de normale methode van het oplossen de bewegingsvergelijkingen van Newton niet meer binnen redelijke tijd te doen is. Moleculen spenderen veel tijd in een kooi en slechts heel af en toe springt er een naar een andere kooi. Voor het berekenen van een gemiddelde diffusie snelheid zouden we over heel veel sprongen moeten middelen, iets wat dus ondoenlijk is. Er zijn echter methoden ontwikkeld die hier anders tegen aan kijken, de zogenaamde "rare-event methoden". Hier wordt eerst gekeken wat de kans is dat je precies op het scheidingsvlak van twee buur kooien zit (in een window), en daarna wordt voor dit molecuul berekend wat de kans is dat als het molecuul uit een kooi kwam, ook daadwerkelijk naar de andere kooi gaat (en niet terugkeert naar de originele kooi). In principe geeft deze methode dezelfde uitkomsten, indien er een voldoende grote scheiding van tijd schalen is (de tijd die een molecuul spendeert in de kooi is veel groter dan in het window). Onze bijdrage bestond uit het feit dat we de rare-event methode toegepast hebben op dit systeem en hebben aangepast voor het gebruik op moleculen die uit meerdere atomen bestaan.

Nu we een betrouwbare simulatie methode hadden ontwikkeld konden we gaan kijken met welke experimenten onze simulaties zouden overeenstemmen. Het verrassende antwoord was: "met Gorrington". Het window-effect in de simulaties was zelfs groter dan gevonden in het experiment: een lineair alkaan met een lengte van 12 C-atomen beweegt meer dan 100.000 keer *sneller* dan een lineair alkane met een lengte van 8 C-atomen. Dit terwijl normaal gesproken in een vloeistof een langer molecuul *trager* beweegt dan een kortere door de toegenomen massa. Aangezien we in een simulatie volledige kennis van het systeem hebben konden we precies de oorzaak van dit verschijnsel vinden. ERI-type zeolieten bestaan uit langwerpige kooien aangesloten door nauwere windows. Kleine moleculen zitten vast in deze kooien en hebben moeite er uit komen. Maar zodra moleculen langer beginnen te worden, beginnen ze de imitatie van de kooi te voelen en uiteindelijk willen nog langere moleculen liever over twee kooien verspreid zitten. Het blijkt dat het grootste molecuul wat nog in een kooi past, de snelste diffusie vertoont. Het ondervindt nauwelijks hinder van de structuur, en hoe je het molecuul ook verplaatst, het zit altijd wel even (on)gunstig. We hebben dat eenvoudig kunnen vaststellen door de grote en type van de zeoliet kooien te variëren. Hoewel we het dus in principe eens waren met Gorrington moesten we ook vaststellen dat de lange moleculen waar Chen zijn kraak experimenten mee deed, helemaal niet in het zeoliet willen! Er was dus een alternatieve verklaring nodig, waarom er geen ketens van een bepaalde lengte worden gevonden. Als de moleculen er niet helemaal in gaan, blijft er nog een andere mogelijkheid over: ze gaan er maar gedeeltelijk in. Moleculen adsorberen aan de buitenkant van het zeoliet, en kraken aldaar in stukken.

In hoofdstuk 6, 7 en 8 besteden we aandacht aan het te gebruiken krachtenveld en methoden. Om realistische simulaties te kunnen doen moeten de krachten tussen atomen in het systeem goed en nauwkeurig beschreven worden. Een te nauwkeurige quantummechanische beschrijving resulteert echter weer in onmogelijk lange rekentijden. In deze hoofdstukken ontwikkelen en stellen we zo'n krachtenveld af om zo goed mogelijk ons systeem te beschrijven. De in de literatuur aanwezige krachtenvelden geven kwalitatief andere uitkomsten, bij sommige krachtenvelden stijgt de diffusie als functie van belading, bij andere daalt de diffusie juist voor een molecuul in een gegeven systeem. Het is dus van belang om een krachtenveld te maken dat uniek gedefinieerd is, en de experimentele data goed reproduceert. Experimenteel blijkt het echter moeilijk te zijn om diffusie goed te meten, verschillende experimentele methoden geven ordes van groottes verschil. Het krachtenveld wat wij geïntroduceerd hebben, en beschreven staat in hoofdstuk 6, 7 en 8

is geparameteriseerd met experimentele data van complete isothermen (de belading van een zeoliet als functie van druk). Hierbij blijkt het mogelijk te zijn unieke parameters te vinden door gebruik te maken van isothermen met buigpunten. Buigpunten in een isotherm geven aan dat er verschillende type adsorptie plekken zijn die als functie van druk verschillend opgevuld worden. De fijngevoeligheid van de methode zorgt er voor dat de parameters heel precies bepaald kunnen worden. Het resulterend krachtenveld is superieur aan andere krachtenvelden in de literatuur voor dit soort systemen.

Tot nu toe waren de berekeningen gedaan in de limiet van oneindige verdunning, dus één molecuul in een oneindig groot zeoliet. In de praktijk is de belading meestal veel hoger. De volgende vier hoofdstukken 9, 10, 11 en 12 breiden de methode van hoofdstukken 3, 4 en 5 uit naar belading. Met deze nieuwe methode kan de diffusie van moleculen op een specifieke belading worden berekend in systemen waar diffusie voldoende traag is. Belangrijker dan dat, in tegenstelling tot conventionele methodes die alleen diffusie-getallen kunnen geven, is deze methode in staat ook diffusie-verklaringen te geven. Zo geeft deze methode informatie over de kans dat een molecuul op een bepaalde plaats in een zeoliet zit, alsmede informatie over de grote van diffusie barrières. In hoofdstuk 11 en 12 wordt met deze methode het verschijnsel van "molecular path control" verklaard. Het blijkt dat in ERI-type zeoliet de diffusie niet in alle richtingen gelijk is. Opzienbarend is dat die mate van "anisotropie" aangepast kan worden door de belading te veranderen. Zo diffunderen moleculen op lage belading twee keer sneller zijwaarts dan voorwaarts door het zeoliet, maar op hogere belading is dit juist omgedraaid. Het blijkt dus mogelijk te zijn de beweging van deeltjes op moleculair niveau te controleren, vandaar de term "molecular path control". Hoewel dit resultaat ook met conventionele methodes is geverifieerd, geeft de methode beschreven in hoofdstuk 9, 10 en 12 de verklaring voor dit gedrag. De kooien van ERI-type zeoliet zijn niet rond, maar langwerpig, met adsorptie sites aan beide kanten van de kooi, op lage beladingen. Aan de ene kant van de kooi zitten drie uitgangen, en ook aan de andere kant zitten er drie, met onderlinge hoeken van 120 graden tussen ieder drie uitgangen. Op lage belading wordt de grootste weerstand tegen beweging gevormd door de uitgangen (windows). Als de belading wordt opgevoerd verschuift dat naar het midden van de kooi. Op hogere belading kunnen moleculen dus vrij makkelijk in het vlak gevormd door de drie uitgangen bewegen, maar heel moeilijk van het ene deel van de kooi naar het andere deel van de kooi. De belangrijkste conclusie van het proefschrift is dat de ontwikkelde methode inzicht geeft in waarom diffusie kan stijgen, dalen, of gelijk kan blijven met een verandering in belading. Iets wat tot nu toe voor mensen werkend in dit onderzoeksgebied volslagen duister was.

15

Acknowledgments

- First of all, I would like to thank my thesis advisor Prof. B. Smit for his contributions to this thesis. Thanks for all the freedom you gave me and the trust in my work.
- Second, I would like to thank all people with whom I have collaborated; Sofía Calero, Thijs Vlugt, Edith Beerdsen, Merijn Schenk, Theo Maessen, R. Krishna, R. Blaak, A. Hoekstra, P. Sloot and Drona Kandhai.
- Third, I would like to thank all present and former colleagues of ITS for the very nice time I had in Amsterdam. Special thanks to those colleagues and friends from Berend's group: Abdon *'Wodka-jus'* Pijpelink, Menno *'Bier, bier, bier, tralalalalala!'* Dreischor, Merijn *'13.30'* Schenk, Thijs *'als je na twee keer iets uitleggen nog steeds er voor kiest om het niet te snappen kun je beter bij de MacDonalds gaan werken'* Vlugt, Sofia *'did i mention i HATE the ketchup-song?'* Calero, Jocelyne *'Jocelijn'* Vreede, Emiel *'NCCC-bowlingkampioen 2001'* Hensen, Rini *'Pantera'* Pool, Edith *'Nodes, nodes !! een koninkrijk voor meer nodes'* Beerdsen, Jan-Willem *'Uruk-Hai'* Handgraaf, Titus *'nog een laatste dan'* van Erp, Daniele *'Captain Bertorelli'* Moroni, Evert *'Mr. Gadget'* Koopman, Marieke *'Molsim'* Kranenburg, Sven *'Schwung'* Jakobtorweihen, Jochem *'practical joke'* Wichers Hoeth, Chris *'mag die muziek wat zachter'* Wijmans, Tim *'werkelijk alles zat tegen'* Tambach, Peter *'Bollie'* Bolhuis, Christopher *'de K(r)ater'* Lowe, Evert Jan *'niet aan David en Menno zeggen dat ik weg ga, he? ik trek het bier niet meer'* Meijer, Ranieri *'de bruuut'* Argentini, Arjen *'itsaio-bierspel-koning'* Berkenbos, Live *'Sigh... Abba is not from Norway, Abdon!'/ 'Drinking? before dinner??!!'* Rekvig, Jasper *'ik wou dat ik die roltrap was, dan was Britney tenminste 1 keer over me heengegaan'* Heuft, Jantien *'prrrr blieb tsjoef prrrr'* Bakker, Bastiaan *'als het tempo niet omhoog gaat ben ik weg, dan kan ik net zo goed thuis een fles opentrekken'* Huisman, Vincent *'zo ken ik De Gennes ja'* Ohm, Jarek *'Jus in your wodka? that's disgusting!!'* Juraszek, Christophe *'woohooooo'* Laforge, Jean-Pierre *'i think your job is finished'* Nicolas, Frank *'Franky...'* Peters, Gadi *'Lord Flashheart'* Rothenberg, Gooitzen Zwanenburg, Elske Leenders, Nabil Khalil, Liu Bei, Luca Ghiringhelli, and Maddalena Venturoli. Also thanks to Richard *'always helping the Dutch economy'* Baur, Jeroen *'Big J.'* Jansen, Huub *'Hubertus'* Hoefsloot, Lars *'NCCC'* van der Zande, Dirk *'Wake-up'* Visser, the Feyenoord Hooligans Henk-Jan Ramaker and Eric van Sprang, and all other people at the university.

Thanks to Sofía Calero for a critical reading of this manuscript.

- Finally, I would like to thank my family and friends that are not related to my research for the support during the last few years; especially my parents.

16

Published Work

Title	Boltzmann approximation of transport properties in thermal lattice gases
Author(s)	R. Blaak and D. Dubbeldam
Source	Physical Review E 63 (2): Art. No. 021109 Part 1, Feb 2001
Abstract	The transport properties of the Grosfils, Boon, and Lallemand model, a two-dimensional isotropic thermal lattice-gas, are evaluated in the Boltzmann approximation. This includes the (self)-diffusion, for which we have introduced an additional and passive color label to the otherwise identical particles in the system. Independently, those results are confirmed by the use of the decay of the velocity autocorrelation function. The theoretical predictions of the dynamical structure factors and results obtained by simulations show an excellent agreement up to fairly large wave vectors. In the hydrodynamic limit of small wave vectors, the Landau-Placzek formulas form an alternative and satisfactory description.
Title	Coupling of thermal and mass diffusion in regular binary thermal lattice gases
Author(s)	R. Blaak and D. Dubbeldam
Source	Physical Review E 64 (6): Art. No. 062102 Part 1, Dec 2001
Abstract	We have constructed a regular binary thermal lattice gas model in which the thermal diffusion and mass diffusion are coupled and form two non-propagating diffusive modes. The power spectrum is shown to be similar in structure as for the one in real fluids, in which the central peak becomes a combination of coupled entropy and concentration contributions. Our theoretical findings for the power spectra are confirmed by computer simulations performed on this model.

Title	Regular binary thermal lattice-gases
Author(s)	R. Blaak and D. Dubbeldam
Source	Journal of Statistical Physics 108 (1-2): 283-315 Jul 2002
Abstract	We analyze the power spectrum of a regular binary thermal lattice gas in two dimensions and derive a Landau-Placzek formula, describing the power spectrum in the long-wavelength, low frequency domain, for both the full mixture and a single component in the binary mixture. The theoretical results are compared with simulations performed on this model and show a perfect agreement. The power spectrums are found to be similar in structure as the ones obtained for the continuous theory, in which the central peak is a complicated superposition of entropy and concentration contributions, due to the coupling of the fluctuations in these quantities. Spectra based on the relative difference between both components have in general additional Brillouin peaks as a consequence of the equipartition failure.
Title	Incommensurate diffusion in confined systems
Author(s)	D. Dubbeldam , S. Calero, T. L. M. Maesen, and B. Smit
Source	Physical Review Letters 90 (24): Art. No. 245901 Jun 20 2003
Abstract	Molecular simulations corroborate the existence of the disputed window effect, i.e., an increase in diffusion rate by orders of magnitude when the alkane chain length increases so that the shape of the alkane is no longer commensurate with that of a zeolite cage. This window effect is shown to be characteristic for molecular sieves with pore openings that approach the diameter of the adsorbate. Furthermore, the physical compatibility between the adsorbate and the adsorbent has a direct effect on the heat of adsorption, the Henry coefficients, the activation energy, and the frequency factors.
Title	Understanding the window effect in zeolite catalysis
Author(s)	D. Dubbeldam , S. Calero, T. L. M. Maesen, and B. Smit
Source	Angewandte Chemie-International Edition 42 (31): 3624-3626 2003
Abstract (provided by Ange- wandte Chemie)	When adsorbates are similar in size to zeolite channels then the surface pores of zeolites only adsorb part of the adsorbate molecule. The not adsorbed section can be cleaved to react further or adsorb elsewhere. The window effect can be examined with the aid of Monte Carlo simulations. For more information see the following communication by D. Dubbeldam et al.

Title	Computer simulation of incommensurate diffusion in zeolites: Understanding window effects
Author(s)	D. Dubbeldam and B. Smit
Source	Journal of Physical Chemistry B 107 (44): 12138-12152 Nov 6 2003
Abstract	Dedicated molecular simulation techniques afford the study of the abnormal adsorption and diffusion of linear alkanes in ERI-, CHA-, and LTA-type zeolites. The exceptionally slow diffusion rates required the development of a combination of rare-event transition-state theory techniques and the configurational-bias Monte Carlo algorithm. The diffusion coefficients computed by this novel method agree well with the nondisputed rates determined experimentally for LTA-type sieves. The computed rates corroborate the nonmonotonic variation of the diffusion rate with alkane chain length published by Goring, that is, the rate increases by orders of magnitude when the molecular and cage shape are no longer commensurate, so a molecule ends up stretched across a cage tethered at opposite windows. The simulations corroborate this "window effect" for both ERI- and CHA-type sieves and suggest that it is characteristic for all sieves with windows approximately 0.4 nm across. They predict that it also occurs for LTA-type sieves provided that the <i>n</i> -alkane is long enough to exceed the diameter of the LTA-type supercage.
Title	Simulating the effect of nonframework cations on the adsorption of alkanes in MFI-type zeolites
Author(s)	E. Beerdsen, D. Dubbeldam , B. Smit, T. J. H. Vlucht, and S. Calero
Source	Journal of Physical Chemistry B 107 (44): 12088-12096 Nov 6 2003
Abstract	We performed configurational-bias Monte Carlo (CBMC) simulations for the adsorption of methane, ethane, propane, butane, and isobutane in MFI-type zeolites with different concentration and nature of nonframework cations. Additional molecular simulations for a mixture of butane/isobutane in these MFI-type zeolites were carried out. The effect of the content-density and nature-of nonframework cations was systematically analyzed, and our results show that even though all of the MFI-type zeolites are structurally similar, differences in the size and concentration of the nonframework cations lead to differences in their adsorptive properties and selectivity performance. For a given cation, the adsorption of alkanes in MFI increases with decreasing the nonframework cation concentration, and for a given Si/Al ratio, the adsorption of alkanes in MFI increases with decreasing atomic weight of the nonframework cation.

Title	United atom force field for alkanes in nanoporous materials
Author(s)	D. Dubbeldam , S. Calero, T. J. H. Vlugt, R. Krishna, T. L. M. Maesen, and B. Smit
Source	Journal of Physical Chemistry B 108 (33): 12301-12313 Aug 19 2004
Abstract	A novel united atom force field affords accurate and quantitative reproduction of the adsorption properties of linear and branched alkanes in nanoporous framework structures. The force field was generated by adjusting the parameters so as to faithfully reproduce the experimentally determined isotherms (particularly the inflection points) on MFI-type zeolite over a wide range of pressures and temperatures. It reproduces extremely well the Henry coefficients, heats of adsorption, preexponential factors, entropies of adsorption, and maximum loading. It is shown that the extension of the force field from MFI to other nanoporous framework topologies is successful, that it affords the prediction of topology-specific adsorption properties, and that it can be an effective tool to resolve the many discrepancies among experimental data sets.
Title	Force Field Parameterization through Fitting on Inflection Points in Isotherms
Author(s)	D. Dubbeldam , S. Calero, T. J. H. Vlugt, R. Krishna, T. L. M. Maesen, E. Beerdsen, and B. Smit
Source	Physical Review Letters 93 (8): Art. No. 088302 Aug 20 2004
Abstract	We present a method to determine potential parameters in molecular simulations of confined systems through fitting on experimental isotherms with inflection points. The procedure uniquely determines the adsorbent-adsorbate interaction parameters and is very sensitive to the size parameter. The inflection points in the isotherms are often related to a subtle interplay between different adsorption sites. If a force field can predict this interplay, it also reproduces the remaining part of the isotherm correctly, i.e., the Henry coefficients and saturation loadings.

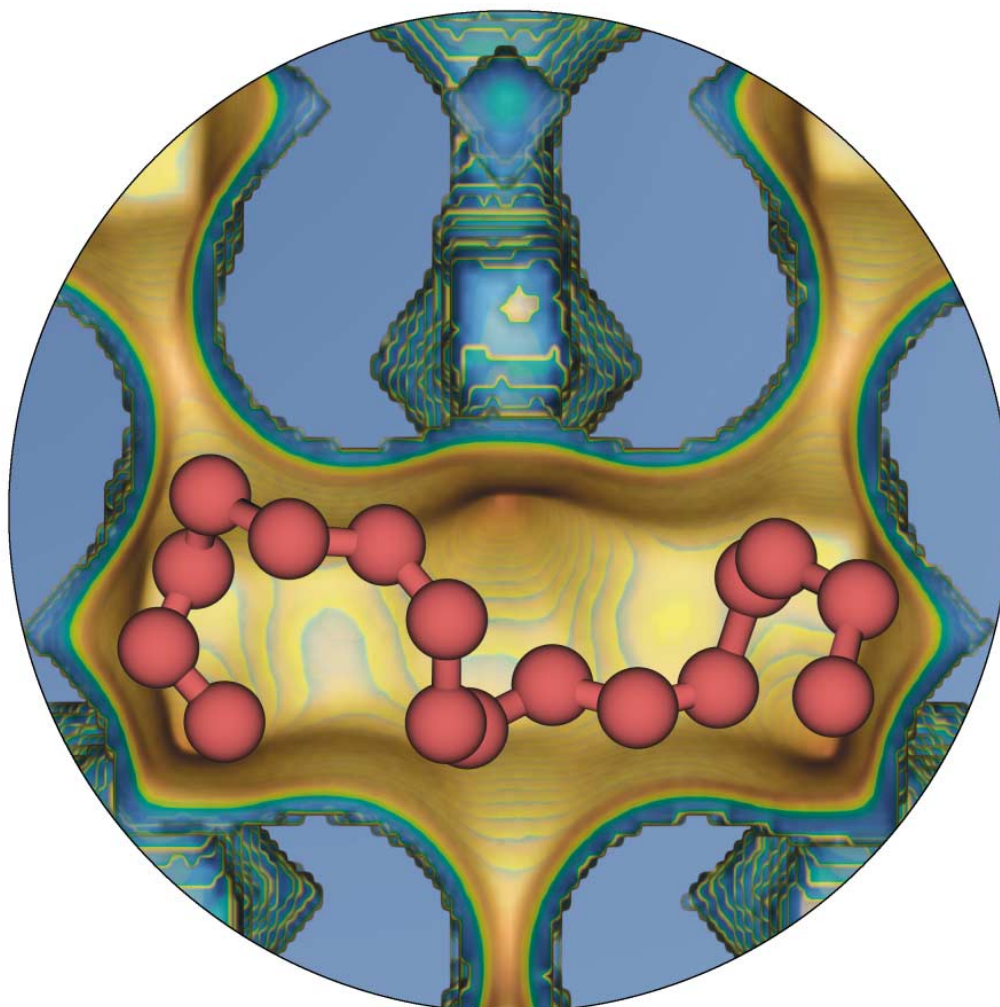
Title	Understanding the Role of Sodium during Adsorption: A Force Field for Alkanes in Sodium-Exchanged Faujasites
Author(s)	S. Calero, D. Dubbeldam , R. Krishna, B. Smit, T. J. H. Vlugt, J. F. M. Denayer, J. A. Martens, and T. L. M. Maesen
Source	Journal of the American Chemical Society 126 (36): 11377-11386 Aug 19 2004
Abstract	We have developed a united atom force field able to accurately describe the adsorption properties of linear alkanes in the sodium form of FAU-type zeolites. This force field successfully reproduces experimental adsorption properties of <i>n</i> -alkanes over a wide range of sodium cation densities, temperatures, and pressures. The force field reproduces the sodium positions in dehydrated FAU-type zeolites known from crystallography, and it predicts how the sodium cations redistribute when <i>n</i> -alkanes adsorb. The cations in the sodalite cages are significantly more sensitive to the <i>n</i> -alkane loading than those in the supercages. We provide a simple expression that adequately describes the <i>n</i> -alkane Henry coefficient and adsorption enthalpy as a function of sodium density and temperature at low coverage. This expression affords an adequate substitute for complex configurational-bias Monte Carlo simulations. The applicability of the force field is by no means limited to low pressure and pure adsorbates, for it also successfully reproduces the adsorption from binary mixtures at high pressure.
Title	Reply to the Comment on "Computer Simulation of Incommensurate Diffusion in Zeolites: Understanding Window Effects"
Author(s)	D. Dubbeldam , T. L. M. Maesen, and B. Smit
Source	Journal of Physical Chemistry B 108 (41): 16330-16330 Oct 14 2004
Title	On the Inflection in the Concentration Dependence of the Maxwell-Stefan Diffusivity of CF ₄ in MFI Zeolite
Author(s)	R. Krishna, J. M. van Baten, and D. Dubbeldam
Source	Journal of Physical Chemistry B 108 (39): 14820-14822 Sep 30 2004
Abstract	The recently published data on the Maxwell-Stefan diffusivity \mathcal{D} of CF ₄ in MFI zeolite (J. Phys. Chem. B 2004, 108, 10613) shows an inflection at a loading $\Theta = 12$ molecules per unit cell, corresponding to the inflection in the adsorption isotherm. We investigate the underlying reasons by performing kinetic Monte Carlo simulations and show that at $\Theta = 12$, the molecular traffic along the zigzag channels comes to a virtual stand-still and further transport occurs only along the straight channels of MFI. The inflection behavior of \mathcal{D} is likely to be a generic characteristic of transport in nanoporous materials in which the adsorption of the diffusant occurs on multiple sites with widely different strengths.

Title	Molecular Simulation of Loading Dependent Slow Diffusion in Confined Systems
Author(s)	E. Beerdsen, B. Smit, and D. Dubbeldam
Source	Physical Review Letters 93 (24): Art. No. 248301 Dec 10 2004
Abstract	A Transition State Theory method is presented that is capable of computing quantitatively the diffusivity of adsorbed molecules in confined systems at non-zero loading. This extension to traditional Transition State Theory is free of additional assumptions and yields a diffusivity identical to that obtained by conventional Molecular Dynamics simulations. While Molecular Dynamics calculations are limited to relatively fast diffusing molecules or small rigid molecules, our approach extends the range of accessible times scales significantly beyond currently available methods. It is applicable in any system containing free energy barriers and for any type of guest molecule.
Title	The selectivity of <i>n</i> -hexane hydroconversion on MOR-, MAZ-, and FAU-type zeolites
Author(s)	S. Calero, M. Schenk, D. Dubbeldam , T. L. M. Maesen, and B. Smit
Source	Journal of Catalysis 228(1): 121-129 15 Nov 2004
Abstract	Analyses of a series of published <i>n</i> -hexane hydroisomerization product slates suggest that MAZ-type zeolites yield more dimethylbutane and less methylpentane than either FAU- or MOR-type zeolites. Molecular simulations do not corroborate the traditional view that these selectivity differences are specifically related to the MAZ-, FAU-, or MOR- type zeolite topology. A scrutiny of the literature indicates that reported variation in selectivity relates to a variation in the efficiency of the (de)hydrogenation function relative to the acid function. The FAU-type zeolite catalyst had the most efficient hydrogenation function. The efficiency of the hydrogenation function on the MAZ-type zeolite was low enough to significantly enhance the 2,3-dimethylbutane yield relative to the methylpentane yield, but not low enough to decrease the 2,2-dimethylbutane yield. The efficiency of the hydrogenation function on the MOR-type zeolite was low enough to do both. Only at a sufficiently high <i>n</i> -hexane hydroconversion does the catalyst with the most efficient hydrogenation function exhibit the highest dimethylbutane yield. This new perspective on the reported hexane hydroconversion selectivities suggests that a FAU-type zeolite catalyst with a highly efficient hydrogenation function is best suited for <i>n</i> -hexane hydroisomerization. The FAU topology has the highest porosity which should afford the highest activity without impairing selectivity.

Title	Elucidating alkane adsorption in sodium exchanged zeolites from molecular simulations to empirical equations
Authors(s)	E. García-Pérez, I. M. Torréns, S. Lago, D. Dubbeldam , T. J. H. Vlugt, T. L. M. Maesen, B. Smit, R. Krishna, and S. Calero
Source	Applied Surface Science (accepted)
Abstract	Configurational-Bias Monte Carlo (CBMC) simulations provide adsorption isotherms, Henry coefficients and heats of adsorption of linear alkanes in sodium exchanged MFI- and FAU-type zeolites. These simulations were carried out using our newly developed force field that reproduces experimental sodium positions in the dehydrated zeolites, and successfully predicts alkane adsorption properties over a wide range of sodium cation densities, temperatures, and pressures. We derived empirical expressions from the simulation data to describe the adsorption of linear alkanes in MFI- and FAU-type zeolites. These expressions afford a suitable substitute for complex CBMC simulations. In the low coverage regime we provide simple expressions that adequately describe the Henry coefficient and adsorption enthalpy of <i>n</i> -alkanes as a function of sodium density and temperature. The predicted Henry coefficients and heats of adsorption compare extremely well to available experimental data. In the high coverage regime we provide an expression for saturation capacities of linear alkanes in the zeolite. This expression, combined with the expression for the Henry coefficients, gives a direct estimation of the complete adsorption isotherms of pure adsorbents and mixtures, in good agreement with the adsorption isotherms obtained from CBMC.
Title	Molecular Simulation of Loading Dependent Diffusion in Nanoporous Materials using Extended Dynamically Corrected Transition State Theory
Authors(s)	D. Dubbeldam , E. Beerdsen, T. J. H. Vlugt, and B. Smit
Source	Journal of Chemical Physics 122: 224712 2005
Abstract	A dynamically corrected Transition State Theory method is presented that is capable of computing quantitatively the self-diffusivity of adsorbed molecules in confined systems at non-zero loading. This extension to traditional Transition State Theory is free of additional assumptions and yields a diffusivity identical to that obtained by conventional Molecular Dynamics simulations. While Molecular Dynamics calculations are limited to relatively fast diffusing molecules, our approach extends the range of accessible times scales significantly beyond currently available methods. We show results for methane, ethane, and propane in LTL- and LTA-type zeolites over a wide range of temperatures and loadings, and demonstrate the extensibility of the method to mixtures.

Title	Molecular Path Control in Zeolite Membranes
Authors(s)	D. Dubbeldam , E. Beerdsen, S. Calero, and B. Smit
Source	Proc. Natl. Acad. Sci. U.S.A. 102 (35): 12317-12320, Aug 2005
Abstract	We report molecular simulations of diffusion in confinement showing a phenomenon which we denote as Molecular Path Control (MPC); depending on loading, molecules follow a preferred pathway. MPC raises the important question to which extent the loading may affect the molecular trajectories in nanoporous materials. Through MPC one is able to manually adjust the ratio of the diffusivities through different types of pores, and as an application one can direct the flow of diffusing particles in membranes forward or sideward by simply adjusting the pressure, without the need for mechanical parts like valves. We show that the key ingredient of MPC is the anisotropic nature of the nanoporous material which results in a complex interplay between different diffusion paths as a function of loading. These paths may be controlled by changing the loading, either through a change in pressure or temperature.
Title	Applying Dynamically Corrected Transition State Theory in Complex geometries
Authors(s)	D. Dubbeldam , E. Beerdsen, S. Calero, and B. Smit
Source	Submitted
Abstract	We apply the dynamically corrected Transition State Theory to confinements with complex structures. This method is able to compute self-diffusion coefficients for adsorbate-adsorbent system far beyond the timescale accessible to Molecular Dynamics. Two exemplary cage/window-type confinements are examined: ERI- and CHA-type zeolites. In ERI-type zeolite each hop in the z direction is preceded by an hop in xy -direction, and diffusion is anisotropic. We show that the crystallographic symmetries (monoclinic and trigonal, respectively) can be exploited to simplify the description of the hopping mechanism. The free energy profiles are more easily evaluated in fractional, dimensionless space. The lattice for CHA-type zeolite is a rhombohedral Bravais lattice, and diffusion is anisotropic, albeit only slightly, but the orientational averaged diffusion coefficient is unaffected compared to a cubic lattice. The anisotropical behavior of ERI-type cages reverse with loading, i.e. at low loading the diffusion in the z -direction is two times faster than in the xy -direction, while for higher loadings this changes to a z -diffusivity that is more than two times slower. At low loading the diffusion is impeded by the eight-ring windows, i.e. the exits out of the cage to the next, but at higher loadings the barrier is formed by the center of the cages.

Communications



When adsorbates are similar in size to zeolite channels then the surface pores of zeolites only adsorb part of the adsorbate molecule. The not adsorbed section can be cleaved to react further or adsorb elsewhere. This window effect can be examined with the aid of Monte Carlo simulations. For more information see the following Communication by D. Dubbeldam et al.

